

**ISSN: 2249-6645**

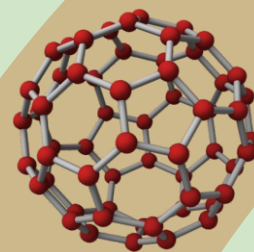


# **International Journal of Modern Engineering Research (IJMER)**

Volume 4

Issue 9

September 2014





# International Journal of Modern Engineering Research (IJMER)

Volume : 4 Issue : 9 (Version-1)

ISSN : 2249-6645

September- 2014

## Contents :

<b>Design and Impact Analysis of a Car Door</b> <i>M. Raghuveer, Ganti Satya Prakash</i>	01-08
<b>Improved Kalman Filtered Neuro-Fuzzy Wind Speed Predictor For Real Data Set Collected At Egyptian North-Western Coast</b> <i>Mohamed I. Awaad<sup>1</sup>, Omar M. Salim, Ossama E. Gouda, Ebtisam M. Saied</i>	09-18
<b>Helicopter Flapping Under Dynamic Stall</b> <i>Jibin Babu, Blesson Joseph Thomas</i>	19-26
<b>Noval Method for Fabrication of 3-D Spacer Fabric Composite and Investigation of Mechanical Property</b> <i>A. Vivek Anand, G. Venkatesh, P. Anand</i>	27-31
<b>Optimization of cutting tool material in lathe machine by T-test</b> <i>Ivan Sunit Rout, Sidhartha Sankar Padhi, Jitendra Narayan Biswal, Tushar Kanti Panda</i>	32-36
<b>Performance Analysis of 4 Stroke Single Cylinder Diesel Engine Using Blend Of Soya Oil with Diesel</b> <i>Prof. C. S. Koli, Arvind Pathak, Prof. Sanjay Bhatele</i>	37-49
<b>Optimization of Machining Parameters of 20MnCr5 Steel in Turning Operation using Taguchi technique</b> <i>Narayana Reddy. A R, Ganti satya prakash</i>	50-60
<b>Stress Analysis of Precast Prestressed Concrete Beams during Lifting</b> <i>V. M. Gaykar, J. G. Solanki</i>	61-68
<b>Performance and Emissions Analysis Using Diesel and Tsome Blends</b> <i>Nirmal kumar. R, Sarathbabu. R. T</i>	69-80
<b>Case Study of MHD Generator for Power Generation and High Speed Propulsion</b> <i>Md Akhtar khan, Kavya vaddadi, Avinash gupta, karrothu vigneshwara</i>	81-90
<b>Bit Error Rate Analysis in WiMAX Communication at Vehicular Speeds using modified Nakagami-m Fading Model</b> <i>Manjeet Singh, Dr. Jyotsna Sengupta</i>	91-95

## Design and Impact Analysis of a Car Door

M. Raghuv<sup>1</sup>, Ganti Satya Prakash<sup>2</sup>

<sup>1</sup>M.Tech student, Dept of Mech. Engg, CMR Institute of Technology, Hyderabad, IN

<sup>2</sup>Asst. prof, Dept of Mech. Engg, CMR Institute of Technology, Hyderabad, IN

**Abstract:** Car door is one of the main parts which are used as protection for passengers from side collisions. Presently steel is used for car doors construction. The aim of the project is to analyze the car door with presently used material steel and replacing with composite materials like Aluminum, Carbon Epoxy, S-glass epoxy, E-Glass epoxy. Impact analysis is conducted on door for different speeds by varying the materials. Best of the result we will consider for the door design. Also we are going to reduce weight of the door by using composite materials replacing with steel. By this we have to reduce the damage percentage of the car and passenger protection. In this project, the Car door is modeled using parametric modeling software Pro/Engineer. Pro/ENGINEER is the standard in 3D product design, featuring industry-leading productivity tools that promote best practices in design. We have to variety the materials of the car door and speed to impacting of door.

**Keywords:** We are doing impact analysis in the software COSMOS (SOLID WORKS).

### I. Introduction

The A vehicle door is a type of door, typically hinged, but sometimes attached by other mechanisms such as tracks, in front of an opening which is used for entering and exiting a vehicle. A vehicle door can be opened to provide access to the opening, or closed to secure it. These doors can be opened manually, or powered electronically. Powered doors are usually found on minivans, high-end cars, or modified cars. Unlike other types of doors, the exterior side of the vehicle door contrasts sharply from its interior side (the interior side is also known as the car door panel): The exterior side of the door is designed of steel like the rest of the vehicle's exterior. In addition, its decorative appearance, typically colored with a design, is intended to match with the rest of the vehicle's exterior, the central purpose being to add to the overall aesthetic appeal of the vehicle exterior.

On the other hand, the vehicle door's interior side is typically made up of a variety of materials, sometimes vinyl and leather, other time's cloth and fabric. Because the car door panel is typically intended to match the rest of the styles used in the car's interior, the choice of cover materials depends on the rest of the styles used in the vehicle's inner body like the dashboard, carpet, seats, etc. However, unlike the material used on the exterior side of the vehicle door, the material on the interior side serves a greater purpose other than just aesthetic appeal. While the materials that makes up the interior side are intended to match their surroundings and contribute to the overall aesthetic appeal, there's an additional purpose of coziness and comfort. This is to say, a car door panel has interior parts that contribute to the overall functionality and ergonomics of the ride, such as: armrests; various switches; lights; electronic systems like the window controls and locking mechanism; etc.

### II. Literature Review

Previous studies by different researches show that the efficient design and increase use of composite materials into the automotive parts directly influences the car safety, weight reduction and gas emission, because the efficient design can absorb more deformation and composite materials have high specific strength (strength to density) and high specific stiffness (stiffness/density). They also have very high impact load absorbing and damping properties.

The side impact door should have the ability to absorb as much deformational energy as possible without breaking. Steel is still the most widely used material for beam members, but the steel increases the total weight of the car. However, breakthroughs in the application of lighter materials, such as composite, are being initiated in the automotive industry. Correct fiber orientation and stacking sequence of the cross-ply laminate contribute to higher energy absorption when compared to steel equivalent.

The composite materials have high specific energy absorption when compared to steel. The properties like high specific strength and high specific stiffness are attractive for the construction of lightweight and fuel

efficient vehicle structures. The energy absorption capability of the composite materials offers a unique combination of reduced weight and improves crashworthiness of the vehicle structures. Fuel efficiency of the vehicle directly depends on the weight of the vehicle. The carbon fiber composite body structure is 57% lighter than steel structure of the same size and providing the superior crash protection, improved stiffness and favorable thermal and acoustic properties. The composite materials are replacing most of the steel structures. Rotors manufactured using RTM (Resin Transfer Molding) for air compressor or superchargers of cars are used to substitute for metal rotors which are hard to manufacture. The composite material was for the first time introduced to the formula-1 in 1980 by McLaren team. Since then the crashworthiness of the racing cars has improved beyond all recognition. They used the carbon fiber composite to manufacture the body, which is low weight, high rigidity and provided the high crash safety standards. The lightweight composite materials are already finding the exciting break in the automotive field as a means to increase the fuel efficiency. The vehicle weight directly contributes about 75 percent of fuel consumption. The vehicle industry can anticipate an aggressive 6 to 8 percent reduction in fuel consumption with 10 percent decrease in vehicle weight. This reduces around 20 kilogram of carbon dioxide emission per kilogram reduction in weight over the vehicle's lifetime. The report from the united states and Canada predicted that plastics and composites would be widely used applied to body panels, bumper systems, flexible components, trims, drive shaft and transport parts of cars. Also rotors manufactured using RTM (Resin Transfer Moldings) for air compressor or superchargers of cars have been used to substitute for metal rotors which are difficult to machine. Composites have been used to substitute flexi spline materials in harmonic drives.

### III. Modeling Of Car Door

#### The specification of DOOR for CAR below

The software used for Modelling of car door is Pro-E and software it is developed by **Parametric Technology Corporation**

This is CAD/CAM/CAE software but we are using this for only 3-D part modelling (CAD).

This CAD includes.

1. Sketcher
2. Part modelling (part design)
3. Surface Design
4. Assembly Design
5. Drafting

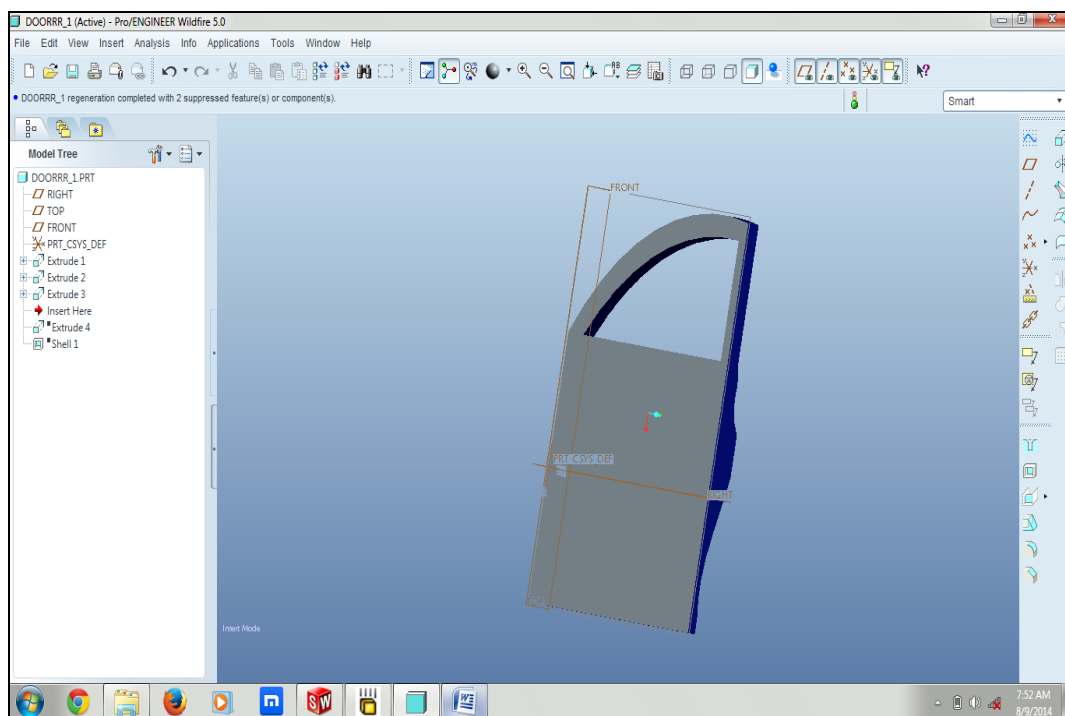


**Figure 1:** 3-D model of Car Door using Solid works-Design 1-Original

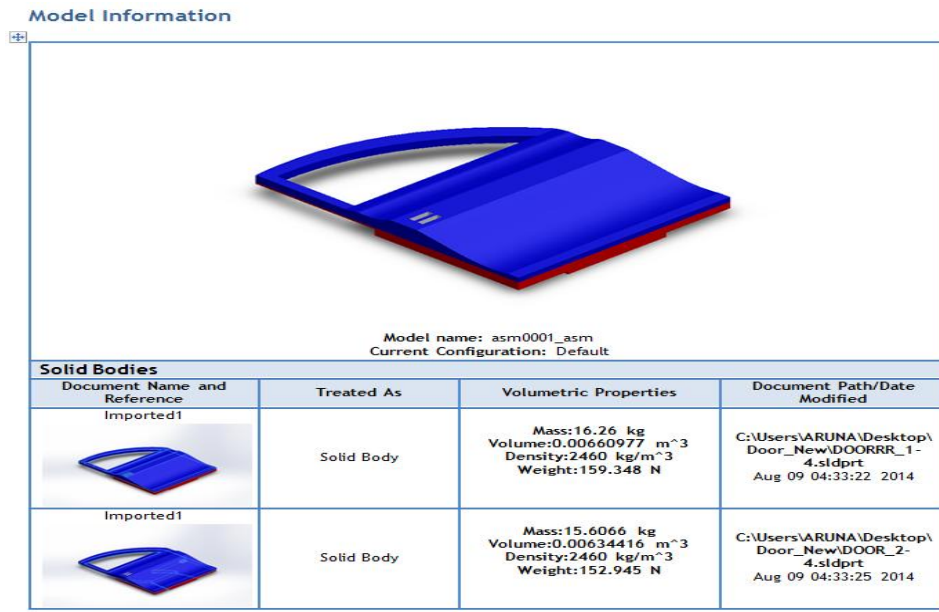


Figure 2: 3-D model information of Car Door with mass 16.26Kg

#### IV. Meshing Of Car Door

The Figure.3 shows the meshed model of door. The Discretization (Mesh generation) is the first step of Finite Element Method. In this step the component or part is divided into number of small parts. In discretization the no of elements are 9095, and 7688 nodes. The effect of force on each portion of the component is not same. The purpose of discretization is to perform the analysis on each small division separately

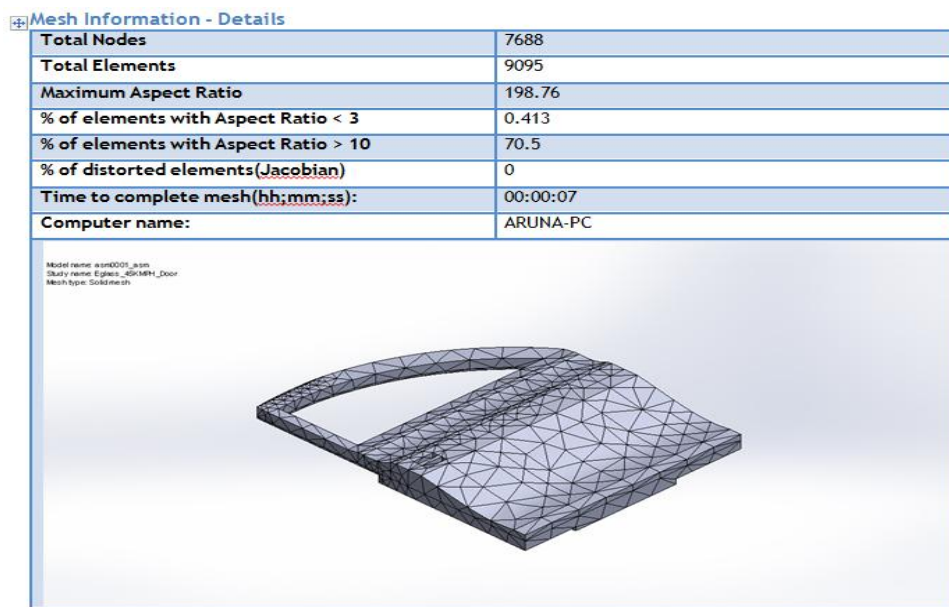


Figure 3: 3-D Meshing model information of Car Door

The Figure.4,5,6: shows the study model of door. After the application of boundary conditions and force, the next step is to perform the structural analysis of door. In this structural analysis, we are mainly concern with the total deformation and the stresses acting on the door (von-misses stresses). When the force is applied, the slight deformation and also the stresses take place in the crankshaft. The total deformation of crankshaft is shown in Figure.4. The deformation in the door is not same throughout. The portion in red color shows that the deformation at that region is maximum and the portion in blue color shows that the deformation is minimum in that region.

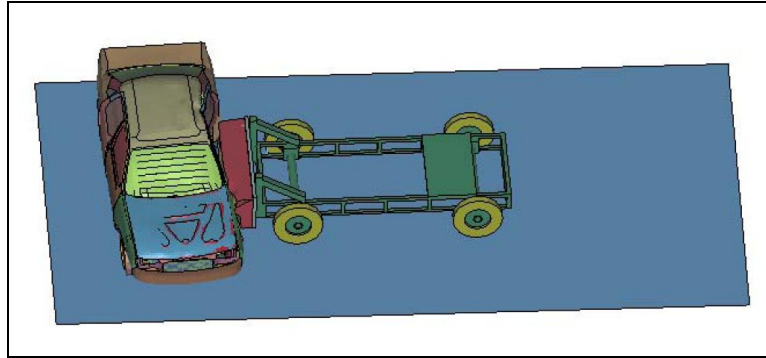


Figure 4: 3-D model stress study of Car Door

### V. Study Stress Of Car Door

#### Study Results

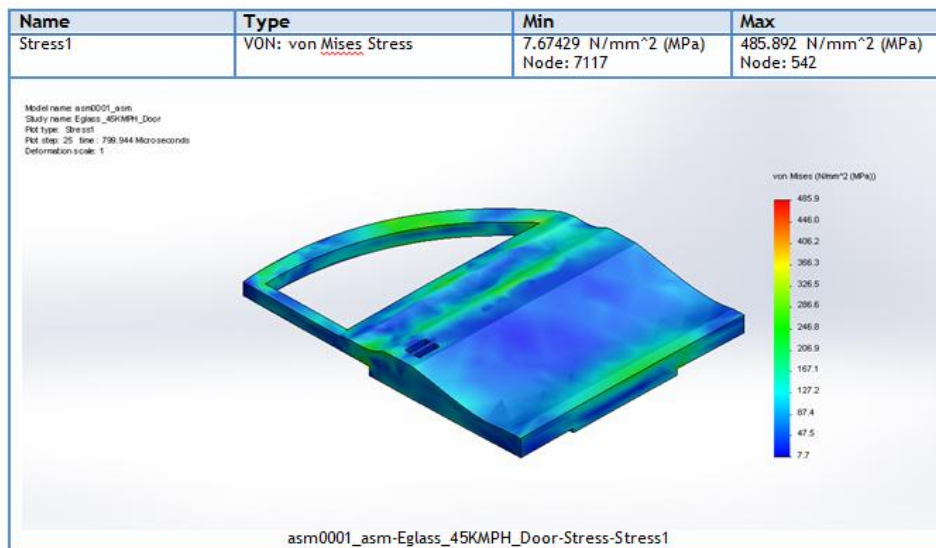


Figure 5: 3-D model stress study of Car Door Min 7.674 & Max 485.49(Mpa)

### VI. Displacement Stress Of Car Door

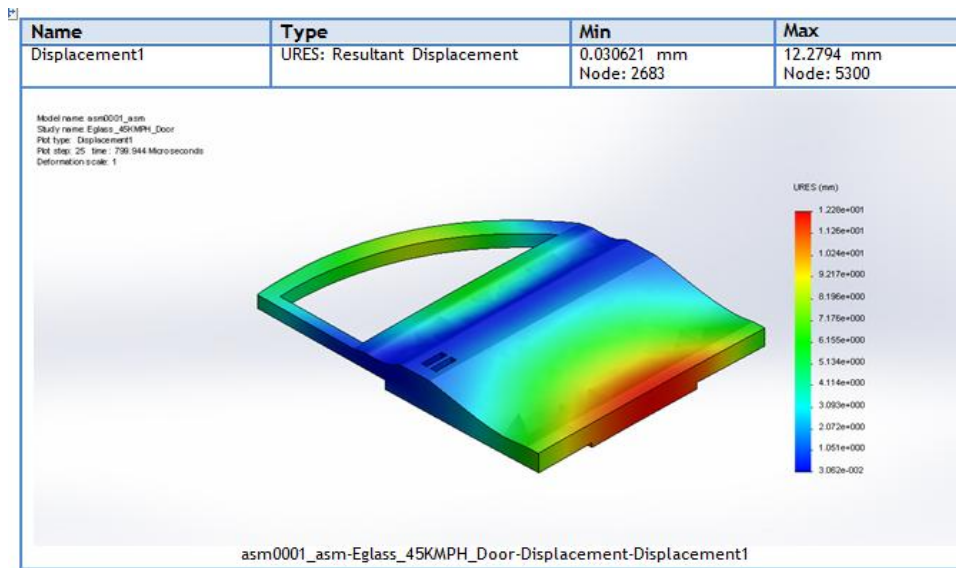


Figure 6: 3-D model Displacement study of Car Door Min 0.030 & 12.27(Mpa)

VII. Displacement Stress Of Car Door

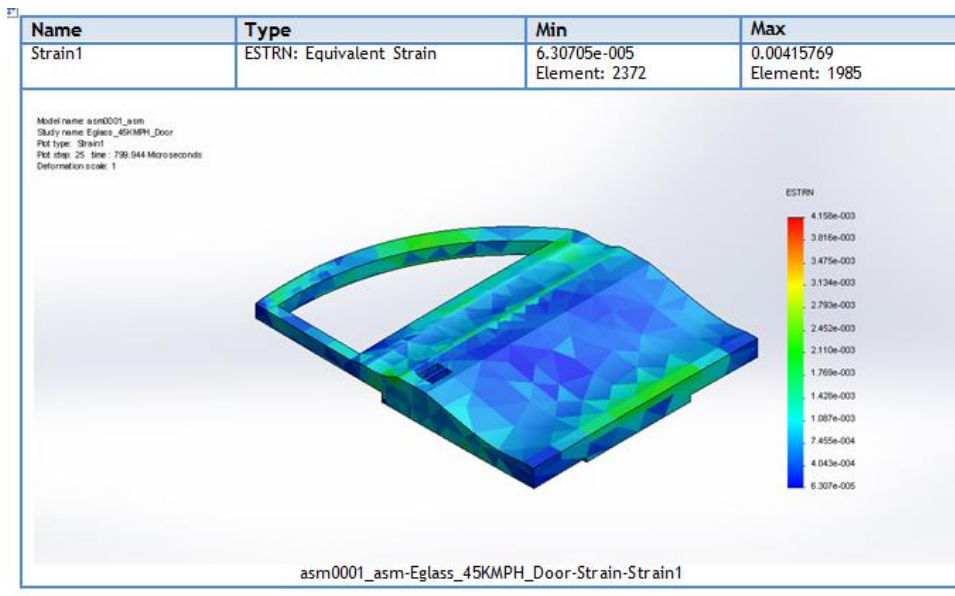


Figure 7: 3-D model strain study of Car Door Min 6.307 & Max 0.0041(Mpa)

The stress acting on the Design1Original door is shown in Figure.5, 6, and 7.

VIII. FIGURES AND TABLES

After applying loading and boundary conditions results from Solid works were obtained and compiled in table

Eglass Epoxy:

Speed	Stress		Displacement		Strain	
Material (Eglass Epoxy)	Stress Min( $\sigma$ )MPa	Stress Min ( $\sigma$ )MPa	Displacement Min Mm	Displacement Minm	Strain(min)	Strain(max)
45	7.66411 N/mm <sup>2</sup>	486.55 N/mm <sup>2</sup>	0.0414237 mm	12.0775 mm	8.54216e-005	0.00470882
60	10.5646 N/mm <sup>2</sup>	707.566 N/mm <sup>2</sup>	0.110908 mm	18.0986 mm	0.000103121	0.00665921
80	5.94308 N/mm <sup>2</sup>	1059.51 N/mm <sup>2</sup>	0.152936 mm	24.6295 mm	0.000101913	0.00883602
100	15.7078 N/mm <sup>2</sup>	1348.39 N/mm <sup>2</sup>	0.267476 mm	31.2923 mm	0.000149278	0.0109856

Table1: Results obtained from SOLID WORKS

Sglass Epoxy:

Speed	Stress		Displacement		Strain	
Material (Sglass Epoxy)	Stress Min ( $\sigma$ )MPa	Stress Min ( $\sigma$ )MPa	Displacement Min Mm	Displacement Min m	Strain(min)	Strain(max)
45	7.67429 N/mm <sup>2</sup>	485.892 N/mm <sup>2</sup>	0.030621m	12.2794 mm	6.30705e-005	0.00415769
60	11.5391N/mm <sup>2</sup>	610.998 N/mm <sup>2</sup>	0.0398429m	18.3876 mm	5.34882e-005	0.00484095
80	11.2458 N/mm <sup>2</sup>	886.518N /mm <sup>2</sup>	0.152936m	24.6295 mm	0.000101913	0.00883602
100	10.1045 N/mm <sup>2</sup>	1114.93N /mm <sup>2</sup>	0.11594mm	30.9996 mm	7.59825e-005	0.00992091

Table1: Results obtained from SOLID WORKS

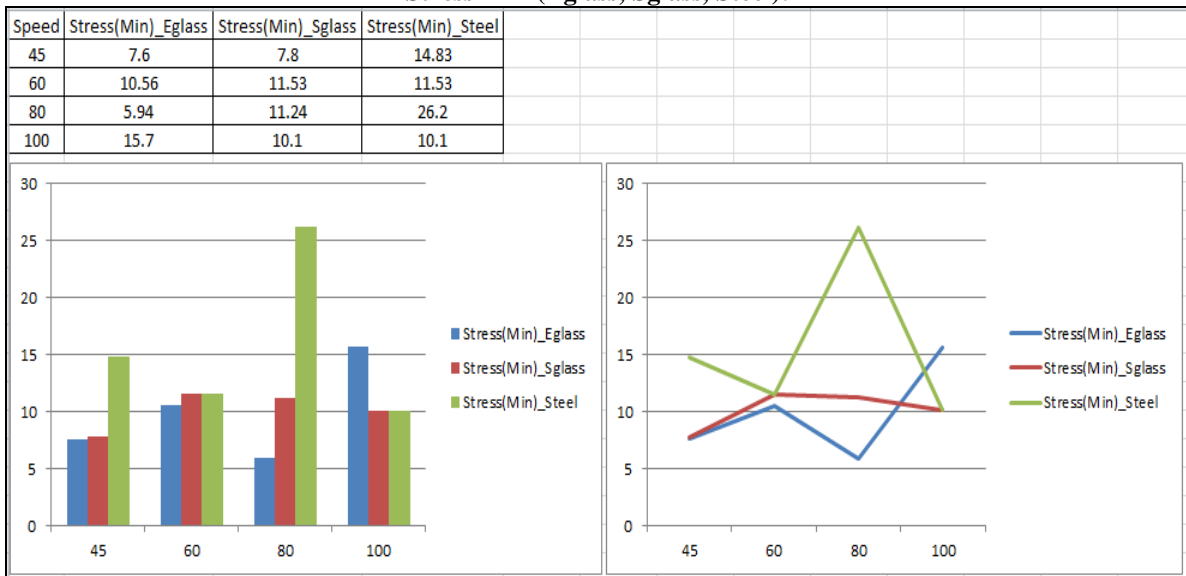
**Steel Epoxy:**

Speed	Stress		Displacement		Strain	
Material (Steel)	Stress Min (σ)MPa	Stress Min (σ)MPa	Displacement Min Mm	Displacement Min m	Strain(min)	Strain(max)
45	14.8305N/mm <sup>2</sup>	1922.55 N/mm <sup>2</sup>	0.0185283 mm	11.2098 mm	3.86505e-005	0.0059074
60	11.5391N/mm <sup>2</sup>	610.998 N/mm <sup>2</sup>	0.0398429m	18.3876 mm	5.34882e-005	0.00484095
80	26.2071 N/mm <sup>2</sup>	3092.92 N/mm <sup>2</sup>	0.0283487 mm	22.4748 mm	4.94524e-005	0.00971505
100	10.1045 N/mm <sup>2</sup>	1114.93 N/mm <sup>2</sup>	0.11594mm	28.982 mm	7.59825e-005	0.00992091

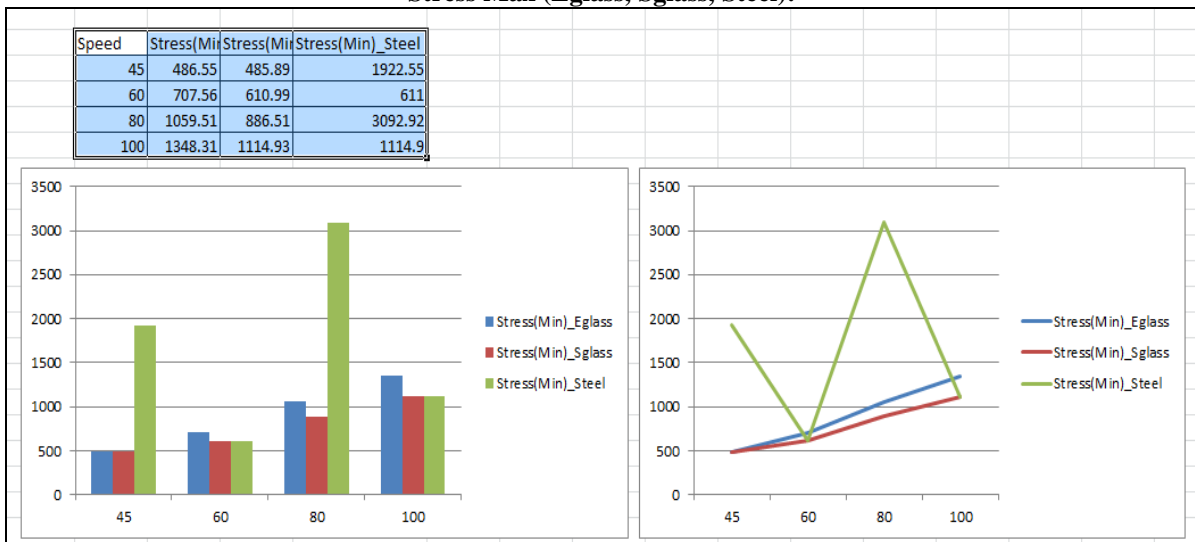
**Table1:** Results obtained from SOLID WORKS

**GRAPHS:**

**Stress Min (Eglass, Sglass, Steel):**

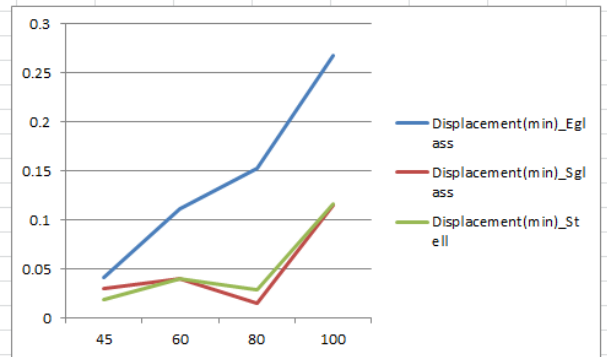
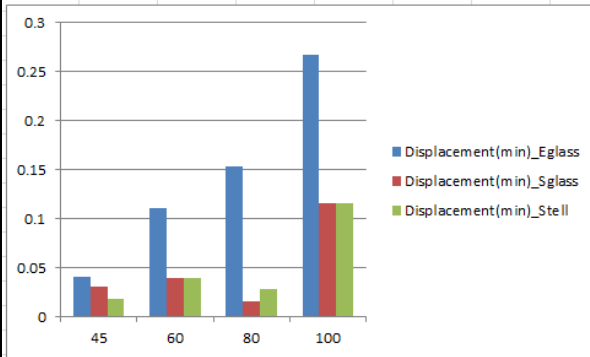


**Stress Max (Eglass, Sglass, Steel):**



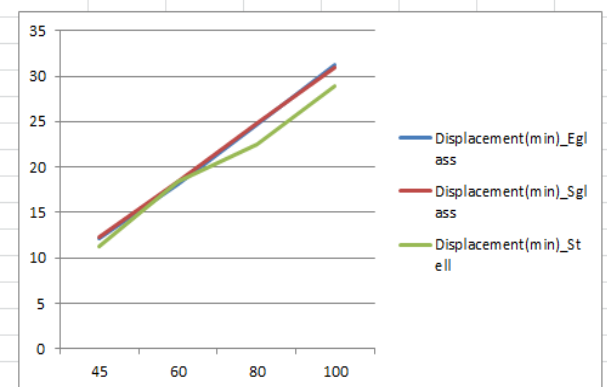
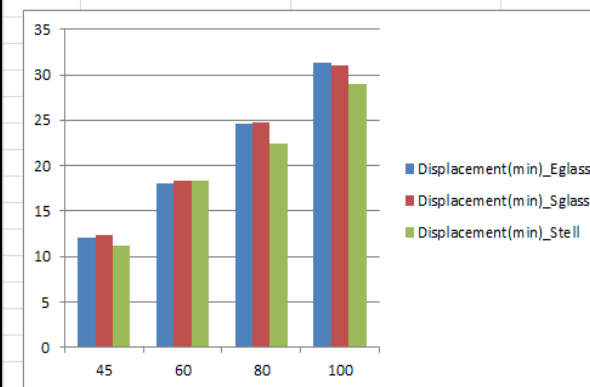
**Displacement Min(Eglass, Sglass, Steel):**

Speed	Displacement	Displacement	Displacement(min)_Stell
45	0.0414	0.0306	0.0183
60	0.1109	0.0398	0.0398
80	0.1529	0.0152	0.0283
100	0.2674	0.1154	0.1159



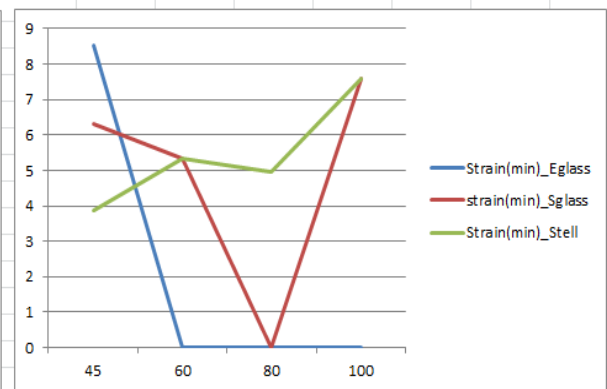
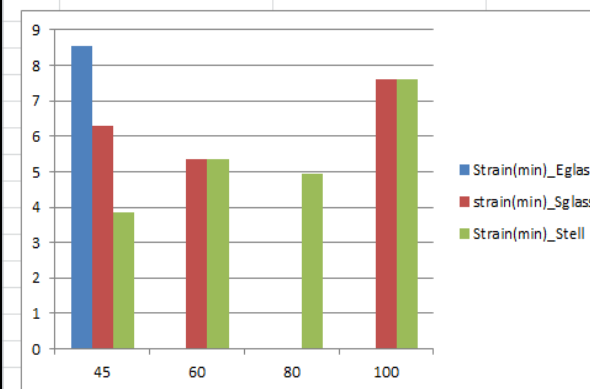
**Displacement Max(Eglass, Sglass, Steel):**

Speed	Displacement(min)_Eglass	Displacement(min)_Sglass	Displacement(min)_Stell
45	12.077	12.279	11.209
60	18.098	18.387	18.387
80	24.629	24.762	22.474
100	31.292	30.999	28.982

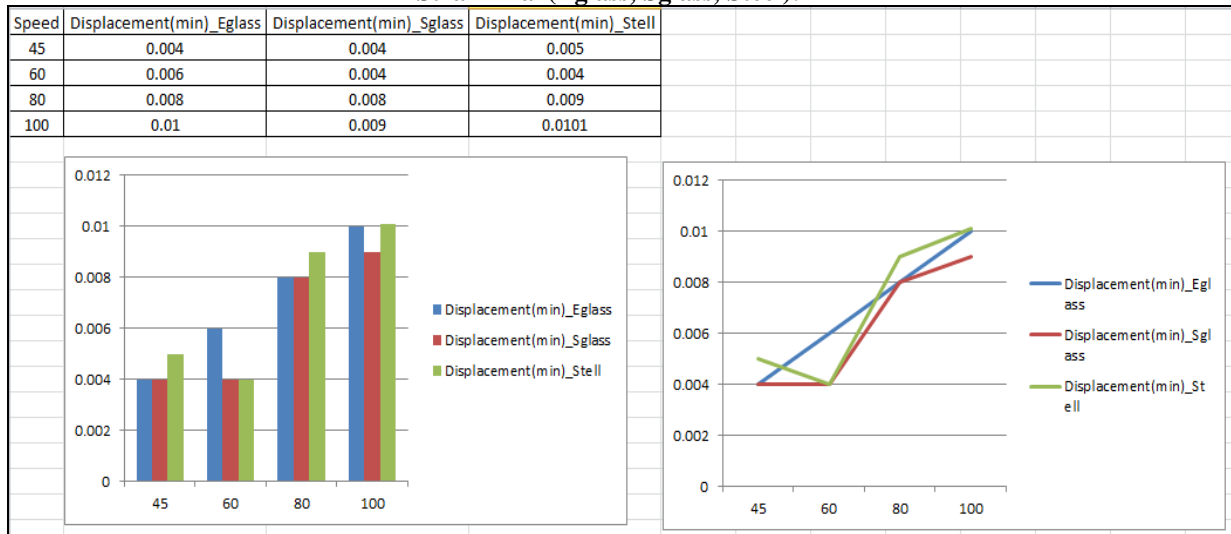


**Strain Min(Eglass, Sglass, Steel):**

Speed	Strain(min)_Eglass	strain(min)_Sglass	Strain(min)_Stell
45	8.524	6.307	3.865
60	0.0001	5.348	5.348
80	0.0001	0.0001	4.945
100	0.0001	7.598	7.598



**Strain Max(Eglass, Sglass, Steel):**



**IX. CONCLUSION**

Finite Element analysis of the impact of the car door has been done using FEA tool SOLID WORKS. From the results obtained from FE analysis, many discussions have been made.

In this study, Steel, Eglass, Sglass epoxy materials are used for side-door impact, for passenger cars, was designed to reduce weight, as well as to improve impact energy absorption; Structural modifications were tidied using FEA, in order to determine a suitable cross-section for the side-door impact. Furthermore, the impact energy absorption characteristics of Steel, Eglass, Sglass Epoxy were also investigated using impact test.

1. Results show the improvement in the strength of the door as the maximum limits of stresses. The value of von-misses stresses that comes out from the solid works is far less than material yield stress so our design is safe.
2. The strength of the car door is also increased (weight Reduction) from change of material from steel to Eglass epoxy and sglass epoxy.
3. As the cost of the car door is increased by using the composite materials for the car door manufacturing and decrease the risk from the collisions.
4. Above Results shows that FEA results conformal matches with the theoretical calculation so we can say that FEA is a good tool to reduce the time consuming theoretical work.

**Acknowledgements**

The support extended by the guide (Smt. Satya Prakash) and college authorities is highly appreciated and acknowledged with due respect.

**REFERENCES**

- [1] S. Acierno, R. Kaufmanc, F.P. Rivara, D.C. Grossman, and C. Mock, Vehicle mismatch: Injury patterns and severity, *Accid. Anal. Prev.* 36 (2004), pp. 761–772.
- [2] M.D. Buhmann, *Radial Basis Functions: Theory and Implementations*, Cambridge University Press, New York, 2003.
- [3] H. Fang, M. Rais-Rohani, Z. Liu, and M.F. Horstemeyer, A comparative study of metamodeling methods for multiobjective crashworthiness optimization, *Comput. Struct.* 83 (25–26) (2005), pp. 2121–2136.
- [4] H. Fang, K. Solanki, and M.F. Horstemeyer, Numerical simulations of multiple vehicle crashes and multidisciplinary crashworthiness optimization, *Int. J. Crashworthiness* 10 (2) (2005), pp. 161–171.
- [5] H. Fang and M.F. Horstemeyer, A generic optimizer interface for programming-free optimization systems, *Adv. Engg. Software* 37 (6) (2006), pp. 360–369.
- [6] H. Fang and M.F. Horstemeyer, Global response approximation with radial basis functions, *Engg. Optimiz.* 38 (4)(2006), pp. 407–424.

## Improved Kalman Filtered Neuro-Fuzzy Wind Speed Predictor For Real Data Set Collected At Egyptian North-Western Coast

Mohamed I. Awaad<sup>1</sup>, Omar M. Salim<sup>2</sup>, Ossama E. Gouda<sup>3</sup>, Ebtisam M. Saied<sup>4</sup>

<sup>1,2</sup>Electrical Power and Control Department, Benha Faculty of Engineering, Benha University, Egypt

<sup>3</sup>Electrical Power and Machines, Cairo Faculty of Engineering, Cairo University, Egypt

<sup>4</sup>Electrical power Department, Shoubra Faculty of Engineering, Benha University, Egypt

**Abstract:** Wind energy plays an important role as a contributing source of energy, as well as, and in future. It has become very important to predict the speed and direction in wind farms. Effective wind prediction has always been challenged by the nonlinear and non-stationary characteristics of the wind stream. This paper presents three new models for wind speed forecasting, a day ahead, for Egyptian North-Western Mediterranean coast. These wind speed models are based on adaptive neuro-fuzzy inference system (ANFIS) estimation scheme. The first proposed model predicts wind speed for one day ahead twenty four hours based on same month of real data in seven consecutive years. The second proposed model predicts twenty four hours ahead based only one month of data using a time series predication schemes. The third proposed model is based on one month of data to predict twenty four hours ahead; the data initially passed through discrete Kalman filter (KF) for the purpose of minimizing the noise contents that resulted from the uncertainties encountered during the wind speed measurement. Kalman filtered data manipulated by the third model showed better estimation results over the other two models, and decreased the mean absolute percentage error by approximately 64 % over the first model.

**Keywords:** Kalman Filtering, Forecasting, State Estimation, Time series, Adaptive Neuro-Fuzzy Inference System.

### I. Introduction

Exponential increase in energy demand globally is leading to rapid depletion of existing fossil fuel resources [1], [2]. This has led the power industry to explore renewable energy sources such as wind, solar, and tidal energies. Renewable energy resources attracted more attention recently owing to their pollution free energy generation capabilities. Wind as a potential source for electricity generation on a large scale has been receiving much attention recently. [1], [3]

Egypt now relies on burning fossil fuels to satisfy about 85% of its electricity demand, which is growing at a rate of 8% per year [4]. The Arab countries' fossil fuel supply is expected to dry up within the next 30-50 years [4]. The National Renewable Energy Authority (NREA) states that Egypt generated 600 MW of power from wind in 2010 with a goal to generate 7.2 GW of wind power by 2020, about 12% of its total electricity production [4].

Due to the unpredictable nature of wind gust, accurate wind prediction is difficult but much needed. Therefore, researchers have focused on deriving accurate stochastic models for wind speed, wind direction, and consequently wind power prediction. These wind models are based on soft-computing either using probabilistic modeling (using random process estimation theories) or based on approximate reasoning using expert systems like neural networks, fuzzy logic, and hybrid systems [4].

In this paper, new time series forecast models for wind-speed prediction are proposed for Egypt's north-western coast, since Egypt is a very promising country for wind energy generation. All models are based on real data gathered for that site. The proposed method doesn't require much data in order to give a prediction with respectable accuracy; the inputs are correlated over several years to take into account seasonal changes. The resultant models are used to predict twenty four hours ahead based on same month of real data in seven consecutive years and predicts twenty four hours ahead based only one month of data using a time series predication schemes. The predicted wind-speed is compared to the actual data to validate the obtained models.

### II. Wind-Speed Forecasting

Integration of accurate wind prediction in the management and control regimes involved in the wind energy conversion system (WECS) provides a significant tool for optimizing operating costs and improving

reliability [5]. However, due to highly complex interactions and the contribution of various meteorological parameters, wind forecasting is a very difficult task. Stochastic techniques depend on collecting wind-speeds data for wind atlas preparations, wind sites monthly and annual production, and wind turbines optimum sites prediction using a Weibull statistical model for predicting the performance of hybrid wind systems and their annual production, consumption of fuel, and costs [4].

Very short-term forecasting is defined as look ahead periods from a few minutes up to an hour, while short-term forecasting, which is proposed in this paper, will indicate hours out to a few days ahead. This difference between the two forecasting time periods is important when trying to create a prediction system. Three main classes of techniques have been identified for wind forecasting. These techniques are numeric weather prediction (NWP) methods, statistical methods, and methods based upon artificial intelligence [6].

Fuzzy sets were introduced to represent and manipulate data and information that possesses non-statistical uncertainty. Fuzzy sets are a generalization of conventional set theory that was introduced as a new way to represent vagueness in the data. It introduces vagueness (with the aim of reducing complexity) by eliminating the sharp boundary between the members of the class from nonmembers [4]. These approaches are problem dependent to a large extent and converge slowly and even may diverge in certain cases.

Weibull distribution is the most commonly used probability density function to describe and evaluate the frequency of wind-speed at the selected sites [4]. Weibull distribution can be described by (1) [7];

$$f_{wB}(w) = \frac{v}{\zeta} \left(\frac{w}{\zeta}\right)^{v-1} e^{-\left(\frac{w}{\zeta}\right)^v} \quad (1)$$

Where  $v$  is a shape parameter,  $\zeta$  is a scale parameter, and independent variable  $w$  is the wind-speed. If the shape parameter equals 2, the Weibull distribution is known as the Rayleigh distribution. For the Rayleigh distribution the scale factor,  $c$ , given the average wind speed ( $\bar{w}$ ) can be found from ( $v=2$ , and  $\zeta = \frac{2}{\sqrt{\pi}}\bar{w}$ ) [4].

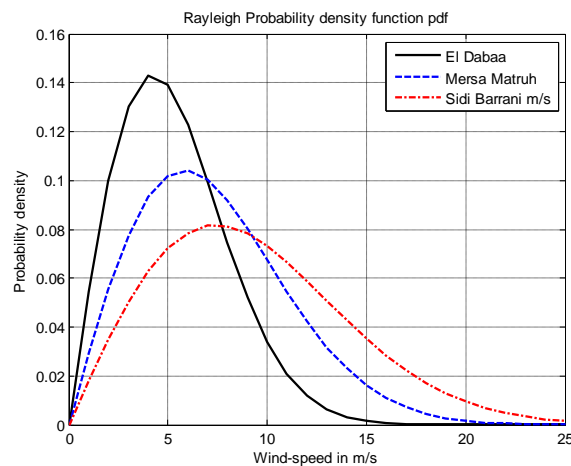


Figure 1. Probability density of the Rayleigh distribution for selected sites

In Fig. 1, the wind-speed probability density function (pdf) of the Rayleigh distribution is plotted. The average wind speeds in the figure are 5m/s, 5.3 m/s, and 5.4 m/s correspond to the wind speed in SidiBarrani, MersaMatruh and El Dabaaas three important candidate regions in Egypt’s North-Western coast [7].

In this paper, three different wind-speed prediction models are proposed. The differences between these models are the size of wind-speed data block required and the scheme by which ANFIS is implemented. All proposed models are short-term based models, twenty four hours ahead of wind-speed forecasting.

### III. Proposed Approach

The proposed approach in this paper is based on Kalman filter and ANFIS as a superior soft-computing technique. 3.1) Kalman Filter (KF)

The Kalman filter was created by Rudolf E. Kalman in 1960, though Peter Swerling actually developed a similar algorithm earlier [8]. It was developed as a recursive solution to the discrete-data linear filtering problem. Kalman filter is based on recursive data processing algorithm and Generates optimal estimate of desired quantities given the set of measurements.

Kalman Filtering is so popular because Good results in practice due to optimality and structure.

In order to use the KF to estimate the internal state of a process given only a sequence of noisy observations; the following matrices must be specified, which is represented as a linear stochastic difference equation.

$$x_k = A_k x_{k-1} + B_k u_k + w_k \quad (2)$$

Where:

$x_k$  = state vector

$A_k$  = state transition model which is applied to the previous state  $x_{k-1}$

$B_k$  = control-input model which is applied to the control vector  $u_k$

$w_k$  = process noise which is assumed to be drawn from a zero mean multivariate normal distribution with covariance  $Q$ ,  $P(w) \square N(0, Q)$

The relationship between the process state and the measurement values can be represented as [8]:

$$Z_k = H_k x_k + v_k \quad (3)$$

Where:

$Z_k$  = measurement of system state

$H_k$  = the observation (or measurement)  $z_k$  of the true state space into the covariance  $R$

$v_k$  = measurement noise;  $p(v) \sim N(0, R)$

To find an equation that computes an a posteriori state estimate as  $\hat{x}_k$  a linear combination of an a priori estimate  $\hat{x}_k^-$  and a weighted difference between the actual measurement  $z_k$  and a measurement prediction  $H\hat{x}_k^-$  [8].

$$\hat{x}_k = \hat{x}_k^- + K(Z_k - H\hat{x}_k^-) \quad (4)$$

The difference  $(z_k - H\hat{x}_k^-)$  is called innovation or residual. Residual of zero; means that, the two terms are in complete agreement and  $k$  is the gain or blending factor that minimizes the posteriori error covariance.

Matrix  $k$  is the gain that minimizes the a posteriori error covariance. The equation that needs to be minimized,

$$\hat{x}_k = \hat{x}_k^- + K(Z_k - H\hat{x}_k^-) \quad (5)$$

Ongoing Discrete Kalman Filter Cycle Project the state ahead,

$$\hat{x}_k^- = A_k \hat{x}_{k-1} + B_k u_k \quad (6)$$

Project the error covariance ahead

$$P_k^- = A_k P_{k-1} A_k^T + Q \quad (7)$$

Compute the Kalman gain

$$K_k = P_k^- H^T (H P_k^- H^T + R)^{-1} \quad (8)$$

Update estimate with measurement  $z_k$

$$\hat{x}_k = \hat{x}_k^- + K_k (z_k - H\hat{x}_k^-) \quad (9)$$

Update the error covariance [8]

$$P_k = (1 - K_k H) P_k^- \quad (10)$$

### 3.2) Adaptive Neuro-Fuzzy Inference Systems (ANFIS)

Adaptive Neuro Fuzzy Inference System (ANFIS) is a fuzzy mapping algorithm that is based on Tagaki-Sugeno-Kang (TSK) fuzzy inference system. ANFIS is integration of neural networks and fuzzy logic and have the potential to capture the benefits of both these fields in a single framework. ANFIS utilizes linguistic information from the fuzzy logic as well learning capability of an ANN for automatic fuzzy if-then rule generation and parameter optimization [9].

A conceptual ANFIS consists of five components: inputs and output database, a Fuzzy system generator, a Fuzzy Inference System (FIS), and an Adaptive Neural Network. The Sugeno-type Fuzzy Inference System, which is the combination of a FIS and an Adaptive Neural Network, was used in this study for rainfall-runoff modeling. The optimization method used is hybrid learning algorithms [9].

For a first-order Sugeno model, a common rule set with two fuzzy if-then rules is as follows:

Rule 1: If  $x_1$  is  $a_1$  and  $x_1$  is  $b_1$ , then

$$f_1 = a_1 x_1 + b_1 x_1 + c_1 \quad (11)$$

Rule 2: If  $x_1$  is  $a_2$  and  $x_2$  is  $b_2$ , then

$$f_2 = a_2 x_2 + b_2 x_2 + c_2 \quad (12)$$

Where,  $x_1$  and  $x_2$  are the crisp inputs to the node and  $a_i, b_i, a_2, b_2$  are fuzzy sets,  $a_i, b_i$  and  $c_i$  ( $i = 1, 2$ ) are the coefficients of the first-order polynomial linear functions.

It is possible to assign a different weight to each rule based on the structure of the system, where, weights  $w_1$  and  $w_2$  are assigned to rules 1 and 2 respectively and  $f$  = weighted average .

ANFIS network is composed of five consequent layers. Each layer contains several nodes described by the node function. Let  $O_i^j$  denote the output of the  $i^{\text{th}}$  node in layer  $j$  [9], [10].

In layer 1, every node  $i$  is an adaptive node with node function

$$O_i^1 = \mu A_i(x), \quad i = 1, 2 \quad (13)$$

Or

$$O_i^1 = \mu B_{i-2}(y), \quad i = 3, 4 \quad (14)$$

Where  $x$  (or  $y$ ) is the input to the  $i^{\text{th}}$  node and  $A_i$  (or  $B_{i-2}$ ) is a linguistic label associated with this node. The membership functions for A and B are usually described by generalized bell functions [11], e.g.

$$\mu A_i(x) = \frac{1}{1 + \left| \frac{x - r_i}{p_i} \right|^{2q_i}} \quad (15)$$

where  $\{p_i, q_i, r_i\}$  is the parameter set. Any continuous and piecewise differentiable functions, such as triangular-shaped membership functions, are also qualified candidates for node functions in this layer [4]. Parameters in this layer are referred to as premise parameters.

In layer 2, each node  $\prod$  multiplies incoming signals and sends the product out

$$O_i^2 = w_i = \mu A_i(x) \times \mu B_i(y), \quad i = 1, 2 \quad (16)$$

Each node output represents the firing strength of a rule.

In layer 3, each node  $N$  computes the ratio of the  $i^{\text{th}}$  rule firing strength to the sum of all rules' firing strengths

$$O_i^3 = \bar{w}_i = \frac{w_i}{w_1 + w_2}, \quad i = 1, 2 \quad (17)$$

The outputs of this layer are called normalized firing strengths. In layer 4, each node computes the contribution of the  $i^{\text{th}}$  rule to the overall output

$$O_i^4 = \bar{w}_i z_i = \bar{w}_i (a_i x + b_i y + c_i), \quad i = 1, 2 \quad (18)$$

Where  $\bar{w}_i$  is the output of layer 3 and  $\{a_i, b_i, c_i\}$  is the parameter set. Parameters of this layer are referred to as consequent parameters.

In layer 5, the single node  $\sum$  computes the final output as the summation of all incoming signals

$$O_i^5 = \sum_i \bar{w}_i z_i = \frac{\sum_i w_i z_i}{\sum_i w_i} \quad (19)$$

Thus, an adaptive network is functionally equivalent to a Sugeno-type fuzzy inference system. ANFIS is an embedded tool in the MATLAB fuzzy toolbox. This approach is based on using the neural networks training capability to adjust the membership functions' (MF) parameters of the proposed fuzzy inference system (FIS).

The proposed ANFISs utilize a subtractive clustering technique in which Gaussian MFs are used. Subtractive clustering generates an initial model for ANFIS training. This subtractive clustering method partitions the data into groups called clusters, and generates an FIS with the minimum number of rules required to distinguish the fuzzy qualities associated with each of the clusters. Subtractive clustering avoids the curse of dimensionality of grid partitioning method. Subtractive clustering is a fast, one-pass algorithm for estimating the number of clusters and the cluster centers in a set of data. It is especially used if there is no clear idea about how many clusters should be assigned for a given set of data.

The real-data sets used to build the proposed models were obtained through a huge database website for weather recordings that covers almost all countries around the globe [12]. These recordings are based on real hourly-based measurements for the corresponding sites. The study proposed is done for MersaMatruh site as one of the candidate sites in Egypt that has sufficient wind resources [7].

#### IV. Simulation Results And Discussions

In this paper the study is based on a real wind speed data gathered from Egypt north-western coast [12]. This location has been selected based on the evaluation done in [7], as it can be considered one of the most promising locations at the north coast. Each subsection has a model to forecast the wind-speed for a certain period of time and a different data block size to obtain with four different models by the end of this section.

**1.1. Model-I: 24-Hrs Ahead Based on Yearly Data Recordings**

The first model is based on a single month’s wind-speed data in seven consecutive years e.g. the month of July of years 2007, 2008, 2009, 2010, 2011, 2012 and 2013. In order to train an ANFIS, complete data sets of inputs along with their corresponding desired output data are needed. Thus, wind-speed data from 2007-2012 are used as six inputs with data sets of 2013 are used as a corresponding output. Since July is 31 days, only 30 days data (5040 data points) were used for training and the 31<sup>st</sup> whole day is to be predicted using the obtained model. The monthly data is selected in the same season to avoid the climate change between seasons.

$$Data(k) = [x_1 \ x_2 \ x_3 \ x_4 \ x_5 \ x_6] \tag{20}$$

The output training data corresponds to the trajectory prediction.

$$T \ arg \ et(k) = [x_7] \tag{21}$$

Where:  $x_1$  through  $x_7$  are wind-speed data in seven consecutive years e.g. the month of July of years 2007, 2008, 2009, 2010, 2011, 2012 and 2013 respectively.

The training input/output data is a structure whose first component is the six-dimensional input  $Data(k)$  as in (20), and its second component is the output  $T \ arg \ et(k)$  as in (21).

Fig. 2 presents the wind-speed data sets in m/s for July in 2007 through 2013 from upper graph down respectively, these data sets were obtained from [9]. The data are hourly recordings, thus for 31 days a total of 744 data point are shown per graph, but only 720 points per graph are used for training purposes and the last 24 hours are to be predicted. Fig. 3 shows the generated FIS using subtractive clustering using ANFIS toolbox that provides a single output Takagi-Sugeno-Kang (TSK) type with linear MFs for the output.

The upper graph of Fig. 4 shows the root mean square error (RMSE) that resulted during the ANN training epochs. The resultant ANFIS model is used for the purpose of testing and validation to predict 24-Hrs ahead. The middle graph of Fig. 4 shows the wind-speed forecasting in m/s for one complete day ahead for the end of July. The error over one day between actual and predicted wind-speed is shown in the lower graph of Fig. 4. The mean value of the error (ME) is found to be around 0.2645 m/s with a mean absolute error (MAE) of 1.6319 m/s. Figure 5 gives scattered plot for actual speed verses predicted speed month data.

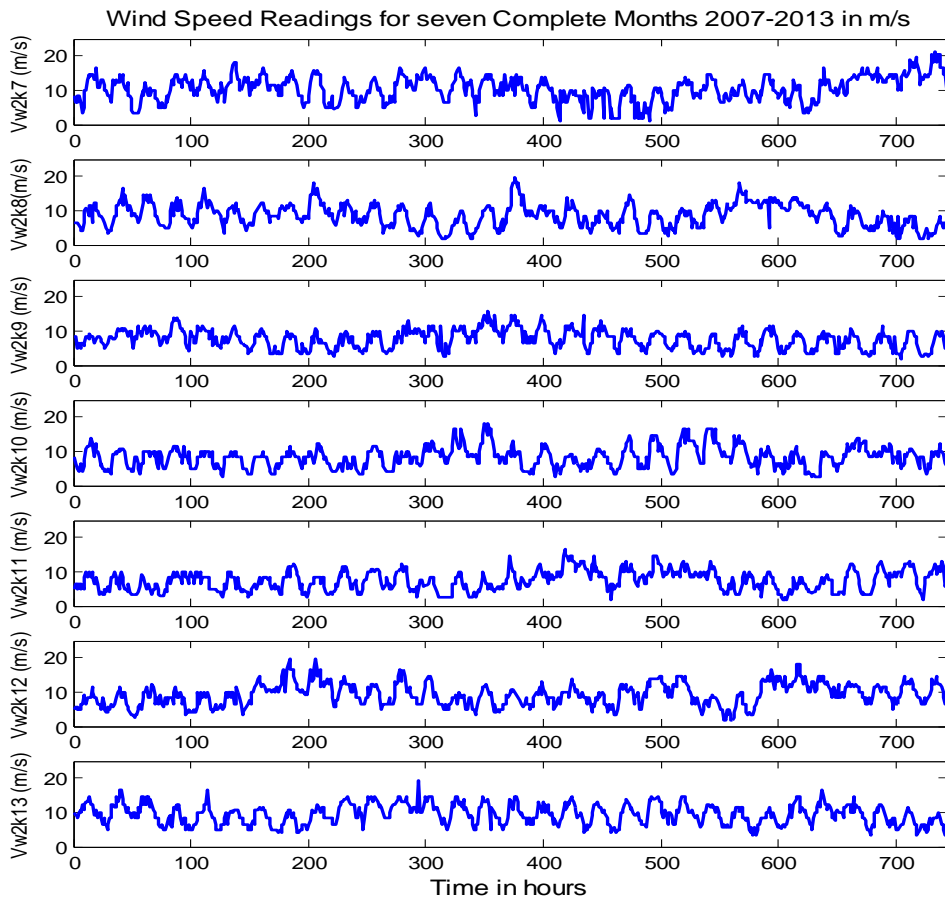


**Figure 2.** Real wind-speed data for 7 months all in July (2007-2013).

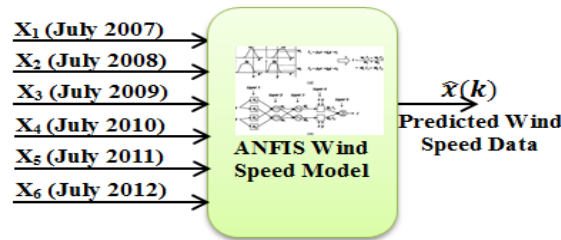


Figure 3. Proposed TSK-FIS for model-I based on Real Wind Speed Data Input

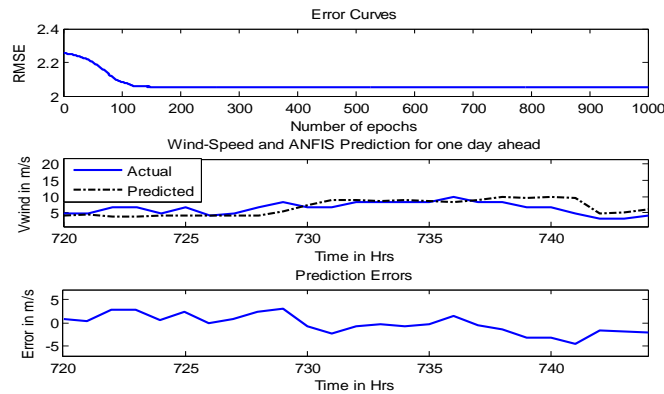


Figure 4. Upper graph is RMSE result for the model-I, Middle graph is actual and prediction of 24-Hrs ahead, where the lower graph shows the prediction error

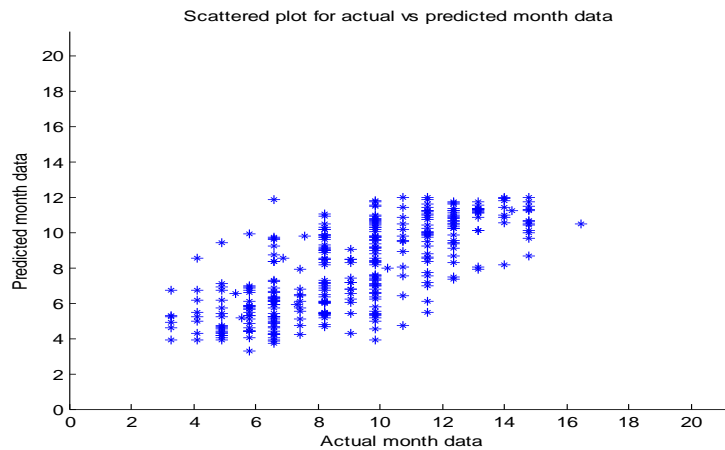


Figure 5. Scattered plot for actual vs predicted month data

1.2. Model-II: 24-Hrs Ahead Based on one month Data

This model is based on only one month wind-speed data, e.g. July 2013. In this model, one month of hourly based wind-speed recordings are required. Data are rearranged to create a mapping from 4 samples wind-speed data points, sampled every 24 hours, to a predicted future of 24 hours as shown in Fig. 6.

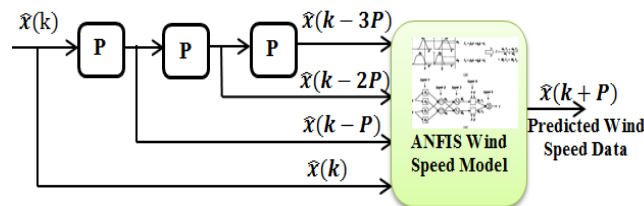


Figure 6. Block diagram of ANFIS without Kalman Filter (KF)

$$Data(k) = [x(k-3p) \quad x(k-2p) \quad x(k-p) \quad x(k)] \tag{22}$$

The output training data corresponds to the trajectory prediction.

$$Target(k) = x(k + P) \tag{23}$$

Where  $k$  is the time instant in hours and  $P$  is the period to be predicted ( $P = 24$  in this case). The training input/output data is a structure whose first component is the four-dimensional input  $Data(k)$  as in (22), and its second component is the output  $Target(k)$  as in (23). There are 720 input/output data points. These data points are used for the ANFIS training (these became the training data set), while only part of them are used as checking data to validate the identified fuzzy model.

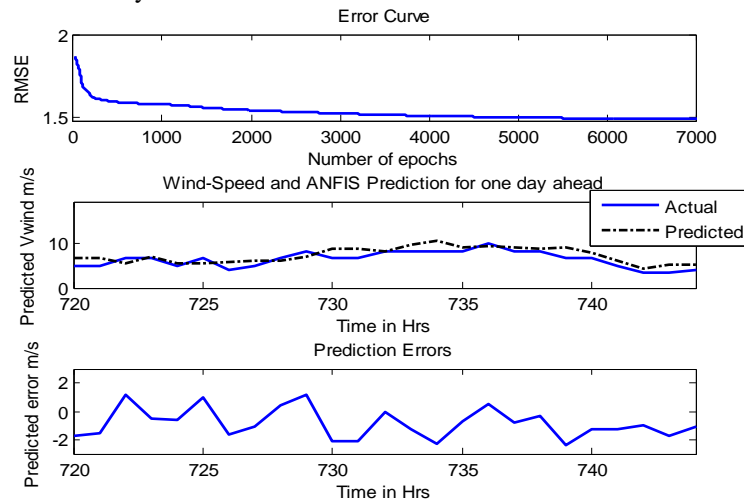


**Figure 7.** Upper graph is RMSE result for the model-I, Middle graph is actual and prediction of 24-Hrs ahead, where the lower graph shows the prediction error

The one month data points (July 2013) were plotted earlier as the last graph of Fig. 2 to illustrate the data used for the training. These data points are then rearranged as five vectors of shifted wind-speed recordings (each vector is 24-Hrs shifted from its corresponding consequent vector). Training the ANFIS is done based on the concept of time-series prediction. RMSE resulted from the training epochs of the ANN is shown in the upper graph of Fig. 7. Data is then used to validate the ANFIS by predicting 24-Hrs ahead. The prediction of July 31st is shown in middle graph of Fig. 7, while the lower graph illustrates the prediction error which shows a quite similar prediction error for model-II as for model-I. The mean value of the error is found to be around 0.8545 m/s with MAE of 1.1975 m/s. The results obtained by model-II is similar to the results of the previous model (model-I), but it has a significant advantage over model-I. This advantage is that model-I has much more data points used in the training step (model-II uses only 14% of model-I data points). Thus, model-II is preferred over model-I. Figure 8 gives scattered plot for actual speed versus predicted speed month data of model II

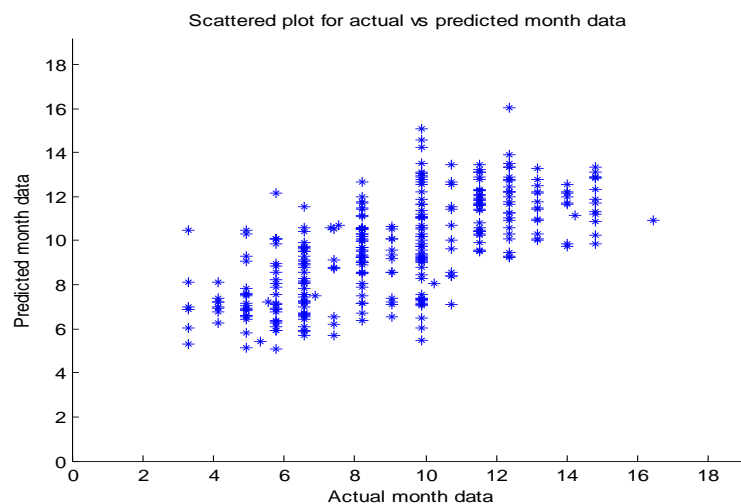


**Figure 8.** Scattered plot for actual vs predicted month data

### 1.3. Model-III: 24-Hrs Ahead Based on one month Data with Kalman Filter

The statistical uncertainty is the randomness or error that comes from different sources; the five types of uncertainty that emerge from the imprecise knowledge are:

- Process uncertainty: dynamic randomness.
- Modeling uncertainty: wrong specification of the model structure.
- Measurement uncertainty: error on observed quantities.
- Implementation uncertainty: consequence of the variability.
- Estimate uncertainty: appear from any source of uncertainties or a combination of them, and it is called inexactness and imprecision.

Wind speed measurements obtained from [12], are subjected to some sort of uncertainties which are presented as vagueness of the wind speed value due to noise contents. KF is commonly used to filter out noisy data as it is considered the best linear unbiased estimator (BLUE). In Model-II; data set is allowed to pass initially through KF for the purpose of minimizing the error covariance exhibited by the data set as shown in Fig. 9. Estimated (filtered) data are then rearranged to create a mapping from four samples wind-speed data points, sampled every twenty four hours, to a predicted future of twenty four hours.

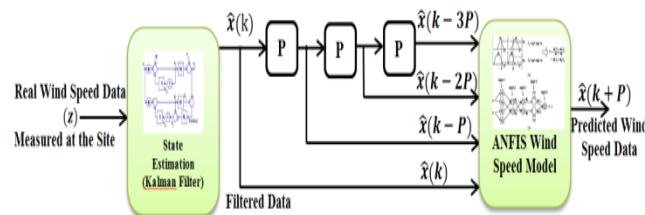


Figure 9. Block diagram of ANFIS with Kalman Filter (KF)

$$E_{Data}(k) = [\hat{x}(k-3p) \quad \hat{x}(k-2p) \quad \hat{x}(k-p) \quad \hat{x}(k)] \tag{24}$$

Where:

$$E_{Data}(k) = \text{Estimated data Vector}$$

The output training data corresponds to the trajectory prediction.

$$\text{Estimated Target (k)} = \hat{x}(k+p) \tag{25}$$

Where  $k$  is the time instant in hours and  $p$  is the period to be predicted ( $p = 24$  in this case). The training input/output data is a structure whose first component is the four-dimensional input  $E_{Data}(k)$  as in (24), and its second component is the output Estimated Target (k) as in (25). There are 720 input/output data points. These data points are used for the ANFIS training (these became the training data set), while only part of them are used as checking data to validate the identified fuzzy model.

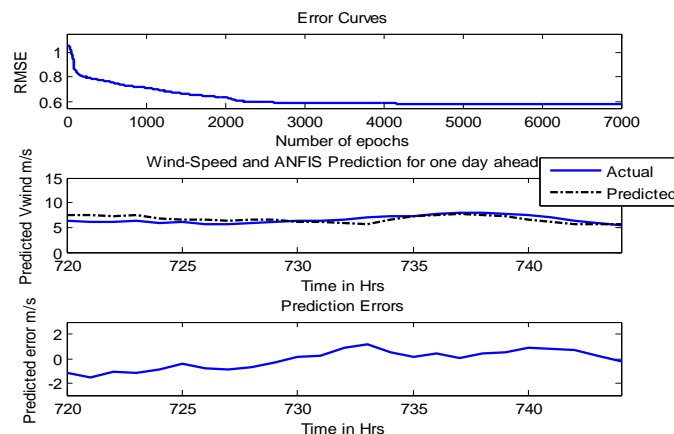


Figure 10. Upper graph is RMSE result for the model-I, Middle graph is actual and prediction of 24-Hrs ahead, where the lower graph shows the prediction error

RMSE resulted from the training epochs of the ANN is shown in upper graph of Fig.10. Data is then used to validate the ANFIS by predicting 24-Hrs ahead. The prediction of July 31st is shown in middle graph of Fig. 10, while the lower graph illustrates the prediction error. The mean value of the error is found to be around

0.0804 m/s with MAE of 0.6624 m/s. The results obtained by model-III are better than the results of the previous model (model-II), because it has a significant advantage over model-II. This advantage is that model-III has low mean absolute error this means the prediction is more accurate by 55.5%. Thus, model-III is preferred over model-II. Figure 11 gives scattered plot for actual speed versus predicted speed month data of model III

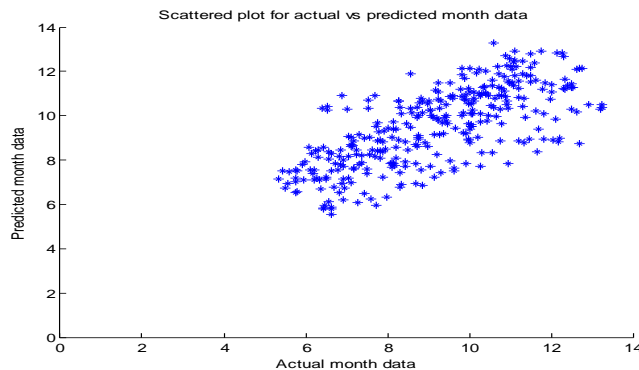


Figure 11. Scattered plot for actual vs predicted month data

Table I. shows accuracy study between the three proposed models including the used forecasting period which is twenty four hours during seven months for the first model and one month for the next both of models. The comparison discusses: RMSE, ME, MAE and Mean Absolute Percentage Error (MAPE).

Model-III using KF showed better accuracy based on error calculation. Thus; model-III is better than model-I because MAPE has been improved by 51.45% as shows in equation (26):

$$\begin{aligned} \text{Enhancement Ratio} &= \left(1 - \frac{\text{MAPE of Model-III}}{\text{MAPE of Model-I}}\right) & (26) \\ &= \left(1 - \frac{10.31}{28}\right) = 63.17\% \end{aligned}$$

And model-III is better than model-II because MAPE has been improved by 51.45% as shows in equation (27):

$$\begin{aligned} \text{Enhancement Ratio} &= \left(1 - \frac{\text{MAPE of Model-III}}{\text{MAPE of Model-II}}\right) & (27) \\ &= \left(1 - \frac{10.31}{21.24}\right) = 51.45\% \end{aligned}$$

Table I. Accuracy study for wind-speed forecasting.

	<b>Model-I</b>	<b>Model-II</b>	<b>Model-III</b>
<b>Forecasting Period</b>	24-Hrs	24-Hrs	24-Hrs
<b>Amount of data points</b>	5040	720	720
<b>RMSE (m/s)</b>	1.9782	1.3466	0.7652
<b>Mean Error (m/s)</b>	0.2645	0.8545	0.0804
<b>MAE (m/s)</b>	1.6319	1.1975	0.6624
<b>MAPE (%)</b>	28.00	21.24	10.31

## V. Conclusion

In this paper, three effective time series stochastic wind models for Egypt's north-western coast were proposed and optimized using ANFIS and Kalman filter.

Model-I based on real wind-speed data sets for the month of July in the years 2007 through 2013; the target was to predict wind-speed 24-Hrs ahead. Model-I accuracy (MAE) is 1.6319 m/s. Model-II and model-III are both based on one month of data to predict 24-Hrs (July 2013); which have the advantage of using only 14% of the data block size and improve the accuracy in the same time. In model-III an initial stage of kalman filter has been added. KF stage has filtered out noise exhibited from measurement uncertainty. Model-III showed better accuracy over model-I by approximately 63.17% mean absolute error and by approximately 51.45% mean absolute error for model-II.

## REFERENCES

- [1] Sivanagaraja Tatinati and Kalyana C. Veluvolu, "A Hybrid Approach for Short-Term Forecasting of Wind Speed," Hindawi Publishing Corporation, The ScientificWorld Journal, Volume 2013, Article ID 548370.
- [2] J. Szarka, "Wind power, policy learning and paradigm change," Energy Policy, vol. 34, no. 17, pp. 3041–3048, 2006.
- [3] S. Akpinar and E. K. Akpinar, "Estimation of wind energy potential using finite mixture distribution models," Energy Conversion and Management, vol. 50, no. 4, pp. 877–884, 2009.
- [4] O.M. Salim, M.A. Zohdy, H.T. Dorrah and A.M. Kamel, "Adaptive Neuro-Fuzzy Short-Term Forecasting for Egypt's East-Coast," international Journal of Sustainable Energy, *iFirst*, 2011, 1–19.
- [5] Thanasis G. Barbounis, J. B. Theocharis, M. C. Alexiadis, P. S. Dokopoulos, "Long-Term Wind Speed and Power Forecasting Using Local Recurrent Neural Network Models," IEEE TRANSACTIONS ON ENERGY CONVERSION, VOL. 21, NO. 1, pp. 273-284, 2006.
- [6] M. Negnevitsky and C. W. Potter, "Very Short-Term Wind Forecasting for Tasmanian Power Generation," IEEE Transactions on Power Systems, vol. 21, no. 2, pp. 965–972, 2006, .
- [7] Ahmed Shata, "Theoretical investigation and mathematical modelling of a wind energy system Case study for Mediterranean and Red Sea," ACWE11-2009, 11th Americas Conference on Wind Engineering, San Juan, Puerto Rico, June-2009.
- [8] Greg Welch, Gary Bishop, "An Introduction to the Kalman Filter", Department of Computer Science, University of North Carolina at Chapel Hill, Chapel Hill, NC 27599-3175 ,2006.
- [9] Kumar, P., D. Kumar, Jaipaul, A. K. Tiwari, " Evaporation Estimation Using Artificial Neural Networks and Adaptive Neuro-Fuzzy Inference System Techniques," Pakistan Journal of Meteorology , Vol. 8, Issue 16: Jan 2012.
- [10] F. Castellanos1 and N. James , "Average Hourly Wind Speed Forecasting with ANFIS," ACWE11-2009, 11th Americas Conference on Wind Engineering, San Juan, Puerto Rico, June-2009.
- [11] D.K.Chaturvedi1, Sinha Anand Premdayal2 and Ashish Chandio3 , " Short Term Load Forecasting using Neuro-fuzzy-Wavelet Approach," International Journal of Computing Academic Research (IJCAR),ISSN 2305-9184 Volume 2, Number 1 (February 2013), pp. 36-48
- [12] Weather Underground website, www.wunderground.com

## Helicopter Flapping Under Dynamic Stall

Jibin Babu<sup>1</sup>, Blesson Joseph Thomas<sup>2</sup>

<sup>1,2</sup>Department of Mechanical Engineering, Amal Jyothi College of Engineering, Kanjirappally, Kerala

**Abstract:** A helicopter is an aircraft that is lifted and propelled by one or more horizontal rotors, each consisting of two or more rotor blades. The main objective of this seminar topic is to study the basic concepts of helicopter aerodynamics. The forces acting on helicopter i.e. lift, drag, thrust and weight are considered for developing analytic equations. The main topics that are discussed include blade motions like blade flapping, feathering and lead-lag. The effect of stall on helicopter blade flapping is studied and it was noticed that there is a sudden lift drop at this stall condition. It was also found that dynamic stall occurs due to rapidly changing angle of attack, which in turn affect the air flow over the airfoil. Blade flapping angle and induced angle of attack are the main parameters concerned with stall. The theory behind blade element analysis has been inferred in detail. The importance of all these in the present scenario are also taken into consideration.

**Keywords:** Flapping, Dynamic stall, angle of attack, airfoil, lift, drag.

### I. Introduction

The science of aerodynamics is the fundament of all flight. Ignor Sikorsky's vision of rotating wing aircraft that could safely hover and perform other desurable flight maneuvers under full control of the pilot took thirty years to be achieved. This rotating aircraft we know it today as helicopter. The great Leonardo da Vinci years back in his drawing showed a basic human carrying helicopterlike machine an obvious elaboration of Archimedes water-screw. The origin of sucessful helicopters can be traced from the achievements of Lilienthal, Langly then to the first pilot controlled aircraft by the Wright Brothers in 1903 to the present date.

#### 1.1 Background and scope

A helicopter is an aircraft that is lifted and propelled by one or more horizontal rotors, each rotor consisting of two or more rotor blades. A helicopter works by having its wings move through air while the body stays still. The helicopter blades are called main rotor blades. During flight there are four forces on the helicopter and those forces are

- lift
- drag
- thrust
- weight

Helicopters are in wide usage in present era. Due to its rapid action and novelty it has created a great impact in the upper class. Rapid flight action inturn results in a special type of stalling process called dynamic stall. A helicopter flies because aerodynamic forces necessary to keep it aloft are produced when air passes about the rotor blades. The rortor blade is an aerodynamic structure that makes flight possible. Its shape produces necessary lift when it passes through the air. Helicopter blades have airfoil sections designed for a specific set of flight characteristics. In this report we are going to study in detail helicopter flapping and the effect of dynamic stall on it.

The topic involves the basic understanding of helicopter blade characteristics i.e. structure, nomenclature and its action under fluid flow and stall. This literature survey deals with the basic study related with helicopter aerodynamics. These factors are the main criteria on which the design and development of helicopters depend. For a helicopter in motion, there are different types of blade movements that occur. In order to study and understand the topics related, various jornals and books have been referred, as illustrated in 'REFERENCES' chapter -6.

#### 1.2 Dynamic stall and its effect

The main journal *Helicopter blade flapping with and without small angle assumption in the presence of dynamic stall* by Jyoti Ranjan Majhi, Ranjan Ganguli(1) deals with the general flapping equation without taking into account the small angle assumptions. The validity of the small induced inflow angle of attack assumption is

investigated in various flight regimes. Moreover it's better to assume that the flap angle and inflow angle are large angles in helicopter dynamics.

In the journal *Dynamic stall on a fully equipped helicopter model* by K.Mulleners, K.Kindler, M.Raffel (2) tells about three dimensional stall observed on the rotor of a fully equipped helicopter model. It's said that dynamic stall on an airfoil comprises a series of complex aerodynamic phenomena into an unsteady change of the angle of attack. Finite wing and rotational effects as well as blade lag motion should be considered for a comprehensive understanding of dynamic stall on retreating helicopter rotor blades.

In *Shallow and deep dynamic stall for flapping low Reynolds number airfoils* by Michael V, Luis Bernal, Chang-Kwon Kang (3) its described about various experiments based on flow visualisation and direct force measurement. Comparison of classical unsteady aerodynamic theory, for an airfoil spanning the test section seek to elucidate the impact of flow separation on the validity of the various approaches and on prediction of lift coefficient time history.

### 1.3 Air foil

An airfoil is the shape of a wing or blade of propeller, rotor, turbine or sail as seen in cross section.

An airfoil-shaped body moved through a fluid produces an aerodynamic force. The component of this force perpendicular to the direction of motion is called lift. The component parallel to the direction of motion is called drag. The lift on an airfoil is primarily the result of its angle of attack and shape. When oriented at a suitable angle, the airfoil deflects the oncoming air, resulting in a force on the airfoil in the direction opposite to the deflection. Most foil shapes require a positive angle of attack to generate lift, but cambered airfoils can generate lift at zero angle of attack. This turning of the air in the vicinity of the airfoil creates curved streamlines which results in lower pressure on one side and higher pressure on the other. The thicker boundary layer also causes a large increase in pressure drag, so that the overall drag increases sharply near and past the stall point.

As a wing moves through air, the air is split and passes above and below the wing. The wing's upper surface is shaped so the air rushing over the top speeds up and stretches out. This decreases the air pressure above the wing. The air flowing below the wing moves in a straighter line, so its speed and air pressure remains the same. Since high air pressure always moves toward low air pressure, the air below the wing pushes upward toward the air above the wing. The wing is in the middle, and the whole wing is "lifted." The faster an airplane moves, the more lift there is. And when the force of lift is greater than the force of gravity, the airplane is able to fly.

Airfoil design is a major facet of aerodynamics. Various airfoils serve different flight regimes. Asymmetric airfoils can generate lift at zero angle of attack, while a symmetric airfoil may better suit frequent inverted flight as in an acrobatic airplane. Modern aircraft wings may have different airfoil sections along the wing span, each one optimized for the conditions in each section of the wing. Movable high-lift devices, flaps and sometimes slats, are fitted to airfoils on almost every aircraft.

### 1.4 Airfoil Terminology

The various terms associated with airfoil are:

- The *suction surface* is generally associated with higher velocity and lower static pressure.
- The *pressure surface* has a comparatively higher static pressure than the suction surface. The pressure gradient between these two surfaces contributes to the lift force generated for a given airfoil.
- The leading edge is the point at the front of the airfoil that has maximum curvature.
- The *trailing edge* is defined similarly as the point of maximum curvature at the rear of the airfoil.
- The *chord line* is a straight line connecting the leading and trailing edges of the airfoil.
- The *chord length* is the length of the chord line.
- The *mean camber line* is the locus of points midway between the upper and lower surfaces.
- *Pitch angle*: The mechanical angle between the chord line of the airfoil and the plane of rotation of the rotor.
- *Angle of attack*: The acute angle formed between the chord line of an airfoil and the resultant relative wind

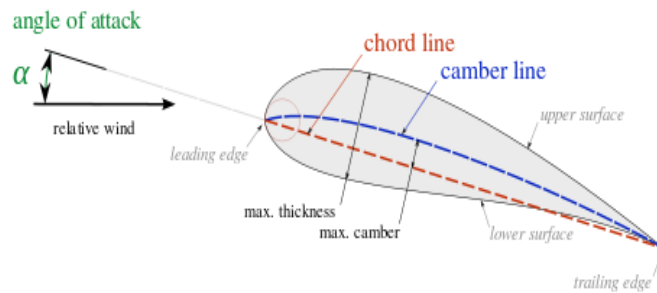


Fig .1: Airfoil nomenclature

## II. Theoretical Study

### 2.1 Helicopter Rotor

A helicopter main rotor is the combination of a rotary wing and a control system that generates the aerodynamic lift force that supports the weight of the helicopter, and the thrust that counteracts aerodynamic drag in forward flight. Each main rotor is mounted on a vertical mast over the top of the helicopter, as opposed to a helicopter tail, which connects through a combination of drive shaft and gearboxes along the tail boom. A helicopter's rotor is generally made of two or more rotor blades. The blade pitch is typically controlled by a swashplate connected to the helicopter flight controls. Helicopters are one of the major examples of rotary-wing aircraft.

The helicopter rotor is powered by the engine, through the transmission, to the rotating mast. The mast is a cylindrical metal shaft that extends upward and is driven by the transmission. At the top of the mast is the attachment point for the rotor blades called the hub. The rotor blades are then attached to the hub.

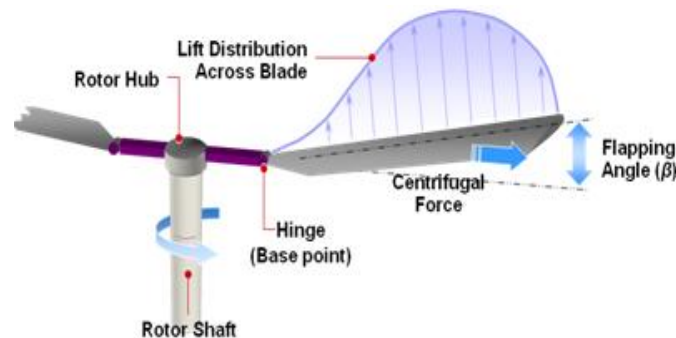


Fig 2.1: Helicopter rotor

#### Limiting conditions

1. Helicopters with teetering rotors must not be subjected to low-g condition because such rotor systems do not control the fuselage attitude.
2. When operating in sandy environments, sand hitting the moving rotor blades erodes their surface. This can damage the rotors and presents serious and costly maintenance problems.

### 2.2 Blade motions

A rotating blade can have the following three types of motions:

- Flapping
- Feathering
- Lead and lag

#### 2.2.1 Helicopter Flapping

In order to get a clear idea of blade flapping we must be clearly know the concept of *dissymmetry of lift*. Dissymmetry of lift is the difference in lift that exists between the advancing half of the rotor disk and the retreating half. It is caused by the fact that in directional flight the aircraft relative wind is added to the rotational relative wind on the advancing blade, and subtracted on the retreating blade. All rotor systems are subject to Dissymmetry of Lift in forward flight. At a hover, the lift is equal across the entire rotor disk. As the helicopter

gain air speed, the advancing blade develops greater lift because of the increased airspeed and the retreating blade will produce less lift, this will cause the helicopter to roll.

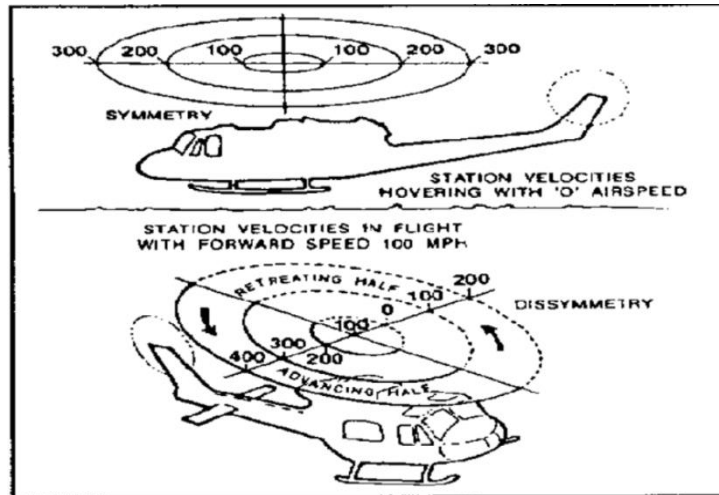


Fig 2.2: Symmetry and Dissymmetry of "LIFT"

Dissymmetry of lift in helicopter aerodynamics refers to an uneven amount of lift on opposite sides of the rotor disc. The dissymmetry is caused by differences in relative airspeed between the advancing blade and the retreating blade.

Dissymmetry of lift is compensated by *blade flapping*, because of the increased airspeed and lift on the advancing blade will cause the blade to flap up and decreasing the angle of attack. The decreased lift on the retreating blade will cause the blade to flap down and increasing the angle of attack. The combination of decreased angle of attack on the advancing blade and increased angle of attack on the retreating blade through blade flapping action tends to equalize the lift over the two halves of the rotor disc. Thus Flapping is the up and down movement of the rotor blades about a flapping hinge (or flexible hub). Blades flap in response to changes in lift caused by changes in velocity of the relative wind across the airfoil, or by cyclic feathering. No flapping occurs when the tip path plane is perpendicular to the mast.

### 2.2.2 Helicopter feathering

Blade feathering is the term for changing blade angle. It influences the blade's angle of attack. A blade feathers along its longitudinal axis, and a bearing is usually used to support this. The blade angle is set by the control rod, which is connected to the swashplate. Changing the blade pitch will result in a change in blade flapping behaviour. The place where the control rods connect to the blade, and the position of the flapping axis both influence feathering and, therefore, blade angle. Feathering is the rotation of the blade about its span-wise axis. Feathering can be uniform throughout the rotor through collective inputs. Feathering can be adjusted differentially through cyclic manipulation.

### 2.2.3 Lead Lag

Coriolis force tends to make a rotor blade want to speed up and slow down its rotation around the mast. If the blade is rigidly attached to the mast but isn't strong enough, it could develop stresses large enough to break the blade. A lead lag hinge simply is a hinge which allows the blade to pivot slightly forward and backward.

### 2.3 Stall

A stall is a condition in aerodynamics wherein the angle of attack increases beyond a certain point such that the lift begins to decrease. The angle at which this occurs is called the critical angle of attack. This critical angle is dependent upon the profile of the wing, its planform, its aspect ratio, and other factors, but is typically in the range of 8 to 20 degrees relative to the incoming wind for most subsonic airfoils. The critical angle of attack is the angle of attack on the lift coefficient versus angle-of-attack curve at which the maximum lift coefficient occurs. Flow separation begins to occur at small angles of attack while *attached* flow over the wing is still dominant. As angle of attack increases, the separated regions on the top of the wing increase in size and hinder the wing's ability to create lift. At the critical angle of attack, separated flow is so dominant that further increases in angle of attack produce less lift and vastly more drag.

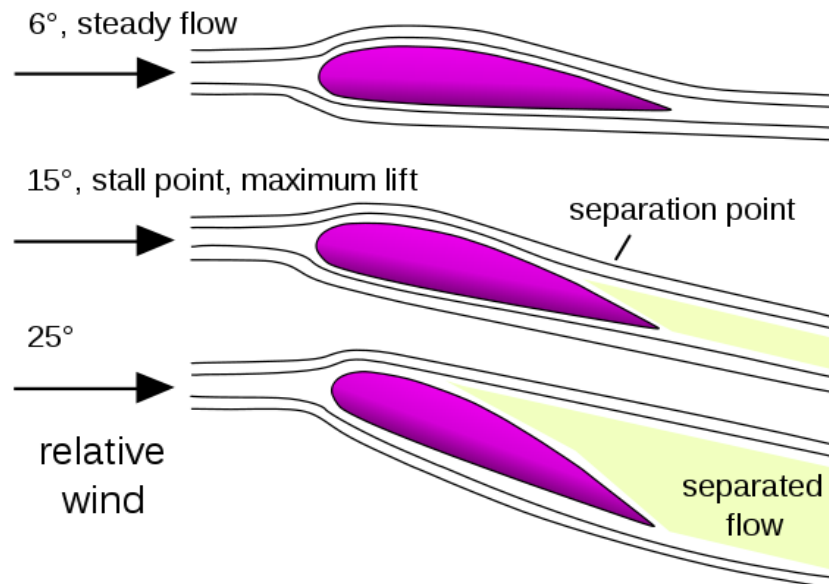


Fig 2.3: Stall formation

One symptom of an approaching stall is slow and sloppy controls. As the speed of the aircraft decreases approaching the stall, there is less air moving over the wing, and, therefore, less air will be deflected by the control surfaces at this slower speed. Some buffeting may also be felt from the turbulent flow above the wings as the stall is reached.

### 2.4 Dynamic Stall

Dynamic stall is a non-linear unsteady aerodynamic effect that occurs when airfoils rapidly change the angle of attack. The rapid change can cause a strong vortex to be shed from the leading edge of the airfoil, and travel backwards above the wing. The vortex, containing high-velocity airflows, briefly increases the lift produced by the wing. As soon as it passes behind the trailing edge, however, the lift reduces dramatically, and the wing is in normal stall.

A dynamic stall is a stalled condition different from a statically stalled condition. It is a transient, non-permanent condition. Airfoil stalls at a given angle of attack. This critical angle of attack is the angle of attack that gives the highest coefficient of lift, ie, beyond this angle of attack, the CL decreases due to increased airflow separation on the upper side of the airfoil. This is measured in a static, steady-state, constant system. However, the airflow separation on top of the wing is in reality dynamic and always changing, and during these changes we may see conditions, beyond the nominated critical angle of attack, where the airflow is less separated than in the above steady-state scenario.

Dynamic stall is mostly associated with helicopters and flapping wings. During forward flight, some regions of a helicopter blade may incur flow that reverses, and thus includes rapidly changing angles of attack. Stall delay can occur on airfoils subject to a high angle of attack and a three-dimensional flow. When the angle of attack on an airfoil is increasing rapidly, the flow will remain substantially attached to the airfoil to a significantly higher angle of attack than can be achieved in steady-state conditions. As a result, the stall is delayed momentarily and a lift coefficient significantly higher than the steady-state maximum is achieved. Helicopter, flapping wings, oscillating wings of insects, propellers are all associated with dynamic stall.

## III. Case Study

### 3.1 Blade element analysis

The blade element theory is used to obtain the loads acting on a blade section. Blade element theory involves breaking a blade down into several small parts then determining the forces on each of these small blade elements. These forces are then integrated along the entire blade and over one rotor revolution in order to obtain the forces and moments produced by the rotor. If the blade element method is applied to helicopter rotors in forward flight it is necessary to consider the flapping motion of the blades as well as the longitudinal and lateral distribution of the induced velocity on the rotor disk.

The blade cross section consists of an airfoil section:

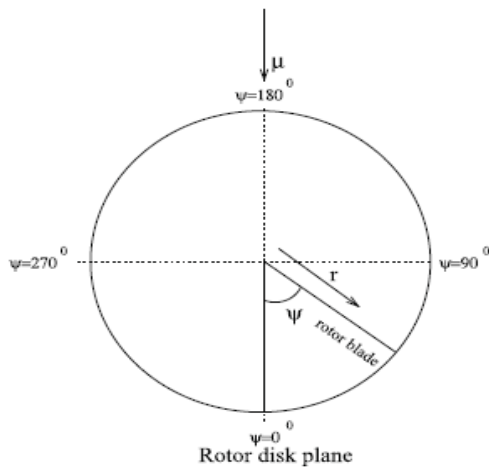


Fig 3.1: Rotor disc plane

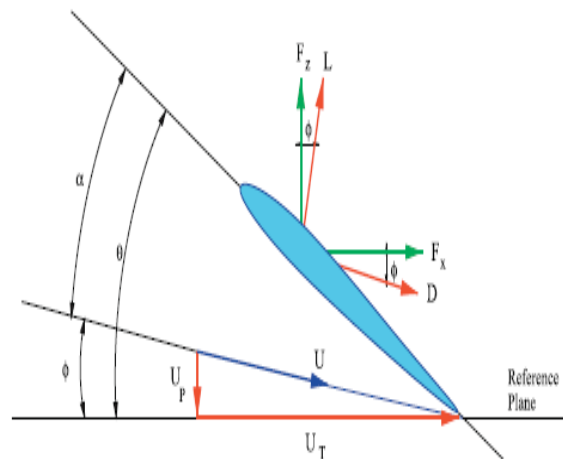


Fig 3.2: Blade element velocity and forces

### 3.1.1 Blade element velocity components

There are three dimensional components of velocity, an in plane component of velocity  $U_T$ , an out of plane component,  $U_P$  and a radial component  $U_R$   $U_R = (\Omega R)\mu \cos \Psi$

$$U_P = (\Omega R)(\lambda \cos \beta + r\beta + \mu \sin \beta \cos \Psi)$$

$$U_T = (\Omega R)(r \cos \beta + \mu \sin \beta) \quad \text{where } \mu = \frac{v_{\infty} \cos \alpha}{\Omega R}$$

### 4.1.2 Blade element forces

Lift and drag forces per unit blade span are:

$$L = \frac{1}{2} \rho U^2 C_{L}$$

$$D = \frac{1}{2} \rho U^2 C_{D}$$

where,  $U$  = resultant velocity

$$C_L = C_L(\alpha)$$

$$C_D = C_D(\alpha)$$

The lift and drag forces act perpendicular and parallel, respectively, to the direction of the resultant flow velocity.

## 3.2 Graphical study

The main objective of this paper is to address two issues:

- The validity of small  $\beta$  assumption
- The validity of the small  $\phi$  assumption.

These assumptions are investigated in the foregoing sections.

### 3.2.1 Flapping response

In the following case study, a uniform inflow model is used. We see that  $\theta_0$  increases from 1 degree to 16 degree. For low  $\theta_0$  the effect is primarily on the phasing of the flap response but at higher  $\theta_0$ , it affects both magnitude and phasing. The small  $\beta$  assumption over predicts the effective angle of attack which results in appropriate lift prediction which in turn brings out an erroneous flap response.

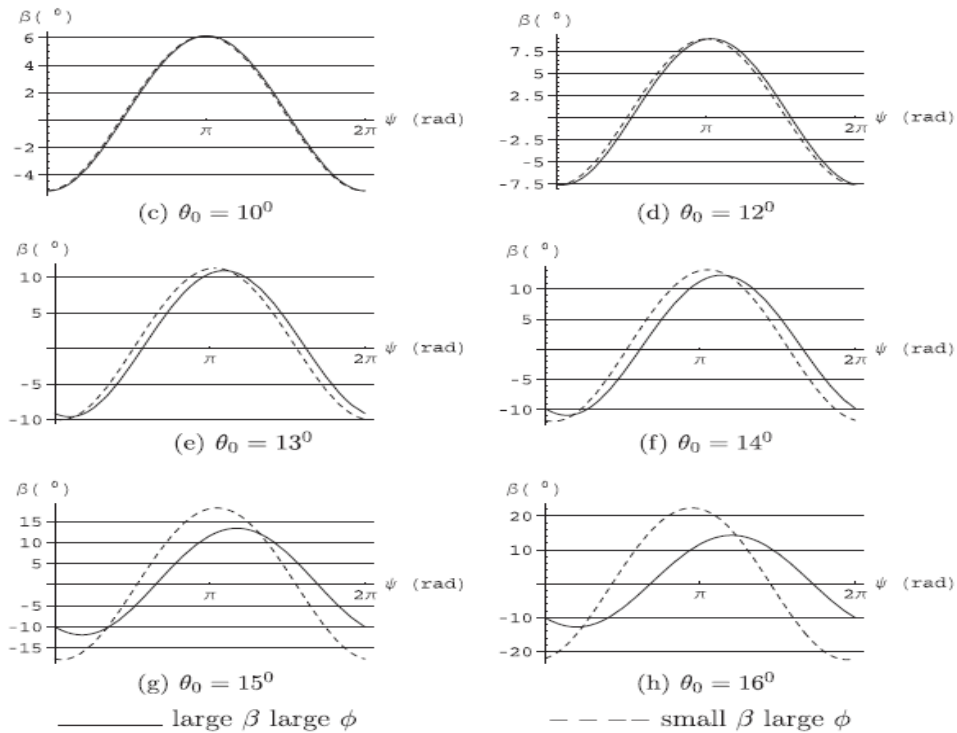


Fig 3.3: Variation of  $\phi$  with azimuth for collective pitch.

### 3.2.2 Induced inflow angle

In this the small flap angle approximation formulation is not always valid.  $\Phi$  is assumed to be large. The nature of the induced inflow angle that is whether it is really large or a small angle approximation can be made which reduces the mathematical complications involved in this study.

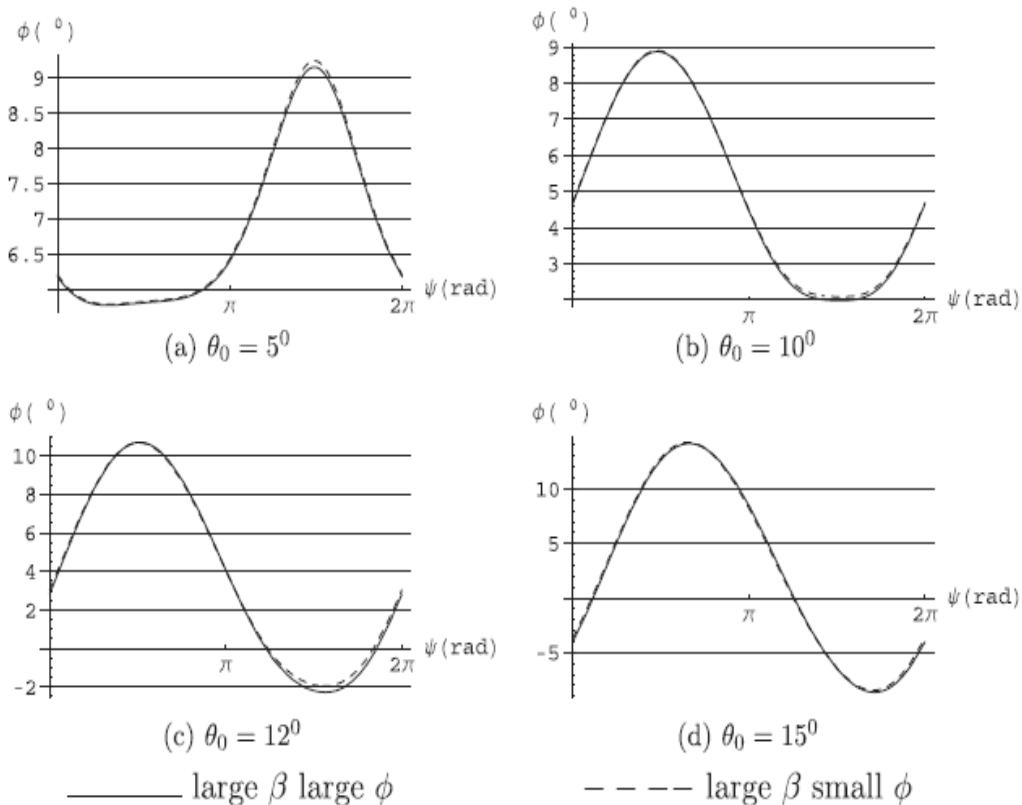


Fig 3.4: Variation of  $\phi$  with azimuth for  $\frac{c}{\sigma}=0.15$

#### IV. Conclusion

In this report, the basic concepts related to helicopter aerodynamics is described and studied. Details regarding airfoil, helicopter rotor, blade motions are known. A complete justification to the seminar topic “helicopter flapping under dynamic stall” is done. Flapping of helicopter blades and the effect of stall on the helicopter motion is discussed in detail. Dynamic stall is given the prime emphasis.

The conclusions assessed from the above Chapters are given below:

- There are three components of velocities:
  1. Radial component  $U_R$
  2. Tangential component  $U_T$
  3. Perpendicular component  $U_P$
  
- There are mainly three forces acting on an element:
  1. Inertia force (opposing the flapping motion)
  2. Centrifugal force (acting radially outwards)
  3. Aerodynamic force (normal to the blade)
  
- Blade element forces
  1. Lift (act perpendicular to direction of the flow velocity)
  2. Drag (act parallel to direction of the flow velocity)
  
- Rotating blades of helicopter mainly has three types of motions
  1. Blade flapping
  2. Blade feathering
  3. Lead and lag

Dissymmetry of lift in helicopter is compensated by the flapping of blades. It is better to assume that the flap angle  $\beta$  and inflow angle  $\phi$  are larger angles in helicopter dynamics. No flapping occurs when the tip path plane is perpendicular to the mast. A stall occurs at the critical angle of attack. At this point lift force suddenly reduces and the drag force increases. Dynamic stall occurs when airfoil rapidly changes the angle of attack. When dynamic stall occurs, the vortex containing high velocity airflows increase the lift, which further decrease after passing the trailing edge.

#### Acknowledgements

This is to acknowledge our indebtedness to our guide Mr. Ashok Chitharenjan, Assistant Professor, Department of Mechanical Engineering for his guidance and cooperation for preparing this report. We are highly thankful for his guidance and encouragement provided to us throughout the completion of the seminar. We express our sincere thanks to Dr. Jippu Jacob, Head of the Department of Mechanical Engineering for supporting us in the completion of this work. We also express our sincere gratitude to all the faculty members of Mechanical Engineering Department.

#### REFERENCES

##### Journal Papers:

- [1] Jyothi Ranjan Majhi, Rajan Ganguli, Helicopter blade flapping with and without small angle assumption in the presence of dynamic stall, *Applied Mathematical Modelling*, 2010, 3726-3740.
- [2] K. Mulleners, K. Kindler, M. Raffel J, *Dynamic stall on fully equipped helicopter model*, Aerospace science and technology 2009, 72-76.
- [3] Michael V. Luis Bernal, Chang-Kwon Kang, *Shallow and deep dynamic stall for flapping low Reynolds number airfoils* 2009, 833-901.

## Noval Method for Fabrication of 3-D Spacer Fabric Composite and Investigation of Mechanical Property

A. Vivek Anand<sup>1</sup>, G. Venkatesh<sup>2</sup>, P. Anand<sup>3</sup>

<sup>1, 2, 3</sup> Aeronautical Department, Bannari Amman Institute of Technology/ Anna University, India

**Abstract:** The paper deals with the fabrication and flexural property studies of 3D Spacer fabrics with three different stiffener height, i.e., 5mm, 10mm and 15mm. The specimens were fabricated over two bidirectional woven fabric surfaces of glass fiber reinforced composite face sheet which were mechanically connected with vertical threads. An innovative stitching technique was used. The flexural strength and deflection of fabricated specimens were determined through three point bending test (ASTM C 393-62). A significant increase in flexural rigidity was observed when it compared with other panels, and found it is highest for 3D Spacer fabric with stiffener height 3415mm. Also, the results proved that flexural strength of 3D Spacer fabric increases with respect to the height of the stiffener. Also the results were compared with simply glued sandwich composite of thickness 15mm and found a significant improvement in flexural strength of 3D spacer fabric composite compared to glued composite.

**Keywords:** Deflection, Elastic modulus, Flexural rigidity, Stitched core sandwich, 3-point bending

### I. INTRODUCTION

The concept of use spacer fabrics in composite sandwich structures was first devised in 1985 in both katholieke universiteit leuven (Belgium) and university of Stuttgart and MBB (Germany). Some researchers have evaluated drum- peel strength, flat-wise compressive strength and transverse shear modulus of the mono-spacer fabric composite panels. It was proved that the fabric composites featured a very high skin core debonding resistance and the pile played an important role on the flat wise compression and shear properties. 3D spacer fabric constructing is a newly developed concept. The fabric are strongly connected to each other by the vertical pile fibers which are interlinked with the skins.

In comparison with the face sheet reinforcement spacer fabric composite, here the composite without additional weaves is called monospacer fabric composite two kinds of mono-spacer composites with integrated hollow cores have been developed, one with 8-shaped piles and the other with corrugated piles. The mechanical characteristics and the damage modes of these mono-spacer fabric composites under different load conditions show considerable change in results. Besides, effects of pile distribution density and pile structure on the composite mechanical performances were different.[1]

Mechanical properties of 3-D spacer fabric, a new sandwich structure, developed by integrally woven technique composites have super-high specific strength and specific stiffness. Face sheet-reinforced 3-D spacer fabric composites were investigated experimentally by laminating additional glass weave at the skin sheets. Effects of various factors on the mechanical properties, such as the additional layer number, the type of glass weave, and the lay-up type were also discussed. Furthermore, an innovative integral multi-face sheet structure composite was developed by directly weaving three uniformly spaced factsheets' in one construction. The mechanical performance was compared with bonded multi-face sheet spacer fabric composite and mono-spacer fabric composite under the same conditions. The results indicated that additional weaves could strengthen the composite face sheets greatly, and the multi-face sheet structure could improve the properties correlated with the piles effectively.[2]

Compressive behaviors of 2-D basalt fiber laminated plain woven composite and 3D basalt fiber orthogonal woven composite were tested under various strain rates and compressive stress strain curves were obtained at various strain rates ranging. The compressive curves exhibited strong strain-rate sensitivity. Compression modulus and failure stress of the 2D woven composites are both greater than those of the 3D woven composite under the same strain rate. The main failure mode of the 2D woven composite is delamination both along in-plane direction and through thickness direction. As the impact velocity increases, the 2D woven composite will be in debris owing to the resin cracks, whereas for that the 3D orthogonal woven, there is no delamination between each layer because of the binds of Z-yarns. The 3D woven composites will also be in debris under high strain rate compression when the Z-yarns break.[3]

The characteristics of different spacer fabrics including low-stress mechanical properties, air permeability and thermal conductivity were investigated in three dimensional spacer. Low-stress mechanical properties obtained by the KES-fabric evaluation system revealed that all tensile, bending and compression properties of spacer fabrics are greatly depending on the type of spacer fabric, the type of spacer yarn used, the yarn count of the spacer yarn, the stitch density and the spacer yarn configuration. Air permeability and thermal conductivity of spacer fabric are closely related to the fabric density. This experimental work suggests that carefully selecting the spacer fabric according to the envisaged application is of primary importance.[4]

## II. MATERIALS AND EXPERIMENT

Three-dimensional sandwich composite is a newly developed sandwich structure, the reinforcement of which is integrally woven by advanced textile technique. Two face-sheets are connected by continuous fibers, named pile in the core, providing excellent properties like outstanding integrity, debonding resistance, lightweight, good design ability and so on. In this paper, specimens were fabricated with various stitching orientation with glass fiber reinforced face sheet and Divinycell core and compared with unstitched sandwich composite. Both the fabrication and testing methods are mentioned in following paragraph.

### 1. Preparation of 3D Spacer Fabric Composite Specimen

Divinycell closed-cell 'H' grade foam core (density = 80kg/m<sup>3</sup>, thickness = 10 mm) was used as the core material along with the woven open form glass fabric face sheets of 10 mils thickness. Panels with closed cell foam sandwiched between two layers of bi-directionally woven glass fabric on each side were put for fabrication. Newly developed fixture was used for stitching the sandwich panels with stiffener height 5mm, 10mm and 15mm as shown in Figure-1. The fixture consists of two wooden slots. The material has to be placed in between them. The rubber dampers had been used for to give additional stiffness for stitching. The Glass Yarn G37 1/5 3.8S was used for the stitching of the sandwich panels. A low viscous epoxy resin based on bisphenol constituent and modified with aromatic glycidyl ether called Araldite GY257 with hardner C2963 manufactured by Huntsman, Australia, was used for the fabrication of the panels. The resin and hardener was mixed in a proportion of 100:45 respectively. After stitching, the spacer fabric composites were prepared using the hand layup process. The specimens were allowed to pre cure for 24 hours at room temperature conditions at laboratory, and then kept for 7 days for post cure before taken out for experimental studies. The configuration of 3D spacer fabric composite specimen are shown in Fig. 2 and 3, respectively.

### 2. Tension Test

3D spacer fabrics were prepared and tested according to ASTM C297 to determine the tensile properties. The 3D spacer fabrics were cut such that the properties in the direction perpendicular to rise would be the direction of flexural stresses in the sandwich panel. The specimen had a 70 x 70 mm cross-section.. The tests were conducted in Universal Testing Machine with wedge-type mechanical grips and with a displacement rate of 0.5 mm/min at Microlab, Ambattur industrial estate, Chennai as shown in Fig. 4 The force - strike curves were obtained for each stiffener height as shown in Fig. 5, 6 & 7.

### 3. Flexural Test Procedure

The sandwich panels were tested in a 3-point bending test as per ASTM standard C393-63. The support span dimension  $a_1$  was calculated from equation 1.

$$a_1 = 2fF/S \quad (1)$$

The allowable facing stress F (182Mpa) for the E glass fabric was found out by 3-point bending test using ASTM D790M, f represents facing sheet thickness (0.4 mm). The allowable core shear stress S (1.15 Mpa) was taken from the manufacture's data sheet (24). The 3-point bending test was conducted. The theoretical flexural rigidity (D) value was found as shown in equation 3.

$$\delta = \frac{Pl^3}{48EI} \quad (3)$$

$$EI = \frac{Pl^3}{\delta 48} \quad (4)$$

Where  $P$  is the load,  $l$  is the length of the specimen,  $\delta$  is the deflection,  $E$  is the Young's modulus and  $I$  is the moment of inertia. Five specimens of each type of sandwich composite were tested in three point bending test and average results were presented in Table 1.

### III. RESULTS AND DISCUSSIONS

The flexural stiffness of sandwich composite is an essential determining factor for application of the material on design. Generally, the compositions of sandwich material have higher elastic modulus of face sheet compare to elastic modulus of face core. Here, it is approximately 243 times higher as observed from experiment. In addition, the thickness of the face sheet (i.e., only 0.4mm) is quite small compare to the thickness of core material (i.e., 10 mm). It has been observed that the 3D space fabric with stiffener height 15 mm has highest flexural rigidity compared to all other specimen tested.

### IV. FIGURES AND TABLES



Fig. 1



Fig. 2



Fig. 3



Fig. 4

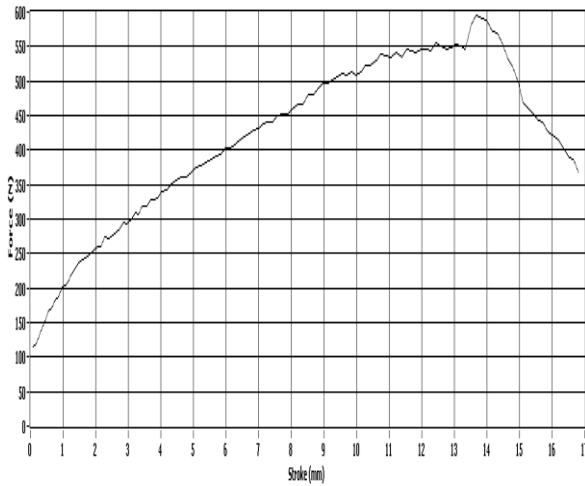


Fig. 5

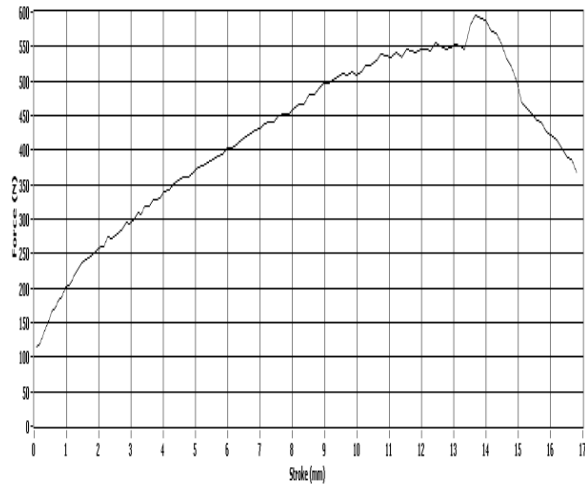


Fig. 6

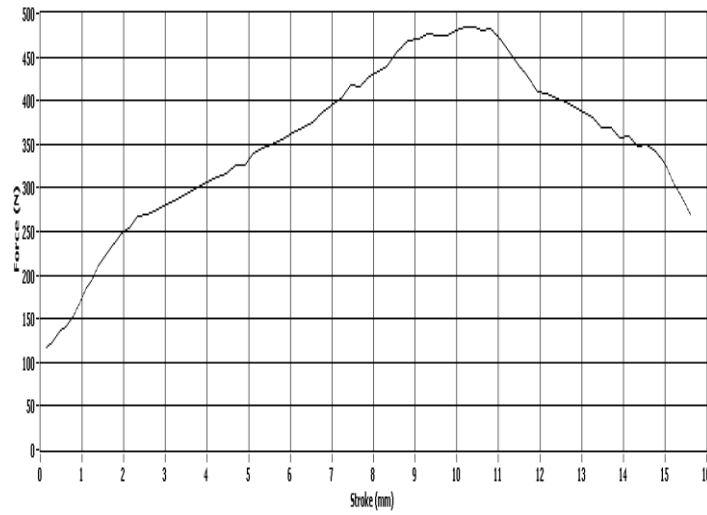


Fig. 7

Specimen	Length mm	Width Mm	Thickness Mm	C.S Area mm <sup>2</sup>	Flexural Rigidity (E*I) Nmm <sup>2</sup>
Stiffener height 5 mm	300	36	396	50	3645000
Stiffener height 10 mm	300	36	420	50	5062500
Stiffener height 15 mm	300	36	576	50	5315625
Sandwich with thickness 15mm	300	36	612	50	4339285

Table 1

## V. CONCLUSION

The present paper focused on the mechanical experimental characterization and numerical simulation of Divinycell closed - cell 'H' grade foam/glass fibre composite sandwich conceived as a lightweight material for various engineering applications. The experimental campaign confirmed the remarkable potentialities of the innovative sandwich structure with core and skins interconnected by transverse stitched plies. Based on the experimental and numerical analysis the following concluding remarks revealed.

1. If the thickness of the 3D spacer fabric increases the flexural rigidity of the specimen will also lead to increase.
2. The failure mode of the 3D spacer fabric composite has distinct into two different categories as the face sheets failed by compressive and tensile load whereas the core failure occurred due to shear failure.
3. The use of foam to fill the sandwich core appears to increase the sandwich stiffness and strength quite remarkably with respect to lighter but weaker solutions: at the same time it furnishes a drastic weight saving with respect to a fully laminated glass fibre reinforced plate.
4. As a main point of remark from the experimental studies, it emerges the considerable weakness of the sandwich extra-skins in real engineering applications could then be quite relevant this should be at least partially eliminated or reduced by improving the production technology on this specific aspect.

## REFERENCES

### Journal Papers:

- [1] Min Li, Shaoki Wang, Zuogang Zhang and Boming Wu, Effect of Structure on the Mechanical Behaviors of Three-Dimensional Spacer Fabric Composites, *Applied Composite Materials*, Volume 16, Issue 1, pp.1-14.
- [2] Shaokai Wang, Properties of face sheet reinforced 3-D spacer fabrics composite and the integral Multi-face sheet structures, Belgium, China.
- [3] Baozhong Sun, Zhilin Niu, Lvtao Zhu and Bohong Gu, Mechanical Behaviors of 2D and 3D Basalt Fiber Woven Composites Under various Strain Rates, Zhongyuan Institute of Technology, Henan Province, China.
- [4] Joanne Yip and Sun-Pui Ng, Study of Three Dimensional Spacer Fabrics Physical and Mechanical Properties, ACE Style Institute of Intimate Apparel, Institute of Textiles & Clothing, The Hong Kong Polytechnic University, Hong Kong.
- [5] Frisch-Fay R. 1962. *Flexible Bars*, Butterworth, Washington, DC, USA.
- [6] Gdoutos E.E., Daniel I.M., Wang K.A. and Abot J. L. Nonlinear Behavior of Composite Sandwich Beams in Three-point Bending, *Experimental Mechanics*. 41(2): 182-189.
- [7] Grediac M. and Dufort L, Experimental Evidence of Parasitic Effects in the Shear Test on sandwich Beams, *Experimental Mechanics*.186-193.
- [8] Johnny Jakobsen, Elena Bozhevolnaya, Ole T.Thomsen, New crack stopper concept for sandwich structure, Department of Mechanical Engineering, Aalborg University, Denmark
- [9] Technical data for Divinycell H grade. available from :<http://www.diabgroup.com>.
- [10] B. Lascoup, Z. Aboura, K. Khelli, M .Benzeggagh, J. Maquet, On the interest of stitched sandwich panel, *Dep GM - Polymères et Composites BP 20529 - 60205 Compiègne Cedex, France*.
- [11] Aaron Halvorsen, Amin Salehi- hojn, Mohammad Mahinfalah, Reza Nakhaei-Jazar, Temperature effects on the impact behaviour of fibre class and Fibre glass/Kevlar sandwich composite, *Applied Composite Materials* November 2006, Volume 13, Issue 6, pp 369-383.
- [12] Cemal Basaran, Shihua Nie and Clyde S. Hutchins, Time Dependent Behavior of a Particle Filled Composite PMMA/ATH at Elevated temperatures, DuPont Surfaces, Yerkes R&D Laboratory, Buffalo, New York, USA.
- [13] ASTM C 393-62. Standard test method for flexural properties of sandwich construction. ASTM International, PA, USA.

## Optimization of cutting tool material in lathe machine by T-test

Ivan Sunit Rout<sup>1</sup>, Sidhartha Sankar Padhi<sup>2</sup>, Jitendra Narayan Biswal<sup>3</sup>,  
Tushar Kanti Panda<sup>4</sup>

<sup>1,2,3,4</sup>(Assistant Professor, Department of Mechanical Engineering, C. V. Raman College of Engineering,  
Bhubaneswar, India)

**Abstract:** Modern manufacturers, seeking to remain competitive in the market, rely on their manufacturing engineers and production personnel to quickly and effectively set-up manufacturing processes for new products. T-test method is a powerful and efficient method for optimizing quality and performance output of a manufacturing process, thus a powerful tool for meeting this challenge. This paper discusses an investigation into the use of t-test method for optimizing controlled dia of workpiece in a lathe machine. Control parameters being considered in this paper are spindle speed, feed rate and depth of cut. After experimentally turning sample work pieces using the selected parameters, this investigation produced an optimum combination of controlled parameter for the cutting tool.

**Keywords:** Depth of cut, Dia of work, Feed rate, Spindle speed, T-test

### I. INTRODUCTION

In lathe machine, a cylindrical workpiece rotates along its axis and the tool removes material from the workpiece to form it into a specific shape. On metal working lathes, the cutting tools are held rigidly in a tool holder that is mounted on a movable platform called the carriage. The tool is moved in and out by means of hand cranks and back and forth either by hand cranking or under power from the lathe. The result is that material is removed from the workpiece under very precise control to produce shapes that are truly precision made. Because of the inherent rotational nature of a lathe, the vast majority of the work produced on it is basically cylindrical in form. Single point tools are used in turning, shaping, planning and similar operations, and remove material by means of one cutting edge. Cutting tools must be made harder than the material which is to be cut and the tool must be able to withstand the heat generated in the metal cutting process. Also the tool must have a specific geometry, with clearance angles designed so that the cutting edge can contact the workpiece without the rest of the tool dragging on the workpiece surface.

#### 1.1 Turning Process

Turning is a form of machining, a material removed process, which is used to create rotational parts by cutting away unwanted material. The turning process requires a turning machine or lathe, workpiece, fixture and cutting tool. The workpiece is a piece of preshaped material that is secured to the fixture, which itself is attached to the turning machine, and allowed to rotate at high speeds. The cutter is typically a single point cutting tool that is also secured in the machine. The cutting tool feeds into the rotating workpiece and cuts away material in the form of small chips to create the desired shape.

#### 1.2 Turning Machine

This machine typically referred to as lathe can be found in a variety of sizes and designs. While most lathes are horizontal turning machines, vertical machines are sometimes used, typically for large diameter workpieces. Turning machines can also be classified by the type of control that is offered. A manual lathe requires the operator to control the motion of the cutting tool during turning operation. Turning machines are also able to be computer controlled, in which case they are referred to as a computer numeric control (CNC) lathe. CNC lathes rotate the workpiece and move the cutting tool based on commands that are preprogrammed and offer very high precision. In this variety of turning machines, the main components that the workpiece to be rotated and the cutting tool to be fed into the workpiece remain the same.

#### 1.3 Turning Cutting Tool

All cutting tools that are used in turning can be found in a variety of materials, which will determine the tool's properties and the workpiece materials for which it is best suited. This properties include the tool's hardness, toughness and resistance to wear. The most common tools that are used include the following:

### **1.3.1 High Speed Steel**

These are so named primarily because of their ability to machine materials at high cutting speeds. These are complex iron-base alloys of carbon, chromium, vanadium, molybdenum, tungsten or combinations thereof, and in some cases substantial amounts of cobalt. The carbon and alloy contents are balanced at levels to give high attainable hardening response, high wear resistance, high resistance to the softening effect of heat, and good toughness for effective use in industrial cutting operations. The recognized standard high speed tool steel, which serves almost all applications under mild to severe metal cutting conditions.

### **1.3.2 Silicon Carbide**

This is also known as carborundum is a composed of silicon and carbon with chemical formula SiC. It occurs in nature as the extremely rare mineral moissanite. Silicon carbide powder has been mass-produced since 1983 for use as an abrasive. Grains of silicon carbide can be bonded together by sintering to form very hard ceramics which are widely used in applications requiring high endurance, such as car brakes, car clutches and ceramic plates in bulletproof vests. The high sublimation temperature of SiC (approximately 2700°C) makes it useful for bearings and furnace parts. Silicon carbide does not melt at any known pressure. It is also highly inert chemically. There is currently much interest in its use as a semiconductor material in electronics, where its high thermal conductivity, high electric field breakdown strength and high maximum current density make it more promising than silicon for high powered devices. SiC has a very low coefficient of thermal expansion ( $4.0 \times 10^{-6}$  K) and experiences no phase transitions that would cause discontinuities in thermal expansion.

### **1.3.3 Alloy Steel**

These are steels with alloying elements other than carbon and iron. When various alloying elements are added to steel, these usually become stronger and harder than plain carbon steels. As the alloy content increases slightly, then gradually ductility reduces and with a total alloy content of 2-4%, hardness of 250 HB and tensile strengths to 850 N/mm<sup>2</sup> are found. Alloy steels within this range are those which have been hardened and tempered to give enhanced tensile strengths. Also included are the highly alloyed tool steels in their annealed condition. Nickel-chrome alloy steels with a total alloy content of 3-4% can be heat treated to give various hardness and tensile strengths by tailoring the tempering temperature to give the desired balance between hardness and ductility. Alloy tool steels with high carbon levels and a total alloy content of more than 5% also fall into this grouping, provided they are in the fully annealed (softened) state.

## **1.4 Turning Material**

In turning, the raw form of the material is a piece of stock from which the workpieces are cut. This stock is available in a variety of shapes such as solid cylindrical bars and hollow tubes. Custom extrusions or existing parts such as castings or forgings are also sometimes used. Turning can be performed on a variety of materials, including most metals. Common materials that are used in turning include aluminium, brass, magnesium, nickel, steel, thermoplastics, titanium and zinc. When selecting a material, several factors must be considered, including the cost, strength, resistance to wear and machinability. The machinability of a material is difficult to quantify, but can be said to possess the following characteristics:

- Should result in a good surface finish.
- Promotes long tool life.
- Requires low force and power to turn.
- Provides easy collection of chips.

## **II. METHODOLOGY**

### **2.1 Stylus Instruments**

These instruments are based on the principle of running a probe across a surface in order to detect variations in height as a function of distance. One of the stylus instruments contains a transducer which converted vertical displacement into an electric signal. This signal can then be processed by the instrument electronics to calculate a suitable roughness parameter. This type of transducer used largely affects instrument performance. Piezoelectric crystal is often used as the transducer in the less expensive instruments. Other transducer mechanisms include moving coil transducers, capacitance transducers, and linear variable differential transducers. The resolution of a stylus instrument depends on its manufacturer and model.

## 2.2 Depth of Cut

The thickness of the material that is removed by one pass of the cutting tool over the workpiece. The depth of cut is the distance that a tool penetrates into the workpiece. It is calculated by

$$\text{DOC} = \frac{D_1 - D_2}{2}$$

Where  $D_1$  = initial dia of work

$D_2$  = final dia of work

## 2.3 Tool Wear

It is one of the critical factors in machining process, affecting cost and productivity. The research on tool wear has improved the understanding of wear mechanisms for different work and tool materials in various machining operations. Machining is carried out under chatter conditions owing to very low dynamic rigidity of the machining system. This means that, in order to reduce the cycle time material removal rates higher than the stable limits are used. Tool wear includes:

- Flank wear in which portion of the tool in contact with the finished part erodes, can be described using the tool-life expectancy.
- Crater wear in which contact with chips erodes the rake face. This is somewhat normal for tool wear, and does not seriously degrade the use of a tool until it becomes serious enough to cause a cutting edge failure.

## 2.4 T-Test

A t-test is a statistical hypothesis test in which the test static follows a student's t-distribution if the null hypothesis is supported. It can be used to determine if two sets of data are significantly different from each other, and is most commonly applied when the test static would follow a normal distribution if the value of a scaling term in the test static were known. When the scaling term is unknown and is replaced by an estimate based on the data, the test static follows a student's t-distribution. A statistical test involving means of normal populations with unknown standard deviations; small samples are used, based on a variable t equal to the difference between the mean of the sample and the mean of the population divided by a result obtained by dividing the standard deviation of the sample by the square root of the number of individuals in the sample. A normal distribution plays a prominent role in tests of hypothesis that involve the mean of a population. In particular, if a random sample of observations is normally distributed, statistical inferences for the sample mean can be made by constructing a Z-test statistic that follows a standard normal distribution. However, the use of this statistic requires knowledge of the true variance of population from which the observations were sampled.

$$t \text{ value} = (\text{Difference between the group means}) / (\text{Variability of the groups})$$

The higher the denominator, the lower will be the t value. The lower the t value, the less likely it is that the two means are different. The means are considered different if the t value is greater than the critical t value. It is the t value comparison with the critical t value that determines whether there really is a difference between the means. The t value's numerator and denominator are calculated in different ways for the different types of t tests. The t test has a number of variations but the most common t test is used to determine whether the means of two normally distributed populations are equal.

## III. RESULTS AND DISCUSSION

It is seen that the work dia is maximum in high speed steel when rake angle is  $2^\circ$  and minimum in silicon carbide. Hence it is known that material removal rate is higher in silicon carbide than other materials due to which work dia is less in silicon carbide but in high speed steel work dia is more as high speed steel requires greater rake angle nevertheless tool wear occurs.

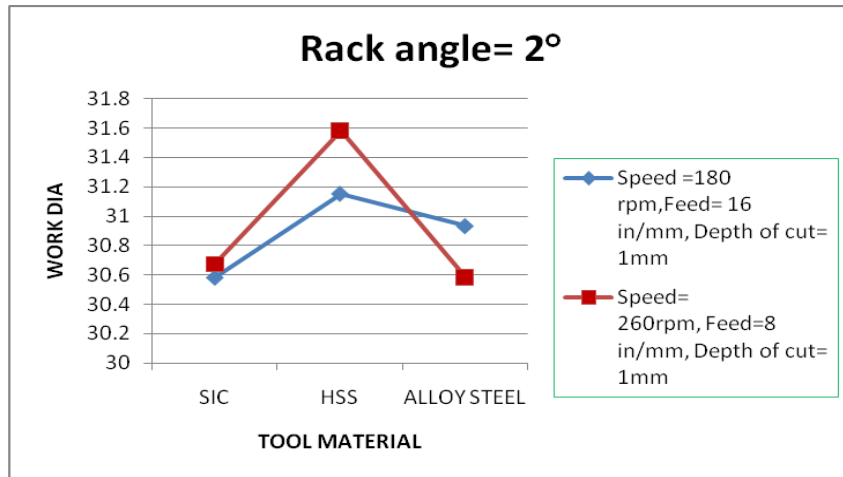


Fig 1: Effect of tool impact with rake angle=2° on work dia

It is seen that when rake angle is 10° work dia is maximum in HSS when speed is 180 rpm and maximum in SiC when speed is 260 rpm. It might be due to the fact that due to high thermal conductivity in SiC tool wear occurred due to which the work dia became more.

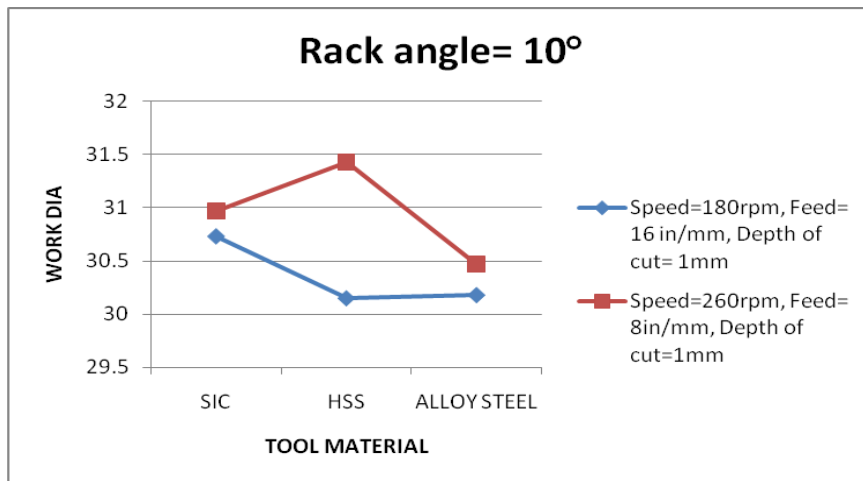


Fig2: Effect of tool impact with rake angle=10° on work dia

It is seen that when rake angle is 18° work dia is maximum in alloy steel and minimum in high speed steel. This is due to the machining speed of HSS greater material removal rate takes place and alloy steel tool wear occurred due to which work dia became more.

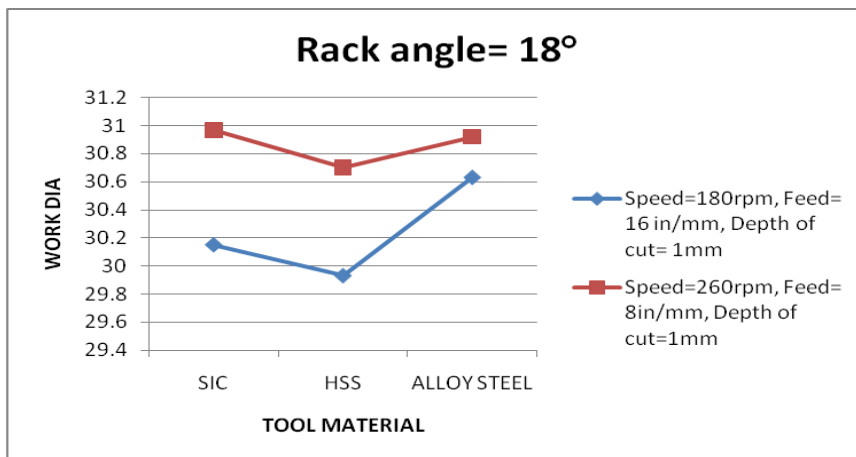


Fig 3: Effect of tool impact with rake angle=18° on work dia

The probability shows that silicon carbide tool is the best and optimum tool material in comparison to high speed steel and alloy steel on the basis of tool wear at different spindle speeds, feed rate and rake angle of the cutting tool. This graph also predicts that silicon carbide has a prolonged tool life than HSS and alloy steel for which accurate depth of cut and material removal rate to the extent is achieved.

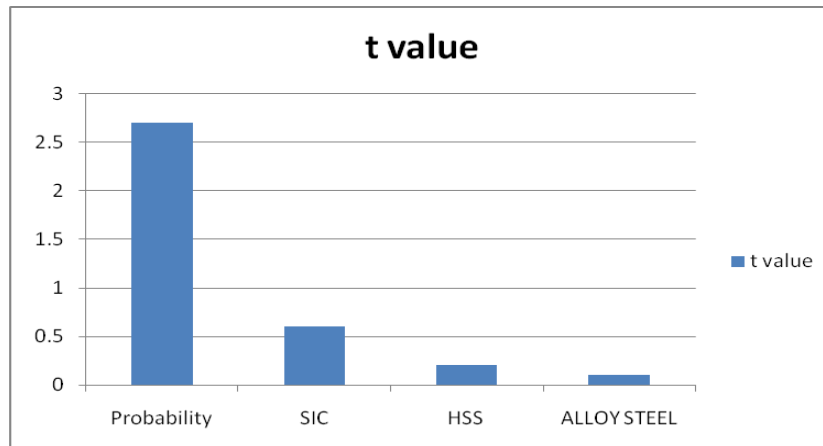


Fig 4: Comparison of probability used on t test with the effect of variation in work dia

#### IV. CONCLUSION

The t-test conducted for the cutting tool showed that silicon carbide produced optimum material removal rate on the mild steel workpiece due to its toughness and anti-corrosion property than high speed and alloy tool steels. The t-test conducted for the cutting tool also showed that silicon carbide has the least tool wear after performing the operation on the mild steel workpiece since it is hard and has better wear resistance than high speed and alloy tool steels.

#### REFERENCES

- [1] Z.Q.Liu, X.Ai, H.Zhang, Z.T.Wang and Y.Wan, Wear patterns and mechanisms of cutting tools in high speed face milling, Journal of Material processing technology, 129,2002, 222-226
- [2] Nexhat Qehaja, Hakif Zeqiri, Hysni Osmani, Jorgaq Kacani and Fitim Zeqiri, Comparative analysis of metal cutting tools reliability during processing by turning in laboratory conditions and exploitation, 14<sup>th</sup> International Research/Expert Conference on trends in the development of machinery and associated technology, Mediterranean Cruise, 2010, 677-680.
- [3] Noemia Gomes de Mattos de Mesquita, Jose Eduardo Ferreira de Oliveira and Arimatea Quaresma Ferraz, Life prediction of cutting tool by the workpiece cutting condition, Advanced Material Research, 223, 2011, 554-563.
- [4] Predrag Basic, Analysis of wear cutting conditions by complex power exponential function for finishing turning of the hardened steel 20CrMo5 by mixed ceramic tools, The Annals of University "Dunarea De Jos" of Galati, Fascicle VIII, 2006 (XII).
- [5] P.N.Rao, Manufacturing Technology Volume 2 Metal cutting and Machine Tools (Tata McGraw Hill Education Private Limited, 2009)
- [6] Amitabha Ghosh and Asok Kumar Mallik, Manufacturing Science (East west Press private limited, 2010)
- [7] P.C.Sharma, A textbook of production technology (Manufacturing processes) (S. Chand and Company Ltd, 2008)
- [8] P.C.Sharma, A textbook of production engineering (S.Chand and Company Ltd, 2012)
- [9] K.B.Ahsan, A.M.Mazid, R.E.Clegg and G.K.H.Pang, Study on carbide cutting tool life using various cutting speeds for  $\alpha$ - $\beta$  Ti-alloy machining, Journal of achievements in materials and manufacturing engineering,55(2),2012, 600-606.
- [10] M.Narasimha, K.Sridhar, R.Reji Kumar and Achamyelah Aemro Kassie, Improving cutting tool life a review, International journal of engineering research and development, 7(1), 2013, 67-75.

## “Performance Analysis of 4 Stroke Single Cylinder Diesel Engine Using Blend Of Soya Oil with Diesel”

Prof. C. S. Koli<sup>1</sup>, Arvind Pathak<sup>2</sup>, Prof. Sanjay Bhatele<sup>3</sup>

<sup>1,3</sup>Asst. Prof. Mech. Engg. Deptt. SRCEM, Banmore

<sup>2</sup>Research Scholar, Mech.Engg. Deptt. SRCEM, Banmore

**Abstract:** In current scenario, there are continuously increasing the number of automobiles and correspondingly increasing the fuel consumption as well as fuel prices. In this regard, biodiesel is found as an alternative fuel derived from natural fats or vegetable oils and it is considered as an attractive alternative to replace diesel fuel.

In this work, biodiesel prepared from soya oil by Transesterification process with methyl alcohol. Processed soya oil is blended with diesel in different proportions as B-10, B-20, B-30, B-40 and B-50. Thermodynamic analysis of 4stroke single cylinder diesel engine, By using different blends of diesel & soya oil has been carried out the effect of B-10,B-20,B-30,B-40,B-50 on the Brake Power, Thermal Efficiency, Brake Specific Fuel Consumption and Total Fuel Consumption has been absorbed. The experimental result shows that at B-40, the optimum BTE (12.09), maximum BP (1.221) and minimum BSFC (0.694).

**Key word:** Soybean oil, Transesterification Process, 4-stroke Diesel engine, Biodiesel Blends.

### I. Introduction

#### 1.1 Background

The idea of using vegetable oil as fuel for diesel engines is not a new one. Rudolph Diesel used peanut oil as fuel in his engine at Paris Exposition of 1900<sup>[4]</sup>. In spite of the technical feasibility, vegetable oil as fuel could not get acceptance, as it was more expensive than petroleum fuels. Later various factors as stated earlier, renewed the interests of researchers in using vegetable oil as substitute fuel for diesel engines. In recent years, systematic efforts have been made by several researchers to use vegetable oils of Sunflower, Peanut, Soyabean, Rapeseed, Olive, Cottonseed, Jatropha, Pongamia, Rubber seed, Jojoba etc as alternate fuel for diesel. Many types of vegetable oils are edible in nature. Continuous use of them causes shortage of food supply and proves far expensive to be used as fuel at present. So far few types of non-edible vegetable oils have been tried on diesel engine leaving a lot of scope in this area. Testing of diesel engines with preheating, blending with diesel and blending with preheating improves the performance and reduces the emissions compared to neat vegetable oil [1].

Biodiesel is produced by Transesterification of oil, where one mole of oil is chemically reacted with three moles of an alcohol in presence of a catalyst. In this reversible reaction, the glycerol moiety of the triglyceride molecule is replaced with an alkali radical of the alcohol used, giving alkyl based monoesters.

Biodiesel has others advantages, compared to conventional diesel fuel, such as: portability, ready availability, renewability, biodegradability, lower sulphur content, higher cetane number, flash point, cloud point and cold filter plugging point<sup>[15]</sup>. Since biodiesel comes from a renewable energy source, its production and use as a replacement for fossil fuel provides three main benefits: reduces economic dependence on petroleum oil; decreases gas emissions that cause the greenhouse effect; and diminishes the proliferation of diseases caused by the pollution of the environment<sup>[3]</sup>.

To ascertain the possibility of use of modified karanja oil as fuel for compression ignition engine the performance test were conducted. The comparison of the test fuels made with diesel fuel. Test fuels' performance analyzed for esters of karanja oil, blends of karanja oil, and the diesel oil as baseline at varying loads performed at governor controlled speed. The variations in the injection parameters were analyzed to observe its influence on the engine performance with different fuels [7]. Results show that diesel engine gives poor performance at lower Injection Pressure than, esterified karanja oil and its blends with diesel. Specific energy consumption is a more reliable parameter for comparison. A comparison of physical and fuel properties of vegetable oils with those of diesel fuel indicates that the vegetable oil are quite similar in nature to diesel fuel. However, vegetable oils have exceptionally high viscosity. After esterification of karanja oil, the specific gravity reduced to 0.895 at 280°C and for diesel at the same temperature was 0.84. The calorific value of esterified

karanja oil found to be 36.76 MJ/kg, which is 17.95% lower than that of diesel. The specific Energy consumption is higher for pure karanja methyl ester as well as for its blends with diesel [5].

## 1.2 Objectives

The aim of this work is to evaluate the performance using different blends of biodiesel with pure diesel in a CI engine. The biodiesel is treated from the soyabean oil by Transesterification process. The following are the major objectives to fulfil the aim of this work.

1. Extraction of soya oil from soya seeds.
2. Determination of physical properties of soya oil and diesel.
3. Study of effect of dilution on properties of blending of soya oil with diesel.
4. Performance evaluation of Diesel engine using different blends of soya oil with diesel.

## 1.3 Biodiesel

Biodiesel is a non-petroleum based diesel fuel which consists of the mono alkyl esters of long Chain fatty acids derived from renewable lipid sources. Biodiesel is typically produced through the reaction of a vegetable oil or animal fat with methanol in the presence of a catalyst to yield glycerine and biodiesel (chemically called methyl esters). Biodiesel is registered with the US Environmental Protection Agency as a pure fuel or as a fuel additive and is a legal fuel for commerce. Biodiesel is an alternative fuel which can be used in neat form, or blended with petroleum diesel for use in compression ignition (diesel) engines. Its physical and chemical properties as it relates to operation of diesel engines are similar to petroleum based diesel fuel. The specification for biodiesel is approved by the American Standards for Testing and Materials (ASTM) under code number 6751.

Biodiesel is a domestically produced, renewable fuel that can be manufactured from new and used vegetable oils, animal fats, and recycled restaurant grease. Biodiesel's physical properties are similar to those of petroleum diesel, but the fuel significantly reduces greenhouse gas emissions and toxic air pollutants. It is a biodegradable and cleaner-burning alternative to petroleum diesel.

## II. Literature Review

S. KIRANKUMAR [1] have presented an experimental investigates of the bio-diesel preparation from vegetable oil i.e. Soya oil by using the Trans esterification process. In the initial stage tests are to be conducted on the four stroke single cylinder direct ignition diesel engine and base line data is generated. Further in second stage the test was conducted on the same engine at same operating parameters by using the diesel blended with the soy esters with different blending ratios such as S10, S20, S30 and the performance parameters (Brake Thermal Efficiency, Brake Specific Fuel Consumption) and also emission parameters (CO, HC, NO<sub>x</sub>, CO<sub>2</sub>, unused oxygen and smoke density) are evaluated. Among all the blends S30 has shown the better performance in the parameters and also in the emissions. So S30 is taken as the optimum blend. Finally the performance and emission parameters obtained by the above test are compared with the base line data obtained earlier by using diesel.

Jiantong Song al.[2] have investigated the power and fuel economies performances of a diesel fuelled with soybean biodiesel Experimental results show that, compared with diesel fuel, with increase in the biodiesel in the blends, the brake power and torque and the brake specific energy consumption increase, the smoke density under free acceleration decreases except B10, the NO<sub>x</sub> emissions increase. The trade-off relationship is clear between the NO<sub>x</sub> and smoke densities when the diesel engine fuelled with different biodiesel percentage in the blends. From the trade-off relationship between NO<sub>x</sub> and smoke density, the optimum blend ratio is B20 in the experimental study.

K. Dilip Kumar. al. [3] have of the engine performance and exhaust emission characteristics for various blends. Experiment set up was developed to carryout engine performance and emission characteristic studies on selected fuel blends at different load conditions. The present work has resulted in giving a good insight into the performance and emission characteristics of the C.I. engine using ethanol, biodiesel, diesel fuel blends. As fuel property point of view density and pour point of all the fuel blends are under the standard limits for diesel fuel. Heat of combustion of all blends is found to be lower than that of diesel fuel alone. D70B20E10 give lower CO and HC emission and slightly higher thermal efficiency than other blends

### III. Experimentation

#### 3.1 Transesterification

Trans-esterification also called alcoholysis is the displacement of alcohol from an ester by another alcohol in a process similar to hydrolysis. This process has been widely used to reduce the viscosity of triglycerides. The transesterification reaction is represented by the general equation, which is the key reaction for bio-diesel production.



If methanol is used in the above reaction, it is termed methanolysis. The reaction of triglyceride with methanol is represented by the general equation.

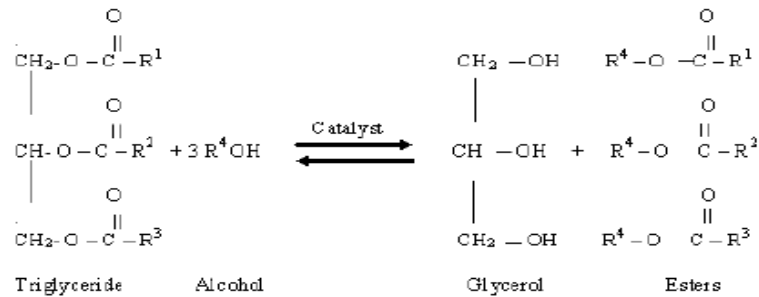


Fig.1 Flow diagram of preparation of bio-diesel

#### 3.2 Contents of Biodiesel

- NaOH 150ml
- Methanol 250ml
- Soabean oil 1 lit.

#### 3.3 Preparation of Bio-Diesel from Soya Oil

For the trans-esterification of mustard oil, Dr. Peeper's style has been followed in our work. First 250ml (90% pure) methanol was mixed with 150ml NaOH. This mixture was swirled in a glass container until NaOH is fully dissolved in methanol. As this is an exothermic reaction, so the mixture would get hot. This solution is known as methoxide, which is a powerful corrosive base and is harmful for human skin. So, safety precautions should be taken to avoid skin contamination during methoxide producing. Next, methoxide was added with I liter of mustard oil, which was preheated about 55 degree Celsius. Then the mixture was jerked for 5 minutes in a glass container. After that, the mixture was left for 24 hours for the separation of glycerol and ester. This mixture then gradually settles down in two distinctive layers. The upper more transparent layer is 100% bio-diesel and the lower concentrated layer is glycerol. The heavier layer is then removed either by gravity separation or with a centrifuge. In some cases if the soyabean oil contains impurities, then a thin white layer is formed in between the two layers. This thin layer composes soap and other impurities.



Figure1: crop of Soya Bean

### 3.4 Specification of Test Rig

**1. ENGINE-**The engine is water cooled single cylinder four stroke constant speed diesel engine 5 HP Make Kirloskar.



Figure 2: Engine

**Table3.4.1: Engine Specifications**

Sr. no.	Items	Specifications
1	Model	KIRLOSKAR, AV1
2	Compression ratio	19:1
3	Method of starting	Hand starting
4	Type, no. of cylinders	Vertical – 4 stroke, 1 cylinder
5	Bore x stroke(mm)	87.5x110
6	Cubic capacity	624
7	Maximum power	5 Hp
8	Nominal speed	1500 rpm
9	Cooling system	Water-cooled
10	Fuel filter	Present
11	Lube oil filter	Present

**2. Rope Brake Dynamometer-**A rope brake dynamometer is supplied with the engine coupled with the flywheel of engine.

**3. Load indicator-**It indicates the load in kg range 0-20 kg Make Harrison.

**4. M.S. Base Frame-**The engine and the dynamometer are mounted on a solid M.S. Channel Base Frame.

**5. Instrumentation for measuring various inputs/outputs-** All instrumentation is incorporated on a control panel. The various factors to be measured are as follows:

**(a) Fuel measurement:** This is done by using burette mounted on the control panel. The fuel tank is mounted on panel. The fuel is supplied to engine using fuel line to fuel injection system. The amount of fuel consumed is determined by the change in the readings shown on the burette. A three –way cock is used both to fill the burette and to allow the fuel to flow to the engine.

**(b) Air flow measurement:** Air flow is measured using an air box Orifice fixed in the inlet of air box. Suction pressure difference across the orifice is read on the U-tube manometer mounted on the panel. The outlet of the air suction box goes to the engine through the flexible hose for air suction.

**(c) Temperature measurement:** For heat balance analysis the PT-100 sensors are connected at exhaust gas calorimeter and engine cooling.

**(d) Tachometer:** It is measured the RPM of crank shaft



Figure 3: Tachometer

**(e) Pensky Martins:** This is used for measuring the flash point of biodiesel



Figure 4: Pensky Martins

**(f) Stopwatch:** It is used to measure the time when fuel is consumed in the engine



Figure 5: Stopwatch

(f) **Pycnometer:** It is used to measure the density of biodiesel & different blends



Figure 6: Pycnometer

### 3.5 Testing and inspection of experiment setup

After settling all the instruments, observation is about to start but before starting any experiment on the setup it is very necessary to inspect all the places where care should be taken to avoid any danger during the observation process. The step of inspection of experiment setup is completed by checking all the important places of experiment setup in a regular time interval during whole process of taking observation. The way of inspection is described here.

- a. Tightening all nuts on foundation structure coupled with engine frame.
- b. Checking the level of oil in the tank to maintain proper level of oil on burette.
- c. Checking the level of cooling water in water jacket.
- d. Checking the leak points of oil in various gate valves where pipes are connected
- e. Insure all switches kept off in electrical load panel before starting the engine.
- f. Check and control speed of engine by adjusting the fuel supply before taking the observation.

### 3.6 Measurement of required variables in different locations-

#### 3.6.1 Measurement of fuel consumption

Experiment starts from first step of measurement of fuel consumption by filling the fuel in the burette. As the fuel is filled in the burette time is started in the stop watch from 0 to 20 ml fuel consumed in the burette. In this way fuel consumption in terms of ml/sec is noted from no load to maximum load (2 to 10 Kg). Same process is repeated for number of observations taken at different load condition.

#### 3.6.2 Measurement of engine shaft speed-

Speed of the engine is measured in terms shaft speed as RPM (Revolution per minute). In the experiment speed of flywheel is measured which is mounted on crank shaft. For measuring the speed of flywheel a digital tachometer is used which is directly subjected to the rotating flywheel. A small reflecting strip is attached to outer side of the flywheel which reflects red rays coming from digital tachometer and counts the number of revolutions per minute of the flywheel. Hence the speed of crank shaft is estimated.

#### Abbreviations:

- T<sub>1</sub>=Exhaust gas temperature at inlet of the calorimeter  
T<sub>2</sub>=Exhaust gas temperature at outlet of the calorimeter  
T<sub>3</sub>=Temperature of water at the inlet of calorimeter  
T<sub>4</sub>=Temperature of water at the outlet of calorimeter  
T<sub>5</sub>=Temperature of water at the inlet of engine housing  
T<sub>6</sub>=Temperature of water at the outlet of engine housing

#### IV. Calculation

The basic performance parameters that were determined for performance evaluation of engine are:

- Brake Power
- Brake thermal efficiency
- Brake specific fuel consumption
- Total fuel consumption

Various formulae that were used for performance evaluation are listed below:

The brake power is calculated by measuring load on dynamometer and engine speed and then putting these values in,

$$BP = \frac{(W-s) \times \pi (D+d) N}{60 \times 1000} \text{ KW} \text{----- (i)}$$

Where,

D =Dia. of drum = 340mm

d =Dia. of rope = 20mm

W =Weight applied on spring balance

(W-S) =Net load reading

N =rpm of Crank Shaft

C.V. of diesel = 44000kJ/Kg<sup>[1]</sup>

C.V. of Biodiesel = 38400 kJ/Kg<sup>[1]</sup>

The fuel consumption rate is noted for each loading and then brake specific fuel consumption is calculated as,

$$BSFC = \frac{TFC}{BP} \times 3600 \text{ kg/kw-hr} \text{ ---- (ii)}$$

The brake thermal efficiency of the engine is calculated as,

$$BTE = \frac{BP}{TFC \times CV} \times 100 \text{ ----- (iii)}$$

Total fuel consumption,

$$TFC = \frac{cc(ml)}{time} \times \frac{(specificgravity) kg}{1000} / sec \text{ ---- (iv)}$$

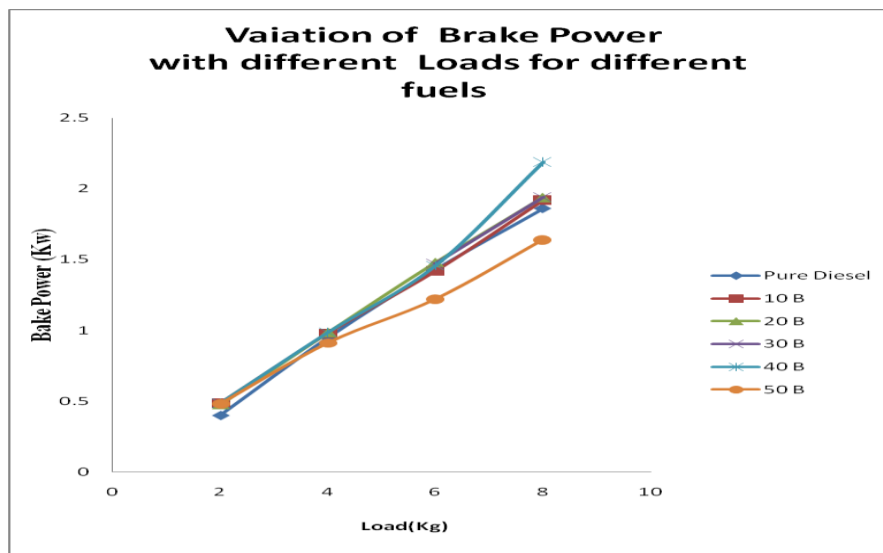


Figure 4.1: Variation of Brake Power with Different loads for different fuels

**FIGURE 4.1,** Depicts the variation in BP with Different loads for different blends. From the curve it is observed the BP is increasing from B10 to B40, after that as blending ratio increases, decrease in the BP, So that the maximum BP achieved at B 40.

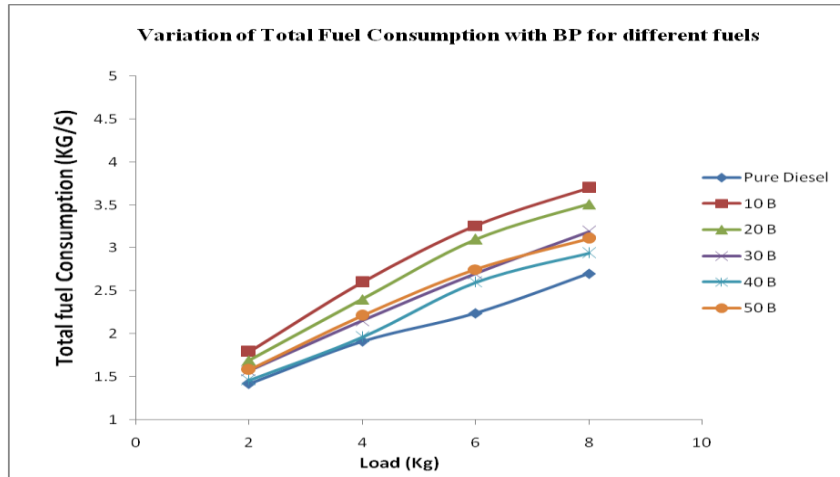


Figure 4.2: Variation of Total Fuel Consumption with different loads for different blends

**FIGURE 4.2,** Depicts the variation in total fuel consumption with different loads for different blends. From the curve it is observed that Total Fuel Consumption decreases from B10 to B40, after that as blending ratio increases, increase in the total fuel consumption.

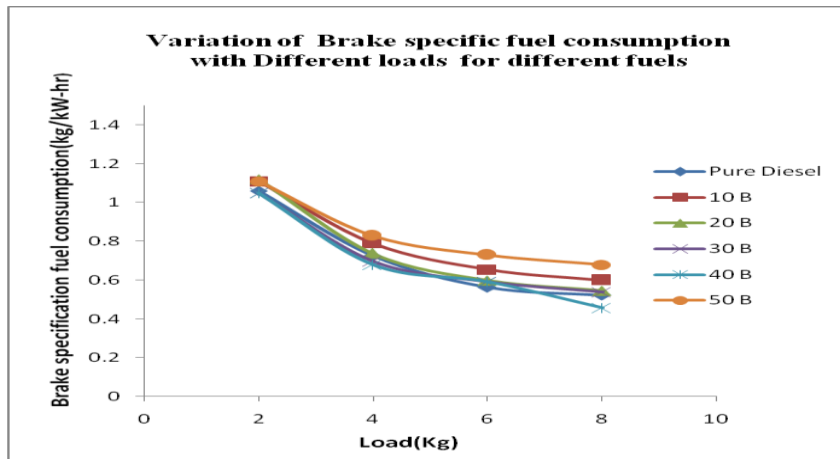


Figure 4.3: Variation of Brake specific fuel consumption with Different loads for different fuels

**FIGURE 4.3,** Depicts the variation in Brake specific fuel consumption with Different loads for different fuels. From the curve it is observed that the Brake specific fuel consumption decreases from B10 to B40, after that as the blending ratio increases, increase in the Brake specific fuel consumption.

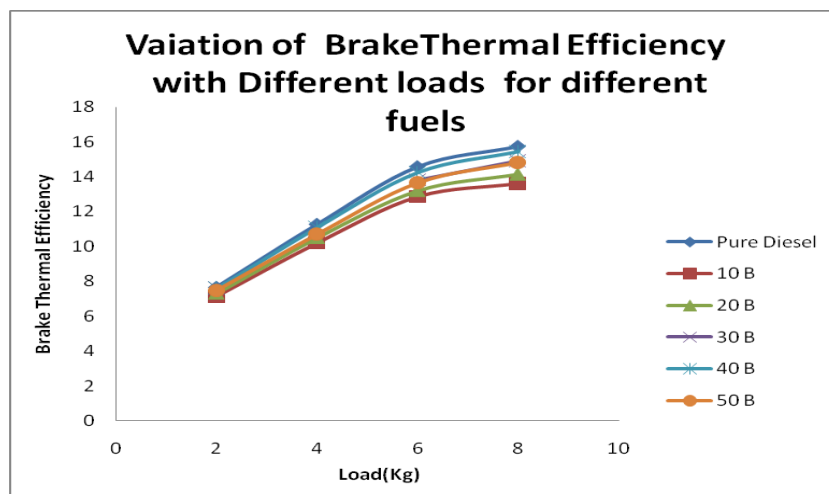


Figure 4.4: Variation of Brake Thermal Efficiency with Different loads for different fuels

**FIGURE 4.4,** Depicts the variation in Brake thermal efficiency with Different loads for different fuels. From the curve it is observed that the Brake thermal efficiency increases from B10 to B40, after that as blending ratio increases, decrease in the Brake thermal efficiency.

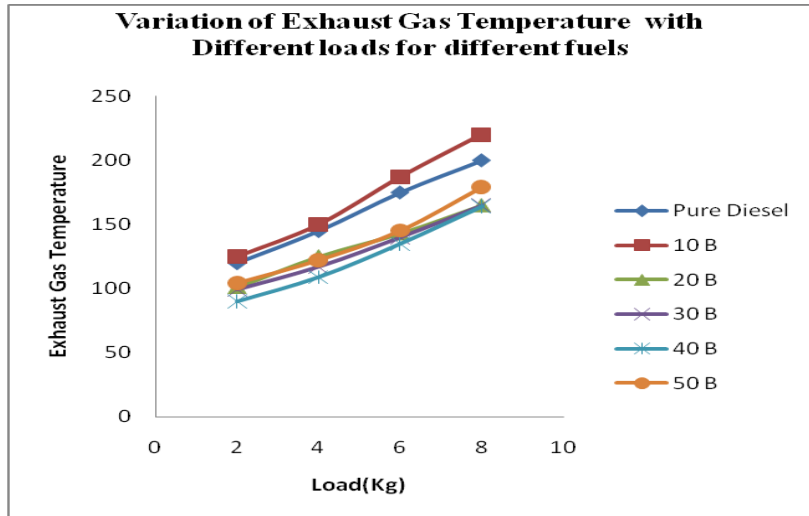


Figure 4.5: Variation of Exhaust gas temperature with Different loads for different Blends

**FIGURE 4.5,** Depicts the variation in Exhaust gas temperature with Different loads for different fuels. From the curve it is observed that the Exhaust gas temperature decreases from B10 to B40, after that as blending ratio increases, increase in the Exhaust gas temperature.

#### 4.1 Performance Analysis

**Table 4.1.1: Performance Analysis for calorific values of different composition of blends**

Vegetable oil Blend	Calorific Value (KJ/kg)
Pure Diesel	44000
10 B	38400
20 B	40890
30 B	40480
40 B	39970
50 B	39540

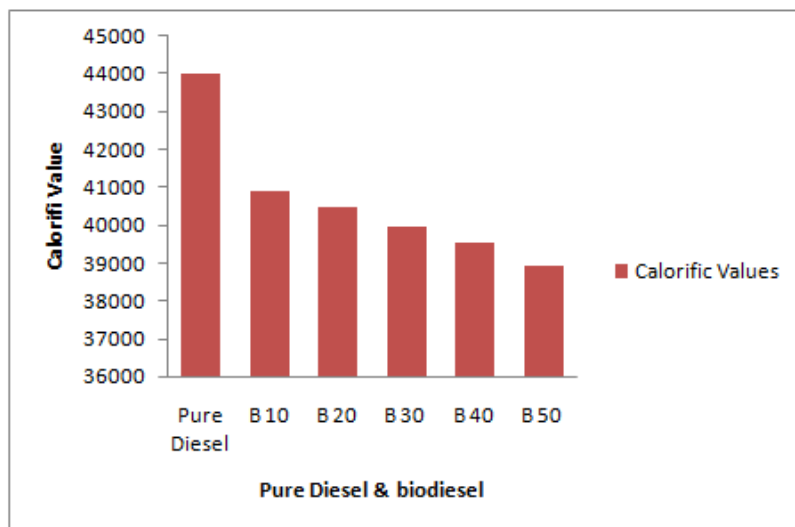


Figure 4.6 Graphical representation of Calorific value of different fuel

## **RUNNING COST OF ENGINE WITH DIFFERENT BLENDS**

<b>Fuel</b>	<b>Cost (Rs./lr.)</b>
Diesel	63.01
Biodiesel	70.22
B10	63.7
B20	64.4
B30	65.1
B40	65.8
B50	65.5

### **V. Conclusion**

Biodiesel is an alternating fuel, currently available in tremendous amount in the form of human producible domestic natural sources. There are many edible oils, such as palm oil, Ghee, neem oil, castor, sunflower oil, coconut oil, mustered oil and soya bean oil etc. These varieties of bio lipids can be used to produce biodiesel. These types of alternative source of energy can help in future as a working fluid for conversion of energy.

In the above experimental work different blends of soya bean transesterified oil (TES) with diesel such as B10, B20, B30, B40 and B50 used as an alternative fuel and investigated different performance parameters such as Brake Thermal Efficiency (BTE), Brake Power (BP), Total Fuel Consumption (TFC) and Brake Specific Fuel consumption (BSFC) at different loads. From the first set of results it can be concluded that the blend B40 has given the performance near to diesel in the sense of brake thermal efficiency, brake specific fuel consumption, Brake Power and Total fuel consumption. Conclusions extracted from the investigation are as follows:-

- Soya bean oil is transesterified in the presence of methyl alcohol. By this process physical property of soya oil has been changed as in table no.
- It has been observed that Brake Power increases from B10 to B40, further increase in blend ratio, decreases the BP. So that the maximum BP achieved at B 40.
- It has been observed that Total Fuel Consumption decreases from B10 to B40, further increase in blend ratio, increases the total fuel consumption. So that minimum TFC achieved at B40.
- It has been observed that the Brake specific fuel consumption decreases from B10 to B40, further increase in blend ratio, increases the BSFC. So that minimum BSFC achieved at B40.
- It has been observed that brake thermal efficiency increases from B10 to B 40, further increase in blend ratio, decreases the BTE. So that the maximum BTE achieved at B40.
- It has been observed that exhaust gas temperature decreases from B10 to B 40, further increase in blend ratio, increases the exhaust gas temperature which is lower than the diesel exhaust gas temperature. This concluded that the TES at B40 giving less emission in the environment as compared to Diesel.

### **REFERENCES**

- [1] S. Kirankumar Jan 2014 "Performance, Combustion Characteristics Of Diesel Engine By Using Soy-biodiesel" International Journal of Mechanical Engineering (IJME) ISSN(P): 2319-2240; ISSN(E): 2319-2259 Vol. 3, Issue 1, 25-34 © IASET.
- [2] Sunilkumar R. Kumbharet. al. March 2014 "Performance Analysis Of single Cylinder Diesel Engine, Using Diesel Blended with Thumba Oil" International Journal of Soft Computing and Engineering (IJSCE) ISSN: 2231-2307, Volume-4, Issue-1.
- [3] A.F.Sherwani et. al 2013 "Experimental Study On The Performance And Emission characteristics of a Four Stroke Diesel Engine running With MahuaOilethyl Esterk" Special Issue of International Journal of Sustainable Development and Green Economics (Ijsdge), Issn No.: 2315-4721, V-2, I-1, 2.
- [4] H.B.ParikhEt. Al. Apr-2013 "Performance Evaluation And Emission Analysis Of 4- S, I.C. Engine Using Ethanol Bio-diesel Blended With Diesel Fuel Ijret: International Journal Of Research In Engineering And Technology ISSN: 2319-1163.
- [5] KhiraiyaKrunal B. et. al. Jan 2013 "A Review of Recent Research on Palm oil Biodiesel as Fuel for CI Engine" International Journal of Applied Research & Studies ISSN 2278 – 9480, iJARS/ Vol. II/ Issue I/293.
- [6] Lovekush Prasad et. al.July-August 2012 "Experimental Investigation of Performance of Diesel Engine Working On Diesel and Neem Oil Blends" IOSR Journal of Mechanical and Civil Engineering (IOSRJMCE) ISSN : 2278-1684 Volume 1, Issue 4, PP 48-51.
- [7] K.ArunBalasubramanian 2012 "Dual Biodiesel Blends in Diesel Engine - Performance and Emission Analysis" European Journal of Scientific Research ISSN 1450-216X Vol.75 No.3 (2012), pp. 400-408 © EuroJournals Publishing, Inc..

- [8] Radha KK, Sarada SN, Rajagopal K, Nagesh el 2011. "Performance and Emission Characteristics of CI Engine Operated On Vegetable Oils as Alternate Fuels", *Inte. J. Automotive and Mech. Engin.* 4: 414-427.
- [9] P. K. Devan and N. V. Mahalakshmi, 2009 "Performance, emission and combustion characteristics of poon oil and its diesel blends in a DI diesel engine", *Fuel*, Vol. 88, 861-867.
- [10] JawadNagiet. al. 2008 "Palm Biodiesel an Alternative Green Renewable Energy for the Energy Demands of the Future" *International Conference on Construction and Building Technology, ICCBT - F - (07) – pp79-94.*
- [11] Canakei, M. and Van Gerpen, J. 2003 "Comparison of engine performance and emissions for petroleum diesel fuel, yellow grease biodiesel and soybean oil biodiesel" *American Society of Agricultural Engineers.* 46(4): 937-944.
- [12] F. Karaosmanoglu, G. Kurt and T. Ozaktas, 2000 "Long term C.I engine test of sunflower oil", *International journal of Renewable Energy*, Vol. 19, 219-221.
- [13] O. M. I. Nwafor and G. Rice, 1995 "Performance of rapeseed oil methyl ester in diesel engine", *International journal of Renewable Energy*, 0960-1481 Vol. 95,00022-4.
- [14] Khan MY, Khan SY, Ahmad N 2006 "Performance characteristics of compression ignition engine when operated on preheated Neem oil", *Proceeding of International Conference on Advances in Mechanical Engineering*, Punjab, Dec 1-3.
- [15] T. Vaughn, M. Hammill, M. Harris and A.J. Marchese. 2006 "Ignition delay of bio-ester fuel droplets" *SAE Paper-2006-01-330.*
- [16] S. Sinha and A.K. Agarwal.2005 "Combustion characteristics of rice bran oil derived biodiesel in a transportation diesel engine" *SAE Paper-2005-26-354.*
- [17] Rahman, M. N. Nabi and M.R.A. Beg. 2004 "Performance Study of a Diesel Engine with Diesel-Vegetable oil Blends as Alternative Fuel" *2nd BSME-ASME International conference on Thermal Engineering*, 2-4 January, Dhaka, Bangladesh.
- [18] AnjanaShrivastava and Ram Prasad.2004 "Triglycerides based diesel fuels", *Renewable and sustainable energy reviews*, Vol.4, pp.111-133.
- [19] F. N. da Silva, A.S. Prata and J. R.Teixeira. 2003 "Technical feasibility assessment of oleic neem methyl ester utilizations in diesel bus engines" *Energy Conversion and Management.* 44: 2857-2878.M.S.
- [20] Mustafa Ertunc Tat and John H. Van Gerpen. 2002. Physical properties and composition detection of biodiesel-diesel fuel blends. *Annual International Meeting Presentation, Hyatt Regency Chicago, Chicago, Illinois, USA. 28-31 July, Paper No. 026084.*

**APENDIX**

**Table 1: PROPERTIES OF DIESEL, BIODIESEL AND ITS BLENDS**

Fuel	Density(Kg/m <sup>3</sup> )	Calorific value(KJ/Kg)	Flash Point( <sup>0</sup> C)	Fire Point( <sup>0</sup> C)
Diesel	830	44000	60	62
Biodiesel	856	38400	156	158
B 10	833.50	40890	58	64
B 20	835.20	40480	62	67
B 30	837.80	39970	64	70
B 40	840.40	39540	66	73
B 50	843	38940	68	76

**Table 2: Data obtained From Experimental Setup Using Pure Diesel**

Sr. No.	LOAD W(kg)	Spring Load (kg)	N (RPM)	FUEL (ml)	TIME (sec)	T <sub>1</sub> ( <sup>0</sup> C)	T <sub>2</sub> ( <sup>0</sup> C)	T <sub>3</sub> ( <sup>0</sup> C)	T <sub>4</sub> ( <sup>0</sup> C)	T <sub>5</sub> ( <sup>0</sup> C)	T <sub>6</sub> ( <sup>0</sup> C)
1.	2	0.2	1466	20	117	100	57	28	30	28	38
2.	4	0.4	1464	20	87	124	66	28	30	28	40
3.	6	0.6	1454	20	78	159	80	28	31	28	41
4.	8	0.9	1444	20	57	191	94	28	32	28	43
5.	10	2.4	1432	20	50	228	109	28	33	28	46

**Table 3: Data obtained From Experimental Setup Using B 10**

Sr. No.	LOAD W(kg)	SPRING LOAD (kg)	N (RPM)	FUEL (ml)	TIME (sec)	T <sub>1</sub> ( <sup>0</sup> C)	T <sub>2</sub> ( <sup>0</sup> C)	T <sub>3</sub> ( <sup>0</sup> C)	T <sub>4</sub> ( <sup>0</sup> C)	T <sub>5</sub> ( <sup>0</sup> C)	T <sub>6</sub> ( <sup>0</sup> C)
1.	2	0.1	1464	20	109	138	55	18	20	19	32
2.	4	0.2	1450	20	77	157	62	19	22	19	35
3.	6	0.4	1442	20	64	192	72	20	23	20	40
4.	8	0.6	1430	20	52	232	84	20	24	20	50
5.	10	0.8	1422	20	40	260	92	20	24	20	54

**Table 4: Data obtained From Experimental Setup Using B 20**

Sr. No.	LOAD W(kg)	SPRING LOAD (kg)	N (RPM)	FUEL (ml)	TIME (sec)	T <sub>1</sub> (°C)	T <sub>2</sub> (°C)	T <sub>3</sub> (°C)	T <sub>4</sub> (°C)	T <sub>5</sub> (°C)	T <sub>6</sub> (°C)
1.	2	0.2	1470	20	113	101	50	19	21	19	30
2.	4	0.4	1460	20	83	125	56	20	22	20	32
3.	6	0.5	1450	20	67	143	61	20	22	20	35
4.	8	0.6	1438	20	56	165	68	20	23	20	36
5.	10	0.8	1428	20	50	184	75	20	24	20	38

**Table 5: Data obtained From Experimental Setup Using B 30**

Sr. No.	LOAD W(kg)	SPRING LOAD (kg)	N (RPM)	FUEL (ml)	TIME (sec)	T <sub>1</sub> (°C)	T <sub>2</sub> (°C)	T <sub>3</sub> (°C)	T <sub>4</sub> (°C)	T <sub>5</sub> (°C)	T <sub>6</sub> (°C)
1.	2	0.2	1472	20	117	108	50	21	23	21	35
2.	4	0.3	1464	20	86	124	55	21	23	21	35
3.	6	0.4	1448	20	69	148	65	21	24	21	37
4.	8	0.6	1438	20	57	179	75	21	26	21	39
5.	10	1.2	1410	20	48	205	85	21	27	21	42

**Table 6: Data obtained From Experimental Setup Using B 40**

Sr. No.	LOAD W(kg)	SPRING LOAD (kg)	N (RPM)	FUEL (ml)	TIME (sec)	T <sub>1</sub> (°C)	T <sub>2</sub> (°C)	T <sub>3</sub> (°C)	T <sub>4</sub> (°C)	T <sub>5</sub> (°C)	T <sub>6</sub> (°C)
1.	2	0.2	1474	20	118	90	43	19	21	20	31
2.	4	0.3	1460	20	90	109	50	19	22	20	33
3.	6	0.5	1457	20	70	135	60	19	23	20	36
4.	8	1.2	1436	20	60	164	70	20	24	20	40
5.	10	1.6	1410	20	54	190	85	20	24	20	44

**Table 7: Data obtained From Experimental Setup Using B 50**

Sr. No.	LOADW (kg)	SPRING LOAD (kg)	N (RPM)	FUEL (ml)	TIME (sec)	T <sub>1</sub> (°C)	T <sub>2</sub> (°C)	T <sub>3</sub> (°C)	T <sub>4</sub> (°C)	T <sub>5</sub> (°C)	T <sub>6</sub> (°C)
1.	2	0.2	1462	20	113	104	53	24	26	24	34
2.	4	0.6	1464	20	80	122	59	24	36	24	38
3.	6	1.4	1460	20	67	145	68	24	27	24	40
4.	8	1.8	1452	20	54	179	81	24	27	24	44
5.	10	2.4	1448	20	50	197	87	24	28	24	45

**Table 8: Brake Power & different Loads of Different blending ratio with Diesel**

	Diesel	B-10	B-20	B-30	B-40	B-50
Load (kg)	BP (kW)					
2	0.4	0.483	0.474	0.483	0.483	0.479
4	0.948	0.978	0.984	0.99	0.984	0.91
6	1.43	1.419	1.479	1.47	1.457	1.22
8	1.86	1.92	1.939	1.94	1.96	1.64

**Table 9: Total Fuel Consumption & Different loads for Different blending Ratio with Diesel**

	Diesel	B-10	B-20	B-30	B-40	B-50
Load (Kg)	TFC kg/s					
2	1.42	1.52	1.48	1.42	1.42	1.48
4	1.92	2.15	2.02	1.92	1.86	2.1
6	2.24	2.58	2.46	2.42	2.4	2.48
8	2.7	3.2	2.94	2.9	2.78	3.1

**Table 10: BSFC & Different loads of different blending ratio with Diesel**

	<b>Diesel</b>	<b>B-10</b>	<b>B-20</b>	<b>B-30</b>	<b>B-40</b>	<b>B-50</b>
<b>Load(kg)</b>	<b>BSFC (kg/kW-hr)</b>					
2	1.06	1.11	1.12	1.05	1.05	1.11
4	0.725	0.791	0.791	0.698	0.680	0.83
6	0.563	0.654	0.599	0.592	0.592	0.73
8	0.522	0.6	0.545	0.538	0.457	0.680

**Table 11: BTE & Different loads of different blending ratio with Diesel**

	<b>Diesel</b>	<b>B-10</b>	<b>B-20</b>	<b>B-30</b>	<b>B-40</b>	<b>B-50</b>
<b>Load (Kg)</b>	<b>BTE</b>	<b>BTE</b>	<b>BTE</b>	<b>BTE</b>	<b>BTE</b>	<b>BTE</b>
2	7.68	7.15	7.3	7.48	7.59	7.47
4	11.28	10.20	10.50	10.75	11.10	10.70
6	14.58	12.85	13.20	13.80	14.25	13.65
8	15.74	13.60	14.15	14.90	15.45	14.82

**Table 12: Exhaust Gas Temperatures & Different loads of different blending ratio with Diesel**

	<b>Diesel</b>	<b>B-10</b>	<b>B-20</b>	<b>B-30</b>	<b>B-40</b>	<b>B-50</b>
<b>Load(Kg)</b>	<b>Temperature (°C)</b>					
2	120	125	101	99	90	104
4	145	150	125	117	109	122
6	175	187	143	140	135	145
8	200	220	165	165	164	179

## Optimization of Machining Parameters of 20MnCr5 Steel in Turning Operation using Taguchi technique

Narayana Reddy. A R<sup>1</sup>, Ganti satya prakash<sup>2</sup>

<sup>1</sup>M.Tech student, Dept of Mech. Engg, CMR Institute of Technology, Hyderabad, India

<sup>2</sup>Associate. prof, Dept of Mech. Engg, CMR Institute of Technology, Hyderabad, India

**Abstract:** Now-a-days increasing the productivity and the quality of the machined parts are the main challenges of metal cutting industry during turning processes. Optimization methods in turning processes, considered being a vital role for continual improvement of output quality in product and processes include modeling of input-output and in process parameters relationship and determination of optimal cutting conditions. This paper present on Experimental study to optimize the effects of cutting Parameters on Surface finish and MRR of 20MnCr5 Steel alloy work material by employing Taguchi techniques. The orthogonal array, signal to noise ratio and analysis of variance were employed to study the performance characteristics in turning operation. Five parameters were chosen as process variables: Cutting Speed, Feed, Depth of cut, Hardness of cutting Tool, Cutting environment (wet and dry). The experimentation plan is designed using Taguchi's L9 Orthogonal Array (OA) and Minitab statistical software is used. Optimal cutting parameters for minimum surface roughness (SR) and maximum material removal rate were obtained. Finally, the relationship between factors and the performance measures were developed by using multiple regression analysis.

**Keywords:** orthogonal array, surface roughness, MINITAB, regression model, turning, coolant

### I. INTRODUCTION

In this work, the Taguchi methods, a powerful statistical tool to design of experiments for quality, is used to find the optimal cutting parameters for turning operations. Even though the present not only optimize cutting parameters for turning operations but also the main cutting parameters and its interaction that affect the cutting performance is the highlight of the work. Experimental results are provided to confirm the effectiveness of Taguchi's approach. Every manufacturing industry aims at producing a large number of products within relatively lesser time. But it is felt that reduction in manufacturing time may cause severe quality loss. In order to embrace these two conflicting criteria it is necessary to check quality level of the item either on-line or off-line. The purpose is to check whether quality lies within desired tolerance level which can be accepted by the customers. Quality of a product can be described by various quality attributes. The attributes may be quantitative or qualitative. If quality falls down the expected level the controller supplies a feed back in order to reset the process environment. In off-line quality control the method is either to check the quality of few products from a batch or lot (acceptance sampling) or to evaluate the best process environment capable of producing desired quality product. This invites a optimization problem which seeks identification of the best process condition or parametric combination for the said manufacturing process. If the problem is related to a single quality attribute then it is called single objective or single response optimization.

### II. LITERATURE REVIEW

Machining parameters in metal turning are cutting speed, feed and depth of cut. The setting of these parameters determines the quality characteristics of turned parts. Consideration of machining parameter optimization started out as early as 1907 when (Taylor, 1907) [1] acknowledged the existence of an optimum cutting speed for maximizing material removal rate in single pass turning operations. Research on machining parameter optimization has increased since the 1950's.

In 1950 (Gilbert, 1950) [2] presented a theoretical analysis of optimization of machining process and proposed an analytical procedure to determine the cutting speed for a single pass turning operation with fixed feed rate and depth of cut by using two different objectives maximum production rate and minimum machining cost.

P. G. Benardos and G. C. Vosniakos, [3] this paper presents the set of parameters that are influence the surface Roughness and also they diagrammatically displayed in Fishbone Diagram.

Aman Aggarwal and Hari Singh, [4] this paper presents that Fuzzy Logic, Genetic Algorithm, scatter search and Taguchi technique are the latest optimization Techniques.

Mahendra Korat and Neeraj Agarwal (2012) [5] investigated the effects of the process parameters viz., coolant condition, cutting speed, feed, depth of cut, nose radius, on response characteristics viz., material removal rate, surface roughness, on EN24 material in CNC turning. ANOVA results shows that nose radius, feed rate, depth of cut, cutting speed and coolant condition affects the surface roughness by 65.38%, 25.15%, 3.06%, 1.41% and 0.09% respectively.

Sahoo et al. (2008) [9] studied for optimization of machining parameters combinations emphasizing on fractal characteristics of surface profile generated in CNC turning operation. The authors used L27 Taguchi Orthogonal Array design with machining parameters: speed, feed and depth of cut on three different work piece materials viz., aluminum, mild steel and brass. It was concluded that feed rate was more significant influencing surface finish in all three materials.

### III. TAGUCHI TECHNIQUE

The Taguchi experimental design method, by Genichi Taguchi is a well-known, unique and powerful technique for product or process quality improvement. It is widely used for analysis of experiment and product or process optimization. Genichi Taguchi is a Japanese engineer who has been active in the improvement of Japan's industrial products and processes since the late 1940s.

Taguchi introduces his concepts to:

- Quality should be designed into a product and not inspected into it.
- Quality is best achieved by minimizing the deviation from a target.
- Cost of quality should be measured as a function of deviation from the standard and the losses should be measured system wide.

### IV. EXPERIMENTAL DETAILS

#### 4. 1: Material

20MnCr5 is categorized as case hardened steel produced by casting, it is easily machinable and can have a wide variety of surface finishes. It also has high strength and stiffness. It is used in the field of high stressed components in automobile industry like small gear, shafts, crankshafts, connecting rods, cam shafts, piston bolts, spindles and other mechanical controlling parts.

Carbon	0.220%
Manganese	1.112%
Silicon	0.244%
Sulphur	0.026%
Phosphorus	0.028%
Chromium	1.154%

Table 1: Chemical composition of 20MnCr5

#### 4. 2: Cutting tool inserts

Inserts are individual cutting tools with several cutting points. Inserts are usually clamped on the tool shank with various locking mechanisms. Most of high performance cutting tools use the insert method. Here there are three type cutting insrets are using they are

1. SUMITOMO AC700G – CARBIDE COATED
2. KORLOY PC9030 – PVD COATED STEEL GRADE
3. TAGUETEC CT3000 – CERAMIC UNCOATED

**4. 3: Machine tool**



Fig1: CNC Horizontal turning lathe LL 15T L3

**4.4: Cutting parameters and their levels**

Symbol	Cutting Parameter	Unit	Level 1	Level 2	Level 3
A	Cutting Speed	rpm	1000	2000	3000
B	Feed	mm/rev	0.05	0.1	0.15
C	Depth of Cut	mm	0.2	0.4	0.6
D	Hardness of Cutting Tool	HRC	65 (Ceramic Uncoated)	71 (PVD Coated Steel Grade)	76 (Carbide Coated)

Table 2 : Cutting parameters and their levels

**4. 5: To find Minimum number of Experiments to be conducted**

Parameter	Number of Levels	Degree of Freedom
Cutting Speed	3	2
Feed	3	2
Depth of Cut	3	2
Hardness of Cutting Tool	3	2
	Total Degrees of Freedom	8
	Minimum no. of Experiments	9

Table 3: Factors, levels and Degree of freedom

4. 6: Orthogonal array

Trial no.	Cutting Speed (m/min)	Feed (mm/rev)	Depth of Cut (mm)	Hardness of Cutting tool (HRC)
1	1	1	1	1
2	1	2	2	2
3	1	3	3	3
4	2	1	2	3
5	2	2	3	1
6	2	3	1	2
7	3	1	3	2
8	3	2	1	3
9	3	3	2	1

Table 4: standard L9 orthogonal array

V. FORMULAS USED

1) MRR (a) represents Actual Material Removal Rate in mm3/min

$$MRR (a) = \frac{[Initial\ Weight\ of\ workpiece\ (gm) - Final\ Weight\ of\ workpiece\ (gm)]}{Density(gm/mm^3) \times Machining\ Time\ (min)} \text{ mm}^3/min$$

2) MRR (t) represents Theoretical Material Removal Rate in mm3/min

$$MRR (t) = f * d * v * 1000 \text{ mm}^3/min$$

Here ‘f’ denotes feed in mm/rev, ‘d’ denotes depth of cut in mm and ‘v’ denotes cutting speed in m/min

3) To calculate Machining time (t) (theoretical) following formula is used

$$t = \frac{L}{f * N} \text{ in min}$$

L = Distance travelled by the tool in the direction of feed in single cut.

F = Feed in mm/rev

N = speed in rpm

VI. RESULTS AND DISCUSSION

In the first run experiment is performed using coolant APPRO SOL XL. Readings are tabulated in table5. Surface roughness is measured and MRR values are calculated using formulae.

Trial no	Surface Roughness In $\mu m$	Initial Weight gms	Final Weight gms	Machining Time (actual) in sec	Machining Time (theoretical) in sec	MRR (a) mm3/min	MRR (t) mm3/min
1	1.61	907.00	885.90	148.00	150.00	1089.69	984.38
2	1.56	907.00	883.60	74.00	75.00	2416.94	3937.50
3	2.23	907.00	867.10	50.00	50.00	6099.36	8859.38

4	1.62	907.00	876.50	76.00	75.00	3067.38	3937.50
5	0.70	907.00	866.70	37.00	37.50	8325.01	11812.50
6	0.79	907.00	893.40	24.00	25.00	4331.21	5906.25
7	0.22	907.00	873.90	50.00	50.00	5059.87	8859.38
8	0.43	907.00	889.30	25.00	25.00	5411.46	5906.25
9	1.15	907.00	878.30	17.00	16.67	12903.71	17718.75

Table 5: Experiment results when coolant is ON

Tri al no	Surface Roughness In $\mu\text{m}$	Initial Weigh t gms	Final Weigh t gms	Machinin g Time (actual) In sec	Machining Time (theoretical ) In sec	MRR (a) mm3/mi n	mrr(t) mm3/mi n
1	1.64	907.00	887.00	148.00	150.00	1032.88	984.38
2	1.59	907.00	876.50	74.00	75.00	3150.28	3937.50
3	2.26	907.00	865.80	50.00	50.00	6298.09	8859.38
4	1.62	907.00	877.10	76.00	75.00	3007.04	3937.50
5	0.74	907.00	869.20	37.00	37.50	7808.57	11812.50
6	0.83	907.00	887.10	24.00	25.00	6337.58	5906.25
7	0.25	907.00	867.40	50.00	50.00	6053.50	8859.38
8	0.47	907.00	884.60	25.00	25.00	6848.41	5906.25
9	1.18	907.00	879.10	17.00	16.67	12544.02	17718.75

Table 6: Experiment results when coolant is OFF

In the Second run experiment is performed in dry condition. Readings are tabulated in table6 Surface roughness is measured and MRR values are calculated using formulae.

REGRESSION MODELS

The regression equation for surface roughness when coolant is ON given by:

$$\text{Surface Roughness } (\mu\text{m}) = 0.42 - 0.00610 \text{ Cutting Speed 'A' (m/min)} + 2.40 \text{ Feed 'B' (mm/rev)} + 0.27 \text{ Depth of Cut 'C' (mm)} + 0.0224 \text{ Tool Hardness 'D'}$$

The regression equation for MRR when coolant is ON given by:

$$\text{MRR (a) mm}^3/\text{min} = 10621 + 23.31 \text{ cutting speed 'A' ( m/min)} + 47058 \text{ feed 'B' (mm/rev)} + 7210 \text{ depth of cut 'C' (mm)} - 246 \text{ tool hardness 'D'}$$

The regression equation for surface roughness when coolant is OFF given by:

$$\text{Surface Roughness} = 0.49 - 0.00608 \text{ cutting speed 'A' (m/min)} + 2.53 \text{ feed 'B' (mm/rev)} + 0.26 \text{ depth of cut 'C' (mm)} + 0.0215 \text{ tool hardness 'D'}$$

The regression equation for MRR when coolant is OFF given by:

MRR (a) mm<sup>3</sup>/min = 5491 + 25.3 cutting speed 'A' ( m/min) + 50288 feed 'B'( mm/rev) + 4951 depth of cut 'C' (mm) - 164 tool hardness 'D'

Source	DF	Seq SS	Adj SS	Adj MS	%p	Rank
Cutting speed(A)	2	2.2134	2.2134	1.1067	63.56	1
Feed(B)	2	0.3652	0.3652	0.1826	10.48	4
Depth of cut(C)	2	0.4161	0.4161	0.2080	11.94	3
Tool ardness(D)	2	0.4876	0.4876	0.2438	14.00	2
Total	8	3.4822				

Table 7: Analysis of Variance for surface roughness

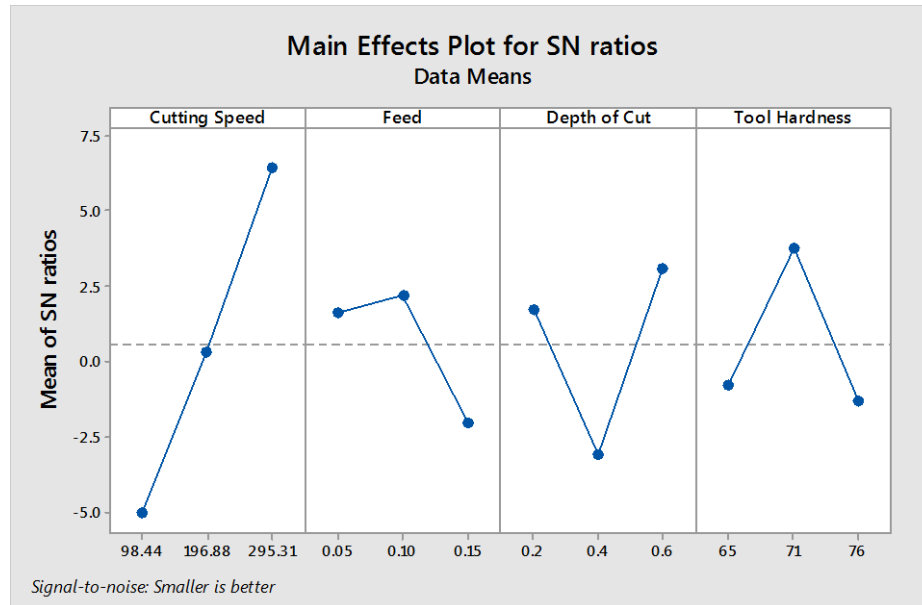


Fig.2: Effect of process parameters on surface roughness

Level	Cutting Speed (m/min) 'A'	Feed (mm/rev) 'B'	Depth of Cut (mm) 'C'	Hardness of Cutting tool (HRC) 'D'
1	-4.9884	1.6082	1.7472	-0.7508
2	0.3184	2.1887	-3.0889	3.7788
3	6.4227	-2.0442	3.0495	-1.2753
Delta	11.4111	4.2329	6.1834	5.0541
Rank	1	4	2	3

Table 8: Response table for surface roughness

Source	DF	Seq SS	Adj SS	Adj MS	%p	Rank
Cutting speed(A)	2	31728492	31728492	15864246	31.87	2
Feed (B)	2	33219867	33219867	16609933	33.37	1
Depth of cut(C)	2	14793873	14793873	7396936	14.86	4
Tool Hardness(D)	2	19783672	19783672	9891836	19.87	3
Total	8	99525902	99525902			

Table 9: Analysis of Variance for MRR

Level	Cutting Speed (m/min) 'A'	Feed (mm/rev) 'B'	Depth of Cut (mm) 'C'	Hardness of Cutting tool (HRC) 'D'
1	68.04	68.19	69.38	73.79
2	73.63	73.58	73.20	71.49
3	76.99	76.88	76.07	73.27
Delta	8.95	8.70	6.68	2.30
Rank	1	2	3	4

Table 10: Response table for MRR

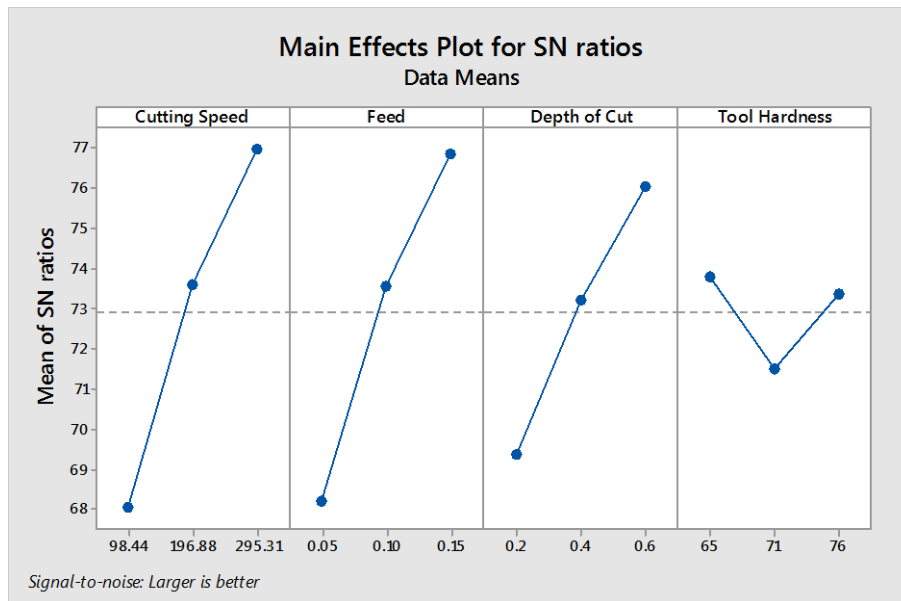


Figure 3: Effect of process parameters on MRR

Source	DF	Seq SS	Adj SS	Adj MS	%p	Rank
Cutting speed(A)	2	2.20469	2.20469	1.10234	64.37	1
Feed (B)	2	0.36029	0.36029	0.18014	10.52	4
Depth of cut(C)	2	0.38869	0.38869	0.19434	11.34	3
Tool Hardness(D)	2	0.47096	0.47096	0.23548	13.75	2
Total	8	3.42462				

Table 11: Analysis of Variance for surface roughness

Level	Cutting Speed (m/min) 'A'	Feed (mm/rev) 'B'	Depth of Cut (mm) 'C'	Hardness of Cutting tool (HRC) 'D'
1	-5.13566	1.18467	1.29320	-1.03972
2	0.01450	1.71516	-3.21863	3.21057
3	5.72053	-2.30046	2.52480	-1.57148
Delta	10.85620	4.01561	5.74343	4.78204
Rank	1	4	2	3

Table 12: Response table for surface roughness

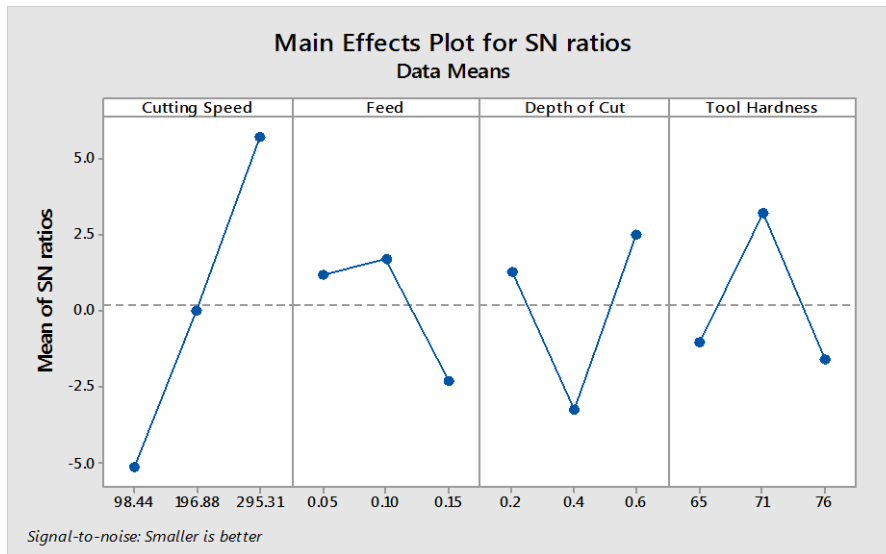


Fig.4: Effect of process parameters on surface roughness

Source	DF	Seq SS	Adj SS	Adj MS	%p	Rank
Cutting speed(A)	2	37469560	37469560	18734780	42.25	2
Feed(B)	2	37939065	37939065	18969532	42.78	1
Depth of cut(C)	2	6391089	6391089	3195545	7.20	4
Tool Hardness(D)	2	6877952	6877952	3438976	7.756	3
Total	8	88677667				

Table 13: Analysis of Variance for MRR

Level	Cutting Speed (m/min) 'A'	Feed (mm/rev) 'B'	Depth of Cut (mm) 'C'	Hardness of Cutting tool (HRC) 'D'
1	-5.13566	1.18467	1.29320	-1.03972
2	0.01450	1.71516	-3.21863	3.21057
3	5.72053	-2.30046	2.52480	-1.57148
Delta	10.85620	4.01561	5.74343	4.78204
Rank	1	4	2	3

Table 14: Response table for MRR

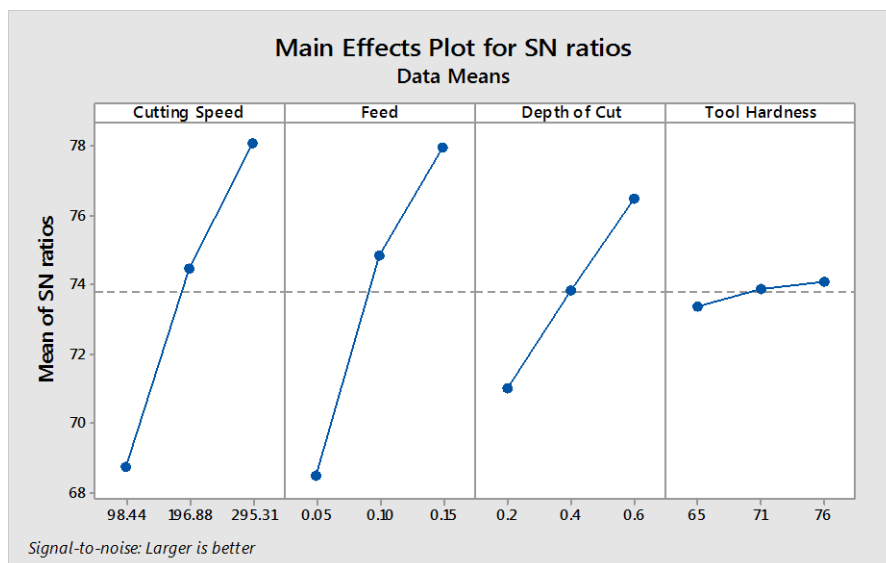


Fig 5: Effect of process parameters on MRR

Trial no	Surface roughness Ra (µm) Coolant ON	Surface roughness Ra (µm) Coolant OFF	%age improvement in Ra when coolant is used
1	1.612	1.64	1.71
2	1.56	1.59	1.89
3	2.23	2.26	1.33
4	1.62	1.62	0.00
5	0.7	0.74	5.41
6	0.79	0.83	4.82
7	0.22	0.25	12.00
8	0.43	0.47	8.51
9	1.15	1.18	2.54

Table 15: shows the effect of coolant on Surface roughness

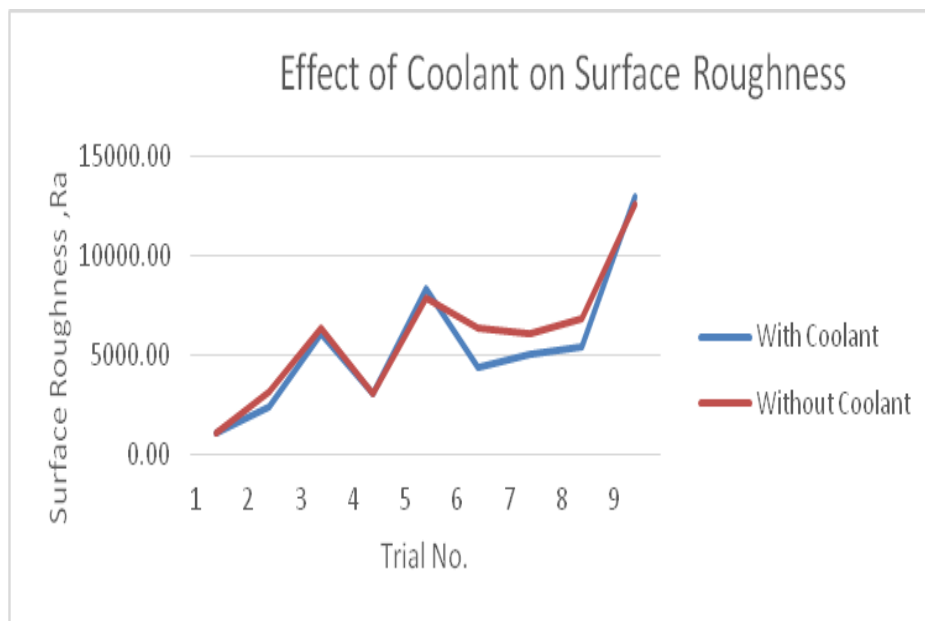


Fig 6: Effect of coolant on MRR

Trial no	MRR (a) (mm <sup>3</sup> /min) Coolant ON	MRR (a) (mm <sup>3</sup> /min) Coolant OFF
1	1089.69	1032.88
2	2416.94	3150.28
3	6099.36	6298.09
4	3067.38	3007.04
5	8325.01	7808.57
6	4331.21	6337.58
7	5059.87	6053.50
8	5411.46	6848.41
9	12903.71	12544.02

Table 16: shows the effect of coolant on MRR

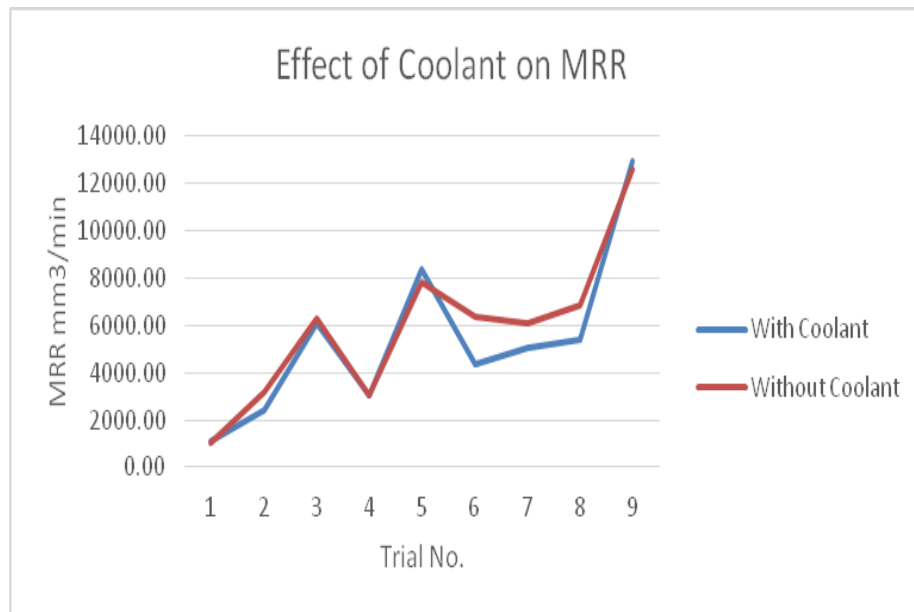


Fig 7: Effect of coolant on MRR

## VII. CONCLUSION

The effect of process parameters cutting speed, Feed, Depth of cut and Tool Hardness on response Characteristics MRR and Surface roughness were studied on 20MnCr5 steel alloy in CNC Turning. Based on results obtained, the following conclusions can be drawn:

- The experimental results showed that the Taguchi parameter design is an effective way of determining the optimal cutting parameters for achieving low surface roughness and maximum material removal rate.
- The relationship between cutting parameters (cutting speed, feed, depth of cut and hardness of cutting tool) and the performance measures (surface roughness and material removal rate) are expressed by multiple regression equation which can be used to estimate the expressed values of the performance level for any parameters levels.
- ANOVA suggests that cutting speed is the most significant factor and feed is most insignificant factor for surface roughness and cutting speed is the most significant factor and tool hardness is the most insignificant factor for MRR when the coolant is ON.
- ANOVA suggests that cutting speed is the most significant factor and feed is most insignificant factor for surface roughness and cutting speed is the most significant factor and feed is the most insignificant factor for MRR when the coolant is OFF.
- ANOVA (S/N Data) results shows that cutting speed, feed, depth of cut and tool hardness affects the surface roughness by 63.56%, 10.48%, 11.94% and 14% respectively when the coolant is ON.
- ANOVA (S/N Data) results shows that cutting speed, feed, depth of cut and tool hardness affects the MRR by 31.87%, 33.37%, 14.86% and 19.87% respectively when the coolant is ON.
- ANOVA (S/N Data) results shows that cutting speed, feed, depth of cut and tool hardness affects the surface roughness by 64.37%, 10.52%, 11.34% and 13.75% respectively when the coolant is OFF.
- ANOVA (S/N Data) results shows that cutting speed, feed, depth of cut and tool hardness affects the MRR by 42.25%, 42.78%, 7.20% and 7.756% respectively when the coolant is OFF.
- The result shows that surface roughness is good when coolant is used. An average improvement of 4.24% in surface roughness was found when coolant is used.
- The result shows that MRR is almost same when coolant is ON and coolant is OFF. Therefore it can be concluded that MRR does not depend much on coolant.

## Acknowledgements

The support extended by the guide (Mr.Ganti satya prakash) and college authorities is highly appreciated and acknowledged with due respect.

## REFERENCES

- [1]. Taylor F W (1907), "On the Art of Cutting Metals", Transactions of the American Society of Mechanical Engineers, Vol. 28, pp. 31-35
- [2]. Gilbert W W (1950), "Economics of Machining-Machining Theory and Practice", American Society of Metals, pp. 465-485
- [3]. P. G. Benardos, G. C. Vosniakos. "Predicting Surface Roughness in Machining: a review", International Journal of Machine tools and Manufacture 43 (2003) 833-844
- [4]. Aman Aggarwal and Hari Singh. "Optimization of Machining techniques- A retrospective and literature review", Sadhana Academy Proceedings in Engineering Sciences, 2005; 30(6): 699-711
- [5]. Mahendra Korat, Neeraj Agarwal. "Optimization of Different machining parameters of EN24 Alloy Steel in CNC Turning by use of Taguchi method", International journal of Engineering Research and applications (IJERA) Vol. 2, Issue 5, September- october 2012, pp. 160-164
- [6]. Farhad Kolahan, Mohsen Manoochehri, Abbas Hosseini. "Simultaneous Optimization of Machining Parameters and Tool Geometry Specifications in turning operation of AISI1045 Steel", World Academy of Science, Engineering and Technology 50 2011 785-788
- [7]. Yang W H and Tang Y S (1998), "Design Optimization of Cutting Parameters for Turning Operations Based on the Taguchi Method", Journal of Materials Processing Technology, Vol. 84, pp. 122-129
- [8]. Thamizhmanii S, Saparudin S and Hasan S (2007), "Analysis of Surface Roughness by Using Taguchi Method", Achievements in Materials and Manufacturing Engineering, Vol. 20, Nos. 1-2, pp. 503-505
- [9]. Sahoo P, Barman T K and Routara B C (2008), "Taguchi Based Practical Dimension Modelling and Optimization in CNC Turning", Advance in Production Engineering and Management, Vol. 3, No. 4, pp. 205-217
- [10]. Philip Selvaraj D and Chandramohan P (2010), "Optimization of Surface Roughness of AISI 304 Austenitic Stainless Steel in Dry Turning Operation Using Taguchi Design Method", Journal of Engineering Science and Technology, Vol. 5, No. 3, pp. 293-301
- [11]. Marinkovic Velibor and MadicMilos (2011), "Optimization of Surface Roughness in Turning Alloy Steel by Using Taguchi Method", Scientific Research and Essays, Vol. 6, No. 16, pp. 3474-3484
- [12]. Adarsh Kumar K, Ratnam Ch, Murthy B S N and Satish Ben B (2012), "Optimization of Surface Roughness in Face Turning Operation in Machining of EN-8", International Journal of Engineering Science & Advanced Technology, Vol. 2, No. 4, pp. 807-812
- [13]. Sreenivasa Murthy T, Suresh R K, Krishnaiah G and Diwakar Reddy V (2013), "Optimization of Process Parameters in Dry Turning Operation of EN 41B Alloy Steels with Cermet Tool Based on the Taguchi Method", International Journal of Engineering Research and Applications (IJERA), pp. 1144-1148

## Stress Analysis of Precast Prestressed Concrete Beams during Lifting

V. M. Gaykar<sup>1</sup>, J. G. Solanki<sup>2</sup>

<sup>1</sup>M.tech Student, Structural Engineering Department, Veermata Jijabai Technological Institute, India

<sup>2</sup>Asst. Professor, Structural Engineering Department, Veermata Jijabai Technological Institute, India

**Abstract:** The use of long span prestressed beams in bridge construction is very common. Even if the sections are economical the erection of the beam still poses a challenge in construction. Not much work has been done in the analysis of stress and deflection at erection stage. This paper deals with the behavior of precast prestressed beams during lifting. Since the spans of these beams are large, it may fail due to cracking during erection. In this paper a detailed 3-dimensional Finite Element Analysis of 2 prestressed beam sections was done with incorporating the effect of initial imperfections and prestress. Results were obtained for both prestressed beam and non-prestressed beam and were compared with Moen's formulae. To include the effect of prestressing cables in the beam new additional formulae were introduced and used in combination with the Moen's. The results obtained were approximately validated with the Finite Element Analysis results. It is seen that the prestressing cables have a significant effect on the behavior of a beam during lifting. For a prestressed beam the overhang length should be kept minimum for safe erection which is opposite in the case of a normal beam.

**Keywords:** Deflection, Finite Element Analysis, Initial Imperfections, Lifting, Prestressed beam.

### I. INTRODUCTION

The use of precast prestressed beams is wide in bridge construction. These beams are long with imperfections and tend to deflect about both major and minor axis during lifting. Moreover the prestressing cable causes the beam to get highly stressed which in turn results in cracking. Thus for safe erection, it is necessary to study the deflection and stress behavior of the prestressed beam.

Many numerical formulae are available in previous literature for analyzing lateral behavior of the beam at lifting.[1]–[7] Also it is found that the camber due to prestress has a considerable effect on the deflection of the beam. [5], [8]. The previous literature also contains an experimental study on initial imperfection.[9]

In this paper, two beam sections viz. 77in. PCI Bulb Tee and Type IV AASHTO beam [9] are numerically modeled using Abaqus software to study its behavior. This study compares the finite element analysis results with the analytical solutions from previous literature and also studies the difference in the stress behavior and deflection of beams due to prestress. The effect of prestress on the deflection of the beam about both major and minor axis is also studied.

### II. NUMERICAL MODELLING

Numerical analysis was carried out on two sections of precast prestressed beams of length 42.36m and 31.7m respectively. The initial imperfection in the beam is considered in the form of a radial curvature with sweep of L/1060 and L/790 respectively. The details of the beams are obtained from 'Lifting Analysis of Precast Prestressed Concrete Beams' [9]. The beams are prestressed using low relaxation strands with 0.6 inch diameter and the strands are harped at 1.524m from mid-span. The compressive strength of concrete for both beams is assumed to be  $f_c = 55 \text{ N/mm}^2$  with initial compressive strength of  $f_{ci} = 45 \text{ N/mm}^2$ .

Finite element models of both beams were made with and without considering the prestressing force. A 3D model was preferred to 2D and 1D model, as the prestressing cables were to be included. The FE model consisted of 3 parts viz. beam, prestressing cables and lifting loops. C3D8R (8 node linear brick element, reduced integration) hexahedral element was used for the beam formation and C3D4 (4 node linear tetrahedron) element for loop formation. For prestressing cables T3D2 (2 node truss) element was used. Initial condition of stress was applied to the cables, so as to get the effect of prestress [10]. The interaction between cables and beam and loop and beam is done by embedded constraint. Thus a perfect bond is assumed between the different parts without any bond slippage. Pinned boundary conditions were applied to the hooks to get the

effect of hanging from cables under the effect of gravity load. M55 grade concrete was used for beam and modulus of elasticity of prestressing steel was taken as 195GPa. The behavior for both materials was assumed to be linear. Fig.1 and Fig.2 shows the details of 77in. PCI Bulb Tee and Type IV AASHTO beam respectively.

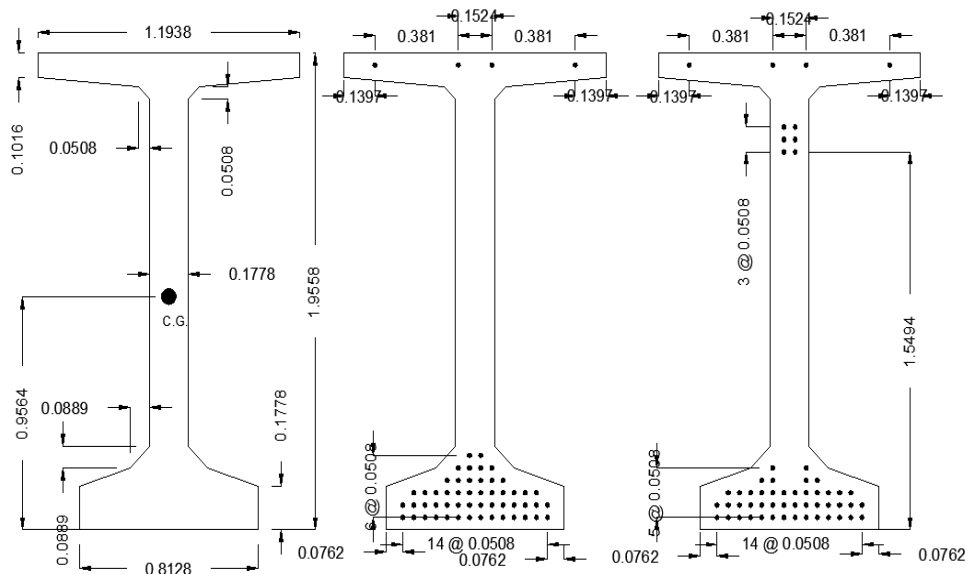


**Fig. 1** Beam details of 77in. PCI Bulb Tee

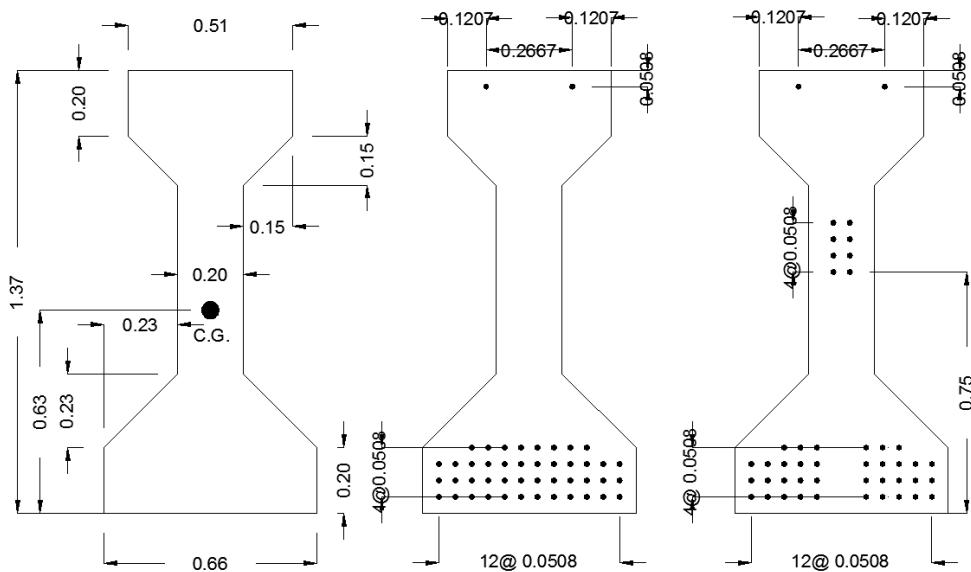


**Fig. 2** Beam details of Type IV AASHTO beam

### III. RESULTS AND DISCUSSIONS

The Numerical modelling was done as explained above. To verify the prestressing condition, first the beams were analysed as simply supported and convergence study was carried out. The results so obtained were compared with the manual analysis. Thus, similar analysis for hanging condition was carried out with pinned boundary conditions for the lifting loops. Only self-weight was considered under static condition for analysis. Also, analysis was carried out both conditions i.e. by considering and not considering the effect of prestressing cables. Fig.3 shows an isometric view of FE model for both beams.

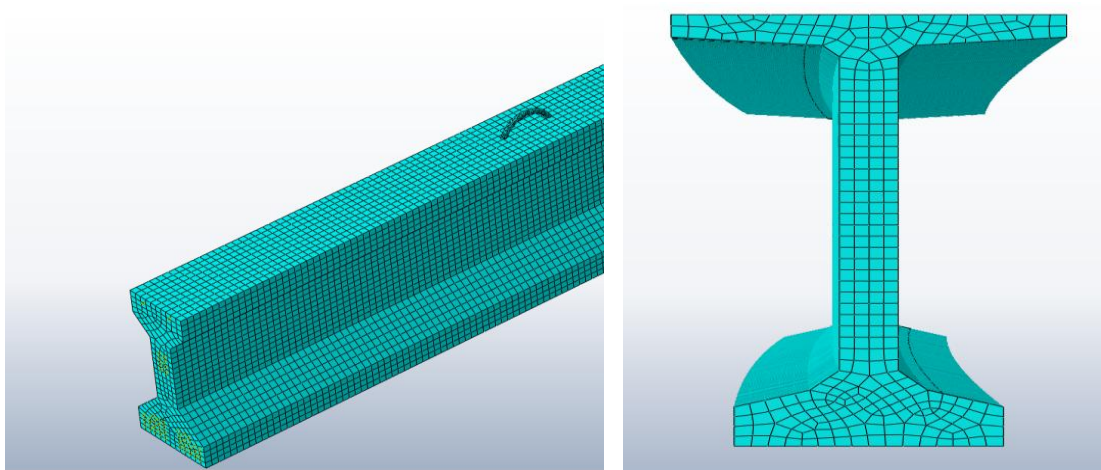


Fig. 3 a) Isometric view of FE model of Type IV AASHTO beam & b) side view of FE model of 77in. PCI Bulb Tee

### 1.1 Finite Element Analysis results

The FEA results for beam without prestressing force shows that as the overhang increases, the tension zone in the beam reduces along with deflection. The stress contours can be seen in Fig.4 and Fig.5 where red zone is tension and blue zone is compression. Fig.4 shows Bulb Tee beam with  $a/L$  ratio 0.05 and 0.12 and Fig.5 shows Type IV AASHTO Beam with  $a/L$  ratio 0.06 and 0.16. It can be seen that the red zone (tension zone) decreases. This happens because as the overhang increases the internal span reduces which in turn cause a reduction in the self-weight bending moment, thus the flexural stress decreases. Hence the compression stresses at the top and the tension stresses at the bottom also reduces.

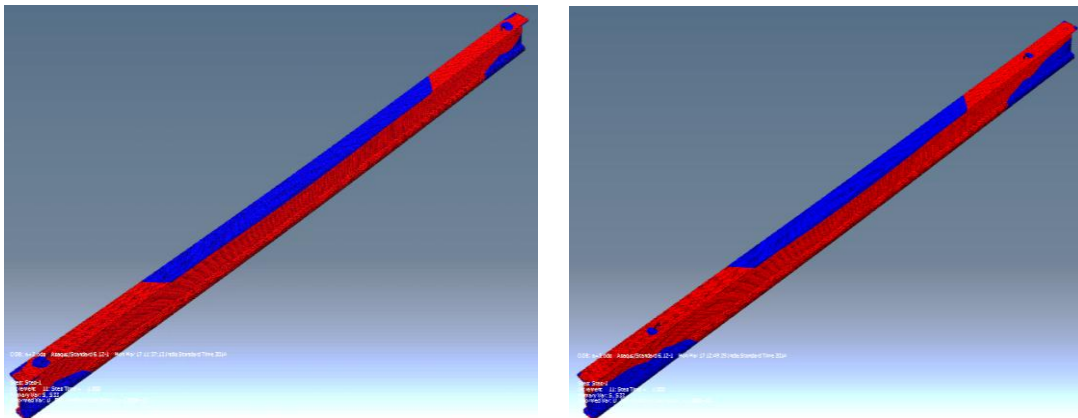


Fig. 4 77in. Bulb Tee Beam at  $a/L=0.05$  &  $a/L=0.12$  respectively

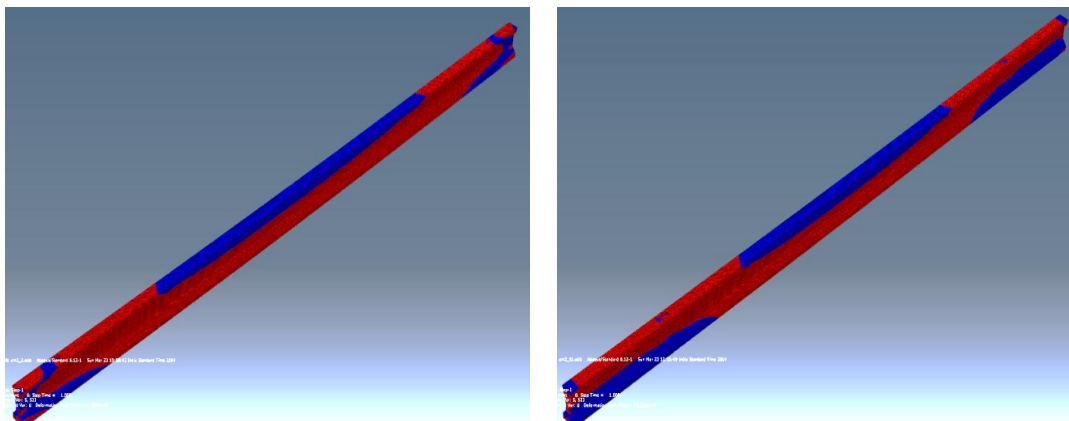


Fig. 5 Type IV AASHTO Beam at  $a/L=0.06$  &  $a/L=0.16$  respectively

For prestressed beam the behaviour seen is opposite. From FEA results the contours in Fig.6 & Fig.7 shows that the red zone increases as the overhang increases. Fig.6 shows Bulb Tee beam at a/L ratio 0.07 and 0.17 and Fig.7 shows Type IV AASHTO Beam at a/L ratio 0.09 and 0.22 respectively. In prestressed beam there is already a negative bending moment due to the prestress, hence there is tension at top and compression at bottom. The stress due to self-weight tries to counteract the stress due to prestress. Thus as the mid-span reduces, the resulting tensile stresses at the top fibre increases and the resulting compression stresses at the bottom fibre increases. This effect is due to the reduction of the bending moment due to self-weight since the mid-span reduces.

**1.2 Analytical results**

During manual analysis the bending moment in the beam at lifting was calculated using Moens formula [3]. Thus, bending stresses were calculated and then added up to the stress due to prestress. The formulae so obtained and used are given below. Here compression is taken as negative and vice-verse. Also the effect of stress due to lateral bending is neglected.

$$\sigma_{top} = -\frac{P}{A} + \frac{P.e}{Z_t} - \frac{M}{Z_t} \tag{1}$$

$$\sigma_{bottom} = -\frac{P}{A} - \frac{P.e}{Z_b} + \frac{M}{Z_b} \tag{2}$$

- where,
- M = bending moment about strong axis
  - P = prestressing force
  - e = eccentricity of the cable
  - A = cross-sectional area
  - Z<sub>t</sub> , Z<sub>b</sub> = Section modulus at top and bottom respectively

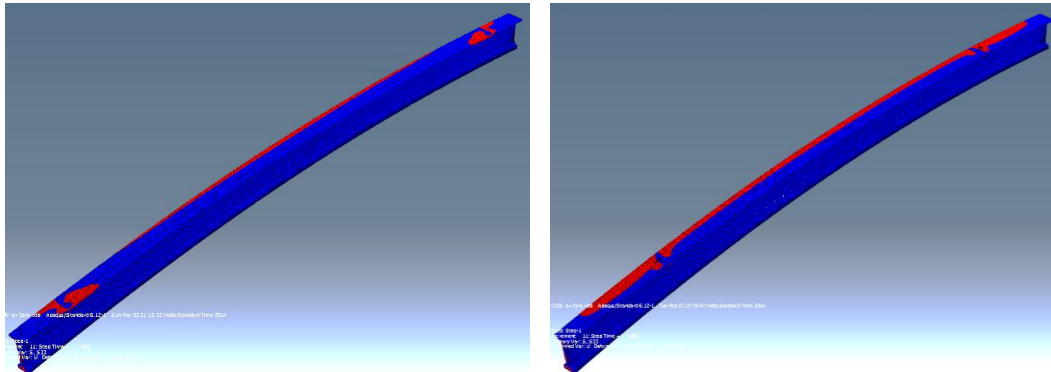


**Fig. 6** 77in.Bulb Tee Beam (prestressed) at a/L=0.071 & a/L=0.165 respectively

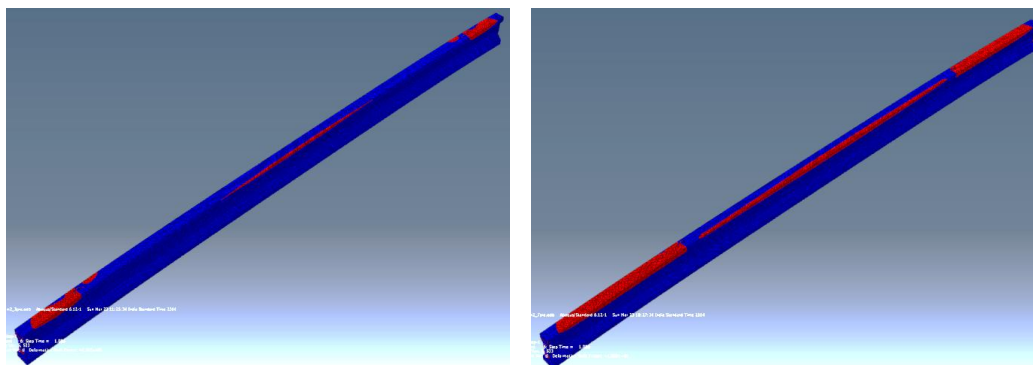


**Fig. 7** Type IV AASHTO Beam (prestressed) at a/L=0.09 & a/L=0.22 respectively

Using these formulae stresses were calculated for varying 'a/L'. The analytical results obtained were compared with FEA results for both sections, as shown in Fig.8 The stresses at a particular section goes on increasing as the 'a/L' ratio increases. Also, the values obtained using the given formulae gives conservative results as compared to abaqus. Both compression and tension stresses appears to be higher side. The reason behind this is the assumption differences in calculating the analytical values like not considering the effect of lifting loop and also neglecting the stresses due to lateral bending. Finite element analysis considers the effect of the lifting loops.

Following Fig.8 shows the stress variation at mid-section for both PCI Bulb Tee and Type IV AASHTO beam respectively. It can be seen that from abaqus analysis that the top fiber is in compression, this is possible due to the local effect of top prestress cables in the top flange. Manual analysis does not take this into consideration.

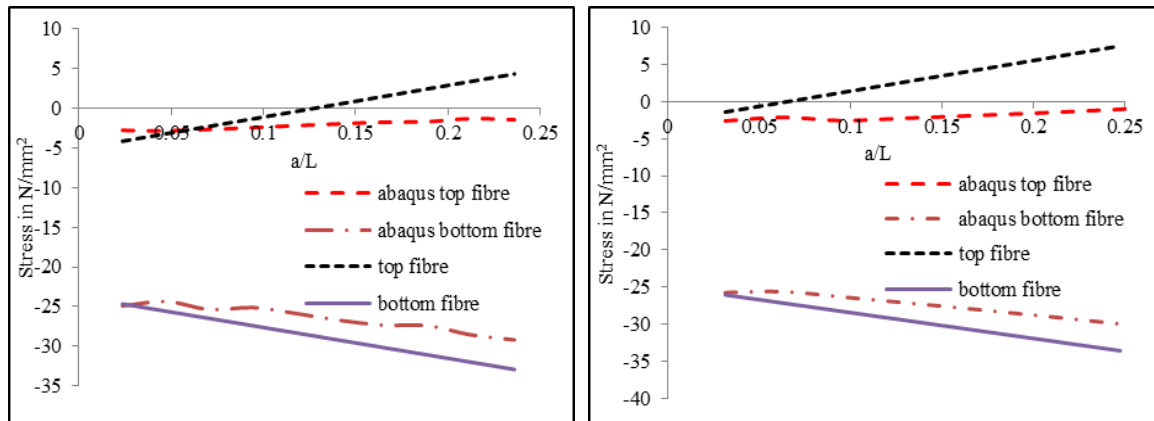
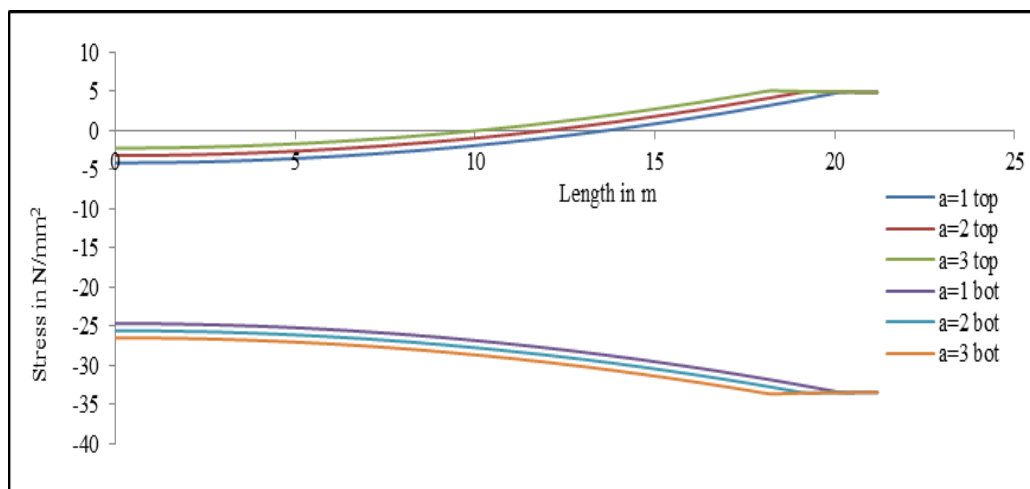


Fig. 8 Stress variation at mid-section (77in. PCI Bulb Tee & Type IV AASHTO Beam respectively)

The stress variation of the both beams along the length is given in Fig.9 & Fig.10. These values are obtained analytically. Here the zero distance indicates mid-span. Thus the distance along X-axis is given from mid-span of the beam. It can be seen that, as the value of 'a' increases (i.e. overhang increases) the stress at both top and bottom fiber increases for all the sections. Maximum tension and compression are obtained at the lifting points.

From Fig.9 & Fig.10 it is clear that in prestressed beams, stresses goes on increasing as the overhang distance increases which is opposite to the behavior of normal R.C.C. beam. As the span increases, the tension in the bottom fiber and compression in the top fiber due to self-weight increases. This helps to counteract the stress produced by the prestressing strands, explaining this behavior of the prestressed beam to that of a normal beam. This behavior is verified by both analytical and FEA results.



zFig. 9 Variation of stress along the length (77in. PCI Bulb Tee)

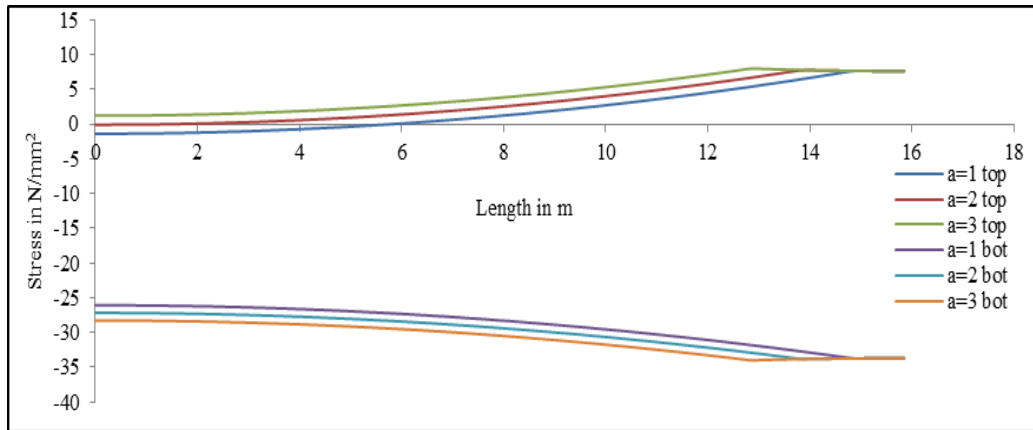


Fig. 10 Variation of stress along the length (Type IV AASHTO Beam)

Along with the stresses the deflections were also compared. Also the observed FEA results of downward deflection are found to be approximately same to the analytical results. Both lateral and downward deflection for both sections reduces at mid-span as the overhang increases. This behaviour is observed for both prestressed and non-prestressed beams.

Fig.11 & Fig.13 shows lateral deflection for both the beams. We can see that the behaviour of lateral deflection is same as analytical but in opposite direction. This difference is due to the downward deflection of the beam, which results in the shift of centroid below the roll axis hence radially inward deflection. From both figures it can be seen that the lateral deflection reduces as the 'a/L' ratio increases. Here positive value means radially outward deflection and vice-verse.

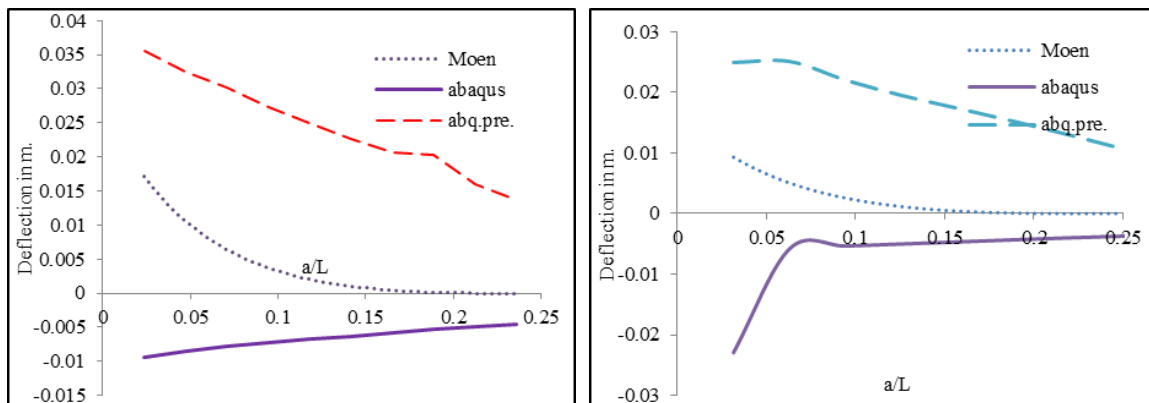


Fig. 11 Lateral Deflection at midsection (77in. PCI Bulb Tee & Type IV AASHTO Beam respectively)

Similar behavior is observed from Fig.12 & Fig.14 for downward deflection for both beams. Here negative value was considered downward deflection and vice-verse. The deflection in prestressed beam was observed to be upward due to the effect of prestress cables. For calculating the net downward deflection due to gravity and prestress following formula was used. This formula gives the deflection due to prestress; this deflection was then added to the deflection due to gravity. The result and behavior obtained were very much similar.

$$v = -\frac{Pex^2}{2EI} + \frac{PeLx}{2EI} \tag{3}$$

where,

v = deflection due to prestressing cables

P = total prestressing force in the cables

e = eccentricity of the cables

L = Total length of the beam

x = distance of section from the end

E,I= modulus of elasticity and moment of inertia about strong axis of the section

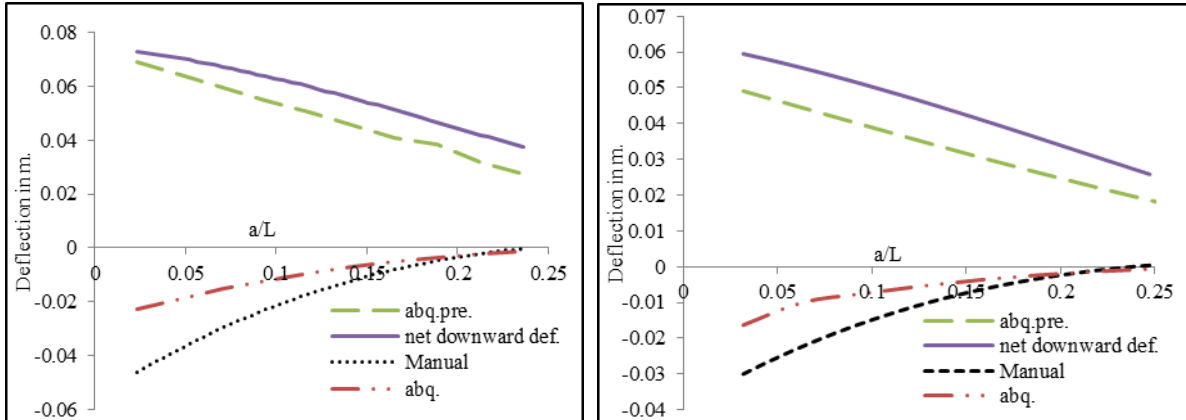


Fig. 12 Downward Deflection at midsection (77in. PCI Bulb Tee & Type IV AASHTO Beam respectively)

Following Fig.13 shows lateral deflection at end-sections. The deflection behaviour for non-prestressed beam is observed to be same, whereas for prestressed beam it goes on increasing as a/L ratio increases. Thus the effect due to prestress observed is significant.

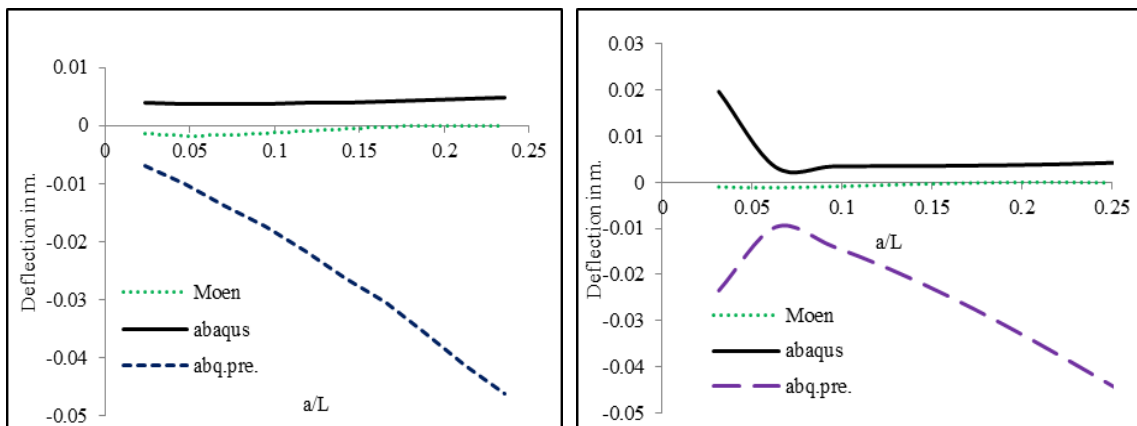


Fig. 13 Lateral Deflection at end section (77in. PCI Bulb Tee & Type IV AASHTO Beam respectively)

Fig.14 shows the downward deflection at end-section for both beams. It is seen that the deflection observed in non prestressed beam is approximately same, but in prestressed beam the deflection observed is in opposite direction and increases drastically as 'a/L' ratio increases.

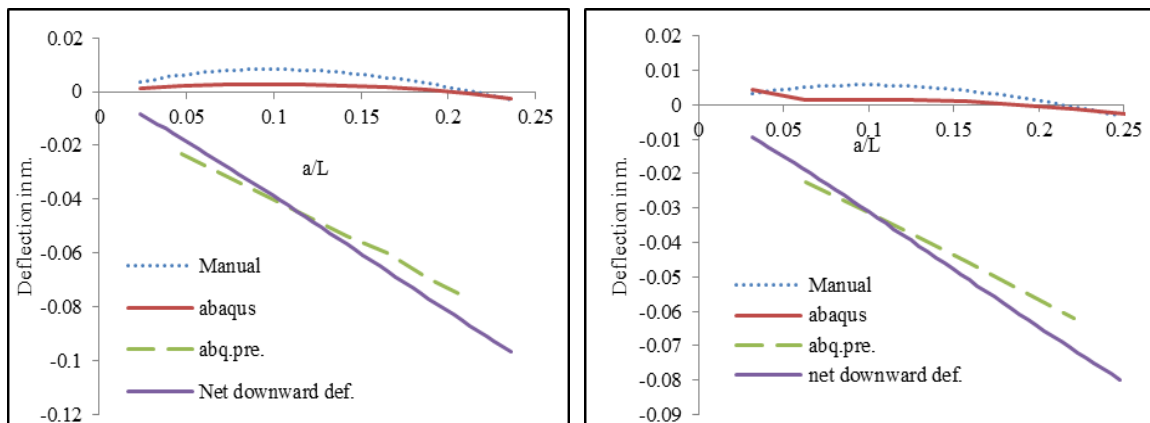


Fig. 14 Downward Deflection at end section (77in. PCI Bulb Tee & Type IV AASHTO Beam respectively)

#### IV. CONCLUSIONS

The Finite Element Analysis results are compared with the analytical equations obtained from Moen [3]. The results verify that the stress behaviour of both prestressed and non prestressed beams between analytical and Finite Element Analysis is same.

It is observed that for a prestressed beam the lifting loops should be far from the mid-section i.e. the 'a/L' ratio should be less than 0.2 to 0.25. Thus the stresses will be under permissible limits. On the contrary a beam without prestressing shows lesser deflection and stresses when the overhang normalized ratio is near by 0.2 to 0.25.

Also the behaviour for lateral and downward deflection shown by the finite element analysis and the formulae are same along the length, except the finite element analysis shows lateral deflection in opposite direction due to the effect of gravity.

The above given formulae combined with Moen's formulae can be used to calculate the deflection and stresses of any precast prestressed as well as non-prestressed beam at any section at hanging stage. Thus the results obtained should be useful in deciding the lift points of the prestressed beam to avoid cracking and collapse.

### REFERENCES

- [1] R. R. Imper and G. Laszlo, "Handling and shipping of long span bridge beams," PCI J., vol. 32, no. 6, pp. 86–101, 1987.
- [2] R. F. Mast, "Lateral stability of long prestressed concrete beams, Part 1," PCI J., vol. 34, no. 1, pp. 34–53, 1989.
- [3] R. Plaut and C. Moen, "Analysis of Elastic, Doubly Symmetric, Horizontally Curved Beams during Lifting," J. Struct. Eng., vol. 139, no. 1, pp. 39–46, 2013.
- [4] R. Plaut, C. Moen, and R. Cojocar, "Beam deflections and stresses during lifting," Eng. J., vol. 49, no. 4, p. 187, 2012.
- [5] R. V. Southwell, H. P. J. Taylor, C. J. Burgoyne, and T. J. Stratford, "Stability Design of Long Precast Concrete Beams.," Proc. ICE - Struct. Build., vol. 134, no. 2, pp. 155–168, Jan. 1999.
- [6] T. J. Stratford, SOUTHWELL, and C. J. Burgoyne, "Lateral Stability of Long Precast Concrete Beams.," Proc. ICE - Struct. Build., vol. 134, no. 2, pp. 169–180, Jan. 1999.
- [7] R. Swann and W. Godden, "The lateral buckling of concrete beams lifted by cables," Struct. Eng., vol. 44, no. 1, pp. 21–33, 1966.
- [8] W. Peart, E. Rhomberg, and R. James, "Buckling of Suspended Cambered Girders," J. Struct. Eng., vol. 118, no. 2, pp. 505–528, 1992.
- [9] R. Cojocar, "Lifting Analysis of Precast Prestressed Concrete Beams," masters diss., Virginia Polytechnic Institute and State University, Blacksburg, VA, 2012.
- [10] P. Riva and F. Minelli, "Numerical modeling of prestressed fiber reinforced high performance concrete beams subjected to shear."

## Performance and Emissions Analysis Using Diesel and Tsome Blends

Nirmal kumar. R<sup>1</sup>, Sarathbabu. R. T<sup>2</sup>

<sup>1</sup>Department of Mechanical Engineering, Trumalai Engineering College, Kiambi, Kanchipuram Dist, Tamil Nadu, INDIA

<sup>2</sup>Department of Mechanical Engineering, Trumalai Engineering College, Kiambi, Kanchipuram Dist, Tamil Nadu, INDIA

**Abstract:** The present study covers the various aspects of biodiesels fuel derived from crude Tobacco oil and performance emissions study on four stroke compression ignition engine with Tobacco seed oil. Crude Tobacco oil is converted to Tobacco seed oil methyl esters by transesterification process. The obtained bio-diesel fuel properties are measured.

The performance and emission parameters obtained by the above are compared with the base line data obtained earlier by using diesel and optimum Tobacco seed oil blend is obtained. The performance parameters obtained by the above tests are to be compared with diesel base line data and optimum blend B5.

**Keywords:** blend, TSOME, CI Engine, emission, performance

### I. INTRODUCTION

Diesel fuel has an essential function in the industrial economy of a developing country and used for transport of industrial and agricultural goods and operation of diesel tractors and pump sets in agricultural sector. The requirement of petro diesel in India is expected to grow from 39.815 MMT in 2001-02 to 52.324 MMT in 2006-07 and just over 66 MMT in 2011-12. The domestic supply of crude oil will satisfy only about 22% of the demand and the rest will have to be met from imported crude. This has stimulated recent interest in alternative sources to replace petroleum-based fuels. Of the alternative fuels, bio-diesel obtained from vegetable oils holds good promises as an eco-friendly alternative to diesel fuel Vegetable oil is a promising alternative fuel for CI engine because it is renewable, environment friendly and can be produced in rural areas. The use of non-edible vegetable oils compared to edible oils is very significant in developing countries because of the tremendous demand for edible oils as food and they are too expensive to be used as fuel at present. The term, bio-diesel, was first introduced in the United States during 1992 by the National Soy Development Board (presently National Biodiesel Board), which has pioneered the commercialization of biodiesel in the USA.

Tobacco seeds an excellent source of oil. The work done so far at CTRI has brought out tremendous scope for exploiting the crop for extraction of oil. In this background, emphasis will be laid on tobacco seed oil and suitable R&D initiatives are envisaged. India is the third largest consumer of edible oils and will account for 11% of global edible oil demand and 16% of global imports. The demand for edible oils in India has shown a steady growth at the rate of 4.43% over the period from 2001 to 2011. The current per capita consumption levels of India (at 13.3 Kg/year for 2009-10) are lower than global averages (24 kg/year). In terms of volumes, palm oil, soybean oil and mustard oil are the three largest consumed edible oils in India. There has been a significant gap between demand and supply of edible oil because of limited availability of oil seeds and shifting of acreage to other crops in the domestic market. This gap has been met through imports, which account for almost 45-50% of the total oil consumption. The dependence on imported oils to continue in the foreseeable future due to anticipated domestic supply constraints and the high cost competitiveness of imported oils.

Tobacco seed is a rich source of oil. Tobacco seeds contain about 35% semi-drying oil which is nicotine free. Tobacco seed is very small. There are about 3,00,000 seeds in one ounce, or more than 10,000 seeds per gram. One tobacco plant may produce one-half an ounce, or about 1,50,000 seeds, which is enough for 100 square yards of seedbed area. Under favourable conditions seeds from one plant may provide enough seedlings from 2 to 5 acres of field tobacco. In the recent year some new industrial uses of tobacco have been envisaged as a strategic development in case the anti-tobacco movement curbs its conventional use so that tobacco leaf farmer do not suffer by producing crop. The strategy does not make tobacco leaf available for

smoking but produce socially relevant useful products like good grade proteins and edible oils. It is appropriately named as “alternate use of tobacco.”

Tobacco seed oil has low toxicity, and its smell is rather strong. It is burnt in lamps throughout India, and acts as good charcoal. The high calorific value of tobacco seed oil matches diesel. It blends with diesel, substituting for nearly 35% of the later, and has been suggested for use without any major engine modification and without any worthwhile drop in engine efficiency. A mature tobacco plant may produce 0.5- 1 kg of fruit each year. Tobacco seeds yield 35% oil. Presently, billions of tobacco seeds are wasted in India, because of the lack of a proper collect.

Biodiesel was produced from non-edible tobacco seed oil having a free fatty acid content of 19% in a two-step process, as free fatty acid of more than 1% in the feedstock adversely affects the single step alkali catalyzed transesterification process by soap formation. The first step of acid catalysed esterification reduced the free fatty acid content of tobacco seed oil to below 1%. The optimum combinations of parameters for pre-treatment were found to be 0.60 volume by volume (v/v) methanol-to-oil ratio, 1% v/v KOH acid catalyst and 1 hr reaction time. The next base catalysed transesterification process converted the pre-treated oil to tobacco seed biodiesel. The optimum combination of parameters for transesterification was found to be 0.24 v/v methanol to- oil ratio, 1.08% weight by volume (w/v) catalyst concentration and 60 min reaction time. This two-step process gave an average yield of 90%. The fuel properties of tobacco seed biodiesel were found to be comparable to those of diesel, and conform to the latest American Standards for Testing of Materials Standards.

## II. History of Tobacco

The genus *nicotiana* is one of the five major genera of the family *solanaceae*. *N. Tabacum* l. And *n. Rustica* l. Are the only two cultivated species in the genus and several commercial varieties of them are being cultivated throughout the world. Among the sixty four or more species of *nicotiana*, *n. Tabacum* is the most widely grown for commercial use. *N. Rustica* is grown commercially only in limited areas of china, india and the ussr. *N. Tabacum* is a natural amphidiploid ( $2n = 48$ ) thought to have arisen by hybridization of wild progenitor species. Different types of tobaccos grown commercially are defined to a large extent by region of production, method of curing and intended use in the manufacturing as well as some distinct morphological characters and chemical differences. As the country is endowed with diverse agro-climatic zones, it grows all types of tobacco, which are broadly classified as flue-cured virginia (fcv) and non-fcv types.

Tobacco is one of the most economically important agricultural crops in the world. It provides livelihood for millions of people, billions of dollars in trade and trillions of dollars in business. Tobacco is a native of the subtropical zone. For economic reasons it is now being produced commercially in about every corner of the earth. Evidence suggests it originated from south america.

Tobacco is an important commercial crop of india with an area of about 4 lakhs ha and producing about 750 million kg. India stands at 2nd and 3rd position at world level for production and exports of tobacco respectively. Tobacco is contributing annually about rs. 20,000/- crores as excise duty and about rs.4020/- crores towards foreign exchange. Different types of tobacco *viz.* Flue-cured virginia (fcv), burley, bidi, natu, cheroot, hookah, cigar-wrapper, cigar-filler and chewing are being cultivated under different agro climatic conditions. In india, tobacco is grown mostly in andhra pradesh, gujarat, karnataka, tamil nadu, bihar, orissa, maharashtra, uttar pradesh and west bengal.

- The plant of tobacco for energy applications, contrary to the tobacco for the cigarettes industry, maximizes the production of flowers and seeds to the detriment of the leaves production and quality
- Its tobacco seed has a diameter of about 0.6 mm and is produced by the inflorescence in capsules 1.5 cm long, each capsule holds 0.5 g of seeds and each inflorescence more than 100 capsules
- The plant is extremely robust, able to grow in various climates and soils, as a matter of fact it can be cultivated on marginal lands which cannot be used for food production
- It is an annual plant, with the harvest in the same year of the sow, allowing farmers to plan every year the size of dedicated fields

Tobacco seeds maintain high viability under proper storage conditions. Kincaid (1958) reported tobacco seed maintained high viability for 25 years in tight containers, either refrigerated or desiccated or both. Seed stored in a paper envelope or a cloth bag in the laboratory deteriorated rapidly, while those in the refrigerator maintained high viability for 15 years but not for 20 years. Free access of air appeared unfavourable to maintenance of viability for more than 15 years. The two principle factors affecting viability of seeds in storage are seed moisture and temperature. Under ideal storage conditions both the seed moisture

content and temperature are kept low, but in practice it is often sufficient to control only one of these factors. It is the common practice to store tobacco seed at low moisture content (approximately 4%) with temperature below 21°C (70°F) in an air tight container. The seed contain reserve store of lipids, proteins, carbohydrates etc. To provide nourishment for the growing embryo. The degradation of these components influences viability.

Ageing is the major cause of loss of viability in seed. Ageing in all organism is the sum total of deteriorative process that eventually leads to death. Seeds are considered dead when in the absence of dormancy they fail to germinate under optimal conditions. Ageing and the consequent biochemical deterioration in the seeds gets accelerated at higher temperature and moisture content. At temperatures more than critical seed moisture level, seed respiration proceeds at faster than normal level and complex molecules like fats, proteins, and carbohydrates get broken down into simpler molecules (free fatty acids, amino acids and simple sugars). Membrane integrity and cellular compartment in the seed is slowly broken down on imbibition of water and the seed loses its food reserve into the surrounding medium resulting in the lack of nourishment for the embryo to grow and germinate. The result of ageing is accumulation of free fatty acids, amino acids and sugars in the seeds. The seed is thus central to crop production.

Tobacco seed is a rich source of oil. Tobacco seeds contain about 35% semi-drying oil which is nicotine free. The seeds also contain a few protein species that are present in high amounts and provide a store of amino acids for use during germination and seedling growth. These storage proteins are of particular importance not only because they comprise nearly the total protein content of the seed but also because they determine its quality for various uses (shewry et al., 1995). Seed proteins have been classified in many different ways. Osborne's classification, based on solubility, dates from the turn of the century and one of the most useful methods. By solubility criteria, proteins are classified into groups on the basis of their extraction and solubility in water (albumins), dilute saline solutions (globulins), alcohol/water mixtures (prolamins) and dilute acid or alkali solutions (glutelins) (ashton, 1976). However, the divisions between these groups of protein are not always clearly defined. For instance, the extraction depends on the sequence in which the solvents are used, on the vigor of the extraction and on the conditions of the starting material (padhye and salunkhe, 1979; shewry et al; 1995). On the other hand, the globulins from different plant sources usually require salt solutions of different ionic strength to solubilise completely (danielson, 1955).

In the recent years some new industrial uses of tobacco have been envisaged as a strategic development in case the anti-tobacco movement curbs its conventional use so that tobacco leaf farmer do not suffer by producing the crop. the strategy does not make tobacco leaf available for smoking but produces socially relevant useful products like good grade proteins and edible oils. it is appropriately named as "alternate use of tobacco.



Fig 1. Tobacco seeds

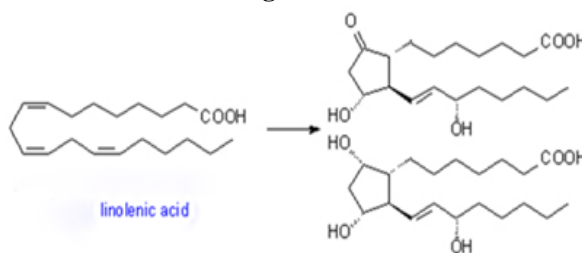


Fig 2 Chemical Structure of Tobacco seed Oil

## 2.1 Properties of Tobacco Seed Oil

Appearance:-	:yellow
Melting point:	:19°C
Boiling point:	: 320°C
Specific Gravity (gm. cm <sup>-3</sup> )	:0.917
Flash point:	:210°C
Auto-ignition temperature:	:343°C
Stability:	: Generally stable, but polymerizes gradually upon Exposure to air.
Combustibility:	: Incompatible with strong oxidizing agents. Reacts Violently with chlorine. Rags or paper impregnated with seed oil may spontaneously combust after a long period due to gradual exothermic reaction with oxygen.
Toxicology	: Skin irritant (not in all cases). May be allergenic.
Transport information:	: Non-hazardous for air, sea or road freight.
Personal protection:	: Gloves and adequate ventilation.

Tobacco seed Oil is also a valuable tool in the preservation of concrete. An application of seed oil penetrates the surface of the concrete forming barrier to water. It stabilizes the surface of the concrete, reduces the formation of dust and prevents corrosive breakdown of the steel reinforcing rods.

## 2.2 Steps in Production Of Bio-Diesel

1. Transesterification.
2. Settling and Separation of esters and glycerin.
3. Washing of bio-fuel
4. Heating.

The most common derivatives of agricultural oil for fuels are methyl esters. These are formed by trans esterification of the oil with methanol in the presence of a catalyst (usually basic) to give methyl ester and glycerol. Sodium hydroxide (NaOH) is the most common catalyst, though others such as potassium hydroxide (KOH) can also be used. Contents used in trans esterification process are

Veg oil: Cotton seed oil, sun-flower oil.

Alcohols: Methanol.

Catalyst: Sodium hydroxide, Potassium hydroxide.

100gr oil+25gr methanol+1gr KOH a 95gr biodiesel+26gr glycerine

## 2.3 Steps Involved In Transesterification

1. Catalyst is dissolved in alcohol using a standard agitator or a mixer.
2. Alcohol catalyst mix is then charged into a closed reaction vessel and bio lipid (Vegetable or animal oil or fat) is added.
3. Reaction mixture is kept just above the boiling point of alcohol with a recommended reaction of around 1-8 hours.
4. Un-reacted or excess alcohol is recovered by distillation which is recycled back.
5. The products containing the glycerol and ester namely the biodiesel are separated using a continuous decanter (with glycerin as underflow and biodiesel as overflow). Centrifuge is used to separate the two materials faster. Once separated from glycerin biodiesel is purified by washing gently with warm water to remove residual catalyst or soaps, dried and sent to storage.

We made the oil by extracting from the seeds by crushing process. Then the produced crude oil is filtered by using the serigraphy papers (A1,A2) filtered oil is preheated by direct heating. The molar ratio 16:1 we mixed methanol and KOH by the titration up to dissolving the KOH completely. This solution is mixed with tobacco crude oil

This solution is heated further to separate the glycerine and other fatty acids about 6hr. At constant temperature 60°C-75°C. The mixture solutions is cooled by using conical flask for 1daya keeping in atmosphere.

Then it formed 2 layers glycerine and pure bio-diesel. now the bio-fuel is separated and the blends are prepared with these tobacco bio-fuel.

blends are (B5, B10, B20, B30, B40) in the performance and analysis criteria

### 2.3.1 Equipment for Constant Heating

In transesterification process we need constant heating to separate the esters, for this we used a steam bath it is shown in plate 3.2



**Fig 3. Steam Bath**

### 2.3.2 Separation of ethyl esters

After transesterification the mixture at the end is settle for at least 10 hours. The lower layer will be of glycerin and the upper layers methyl ester (bio-fuel). After settling we have to separate the methyl ester from the glycerine shown in plates 3.2(a) and 3.2(b). The mixture is separated by using a separating flask.



**Fig 4 Process of Separation**



**Fig 5 Formation of Glycerin**

Glycerin is the useful by-product produced in process of making bio-diesel, which is used in the making of soap's and many other beauty products.

## III. Preparation of Blends with Diesel

The obtained Bio- Diesel is blended for conducting the performance test, the Tobacco seed Bio- Diesel is mixed in proper proportions.

### 3.1 Procedure

1. The Bio- Diesel is first filtered form impurities.
2. Required amount of fuel and Bio- Diesel is taken into the measuring jar and mixed thoroughly the amount of proportions shown in table 3.3(a) & 3.3(b).
3. Obtained TSOME fuel properties are find out and these values are tabulated in tables 3.10 to 3.13.

**Table3.1 Blending Percentage of Fuel**

Notation	Fuel Quantity	Bio-Diesel Quantity	Diesel Quantity
B5	1 LITRE FUEL	50 ml	950ml
B10	1 LITRE FUEL	100 ml	900 ml
B20	1 LITRE FUEL	200 ml	800 ml
B30	1 LITRE FUEL	300ml	700ml
B40	1 LITRE FUEL	400ml	600ml

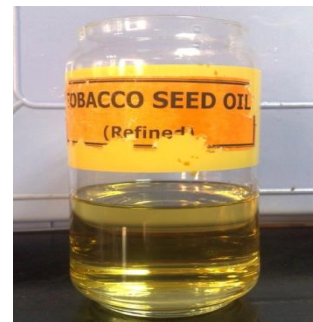
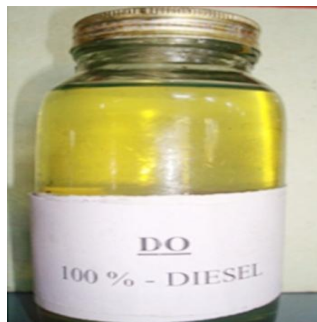


Fig 5 Tobacco seed Oil Blends (B5, B10, B20, B30, B40)      fig 7 Diesel and Tobacco crude oil

### 3.2 Specificgravity- Result

Table 3.2 Results of Specific Gravity for TSOME and Diesel

S.No	Oil	Blend	Specific Gravity
1.	Diesel	D100	0.835
2.	Tobacco Oil Crude		0.917
3	Tobacco seed Oil Methyl Ester Blends With Bio-Diesel (TSOME)	B5	0.6859
		B10	0.6988
		B20	0.7111
		B30	0.7282
		B40	0.7454

### 3.3 Viscosity – Results

Table3.3 Results of Viscosity for TSOME and Diesel at 40°C

S.NO	OIL		Kinematic Viscosity (stokes)	Dynamic Viscosity (Poise)
1	Diesel	D100	0.364	0.652
2.	Tobacco Oil Crude		0.484	0.738
3	Tobacco seed Oil Methyl Ester Blends With Bio- Diesel (TSOME)	TSOME	0.80	0.64

### 3.4 Flash Ans Fire Points – Results

Table3.4 Results of Flash Point and Fire of TSOME and Diesel

S.No	Oil		Flash Point °C	Fire Point °C
1.	Diesel	D100	58	62
2.	Tobacco Oil Crude	B100	185	192
3	Tobacco seed Oil Methyl Ester Blends With Bio- Diesel (TSOME)	TSOME	50	56

### 3.5 Carbon Percentages – Results

Table 3.5 Results of Carbon Residue for TSOME and Diesel

Oil		% of Carbon
Diesel	D100	0.12
Tobacco seed Oil Methyl Ester Blends With Bio- Diesel (TSOME)	TSOME	0.22

### 3.6 Calorific Value Results

Table 3.6 Results of Calorific Value in kJ/kg for TSOME and Diesel

	Crude	B5	B10	B20	B30	B40
Tobacco seed oil kJ/kg	38438	42181	41862	41224	40586	39948
Diesel kJ/kg	42500	42500	42500	42500	42500	42500

After find all properties of TSOME then next stage performance and emissions parameters are find with the help of 4-stroke single cylinder compression ignition diesel engine, gas analyser and smoke meter.

## IV. Experimental Setup and Procedure

### 4.1 Introduction

Using TSOME oil tests are to be conducting on different equipment's, to be found some of the fuel properties. Later performance and emission tests were conducted on 4- stroke single cylinder water cooled diesel engine coupled with a rope brake dynamometer, with the help of Smoke meter and multigas analyzer.

### 4.2 Diesel Engine

Experimental set up consists of a water cooled single cylinder vertical diesel engine coupled to a rope pulley brake arrangement it shown in plate 4.6, to absorb the power produced necessary weights and spring balances are induced to apply load on the brake drum suitable cooling water arrangement for the brake drum is provided. A fuel measuring system consists of a fuel tank mounted on a stand, burette and a three way cock. Air consumption is measured by using a mild steel tank which is fitted with an orifice and a U-tube water manometer that measures the pressures inside the tank. For measuring the emissions the gas analyser is connected to the exhaust flow.

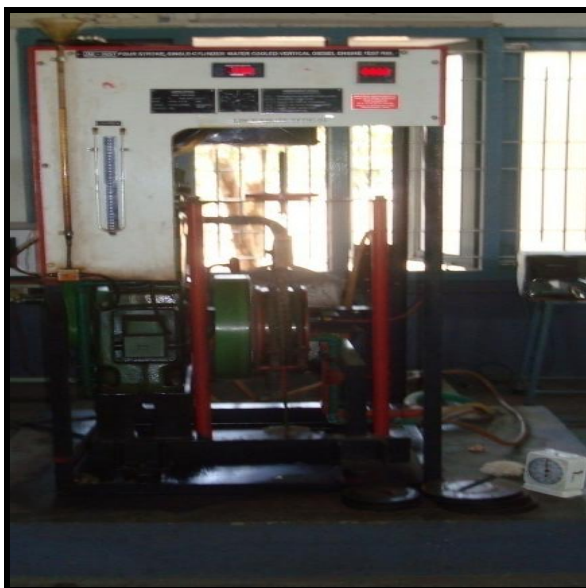
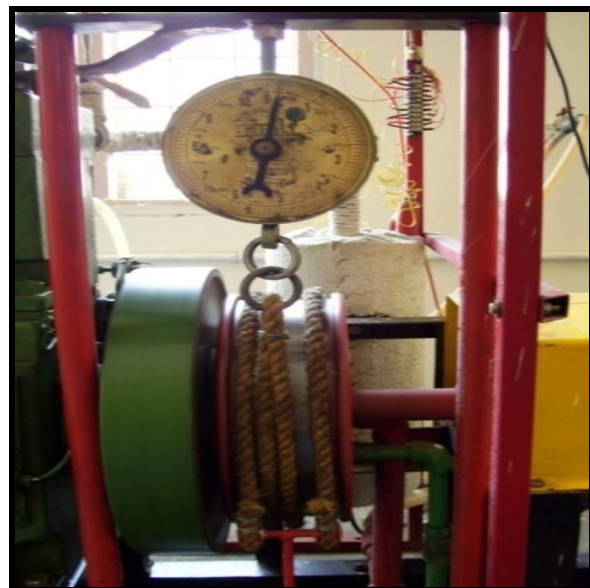


Fig 8 (a) 4- Stroke diesel engine



(b) Dynamometer

#### **4.2.1 Description**

This is a water cooled single cylinder vertical diesel engine is coupled to a rope pulley brake arrangement to absorb the power produced necessary weights and spring balances are induced to apply load on the brake drum suitable cooling water arrangement for the brake drum is provided. Separate cooling water lines are provided for measuring temperature. A fuel measuring system consists of a fuel tank mounted on a stand, burette and a three way cock. Air consumption is measured by using a mild steel tank which is fitted with a orifice and a U-tube water manometer that measures the pressures inside the tank. Also digital temperature indicator with selector switch for temperature measurement and a digital rpm indicator for speed measurement are provided on the panel board. A governor is provided to maintain the constant speed. For measuring the emissions the gas analyser is connected to the exhaust flow.

#### **4.2.2 Procedure**

Note down engine specifications and ambient temperature.

1. Calculate full load (W) that can be applied on the engine from the engine specifications.
2. Clean the fuel filter and remove the air lock.
3. Check for fuel, lubricating oil and cooling water supply.
4. Start the engine using decompression lever ensuring that no load on the engine and supply the cooling water
5. Allow the engine for 10 minutes on no load to get stabilization.
6. Note down the total dead weight, spring balance reading, speed, time taken for 20cc of fuel consumption and the manometer readings.
7. Repeat the above step for different loads up to full load.
8. Allow the engine to stabilize on every load change and then take the readings.
9. Before stopping the engine remove the loads and make the engine stabilized.
10. Stop the engine pulling the governor lever towards the engine cranking side. Check that there is no load on engine while stopping

### **V. Experimental Observation**

#### **5.1 Introduction**

The engine was first operated on diesel fuel with no load for few minutes at rated speed of 1500 rpm until the cooling water and lubricating oil temperatures comes to certain temperature. The same temperatures were maintained throughout the experiments with all the fuel modes. The baseline parameters were obtained at the rated speed by varying 0 to 100% of load on the engine.

The diesel fuel was replaced with the Tobacco seed oil biodiesel (B5) and test was conducted with the blend of 95% diesel and 10% biodiesel by varying 0 to 100% of load on the engine with an increment of 20%. After the Tobacco seed oil biodiesel, the test was conducted with the blend of 90% diesel and 10% biodiesel (B10). After the Tobacco seed oil biodiesel, the test was conducted with the blend of 80% diesel and 20% biodiesel (B20). After the Tobacco seed oil biodiesel, the test was conducted with the blend of 70% diesel and 30% biodiesel (B30) and after the Tobacco seed oil biodiesel, the test was conducted with the blend of 60% diesel and 40% biodiesel (B40).

The directly blended fuel does not require any modifications to diesel engines. Hence direct blending method was used in this test. The tests were conducted with these three blends by varying the load on the engine. The brake power was measured by using an electrical dynamometer. The mass of the fuel consumption was measured by using a fuel tank fitted with a burette and a stop watch. The brake thermal efficiency and brake specific fuel consumption were calculated from the observed values. The exhaust gas temperature was measured by using an iron-constantan thermocouple.

The exhaust emissions such as carbon monoxide, carbon dioxide, nitrogen oxides, hydrocarbons and unused oxygen were measured by exhaust an analyser and the smoke opacity by smoke meter. The results from the engine with a blend of diesel and biodiesel and compared with the baseline parameters obtained during engine fuelled with diesel fuel at rated speed of 1500 rpm. Out of these three blends best blend is obtained on the basis of performance parameters. In this experiment B5 shows the best results. and compared with the baseline parameters obtained during engine fuelled with diesel fuel at rated speed of 1500 rpm.

## VI. Results and Discussion

### 6.1 Introduction

The experiments are conducted on the four stroke single cylinder water cooled diesel engine at constant speed (1500 rpm) with varying 0 to 100% loads with diesel and different blends of TSOME like B5, B10, B20, B30

and B40. The performance parameters such as brake thermal efficiency and brake specific fuel consumption were calculated from the observed parameters and shown in the graphs.

The other emissions parameters such as exhaust gas emissions such as Carbon monoxide, hydrocarbons, and oxides of nitrogen, carbon dioxide, unused oxygen and smoke were represented in the form of graphs from the measured values. The variation of performance parameters and emissions are discussed with respect to the brake power for diesel fuel, diesel-biodiesel blends and obtained optimum blend are discussed in below article.

### 6.2 Performance Analysys Using Pure Diesel and Its Blends of Tsome

In this stage various performance parameter characteristics are discussed in below for diesel, TSOME -diesel blends.

#### 6.2.1 Brake Thermal Efficiency

The variation of brake thermal efficiency with brake power for different fuels is presented in Fig.6.1. In all cases, it increased with increase with brake power. This was due to reduction in heat loss and increase in power with increase in load. The maximum thermal efficiency for B5 at full load 44.27%, was higher than that of diesel (32.16%). Increase in thermal efficiency due to % of oxygen presence in the biodiesel, the extra oxygen leads to causes better combustion inside the combustion chamber. The thermal efficiency of the engine is improved by increasing the concentration of the biodiesel in the blends and also the additional lubricity provided by biodiesel. The reason may be the leaner combustion of diesel and extended ignition delay resulting in a large amount of fuel burned.

The increment of BTE was observed with B5 at full load is 12.11% higher than that of diesel fuel.

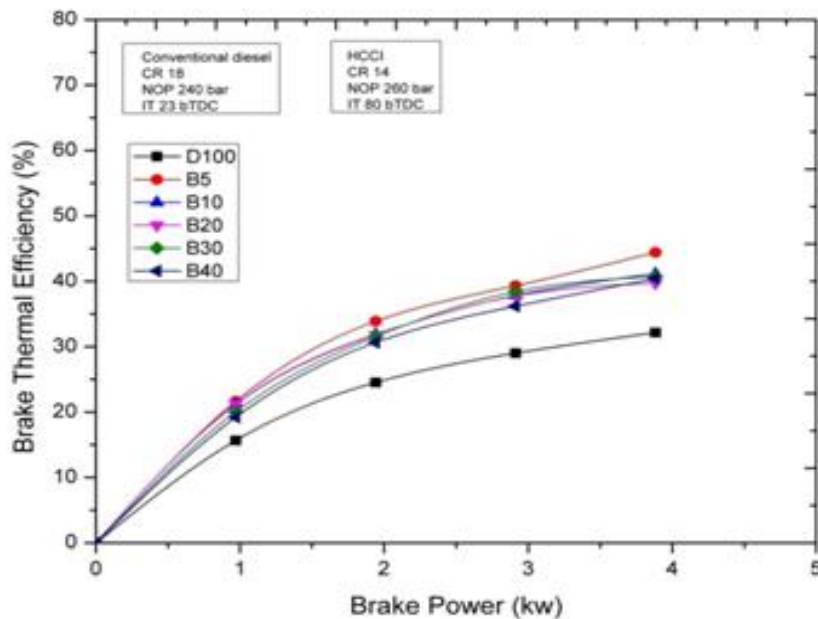


Fig.9 Variation of Brake Themral Efficiency with Brake power using TSOME Blends

#### 6.2.2 Brake Specific Fuel Consumption

The variation in BSFC with brake power for different fuels is presented in Fig.6.3. Brake-specific fuel consumption (BSFC) is the ratio between mass fuel consumption and brake effective power, and for a given fuel, it is inversely proportional to thermal efficiency. BSFC decreased sharply with increase in brake power for all fuels. The main reason for this could be that the percent increase in fuel required to operate the engine is less than the percent increase in brake power, because relatively less portion of the heat is lost at higher loads.

It can be observed that the BSFC of 0.256kg/kW-hr were obtained for diesel and 0.1324 kg/kW-hr B5 at full load. It was observed that BSFC decreased with the increase in concentration of TSOME in diesel. The BSFC of Bio-diesel is decreases up to 18.52% as compared with diesel at full load condition.

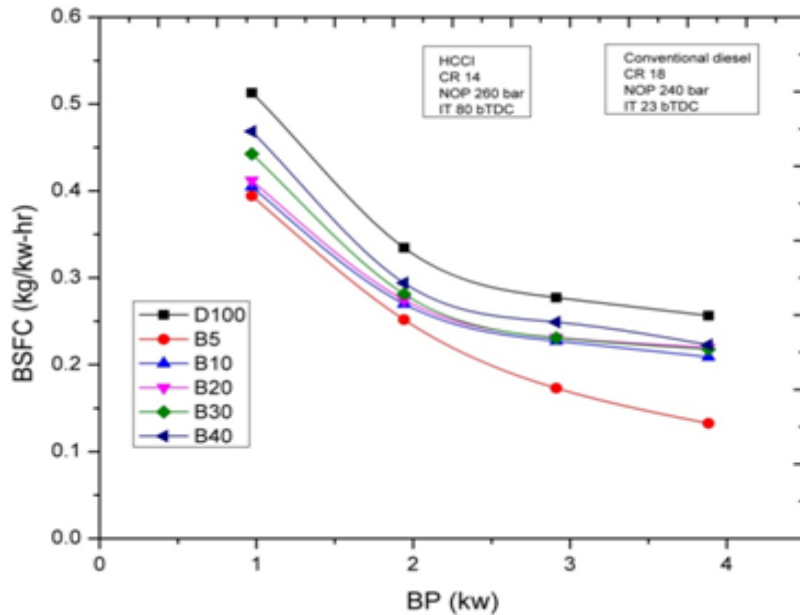


Fig.10 Variation of Brake specific fuel consumption with Brake Power using TSOME Blends

### 6.2.3 Air-Fuel Ratio

The A/F ratio that was obtained from calculations is plotted against brake power and compared the results for different blends of fuels as shown in Fig.6.6. As the percentage of TSOME is increased in blends A/F ratio increased negligibly for B10,B20,B30 and B40 blends at constant injection pressure. A/F for diesel is 23.16, where as in case of B5 40.23 from that it is observed decrease in A/F up to 5.56% compares with diesel at full load condition. In the same way decrement of A/F occurred in B10 and B40.

The air fuel ratio decreases due to increase in load because of the compensation of load can only be done with increasing the quantity of fuel injection to develop the power required to bare the load.

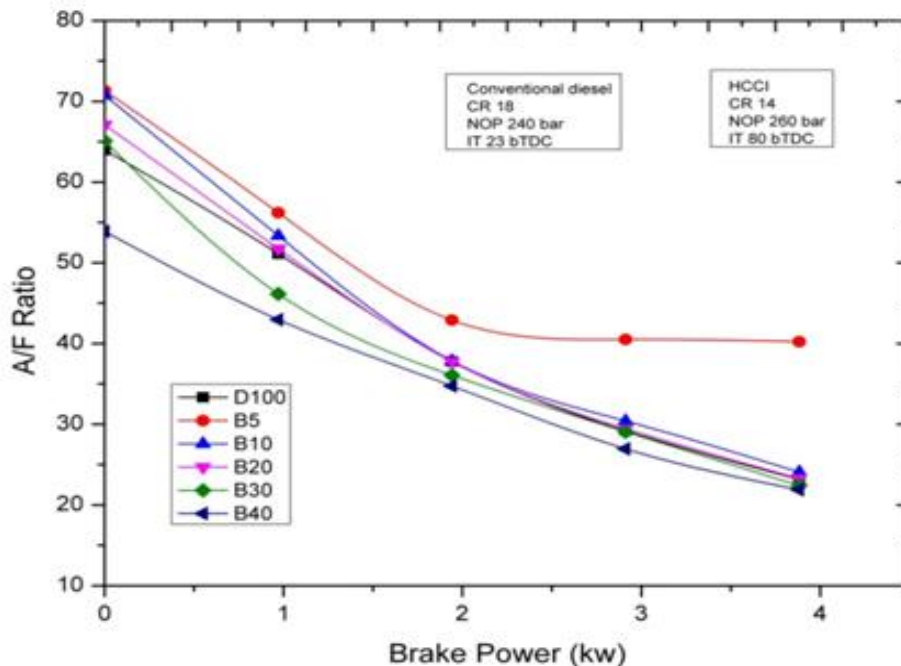


Fig.11 Variation of Air-Fuel Ratio with Brake Power using TSOME Blends

#### 6.2.4. Smoke Density

The variation of Smoke density emissions with brake power for diesel fuel, biodiesel-blends is shown in the Fig.6.12. The smoke is formed due to incomplete combustion in engine.

The smoke density is lower for B5 compared to B10 and D100. The maximum smoke density recorded for the diesel was 83.57 HSU, 64.37HSU for B10, 60.65 HSU for B20, 50.36 HSU for B30, 65.57 HSU for B40 and 45.69 HSU for B5 at maximum load. The decrease in smoke density of B5, B10, B20, B30 and B40 is 45.32%, 22.97%, 27.42%, 39.72% and 21.53% respectively compared with diesel fuel at full load. In case of TSOME, the smoke emission is low. This is because of better combustion of TSOME. The smoke density increased with the load for diesel fuel and diesel blends. The smoke opacity of the pure biodiesel was higher than those of all the other fuels used generally. Smoke opacity of the blends B5, B10, B20, B30 and B40 were lower than those of the diesel fuel at all loads on the engine.

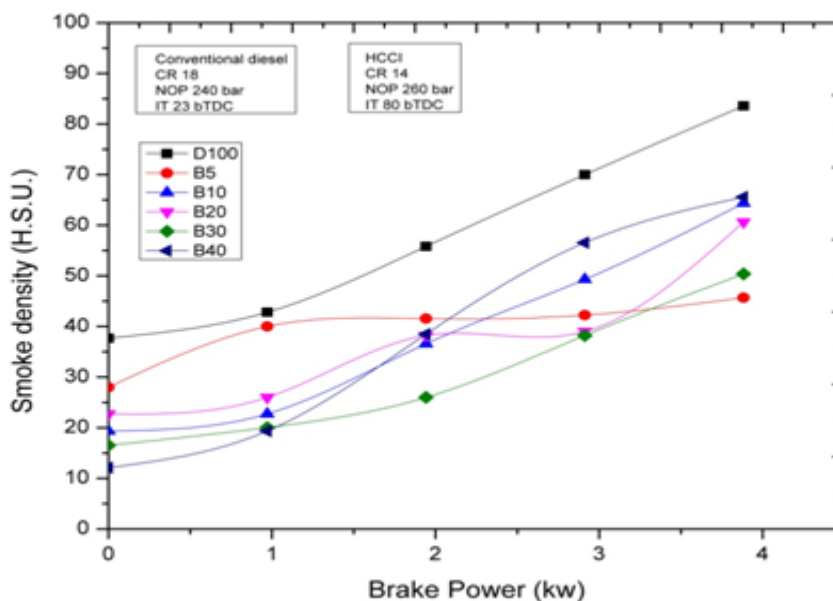


Fig.12 Variation Smoke deensity with Brake power using TSOME Blends

### VII. Performance And Emissions Analysis Using Diesel And Tsome Blends

In this experimental study, the effect of Tobacco seed oil Methyl ester blends and diesel fuel on engine performance and exhaust emissions were investigated on single cylinder ,water cooled and direct injection at constant speed of 1500 rpm. Out of all blends of Tobacco oil methyl esters B5 shows best results in performance and Smoke Density parameters.

The conclusions of this investigation are compared with diesel base line data at full load as follows:

- The maximum brake thermal efficiency for B5 (44.42%) was higher than that of diesel.
- The brake thermal efficiency increased in 12.11% compared with diesel.
- Brake specific fuel consumption is decreases in blended fuels. In B5 fuel the BSFC is lower than the diesel in 18.52%.
- Significant reductions were obtained in smoke Density, Smoke Density was increased by 45.32% with B5 compared to diesel at maximum load of the engine.

### VIII. Conclusion

The performance and emission characteristics of conventional diesel, diesel and biodiesel blends were investigated on a single cylinder diesel engine. The conclusions of this investigation at full load are as follows:

- The brake thermal efficiency increases with increase biodiesel percentage. Out of all the blends B5 shows best performance and emissions parameters. The maximum brake thermal efficiency obtained is 44.42% with B5 blend.
- As a CI engine fuel, B5 blend results in an average reduction of 21.53% smoke densities.
- Since B5 blend reduces the environmental pollution, high in thermal efficiency when compared with diesel it will be a promising renewable energy source for sustaining the energy.

## REFERENCES

### Journal Papers:

- [1] Vern Hofman and Elton Solseng “Biodiesel Fuel Use In an Unmodified Diesel Engine”. An ASAE /CSAE Meeting Presentation, Paper No: MBSK 02-109.
- [2] S.Jaichandar and K.Annamalai, “The Status of Biodiesel as an Alternative Fuel for Diesel Engine –An Overview” *Journal of Sustainable Energy & Environment* 2 (2011) pages no:71-75.
- [3]. N.L. Panwar a,\*, Hemant Y. Shrirame a, N.S. Rathore a, Sudhakar Jindal b, A.K. Kurchania, Performance evaluation of a diesel engine fueled with methyl ester of castor seed oil, *Applied Thermal Engineering* 30 (2010) ,pp245–249
- [4]. F. Karaosmanogĭ lu, G. Kurt, T. OÈ zaktas, Long term CI engine test of sunflower oil, *Renewable Energy* 19 (2000) ,pp219-221
- [5]. A.S. Ramadhas , S. Jayaraj, C. Muraleedharan, Use of vegetable oils as I.C. engine fuelsA review, *Renewable Energy* 29 (2004) ,pp727–742
- [6]. Murat Karabektas , Gokhan Ergen , Murat Hosoz ,The effects of preheated cottonseed oil methyl ester on theperformance and exhaust emissions of a diesel engine, *Applied Thermal Engineering* 28 (2008) ,pp2136–2143
- [7]. M. Mani a,\*, C. Subash b, G. Nagarajan b , Performance, emission and combustion characteristics of a DI diesel engine using waste plastic oil, *Applied Thermal Engineering* 29 (2009) 2738–2744.
- [8]. M.H. Mat Yasin a,†, Talal Yusaf b, R. Mamat a, A. Fitri Yusop a, Characterization of a diesel engine operating with a small proportion of methanol as a fuel additive in biodiesel blend, *Applied Energy* xxx (2013) xxx–xxx
- [9]. H. An, W.M. Yang †, A. Maghbouli, J. Li, S.K. Chou, K.J. Chua, Performance, combustion and emission characteristics of biodiesel derived from waste cooking oils *Applied Energy* xxx (2013) xxx–xxx.
- [10]. Alireza Shirneshana , a , HC, CO, CO2 and NOx Emission evaluation of a diesel engine fueled with waste frying oil methyl ester, *Procedia - Social and Behavioral Sciences* 75 ( 2013 ) 292 – 297
- [11]. Cenk Sayin, Metin Gumus,Impact of compression ratio and injection parameters on the performanceand emissions of a DI diesel engine fueled with biodiesel-blended diesel fuel, *Applied Thermal Engineering* 31 (2011),pp 3182-3188
- [12]. 05Octavio Armas , Reyes García-Contreras, Ángel Ramos, Impact of alternative fuels on performance and pollutant emissionsof a light duty engine tested under the new European driving cycle, *Applied Energy* 107 (2013) ,pp183–190
- [13]. 07A.M. Liaquat\*, H.H. Masjuki, M.A. Kalam, I.M. Rizwanul Fattah, M.A. Hazrat,M. Varman, M. Mofijur, M. Shahabuddin, Effect of coconut biodiesel blended fuels on engine performance and emission characteristics, *Procedia Engineering* 56 ( 2013 ) ,pp583 – 590
- [14]. T.T. AL-Shemmeri\*, S. Oberweis,Correlation of the NOx emission and exhaust gas temperature for biodiesel, *Applied Thermal Engineering* 31 (2011) 1682e1688.
- [15]. Yimin Liu , Gloria E. Helfand , A hedonic test of the effects of the Alternative Motor Fuels Act, *Transportation Research Part A* 46 (2012) ,pp1707–1715
- [16]. K. Pramani, Properties and use of jatrophacurcas oil and diesel fuel blends in compression ignition engine, *Renewable Energy* 28 (2003) 239–248.
- [17]. H. An, W.M. Yang †, S.K. Chou, K.J. Chua, Combustion and emissions characteristics of diesel engine fueled by biodiesel at partial load conditions, *Applied Energy* 99 (2012) 363–371.
- [18]. O.M.I. Nwafor, Efect of choice of pilot fuel on the performance of natural gas in diesel engines, *Renewable Energy* 21 (2000),pp 495-504
- [19]. D.John Panneer Selvam a and K.Vadivel, Performance and emission analysis of DI diesel engine fuelled with methylester of beef t allowand diesel blends, *Procedia Engineering* 38 ( 2012 ) ,pp342 – 358
- [20] C.V. Sudhir,N.Y. Sharma and P.Mhonanan, “Potential of waste Cooking Oils as Biodiesel Feed Stock,”*Emirates Journal for Engineering Research*, 12 (3) (2007),pages no: 69-75

## Case Study of MHD Generator for Power Generation and High Speed Propulsion

Md Akhtar khan<sup>1</sup>, Kavya vaddadi<sup>2</sup>, Avinash gupta<sup>3</sup>, karrothu vigneshwara<sup>4</sup>

<sup>1</sup>Assistant Professor@GITAM University-Hyderabad,

<sup>2</sup>Student@MLRIT,<sup>3</sup>Student@GITAM UNIVERSITY

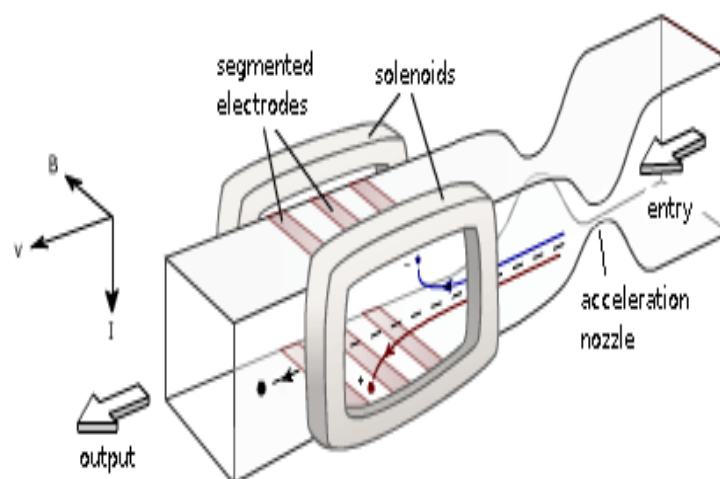
<sup>4</sup>Student@GNITC

**Abstract:** The main scope of the project is calculating the output power or the capacity of Eco-friendly Magneto Hydrodynamic Generator. Capacity of Thermal power station in India is compared with Eco-MHD. Modern society requires a variety of goods and services which require energy as the diversity of range of services increases so is the demand for energy. Electrical energy because of its versatility takes major share. About 75% of electrical energy is generated by thermal stations. Coal has to be transported to thermal stations located away from coalfields by railways and power has to be transmitted over large distances from pithead stations. These problems can be eliminated or reduced by converting coal into SNG (synthetic natural gas) at pithead and transporting the gas by pipe-grid to all thermal stations. The efficiency of power station can be increased by adopting combined cycle. Topping combined cycle by MHD generators failed to materialize. Eco friendly Magneto hydrodynamic generator is now suggested for development as a topping addition for combined cycle to further improve the efficiency.

**Keywords:** MHD Generator, MHD aerodynes, High speed propulsion, sunspot modelling, Hypersonic vehicle

### I. Introduction

The MHD (magneto hydrodynamic) generator transforms thermal energy and kinetic energy directly into electricity. MHD generators are different from traditional electric generators in that they operate at high temperatures without moving parts. MHD was developed because the hot exhaust gas of an MHD generator can heat the boilers of a steam power plant, increasing overall efficiency. MHD was developed as a topping cycle to increase the efficiency of electric generation, especially when burning coal or natural gas. MHD dynamos are the complement of MHD propulsor, which have been applied to pump liquid metals and in several experimental ship engines.[1]



**MHD Generator**

Faraday linear nozzle with segmented electrodes

Fig.1 MHD generator [7]

An MHD generator, like a conventional generator, relies on moving a conductor through a magnetic field to generate electric current. The MHD generator uses hot conductive plasma as the moving conductor. The mechanical dynamo, in contrast, uses the motion of mechanical devices to accomplish this. MHD generators are technically practical for fossil fuels, but have been overtaken by other, less expensive technologies, such as combined cycles in which a gas turbine's or molten carbonate fuel cell's exhaust heats steam to power a steam turbine. Natural MHD dynamos are an active area of research in plasma physics and are of great interest to the geophysics and astrophysics communities, since the magnetic fields of the earth and sun are produced by these natural dynamos.

The Lorentz Force Law describes the effects of a charged particle moving in a constant magnetic field. The simplest form of this law is given by the vector equation.

$$\mathbf{F} = Q \cdot (\mathbf{v} \times \mathbf{B})$$

Where,

- $\mathbf{F}$  is the force acting on the particle.
- $Q$  is the charge of the particle,
- $\mathbf{v}$  is the velocity of the particle, and
- $\mathbf{B}$  is the magnetic field.

The vector  $\mathbf{F}$  is perpendicular to both  $\mathbf{v}$  and  $\mathbf{B}$  according to the right hand rule.

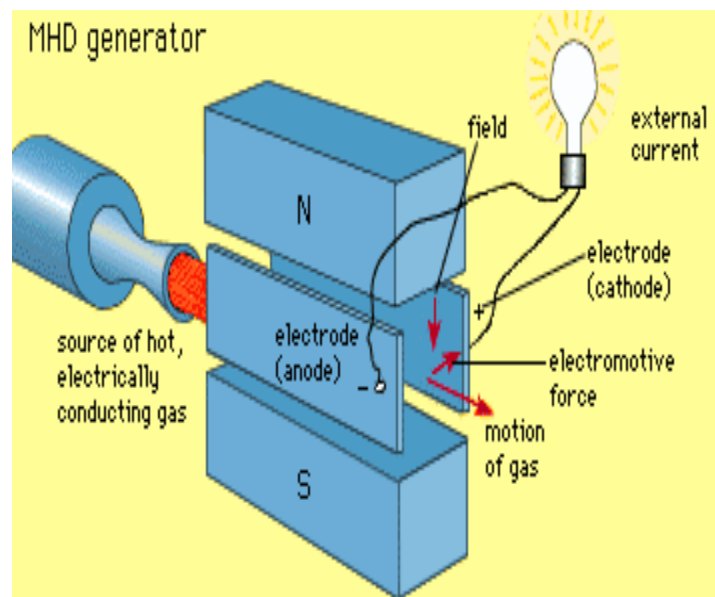


Figure-2 MHD generator producing electricity [1]

## II. Power Generation

Typically, for a large scale power station to approach the operational efficiency of computer models, steps must be taken to increase the electrical conductivity of the conductive substance. The heating of a gas to its plasma state or the addition of other easily ionisable substances like the salts of alkali metals can accomplish this increase. In practice, a number of issues must be considered in the implementation of an MHD generator: generator efficiency, economics, and toxic by products. These issues are affected by the choice of one of the three MHD generator designs: the Faraday generator, the Hall generator, and the disc generator.

It has been sixty years since various methods have been investigated in view of lowering heat transfer to high-speed Flying bodies. Hypersonic magnetized plasmas have been initially studied for space capsules equipped with Electromagnetic shields, around which air is naturally ionized due to subsequent heat behind shock waves, Later Work focused on detaching shock waves from leading edges of blunt bodies with upstream non-magnetized Plasma "air-spike" acting like a protective cushion for the materials. Ionization is then obtained through many means, including applying high voltage discharges, high frequency electromagnetic waves or lasers. Moreover, the modification of gas-dynamic through microwave radiation heats up the plasma and modifies the local value of the sound velocity, which attenuates the recompression behind a soft shock wave. But none of these methods really acts on the flow to truly impose one way or another to it.

A first category of plasma-aerodynamic devices actively acting upon the flow uses electro hydrodynamics. Those EHD accelerators are generally known as plasma actuators. They use properties of electric fields only (par electric body force, DC ion mobility drift or RF peristaltic waves) to carry the ions and the neutral gas through Lorentzian collisions upon a thin layer. Peristaltic EHD devices can theoretically

accelerate air in the boundary layer up to Mach 1.0 (neglecting heating and viscous effects which lower the real effect). But magneto hydrodynamics, involving both applied electric and magnetic fields combined into Lorentz forces  $J \times B$ , is preferred to control airflows up to hypersonic regimes.

Next-generation aircrafts of a new kind are described which, if supplied by a powerful energy source, could flight silently at high Mach numbers in dense air without shock wave nor turbulence, fully driven by MHD force fields controlling the flow around their whole body. In relation with such devices, original solutions to classical problems raised by plasma instabilities in the presence of powerful magnetic fields are proposed.

Among applications of MHD converters described in this paper: wave drag and wake turbulence cancellation, flow laminarization, engine inlet control, combination of accelerators and generators into MHD-bypass systems, HV plasma protection of leading edges, electromagnetic braking for atmospheric re-entry. The association of all these techniques leads to a unique device combining a space launcher, a plane and an atmospheric re-entry capsule into one fully reusable vehicle taking-off and landing on its own steam, successor of conventional rockets.

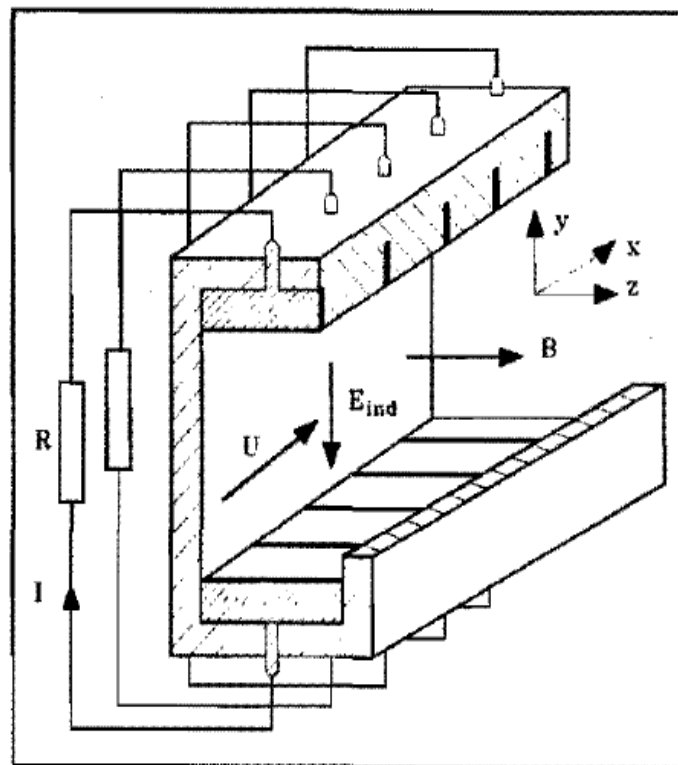


Fig.3 Principle of MHD generator[9]

When an electrical conductor is moved so as to cut lines of magnetic induction, the charged particles in the conductor experience a force in a direction mutually perpendicular to the  $B$  field and to the velocity of the conductor. The negative charges tend to move in one direction, and the positive charges in the opposite direction. This induced electric field, or motional emf, provides the basis for converting mechanical energy into electrical energy. At the present time nearly all electrical power generators utilize a solid conductor which is caused to rotate between the poles of a magnet. In the case of hydroelectric generators, the energy required to maintain the rotation is supplied by the gravitational motion of river water.

One of the earliest serious attempts to construct an experimental MHD generator was undertaken at the Westinghouse laboratories in the period 1938-1944, under the guidance of Karlovitz (see Karlovitz and Halasz, 1964). This generator (which was of the annular Hall type) utilized the products of combustion of natural gas, as a working fluid, and electron beam ionization. The experiments did not produce the expected power levels because of the low electrical conductivity of the -gas and the lack of existing knowledge of natural gas, as a working fluid, and electron beam ionization.

### III. MHD Generator Description

If gas flows in x direction and magnetic field B acts in y direction, the force on the particle acts in z direction.

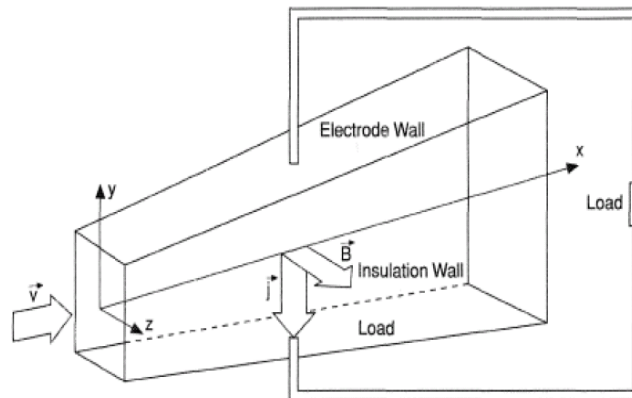


Fig.4 Direction of magnetic field, gas velocity and force in MHD system

#### MHD design problems:

- Efficiency attained are so far have been relatively low and life of the equipments has been short.
- Combustor, MHD-generator, channel, electrodes and air-prep-heater are exposed to corrosive gases at very high temperature. So material must be developed to permit long operating life.
- The ash (slag) residue from the burning coal is carried over with combustion gases and cause erosion of the exposed surface.

### IV. MHD For High speed Propulsion

#### 1. MHD Aerodynes

MHD (Magneto Hydrodynamic) propulsion has been extensively studied since the fifties. To shift from propulsion to an MHD Aerodyne, one only needs to accelerate the air externally, along its outer skin, using Lorentz forces. A set of successful experiments, obtained on a disk shaped model, placed in low density air, dealt with various problems: wall confinement of two-temperature plasma obtained by inversion of the magnetic pressure gradient, annihilation of the Velikhov electro thermal instability by magnetic confinement of the streamers, establishment of a stable spiral distribution of the current, obtained by an original method. Another direction of research is devoted to the study of an MHD-controlled inlet which, coupled with a turbofan engine and implying an MHD-bypass system, would extend the flight domain to hypersonic conditions.[3]

During the sixties it was shown that if the electrical conductivity of the gas was large enough (3,000S/m), Lorentz forces  $J \times B$  ( $B = 2$  teslas) could deeply modify the gas parameters of a supersonic flow ( $M = 1.4$ ) in a Faraday MHD converter. In a constant cross section channel, when slowing down the gas (short duration argon flow,  $T = 10,000^\circ\text{K}$ ,  $p = 1$  bar,  $V = 2750$  m/s, delivered by a shock driven wind tunnel) when slowing down, the deceleration was strong enough to create a front shock wave, without any obstacle. Accelerating the gas, velocity gain of 4,000 m/s was obtained along a 10 cm MHD channel. In supersonic flows, shock waves occur when the local slowing down is strong enough to produce self crossing of Mach lines.

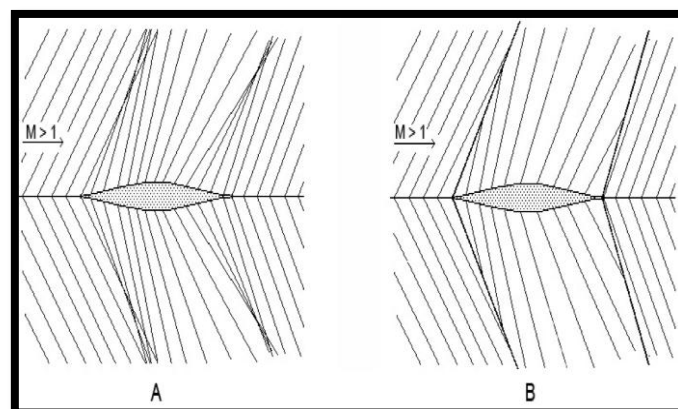


Fig.5-Two dimensional flows around a flat wing. Mach lines computed from Navier-stokes .[4]

It was shown, based on 2d-numerical calculation and hydraulic simulation that those shock waves could be eliminated if a suitable Lorentz force was applied around the model.

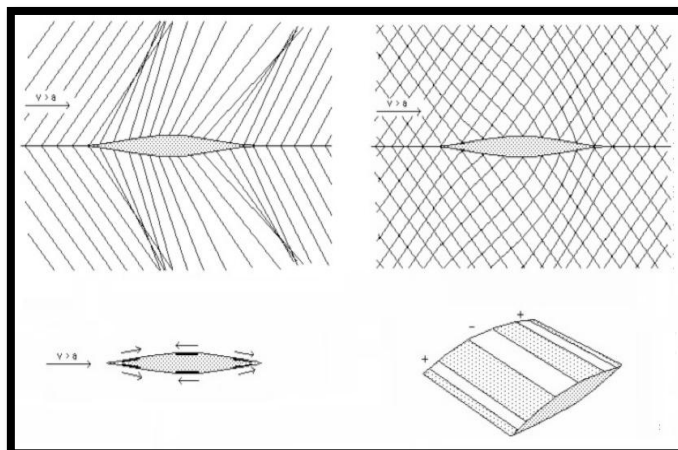


Fig.6 Elimination of shocks around a flat wing by convenient Lorentz force field

Elimination of shocks around a flat wing by convenient Lorentz force field. The gas must be accelerated around the leading edge and the bottom, and slowed down between the two to prevent the expansion fan. By the way, this introduced the concept of MHD bypass. In the eighties it was planned to use a shock tube as a supersonic, high electrical conductivity gas flow generator, to operate this key-experiment [5]. But, due to the connection to UFO phenomenon (supersonic silent flight, as reported by witnesses) this was no longer possible in institutional structures. Years after, the Lambda Laboratory was created in 2007, with private funding. The use of a shock tube was too complex and expensive, so that the team shifted to experiments in low pressure hypersonic wind tunnel, providing natural high electrical conductivity.

Then disk shaped MHD aerodynes, are more suitable, due to the high Hall parameter conditions. This arises specific difficulties, such tendency of the discharge to be blown away, due to the magnetic field gradient. This was rapidly solved, by wall confinement through inversion of magnetic gradient.

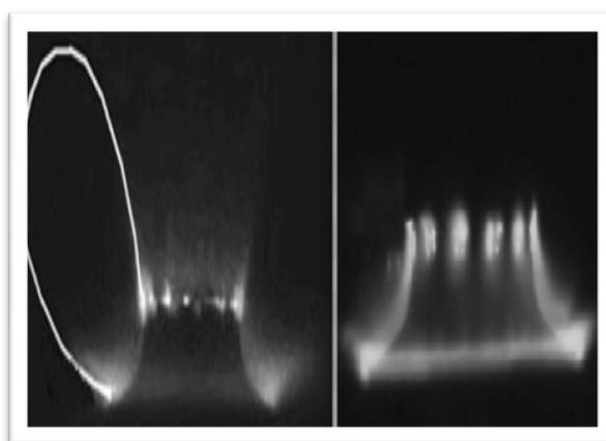


Fig.6 Left: the discharge is blown away by the magnetic gradient.  
Right: wall confinement by inversion of this magnetic gradient

## V. Sunspot Modelling

Sunspots are central to our understanding of solar magnetism in several aspects. Sunspots are the most prominent manifestation of the large scale cyclic solar magnetic field. Understanding their subsurface structure as well as the processes of formation, dynamic evolution, and decay is crucial for connecting them to the dynamo and flux emergence processes in the solar convection zone. On smaller scales sunspots provide an ideal environment for studying magneto-convection for a variety of different field configurations [9]. While quiet Sun regions have been modelled very successfully for almost 3 decades using 3D radiative MHD simulations, such models were only applied to sunspots in the past five years.

## VI. MHD For Space Vehicles

Several Authors have investigated the possibility to utilize MHD energy conversion systems in the space. Many of them proposed a plasma MHD generator feed by fuel in liquid or solid state (liquid hydrogen, liquid oxygen, kerosene, and nuclear fuel). The fuel contained in heavy vessels, have to be carried to space together with MHD generator. To do this a large amount of energy is needed. An electrical power generation on-board system was also considered. The MHD generator proposed is built in supersonic nozzle of rocket engine utilizing liquid hydrogen and liquid oxygen. A. Kantrovitz presented one of the first studies on MHD interaction generated by space vehicles at hypersonic velocities.[6]

During re-entry into atmosphere between 80 and 60 Km of altitude at velocities 7,000-11,000 m/s strong shock waves occur with highly non-uniform flow field. The temperature of air behind the shock reaches 10,000-20,000 K and due to relaxation near vehicle surface is between 10,000 and 5,000 K. This produces sufficient ionization to sustain a significant MHD interaction level.

As a consequence of ionized boundary layer of hypersonic vehicle.

The control of flight of spacecraft can be obtained by creation of drag forces and tangential forces as well as a controlling moment. The external flow structure including shock wave formation can be influenced too. At lower altitudes and velocities the MHD conversion and the flight control would be possible through pre-ionization or seeding of the working media.[8]

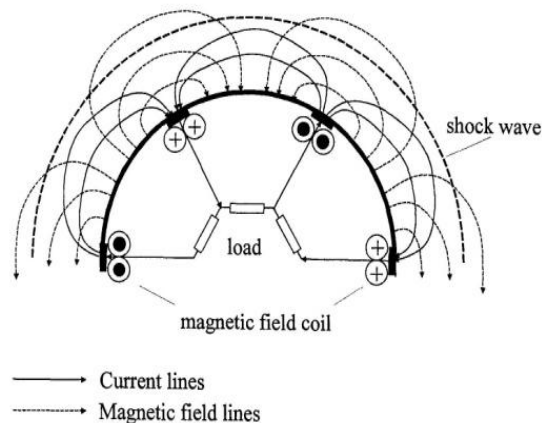


Fig. 7 Scheme of a conversion system realized in Boundary layer of an Hypersonic Vehicle (above: side view - below: cross sectional view)

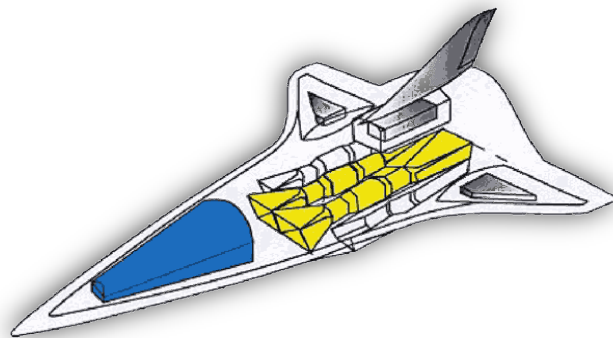


Fig. 8 AJAX spacecraft using MHD[12]

## VII. Magneto-Hydrodynamic Design

1st law of Thermodynamics defines the equivalence between work and heat energy, when work is converted into Heat. But the 2nd law of Thermodynamics explains the conversion of thermal energy into mechanical energy on the basis of temperature gradient. The efficiency of ideal heat engine  $\eta = (K_1 - K_2) / K_1$  where  $K_1$  and  $K_2$  are absolute temperatures in Kelvin scale of source of heat and sink respectively. This equation can also be stated as  $\{1 - (K_2 / K_1)\}$ . If  $Q_1$  is the quantity of heat observed from the heat source then the quantity of heat that can be converted into work is  $Q_1 \{(K_1 - K_2) / K_1\}$  or  $Q_1 \{1 - (K_2 / K_1)\}$ . [10]

That means the entire quantity of heat cannot be converted into work unless  $K_2$  is 0 or  $-273^{\circ}\text{C}$ . The conversion of heat into work is dependent on the temperature gradient.

The fraction ( $K_2/K_1$ ) can be defined as “non-convertible fraction” of heat energy. So, the conversion ratio can be increased only by decreasing the non-convertible fraction ( $K_2/K_1$ ).



Fig. 9 Space vehicle using MHD[10]

### VIII. The Secret Of Hypersonic Flight: MHD

The faster an airplane flies the higher it must climb and cruise. It is not possible to fly at ground level at high Mach number just for mechanical constraint due to high pressure. Over Mach 3-3.5 flight is possible with turbo reactors (up-left figure). At higher Mach numbers these rotating machines cannot be used any longer. One can shift to stato-reactor (right). At Mach number up to Mach 6.5 scramjets can be used (below). The leading edge is cooled by liquid hydrogen an oxygen circulations. The mixture burns in annular combustion chamber at supersonic velocity.[17]

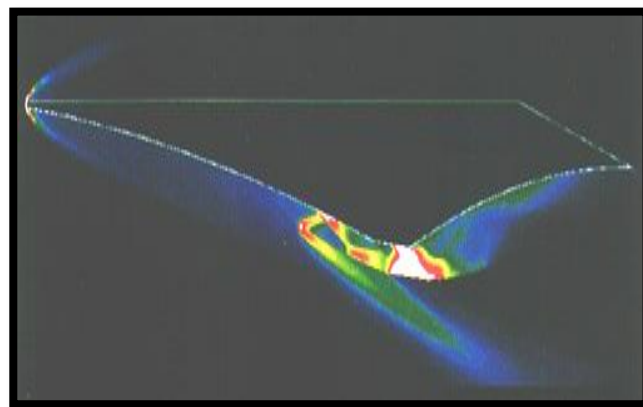


Fig. 10 Ajax with stato

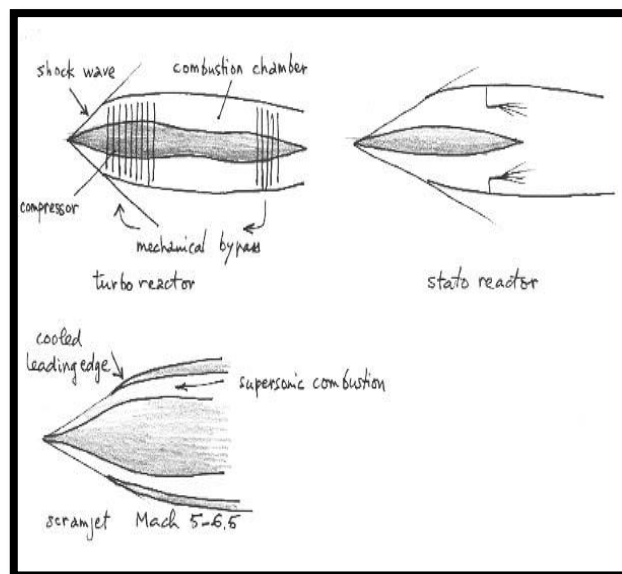


Fig. 11 Turbo Reactors [12]

### IX. Magnetic Plates

The area of each magnetic plate is 3 m<sup>2</sup> and the distance between the plates is 6m. The following are the properties of the magnetic plates:

- The Magnetic plates both together weigh 12,000 tonnes
- The plates are 100,000 times stronger than the Earth's magnetic field,
- stores enough energy to melt 18 tonnes of gold.
- Uses almost twice much iron as the Eiffel Tower.

### X. Basic Formulae Used In MHD Calculations

**Max Power = E<sup>2</sup>/4R**

E and R are calculated as follows:

Open circuit voltage **E = BUD**

Where B is Magnetic Flux density,

D is Distance between plates

Generator resistance **R = D/σ A**

Where σ is Average gas density

A is plate area

#### 6.2 Capacity Calculations:

Plate Area (A)	= 3 m <sup>2</sup>
Distance between plates (D)	= 6 m
Flux density (B)	= 5 Wb/m <sup>2</sup>
Average gas density (U)	= 1000 m/s
Gaseous conductivity (σ)	= 10 Mho/m
Open circuit voltage (E)	= BUD = 5x1000x6 = 30,000 volts
Generator resistance (R)	= D/σ A = 6/ (10x3) = 0.2 ohm
Max Power (P)	= E <sup>2</sup> /4R = (30,000) <sup>2</sup> / (4x0.2) = 1125 MW

### XI. Comparison With Other Magneto Hydro Dynamic Generators

#### 1. Comparison with IITK MHD calculations

##### IITK calculations

A	= 0.25 m <sup>2</sup>
D	= 0.5 m
B	= 2 Wb/m <sup>2</sup>
U	= 1000 m/s
σ	= 10 Mho/m
E	= BUD = 2x1000x0.5 = 1000 volts
R	= D/σ A = 0.5/ (10x0.25) = 0.2 ohm
Max Power	= E <sup>2</sup> /4R = 1000 <sup>2</sup> / (2x0.2) = 1250 KW

##### Eco-MHD calculations

A	= 3 m <sup>2</sup>
D	= 6 m
B	= 5 Wb/m <sup>2</sup>
U	= 1000 m/s
σ	= 10 Mho/m
E	= BUD = 5x1000x6 = 30,000 volts

$$\begin{aligned} R &= D/\sigma A \\ &= 6/(10 \times 3) = 0.2 \text{ Ohm} \\ \text{Max Power} &= E^2/4R \\ &= 30000^2/(4 \times 0.2) \\ &= 1125000 \text{ KW} \end{aligned}$$

A is Plate Area  
D is distance between plates  
B is flux density  
 $\sigma$  is gaseous conductivity  
U is average gas density  
R is generator resistance  
E is open circuit voltage

The Eco-MHD capacity is 1125 MW which is greater than the IITK MHD capacity which is 1250KW.

### Comparison of capacities between Eco-friendly MHD and KTPS

Kothagudem Thermal Power Plant is located at Paloncha in Andhra Pradesh, India. The power plant has an installed capacity of 1,720 MW with 11 units in operation. It is one of the coal based power plants of APGENCO. [14]

In January 2012, it was reported that the Andhra Pradesh government has decided to build additional unit with capacity of 800 MW.

Currently, Kothagudem thermal station space available at the site has been surveyed, it has been confirmed that another unit of 800 MW capacities can come up there.



The calculated Eco-MHD capacity found to be 1125MW, and the KTPS capacity is 800MW  
 $1125 \text{ MW} > 800 \text{ MW}$ .

Thus Eco-friendly MHD has more capacity than the existing Thermal power station capacity.

## XII. Results And Conclusion

The MHD generator Resistance increases with the decrease in the Area of the plates, and increases with increase in the distance between the plates. The open circuit voltage varies increasingly with the Magnetic flux density, average gas density and also the distance between the two plates. The overall capacity or the maximum power generated increases with increase in the Open circuit voltage and decrease in the resistance of the generator.

The Magnetic flux is taken  $5 \text{ Wb/m}^2$ . The two plates, each of area  $3\text{m}^2$  are separated by the distance 6m. The open circuit voltage is calculated to be 30,000 volts, and the Generator resistance 0.2 Ohm.

The Eco-Friendly Magneto Hydrodynamic Generator is capable of producing capacity of 1125MW. The Power generation is Eco-Friendly using the salt water as fuel and capacity is comparatively greater than the existing KTPS (Thermal power station) in India. The possibility of stacking the output of many such systems in series and the absence of many disadvantages associated with non-renewable methods of electric power generation should make MHD using flowing salt water a very attractive alternative for energy generation.

Harnessing power by employing an MHD generator with salt water as its fluid conductor is hugely advantageous in that the source is renewable, it requires no external energy input to facilitate its operation, it has no moving parts and as such does not contribute to mortality of aquatic organisms and finally, it does not pose problems of pollution.

### **XIII. Future-Scope Of Magneto Hydro Dynamic Generator**

The Eco-friendly MHD Generator design, calculations and analysis of the results will be given to an industry which will be able to develop the Eco-friendly power generation using MHD. Power generation capacity has to increase rapidly[16]. To reduce pollution, and to improve overall efficiency the coal has to be gasified at pitheads and the gas, SNG, transported by pipe-grid to all thermal stations. This facilitates conversion of all stations into combined cycles initially. Later MHD generators or thermal cells can be added to the power stations. This is the only way beneficial to one and all. The MHD Generator can be equipped with solar panels, so that the power generation becomes easier.

Recently, sunspot models have undergone a dramatic change. In the past, several aspects of sunspot structure have been addressed by static MHD models with parametrized energy transport. Models of sunspot fine structure have been relying heavily on strong assumptions about flow and field geometry (e.g., flux-tubes, "gaps", convective rolls), which were motivated in part by the observed filamentary structure of penumbrae or the necessity of explaining the substantial energy transport required to maintain the penumbral brightness[15]. However, none of these models could self-consistently explain all aspects of penumbral structure (energy transport, filamentation, Ever shed flow).

In recent years, 3D radiative MHD simulations have been advanced dramatically to the point at which models of complete sunspots with sufficient resolution to capture sunspot fine structure are feasible.

### **REFERENCES**

- [1]. C. Ambasankaran Project Director "Status Report on the Indian MHD Programme" Indian MHD Power Generation Project, Bhabha Atomic Research Centre
- [2]. C.Rajareddy "Eco-Friendly Power Generation: Thermal Cell's Future Role" Proceedings Of The Seminar On Environment Friendly Electric Power Generation.
- [3]. J.P.Petit, J.C.Dore "MHD Aerodynes, With Wall Confined Plasma, Electrothermal Instability Annihilated And Stable Spiral Current Pattern" Lambda Laboratory France
- [4]. Nob. Harada, Le Chi Kien, and M. Hishikawa "Basic Studies on closed cycle MHD Power Generation System For Space Application" 35th AIAA Plasmadynamics and Lasers Conference 28 June-1 July / Portland , Oregon AIAA 2004-2365
- [5]. Harada, Nobuhiro "Magneto hydrodynamics For Advanced Power Generation System" The International Conference on Electrical Engineering 2008 No. O-043
- [6]. Samuel O. Mathew , Obed C. Dike , Emmanuel U Akabuogu , And Jemima N. Ogwo "Magneto Hydrodynamics Power Generation Using Salt Water" ISSN 2186-8476, ISSN 2186-8468 Vol. 1 No. 4, December 2012 Asian Journal of Natural & Applied Sciences
- [7]. Vyacheslav Chernyshev "International Co-Operation in MHD Electrical Power Generation" IAEA Bulletin-Vol.20, No.1 53
- [8]. Ajith Krishnan R, Jinshah BS "Magneto Hydrodynamic Power Generation" International Journal of Scientific and Research Publications, Volume 3, Issue 6, June 2013 1 ISSN 2250-3153
- [9]. P. Satyamurthy "Experimental Facility To Study MHD Effects At Very High Hartmann And Interaction Parameters Related To Indian Test Blanket Module for ITER" Bhabha Atomic Research Centre
- [10]. Vishal. D. Dhareppagol & Anand Saurav "The Future Power Generation With MHD Generators Magneto Hydro Dynamic Generation" ISSN (Print) : 2278-8948, Volume-2, Issue-6, 2013
- [11]. Ebersohn, F., Longmier, B., Sheehan, J., Shebalin, J., Girimaji, S., "Preliminary Magneto hydrodynamic Simulations of Magnetic Nozzles", IEPC-2013-334 33rd International Electric Propulsion Conference, Washington, D.C
- [12]. Sergey O. Macheret, Mikhail N. Shneider, And Richard B. Miles, Aiaa "Mhd Power Extraction From Cold Hypersonic Air Flows with External Ionizers" Department of Mechanical And Aerospace Engineering, Princeton University.
- [13]. Zeigarnik V.A., Novikov V.A., Okunev V.I., Rickman V.Yu, "Mass-Dimension Optimization of Mhd Generators for Hypersonic Aircraft of «Ajax» Concept" High Energy Density Research Center of IvTan-Association and State Hypersonic System Research Institute of "Leninets" Holding Company.
- [14]. Steven J. Schneider "Annular MHD Physics for Turbojet Energy Bypass" NASA/Tm- 2011-217210 AIAA-2011-2230
- [15]. Sheehan, J., Longmier, B., Bering, E., Olsen, C. Squire, J.Carter, M.Cassady.L. "Plasma Adiabaticity in A Diverging Magnetic Nozzle" Iepc-2013-159, 33rd International Electric Propulsion Conference, Washington, D.C., October 6-10, 2013.
- [16]. Gilchrist, B. E., Davis, C., Carlson, D., And Gallimore, A. D., "Electromagnetic Wave Scattering Experiments In Hall Thruster Plasma Plumes" AIAA-98-3642, 34<sup>th</sup> Joint Propulsion Cleveland, Oh, July 12-15, 1998.
- [17]. Brichkin D.I., Kuranov A.L., and Sheikin E.G., "The Potentialities of MHD Control for Improving Scramjet Performance" AIAA Paper 99-4969.

## Bit Error Rate Analysis in WiMAX Communication at Vehicular Speeds using modified Nakagami- $m$ Fading Model

Manjeet Singh<sup>1</sup>, Dr. Jyotsna Sengupta<sup>2</sup>

<sup>1,2</sup>Department of Computer Science, Punjabi university Patiala (147002)

**Abstract:** At high vehicular speeds, rapid changes in surrounding environments, cause severe fading at the receiver, resulting a drastic fall in throughput and unless any proactive measure is taken to combat this problem, throughput becomes insufficient to support many applications, particularly those with multimedia contents. Bit Error Rate (BER) estimation is an integral part of any proactive measure and recent studies suggest that Nakagami- $m$  model performs better for modelling channel fading in wireless communications at high vehicular speeds. No work has been reported in literature that estimates BER at high vehicular speeds in WiMAX communication using Nakagami- $m$  model. In this thesis, we develop and present an analytical model to estimate BER in WiMAX at vehicular speeds using Nakagami- $m$  fading model. The proposed model is adaptive and can be used with resource management schemes designed for fixed, nomadic, and mobile WiMAX communications.

### I. Introduction

WiMAX is basically described as the IEEE 802.16 standard for Broadband Wireless Access (BWA) that was developed to provide high transmission data rates over larger areas and also to those areas users where broadband coverage is not available. MIMO systems are also of major interest in the field of wireless communication as it allows data to be sent and received over different antennas. WiMAX-MIMO systems are mainly developed to increase the performance of simple WiMAX system. This paper analyses WiMAX-MIMO systems under different modulations with different CC code rates for different fading channels ( Rician and Nakagami channel). Spatial Diversity technique of MIMO system is used for the simulation purpose. Signal-to Noise Ratio (SNR) vs Bit Error Rate (BER) plots are analysed for this purpose.

The IEEE 802.16 PHY includes mainly three specifications, which are suited to different operational environments. For frequencies from 10 to 66 GHz, the standard recommends the Wireless MAN-SC PHY, where SC means single-carrier modulation. The typical channel bandwidth is 25 MHz or 28 MHz, and the raw data rates can exceed 120 Mb/s. For frequency band below 11 GHz, two alternatives have been specified: Wireless MAN-OFDM and Wireless MAN- OFDMA. In this frequency range, the wavelength is relatively long, and therefore it is a Non-LOS (NLOS). Hence the impairments like fading and multipath propagation are more prominent in both of these specifications.

Factors such as these include helpful to analyze the cardiovascular disease. In numerous cases, diagnosis is generally based on current test results of the patients & experience of the doctor. Thus the diagnosis becomes a complex task that will require much experience & high skill [6].

Modulation is a fundamental component of a digital communication system. It involves mapping of incoming digital information from interleaver into analog form onto a constellation so it can be transmitted over the channel. Various digital modulation techniques used in our analysis that are M-PSK and M-QAM where M is the number of constellation points in the constellation diagram. After modulation process, code words generated by encoding process are converted into symbols. Inverse process of modulator is called demodulation which is done at the receiver side of Physical layer to recover the transmitted digital information.

### II. Literature Cited

**Suzuki,** Use of a commercial WiMAX equipment in the frequency of 3.5 MHz with a bandwidth of 7 MHz (BW), where link speeds was BPSK -1 / 2 and QPSK 1/2. Research shows that the image size has a significant impact on the performance of WiMAX communication. Communication System WiMAX Rated vehicles for communication, both V2I and V2V infrastructure for road safety project. The experimental design consisted of three WiMAX base stations. The researcher concluded that the proposed architecture meets the requirements of the implementation of version 1.0 WiMAX.

**Charash** studied the behavior and performance for IEEE 802.16e -based unit noise ratio (SNR) in an urban micro cell and determined the SNR switching point between each link speed. The theory is compared to the measurement results of the mobile practice test in an urban cell. Experiments show that 3/4 code rate provides lower performance than the average rate of code.

**Stein** proposed a system for providing roaming wireless high speeds on multiple interfaces, running in the WiMAX system and Wi-Fi technology. The system supports multiple interfaces for mobile devices quickly. It can support fast switch connecting the access point Wi-Fi, and passes seamlessly between access points. Connections use various means, such as Wi-Fi and WiMAX. The proposed system has improved the efficiency of communications technology WiMAX up to 30 %, and the combination of WiMAX and Wi-Fi technology significantly wide band technology.

The study showed that the Flash OFDM solution is a pre-stage gear linkage, such as access to communication on the base WiMAX high-speed Internet is profitable passenger rail operated more. The researcher examined two scenarios, the first that included two mobile nodes support of the application in real time and met. The second scenario has a strong footprint with 40 vehicles. A simulation was performed using two gateways Access Services Network (ASN).

**Malhotra et al.**, Considered based mobile WiMAX DL channel cluster systems based on LS methods using DL-PUSC permutation. The simulation was performed using the Rayleigh fading model. The estimate was made regarding the mean squared error (MSE) and the BER. The results showed that two OFDM symbols has a better performance compared to a single OFDM symbol.

**Sood et al.**, A performance analysis of the application of additive white Gaussian noise (AWGN) and Doppler movement. Tx was developed according to the IEEE standard and the current simulation on M-QAM modulation and RS code CC. The Least Square (LS) and minimum mean square (LMS) method is used for channel estimation. The results show that the performance degrades LS estimator relatively high speed, and provides better performance LMS. The researcher concluded that the interpolation method has a great impact on the estimation of the mobile channel.

### III. Materials And Methods

#### 3.1 WiMAX Technology

High speed wireless communication technologies such as Worldwide Interoperability for Microwave Access (WiMAX) have revolutionized the way of our day-to-day communication and opened opportunities for many innovative applications. The 802.6m version of WiMAX offers data rates up to 1 Gbps for fixed communications and supports mobility up to 350 km/h. While WiMAX technology's capacity to deliver high data rates in a fixed environment is beyond any doubt, the standard is not fully optimized yet for mobile communication at high vehicular speeds.

#### 3.2 Nakagami Channel

Rayleigh fading can't describe the long-distance fading effects that are corrected by the Nakagami by formulating a parametric gamma distribution-based density function thus reducing the effects of multipath propagation. It provides a better explanation to worse conditions than the Rician and Rayleigh fading model and thus fits better in the mobile channel data. This fading originated to describe the amplitude of fading channels.

#### 3.3 Bit error rate estimation

We have dealt with the problem of Bit error rate estimation (BER) in WiMAX communication at vehicular speeds using Nakagami-*m* model. We have followed an analytical model in which I had studied the parameters and equations which had changed the bit error rate at various vehicular speeds for efficient resource management. I have also modified the marginal distribution equation used in the basic model to check its effect. The basic aim and purpose was to change the marginal distribution equation in such a way so that *it increases the throughput of the base model. The modulation method which I had used for calculating the bit rate probability is based on QPSK modulation.*

#### 3.4. Methodology used

We have used a predefined methodology to improve the algorithm and for applying the Nakagami fading for the vehicular traffic. The methodology is given as shown below:

1. Defined the extracted workflow specification according to problem definition
2. Based on that we have defined the newly extracted organizational model

Stored the event log file and generated a simulation model that reflects the process as it is currently enacted. The direct usage of design information avoids mistakes that are likely to be introduced when models are constructed

manually, and the automated extraction of data from event logs allows the calibration of the model based on actually observed parameters.

#### IV. Results And Discussion

We have analyzed WIMAX communications system which can be used for vehicular speed by using a nakagami model. This system is quiet efficient when dealing with the problem of improving the management capacity of the mobility and circulation, improve the condition of travel, and reduce the effects the unfavorable environment in surface transportation systems. Modern research on WIMAX communications system shows that all the components here are connected by wireless communication. Wireless communication can also be used in modern vehicular operations so that its efficiency is improved with time. In most of such applications, data communication takes place between the vehicle (V2V) and vehicle vehicle-infrastructure (V2I) using wireless communication systems.

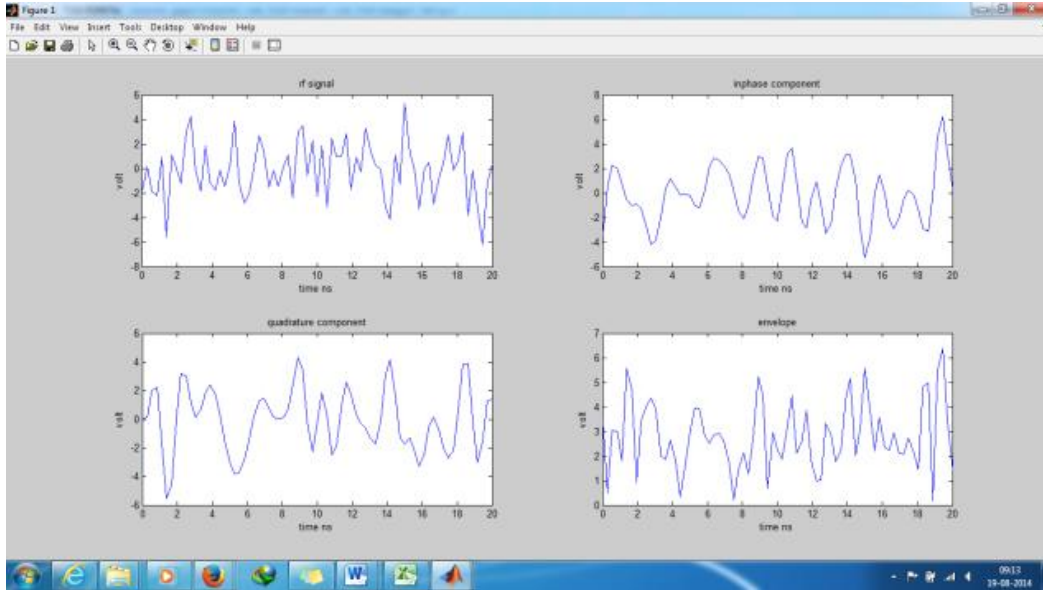


Figure 1: Various parameters of theWiMAX communication at vehicular speeds using Nakagami-*m* model

The performance of the basic WiMAX system with different modulations and different CC code rates, we have calculated the parameters in the form of BER vs SNR plots over Nakagami channel. Our graph shows an improvement in the SNR value using spatial diversity technique of Nakagami model.

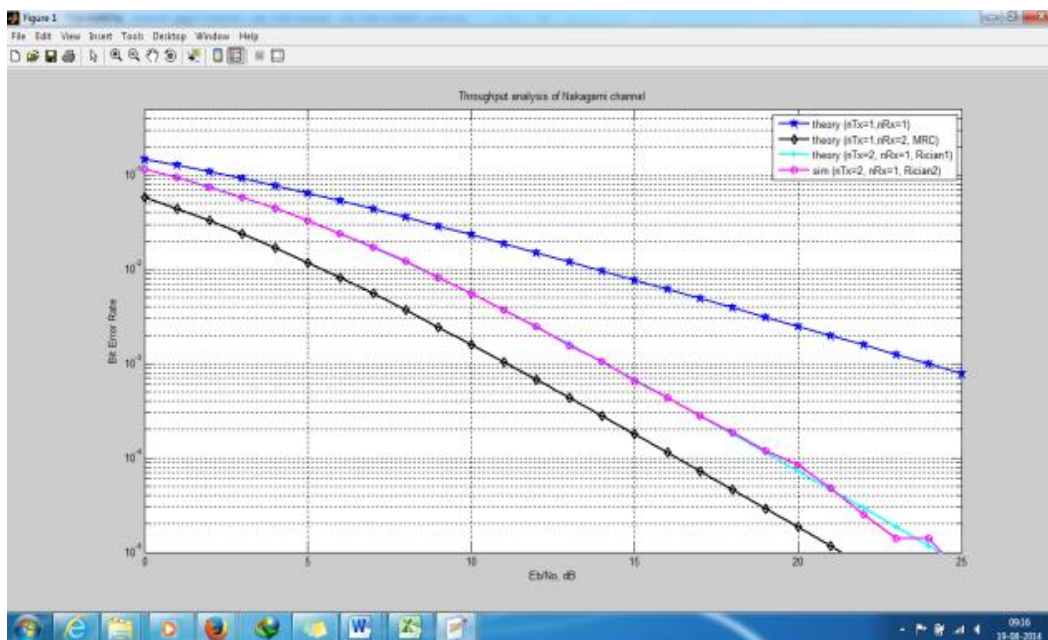


Figure 2: To check the performance of our model with other existing models

In the figure given above, we have tried to compare our model with three other models. By comparison it is shown that BER of our model is less as compared to other three models. It is compared with different parameters so that efficiency of the system as compared to other vehicle is same. We have used the following parameters for the simulation:

**Number of bits used for simulation:  $N = 10^6$**

**EB number values:  $E_b/N_0_{dB} = 0:25$**

**Number of paths:  $numpaths = 10$**

**Frequency of the carrier:  $F_c = 900e6$**

**Sampling Frequency of the carrier:  $F_s = 4 * F_c$**

**Period of sampling:  $T_s = 1/F_s$**

**Time for simulation:  $t = 0: T_s:1999 * T_s$**

**And we have calculated the radian frequency as  $\omega_c = 2 * \pi * F_c$ ;**

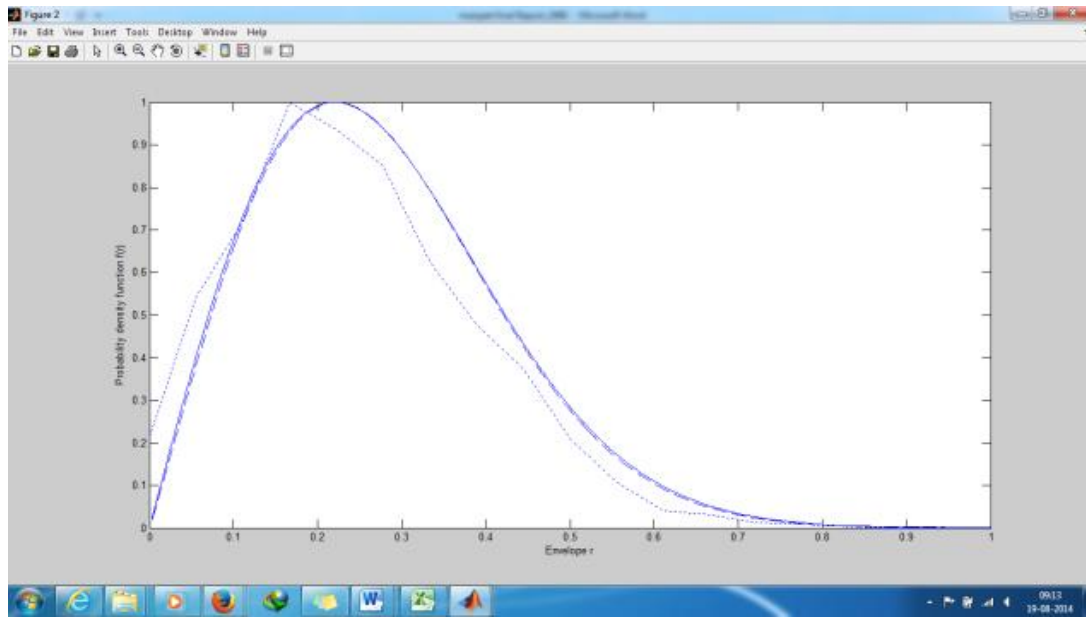


Figure 3: Bit error rate estimation area of WIMAX models for a particular model with different varying parameters.

In this graph we are able to achieve 5 dB improvements in SNR for the envelope and we have used Spatial Diversity technique in WiMAX in the presence of Nakagami model. The performance of the basic WiMAX system with different modulations and different CC code rates, we have calculated the parameters in the form of BER vs SNR plots over Nakagami channel. Our graph shows an improvement in the SNR value using spatial diversity technique of Nakagami model.

## V. Conclusion

At vehicular speeds, however, spectral efficiency of WiMAX becomes low mainly due to multipath fading problem and further research is needed for designing resource management schemes at vehicular speeds so that multimedia applications can be supported at high vehicular speeds. A key requirement for such a resource management scheme is to have an analytical model that can estimate BER at high vehicular speeds so that proactive actions can be taken and proper planning can be done. The proposed analytical model in this thesis is adaptive to reflect fading severity at various speeds and is a perfect fit for WiMAX communication. The proposed model can also be used with long term evolution (LTE) down link channel which uses similar OFDMA technique.

## REFERENCES

- [1] Mohammad Hayajneh and Najah Abu Ali, "Closed-Form Rate Outage Probability for OFDMA Multi-Hop Broadband Wireless, Networks under Nakagami-m Channels"
- [2] Varsha Birla, Prof. RupeshDubey, "Capacity Enhancement of WiMAX System Using Adaptive Modulation and Code Rate", International Journal of Emerging Technology and Advanced Engineering

- [3] Biswojit Bose, Iftexhar Ahmad and DaryoushHabibi, "Bit Error Rate Analysis in WiMAX Communication at Vehicular Speeds Using Nakagami-m Fading Model
- [4] Mr. Firoz Ahmed Mansuri1, Prof. Saurabh Gaur, "BER of OFDM system using concatenated forward error correcting codes (FEC) over Nakagami-m fading channel", International Journal of Engineering Trends and Technology (IJETT) – Volume 4 Issue 9- Sep 2013
- [5] PavaniSanghoi, LavishKansal, " Analysis of WiMAX Physical Layer using Spatial Diversity under Different Fading Channels", International Journal of Computer Applications (0975 – 8887) Volume 45– No.20, May 2012
- [6] Qing Wang, Dapeng Wu and Pingyi Fan, "Effective Capacity of a Correlated Nakagami-m Fading Channel"
- [7] PavaniSanghoi, LavishKansal, "Analysis of WiMAX Physical Layer Using Spatial Multiplexing Under Different Fading Channels"
- [8] Yunxia Chen and ChinthaTellambura, "Distribution Functions of Selection Combiner Output in Equally Correlated Rayleigh, Rician, and Nakagami-m Fading Channels," IEEE TRANSACTIONS ON COMMUNICATIONS, VOL. 52, NO. 11, NOVEMBER 2004
- [9] H. Suzuki, "A statistical model for urban radio propagation," IEEE Trans. Commun., vol. COM-25, pp. 673-680, July 1977.
- [10] U. Charash, "Reception through Nakagami fading multipath channels with random delays," IEEE Trans. Commun., vol. COM-27, pp. 657-670, Apr. 1979.
- [11] S. Stein, "Fading channel issues in system engineering," IEEEJ. Select. Areas Commun., vol. SAC-5, pp. 684-9, Feb. 1987.
- [12] C. Loo, "Statistical model for a land mobile satellite link," IEEE Trans. Veh. Technol., vol. VT-34, pp. 122-127, Aug. 1985.
- [13] <http://dspace.thapar.edu:8080/dspace/bitstream/10266/1227/3/>
- [14] <http://ro.ecu.edu.au/cgi/viewcontent.cgi?article=1531&context=theses>
- [15] JyoteeshMalhotra, Ajay K. Sharma, R.S Kaler, "Investigation on First Order Performance Metrics in the Nakagami-m Fading Channel," In the proceeding of conference of Design Technique for Modern Electronic Devices, VLSI and Communication Systems, 14th-15th May, 2007.



# International Journal of Modern Engineering Research (IJMER)

Volume : 4 Issue : 9 (Version-2)

ISSN : 2249-6645

September- 2014

## Contents :

<b>Failure of Piston in IC Engines: A Review</b> <i>R. C. Singh, Roop. Lal, Ranganath M S, Rajiv Chaudhary</i>	01-10
<b>Big Bang–Big Crunch Optimization Algorithm for the Maximum Power Point Tracking in Photovoltaic System</b> <i>Yacine Labbi, Asma Labbi, Zoubir Becer, Djilani Benattous</i>	11-17
<b>Experimental Investigation and Parametric Analysis of Surface Roughness in CNC Turning Using Design of Experiments</b> <i>Ranganath. M. S, Vipin</i>	18-25
<b>Content Based Message Filtering For OSNS Using Machine Learning Classifier</b> <i>Hajiali Mohammed, T. Sukanya</i>	26-30
<b>Harmonic Analysis of 6-Pulse and 12-Pulse Converter Models</b> <i>Venkatesh P, Dr. M. N. Dinesh</i>	31-36
<b>A Distributed Approach for Neighbor Position Verification in MANETs</b> <i>Mahendranath Chowdry Kundla, Kancharla Kalpana</i>	37-40
<b>Characterization of environmental impact indices of solid wastes in Surulere Local Government Area, Nigeria with GaBi5 LCA modeling technique</b> <i>S. O. Ojoawo, J. S. Bosu, O. A. Oyekanmi</i>	41-49
<b>A Novel Key Management Paradigm for Broadcasting to Remote Cooperative Groups</b> <i>Murala Lavanya, T. Sukanya</i>	50-54
<b>Study of Local Binary Pattern for Partial Fingerprint Identification</b> <i>Miss Harsha V. Talele, Pratvina V. Talele, Saranga N Bhutada</i>	55-61
<b>A Novel Acknowledgement based Intrusion Detection System for MANETs</b> <i>Parveen Pathan, V. Jhansi Lakshmi</i>	62-66

## Failure of Piston in IC Engines: A Review

R. C. Singh<sup>1</sup>, Roop. Lal<sup>2</sup>, Ranganath M S<sup>3</sup>, Rajiv Chaudhary<sup>4</sup>

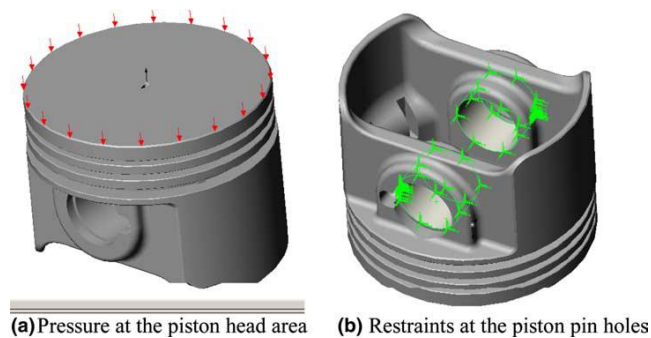
<sup>1</sup>Associate Professor, <sup>2</sup>Assistant Professor, Mechanical Engineering, Delhi Technological University, Delhi, India

**Abstract:** Piston in the internal combustion (IC) engine is robust, dynamically loaded tribo-pair that reciprocates continuously at varying temperature. Study has been made by various researchers on piston design, dynamics, fatigue and wear at the interface with other element in contact along with their effects on IC engines. It was found that the friction coefficient increases with increasing surface roughness of liner surface and thermal performance of the piston increases with increased coating thickness. The free material liberated due to deep scoring between the piston and liner snowballs, leads to seizure failure.

**Keywords:** Piston, Tribo-pair, IC Engines, Fatigue, Wear.

### I. INTRODUCTION

The current trend in the land transportation and power production is to develop IC engines of enhanced “power-capacity” and “reduced emissions” (to follow specified international intrinsic norms). Piston, piston rings and cylinder liner are important components of an IC engine. The prime function of piston is to transmit the motion produced by liberation of chemical energy of fuel to mechanical works. Piston rings dynamically seal the gap between the moving piston and the cylinder liner surface in order to prevent the escape of the combustion gases from the combustion chamber into the crankcase and the leakage of the oil from the crankcase into the combustion chamber.



(a) Pressure at the piston head area (b) Restraints at the piston pin holes  
Fig. 1. Typical engine piston [10]

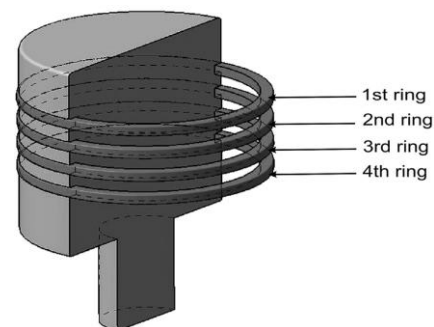


Fig. 2. Schematic illustration of a worn ring piece [ 25 ]

The manufacturing of cylinders includes boring, honing and plateau honing which has received much attention by manufacturers in recent times. The process of the surface changes which occurs during running of the engine is related to the wearing action caused by the piston ring on the bore. This action takes place of “transitional topography” where the surface generated exhibits the influence of the piston ring which modifies the machined surface. This has been made possible by improving the design of piston and reducing the failure i.e. scuffing, sculling, seizure of piston etc. The piston is one of the continuous moving parts of engine, is of pivotal importance. Piston has high dynamic loaded speed and heavy reciprocating weight develop high inertia forces, which are undesirable. The following factors may be considered for proper functioning of piston in IC Engine:

1. The piston should have enormous strength and heat resistance properties to withstand gas pressure and inertia forces. They should have minimum weight to minimize the inertia forces.
2. The material of the piston should have good and quick dissipation of heat from the crown to the rings and bearing area to the cylinder walls. It should form an effective gas and oil seal.
3. Material of the piston must possess good wearing qualities, so that the piston is able to maintain sufficient surface-hardness unto the operating temperatures.
4. Piston should have rigid construction to withstand thermal, mechanical distortion and sufficient area to prevent undue wear. It has even expansion under thermal loads so should be free as possible from discontinuities.

5. Piston should form tribo-pairs and have high reciprocation speed without noise, minimum work of friction and have little or no tendency towards corrosion and pitting-up.

## II. LITERATURE REVIEW

Sunden and R. Schaub [12] presented a selection of some of the more practically orientated principles of the successful manufacture of grey cast iron piston rings greater than 175 mm in diameter, and shown that when considered with the sciences of strength of materials and diesel engineering, the subject of piston rings becomes an embodiment of the wider subject of tribology. A brief description of the most important topics of practical piston ring manufacture, and an indication of the vast size and complicated nature of an industry which concerns itself with one of the cheapest components of a diesel engine has been given. P. C. Nautiyal, et al, [23] investigated a large part of the top piston ring wear of an IC engine which takes place in boundary lubrication around top dead centre (TDC) position. A quantitative assessment of the frictional behavior using actual piston ring and cylinder liner under conditions close to TDC was made. The factors responsible for wear under these conditions have been identified as surface temperature, peak combustion pressure, total energy on the wearing surfaces and other physical properties of the material under sliding. T. H. C. Childs and F. Sabbagh [30] carried out tests to study the wear mechanisms responsible, particularly the relative importance of high cycle metal fatigue and chemical reaction film wear. Two types of cast iron used as piston rings (a grey and a carbidic iron) were used as pins and a cylinder bore material was used as the ring. Specific loads were varied from 20 to 400 MPa and the sliding speed was  $0.4 \text{ m s}^{-1}$ . The wear mechanisms in the two types of test were possibly different, as the engine tests produced worn surfaces which when examined by an optical microscope were bright, whereas the pin-on-ring test surfaces were covered by patchy non-metallic films. Wear rates, friction coefficients, percentage metallic contact and plasticity index were measured in the pin-on-ring tests. Specific wear rates did not correlate with any parameters of contact stress severity.

D. J. Picken and H. A. Hassaan [6] paper described the theory and use of a method for estimating the service life of an internal combustion (i.c.) engine based on experimental evidence and the law of adhesive wear. A simple computer program described, which predicted the overhaul life of an IC engine from its design data and a typical sample of its particular running conditions. The use of the program for an engine generator set operating on biogas at a farm site used as an example. It was considered that the work reported showed that the limit of engine life occurred when the wear of the cylinder liner at the upper position of the piston ring became excessive. Based on this, and assuming marginal lubrication in this area was possible to do a calculation which predicted engine life for any given application. J. E. Willn [13] discussed various methods of characterizing and describing surface finish more accurately for specification purposes. Later, it was hoped that some part of the characterization may also form a correlation with the performance of the ring and bore surfaces with respect to scuffing failure. Complete surface finish characterization was a pre-requisite to ring and liner scuffing tests from which it could be possible to form some correlation between performance and some feature of the surface profile. Meanwhile, a practical and more precise method of specifying finish was required for insuring consistent results in production. Then established random analysis techniques offer a means of characterizing profiles which describe the variations more fully than the simple values of center line average or root mean square. In the majority of cases, the specimen profiles which were examined, varied randomly in amplitude but not in frequency. A. V. Sreenath and N. Raman [2] studied about the conformance between the liner and rings of an internal combustion engine and found that it depend upon mainly on the linear wear (dimensional loss) during running-in. Running-in wear studies, using the factorial design of experiments, on a compression ignition engine showed that at certain dead centre locations of piston rings the linear wear of the cylinder liner increases with increase in the initial surface roughness of the liner. The linear wear of the cast iron liner and rings decreased with increasing load but the mass wear increased with increasing load. Statistical analysis of the linear wear data showed that, during running-in, the initial surface roughness of the liner had a significant effect on running-in wear at and around such dead centre positions of rings where more than one compression ring slide over. It was observed that metal to metal contact occurs at the dead centre positions of rings during running-in. K. J. Stout and T. A. Spedding [17] considered the methods of producing engine bores and the surface profiles obtained by these methods were examined and attempted to characterize their surface topography made. The effects of wear studied and from a consideration of the surface topography of the initial machining process a characterization technique was proposed. The random part of the bored surface has a similar skewness and kurtosis to the honed surface which was due to the similarity of the effects of shearing and deformation on the surface during the two finishing operations.

William G. Agnew [33] reviewed the combustion research conducted by one automotive research laboratory of General Motors. Wieslaw Grabon et al, [32] carried out experiments on a reciprocating tester. The lubricant was supplied into the inlet side of the contact zone. The construction of tribological tester allowed to

measure the friction force between specimen and counter-specimen. Tribological behaviors of cylinder liners with and without oil pockets were compared. Specimens were cut from plateau honed cylinder liners made of grey cast iron. Counter-specimens were cut from grey cast iron piston rings. The results suggested that hydrodynamic oil pocket effect was of prime importance. The positive effect of additional cylinder liner surface texturing on frictional resistance under worse lubrication conditions was smaller. Height and slope of piston ring surface topographies decreased due to wear. S. Mezghani et al, [27] investigated the various aspects of the wear modeling that caused running-in problems in honed surfaces and its implications on ring-pack friction performance. Plateau honing experiments under different conditions were carried out on an instrumented vertical honing machine. The plateau honing experiments characterized the surface modifications during running-in wear of cast-iron engine bores using advanced characterization method. The predictions were in good agreement with the measurement data of plateau and valleys surface-height parameters. The simulation model of piston ring-pack contact developed to predict friction of cylinder surfaces after plateau honing showed that smooth surfaces lead to better friction performances despite the increases of the ratio between plateau and valleys height (non-plateaued surface). E.P. Becker and K.C Ludema [9] used a laboratory simulator to identify the important variables influencing cylinder bore wear. The same characteristics of wear were observed in the simulator as in running engines, even though the simulator did not attempt to duplicate all the conditions found within an engine. A new picture of wear in cylinders was presented, consistent with the data and previous work on boundary lubrication. The qualitative model accounted for the evolution of the cylinder running surface in terms of composition and texture changes. The model was used to determine the relative importance of the many variables that can influence wear behavior, including contributions from lubricant chemistry, material properties, and mechanical loading. J. Galligan et al, [14] developed a bench test in the first part of this work and the time to failure of ring bore contacts lubricated with a fully formulated motor oil. It was found that failure times correlated well with load, frequency, test temperature and quantity of oil, but that the effect of surface finish, though present, was more difficult to quantify. The main findings in this respect were that there is an optimum finish for long life, and that liner surfaces which were initially highly polished lived which are more dispersed than those with standard finishes. The time to failure in a bench test designed to simulate scuffing failure in the bores of IC engines was shown to be linearly related to load, frequency, temperature and quantity of oil. If the first three of these exceed a critical value, or if the quantity of oil falls below a critical value, scuffing was almost instantaneous. The time to scuff was related to liner surface finish as measured by the rms slope of the top half of its profile.

S.G. Chung et al,[29] employed three types of fixed piston samplers at Nakdong River Delta. The retrieved samples were equally divided into 100 mm long pieces. Quality was evaluated using suction, shear wave velocity, and consolidation tests. The constant rate of strain consolidation test, rather than the incremental loading test, produced a better correlation with the nondestructive test results. The results suggested that the difference in sample quality was principally caused by the mechanical disturbance attributed to the different penetration mechanisms (methods) of the sampling tubes. The tip angle of sampling tubes significantly affected sample quality, whereas the length-to-diameter ratio had a relatively insignificant effect. The three methods used are in the following order: oil-operated, mechanical, and hydraulic samplers. The difference in sample quality was primarily caused by the mechanical destructure that occurs because of different penetration mechanisms. Sample quality tends to vary with the in-situ void ratio of the clay. M. Priest, C.M. Taylor [18] reviewed the nature of the surfaces encountered in the piston assembly, valve train and journal bearings of the internal combustion engine. The mathematical models of engine tribology endeavouring to cope with the extreme complexities for the incorporation of surface topography potentially were discussed. U.I. Sjödin, U.L.-O. Olofsson [31] investigated the wear interaction between piston ring and piston groove in a radial piston hydraulic motor in regard to mass loss and changes in form and surface roughness. A test rig was developed to simulate the tilting movements of pistons. The results showed that wear on the piston ring groove can be up to 10 times greater than the wear on the piston ring. Factorial design analysed that the form of the piston groove significantly influences the amount of wear, the dominant wear mechanism was mild wear. The most important design variable was the length of the support surface. The preferred design was a piston groove without any support plane. Zenon Krzyzak and Pawel Pawlus [36] analysed the surfaces of a large number of piston skirts surfaces under the “zero-wear” condition were analysed. The amplitude of worn piston skirt surfaces decreased, the ordinate distribution became asymmetric, summit density increased and lay direction changed from circumferential to axial during wear. The relationship between microgeometry parameters was studied using correlation and regression analysis. It was decided to determine the local wear of piston skirts based on the changes in amplitude parameters. An increase in the initial surface height caused and increase in piston skirt wear. The local linear wear of piston skirts was bigger on the thrust side than on the anti-thrust side of the cylinder. The worn piston skirt surfaces were observed to be smoothed. The ordinate distribution became asymmetric during “zerowear”. The ratio of average slopes in axial and circumferential directions can monitor

piston skirt wear. Piston skirt wear was proportional to initial profile height. Change of height parameter during wear process was bigger on the thrust side than on the anti-thrust side of the cylinder. A. Skopp, et al, [1] compared the tribological behaviour of  $TiO_2$  and  $TiO_{1.95-x}$  coatings under lubricated conditions with uncoated specimen of grey cast iron. The interaction of the pairs with prototype engine oils based on esters and polyglycols were studied under mixed/boundary lubrication using the BAM test method. Lubricants were factory fill engine oils, ester-containing lubricants with low-SAP (sulphur-ash-phosphor) and/or bio-notox properties as well as polyglycole-based lubricants. The ester and polyglycole-based engine oils respond both to bio-no-tox criteria and were polymer-free. They followed different strategies to reduce zinc, phosphorus and sulphur to assure a low ash content. Based on the piston ring/cylinder liner simulation BAM test outside of engines under conditions of mixed/boundary lubrication, it is reasonable that thermally sprayed  $TiO_x$ -based cylinder liner coatings can substitute commonly used uncoated grey cast iron liner materials. The coefficient of friction was more determined by the lubricants or by an individual interaction between lubricants and a specific material or tribopairing.

L. Ceschini, et al, [16] carried out both bench tests and laboratory dry sliding tests on components for hydraulic motors involved in a boundary lubricated sliding contact, with the aim of investigating the tribological behavior and improve the durability of the components. Bench tests were carried out on a rotating shaft, consisting of a quenched and tempered 36CrNiMo4 steel, coated by a Ni7Al layer deposited by Air Flame Spray, sliding against a carburized E470 steel contacting element. Failure analysis of real components after bench tests identified the main wear mechanism as two body abrasion. Laboratory dry sliding tests allowed the investigation of the influence of normal load and sliding distance on friction and wear behavior. Those tests also used in the subsequent steps of the work for ranking candidate alternative materials for the investigated tribo system. Rohollah Ghasemi and Lennart Elmquist [25] investigated the relationship between the deformation of the matrix and the closing tendency of flake graphite.

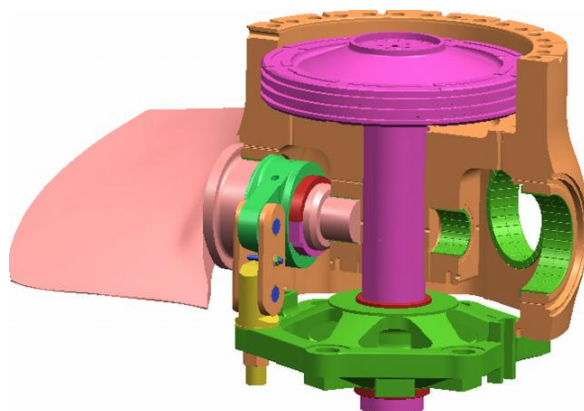


Fig. 3. Blade-control system for one blade.[35]

Two representative piston rings, which belonged to the same two-stroke marine engine but were operated for different periods of time, were studied. Initial micro structural observations indicated a uniform distribution of graphite flakes on unworn surfaces, where as worn surfaces demonstrated a tendency towards a preferred orientation. SEM and EDS analysis indicated substantial deformation of the matrix in the area around the flakes.

An insignificant corrosion attack was observed on both worn piston ring surfaces. As the orientation of the graphite flakes deviated more from the sliding direction, there was a higher chance of them maintaining their intrinsic self-lubricating nature and continuously supplying graphite to the sliding surface. C.W. Huang and C.H. Hsueh [5] selected Piston-on-three-ball tests by the International Organization for Standardization to establish ISO 6872 for the evaluation of the biaxial strength of dentistry-ceramic materials. The formula adopted in ISO 6872 for the fracture load-biaxial strength relationship was an approximate equation originally derived for piston-on-ring tests of mono layered discs. This formula was modified and extended to the case of multilayered discs subjected to piston-on-ring loadings recently. The purpose of their study was to evaluate the adequacy of applying the formula for piston-on-ring to piston-on-three-ball tests for both mono layered and multilayered discs. Finite element analyses were performed to simulate both piston-on-three-ball and piston-on-ring tests. Different degrees of friction between the specimen supporting surface and the loading fixture were considered in the simulations. The results depended on friction when the disc was supported by a ring, however the results became insensitive to friction when the disc was supported by three balls. The maximum tensile stress on the surface of the disc decreased when the friction increased. The results of finite element analyses demonstrated how the friction between the specimen supporting surface and the loading fixture affects the

biaxial strength evaluation in piston-on-ring and piston-on-three-ball tests. Results demonstrated that Hsueh et al.'s formulae predict well the biaxial tensile strength for mono layered systems.

Dacheng Li, et al, [7] proposed a capacity-regulation system based on a novel rotary control valve for reciprocating refrigeration compressor and designed for the first time. The regulation system was mainly composed of a rotary control valve and an adaptive regulation system. The parameters for the design and control of the rotary control valve are theoretically determined. To verify the feasibility and effectiveness of the proposed system, a three-cylinder reciprocating compressor was adopted as a test device. Experimental results showed that the technology was able to realize continuous stepless capacity regulation for the compressor within the range of (0)10e100%, and power consumption decreased correspondingly with the load reduction. S. Mezghania, et. al, [27] developed a prediction friction model in the hydrodynamic contact regime between the ring and cylinder liner taking into account the real topography of the cylinder liner. The properties of groove texture were related to the oil consumption. The friction performance in the piston ring/cylinder liner contact was associated with the plateau formation. Piston ring-pack friction reduction strategies through the cylinder liner groove texture optimization were analyzed. In their study, the groove texture (grooves balance, honing angle, etc.) have been demonstrated to greatly affect friction performance. This model aimed to solve the average Reynolds equation, which depends on the real surface topographies of the cylinder liner, and describes the influence of surface irregularities on the lubricant flow under hydrodynamic lubrication conditions, considering lubricant film rupture and cavitations. Muhammet Cerit [19] determined the temperature and the stress distributions in a partial ceramic coated spark ignition (SI) engine piston. Effects of coating thickness and width on temperature and stress distributions were investigated including comparisons with results from an uncoated piston. It was observed that the coating surface temperature increase with increasing the thickness in a decreasing rate. Surface temperature of the piston with 0.4 mm coating thickness was increased up to 82 °C. The normal stress on the coated surface decreases with coating thickness, up to approximately 1 mm for which the value of stress was the minimum. The optimum coating thickness was found to be near 1 mm under the given conditions. Results indicated that temperature distributions developed at the ceramic coated piston surface can be considerably higher than those of the uncoated piston surface. Thermal analysis results indicated that the coated section of the piston, which is close to the crevice and wall quenching regions, cause an increase in the temperature. As a result of increase in temperature, a slight amount of decrease in carbon monoxide emission may be expected since CO oxidation reactions strongly depend on temperature. The von Misses stress decreased with increased coating thickness. The shear stress which causes lateral cracks increased with the coating thickness increase and reached its maximum level at the inner edge of the coated region at the interface of the substrate. Finally, it was found that the optimum coating thickness for the ceramic coating was slightly below 1 mm.

C. Friedrich a, et al, [4] conducted experiments with coating development and model wear test results from PVD coatings on piston rings for combustion engines. Piston rings were examples for the application of thin films on commonly used mechanical components. The PVD CrxN coatings were deposited by RF magnetron sputtering and characterized by their fundamental mechanical properties like thickness, hardness, residual stress and adhesion, which are important for the tribological behavior of the coating substrate compound. The contact mechanics of the tribological system piston-ring–cylinder were determined by high mechanical loading and changing geometry caused by the sliding kinematics. Therefore, the range of thickness was about 7 mm. The selected rings were made of steel DIN 1.4112 (DIN X 90 Cr Mo V 18) with a bore diameter of 97.5 mm. The results of the coating substrate characterization — high hardness, moderate compressive residual stresses and sufficient adhesion on metallic substrates — provide good behaviour of coatings in this tribological application. This was confirmed by the results of the tribological test procedures which have been performed with ring-on-disc model-wear tests and a short-stroke test rig. The wear of piston rings was investigated with respect to PVD hard coatings as a surface finish with an adjustable profile of mechanical properties. Dhananjay Kumar Srivastava et al,[8] closely related the performance of a combustion engine with the friction force and wear between cylinder liner and piston rings. This friction force was significantly reduced by optimizing the surface topography of cylinder liners. The experiments were carried out for evaluating wear and friction in simulated engine conditions using Cameron–Plint wear testers, Pin-on-disk testers, SRV testers, etc. A non-firing engine simulator was developed in order to simulate engine conditions to a closer extent compared to these machines. This simulator operated at similar linear speed, stroke, and load as real engine and simulated almost all engine operating conditions, except firing pressures. Energy dispersive analysis (EDS) was carried out of liner and top ring for evaluating materials transfer. Coefficient of friction between three different liner segments and ring was evaluated using an SRV wear tester. Coefficient of friction in the piston ring–liner interface increases with increasing average surface roughness for liner. Surface profile and SEM tests were conducted on liner and rings at different stroke position, which reveal that highest amount

wear takes place at TDC location. Even at the BDC location, the wear was higher than the mid-stroke position because of failure of hydrodynamic lubrication regime. The major elements of liner material were iron, manganese, chromium and silicon. During the experiment, concentration of silica went up. In the ring, the hard chrome plating wore out with time and the base metals got exposed towards the end of the experiment. YujunLi et al, [34] developed a novel vibration-based fault diagnostic method to identify the vital components of a diesel engine that have abnormal clearance. The advantage of this method was that it does not require the comparison of current operating parameters to those collected as the baseline. The proposed method employs the timing of impacts caused by two contacting components as the prime diagnostic feature. To extract the features that distinguish the components with abnormal clearance from those with normal clearance, the characteristics of the vibrations generated by a diesel engine typically used in manufacturing were analyzed in this research.

F.S. Silva [10] analysed the fatigue-damaged pistons from petrol/diesel engines, as well as automobiles including trains. The study of damages initiation in the piston at the crown, ring grooves, pin holes and skirt was assessed. An assessment was made through the Case studies as well as the analysis of the thermal/mechanical fatigue damages the pistons. The stress distribution during the combustion was determined through the linear static stress analysis, using ‘‘cosmos works’’. Stresses at the piston crown, pin holes, grooves and skirt was also determined. For the confirmation of the crack initiation sites, a fractographic study was also done. The fatigue was a problem for the engine pistons, however, it was not responsible for being the largest part of the damaged pistons. The limitation of weight reduction promoted thinner walls, which cause higher stresses. The priority of fuel consumption reduction and more power was in contradiction as another constraint. Z.W. Wang et al, [35] predicted the failure conditions in the piston rods, in Kaplan turbines and the stresses were analyzed. The pressure oscillations over the turbine blades transferred the forces to the piston rods. The analysis of the dynamic stresses were done at thirteen operating conditions using CFD analyses of the flow, along with the analysis of the stresses to the dynamic loads.

The predicted position of the maximum stress concentration was in good agreement with the actual fracture position. The excessive dynamic stresses at the rated output resulted the crack to grow ending to fracture, in the AGC mode, The mean and dynamic stresses were smaller than that of the retainer ring structure due to the pre tightening force in the structure. G. Floweday et al, [11] Studied diesel engine piston failures, during a bench dynamometer engine durability test, which was aimed to evaluate the effects of various fuels on the life of the fuel system components in diesel engine cars. During the test, a number of pistons, cylinder heads and turbocharger failures were experienced. The study aimed at finding the reasons of the piston failures during the tests. Investigation of the fractured pistons revealed that due to excessive thermo-mechanical loading, thermo-mechanical fatigue initiation took place as a result of silicon phase cracking and subsequent micro-crack formation. Micro cracks with progressive formations lead to flaws upto sufficient magnitude for initiating the propagation by high cycle fatigue mechanisms.

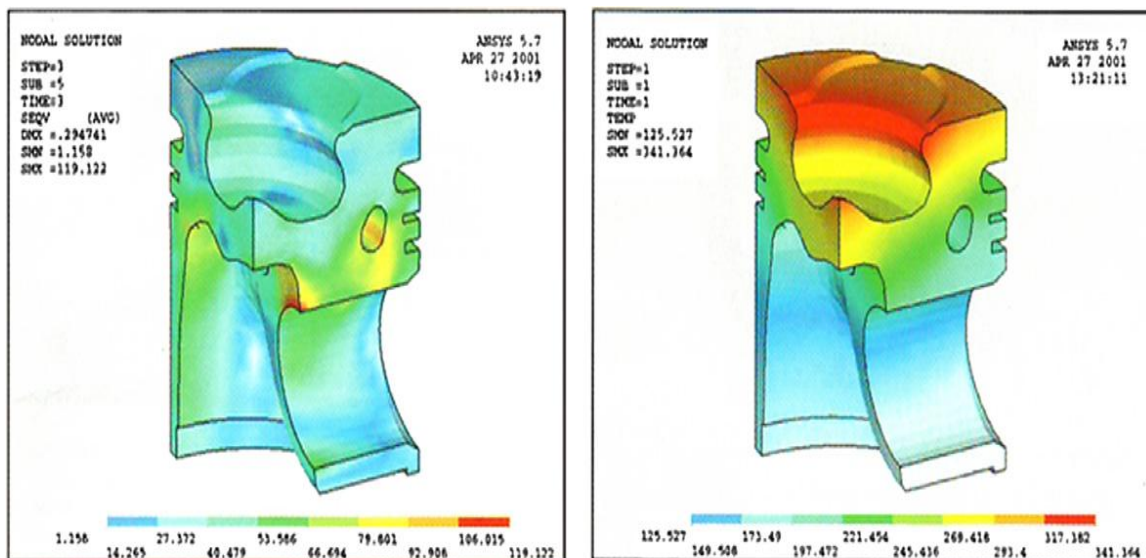


Fig. 4. Contour plot showing the distribution of stress (left) and temperature (right) in a diesel piston due to the combined thermal and pressure loads experienced in an engine. (Reprinted with permission from SAE R-345\_2004 SAE International).[11]

Over-fuelling along with the combination of elevated and poorly controlled post intercooler air temperature caused the excessive thermo-mechanical piston loading. No evidence was found supporting the failures to be related with the test fuel formulations. The piston failure may be attributed to, minor over-fuelling and associated thermo-mechanical overload of the pistons, because of the use of neutral injector codes in the engine ECUs, as it deactivates the ECU's function of recalibration of the fuel injector. The damage of the Surface and hairline cracking of the reference fuelled engine piston, the indications of reduced radiation thermal loading as well as spray penetration with the test fuels gave strong indication that fuel formulations were not contributing to the piston failures. Roop Lal et al, [26] made studies on cylinder liner and piston rings interface. Published data on friction and wear was collected from various researchers and concluded. The oil film thickness played important roll and finally affected the performance of engine. Surface roughness of tribo pair material at the junction producing friction and it varied throughout the stroke length of piston. Loss of power in lubrication had the shear force due to boundary conditions. The tribological performance in IC engine could understood when friction and wear were considered. The necessity to study the factors influencing reliability and performance along with wear was expressed . From the view point of tribo element it was very important to know the specific load, speeds and temperatures for the major components of engine like piston assembly, valve train, the journal bearing and lower viscosity engine oil for lubrication. O.P. Singh et al, [22] investigated experimentally the seizure failure of piston with numerical simulation of thermal elasto-hydrodynamic lubrication (EHL).

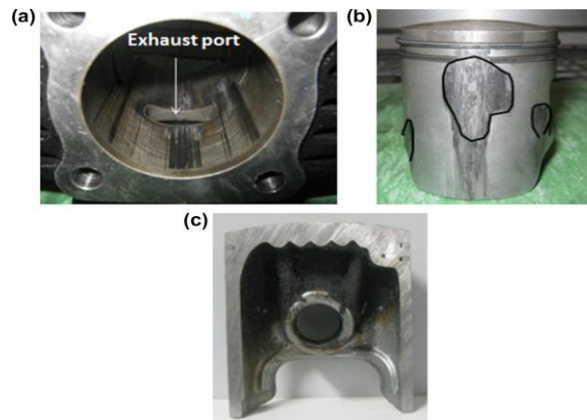


Fig. 5. (a) Seized cylinder liner, (b) seized piston and (c) cut section of the piston showing burnt oil under the crown and skirt. [22]

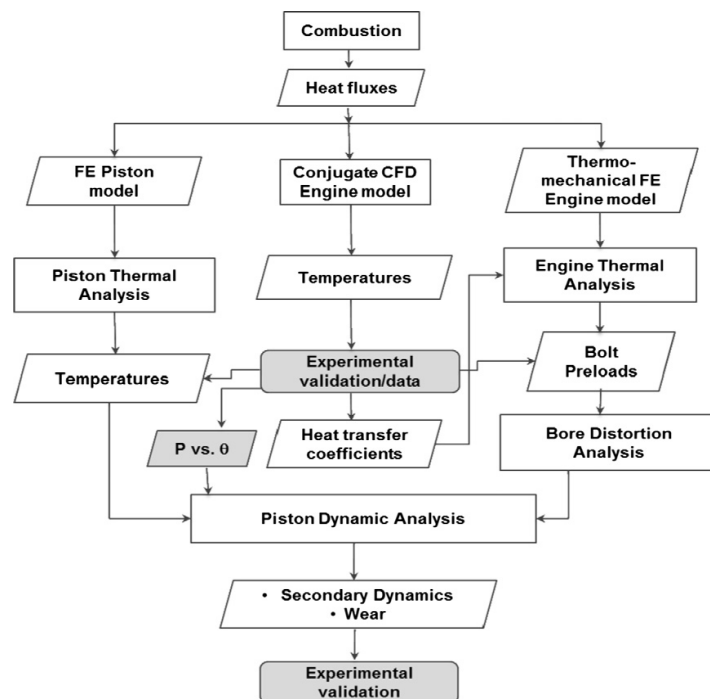


Fig. 6. Flow chart showing steps used in the numerical model of piston hydrodynamic simulation.[22]

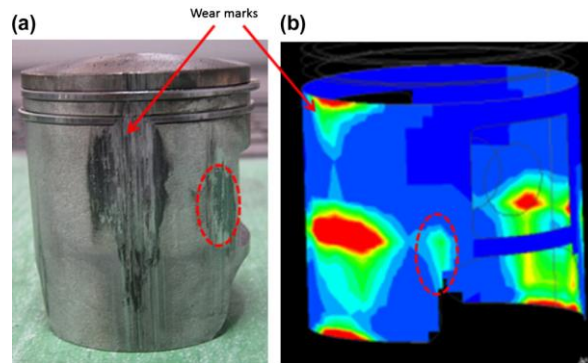


Fig. 7. Correlation of seized marks obtained from the test results and the cumulative wear plot from numerical simulation.[22]

A metallurgical investigation of the piston, rings and liner was done in terms of chemical composition, chemical analysis and hardness. The results indicated large decrease in clearances between the piston and liner at 28°C after TDC. The variation in frictional power over the cycle exhibited sudden increase in magnitude at that location after TDC. The predicted wear mark locations compared well with the test results. The overheating happened to be the root cause of the current piston seizure. Pistons coated with molybdenum material, although enhanced the piston life, but with the problem of skinning off the coating under severe conditions of temperatures and pressures. B. Zhang et al, [3] performed the design as well as experimental validation of a double acting free piston expander in which a slider-based control scheme was used for realizing a full expansion process for the expander. A model was developed for determining the geometric parameters of the expander along with the auxiliary compressor. The results showed that the expander worked stably in a wide range of pressure differences/ratios. R. Mikalsen and A.P. Roskilly [24] reviewed the history of free-piston I C engines, from the air compressors and gas generators used in the mid-20th century Salient features of the free-piston engine has been presented and the effects on engine operation has been discussed, along with comparative advantages and disadvantages with the conventional engines has been discussed.

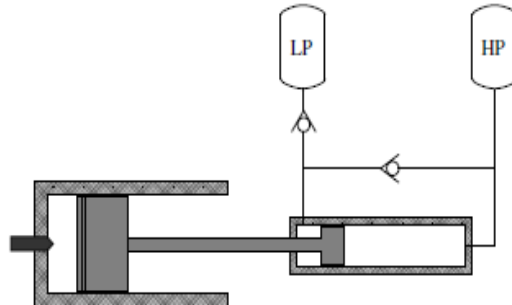


Fig. 8. Single piston hydraulic free-piston engine [24]

Muhammet Cerit and Mehmet Coban [20] improved the performance of a diesel engine, by finding out both temperature and thermal stress distributions on an aluminum piston crown with zirconia coating in a plasma sprayed magnesia-stabilized environment. Effects of the coating thickness varying between 0.2 to 1.6 mm has been investigated, and the results has been compared with that of an uncoated piston, using finite element method. Higher combustion chamber temperature was developed by means of TBC, resulting increase in thermal efficiency of the engine. The engine performance improved with reduction in the piston (substrate) surface temperature. The thermal performance of the piston also increased with increase in coating thickness. From the analysis it was found that the calculated stress values was lower than the allowable stress values of the materials.

### III. SUMMARY

Experiments revealed that friction coefficient increases with increasing surface roughness of liner surface. The linear wear of the cast iron liner and rings decreased with increasing load but the mass wear increased with increasing load.

The thermal stress is related to coating thickness. It increases with the coating thickness on the SUBS. The greatest value of the normal stress which produces spalling of the ceramic is produced on the bond coat. It is nearly twice the value of the maximum normal stress on the substrate. The thermal performance of the piston

increases with increased coating thickness. Stress values obtained from FEA were compared with the mechanical properties of the aluminum alloy and zirconia material and it was concluded that calculated stress values were lower than the allowable stress values of the materials.

The ratio of average slopes in axial and circumferential directions can monitor piston skirt wear. The free material liberated due to deep scoring between the piston and liner snowballs, changes its phase from solid to molten state and finally makes its way into the rings. It locks the rings and thus leading the complete engine seizure failure.

Surface thermal damage and hairline cracking of the reference fuelled engine piston, as well as the indications of marginally reduced radiation thermal loading and spray penetration associated with the test fuels gave strong indication that the fuel formulations did not contribute to the piston failures. The fractographic and microstructural analyses reveal regarding selection of correct material for piston fabrication.

The piston failures were determined to have occurred due to Surface thermal damage of the piston bowl lip, Crack initiation by thermal micro-cracking and erosion of primary silicon particles, leading to threshold flaw size, Propagation by thermo-mechanical high and low cycle fatigue and Brittle fast fracture at the critical crack length. Subsequent fuel and flame impingement resulting in piston burn through and loss of engine compression.

The main causes contributing to the piston wear and failures was the use of neutral injector codes in the engine ECUs which deactivated the ECU's function of automatic recalibration of the fuel injector flow rates, resulting in minor over-fuelling and associated thermo-mechanical overload of the failed pistons. Further poorly controlled post intercooler air temperatures and an elevated set point, resulting in overheating of the piston and other combustion chamber components.

## REFERENCES

- [1] A. Skopp a,1, N. Kelling a,1, M. Woydta,1, L.-M. Berger b., Thermally sprayed titanium sub oxide coatings for piston ring/cylinder liners under mixed lubrication and dry-running conditions, *Wear* 262 (2007) 1061–1070
- [2] A. V. Sreenath And N. Raman, Running-In Wear Of A Compression Ignition Engine: Factors Influencing The Conformance Between Cylinder Liner And Piston Rings, *Wear*, 38 (1976) 271 – 289
- [3] B. Zhang, X. Peng , Z. He, Z. Xing, P. Shu, Development of a double acting free piston expander for power recovery in trans critical CO<sub>2</sub> cycle, *Applied Thermal Engineering* 27 (2007) 1629–1636
- [4] C. Friedrich a., G. Berg a, E. Broszeit a, F. Rick b, J. Holland b, PVD CrxN coatings for tribological application on piston rings, *Surface and Coatings Technology* 97 (1997) 661–668
- [5] C.W. Huang a., C.H. Hsueh b, c, Piston-on-three-ball versus piston-on-ring in evaluating the biaxial strength of dental ceramics, *Dental materials* 27 (2011) e117–e123
- [6] D. J. Picken; H. A. Hassaan, A Method for Estimating Overhaul Life of Internal Combustion Engines including Engines Operating, *J. agric. Engng Res*, 28. (1983), 139-147
- [7] Dacheng Li a., Haiqi Wub, Jinji Gao b, Experimental study on stepless capacity regulation for reciprocating compressor based on novel rotary control valve, *International journal of refrigeration* 36 (2013) 1701 e1715
- [8] Dhananjay Kumar Srivastava a, Avinash Kumar Agarwal a., Jitendra Kumar b, Effect of liner surface properties on wear and friction in a non-firing engine simulator, *Materials and Design* 28 (2007) 1632–1640
- [9] E.P. Becker a., K.C Ludema b, A qualitative empirical model of cylinder bore wear, *Wear*, 225-229 (1999) 387-404
- [10] F.S. Silva , Fatigue on engine pistons – A compendium of case studies, *Engineering Failure Analysis* 13 (2006) 480–492
- [11] G. Floweday a, S. Petrov b, R.B. Tait b., J. Press c, Thermo-mechanical fatigue damage and failure of modern high performance diesel pistons, *Engineering Failure Analysis* 18 (2011) 1664–1674
- [12] H. Sunden and R. Schaub †, Piston rings for slow and speed diesel engines, *Tribology International* February 1979
- [13] J. E. Willn, Characterisation Of Cylinder Bore Surface Finish A Review Of Profile Analysis, *Wear - Elsevier Sequoia S.A., Lausanne - Printed in the Netherlands*
- [14] J. Galligan a, A.A. Torrance a.), G. Liraut b , A scuffing test for piston ring bore combinations: Pt. II. Formulated motor lubrication, *Wear* 236 (1999) 210–220
- [15] Jarosław Milewski, Łukasz Szabłowski, Jerzy Kuta, Control strategy for an Internal Combustion engine fuelled by Natural Gas operating in Distributed Generation, *Energy Procedia* 14 (2011) 1478 – 1483
- [16] L. Ceschini, A. Marconi, C. Martini n, A. Morri, Tribological behavior of components for radial piston hydraulic motors: Bench tests, failure analysis and laboratory dry sliding tests, *Wear* 305 (2013) 238 –247
- [17] K. J. Stout And T. A. Spedding, The Characterization Of Internal Combustion Engine Bores, *Wear*, 83 (1982) 311 – 326
- [18] M. Priest, C.M. Taylor, Automobile engine tribology — approaching the surface, *Wear* 241 (2000) 193–203
- [19] Muhammet Cerit , Thermo mechanical analysis of a partially ceramic coated piston used in an SI engine, *Surface & Coatings Technology* 205 (2011) 3499–3505
- [20] Muhammet Cerit and Mehmet Coban, Temperature and Thermal Stress analysis of a ceramic-coated aluminium alloy piston used in a diesel engine, *International Journal of Thermal Sciences* 77, (2014) 11-18
- [21] Mustafa Canakci , Combustion characteristics of a turbocharged DI compression ignition engine fueled with petroleum diesel fuels and biodiesel, *Bio resource Technology* 98 (2007) 1167–1175
- [22] O.P. Singh a., Yogesh Umbarkar b, T. Sreenivasulu a, E. Vetrivendan a, M. Kannan a, Y.R. Babu a, Piston seizure investigation: Experiments, modeling and future challenges, *Engineering Failure Analysis* 28 (2013) 302–310

- [23] P. C. Nautiyal, S. Singhal and J. P. Sharmat, Friction and wear processes in piston rings, *Tribology International*, 1983
- [24] R. Mikalsen, A.P. Roskilly, A review of free-piston engine history and applications, *Applied Thermal Engineering* 27 (2007) 2339–2352
- [25] Rohollah Ghasemi, Lennart Elmquist. The relationship between flake graphite orientation, smearing effect, and closing tendency under abrasive wear conditions, *Wear* 317 (2014) 153–162.
- [26] Roop Lal, R C Singh, Ranganath M S and S Maji, Friction and Wear of Tribo-Elements in Power Producing Units for IC Engines- A Review, *International Journal of Engineering Trends and Technology (IJETT) – Volume 14 Issue 5, 2014*
- [27] S. Mezghani a, n, I. Demirci a, M. Yousfi a, b, M. El Mansori a, Running-in wear modeling of honed surface for combustion engine cylinder liners, *Wear* 302 (2013) 1360–1369
- [28] S. Mezghania, I. Demircia, H. Zahouanib, M. El Mansoria, The effect of groove texture patterns on piston-ring pack friction, *Precision Engineering* 36 (2012) 210–217
- [29] S.G. Chung, J.M. Lee, W.Y. Jang, Comparing the Quality of Samples obtained by Three Types of Fixed Piston Samplers for Soft Sensitive Clay, Accepted manuscript, *Engineering Geology*, Accepted date: 21 June 2014
- [30] T. H. C. Childs and F. Sabbagh, Boundary-Lubricated Wear Of Cast Irons To Simulate Automotive Piston Ring Wear Rates, *Wear*, 134 (1989) 81 – 97
- [31] U.I. Sjodin, U.L.-O. Olofsson, Experimental study of wear interaction between piston ring and piston groove in a radial piston hydraulic motor, *Wear* 257 (2004) 1281–1287
- [32] Wieslaw Grabon a, Waldemar Koszela a, Pawel Pawlus a, n, Slawomir Ochwat b a, Improving tribological behaviour of piston ring–cylinder liner frictional pair by liner surface texturing, *Tribology International* 61 (2013) 102–108
- [33] William G. Agnew, Fifty Years Of Combustion Research At General Motors, *Proc. Energy Combust. Scie. Vol 4*, pp 115-155, 1978
- [34] Yujun Li a, Peter W. Tse a, Xin Yang b, Jianguo Yang b, EMD-based fault diagnosis for abnormal clearance between contacting components in a diesel engine, *Mechanical Systems and Signal Processing* 24 (2010) 193–210
- [35] Z.W. Wang a, Y.Y. Luo a, L.J. Zhou b, R.F. Xiao a, G.J. Peng a, Computation of dynamic stresses in piston rods caused by unsteady hydraulic loads, *Engineering Failure Analysis* 15 (2008) 28–37
- [36] Zenon Krzyzak, Pawel Pawlus, ‘Zero-wear’ of piston skirt surface topography, *Wear*, 260 (2006) 554-561

# Big Bang–Big Crunch Optimization Algorithm for the Maximum Power Point Tracking in Photovoltaic System

Yacine Labbi<sup>1</sup>, Asma Labbi<sup>2</sup>, Zoubir Becer<sup>3</sup>, Djilani Benattous<sup>4</sup>

<sup>1,4</sup>Department of Electrical Engineering, El-Oued University, Algeria

<sup>2,3</sup>Department of Physics, El-Oued University, Algeria

**Abstract:** This paper presents an intelligent control method for the maximum power point tracking (MPPT) of a photovoltaic system under variable temperature and irradiance conditions. The Big Bang–Big Crunch (BB–BC) optimization algorithm is a new optimization method that relies on the Big Bang and Big Crunch theory, one of the theories of the evolution of the universe. In this paper, a Big Bang–Big Crunch algorithm is presented to meet the maximum power operating point whatever the climatic conditions are from simulation results, it has been found that BB–BC method is highly competitive for its better convergence performance.

**Keywords:** Photovoltaic System, MPPT, Optimization Technique, Big Bang–Big Crunch (BB–BC)

## I. NOMENCLATURE

<i>BB-BC</i>	big bang–big crunch
<i>G</i>	insulation level
<i>I<sub>D</sub></i>	diode current
<i>I<sub>L</sub></i>	photo current
<i>I<sub>o</sub></i>	reverse saturation current
<i>I<sub>sc</sub></i>	short-circuit.
<i>k</i>	boltzmann's constant
<i>l</i>	upper limit
<i>MPPT</i>	maximum power point tracking
<i>PV</i>	solar photovoltaic
<i>q</i>	electronic charge
<i>R<sub>s</sub></i>	cell series resistance
<i>R<sub>sh</sub></i>	cell Shunt resistance
<i>T</i>	cell temperature
<i>V<sub>oc</sub></i>	the open circuit
<i>x<sup>c</sup></i>	center of mass

## II. INTRODUCTION

Photovoltaic energy is a technique, which converts directly the sunlight into electricity. It is modular, quit, non-polluting and requires very little maintenance, for this reason a powerful attraction to photovoltaic systems is noticed. By having a quick glance on both the current-voltage and the power-voltage characteristics of PV arrays, we see clearly the dependence of the generating power of a PV system on both insulation and temperature. [1].

A new optimization method relied on one of the theories of the evolution of the universe namely, the Big Bang and Big Crunch theory is introduced by Erol and Eksin [11] which has a low computational time and high convergence speed. According to this theory, in the Big Bang phase energy dissipation produces disorder and randomness is the main feature of this phase; whereas, in the Big Crunch phase, randomly distributed particles are drawn into an order. The Big Bang–Big Crunch (BB–BC) Optimization method similarly generates random points in the Big Bang phase and shrinks these points to a single representative point via a center of mass in the Big Crunch phase. After a number of sequential Big Bangs and Big Crunches where the distribution of randomness within the search space during the Big Bang becomes smaller and smaller about the average point computed during the Big Crunch, the algorithm converges to a solution. The BB–BC method has been shown to outperform the enhanced classical Genetic Algorithm for many benchmark test functions [2].

In this study, we present an application of a Big Bang–Big Crunch (BB–BC) on a photovoltaic system, which helps to catch the Maximum Power Operating Point (MPOP). This latter change instantaneously with changing radiation and temperature, what implies a continuous adjustment of the output voltage to achieve the

transfer of the maximum power to the load. The justification of this application lies in the fact the I-V and P-V characteristics are non linear because of the nonlinearity of the photovoltaic systems from one hand and because of the instantaneous change of both insulation and temperature from the other hand, what makes the two previous plot in fact fluctuating instead of the simulated smooth ones (Fig. 1 and 2) [3].

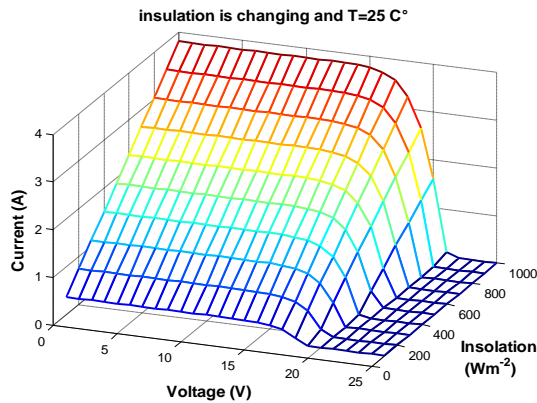


Fig. 1 I-V characteristics when insulation is changing.

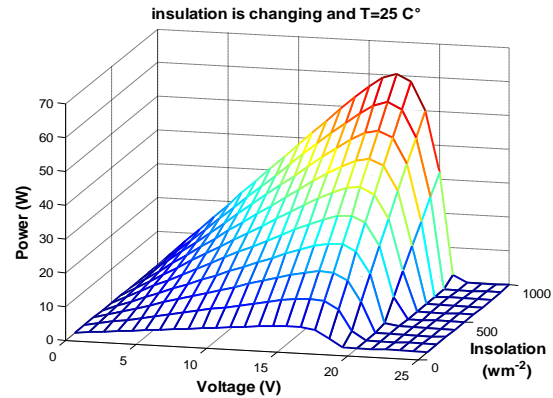


Fig. 2 P-V characteristics when insulation is changing.

The proposed approach is employed in fitting both the I-V and P-V characteristics of a solar module referenced as Solarex MSX 60 with the characteristics shown in the index.

### III. MODELING OF THE PHOTOVOLTAIC GENERATOR

Thus the simplest equivalent circuit of a solar cell is a current source in parallel with a diode. The output of the current source is directly proportional to the light falling on the cell (photocurrent  $I_{ph}$ ). During darkness, the solar cell is not an active device; it works as a diode, i.e. a p-n junction. It produces neither a current nor a voltage. However, if it is connected to an external supply (large voltage) it generates a current  $I_D$ , called diode ( $D$ ) current or dark current. The diode determines the I-V characteristics of the cell.

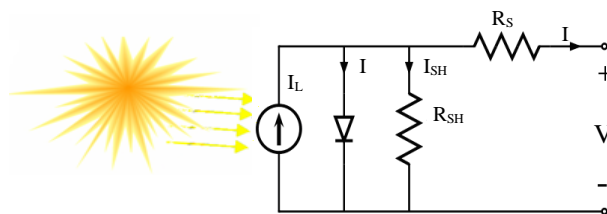


Fig. 3 Circuit diagram of the PV model.

Increasing sophistication, accuracy and complexity can be introduced to the model by adding in turn [4]:

- Temperature dependence of the diode saturation current  $I_0$ .
- Temperature dependence of the photo current  $I_L$ .
- Series resistance  $R_s$ , which gives a more accurate shape between the maximum power point and the open circuit voltage. This represents the internal losses due to the current flow.
- Shunt resistance  $R_{sh}$ , in parallel with the diode, this corresponds to the leakage current to the ground and it is commonly neglected
- Either allowing the diode quality factor  $n$  to become a variable parameter (instead of being fixed at either 1 or 2) or introducing two parallel diodes with independently set saturation currents.

In an ideal cell  $R_s = R_{sh} = 0$ , which is a relatively common assumption [5]. For this paper, a model of moderate complexity was used. The net current of the cell is the difference of the photocurrent,  $I_L$  and the normal diode current  $I_0$ :

$$I = I_L - I_0 \left( e^{\frac{q(V+IR_S)}{nKT}} - 1 \right), \quad (1)$$

The model included temperature dependence of the photo-current  $I_L$  and the saturation current of the diode  $I_o$ .

$$I_L = I_L(T_1) + K_o(T - T_1), \tag{2}$$

$$I_L(T_1) = I_{sc}(T_{1,nom}) \frac{G}{G_{(nom)}}, \tag{3}$$

$$K_o = \frac{I_{sc}(T_2) - I_{sc}(T_1)}{(T_2 - T_1)}, \tag{4}$$

$$I_o = I_o(T_1) \times \left(\frac{T}{T_1}\right)^{\frac{3}{n}} e^{-\frac{qV_o(T)}{nk\left(\frac{1}{T} - \frac{1}{T_1}\right)}}, \tag{5}$$

$$I_o(T_1) = \frac{I_{sc}(T_1)}{\left(e^{\frac{qV_{oc}(T_1)}{nkT_1}} - 1\right)}, \tag{6}$$

A series resistance  $R_s$  was included; witch represents the resistance inside each cell in the connection between cells.

$$R_s = -\frac{dV}{dI_v} - \frac{1}{X_v}, \tag{7}$$

$$X_v = I_o(T_1) \times \frac{q}{nkT_1} e^{\frac{qV_{oc}(T_1)}{nkT_1}} - \frac{1}{X_v}, \tag{8}$$

The shunt resistance  $R_{sh}$  is neglected. A single shunt diode was used with the diode quality factor set to achieve the best curve match. This model is a simplified version of the two diode model presented by Gow and Manning [6]. The circuit diagram for the solar cell is shown in Figure 3.

The I-V characteristics of the module can be expressed roughly by the (1) to (8). the model requires three point to be measured to define this curve [7]:

- The voltage of the open circuit  $V_{oc}$ .
- The current of short-circuit  $I_{sc}$ .
- The point of optimum power ( $I_{opt}$ ,  $V_{opt}$ ).

#### IV. BIG BANG–BIG CRUNCH (BB–BC) OPTIMIZATION ALGORITHM

The BB–BC method developed by Erol and Eksin [2] consists of two phases: a Big Bang phase, and a Big Crunch phase. In the Big Bang phase, candidate solutions are randomly distributed over the search space. Similar to other evolutionary algorithms, initial solutions are spread all over the search space in a uniform manner in the first Big Bang. Erol and Eksin [2] associated the random nature of the Big Bang to energy dissipation or the transformation from an ordered state (a converged solution) to a disorder or chaos state (new set of solution candidates).

Randomness can be seen as equivalent to the energy dissipation in nature while convergence to a local or global optimum point can be viewed as gravitational attraction. Since energy dissipation creates disorder from ordered particles, we will use randomness as a transformation from a converged solution (order) to the birth of totally new solution candidates (disorder or chaos) [2].

The proposed method is similar to the GA in respect to creating an initial population randomly. The creation of the initial population randomly is called the Big Bang phase. In this phase, the candidate solutions are spread all over the search space in an uniform manner [2].

The Big Bang phase is followed by the Big Crunch phase. The Big Crunch is a convergence operator that has many inputs but only one output, which is named as the “center of mass”, since the only output has been derived by calculating the center of mass. Here, the term mass refers to the inverse of the merit function value [8]. The point representing the center of mass that is denoted by  $x_c$  is calculated according to:

$$\bar{x}^c = \frac{\sum_{i=1}^N \frac{1}{f^i} \bar{x}^i}{\sum_{i=1}^N \frac{1}{f^i}}, \tag{8}$$

where  $x_i$  is a point within an n-dimensional search space generated,  $f_i$  is a fitness function value of this point,  $N$  is the population size in Big Bang phase. The convergence operator in the Big Crunch phase is different from ‘exaggerated’ selection since the output term may contain additional information (new candidate or member having different parameters than others) than the participating ones, hence differing from the population members. This one step convergence is superior compared to selecting two members and finding their center of gravity. This method takes the population members as a whole in the Big-Crunch phase that acts as a squeezing or contraction operator; and it, therefore, eliminates the necessity for two-by-two combination calculations [2].

After the second explosion, the center of mass is recalculated. These successive explosion and contraction steps are carried repeatedly until a stopping criterion has been met. The parameters to be supplied to normal random point generator are the center of mass of the previous step and the standard deviation. The deviation term can be fixed, but decreasing its value along with the elapsed iterations produces better results.

After the Big Crunch phase, the algorithm creates the new solutions to be used as the Big Bang of the next iteration step, by using the previous knowledge (center of mass). This can be accomplished by spreading new off-springs around the center of mass using a normal distribution operation in every direction, where the standard deviation of this normal distribution function decreases as the number of iterations of the algorithm increases [8]:

$$x^{new} = x^c + l.r/k, \tag{9}$$

where  $x^c$  stands for center of mass,  $l$  is the upper limit of the parameter,  $r$  is a normal random number and  $k$  is the iteration step. Then new point  $x_{new}$  is upper and lower bounded.

The BB–BC approach takes the following steps [2]:

- Step 1 Form an initial generation of  $N$  candidates in a random manner. Respect the limits of the search space.
- Step 2 Calculate the fitness function values of all the candidate solutions.
- Step 3 Find the center of mass according to (9). Best fitness individual can be chosen as the center of mass.
- Step 4 Calculate new candidates around the center of mass by adding or subtracting a normal random number whose value decreases as the iterations elapse of using (9).
- Step 5 Return to Step 2 until stopping criteria has been met.

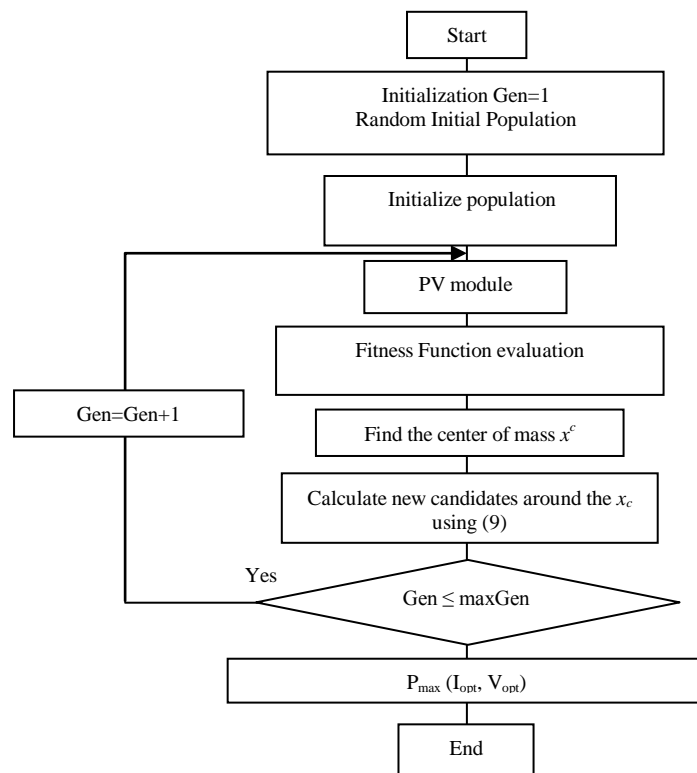


Fig. 4. Flow chart of genetic algorithm

### V. APPLICATION OF BB-BC TO MPOP

The goal is to solve some optimization problem where we search for an optimal solution in terms of the variables of the problem (current and voltage) by imposing the constraints on the current and the voltage which should be both bigger than zero.

To minimize fitness is equivalent to getting a maximum puissance value in the searching process. The objective of BB-BC has to be changed to the maximization of fitness to be used as follows:

$$fitness = \begin{cases} P_{max} / P(V, I); & \text{if } P < P_{max} \\ 0; & \text{otherwise} \end{cases} \quad (10)$$

The above steps and how BB-BC evolves are depicted by the flow chart of Fig. 4. It should be noted that all the parameters involved in the Bang and Big Crunch algorithm can be pre-defined subject to the nature of the problem being solved, which is the controlled equipment and then they are located on a string.

### VI. SIMULATION RESULTS AND DISCUSSION

The program has been executed under Matlab system. The program was written and executed on Pentium 4 having 2.4 GHZ 1GB DDR RAM.

According to simulation, the following parameters in the BB–BC algorithms methods are used :

- The number of generation is 50 iterations and Size of population 20 individuals (candidates).
- The individual having maximum fitness value is chosen for Big–Crunch phase.
- New population (Big Bang phase) is generated by using normal distribution principle with (9):

$$X(k,i) = X_{est}(i) + (X_{max}(i) - X_{min}(i)) \cdot rand / it, \quad (11)$$

Where  $k$  number of candidates,  $i$  number of parameters,  $X_{est}(i)$  value which falls with minimum cost,  $X_{max}(i)$  and  $X_{min}(i)$  are parameter upper and lower limits and  $it$  number of iterations.

The convergence of optimal solution using BB-BC is shown in Fig. 5 and 6, where only about 16 iterations were needed to find the optimal solution.

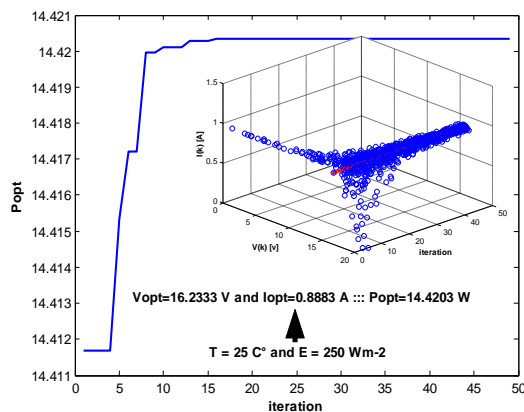


Fig. 5 Convergence of BB-BC for T = 25 C° and E = 250 Wm<sup>-2</sup>

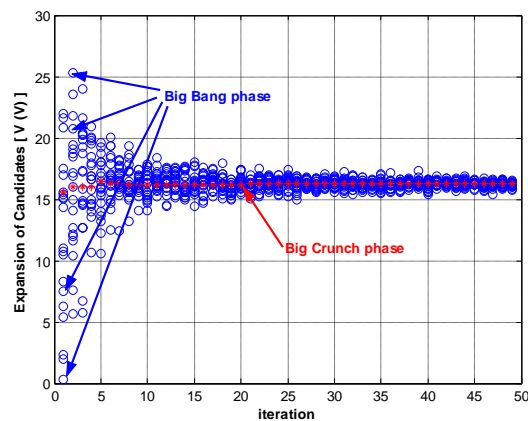


Fig. 6 Expansion of Candidates for iteration.

In order to simulation the system, it is necessary to use the irradiance data for a specific location over 24 a hour period of time, any location will be sufficient to test the model. I chose to use data from Golden, Colorado on March 14, 2010 and July 14, 2009 because the data is easily available, and I can be reasonably confident about the accuracy [9]. The data for July 14, 2009 appears to be a pretty good example of a typical sunny day, while March 14, 2010 is good worst case scenario ( refer to fig. 8 and 9). Both of these days can be useful for simulation purposes.

The resulted values of this optimization problem are Show in simulation 1-2. These simulation results of many sample runs of the BB-BC technique. We see clearly the variation of the MPOP with respect to either insulation or temperature and both of them with great accuracy (Fig. 9-12).

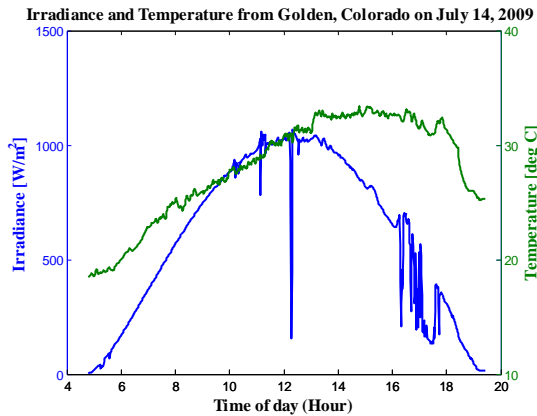


Fig. 7 Irradiance and Temperature data for sunny day. cloudy day.

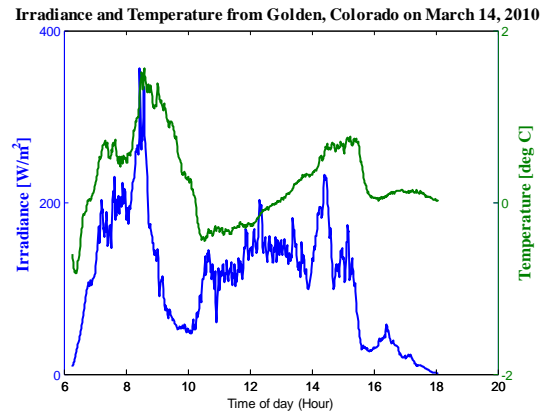


Fig. 8 Irradiance and Temperature data for

**A. Simulation 1 : Sunny day conditions.**

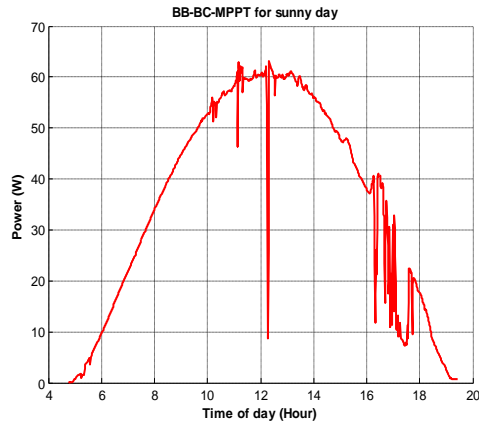


Fig. 9 Power optimal for sunny day simulation purposes.

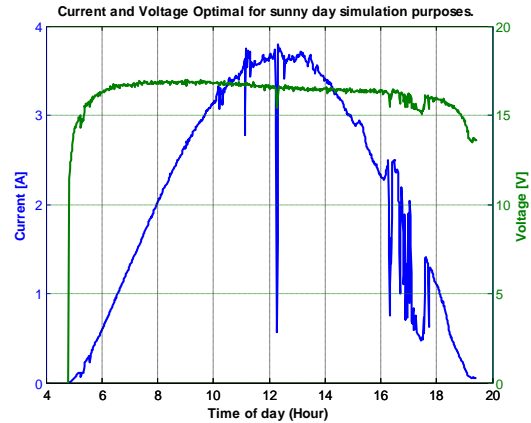


Fig. 10 Current and Voltage optimal for sunny day.

**B. Simulation 2 : Cloudy day conditions.**

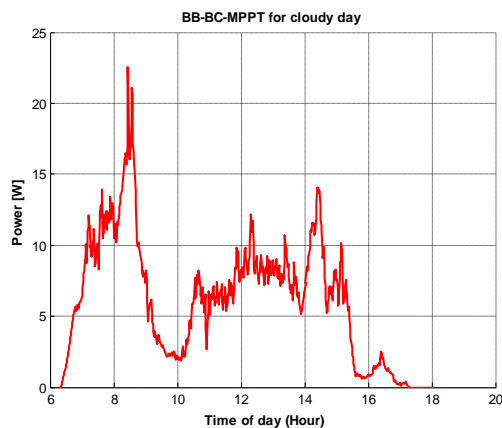


Fig. 11 Power optimal for cloudy day simulation purposes.

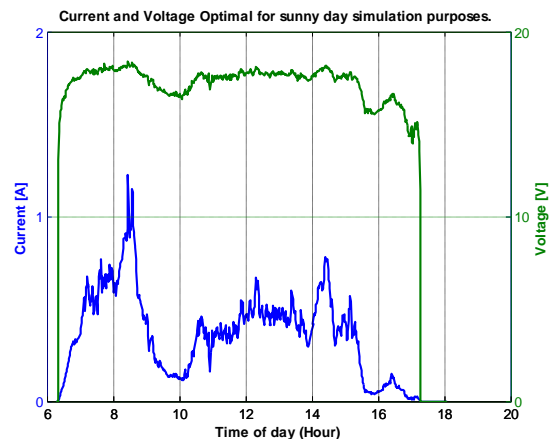


Fig. 12 I and V optimal for cloudy day simulation purposes.

Obviously, the system works much better under sunny conditions. The data used for the cloudy day dropped the power maximal of PV array by about 80 %.

However given the significant decrease in energy produced by the PV array, there may have been another factor (snow for example). Therefore, I would recommend that simulations be run for several more cloudy day

scenarios. Also, a simulation in which cloudy day is followed by a sunny day may give us an idea of how quickly the system would be able to rebound back to normal condition.

## VII. CONCLUSION

This paper introduces a new solution approach based on Big Bang–Big Crunch, which calculates instantaneously the MPOP of a PV module in order to maximize the profits in terms of the power issued from the PV module. Because of the P-V characteristics this method is used to seek the real maximize power and to avoid the wrong values of local maxima. The obtained results of this investigation and depicted in Fig. 9-12.

The BB-BC optimization has several advantages over other evolutionary methods: Most significantly, a numerically simple algorithm and heuristic methods with relatively few control parameters; and the ability to solve problems that depend on large number of variables.

## APPENDIX

### APPENDIX 1. SOLAREX MSX 60 SPECIFICATIONS (1kW/M2, 25°C)

Characteristics	SPEC.
Typical peak power ( $P_m$ )	60W
Voltage at peak power ( $V_m$ )	17.1V
Current at peak power ( $I_m$ )	3.5A
Short-circuit current ( $I_{SC}$ )	3.8A
Open-circuit voltage ( $V_{OC}$ )	21.1V
Temperature coefficient of open-circuit voltage ( $\alpha$ )	-73 mV/°C
Temperature coefficient of short-circuit current ( $\beta$ )	3 mA/°C
Approximate effect of temperature on power	-0.38W/°C
Nominal operating cell temperature (NOCT <sup>2</sup> )	49°C

## REFERENCES

- [1] A. Labouret and M. Viloz, *Energie solaire photovoltaïque, Le manuel du professionnel*, Dunod, Paris, 2003.
- [2] K. Erol Osman, Ibrahim Eksin, *New optimization method : Big Bang-Big Crunch*, Elsevier, *Advances in Engineering Software*, 37, 2006, pp. 106–111.
- [3] D.J. Bellala and M. Chaabanem, "Optimization by continuous Genetic algorithm of the Maximum Photovoltaic Power tracking under different climatic conditions", *Asian Journal of inf tech*, 6(6), 2007, pp. 715-719.
- [4] G. Walker, "Evaluating MPPT converter topologies using a MATLAB PV model", *Journal of Electrical & Electronics Engineering, Australia, IEAust*, 21(1), 2001, pp.49-56.
- [5] CIGRE TF38.01.10, *Modeling New Forms of Generation and Storage*, November. 2000, pp. 26-39.
- [6] J. A. Gow, C. D. Manning, "Development of a photovoltaic array model for use in power electronics simulation studies", *IEE Proceedings on Electric Power Applications*, 146, March 1999, pp. 193-200.
- [7] D. Weiner and A. Levinson, "An optimal operation desing of a photovoltaic D.C. motor coupled water pumping system", *electric Machines and Power Systems, Electric Power Components and Systems*, 24(3), April. 1996 , pp. 277–288.
- [8] A. Kaveha, S. Talataharib, "Size optimization of space trusses using Big Bang–Big Crunch algorithm", *Elsevier, Computers and Structures*, 87, 2009, pp. 1129–1140.
- [9] National Renewable Energy Laboratory (NREL) Daily plot and Raw Data Files March 14, 2010 and July 14, 2009 (downloaded from [http://www.nrel.gov/midc/srrl\\_bms/](http://www.nrel.gov/midc/srrl_bms/)).
- [10] C. Larbes, Ait S.M. Cheikh, T. Obeidi and A. Zerguerras, "Genetic algorithms optimized fuzzy logic control for the maximum power point tracking in photovoltaic system", *Elsevier, Renewable Energy*, 34, 2009, pp. 2093-2100.

## Experimental Investigation and Parametric Analysis of Surface Roughness in CNC Turning Using Design of Experiments

Ranganath. M. S<sup>1</sup>, Vipin<sup>2</sup>

<sup>1</sup>Associate Professor, <sup>2</sup>Professor, Production and Industrial Engineering, Delhi Technological University, Delhi, India

**Abstract:** The manufacturing industries are very much concerned about the quality of their products. They are focused on producing high quality products in time at minimum cost. Surface finish is one of the crucial performance parameters that have to be controlled within suitable limits for a particular process. Surface roughness of machined components has received serious attention of Researchers for many years. It has been an important design feature and quality measure in machining process. There are a large number of parameters which affect the surface roughness. These include cutting tool variables, work piece material variables, cutting conditions etc. Therefore, prediction or monitoring of the surface roughness of machined components has been challenging and unexplored area of research. The present work is therefore in a direction to integrate effect of various parameters which effect the surface roughness. Experiments were carried out with the help of factorial method of design of experiment (DOE) approach to study the impact of turning parameters on the roughness of turned surfaces. A mathematical model was formulated to predict the effect of machining parameters on surface roughness of a machined work piece. Model was validated with the experimental data and the reported data of other researchers. Further parametric investigations were carried out to predict the effect of various parameters on the surface research

**Keywords:** Surface Roughness, Design of Experiments, CNC Turning, Surface Roughness, factorial method,

### I. INTRODUCTION

The manufacturing industries are very much concerned about the quality of their products. They are focused on producing high quality products in time at minimum cost. Surface roughness is one of the crucial parameters that have to be controlled within suitable limits for a particular process. Therefore, prediction or monitoring of the surface roughness of machined components has been an important area of research.

In the present research, modelling the distribution of the resulting surface roughness values, in fine turning of Aluminium 6061, using wiper insert tools has been undertaken. This study will enable the assessment of the process variability with respect to surface roughness in fine turning. Though some studies on this particular aspect have been done, a different approach has been used in the current study. The important parameters discussed here are cutting speed, feed depth of cut, nose radius and rake angle. In the second part of this study, predictive equations for use in predicting the surface roughness values have been developed in terms of five important variables cutting speed, feed, depth of cut, nose radius and rake angle. Use of such predictive equations has been demonstrated with the application of regression techniques. In the third part of the present study, the performance of wiper insert tools is given. Several statistical techniques were used in this study to analyze the data instead of drawing conclusions based on the trends of the graphs as was done in earlier studies. A theoretical approach for predicting the surface roughness values has been discussed in terms of cutting speed, feed, depth of cut, nose radius and rake angle of the tool. Many researchers have indicated different methods of predicting the surface roughness values from various combinations of machining variables using the Design of experiments, ANN and GA. In establishing the predictive equations in the present study, emphasis has been placed on the experimental design. To develop the first order models (log transformed) for predicting the surface roughness values a regression modelling has been done. For establishing the second-order predictive models a full factorial design has been used.

### II. EXPERIMENTAL SETUP

Experimental Setup includes the following: 1. CNC Turning Machine 2. The geometry of tools selected are with the combinations of Nose radius: 0.4mm, 0.8mm, 1.2 mm and Rake angles 16°, 18°, 20°. 3. Work material-Aluminum 6061, Heat Treatable Alloy manufactured in the form of bars by HINDALCO 4. Surface Roughness Measuring Instrument Talysurf Surtronic 3+ 5. Software

The CNC turning machine consists of the machine unit with a three jaw independent chuck, a computer numerically controlled tool slide. CNC System used was Fanuc 0i mate - TD/Siemens 828D Basic T. with turret tooling BTP 80. The cutting tool which provided with the CNC turning lathe was a 25 x 25 mm square tool holder with 60 mm length having the positive tool angles. The tool used was cemented carbide insert type. The geometry of tools selected are with the combinations of three nose radius: 0.4, 0.8, 1.2 and positive Rake angles 16°, 18°, 20°. Plate 3.7 shows the inserts and tool holder.



Figure 1: Inserts and Tool Holder

The Surtronic 3+ is a portable, self-contained instrument for the measurement of surface texture and is suitable for use in both the workshop and laboratory. Parameters available for surface texture evaluation are: Ra, Rq, Rz (DIN), Ry and Sm. The parameters evaluations and other functions of the instrument are microprocessor based. The measurements results are displaced on an LCD screen and can be output to an optional printer or another computer for further results. Minitab 13 was used for analyzing the results.

### III. DESIGN OF EXPERIMENTS

The Design of Experiments were carried according to full factorial design methods.

Table 1: Process Parameters and Levels

Process Parameters Design	Process Parameters	Level (1)	Level (2)	Level (3)
A	Tool Rake angle (Degree)	16	18	20
B	Tool nose Radius (mm)	0.4	0.8	1.2
C	Cutting Speed (m/min)	175	225	275
D	Feed rate (mm/rev.)	0.05	0.1	0.15
E	Depth of cut (mm)	0.1	0.2	0.3

#### Factorial Design

- Factors: 5
- Factor Levels: 3, 3, 3, 3, 3
- Runs: 243
- Replicates: 1
- General Linear Model: Ra versus A, B, C, D, E
- Factor                      Type                      Levels                      Values
- A (Rake angle)            fixed                      3                              1 2 3
- B (Nose Radius)           fixed                      3                              1 2 3
- C (Speed )                   fixed                      3                              1 2 3
- D (Feed )                    fixed                      3                              1 2 3
- E (Depth of Cut )        fixed                      3                              1 2 3

### IV. DATA ANALYSIS

The purpose of developing the mathematical model relating the machining responses and their machining factors was to facilitate the optimization of the machining process. Using the mathematical model, the objective function and process constraints were formulated, and the optimization problem was then solved by using regression analysis.

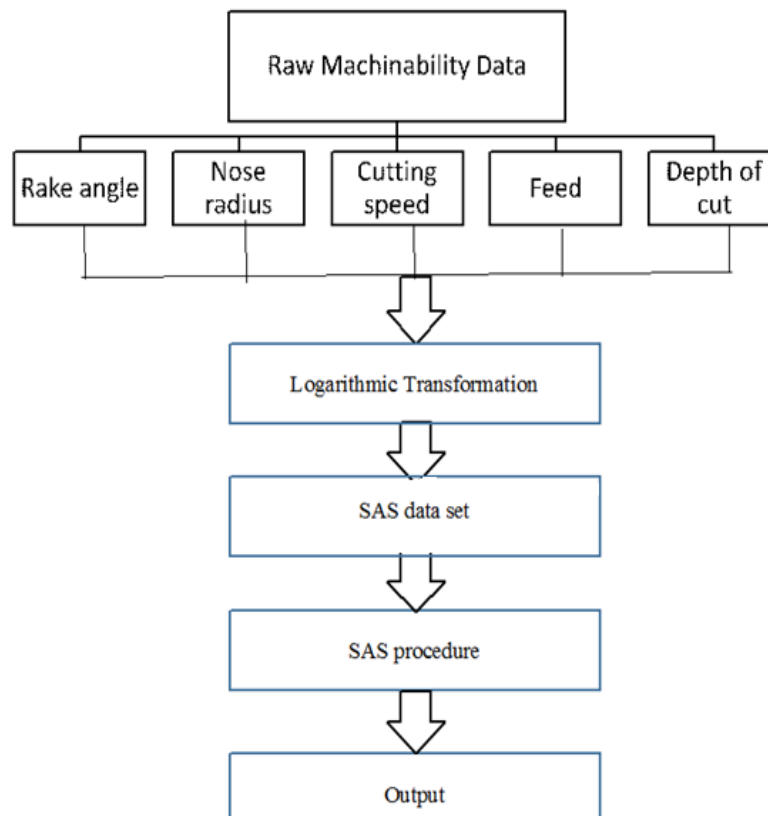


Figure 2: Program data vector for processing in regression analysis [Vipin and Kumar, 2009]

Regression Analysis has been made for Surface Roughness (Ra) versus Rake angle (Rk), Nose radius (Nr), Cutting Speed (V), Feed (f), and Depth of Cut (d). The regression equation obtained is

$$Ra = 478.63 Rk^{-0.653} Nr^{-0.271} V^{-0.539} f^{0.707} d^{0.184}$$

The R-square value of 0.908 indicated that 90.8% of the variability in the surface roughness was explained by the model with factors Rk, Nr, V, f and d. based on the mathematical model, it can be concluded that the feed is a dominant factor in the roughness model of finish turning of Al 6061. The developed regression model is reasonably accurate and can be used for prediction within limits.

Figure 3: (a) shows the main effect plots for Ra. Figure 3: (b) shows the Interaction plots for Ra. The interactions considered between the selected factors are:

Rake angle and Nose Radius (A & B)

Rake angle and Cutting speed (A&C)

Rake angle and Feed (A&D)

Rake angle and Depth of Cut (A&E)

Nose Radius and Cutting speed (B&C)

Nose Radius and Feed (B&D)

Nose Radius and Depth of Cut (B&E)

Cutting speed and Feed (C&D)

Cutting speed and Depth of Cut (C&E)

Feed and Depth of Cut (D&E)

Three-factor interactions ABC, ABD, ABE, ACD, ACE, BCD, BCE, CDE,

Four-factor interaction ABCD, ABCE, ACDE,

Five-factor interaction ABCDE

Main Effects Plot - Data Means for Ra

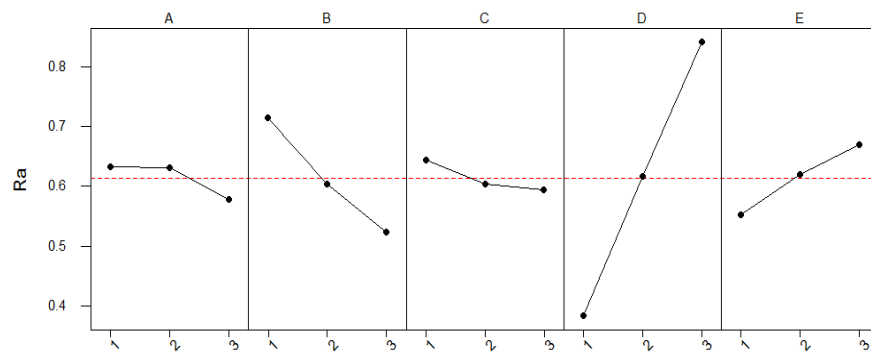


Figure 3: (a) main effect plots for Ra.

Interaction Plot - Data Means for Ra

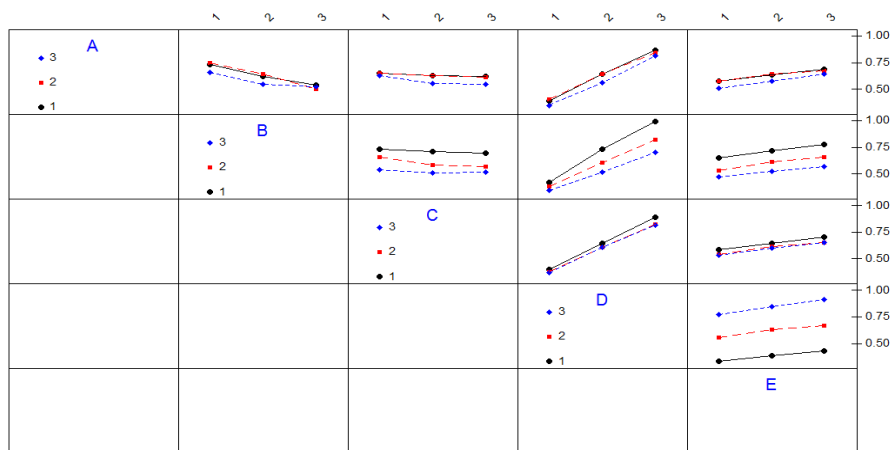


Figure 3: (b) Interaction plots for Ra.

### V. RESULTS AND DISCUSSIONS

In this section the effect of cutting speed, feed, depth of cut, nose radius and rake angle have been discussed through graphs in detail with varying the parameters. Nearly 226 graphs have been produced with different combinations. The following sample graphs have been shown with variations.

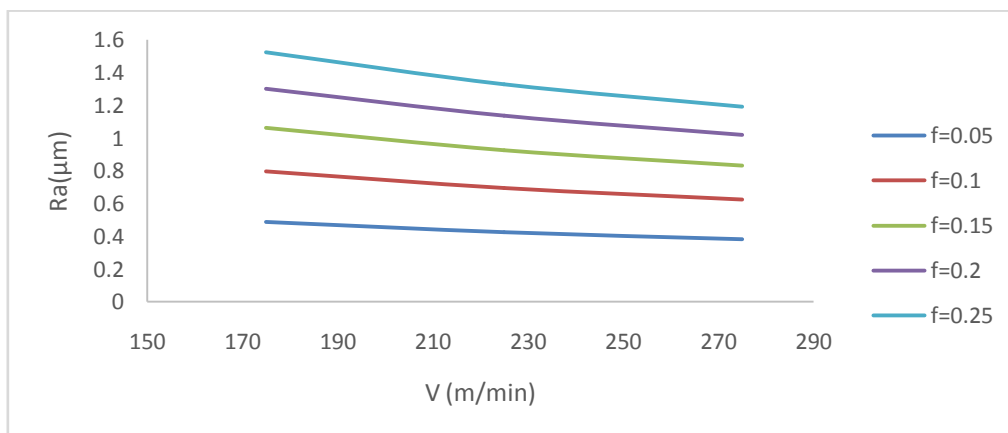


Figure 4: Graph between Surface Roughness and Cutting Speed for different feed values (mm/rev) at constant Rk=16 deg, Nr=0.4mm and d=0.1mm

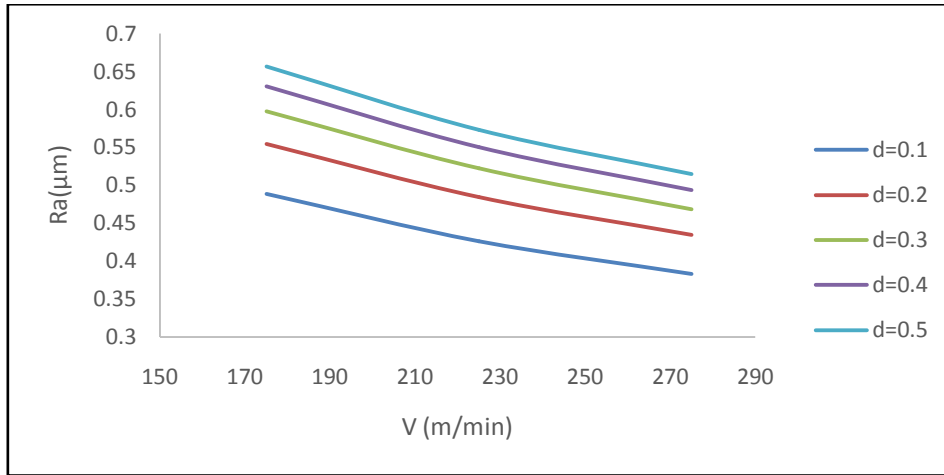


Figure 5: Graph between Surface Roughness and Cutting Speed for different depth of cut values (mm) at constant Rk=16 deg, Nr=0.4mm and f=0.05 mm/rev

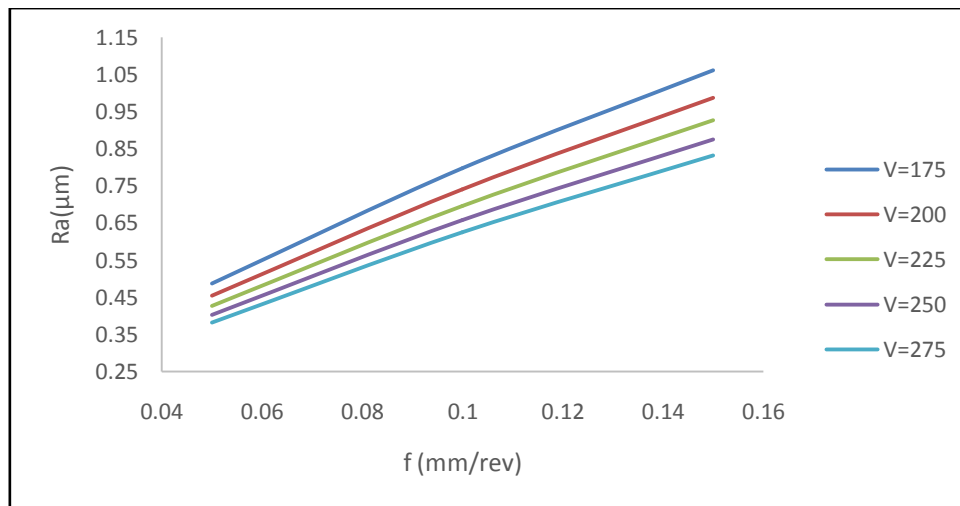


Figure 6: Graph between Surface Roughness and Feed for different cutting speed values (m/min) at constant Rk=16 deg, Nr=0.4mm and d=0.1mm

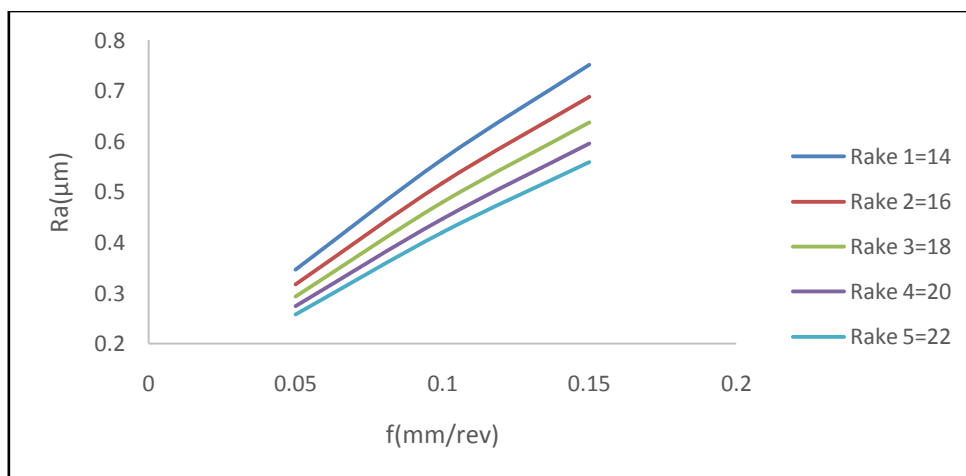


Figure 7: Graph between Surface Roughness and Feed for different rake angle values in (degrees) at constant Nr=1.2mm, V=225m/min and d=0.1

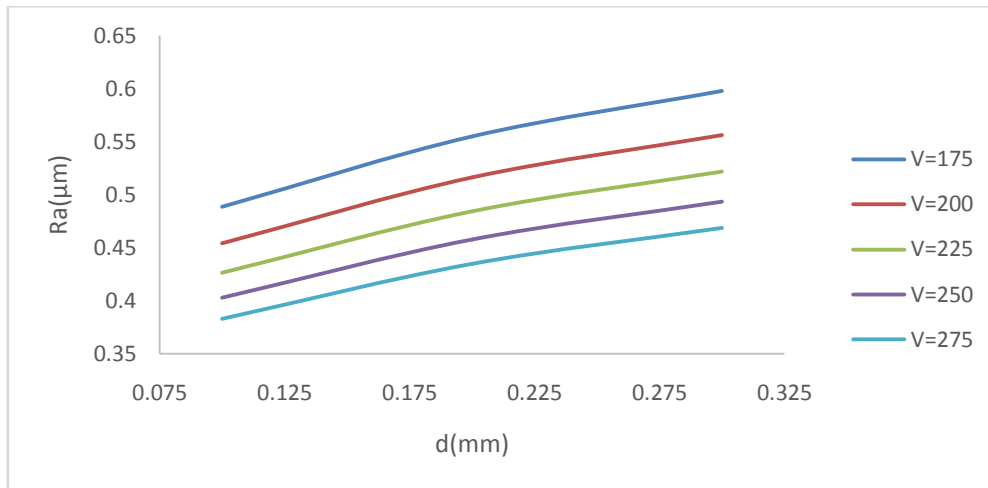


Figure 8: Graph between surface Roughness and Depth of Cut for different cutting speed values (m/min) at constant  $R_k=16$  deg,  $N_r=0.4$ mm and  $f=0.05$ mm/rev

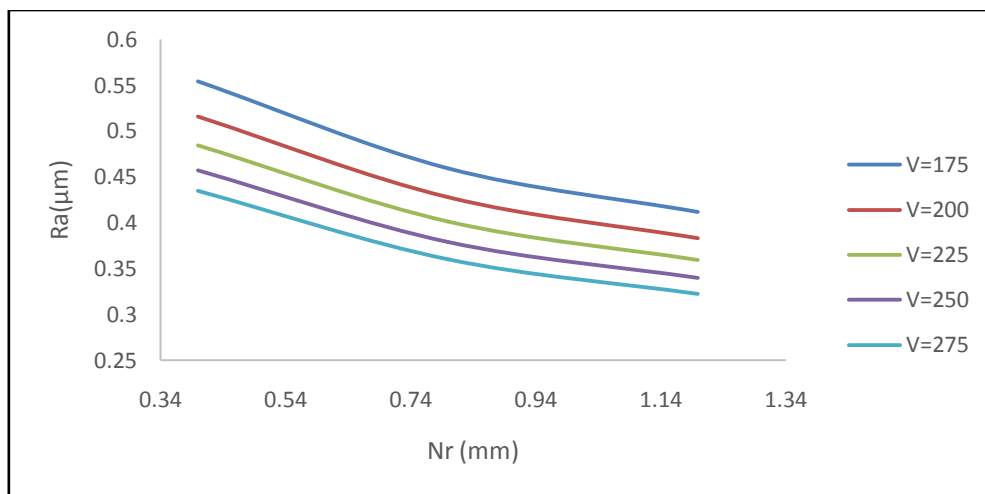


Figure 9: Graph between surface Roughness and Nose Radius for different cutting speed values (m/min) at constant  $R_k=16$  deg,  $f=0.05$ mm/rev and  $d=0.1$ mm

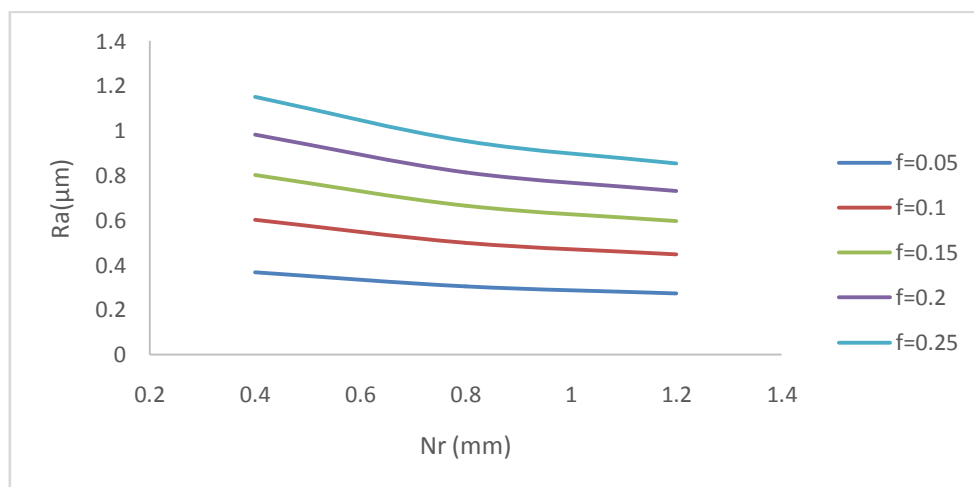


Figure 10: Graph between Surface Roughness and Nose Radius for different feed values (mm/rev) at constant  $R_k=20$  deg,  $V=225$ m/min and  $d=0.1$ mm

## **Results Obtained From Graphs**

### **1. Variation of Roughness values**

- As speed increases from 175m/min to 275 m/min the surface roughness values varies from 0.263 $\mu$ m to 1.865 $\mu$ m.
- As depth of cut increases from 0.1mm to 0.3mm the surface roughness values varies from 0.257 $\mu$ m to 1.865 $\mu$ m.
- As feed increases from 0.05mm/rev to 0.15 mm/rev the surface roughness values varies from 0.257 $\mu$ m to 1.427 $\mu$ m
- As nose radius increases from 0.4mm to 1.2mm the surface roughness values varies from 0.263 $\mu$ m to 1.865 $\mu$ m
- As rake angle increases from 16 degrees to 20 degrees the surface roughness values varies from 0.274 $\mu$ m to 1.427 $\mu$ m

### **2. Minimum and Maximum Ra values**

- The minimum Roughness value 0.257 is at Rk 22, Nr 1.2, V 225, f 0.05 and d 0.1
- The maximum Roughness value 1.865 is at Rk 16, Nr 0.4 V 175 f 0.25 and d 0.3

3. The optimal combination process parameters for minimum surface roughness is obtained at 20<sup>0</sup>, 0.4mm, 275 m/min, 0.05 mm/rev and 0.1mm.

## **VI. CONCLUSIONS**

The following conclusions have been made on the basis of results obtained and analysis performed:

- Increase in cutting speed improves the surface finish, thus the average surface roughness value decreases.
- Impact of Increase in depth of cut effects the surface finish adversely to a small extent, but as depth of cut increases beyond a certain limit surface finish deteriorates to a large extent.
- Small increase in feed rate deteriorates surface finish to a large extent as compared to same amount of increase of depth of cut.
- Surface roughness also decreases as the nose radius increases hence surface finish increases.
- Increase in back rake angle the surface roughness decreases and improves the surface finish.
- The ANOVA and F-test revealed that the feed is dominant parameter followed by depth of cut, speed, nose radius and rake angle for surface roughness.
- The optimal combination process parameters for the work piece under consideration with regards to minimum surface roughness or maximum surface finish is obtained at rake angle of 20<sup>0</sup>, nose radius 0.4mm, cutting speed 275 m/min, feed rate 0.05 mm/rev and depth of cut 0.1mm.

## **REFERENCES**

- [1] A.V.N.L.Sharma, K.Venkatasubbaiah, P.S.N.Raju, Parametric Analysis and Multi Objective Optimization of Cutting Parameters in Turning Operation of EN353 – With CVD Cutting Tool Using Taguchi Method International Journal of Engineering and Innovative Technology (IJEIT) Volume 2, Issue 9, March 2013, ISSN: 2277-3754
- [2] Adnan Jameel, Mohamad Minhat and Md. Nizam Using Genetic Algorithm to Optimize Machining Parameters in Turning Operation : A Review, International Journal of Scientific and Research Publications, Volume 3, Issue 5, May 2013 1, ISSN 2250-3153
- [3] D. Lazarević, M. Madić, P. Janković, A. Lazarević Cutting Parameters Optimization for Surface Roughness in Turning Operation of Polyethylene (PE) Using Taguchi Method Tribology in Industry Vol. 34, No 2 (2012) pp 68-73
- [4] G.M.Sayeed Ahmed, Hakeemuddin Ahmed , Syed Safiuddin Samad Experimental Investigation of Effect of Tool Length on Surface Roughness during Turning Operation and its Optimization , IOSR Journal of Mechanical and Civil Engineering (IOSR-JMCE) Volume 7, Issue 2 (2013), PP 73-80
- [5] Jitendra Verma, Pankaj Agrawal, Lokesh Bajpai Turning Parameter Optimization for Surface Roughness Of ASTM A242 Type-1 Alloys Steel By Taguchi Method International Journal of Advances in Engineering & Technology, March 2012. ISSN: 2231-1963
- [6] K.Manilavanya, R.K.Suresh, A.Sushil Kumar Priya, V.Diwakar Reddy, Optimization of Process Parameters in Turning Operation of AISI-1016 Alloy Steels with CBN Using Taguchi Method And Anova, IOSR Journal of Mechanical and Civil Engineering (IOSR-JMCE), Volume 7, Issue 2 (May. - Jun. 2013), PP 24-27, e-ISSN: 2278-1684, p-ISSN: 2320-334X
- [7] M. Aruna and V. Dhanalaksmi , Design Optimization of Cutting Parameters when Turning Inconel 718 with Cermet Inserts, World Academy of Science, Engineering and Technology 61 2012
- [8] M. Kaladhar, K. VenkataSubbaiah, Ch. Srinivasa Rao, Determination of Optimum Process Parameters during turning of AISI 304 Austenitic Stainless Steels using Taguchi method and ANOVA , International Journal of Lean Thinking Volume 3, Issue 1 (June 2012)

- [9] M. VenkataRamana, A. Venkata Vishnu, G. Krishna Mohan Rao and D. Hanumantha Rao Experimental Investigations, Optimization Of Process Parameters And Mathematical Modeling In Turning Of Titanium Alloy Under Different Lubricant Conditions IOSR Journal of Engineering (IOSRJEN), Vol. 2 Issue 1, Jan.2012, pp. 086-101
- [10] Mustafa Günay, EmreYücel, Application of Taguchi method for determining optimum surface roughness in turning of high-alloy white cast iron, Measurement 46 (2013) 913–919
- [11] Rahul Davis A Parameteric Design Study of Surface Roughness In Dry Turning Operation of EN24 Steel, International Journal of Mechanical Engineering and Technology (IJMET), ISSN 0976 – 6340(Print), ISSN 0976 – 6359(Online) Volume 3, Issue 2, May-August (2012),
- [12] Ranganath M S, and Vipin ,“Experimental Investigations on Surface Roughness for Turning of Aluminium (6061) Using Regression Analysis” Journal of Modeling and Simulation in Design and Manufacturing, Vol 3 No.1&2 (2013), pp 190-196
- [13] Ranganath M S, Vipin , and R S Mishra “Optimization Of Process Parameters In Turning Operation Of Aluminium (6061) With Cemented Carbide Inserts Using Taguchi Method And ANOVA” International Journal of Advance Research and Innovation Website: www.ijari.com ISSN 2347-3258, Volume 1(2013), 13-21
- [14] Ranganath M S, and Vipin , “Optimization Of Process Parameters In Turning Using Taguchi Method And ANOVA: A Review” International Journal of Advance Research and Innovation Website: www.ijari.com ISSN 2347-3258, Volume 1(2013), 31-45,2013
- [15] Ranganath M S, Vipin , and R S Mishra, “Neural Network Process Modelling for Turning of Aluminium (6061) using Cemented Carbide Inserts”, International Journal of Advance Research and Innovation, ISSN 2347 – 3258, Volume 3 (2013) 211-219
- [16] Ranganath M S, Vipin , and R S Mishra, “Application of ANN for Prediction of Surface Roughness in Turning Process: A Review”, International Journal of Advance Research and Innovation, ISSN 2347 – 3258, Volume 3 (2013) 229-233
- [17] Ranganath M S, Vipin , and R S Mishra, “Effect of Cutting Parameters on MRR and Surface Roughness in Turning of Aluminium (6061)”, International Journal of Advance Research and Innovation, ISSN 2347 – 3258, Volume 1 (2014) 32-39
- [18] Ranganath M S, Vipin , and R S Mishra, “Optimization of Surface Roughness and Material Removal Rate on Conventional Dry Turning of Aluminium (6061)”, International Journal of Advance Research and Innovation, ISSN 2347 – 3258, Volume 1 (2014) 62-71
- [19] Ranganath M S, and Vipin , “Measuring Effect of Machining Parameters on Surface Roughness with Turning Process- Literature Survey,” International Journal of Advance Research and Innovation Website: www.ijari.com ISSN 2347-3258, Volume 1 (2014) 313-318
- [20] Ranganath M S, and Vipin , “Effect of Rake Angle on Surface Roughness in CNC Turning,” International Journal of Advance Research and Innovation Website: www.ijari.com ISSN 2347-3258, Volume 2 (2014) 522-530
- [21] Ranganath M S, and Vipin , “Effect of Machining Parameters on Surface Roughness with Turning Process- Literature Review,” International Journal of Advance Research and Innovation Website: www.ijari.com ISSN 2347-3258, Volume 2 (2014) 531-536
- [22] Ranganath M S, Vipin, Nand Kumar and R. Srivastava “Surface Finish Monitoring in CNC Turning Using RSM and Taguchi Techniques” International Journal of Emerging Technology and Advanced Engineering Website: www.ijetae.com (ISSN 2250-2459, ISO 9001:2008 Certified Journal, Volume 4 (9), 2014, pp 171-179
- [23] Srinivasan, A., R.M. Arunachalam, S. Ramesh and J.S. Senthilkumaar, Machining Performance Study on Metal Matrix Composites-A Response Surface Methodology Approach, American Journal of Applied Sciences 9 (4): 478-483, 2012
- [24] T. Sreenivasa Murthy, R.K.Suresh, G. Krishnaiah, V. Diwakar Reddy, Optimization of process parameters in dry turning operation of EN 41B alloy steels with cermet tool based on the Taguchi method, International Journal of Engineering Research and Applications (IJERA), Vol. 3, Issue 2, March -April 2013, pp.1144-1148, ISSN: 2248-9622
- [25] V.R. Chaudhari, Prof. D. B. Gohil , Prediction of Surface Roughness Using Artificial Neural Network: a review, International Journal of Emerging trends in Engineering and Development, Issue 2, Vol.4(May-2012), ISSN 2249-6149
- [26] Vipin and Harish Kumar, “Surface Roughness Prediction Model By Design Of Experiments For Turning Leaded Gun Metal” International Journal Of Applied Engineering Research ISSN 0973-4562 Volume 4 Number12 (2009) Pp. 2621–2628
- [27] Wada Tadahiyo , HiroKazuki and Nakanishi Jun, Cutting Performance of Turning Insert with Three-arcs-shaped Finishing Edge, Applied Mechanics and Materials Vols. 110-116 (2012) pp 1630-1636
- [28] YansongGuoa, JefLoendersb, JoostDufloa, Bert Lauwersa, Optimization of energy consumption and surface quality in finish turning, Available online at www.sciencedirect.com, Procedia CIRP 1 (2012) pp 551–556

## Content Based Message Filtering For OSNS Using Machine Learning Classifier

Hajiali Mohammed<sup>1</sup>, T. Sukanya<sup>2</sup>

<sup>1</sup> M.Tech(CSE), MVR College of Engineering and Technology, A.P., India.

<sup>2</sup>Asst. Professor, Dept. of Computer Science & Engineering, MVR College of Engineering and Technology, A.P., India.

**Abstract:** Online social networking(OSNs) sites like Twitter, Orkut, YouTube, and Face book are among the most popular sites on the Internet. Users of these web sites forms a social network, which provides a powerful means of sharing, organizing, and finding useful information .Unlike web information , the Online social networks (OSN) are organized around more number of users joins the network, shares their information and create the links to communicate with other online users. The resulting social network sites provides a basis for maintaining social relationships, for finding users with similar interests, and for locating content and knowledge that has been contributed or endorsed by other users. In OSNs information filtering can be used for avoiding the unwanted messages sharing or commenting on the user Walls. In this paper, we have proposed a system to filter undesired messages from OSN walls. The system exploits a machine learning soft classifier to enforce customizable content-dependent FRs. Moreover, the flexibility of the proposed system in terms of filtering options is enhanced through the management of BLs.

**Keywords:** Black list, Classifier, Content filtering, GUI, OSN.

### I. INTRODUCTION

Information and communication technology plays a significant role in today's online networked society. It has affected the online interaction between various users, who are aware of security applications and their implications on personal privacy. Online Social networks(OSNs) provide platform to meet different users and share information with them. Communication on these web sites involves exchange of various content including text as well as multimedia content. A social network include private messaging, blogs, chat facility and file, photo sharing functions and other ways to share text and multimedia content. Users of these online networking web sites can express their feelings and can convey their idea in terms of wall messages too. A wall is a section in online site user profile where others can post messages or can attach an image to leave a gift to its wall owner. This OSN wall is a public writing space so others can view what has been written on wall. Therefore in online sites there is possibility of posting illegal or undesirable messages on wall which is visible to others too. There is a need to develop more security techniques for different communication technologies, particularly online social networks. Networking sites provide very little support to prevent unwanted messages on user walls. With the lack of classification or filtering tools, the user receives all messages posted by the users he or she follows. In most cases, the user receives a noisy stream of updates from other users. In this paper, a content based information filtering system is introduced. The system focuses on one kind of feeds-Lists which are a manually selected group of users on networking sites. List feeds tend to be focused on specific topics, however it is still noisy due to undesired messages. Therefore, we present an online filtering system, which extracts the such topics in a list, filtering out irrelevant messages[1].

In networking sites, information filtering can also be used for a different, more sensitive, purpose. This is due to the fact that in networking sites there is the possibility of posting or commenting other posts on particular public or private areas, called in general walls. In the proposed system Information filtering can therefore be used to give various users the ability to automatically control the messages written on their own walls, by filtering out undesired messages. The aim of the proposed work is therefore to propose and experimentally evaluate an automated system, called Filtered Wall (FW), able to filter undesired messages from OSN user walls. We exploit Machine Learning (ML) text categorization techniques [2] to automatically assign with each short text message a set of categories based on its information. The major efforts in developing a robust short text classifier are concentrated in the extraction and selection of a set of characterizing and discriminant features.

## **II. RELATED WORK**

In this section we are going to discuss the recent methods over the content-based filtering in Online Social Networking (OSN). In [3], the authors provide the user to have a straight rule over their own private wall to avoid the unwanted messages.

The main aim of this work is users have a straight control over various messages posted on their own private space. So we are using the automated system called Filtered wall (FW), which have the capacity to filter unwanted messages. This system will blocks only the undesired messages send by the user. Drawback of this paper is user will not be blocked; This means only the content posted by the user will block. content based message filtering and short text classification support by this system.

In [4], the authors use mutual filtering method, but in our proposed system content based filtering is used. It explains the content based proposal system that develops the information pulling out and machine learning technique for text categorization. In [5], the authors provide the system can generally take decision about the message which is blocked due to the acceptance depends up on statistical information. In [6], the authors provides classification of text put in complex and specific terminology; need the application of the learning process. Fractional Matching method is applied which shrink the text message for confining the text characteristic. Fractional matching develops a language model. The output of the fractional matching compression provides consistent care of text classification

In [7], the authors introduce a social network is the common concentration group in network. Two level approaches are stated to combine trust, gloss and origin. The authors state an algorithm for concluding trust relationship with origin content and trust gloss in web social network. Film trust application is introduced which uses trust to video ranking and ordering the review. We consider film trust give the good crop model. In [8], the authors provide the clustering of document is helpful in many field. Two categories of clustering general purpose and text tilting, these both will be used for clustering process of information. Novel heuristic online document clustering is predictable, which is the proficient in clustering of text tilting parallel measures. Presentation measure is done in F-measure, and then it will be counterpart up with the other methods.

## **III. PROPOSED WORK**

### **1. Filtered Wall Architecture**

The architecture of networking site services is a three-tier structure of three layers (Figure 1). These three layers are:

- Social Network Manager (SNM)
- Social Network Application (SNA)
- Graphical User Interface (GUI)

The starting stage is the Social Network Manager Layer provides the essential OSN functionalities (i.e., profile and relationship administration). This layer also maintains all the data regarding to the user profile. After maintaining and administrating all users information will provide for second stage for applying Filtering Rules (FR) and Black lists (BL). In second stage, the Content Based Message Filtering (CMBF) and Short Text Classifier is composed. This is very important stage for the message categorization according to its CMBF filters. Also a Black list (BL) is maintained for the user who sends frequently bad words in message.

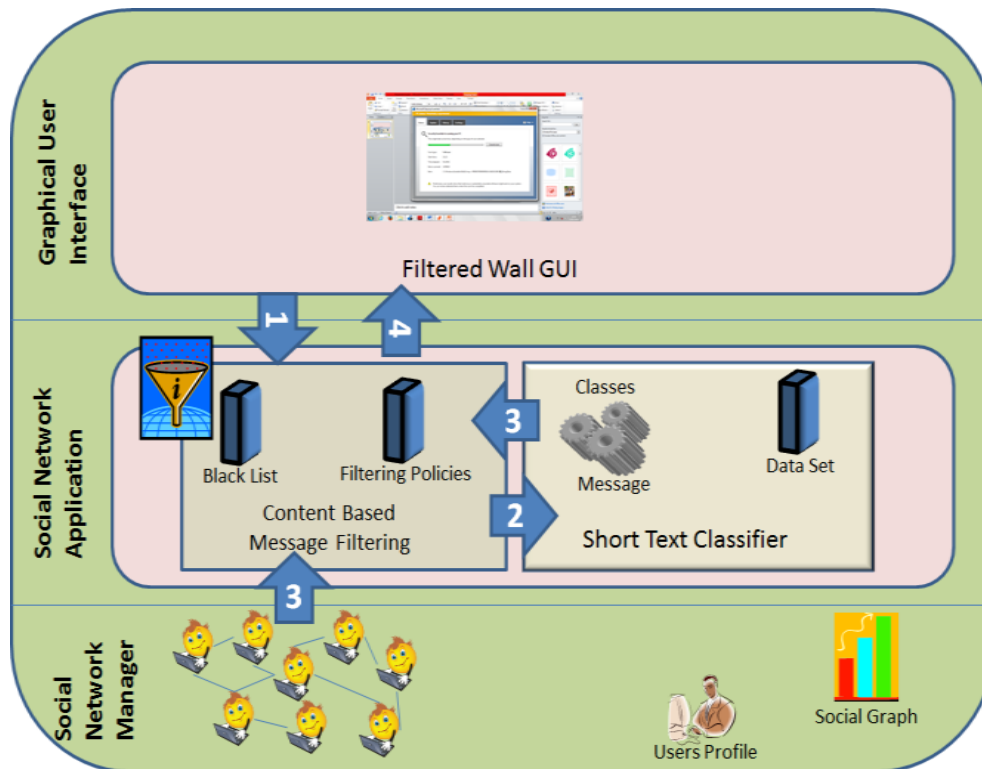


Fig. 1: Architecture of Filtered Wall

The third stage provides Graphical User Interface(GUI) to the user who wants to post his or her messages as a input. In this stage the Filtering Rules (FR) are used to filter the unwanted messages and provide Black list (BL) for the user who are temporally prevented to publish messages on user’s wall. In general, the architecture in support of networking site services is a three-tier configuration. According to this orientation layered structural plan, the proposed system has to be positioned in the second and third layers (Figure 1), as it can be considered as a SNA. Particularly, the users cooperate with the system by means of a GUI setting up their filtering laws, along with which messages have to be filtered out. In addition, the GUI offers users with a FW that is a wall where only legal messages that are authorized according to their filtering rules are published. The core components of the proposed system are the short Text Classifier elements and Content-Based Messages Filtering (CBMF). The latter element aims to categorize the messages according to a set of categories. In compare, the first element exploits the message categorization offered by the STC module to implement the FRs specified by the wall user. As graphically illustrated in Figure 1, the path pursued by a message, it can be summarized as follows:

- After entering the private wall of one of his/her neighbors, the user attempts to post a message, which is captured by FW.
- A ML-based text classifier extracts the metadata from the content of the posted message.
- FW uses metadata provided by the classifier, mutually with data extorted from the social graph and the users’ profiles, to implement the filtering and black list rules.
- Depending on the result of the previous step, the message posted will be available or filtered by FW.

## 2. Short Text Classifier

In short text classifier, it consider three types of features, Document properties (Dp), Bag of words(BoW), and Contextual Features (CF).The first two types of features; they are entirely derived from the data contained within the text of the message. We introduce contextual features modeling information that characterizes the environment where the user is posting. These features play an important role in the semantics of the messages. Text representation is the Vector Space Model (VSM) according to which a text document dj is represented as the vector of binary or real weights:

$$d_j = w_{1j}, \dots, w_{|T|j}$$

where  $T$  is the set of features that occur at least once in at least one text document of the collection  $T_r$  and  $w_{kj}$   $[0, 1]$  represents how much term  $t_k$  contributes to the semantics of the document  $d_j$ . In the bag of words representation, terms are identified with words. In the case of the non binary weighting, the weight  $w_{kj}$  of term  $t_k$  in document  $d_j$  is computed according to the standard term frequency—inverse document frequency (tf-idf) weighting function is defined as follows:

$$f - idf(t_k, d_j) = \#(t_k, d_j) \cdot \log \frac{|T_r|}{\#T_r(t_k)}$$

where  $\#(t_k, d_j)$  denotes the number of times  $t_k$  occurs in document  $d_j$  and  $\#T_r(t_k)$  denotes the document frequency of the term  $t_k$ , i.e., the number of documents in  $T_r$  in which  $t_k$  occurs. Contextual features is not very dissimilar from BoW features describing the nature of data. Therefore, all the formal definitions introduced for the bag of words features also apply to Cfs.

### 3. Filtering Rules

To define the language for filtering rule specification, many issues are considered. First issue may be the text message with different meaning and significance based on who writes it. As a result, filtering rules should allow the user to restrict the message creators. Here the type, depth, and the trust value are recognized by creator Specification.

#### Definition 1: Creator specification

A Creator Specification *CreaSpec*, which denotes a set of networking site users. Possible combinations are one. Set of attributes in the An OP Av form, where An is the user profile attribute name, Av is the profile attribute value and OP is a comparison. Set of relationship of the form (n, Rt, minDepth, maxTrust) indicate site users participating with user n in a relationship of type Rt, depth greater than or equal to minDepth, trust value greater than or equal to maxTrust.

#### Definition 2: Filtering rule

A filtering rule is a tuple ( auth,CreaSpec,ConSpec,action) Auth is the user who states the filtering rule. CreaSpec is the Creator specification(see definition 1). ConSpec is the Boolean expression. Action is the action performed by the system.

Filtering rules will be applied, when the site user profile does not hold value for attributes submitted by a FR. This type of situation will dealt with asking the owner to choose whether to notify or block the messages initiating from the profile which does not match with the wall owners filtering rules, due to missing of attributes.

### 4. Blacklist Management

The main implementation of this paper is to execute the Blacklist Mechanism, which will keep away messages from unwanted creators. Black list are handled undeviating by the system. This will able to decide the users to be inserted in the BL. And it also decides the user preservation in the list will get over. Set of rules are applied to improve the stiffness, such rules are called black list rules. By applying the list rule, the owner can identify which user should be blocked based on the relationship in OSN and the user's profile. The user may have bad opinion about the other users can be banned for an uncertain time period. We have the information based on bad attitude of the user. Two principles are stated as follows First one is within a given time period user will be inserted in black list for numerous times, he /she must be worthy for staying in black list for another sometime. This principle will be applied to user who inserted in black list at least once. Relative Frequency is used to find out that the system, who messages continue to fail the filtering rules. Two measures can be calculated globally and locally, which will consider only the message in local and in global it will consider all the networking site users walls.

A BL rule is a tuple (auth,CreaSpec,CreaB,t),where Auth is a user who state the black list rule. CreaSpec is the creator specification. CreaB have two components ,RF Blocked and minBanned-RFBlocked(RF,mode>window) such that  $RF = \frac{\#bMessages}{\#tMessages}$  Where  $\#tMessage$  is the total number of messages that site User recognized using CreaSpec, whereas  $\#bMessage$  is the number of message in

\*tMessage that have been blocked. A window represents the time interval of the message creation. minBanned= (min,mode>window) min is the minimum number of times in the time interval enumerate in window that site user recognized using CreaSpec .mode indicates all site user. T signify the time period the user recognized by CreaSpec and CreaB which will be banned from authentication wall.

#### **IV. CONCLUSION**

In this paper, we present a system to filter unwanted message in online networking sites wall. The first step of the proposed system is to classify the content using several rules. Next step is to filter the unwanted rules. Finally a Blacklist rule is also implemented. So that owner of the user can insert the user who posts unwanted messages. Better privacy is given to the networking site wall using our proposed system. In future Work, we plan to implement the filtering rules with the aim of bypassing the whole filtering system, so that it can be used only for the purpose of overcome the filtering system.

#### **REFERENCES**

- [1] Measuring semantic similarity between words using web search engines. In WWW '07: Proceedings of the 16th international conference on World Wide Web, pages 757-766, New York, NY, USA, 2007. ACM.
- [2] F. Sebastiani, "Machine learning in automated text categorization," ACM Computing Surveys, vol.34, no. 1, pp. 1–47, 2002.
- [3] Marco Vanetti, Elisabetta Binaghi, Elena Ferrari, Barbara Carminati, an Moreno Carullo, " A System to Filter Unwanted Messages from OSN User Walls",2013.
- [4] R.J.Mooney and L.Roy, "Content-Based Book Recommending Using Learning for Text Categorization", 2000.
- [5] M.Vanetti, E.Binaghi, B.Carminati, M.Carullo, and E.Ferrari, "Content- Based Filtering in On-Line Social Networks", 2010.
- [6] V.Bobicev and M.Sokolova, "An Effective and Robust Method for Short Text Classification," Proc.23rd Nat'l Conf. Artificial Intelligence (AAAI), D.Fox and C.P.Gomes, eds., pp.1444-1445,2008.
- [7] J.Colbeck, "Combining Provenance with Trust in Social Networks for Semantic Web Content Filtering," Proc. Int'l conf. Provenance and Annotation of Data, L.Moreau and IFoster, eds., pp.101-108, 2006.
- [8] M.Carullo, E.Binaghi, and I. Gallo, "An Online Document Clustering Technique for short Web contents," Pattern Recognition Letters,vol.30, pp.870-876, July 2009.

## Harmonic Analysis of 6-Pulse and 12-Pulse Converter Models

Venkatesh P<sup>1</sup>, Dr. M. N. Dinesh<sup>2</sup>

<sup>1</sup>M-Tech, Power Electronics, Department of Electrical and Electronics Engineering. R.V.C.E. Bangalore

<sup>2</sup>Associate Professor, Department of Electrical and Electronics Engineering. R.V.C.E. Bangalore

**Abstract:** This paper discusses the impact of using 6-pulse and 12-pulse rectifier circuit commonly found in HVDC systems. The 12-pulse rectifier circuit is known to be more expensive, but produces the reduced input current harmonics and output voltage ripples. The Multi-pulse configuration consists of several six-pulse converter units in either series or parallel on the DC side. These units are phase-shifted with respect to each other by the transformer connection. This paper presents the modeling and simulation of both 6-pulse and 12-pulse rectifier topologies to compare their input current harmonics, output voltage ripples and also total Harmonic Distortion (THD) as well. The input current waveform, voltage waveform and THD have been observed. The rectifiers are modeled and simulated using MATLAB software to compare their harmonic levels.

### I. Introduction

The transmission and distribution of electrical energy Started with direct current (DC) in late 19<sup>th</sup> century, but it was inefficient due to the power loss in conductors. Alternating current (AC) offered much better efficiency, since it could easily be transformed to higher voltages, with far less loss of power. AC technology was soon accepted as the only feasible technology for generation, transmission and distribution of electrical energy [3].

Diode rectifier used passive component and switching devices for reduce harmonic problem, but they are create more complicated system include in high power grid application. The 6-pulse rectifier is involving most AC drive because of its low cost and simplest structure. The input current THD can exceed 100% with no harmonics filter with 5th, 7th and 11th harmonics at full load condition. Harmonics filter with 5th, 7<sup>th</sup> and 11th harmonics being dominant harmonics component. A 12-pulse rectifier involves two sets of 6-pulse rectifier is very popular for different types high power grid application. The multi-phase transformer can be an autotransformer or an isolated transformer with some phase displacement to provide two three-phase voltage sources that cancel the 5th and 7th harmonics. 12-pulse rectifier with a wye-wye, wye--delta isolation transformer and the resulting input current waveform where 11th and 13th harmonics are the dominant harmonic components [5].

As technology grows every day, the study of power systems has shifted its direction to power electronics to produce the most efficient energy conversion. Power electronics plays a vital role in processing and controlling the flow of electric energy by supplying voltages and currents in a form that is suited for user loads. The goals of using power electronics are to obtain the benefit of lower cost, small power loss and high efficiency. Because of high energy efficiency, the removal of heat generated due to dissipated energy is lower. Other advantages of power electronics are reduction in size, weight, and overall cost [4].

### II. 6--Pulse And 12-Pulse Rectifier Models

The basic configuration for HVDC uses a three phase bridge rectifier or six pulse bridges, containing six electronic switches, each connecting to one of the three phases power supply. A complete switching element is usually referred to as a valve, irrespective of its construction. The simulated diagram of six Pulse Bridge is shown in figure.1. Normally, two diodes in the bridge are conducting at any time, one on the top row (D1, D3 and D5) and another from bottom row (D2, D4 and D6). The two conducting valves connecting to two of three AC phase voltages, in series to the DC terminals. Thus the DC output voltage at any given instant is given by the series combination of two AC phase voltages. For example, if valves D1 and D2 are conducting, then the DC output voltage is given by the voltage of phase 1 minus the voltage of phase 3.

In fact, with a line commutated converter, the firing angle represents the only way of controlling the converter output voltage. Firing angle control is used to regulate the DC voltages of both ends of the HVDC system continuously in order to obtain the desired level of power transfer.

For high power applications such as high voltage DC transmission and DC motor drives, a 12 pulse output is generally required to reduce the output ripples and to increase the ripple frequencies. A three phase bridge gives a six pulse output voltages. An enhancement of the six pulse bridge arrangement uses 12 valves in a twelve pulse bridge. A twelve pulse bridge is effectively two six pulse bridges connected in series on the DC side and arranged with a phase displacement between their respective AC supplies so that some of the harmonics voltages and currents are get cancelled.

The phase displacement between the two AC supplies is usually  $30^\circ$  and is realized by using converter transformer with two different secondary windings. Usually one of the valve winding is star (wye) connected and the other is delta connected.

MATLAB software, particularly Simulink, MATLAB's graphical interface is a Environment for designing and modeling systems, was used to model various aspects of the proposed power generation and transmission system. MATLAB version 2013, release 07.02.2013, equipped with the SimPowerSystems block set, was the software used.

### 3-Phase diode rectifier using 6-diodes

The MATLAB Sim Power Systems software is a subsystem contains numerous demonstration models, including a model of a 3-phase diode rectifier. This model was the inspiration for our simplified models of 3-phase 6-pulse and 12-pulse converters.

Figure1 shows 6-pulse diode bridge rectifier. The three single-phase AC voltage sources, each 120 degrees out of phase with the other, each being rectified through a diode, RL load was used.

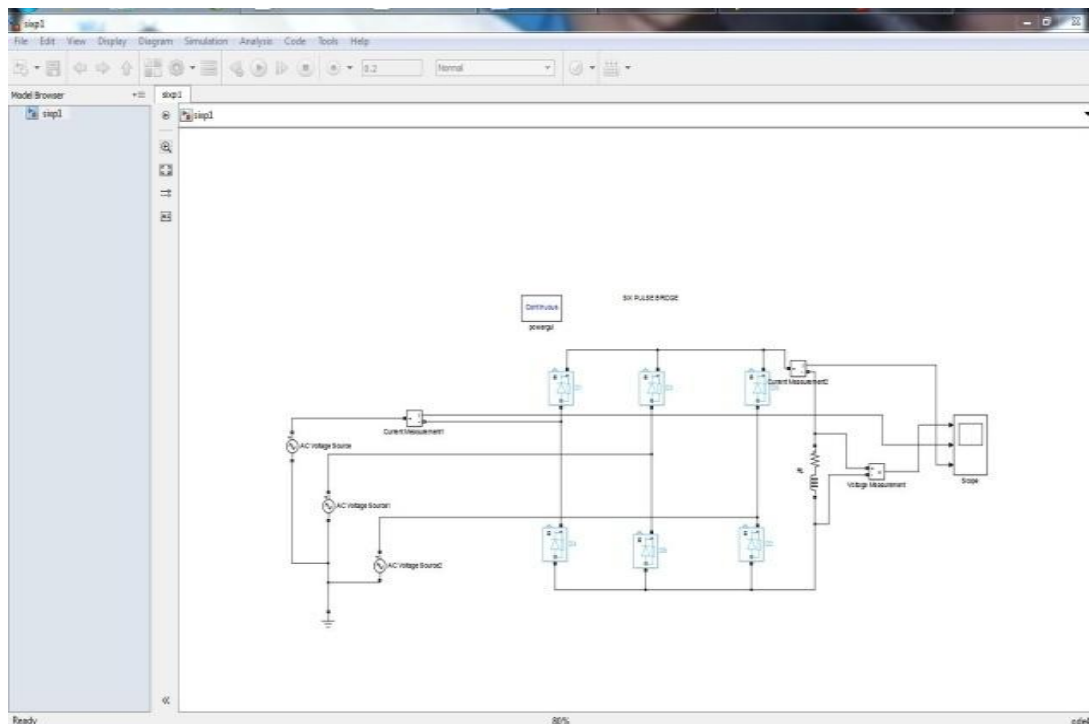


Figure: 1:3-phase diode rectifier using 6-diodes

### 3-Phase diode rectifier using 12-diodes

The MATLAB 3-phase diode rectifier demonstration model, described above, features three single-phase AC voltage sources, each 120 degrees out of phase with the other, each being rectified through a diode and RL load was used.

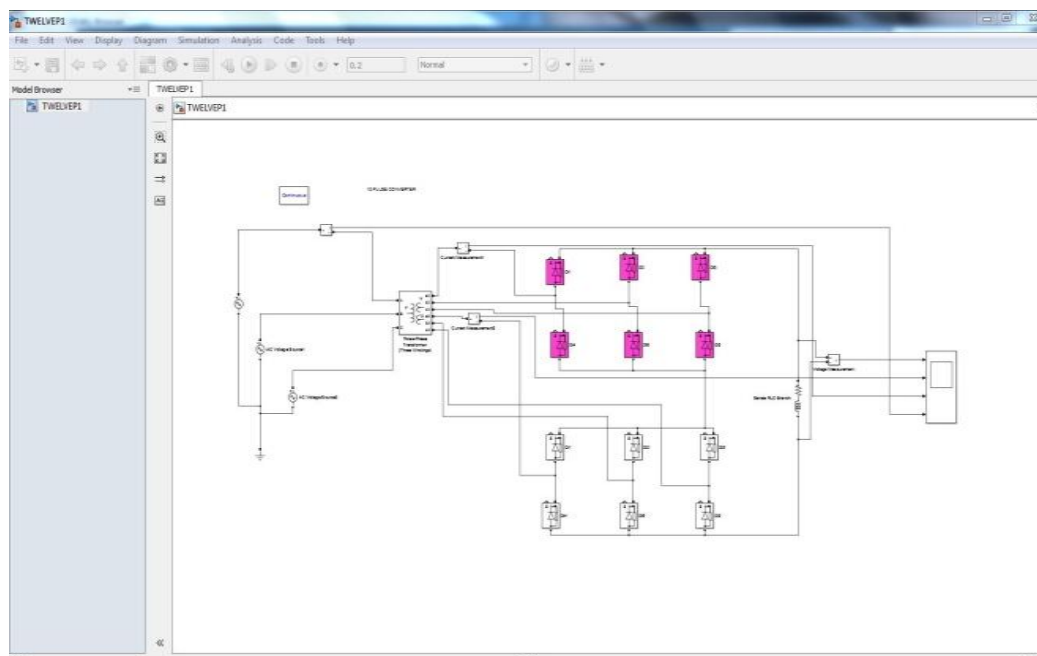


Figure: 2: 3-Phase diode rectifier using 12 diodes.

### 12-pulse converter rectifier, using 12-thyristors

Diodes cannot be used in HVDC converters because the timing of current flow must be precisely controlled, and diodes do not allow this sort of control. 3-Phase diode models using 6-diodes and 12-diodes rectifier models and also 12-pulse rectifier using thyristors model were simulated. Stability is the major problem in diode models, Hence output voltage can be varied in 12-pulse converter using thyristors.

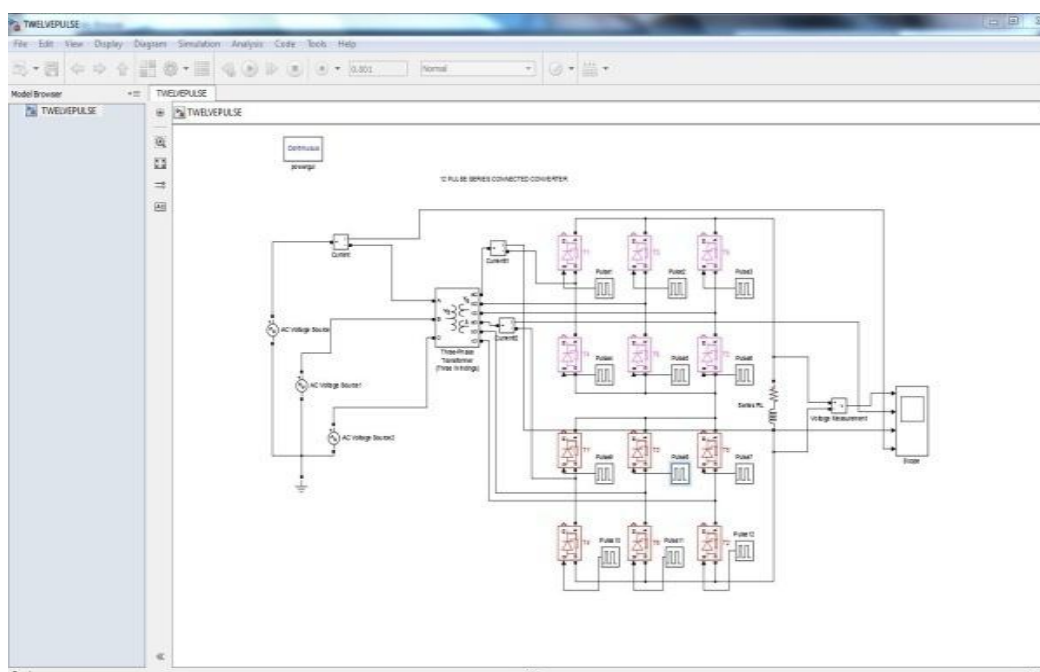


Figure: 3: 12 pulse converter using 12-thyristors.

### III. Simulated Results

Both 6-pulse and 12-pulse rectifier models were simulated. With increasing pulses in the converter, the input side the Total Harmonic Distortion (THD) is reduces and efficiency of the system is increased. For RL type load with  $R= 10 \text{ ohm}$ , and  $L=650\mu\text{H}$ . The results obtained are as follows:

Results obtained for six pulse converter showing output voltage ( $V_d$ ), input current (I), and output current ( $I_d$ ) in figure 4.

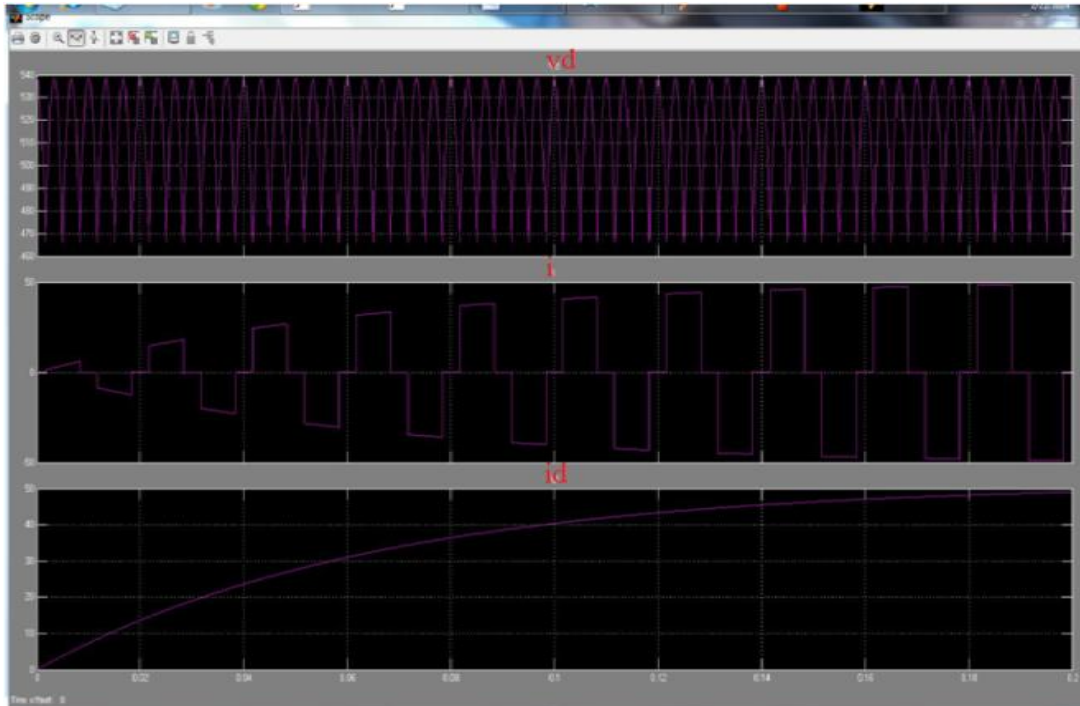


Figure: 4: waveforms of 3-phase diode rectifier using 6-diodes

Results obtained for twelve (12) pulse converter using diodes. Showing output voltage ( $V_d$ ), secondary currents ( $i_1$ ) and ( $i_2$ ), and input current (I) in figure 5.



Figure: 5: waveforms of twelve pulse converter using diodes.

Results obtained for twelve (12) pulse converter using thyristors. Showing output voltage ( $V_d$ ), secondary currents ( $i_1$ ) and ( $i_2$ ) and input current (I) in Figure 6.

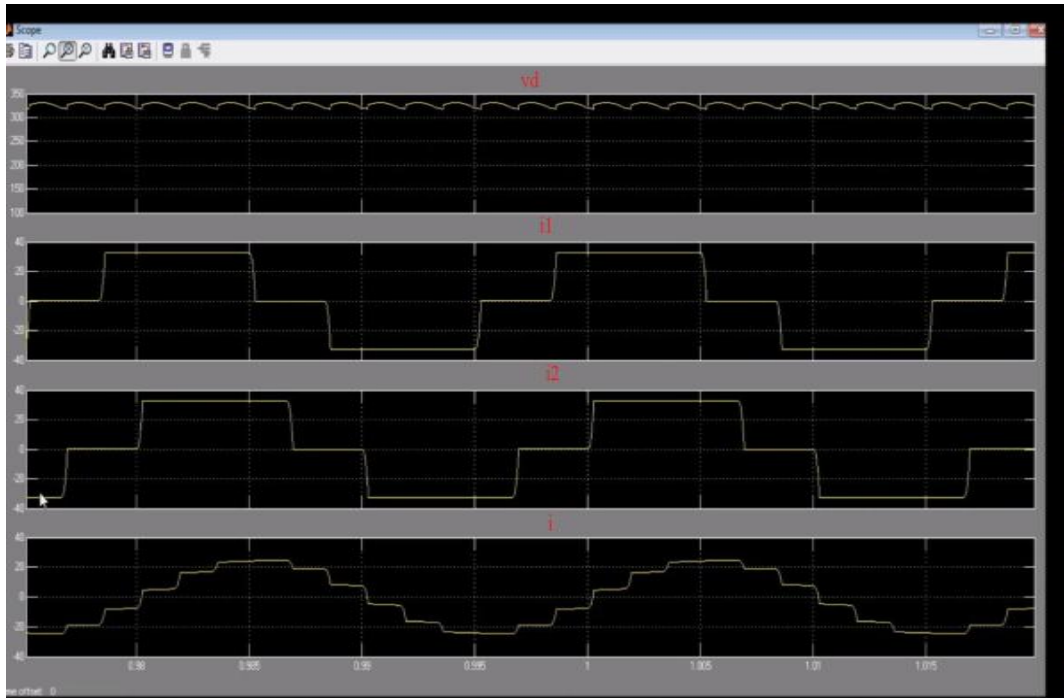


Figure: 6: waveforms of twelve pulse converter using thyristors.

Fast Fourier Transform (FFT) analysis was carried out on both 6-pulse and 12-pulse converters. The analysis shows 11<sup>th</sup> and 13<sup>th</sup> harmonics in 12 pulse converter with 12% of THD.

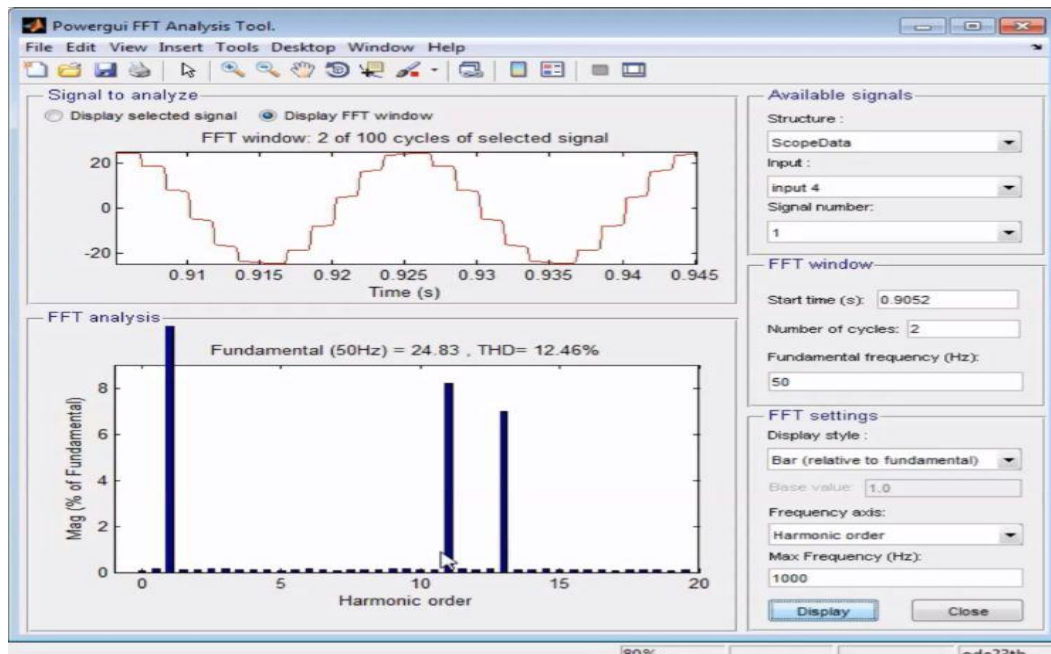


Figure: 7: FFT analysis.

With increasing the pulses in the converter, the input side the Total Harmonic Distortion (THD) has reduces and efficiency of the system is increased. For RL type load with  $R= 10$  ohm,  $L = 650\mu\text{H}$  and the results obtained are as follows:

THD in 6 pulse converter = 36.95 %

THD in 12 pulse converter = 12.48 %

It is observed that the total harmonic distortion (THD) decreases as the number of converter pulses increases and it is within limits as per IEEE standards.

#### **IV. Conclusion**

In the 12-Pulse converter configurations, the output voltage ripple as well as the input phase current harmonic content was much lower as compared to the 6-Pulse converter configurations. As the number of pulses increases, the quality of DC so obtained becomes better as well as the harmonic content in the AC input current is further reduced. Other multi-pulse converter configurations with pulse numbers much higher than 12 and with different configurations, like 18-Pulse, 24- Pulse, 36-Pulse, 48-Pulse configurations, which give much better performance than the 12-Pulse converter. But due to increased circuit complexity and higher number of components involved, their analysis becomes tedious and complex.

#### **REFERENCES**

- [1] Edward Wilson Kim bark, "Direct Current Transmission", Volume 1, Wiley Interscience.
- [2] K.R.Padiyar, "HVDC Power Transmission Systems", New Age, Second Edition.
- [3] N.M. Tabatabaei, M.abedi, N.S.Boushehri and A.jafari, "Mutipulse AC-DC Converters for Harmonics Reduction", International Journal on Technical and physical problems of Engineering, vol.6, no.1, pp. 210-219, Jan.2014.
- [4] Supeed Pyakuryal and Mohammad Matin, "Feedback Controlled for a 3-Phase 6-pulse Rectifier", The International Journal of Engineering and Science, vol.2, no. 8, pp. 23-27, Aug. 2013.
- [5] Madhuri Saxena, Sanjeev Gupta, "Simulation of Mutipulse converter for Harmonic Reduction using controlled rectifier", International Journal of Science and Research (IJSR), India online ISSN: 2319-7064, vol.02, no.04, pp.197-200, 2013.
- [6] Jaime Peralta, Hani Saad, Sebastian Denneteirer, Jean Mahseredjian, and Samuel Nguefeu, "Detailed and Averaged Models for a 401-Level MMC–HVDC System", IEEE transactions on power delivery, vol.27, no.3, pp.1501-1508 July 2012.
- [7] Yong Li, Zhiwen Zhang, Christian Rehtanz, Longfu Luo, Sven Ruberg, and Fusheng Liu, "Study on Steady- and Transient-State Characteristics of a New HVDC Transmission System Based on an Inductive Filtering Method", IEEE Transactions on power electronics, vol.26, no.7, pp.1976-1986 July 2011.
- [8] Hink, Karl M., "Harmonic Mitigation of 12-Pulse Drives with Unbalanced Input Line Voltages", MTE Corporation.
- [9] Tirtharaj Sen, Pijush Kanti Bhattacharjee and Manjima Bhattacharya, "Design and Implementation of Firing Circuit for Single Phase Converter", International Journal of Computer and Electrical Engineering, vol.3, no 3, pp.368-374 June 2011.
- [10] Hui Ding, Yi Zhang, Aniruddha M. Gole, Dennis A. Woodford, Min Xiao Han, and Xiang Ning Xiao, "Analysis of Coupling Effects on Overhead VSC-HVDC Transmission Lines From AC Lines With Shared Right of Way", IEEE Transactions on power delivery, vol.25, no. 4, pp.2976-2986 October 2010.

## A Distributed Approach for Neighbor Position Verification in MANETs

Mahendranath Chowdry Kundla<sup>1</sup>, Kancharla Kalpana<sup>2</sup>

<sup>1</sup> M. Tech (CSE), MVR College of Engineering and Technology, A.P., India.

<sup>2</sup>Asst. Professor, Dept. of Computer Science & Engineering, MVR College of Engineering and Technology, A.P., India.

**Abstract:** Mobile Ad Hoc Network(MANET) is a kind of wireless network where you can find number of base stations which supports the communication of mobile nodes. The mobile node supports the routing process of the communication to improve the throughput of the overall network. The mobile nodes are moving at some speed and towards the direction, which makes the topology of the wireless network gets changing at every fraction of time. Due to this reason there will be number of nodes comes into the coverage area of a base station and leaves, which cannot be trusted for service handling. What the adversary does here is that it replies with the route discovery phase using fake location information with the intension to get participate in the routing process. After gets selected it simply discard the packets received, or manipulate the packets, or else it will never receive the packets because of the false location. This makes the transmission as a failure one and service throughput degrades automatically. Location Based Services are one, which is provided and accessed based on the location content. In a road traffic network the location based service can be accessed in various ways. The routing in the road network becomes more complicated due to the increase in mobile nodes. A mobile node can access a service to know about the traffic and the route to reach a destination by accessing the location based service. The correctness of the node locations is therefore an all important issue in mobile networks, and it becomes particularly challenging in the presence of adversaries aiming at harming the system. This paper presents a protocol for updating the position of the node in dynamic mobile ad hoc networks. The protocol adapts quickly to position changes when node movement is frequent, yet requires little or no overhead during the periods in which hosts move less frequently.

**Keywords:** CST, DST, MANET, Neighbor discovery, NPV.

### I. INTRODUCTION

Mobile adhoc networks (MANET) [1] is a popular technology the world society speaks about due to the technology development. The modern world uses internet technology for everything as a part of their life, and now a day they use mobile technology in place of information technology to get access to the location based service. The kind of sophisticated service increases with the risk rate in accessing the service. The service providers have more challenges in providing the services and maintaining the quality of service parameters. A mobile network is an autonomous collection of mobile users that communicate over relatively bandwidth constrained wireless links. Since the nodes are mobile, the wireless network topology may change rapidly and unpredictably over time. The MANET network is decentralized; where all network activity including discovering the topology and delivering messages must be executed by the nodes themselves. The verification of the node locations is an important issue in mobile networks, and it becomes particularly challenging in the presence of adversaries aiming at harming the system. In order to find out the neighbor nodes and verify them various techniques are proposed.

Neighbour discovery deals with the identification of neighboring nodes with which a communication link can be established or that are within a given distance. An adversarial node could be securely discovered as neighbour node and be indeed a neighbour (within some range), but it could still cheat about its position within the same range. In other words, secure neighbor discovery lets a node assess whether another node is an actual neighbour but it does not verify the location it claims to be at .this is most often employed to counter wormhole attacks. Figure1 shows an example of topological information stored by verifier S at the end of the message exchange and effect of a fake position announcement by M.

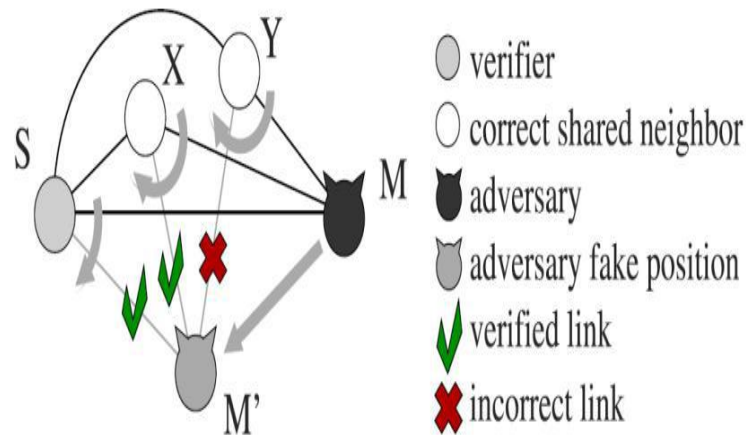


Fig.1: Neighbor discovery in adversarial environment

Neighbor verification [2] schemes often rely on fixed or mobile trustworthy nodes, which are assumed to be always available for the verification of the neighbor positions announced by third parties. In mobile ad hoc environments, however, the pervasive presence of either infrastructure or neighbour nodes that can be aprioristically trusted is quite unrealistic. Thus, a protocol is devised that is autonomous and does not require the trustworthy neighbours. A mobile ad hoc network is the collection of wireless mobile hosts forming a temporary network without the aid of any established infrastructure or centralized administration. In such an environment, it is necessary for one mobile node to enlist the aid of other hosts in forwarding a packet to its destination, due to the limited range of each mobile node's wireless transmissions. In order to procure the position of other nodes while moving, an approach is proposed such a way that it helps in obtaining the position of a dynamic mobile node. This paper presents a protocol for updating the position of the node in dynamic mobile ad hoc networks. The protocol adapts quickly to position changes when node movement is frequent, yet requires little or no overhead during the periods in which hosts move less frequently.

## II. RELATED WORK

In [3], the authors propose an Adaptive Hello Messaging Scheme for Neighbor Discovery in On-Demand MANET Routing Protocols. The authors present an adaptive Hello messaging scheme to suppress unnecessary Hello messages without reduced detectability of the broken links. Simulation results show that the proposed method reduces energy consumption and the network overhead without any explicit difference in throughput. In [4], the authors propose Dynamic Neighbor Positioning In Manet with Protection against Adversarial Attacks. The authors present techniques for finding neighbours effectively in a non priori trusted environment are identified. These techniques will eventually provide security from attacker nodes. The protocol is robust to malicious attacks. This protocol will also update the position of the mobile nodes in an active environment. The performance of the proposed method will be effective one.

In [5], the authors propose Neighbor node discovery and Trust prediction in MANETs. This paper uses the directional antenna algorithm known as scanning based direct discovery algorithm to discover the neighbour nodes. To enable the cooperative working of the various distributed protocols we use trust system to provide the trust level of various mobile nodes, thereby enhancing the cooperation among the nodes. This paper uses the distributed hybrid trust algorithm and also uses relationship maturity concept to compute the trust of the mobile nodes. This paper demonstrates that Trust systems are better than already existing encryption techniques. For the discovery of mobile nodes [6], the authors explored the various attacks possible in the physical and communication medium of the MANETs. The authors classified the neighbor discovery as physical and communication neighbor discovery. Protocols aiming at communication neighbour discovery, which are based on physical discovery protocols, often fail to achieve their objective. This is because that these two types of discovery are not equivalent. At the same time, the protocols for communication neighbour discovery do not fully address the problem at hand. They are very effective only under very specific operational conditions or they do not ensure correctness in all cases.

For the verification of Neighbor position [7] [8], there are techniques that was studied in the context of mobile ad hoc and sensor networks; however, existing Neighbor Position Verification schemes often rely on traditional or mobile trustworthy nodes, which are assumed to be always available for the verification of the positions announced by third parties. In mobile ad hoc environments, however, the pervasive presence of either infrastructure or neighbour nodes that can be aprioristically trusted is quite unrealistic.

### III. PROPOSED WORK

In this paper we propose a fully distributed cooperative scheme for neighbor position verification (NPV), which enables a node, hereinafter called the verifier, to discover and verify the position of its communication neighbors.

#### 1. NPV Protocol

The proposed NPV protocol is designed for spontaneous mobile ad hoc environments, and, as such, it does not rely on the presence of a trusted infrastructure or of a priori trustworthy nodes. This protocol leverages cooperation but allows a node to perform all verification procedures autonomously. This method has no need for lengthy interactions, e.g., to reach a consensus among multiple mobile nodes, making our scheme suitable for both low and high mobility environments. It is reactive, meaning that it can be executed by any mobile node, at any point in time, without prior knowledge of the neighborhood. It is robust against independent and colluding attacks. It is lightweight, as it generates low overhead routing traffic.

##### Algorithm 1:

**Step 1:** node S do

**Step 2:** S  $\rightarrow$ \* : (POLL, K's)

**Step 3:** S : store ts

**Step 4:** When receive REPLY from X E

**Step 5:** S : store txs, cx

**Step 6:** after  $T_{max} + T_{jitter}$  do

**Step 7:** S : ms={ (cx, ix)/txs }

#### 2. Direct Symmetry Test

The Direct Symmetry Test(DST) verifies the direct links with its communication neighbor nodes. To this end, DST checks whether reciprocal to F-derived distances are consistent with each other and with the position advertised by the neighbor node and with a proximity range. The latter corresponds to the maximum nominal transmission range, and upper bounds the distance at which the two nodes can communicate.

##### Algorithm 2:

**Step 1:** node S do

**Step 2:** S:  $F_s < -0$

**Step 3:** For all X E Ns do

**Step 4:** If  $ds_x - dx_s > 2$  or

**Step 5:**  $ps - px / - dx_s > 2$  or

**Step 6:**  $ds_x > R$  then

**Step 7:** S:  $F_s < -X$

#### 3. Cross Symmetry Test

The cross symmetry test(CST) ignores nodes already declared as faulty by the DST and only considers mobile nodes that proved to be communication neighbor nodes between each other, i.e., for which To F derived mutual distances are available. However, pairs of neighbor nodes declaring collinear positions with respect to S are not taken into account. This choice makes our NPV robust to attacks in many particular situations. For all other pair the cross test verifies the symmetry of the reciprocal distances and their consistency with the positions declared by the neighbor nodes and with the proximity range. For each neighbor maintains a link counter and a mismatch counter. The former is incremented at every new crosscheck on X, and records the number of communication links between neighbor and other neighbors. The latter is incremented every time at least one of the cross-checks on distance and the position fails and identifies the potential for neighbor being faulty.

**Algorithm 3:**

**Step 1:** node S do  
**Step 2:** S:Us<- 0, Ws<- 0  
**Step 3:** For all X E Ns, X E Fs do  
**Step 4:** if dxy , dyx and  
**Step 5:** Ps E line(px , py)  
**Step 6:** S:lx=lx+1, ly=ly+1  
**Step 7:** If dxy-dyx > 2x+e or  
**Step 8:** dxy > R then  
**Step 9:** S: mx=mx+1.

#### IV. CONCLUSION

In mobile ad hoc networks(MANETs), position aided routing protocols can offer a significant performance increase over fixed ad hoc routing protocols. As position information is broadcasted including the attacker to receive. Routes may be disconnected due to the dynamic movement of mobile nodes. Such mobile networks are more vulnerable to both internal and external attacks due to presence of the attacker nodes. These mobile nodes affect the performance of the routing protocol in ad hoc networks. So it is essential to identify the neighbor nodes in MANET. The Neighbor Position Verification (NPV) is a routing protocol designed to protect the wireless network from adversary nodes by verifying the position of neighbor nodes to improve security, efficiency and performance in ad hoc network routing.

#### REFERENCES

- [1] Chansu Yu, y Ben Lee , Hee Yong Youn, "Energy Efficient routing protocols for mobile ad hoc networks", Wireless Communications and Mobile Computing, John Wiley & Sons, Ltd, PP-959–973, 2003.
- [2] E. Ekici, S. Vural, J. McNair, and D. Al-Abri, "Secure Probabilistic Location Verification in Randomly Deployed Wireless Sensor Networks," Elsevier Ad Hoc Networks, vol. 6, no. 2, pp. 195-209, 2008.
- [3] Seon Yeong Han, 2013. An Adaptive Hello Messaging Scheme for Neighbor Discovery in On-Demand MANET Routing Protocols, IEEE Transactions on communication, 17(5): 1040-1043.
- [4] Priyadarshani, K., 2013. Dynamic Neighbor Positioning In Manet with Protection against Adversarial Attacks, IJCER, 3(4).
- [5] Thilagavathy, S., 2013. Neighbor node discovery and Trust prediction in manets, International Journal of Science, Engineering and Technology Research (IJSETR), 2(1).
- [6] Poturalksi, M., P. Papadimitratos and J.P. Hubaux, 2008. "Towards Provable Secure Neighbor Discovery in Wireless Networks," Proc. Workshop Formal Methods in Security Eng.
- [7] Chiang, J., J. Haas and Y. Hu, 2009. "Secure and PreciseLocation Verification Using Distance Bounding and Simultaneous Multilateration," Proc. Second ACM Conf. Wireless Network Security (WiSec).
- [8] Capkun, S., K. Rasmussen, M. Cagalj and M. Srivastava, 2008. "Secure Location Verification with Hidden and Mobile Base Stations," IEEE Trans. Mobile Computing, 7(4): 470-483.

## Characterization of environmental impact indices of solid wastes in Surulere Local Government Area, Nigeria with GaBi<sub>5</sub> LCA modeling technique

S. O. Ojoawo<sup>1</sup>, J. S. Bosu<sup>2</sup>, O. A. Oyekanmi<sup>3</sup>

<sup>1,2,3</sup> Department of Civil Engineering, Ladake Akintola University of Technology, Ogbomoso Nigeria

**Abstract:** Life Cycle Assessment (LCA) is currently being used in several countries to evaluate treatment options for specific waste fractions. The application of GaBi<sub>5</sub> (Holistic Balancing) modeling tool is currently apt for the impact assessment of environmental pollution indices arising from wastes. This study focuses on the characterization of environmental impact indices of solid wastes in Surulere, one of the Local Government Area (LGA)s in Nigeria using GaBi<sub>5</sub>.

Waste classification was carried out in the selected houses of the LGA. Tool for the Reduction and Assessment of Chemical and other Environmental Impacts (TRACI) and the Centre of Environmental Science, University of Leiden, Netherlands (CML) methods of LCA inventory assessment were employed in the study. One kg of municipal solid waste of this area was selected as the functional unit. The Scenario considered in this study with its system boundaries is Landfilling. It consists of three main steps: Collection, Transportation and Landfilling. GaBi<sub>5</sub> modeling tool was used to obtain background data for the life cycle inventory and to analyse the wastes completely. Four (4) environmental impact indices evaluated are: Global Warming Potential (GWP), Acidification Potential (AP), Eutrophication Potential (EP) and Ozone Depletion Potential (ODP).

Result of the Scenario's Environmental Impacts shows that the GWP is characterized in the order: Biodegradable > Textile > Wood > Paper > plastic > Metal > Glass. The AP followed similar trend except for paper that is greater than wood wastes. EP has this trend; Metal > Wood > Glass > Biodegradable > Paper > Textile while for ODP it was Textile > Plastic > Paper > Metal > Wood > Biodegradable > Glass. The study also showed that when LCA is applied in conjunction with the waste hierarchy, it can be a useful tool for the planning of municipal waste management plans as it allows municipalities to directly compare the actual environmental impacts of different technologies and planning options. Furthermore, through system expansion, a consequential approach to LCA may encourage municipalities to integrate waste management with processes in other sectors. The GaBi software of LCA solves the problem of imprecision involved in solid waste decision making. The study concludes that the wastes all have detrimental impacts on the 4 measured categories but the highest pollution threat is on the Global Warming Potential. It is recommended that Environmental Protection Agencies at all levels should always analyze and contain the pollution impacts of the solid wastes on the environment.

**Keywords:** Environmental Impact Indices, GaBi<sub>5</sub>, Life Cycle Assessment, Life Cycle Inventory

### I. Introduction

Protecting the environmental and natural resources is increasingly becoming very important through environmental solid waste management programmes. It is necessary to follow the same part with the waste managers, a sustainable approach to waste and integrate strategies that will produce the best practicable option. This is very challenging task since it involves taking into account economic, technical, regulatory, and environmental issues. Solid waste management is a complex and multi-disciplinary problems that should be considered from basis. For a healthy environment, both municipal and industrial waste should be managed according to solid waste management hierarchy (prevention /minimization/ recovery/incineration/landfilling).

Studies on modelling of solid waste management system were started in 1970s and were increased with the development of computer models in 1980s. While models in the 80s were generally based on an economic perspective [1], models that included recycling and other waste management method were developed for planning of municipal solid waste management system in the 1990 [2]. It is accepted that LCA concepts and

techniques provides solid waste planners and decision makers with an excellent framework to evaluate MSW management strategies [3].

The LCA, which is used to determine the optimum municipal solid waste management (MSW) strategy. Environmental LCA is a system analysis tool. It was developed rapidly during the 1990s and has reached a certain level of harmonization and standardization. The LCA of product commences with extracting of raw materials through the process of logging, mining etc and ends with final disposal of products. The life cycle of waste on the other hand, starts when a material is discarded into the waste stream and ends when the material has either been converted into a resource (such as recycled materials or recovered energy) or, when it is finally disposed.

The LCA is currently being used in several countries to evaluate treatment options for specific waste fractions [3-8]. Over the last few years back, some agencies like the Society of Environmental Toxicology and Chemistry (1991), Canadian Standards Association (1994), and the International Organization for Standardisation (ISO) have undertaken the development of standardization methodologies for carrying out the first two phases of life cycle assessment: Goal definition and scoping and life cycle inventories. The third phase of life cycle assessment, impact analysis, is intrinsically more problematic and there is, at this time, no widely accepted methodology for combining the diverse environmental effects into a single measure of environmental performance.

Regularity, technical and environmental constraints characterize LCA models [9]. The regulatory constraints give the minimum percentage of waste recycling; these percentages are proportional to the total waste generated. Also [9] presented a comprehensive mixed integer nonlinear programming problem, whose planning horizon is a year. They gave a detailed description of environmental constraints that cover RDF constraints; the incineration and the SOM constraints.

The model of [10] minimize overall cost (taking into account energy and material recovery) through the solution of a nonlinear programming problem.

The aim of this present study is to select an optimum waste management system for Surulere LGA of Nigeria by evaluating, from an environmental point of view, alternatives to the existing system. Here, the LCA methodology has been used to conduct an environmental comparison of the alternative scenarios in the waste management system of the Study Area. This evaluation was according to TSE EN ISO 14040 that classified LCA into four major stages of goal and scope definition, life cycle inventory, life cycle impact analysis and interpretation of the results.

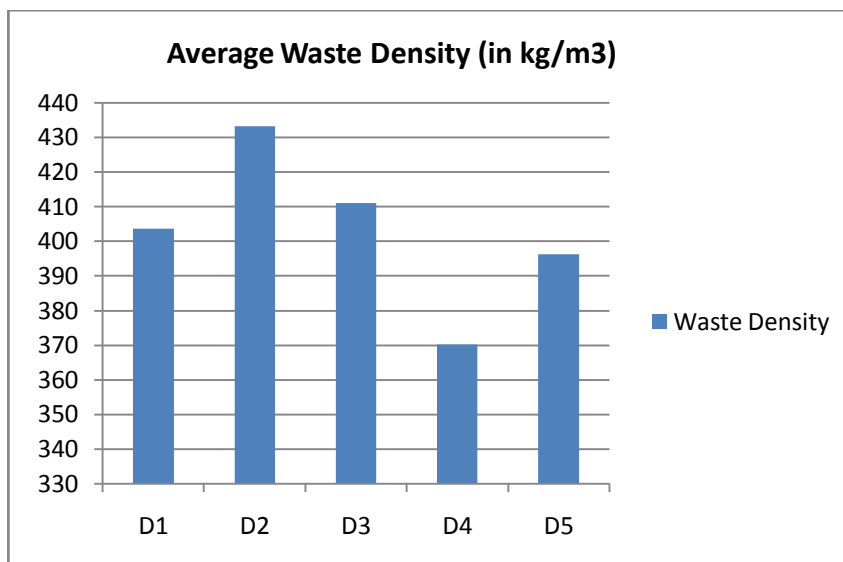
## **II. Methodology**

### **(a) Study Area**

The municipality of Surulere Local Government Area (LGA) in Oyo State of Nigeria is with a population of 180,000 people [11], and is increasing with an annual population rate of 0.15%. The headquarters is situated at Iresa-Adu which is the largest of all the towns in the LGA. The study area has two different seasons; the Wet and Dry season. The wet season lasts about 6 months, April to September that is the period of maximum solid waste generation while the dry season is from October to March with scanty or no rainfall. In the study area, apart from Open – burning, there is only one waste recovery program and the program is widespread throughout the area which is uncontrolled tipping. Wastes are collected in bins or containers and compactor vehicles and are later transported by the Oyo State Environmental Protection Agency (OYSEPA) for land filling with little recovery rate.

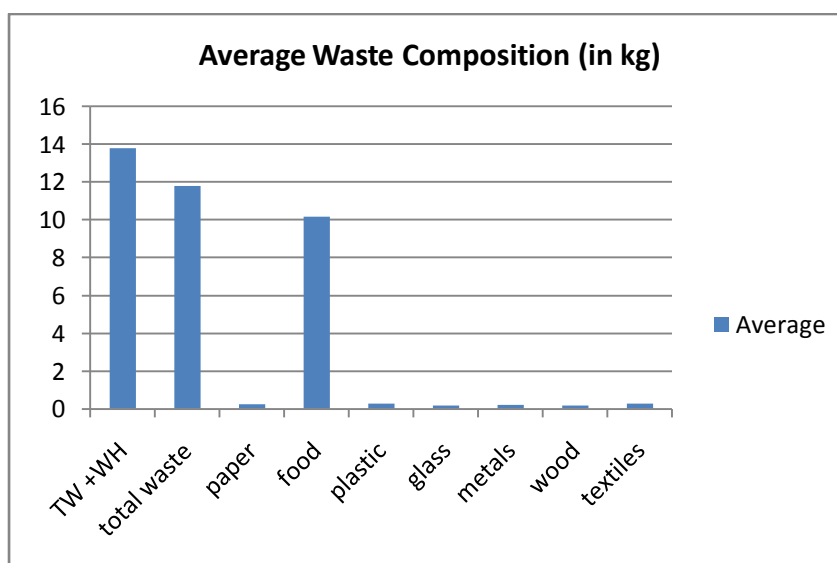
### **(b) Waste Composition in the study area.**

The waste density and composition in municipality of Surulere Local Government Area are given in Figures I and II respectively.



where D1, D2...D5 – Selected Dumpsites

**Figure I: Waste density in selected dumpsites of the Study Area**  
[Source: 12]

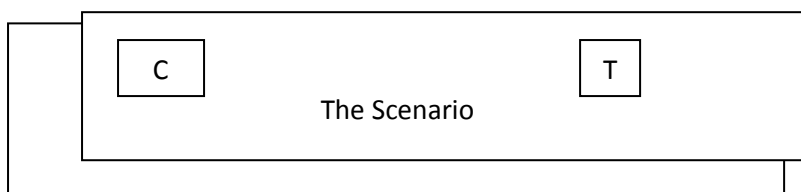


where TW – Total Waste, HW – Headpan Weight.

**Figure II: Composition of waste materials by mass in the Study Area**  
[Source: 12]

### (c) The Life Cycle Assessment (LCA)

The functional unit selected for the comparison of the alternative scenarios is the management of 1kg of municipal solid waste of this area. The scenario that was considered in this study with the system boundaries is illustrated in Figure III. The Scenario is called Landfilling Scenario consists of three main steps: Collection, Transport and Landfilling of MSW. Because of rural nature of the area, the quantities of municipal solid waste of this area are not rising rapidly; it is assumed that approximately 90 tonnes of MSW is generated daily by the 180,000 residents. Most of their wastes are being disposed when going to farm or thrown into the drains during heavy rainfall. Few private vehicles collect wastes in plastic bags that are discarded and piled up on the streets by the residents, and transport the wastes to the unregulated dumping site to dump there at all hours of the day for recycling or other use when they know they have no means of dumping waste materials. There are few unregulated open dumping site where recyclable components (about 7% of total wastes) are partially separated manually under the unhygienic conditions and piled up for recycling.



C: collection, T: transportation

Figure III: the scenario of MSW for the Study

### III. Results And Discussions

The two methods employed to assess the impact of the solid waste generated in the study area are: the Tool for the Reduction and Assessment of Chemical and other Environmental Impacts (TRACI) and the Centre of Environmental Science, University of Leiden, (the Netherlands CML) Methods.

#### (a) Impact assessment of the Scenario with CML method of *GaBi<sub>5</sub>* LCA modelling

11.60kg of waste materials were collected and transported for landfilling purposes. The flow chart of the landfill scenario and the result of Life Cycle Inventory (LCI) as produced from the *GaBi<sub>5</sub>* LCA model are given in Figure IV and Table I respectively.

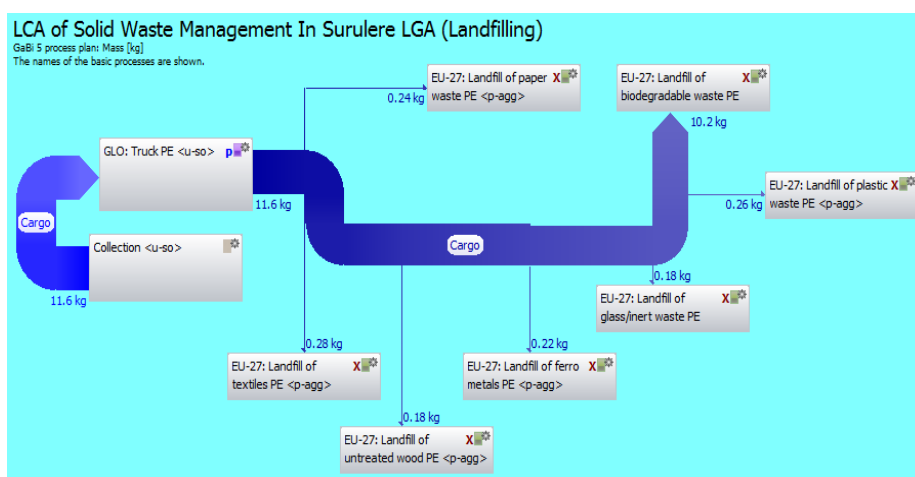


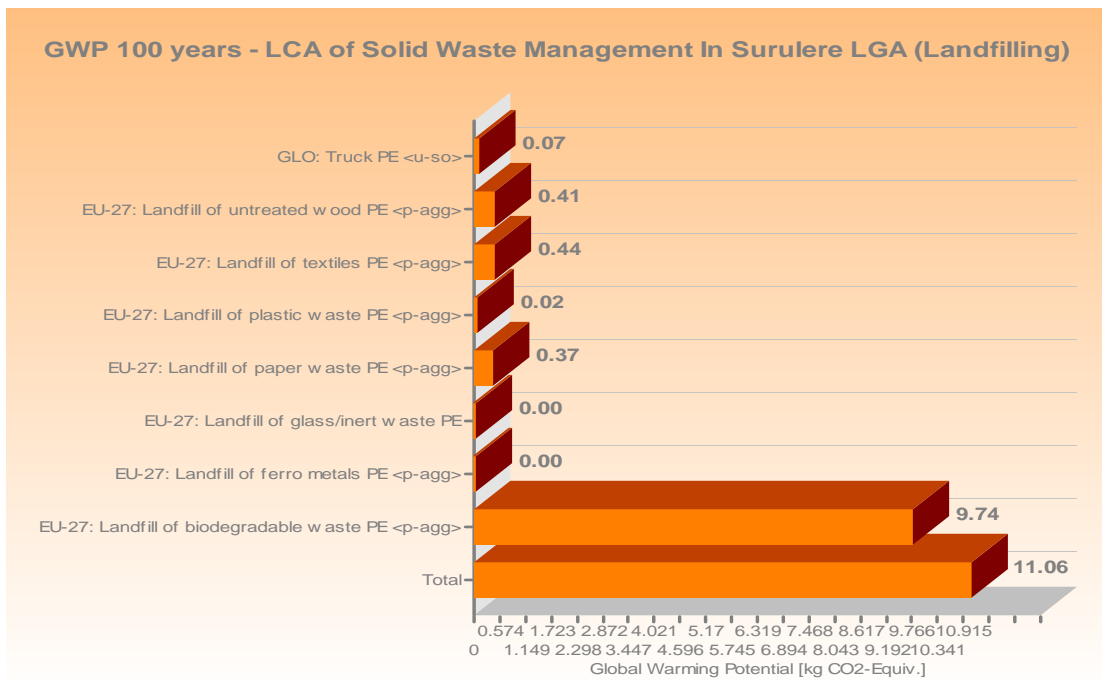
Figure IV: Plan of the LCA of Solid Waste Management in the Scenario

Table I: LCI result for the Scenario

	GWP		AP		EP		ODP	
	CML Kg, CO <sub>2</sub> , eqv	TRACI Kg, CO <sub>2</sub> , eqv	CML Kg, CO <sub>2</sub> , eqv	TRACI I Kg, CO <sub>2</sub> , eqv	CML Kg, CO <sub>2</sub> , eqv	TRACI Kg, CO <sub>2</sub> , eqv	CML Kg, CO <sub>2</sub> , eqv	TRACI Kg, CO <sub>2</sub> , eqv
Biodegradable	9.74	9.17	0.00308	0.186	0.018	0.00774	2.66E-009	2.66E-009
Metal	0.00452	0.00436	1.04E-005	0.000688	8.79E-005	5E-006	6.12E-012	6.12E-012
Glass	0.00251	0.00251	1.53E-005	0.000907	2.1E-006	1.21E-006	2.48E-012	2.48E-012
Paper	0.369	0.347	8.67E-005	0.00541	0.00128	5.4E-005	6.26E-011	6.26E-011
Plastic	0.0194	0.0192	5.62E-005	0.00305	6.91E-005	3.23E-005	6.78E-011	6.78E-011
Textile	0.442	0.416	0.000102	0.0064	0.000657	0.00027	7.3E-011	7.3E-011
Wood	0.414	0.389	8.9E-005	0.00507	4.31E-005	1.82E-005	4.69E-011	4.69E-011

**(i) Global Warming Potential (GWP)**

Using the CML Method, the global warming potential for hundred years in the LCA of solid waste management from *GaBi<sub>5</sub>* LCA model is graphically shown below:



**Figure V: GWP 100years - LCA of Solid Waste Management**

**(ii) Acidification Potential (AP)**

Using the CML Method, the acidification potential in the LCA of solid waste management is graphically shown below:

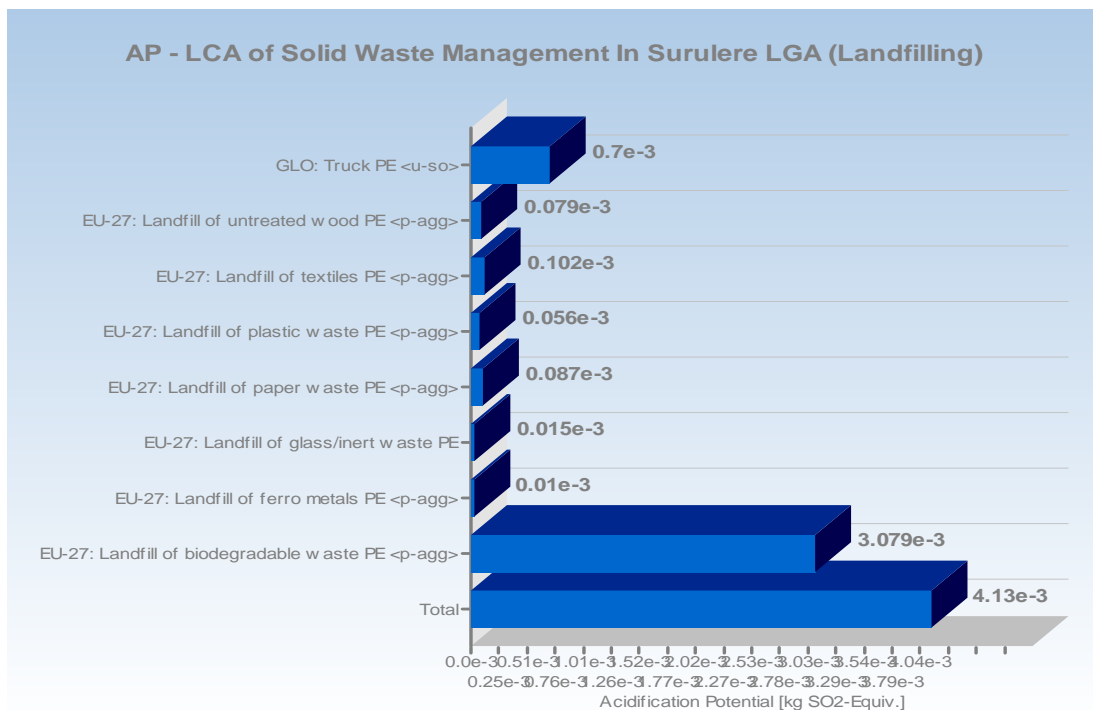


**Figure VI: AP - LCA of Solid Waste Management**

**(iii) Eutrophication Potential (EP)**

Using the CML Method, the eutrophication potential in the LCA of solid waste management is graphically shown below:

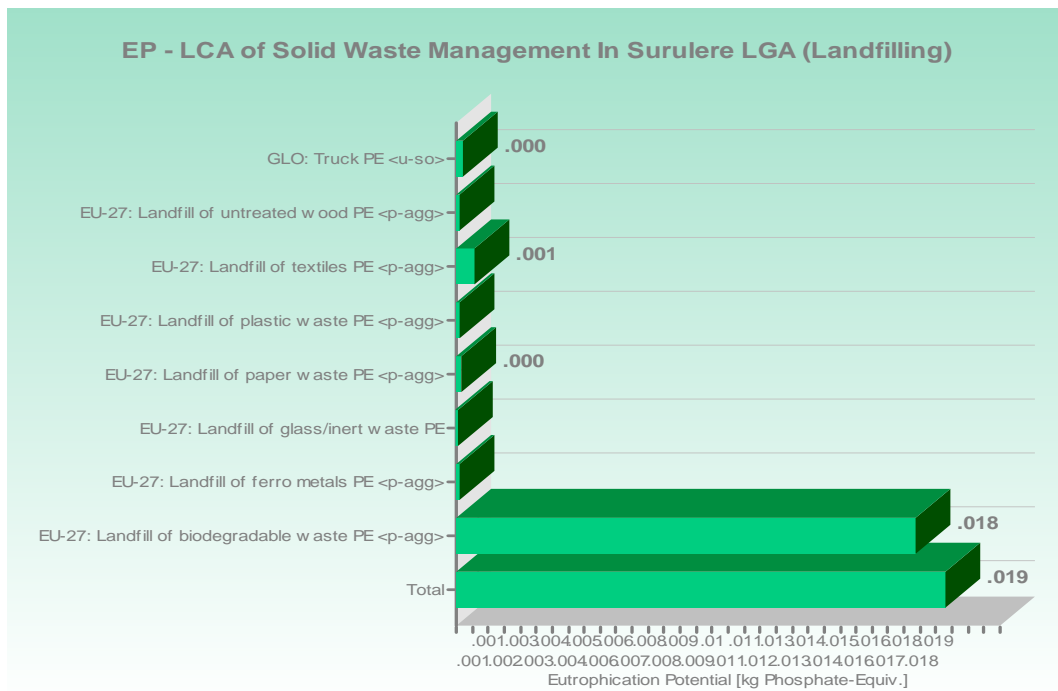


**Figure VII: EP - LCA of Solid Waste Management**

**(iv) Ozone Depletion Potential (ODP)**

Using the CML Method, the Ozone Depletion potential in the LCA of solid waste management is graphically shown below:

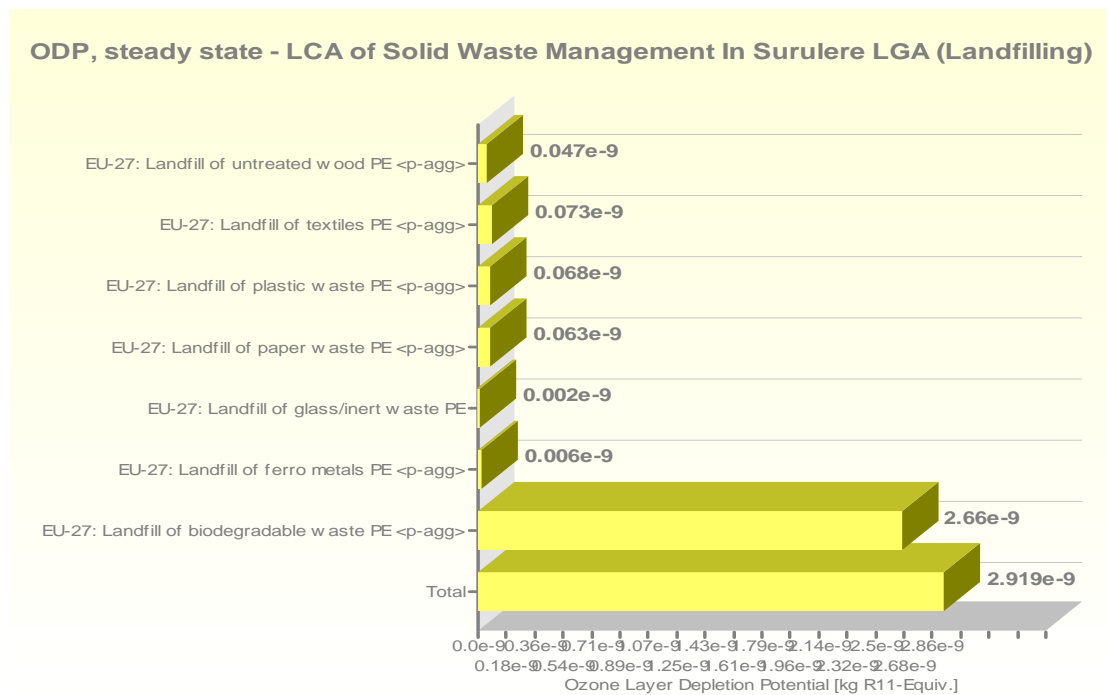


**Figure VIII ODP - LCA of Solid Waste Management**

**(b) Impact assessment of the Scenario with TRACI method of GaBi<sub>5</sub> LCA modelling**

The comprehensive results of the life cycle Impact (LCI) Assessment of the scenario analyzed using the TRACI method are given below:

**(i) Global Warming Potential (GWP)**

Using the TRACI Method, the global warming potential for hundred years in the LCA of solid waste management of Surulere Local Government is expressed as global warming air which is graphically shown below:

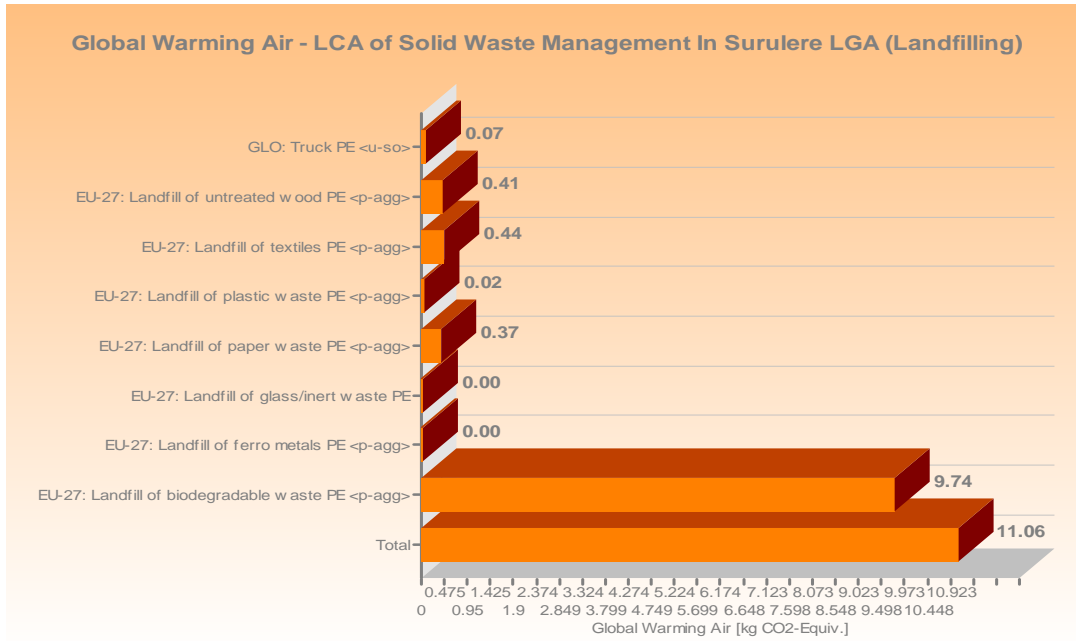


**Figure IX: GWP - LCA of Solid Waste Management**

**(ii) Acidification Potential (AP)**

Using the TRACI Method, the acidification potential in the LCA of solid waste management scenario is graphically shown below:

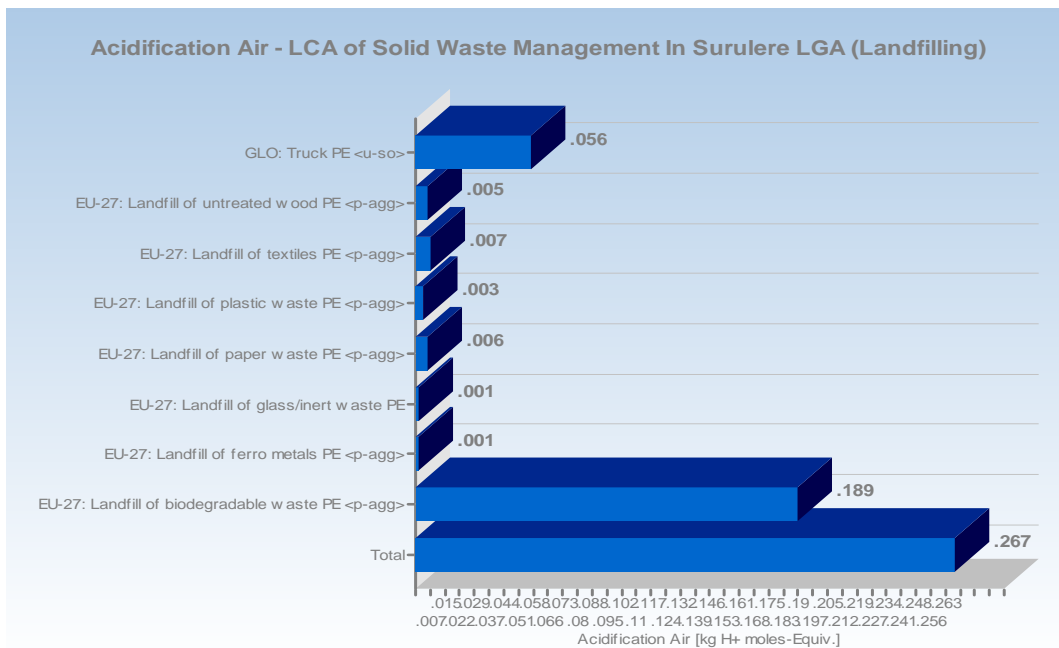


**Figure X: AP - LCA of Solid Waste Management**

**(iii) Eutrophication Potential (EP)**

Using the TRACI Method, the eutrophication potential in the LCA of solid waste management (scenario one) is graphically shown below:

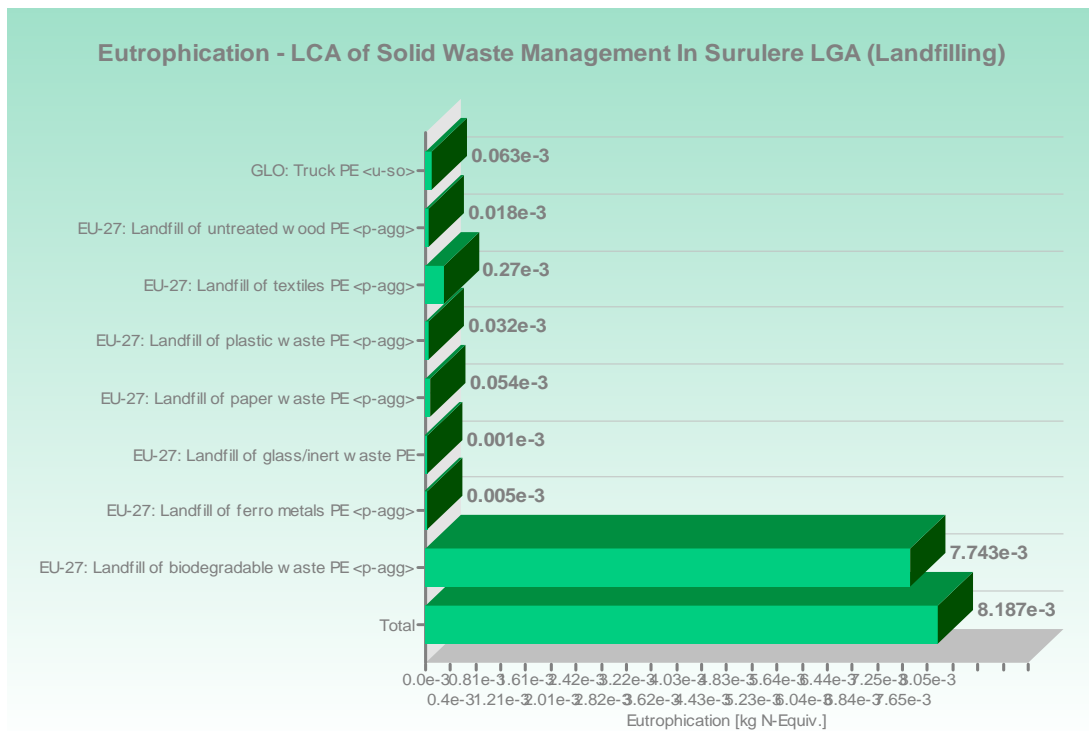


**Figure XI: EP - LCA of Solid Waste Management**

**(iv) Ozone Depletion Potential (ODP)**

Using the TRACI Method, the Ozone Depletion potential in the LCA of solid waste management scenario is graphically shown below:

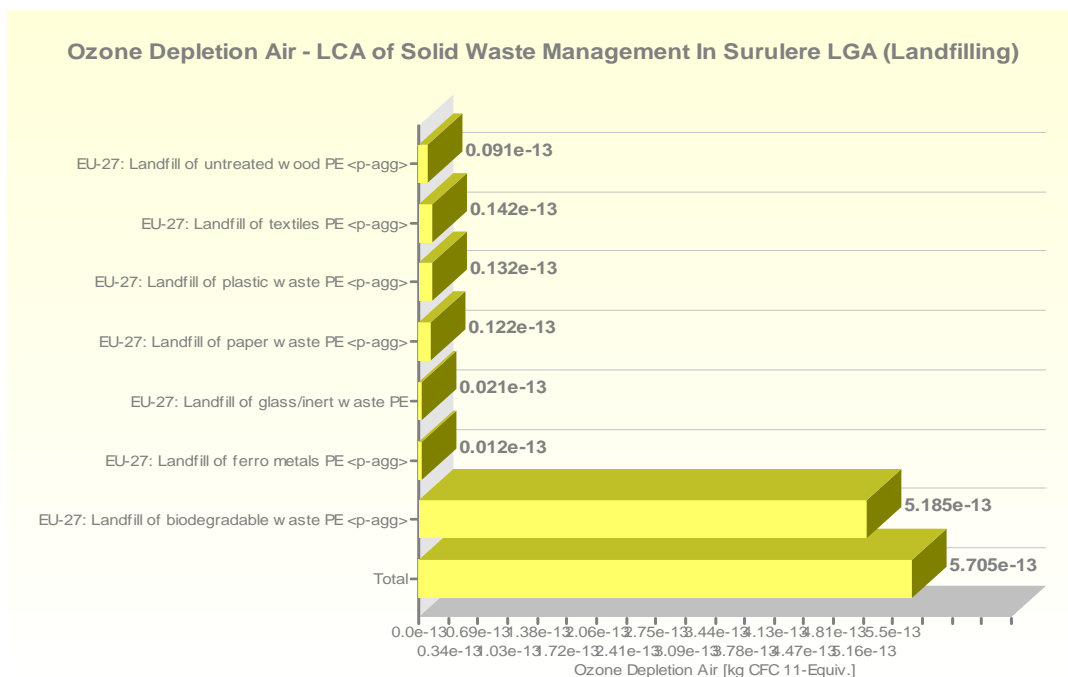


**Figure XII: ODA - LCA of Solid Waste Management**

**(c) Comparison of Environmental impact assessment of both TRACI and CML methods**

**(i) Global Warming Potential(GWP)**

It is generally observed that the GWP for 100years is relatively the same when the solid waste is land filled in respective of the LCI Assessment method used. From Figures V and IX, it is noted that the GWP for 100years is the same for both method of assessment.

**(ii) Acidification Potential (AP)**

From Figures VI and X, it is discovered that the environmental impact in terms of AP is high when TRACI method was used for the LCI assessment while it is lesser when CML method was adopted for the assessment.

**(iii) Eutrophication Potential (EP)**

From Figures VII and XI, it is noted that the EP as result of biodegradable waste and textile waste are high whereas the EP for other type of solid waste as indicated in the Figures are lesser when CML method was used for the LCI assessment; while when the TRACI method was used for the assessment, most of solid wastes have a high EP, with the exception of biodegradable waste and textile waste, when compared with CML method.

**(iv) Ozone Depletion Potential (ODP)**

The potential of ozone depletion as a result of solid waste land filled when assessed by CML method is a little higher than when TRACI method was used for LCI assessment (Figures VIII and XII refers).

#### IV. Conclusion

Application of *GaBi<sub>5</sub>* LCA modelling techniques solves the problem of imprecision involved in solid waste decision making. The study concludes that the wastes all have detrimental impacts on the 4 measured categories but the highest pollution threat is on the Global Warming Potential (GWP). The Scenario's Environmental Impacts shows that the GWP is characterized in the order: Biodegradable > Textile > Wood > Paper > plastic > Metal > Glass. The AP followed similar trend except for paper that is greater than wood wastes. EP has this trend; Metal > Wood > Glass > Biodegradable > Paper > Textile while for ODP it was Textile > Plastic > Paper > Metal > Wood > Biodegradable > Glass. The study also showed that when LCA is applied in conjunction with the waste hierarchy, it can be a useful tool for the planning of municipal waste management system as it allows municipalities to directly compare the actual environmental impacts of different technologies and planning options. Furthermore, through system expansion, a consequential approach to LCA may encourage municipalities to integrate waste management with processes in other sectors. It is therefore recommended that Environmental Protection Agencies at all levels should always analyze and contain the pollution impacts of the solid wastes on the environment.

#### REFERENCES

- [1] Gottinger, H.W., 1988. A computational model for solid waste management with application. *European Journal of Operational Research* 35, 350–364.
- [2] MacDonald, M., 1996. Solid waste management models: a state of the art review. *Journal of Solid Waste Technology and Management* 23 (2), 73–83.
- [3] Obersteiner, G., Binner, E., Mostbauer, P., Salhofer, S., 2007. Land II modelling in LCA – a contribution based on empirical data. *Waste Management* 27, S58–S74.
- [4] Boer, J., Boer, E., Jager, J., 2007. LCA-IWM: A decision support tool for sustainability assessment of waste management systems. *Waste Management* 27, 1032–1045.
- [5] Winkler, J., Bilitewski, B., 2007. Comparative evaluation of life cycle assessment models for solid wastes management. *Waste Management* 27, 1021–1031.
- [6] Borghi, A., Binaghi, L., Borghi, M.G.M., 2007. The application of the environmental product declaration to waste disposal in a sanitary landfill. *International Journal of LCA* 12 (1), 40–49.
- [7] Finnveden, G., 1999. Methodological aspects of life cycle assessment of integrated solid waste management systems. *Resources, Conservation and Recycling* 26, 173–177.
- [8] Ozeler, D., Yetis, U., Demirer, G.N., 2006. Life cycle assessment of municipal solid waste management methods: Ankara case study. *Environment International* 32, 405–411.
- [9] Fiorucci, P., Minciardi, R., Robba, M., Sacile, R. “Solid waste management in urban areas development and application of a decision support system”. *Resources Conservation and Recycling*, 37, 2003, pp 301-328.
- [10] Chang, N. and Wang, S.F. “A fuzzy goal programming approach for the optimal planning of metropolitan solid waste management systems”. *European Journal of Operational Research*, 99, 1997, pp 303-321.
- [11] NPC “Official gazette for 2006 population census”. *National Population Commission*, Nigeria.
- [12] S.O. Ojoawo, O.A Agbede and A.Y Sangodoyin (2011) On the physical composition of solid wastes in selected dumpsites of Ogbomosoland, South-Western Nigeria. *Journal of Water Resource and Protection*, U.S.A, 3 (9): 661-666.

## A Novel Key Management Paradigm for Broadcasting to Remote Cooperative Groups

Murala Lavanya<sup>1</sup>, T. Sukanya<sup>2</sup>

<sup>1</sup> M. Tech (CSE), MVR College of Engineering and Technology, A.P., India.

<sup>2</sup>Asst. Professor, Dept. of Computer Science & Engineering, MVR College of Engineering and Technology, A.P., India.

**Abstract:** A Mobile Ad Hoc Network(MANET) is a system made up of wireless mobile nodes. These MANET nodes have wireless communication and networking characteristics. MANETs have been proposed to serve as an effective networking system facilitating information exchange between mobile devices even without fixed infrastructures. In MANETs, it is important to support group-oriented applications, such as audio/video conference and one-to-many data dissemination in disaster or battlefield rescue scenarios. In the above group oriented communication scenarios, the common problem is to enable a sender to securely transmit secret messages to a remote cooperative group. A solution to the above problem must meet several constraints. First, the sender must be remote and can be dynamic. Second, the message transmission may cross various networks including open insecure networks before reaching the intended recipients. Third, the data communication from the group members to the sender may be limited. Also, the sender may wish to choose only a subset of the overall group as the intended recipients. Furthermore, it is hard to resort to a fully trusted third party to secure the overall communication. In contrast to the above constraints, mitigating features are that the group members are cooperative and the secret communication among them is local and efficient. This paper exploits these mitigating features to facilitate the remote access control of group-oriented communications without relying on a fully trusted secret key generation center.

**Keywords:** Broadcasting, Group communication, Key Management, MANET, VANET.

### I. INTRODUCTION

Mobile Ad Hoc Networks(MANETs) [1] are planned to function good networking system facilitating data exchange between mobile devices without fixed infrastructures. It's most important to support group-oriented applications, audio and video conference and one-to-many data dissemination in disaster or battlefield rescue scenarios. Wireless network communication is broadcast and a certain amount of devices can receive transmitted messages, the risk of unsecured sensitive data being intercepted by unintended recipients is a real concern. So MANET, Vehicular Ad Hoc Network(VANET) [2] having in same near future. This network communication is hard to resort to a fully trusted third party to secure the network communication. And then the group members must be cooperative and the communication among them is local and efficiently. An ad hoc network is a collection of wireless nodes that can dynamically form a network to exchange information without using any pre-existing traditional network infrastructure. It is an autonomous system in which mobile nodes connected by wireless links are free to move randomly and often act as routers at the same time. The traffic types in MANETs are quite different from those in an infrastructure wireless network. Figure 1 shows an example MANET.

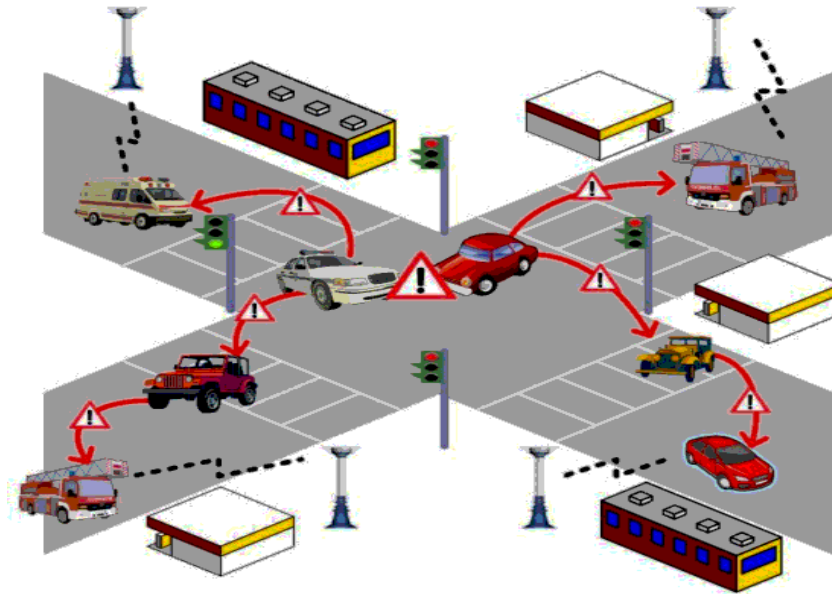


Fig. 1: An example MANET

A Mobile Ad Hoc Network is a type of ad hoc network that can change locations and configure itself on the fly. Because ad hoc networks are mobile, they use wireless connections to connect to various networks. This can be a standard Wi-Fi connection, or another medium, such as a satellite or cellular transmission. A Mobile ad hoc Network (MANET) is a self-configuring infrastructure network of several mobile devices connected by wireless. Ad hoc is Latin and means "for this purpose". Key Management is the major security concept in group oriented Communications. The existing key management systems can be categorised in to two types depending on the approaches. They are: Group Key Agreement and Key Distribution systems. Presently both of these concepts are active research areas and they have huge repositories of literature.

## II. RELATED WORK

In a wireless environment, access control is the most fundamental and critical security issue in group oriented communication [3]. Generally, access control can be achieved by applying cryptographic techniques. A shared key, called group key or traffic encryption key (TEK), is used to cipher the group communication data and is distributed to all legitimate group members. Only the members who own this traffic key can access the communication content. The integrity and confidentiality of the group's communication rely on the safety of the group key. Management of the group key thus plays a vital role in the security of group communication [4]. Key management in group oriented communication is very different from that in the point-to-point communication model. In the point-to-point model, the cipher key can be generated by negotiation through protocols such as the Diffie-Hellman key exchange protocol [5] or it can be generated by one side and then sent to another side. However, in group oriented communication, a group may have many receivers, and the efficient generation, regeneration and distribution of the group keys to all receivers is a complicated and challenging task.

A large number of group key agreement protocols have been proposed in the literature. The earlier efforts in [6] focused on efficient establishment of the initial group key. Later studies in [7] enable efficient member joins, but the cost for a member leave is still comparatively very high. A tree key structure has been further proposed and then improved to achieve better efficiency for member joins and leaves [8]. Broadcast encryption is very essential for key management [9] in priced media distribution [10] and digital rights management [11]. Broadcast encryption schemes in the literature can be classified in 2 categories: symmetric-key broadcast encryption and public-key broadcast encryption. In the symmetric-key encryption, only the trusted center generates all the secret keys and broadcasts messages to all users. Hence, only the key generation center can be the sender or the broadcaster. In the public-key encryption, in addition to the secret keys for each user, the trusted center also generates a public key for all the users so that any one can play the role of a sender or broadcaster .

### III. PROPOSED WORK

#### 1. System Model

In this paper, we create nodes and made ad hoc network. Each and every node has to generate both public and secret key. And allocate a certificate authority person to provide the certificate for public key during data transmission but he does not have secret key, receiver only have that single secret key. The remote sender can retrieve the receiver's public key for checking and validate through the certificate authority. The potential receivers are linked together with the efficient local connections. Using communication infrastructures, they can also join to the heterogeneous networks. Each receiver has a public and secret key pair. The public key is certified by a certificate authority(CA), but the secret key is kept only by the receiver side. A remote sender can get back the receiver's public key from the CA and validate the authenticity of the public key by checking its certificate, which implies that no direct communication from the receivers to the sender is necessary [7]. Then, the sender can send the secret messages to any chosen subset of the receivers. After that officially define the model of the group key agreement based broadcast encryption. Since the heart of the key management is to securely distribute a session key to the intended receivers, it is sufficient to define the system as a session key encapsulation mechanism. Then, the sender can at the same time encrypt any message under the session key, and only the intended receivers can decrypt it. Figure 2 shows our system model.

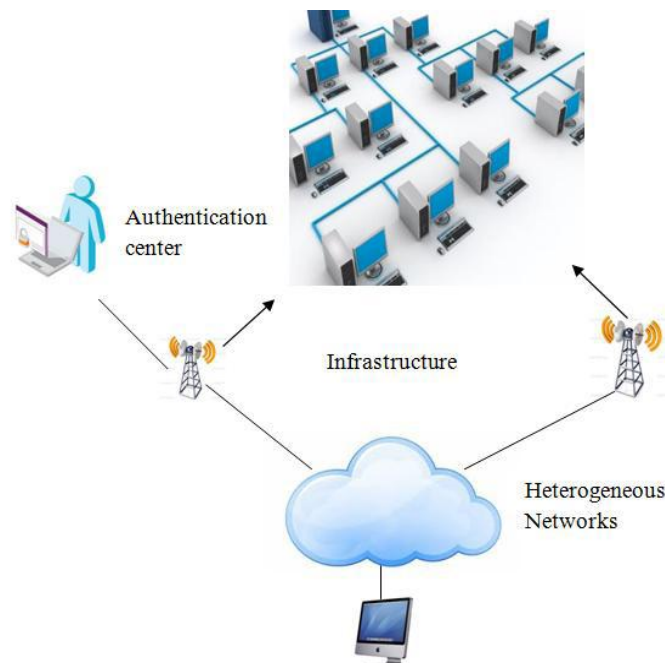


Fig. 2: System Model

#### 2. Key Management

The major security concern in group-oriented communications with access control is the key management. The key management process allowing secure and efficient transmissions to remote cooperative groups by effectively exploiting the mitigating features and circumventing the constraints. In proposed scheme an authentication key is a pair of public and private key and a certificate signed by the base station are pre distributed in each cluster head. The authentication key is used to verify the member sensor node identities. Authentication key is known to all the cluster heads and the base station. The public or private key pair is used to establish pair wise keys among cluster heads. An authentication key and the public key of the base station are pre distributed in each of the member sensor node. Public keys are used to verify the certificates of the cluster heads. Authentication key can be calculated by using the following hash function:

$$KAuth_i = H(ID_i || KCHAuth)$$

#### 3. Key Generation

The key generation algorithm is run by each user  $u_i$  to generate the public and private key pair. The user takes  $n, N$  as their inputs and value  $i$  as the index to generate  $(pk_i, sk_i)$  as their public, private key pair. The

key generation process can be done offline mode before the message transmission starts online. Each user randomly chooses public key  $P_i$  which belongs to the group  $Z_p$  and generates secret key  $S_i$  as

$$S_i = g^{P_i}$$

#### 4. Encryption

The encryption algorithm is run by each sender who wishes to start the communication with the group of receivers. Here a secret session key  $k$  is generated with which messages can be enciphered and sent to the receivers. Only the intended receivers can decrypt that key and hence the secret message. The secret session key is generated as follows:

- Randomly select  $r$ ,  $P_r$  belongs to  $Z_p$  and compute

$$S_{i0} = g^r, Y_{i0} = (S_{i1}/S_{i0}), c = g^{P_r}$$

- Extract the public group encryption key as

$$K = e(S_{i1}, S_{i2})e(S_{i2}, S_{i3}) \dots e(S_{i(n-1)}, S_{in})$$

- Compute

$$S = Ke(S_{in}, S_{i0})e(S_{i0}, S_{i1})$$

- Compute secret session key

$$k = S^r$$

- Broadcast the header

$$\text{Hdr} = (S_{i0}, Y_{i0}, c)$$

#### 5. Decryption

The Decryption algorithm is run by all the receivers' in order to decrypt the secret session key hidden in the header part and thereby decrypt the message. The decryption process is explained as follows.

- Each receiver  $U_{ij}$  publishes

$$Y_{ij} = (S_{ij+1}/S_{ij})S_{ij}$$

- Each receiver indexed by  $ij$  can decrypt the secret session key

$$d = S_{ij-1}^{(n+1)P_{ij}} Y_{ij}^{n-1} Y_{ij+1} \dots Y_{ij-2}$$

- By using  $d$  each receiver can extract the secret session key  $k$  by computing

$$k = e(d, c)$$

### IV. CONCLUSION

The difficulty of effectively, efficiently and securely broadcasting to a remote cooperative group happens in many freshly appearing networks. A foremost dispute in developing such network systems is to overwhelm the obstacles of the potentially restricted connection from the assembly to the sender, the unavailability of a completely trusted key generation center, and the dynamics of the sender. The living key administration paradigms cannot deal with these trials very effectively. In this paper, we circumvent these obstacles and close this gap by suggesting an innovative key management paradigm. This novel key management paradigm is a hybrid of customary broadcast encryption and assembly key agreement. In such a scheme, each constituent sustains a single public or secret key two. Upon seeing the public keys of the group members, an isolated sender can securely broadcast to any proposed subgroup selected in an ad hoc way. Following this form, we instantiate a method that is verified protected in the standard form. Even if all the proposed constituents collude, then they will not extract any helpful data from the conveyed messages. After the public assembly cipher key is extracted, both the computation overhead and the connection cost are independent of the group dimensions.

## REFERENCES

- [1] Chansu Yu, y Ben Lee , Hee Yong Youn, "Energy Efficient routing protocols for mobile ad hoc networks", *Wireless Communications and Mobile Computing*, John Wiley & Sons, Ltd, PP-959–973, 2003.
- [2] L. Zhang, Q. Wu, A. Solanas, and J. Domingo-Ferrer, "A scalable robust authentication protocol for secure vehicular communications," *IEEE Trans. Veh. Technol.*, vol. 59, no. 4, pp. 1606–1617, May 2010.
- [3] Judge, P., and Ammar, M. (2003). Security Issues and Solutions in Multicast Content Distribution: A Survey. *Network*, IEEE, Vol. 17(1), pp. 30-36.
- [4] Bruschi, D., and Rosti, E. (2002). Secure Multicast in Wireless Networks of Mobile Hosts: Protocols and Issues. *Mobile Networks and Applications*, Vol. 7(6), pp. 503-511.
- [5] Diffie, W., and Hellman, M. E. (1976). Multiuser cryptographic techniques. In *Proceedings of the AFIPS*, pp. 109-112.
- [6] M. Burmester and Y. Desmedt, "A secure and efficient conference key distribution system," *Adv. Cryptol.*, vol. 950, EUROCRYPT'94, LNCS, pp. 275–286, 1995.
- [7] M. Steiner, G. Tsudik, and M. Waidner, "Key agreement in dynamic peer groups," *IEEE Trans. Parallel Distrib. Syst.*, vol. 11, no. 8, pp. 769–780, Aug. 2000.
- [8] A. Sherman and D. McGrew, "Key establishment in large dynamic groups using one-way function trees," *IEEE Trans. Softw. Eng.*, vol. 29, no. 5, pp. 444–458, May 2003.
- [9] M. Abdalla, Y. Shavitt, and A. Wool, "Key management for restricted multicast using broadcast encryption," *IEEE/ACM Trans. Netw.*, vol. 8, no. 4, pp. 443–454, Aug. 2000.
- [10] B. M. Macq and J.-J. Quisquater, "Cryptology for digital TV broadcasting," *Proc. IEEE*, vol. 83, no. 6, pp. 944–957, Jun. 1995.
- [11] J. Lotspiech, S. Nusser, and F. Pestoni, "Anonymous trust: Digital rights management using broadcast encryption," *Proc. IEEE*, vol. 92, no. 6, pp. 898–909, Jun. 2004.

## Study of Local Binary Pattern for Partial Fingerprint Identification

Miss Harsha V. Talele<sup>1</sup>, Pratvina V. Talele<sup>2</sup>, Saranga N Bhutada<sup>3</sup>

<sup>1</sup>Department of Computer Science, SSBT's College of Engineering, Jalgaon, Maharashtra

<sup>2</sup>Department of Information Technology, MIT College of Engineering, Pune, Maharashtra

<sup>3</sup>Department of Information Technology, MIT College of Engineering, Pune, Maharashtra

**Abstract:** Fingerprints are usually used in recognition of a person's identity because of its uniqueness, stability. Today also the matching of incomplete or partial fingerprints remains challenge. The current technology is somewhat mature for matching ten prints, but matching of partial fingerprints still needs a lot of improvement. Automatic fingerprint identification techniques have been successfully adapted to both civilian and forensic applications. But this Fingerprint identification system suffers from the problem of handling incomplete prints and discards any partial fingerprints obtained. Level 2 features are very efficient if the quality of achievement decreases the number of level 2 features will not be enough for establishing high accuracy in identification. In such cases pores (level 3 features) can be used for partial fingerprint matching with the help of suitable technique local binary pattern features. Local binary pattern feature is used to match the pore against with full fingerprints. The first step involves extracting the pores from the partial image. These pores act as anchor points and sub window (32\*32) is formed surrounding the pores. Then rotation invariant LBP histograms are obtained from the surrounding window. Finally chi-square formula is used to calculate the minimum distance between two histograms to find best matching score.

**Keywords:** Local Binary Pattern, Pores, Partial Fingerprint, Chi-Square

### I. INTRODUCTION

Fingerprint can be used in forensic science to support criminal investigations, biometric systems such as civilian and commercial identification devices for person identification. It is believed with strong evidences that each fingerprint is unique. Each person has his own fingerprints with the permanent uniqueness. So fingerprints have being used for identification and forensic investigation for a long time. A fingerprint is composed of ridges and valleys on the surface of a fingertip. A fingerprint is a pattern of curving line structures called ridges, where the skin has a higher profile than its surroundings, which are called the valleys. In most fingerprint images, the ridges are black and the valleys are white. The fingerprint of an individual is unique and remains unchanged of over a lifetime. Automatic fingerprint identification is one of the most reliable biometric technologies. This is because of the well known fingerprint distinctiveness, persistence, ease of acquisition and high matching accuracy rates. Fingerprints are unique to each individual and they do not change over time. Even identical twins do not carry identical fingerprints. The uniqueness can be attributed to the fact that the ridge patterns and the details in small areas of friction ridges are never repeated.

The fingerprint identification problem can be grouped into two sub-domains: one is fingerprint verification and the other is fingerprint identification. In addition, different from the manual approach for fingerprint recognition by experts, the fingerprint recognition here is referred as Automatic Fingerprint Recognition System. Fingerprint verification is to verify the authenticity of one person by his fingerprint. The user provides his fingerprint together with his identity information like his ID number. The fingerprint verification system retrieves the fingerprint template according to the ID number and matches the template with the real-time acquired fingerprint from the user. The noise and distortion of captured fingerprints and the inaccurate of extracted features make fingerprint matching a very difficult problem. With the advent of high-resolution fingerprint imaging techniques and the increasing demand for high security, sweat pores have been recently attracting increasing attention in automatic fingerprint recognition.

The main modules of a fingerprint identification system (Figure 1) are:

1. Fingerprint sensing in which the fingerprint of an individual is acquired by a fingerprint scanner to produce digital representation.
2. In preprocessing the input fingerprint is improved and modified to simplify the task of feature extraction.

3. In feature extraction the fingerprint is further processed to generate discriminative properties.
4. Then in matching the feature vector of the input fingerprint is compared against one or more existing templates. Then score is calculated. The templates of approved users of the biometric system, also called clients, are usually stored in a database. Clients fingerprints can be checked against stored fingerprints. [5]

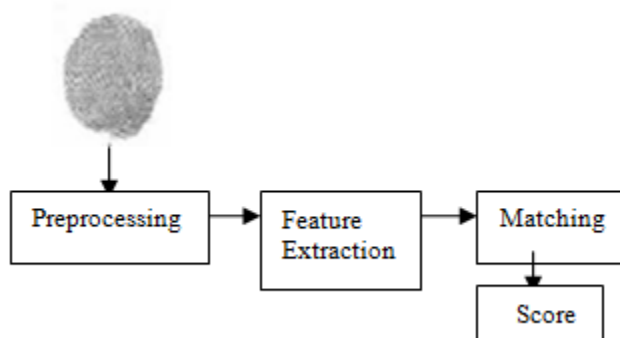


Figure 1: Main Module of Fingerprint Identification System

The need for recognition of partial fingerprints is increasing in both forensic and civilian applications. In forensics, latent fingerprints lifted from crime scenes are often noisy and broken, thus the usable portions are small and partial. In civilian applications, the invention of small hand-held devices, such as mobile phones, PDAs, and miniaturized fingerprint sensors present considerable demands on partial fingerprints processing. However, fingerprint scanners with a sensing area smaller than 1.0"x1.0", which is considered to be the average fingerprint size as required by FBI specifications can only capture partial fingerprints. A method for partial fingerprint recognition, the method comprising the steps of extracting features including ridge orientations, valley images, minutiae, and pores from at least two fingerprint fragments, aligning the fingerprint fragments, matching the pores and minutiae on the fingerprint fragments after applying estimated alignment transformation, calculating a final matching score based on a pore matching score and a minutiae matching score, identifying a person based on a result of the final matching score.

Matching partial fingerprints to a pre-filed complete fingerprint is usually encountered in forensic applications. In many cases, the partial fingerprint images that lifted from crime scenes are broken and unclear. Thus, the useable parts of the partial fingerprint images are restricted in small areas. Matching the partial fingerprint to the pre-filed images in database usually has the following problems:

1. The partial fingerprints obtained from a crime scene are normally small and noisy.
2. The number of minutia points available in such prints is less and further reduces the discriminating power.
3. Difficult to discover correspondence of obtained partial fingerprint to one of the fingers even if ten-prints are available.
4. Loss of core and delta is highly likely, so a robust algorithm that is independent of relying on these singularities is required.
5. Distortions like elasticity and humidity are introduced due to characteristics of the human skin.

The major challenges faced in partial fingerprint matching are the absence of sufficient level 2 feature minutiae and other structures such as core and delta. Thus common matching methods based on alignment of singular structures would fail in case of partial prints. Pores (level 3 features) on fingerprints have proven to be discriminative features and have recently been successfully working in automatic fingerprint identification systems. [7]. The Purpose of our paper is partial fingerprint identification is done by using level 3 feature pores with the help of local binary pattern to improve the matching accuracy.

## II. LITERATURE SURVEY

Level 1 feature, or patterns, is the macro details of the fingerprint such as ridge flow and pattern type. Level 1 level of detail cannot be used to individualize, but it can help narrow down the search. The line scan algorithm is very powerful algorithms that can be used for both full and partial fingerprints. The most notable advantages of these algorithms are the high accuracy in the case of partial fingerprints. At this time, the major drawback of developed algorithms is lack of pre-classification of examined fingers. Therefore, we use minutiae classification scheme to reduce the reference base for given tested finger. In 1892, Galton introduced Level 2 features by defining minutia points as either ridge endings or ridge bifurcations on a local ridge. Level 2 features, unlike Level 1 features, have individualization power and contribute the most in fingerprint matching. On average, a fingerprint generally contains 75-175 minutiae. At times, however, only a small number of

minutiae are available in the captured fingerprint image and the extraction of additional Level 3 features may be necessary.

Locard introduced the science of poroscopy, the comparison of sweat pores for the purpose of personal identification in 1912. Locard confirmed that like the ridge characteristics, the pores are also permanent, immutable, and unique, and are useful for establishing the identity, particularly when a sufficient number of ridges are not available. Then Locard added the variation of sweat pores and proposed four criteria which can be used for pore based identification. The four criteria are the size of the pores, the form of the pores, and the position of the pores on the ridges, and the number or frequency of the pores. It was observed that the number of pores along a centimeter of ridge varies from 9 to 18, or 23 to 45 pores per inch and 20 to 40 pores should be sufficient to determine the identity of a person. Partial fingerprint identification is done by level 3 features based on pores extraction. There are three methods for partial fingerprint identification:

**1. State of the art pore matching method:**

First, gray scale images from the sensor are converted to binary format. The binary image is stored for later use and then processed further, resulting in a skeleton image. Finally, the skeleton image is processed to improve its functionality from a minutia or ridge analysis viewpoint. During the skeleton processing stage, its quality is improved by eliminating “ridge noise” components produced by pores and also by syntactic processing. The state-of-the-art pore matching method was recently proposed by Jain et al. In this method, the fingerprint images were first aligned based on the minutia features on them by using a string-matching algorithm. Then they were matched by using the iterative closest point (ICP) algorithm which is capable to handle sets of points with different numbers of points and can compensate for non-linear deformation between them.

**2. Adaptive pore model method:**

Manually marked and cropped hundreds of pores in several fingerprint images, including both open and closed pores. Based on the appearance of these real pores, we summarized three types of representative pore structures. Pore extraction results include Pores should reside on ridges only. To implement this constraint, we use the binary ridge image as a mask to filter the extracted pores. Pores should be within a range of valid sizes. We measure the size of a pore by counting the pixels in its region. The mean intensity of a true pore should be large enough.

**3. Dots and incipients for partial fingerprint matching method:**

A ridge unit may stay isolated that looks like a dot between normal ridges and thin and often fragmented ridges may also appear between normal ridges, known as incipient. As a result, our extraction algorithm for dots and incipients is designed based on ridge information and local orientation fields. The key component of our extraction algorithm is to estimate the local phase symmetry for ridge pixels. Because dots and incipients are isolated. They present slightly higher local symmetry than normal ridges. As a result, we employ wavelets based on complex valued Log Gabor functions to measure the local phase symmetry. Once local symmetry is estimated, it is multiplied with the skeletonized valley image. This is because dots and incipient ridges only occur in valleys between normal friction ridges.

However all these methods require high quality fingerprints so we use an automatic extraction of Local Binary Pattern of a pore for partial fingerprint identification.

### **III. METHODOLOGY**

Pores appear on fingerprint images as drops on the ridge. Pores are extracted from partial fingerprint image by using marker controlled watershed segmentation method. The concept of watershed is used in the field of topography. It determines a drop of water which is fall into a particular region. The watershed transform produces closed and adjacent contours including all image edges. The watershed produces a severe over segmentation.

**1. Marker Controlled Watershed Segmentation:**

The marker-controlled watershed segmentation method is strong and flexible for segmentation of objects with closed contours, where the boundaries are represented as ridges. Markers are placed inside an object of interest. Internal markers are used to limit the number of regions by specifying the objects of interest and external markers are those pixels we are confident to belong to the background. After segmentation, the boundaries of the watershed regions are arranged on the desired ridges, thus separating each object from its neighbors.

## 2. Creating Markers:

The marker image used for watershed segmentation is a binary image consisting of either single marker points or larger marker regions, where each connected marker is placed inside an object of interest. Each initial marker has a one-to-one relationship to a specific watershed region, thus the number of markers will be equal to the final number of watershed regions. After segmentation, the boundaries of the watershed regions are arranged on the desired ridges, thus separating each object from its neighbors. The markers can be manually or automatically selected, but high throughput experiments often use automatically generated markers to save human time and resources. Various methods have been used for computing internal and external markers, many of which involve the linear filtering, non linear filtering and morphological processing.

## 3. Pore Extraction:

We used simple algorithm to create foreground and background markers using Morphological image reconstructions. Read the original image as shown in Figure 3.1 (a). Then the watershed transform of the gradient fingerprint image is computed without any other processing. Watershed lines obtained which result in over segmented image as shown Figure 3.1 (b). Each connected region contains one local minimum in the corresponding gradient image. By computing the location of all regional minima in the fingerprint image as shown in Figure 3.1(c), we found that most of the regional minima are very shallow and represent detail which is irrelevant to our segmentation problem. The extraneous minima is eliminated by computing the set of low spots in the image that are deeper by a height threshold = 2. Then the markers are superimposed on the original fingerprint image. Next, background markers are created. The approach followed here is to mark the background by finding pixels that are exactly midway between the internal markers. This is done by computing the watershed transform of the internal marker image. The resulting watershed ridge lines appear in midway between the pores and hence they serve well as external markers. The marker image is shown in Figure 3.1 (d)

The internal and external markers are then used to modify the gradient fingerprint image using a procedure called minima imposition. The minima imposition technique modifies a fingerprint image so that regional minima occur only in marked locations. Other pixel values are pushed up as necessary to remove all other regional minima. The gradient fingerprint image is then modified by imposing regional minima at the locations of both the internal and the external markers. Finally watershed transform of the marker-modified gradient fingerprint image is computed. After superimposing the watershed ridgelines on the original fingerprint image, a much improved pore extraction is obtained as shown in Figure 3.1 (e)

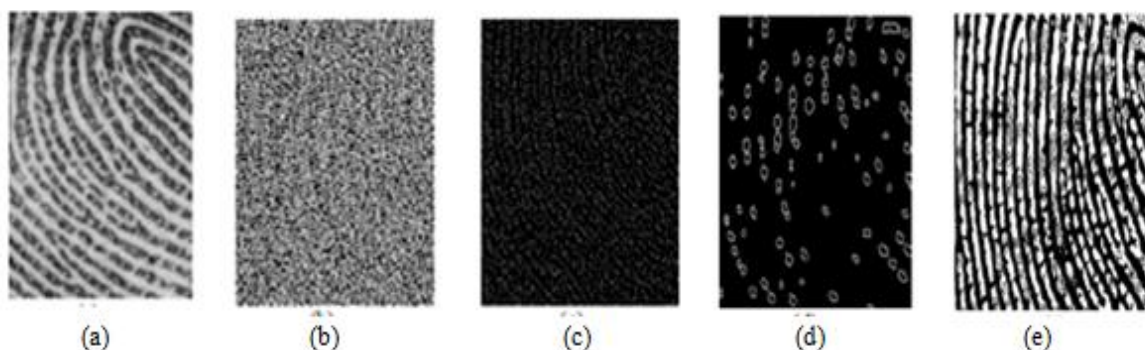


Figure 3.1: Pore extraction results (a) Original image (b) Over segmented image (c) Regional minima (d) Marker image (e) Extracted pores

### Algorithm:

1. Read the original image.
2. Develop gradient fingerprint images using appropriate edge detection function.
3. Compute the watershed transform of the gradient fingerprint image without any other processing which gives over segmented image.
4. Watershed lines obtained from gradient fingerprint images. Use the obtained watershed line as external markers by calculating regional minima.
5. Superimpose the foreground marker image on binarized fingerprint image.
6. Clean the edges of the markers using edge reconstruction.
7. Compute the background markers.
8. Compute the watershed transform of the function.[2]

#### IV. IMPLEMENTATION

A common challenge to the pore-based fingerprint recognition systems is how to accurately and robustly extract pores from fingerprint images. Based on the position on the ridges, pores are often divided into two categories: open and closed. A closed pore is entirely enclosed by a ridge, while an open pore intersects with the valley lying between two ridges as shown in Figure 4.1.

##### 1. Local Binary Pattern:

The local binary pattern (LBP) operator was first introduced by Ojala et al. 1996. LBP is a powerful method of texture description. The original 3X3 neighborhood is thresholded by the value of the center pixel. The values of the pixels in the thresholded neighborhood are multiplied by the binomial weights given to the corresponding pixels. Finally, the values of the eight pixels are summed to obtain the LBP number for this neighborhood. [1]

The standard version of the LBP of a pixel is formed by thresholding the 3X3 neighborhood of each pixel value with the center pixel's value. Let  $g_c$  be the center pixel gray level and  $g_p$  ( $p = 0,1,..7$ ) be the gray level of each surrounding pixel. Fig.1 illustrate the basic LBP operation. If  $g_i$  is smaller than  $g_c$ , the binary result of the pixel is set to 0 otherwise set to 1. All the results are combined to get 8 bit value. The decimal value of the binary is the LBP feature.

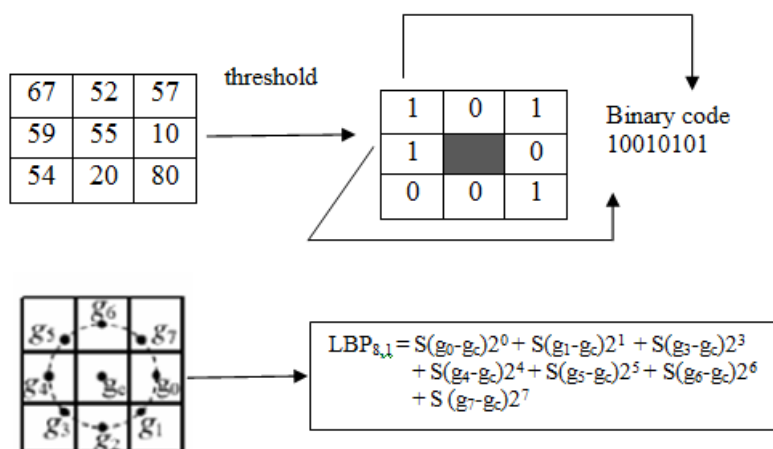


Figure 4.1: LBP operator of a pixel circular neighborhood with  $r=1, p=8$

Let  $LBP_{p,r}$  denote the LBP feature of a pixel 's' circularly neighborhoods, where  $r$  is the radius and  $p$  is the number of neighborhood points on the circle. From Figure 4.1 we can write,

$$LBP(P, R) = \sum_{p=0}^{p-1} S(g_p - g_c) 2^p$$

The concept of uniform patterns is introduced to reduce the number of possible bins. Any LBP pattern is called as uniform if the binary pattern consists of at most two bitwise transitions from 0 to 1 or vice versa. For example if the bit pattern 11111111 (no transition) or 00110000 (two transitions) are uniform where as 10101011 (six transition) are not uniform.

##### 2. Derivation of LBP Operator:

Let us define texture  $T$  as the joint distribution of the gray levels of  $P$  ( $P > 1$ ) image pixels:

$$T = t(g_c, g_0, \dots, g_{p-1})$$

where gray value  $g_c$  corresponds to the gray value of the center pixel of the local neighborhood and  $g_p$  ( $P=0,1,..P-1$ ) correspond to the gray values of  $P$  equally spaced pixels on a circle of radius  $R$  ( $R > 0$ ). that form a circularly symmetric neighbor set.

Without losing information, the gray value of the center pixel ( $g_c$ ) from the gray values of the circularly symmetric neighborhood  $g_p$  gives:

$$T = t(g_c, g_0 - g_c, g_1 - g_c, \dots, g_{p-1} - g_c)$$

Next, we assume that differences  $g_p - g_c$  are independent of  $g_c$ , which allows us to factorize the above equation :

$$T = t(g_c) t(g_0 - g_c, g_1 - g_c, \dots, g_{p-1} - g_c)$$

Since  $t(g_c)$  describes the overall luminance of an image, which is unrelated to local image text so it can be ignored and therefore does not provide useful information for image analysis :

$$T = t(g_0 - g_c, g_1 - g_c, \dots, g_{p-1} - g_c)$$

Signed differences  $g_p - g_c$  are not affected by changes in mean luminance; hence, the joint difference distribution is invariant against gray-scale shifts. We achieve invariance with respect to the scaling of the gray scale by considering just the signs of the differences instead of their exact values:

$$T = t( s(g_0 - g_c), s(g_1 - g_c), \dots, s(g_{p-1} - g_c) )$$

Where,

$$S(x) = \begin{cases} 1, & \text{if } X \geq 0 \\ 0, & \text{Otherwise} \end{cases}$$

By assigning a binomial factor  $2^p$  for each sign  $S(g_p - g_c)$ , we transform the above equation into a unique  $LBP_{P,R}$  number that characterizes the spatial structure of the local image :

$$LBP(P,R) = \sum_{p=0}^{p-1} S(g_p - g_c) 2^p \quad S(x) = \begin{cases} 1, & \text{if } X \geq 0 \\ 0, & \text{Otherwise} \end{cases}$$

The name ‘‘Local Binary Pattern’’ reflects the functionality of the operator, i.e., a local neighborhood is thresholded at the gray value of the center pixel into a binary pattern.[3]

### 3. LBP Feature Extraction:

However, adjacent LBP descriptors are not overlapped. Firstly, given an image, we split the image into several non-overlapped blocks. Then we extract the pores from fingerprint image by using marker controlled watershed segmentation method. Extracted pores are used as anchor points for mapping to full image. For each pore, a sub window is formed centered at that pore. Then for each block the feature histogram is calculated using local binary pattern. Through comparing the pixels between the neighbor points and central point, different weights are given according to different locations. We usually describe the neighborhood by a couple (P,R), where P denotes the number of the sampled pixels in the area and R denotes the radius of neighbor. It is obvious that different types of images contain different feature details. Thus, it is the key issue that how to deal with the details in order to get good recognition performance and high efficiency. Specifically, we define the different weight on each block. Then we enhance the histogram vector according to the weight so as to strengthen the key information and eliminate the ineffective information. The single block strategy that segments a whole image symmetrically which obtain most of the features but still there are some problems.

The single-blocked strategy exacts the features in a easy way which leads to the decreasing of the recognition accuracy. Thus we can introduce the multi-blocked strategy that is to partition the same image into different blocks, and take the LBP feature vectors exacted by different partition into consideration. After that we deal with the problems bring by the single-blocked efficiently. In multi-blocked way, we need to combine the enhanced histogram in order to get the multi-blocked enhanced histogram. The resultant histogram is stored in the template of the partial image. Thus finally in the template for the partial image we have a set of histograms corresponding to all pores.

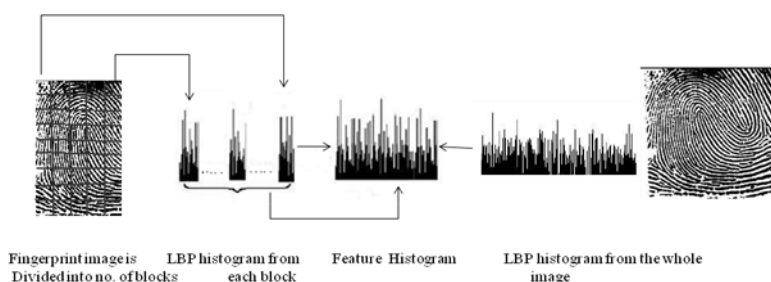


Figure 4.2: A fingerprint image is divided into number of blocks from which LBP histograms are extracted and concatenated into a single histogram

In the case of LBP, the matching of an image pair is done by computing the distance between the two LBP feature histograms of training and test samples. The larger the distance between the histograms the more dissimilar are the images. The algorithm for matching a partial and full image pair is based on distance between two lbp feature histograms. Minimum distance corresponds to best match. To get distance between two histograms, chi-square formula is used.

The Chi-Square distance between the two histograms S and M can be defined as:

$$\chi^2(S, M) = \sum_{i=1}^n \frac{(S_i - M_i)^2}{(S_i + M_i)}$$

Where  $S_i$  and  $M_i$  denote the  $i^{\text{th}}$  bin value for two histograms respectively and  $n$  is the number of elements in the histogram. Chi square distance is an effective measurement of similarity between a pair of histograms, hence it is suitable for nearest neighbor. The “ $\chi$ ” is the Greek letter chi; the “ $\sum$ ” is a sigma. Here we find out the distance between observed value and expected value and then sum all the value. For identifying a partial image in the set of full images, match score corresponding to each (partial image, full image) pair is obtained. The full fingerprint with maximum match score is identified as the best match.

Let  $P_p$  and  $F_p$  are list of histogram for pores in partial and full fingerprint image respectively.

for  $p$  in  $P_p$

dis = min(chi-square-distance( $p$ ,  $F_p$ ))

if dis < threshold

$p$  is matched with distance dis

else  $p$  is non-matched

NIST special database 30 is used. It include all ten rolled fingerprints and the plain impressions at the bottom of the card scanned at both 500 dpi and 1000 dpi. This database has 36 paired fingerprint cards scanned at both resolutions and segmented into individual fingerprint images. Each partial fingerprint was matched with full fingerprint and then match score was calculated. [4]

Match Score = No. of Matched pores / Total No. of pores

Match scores represent the percentage of total number of pore matched out of total number of pores in partial image, it was necessary to choose threshold such that the match score was sufficiently high for all successful matches. The true detection rate  $RT$  means the ratio of the number of detected true pores to the number of all true pores and the false detection rate  $RF$  means the ratio of the number of falsely detected pores to the number of all detected pores were calculated on the fingerprint images.

## V. CONCLUSION

We present the partial fingerprint identification using local binary pattern features of pores. LBP feature provide good identification rate rather than other methods. This pore extraction method can detect pores more accurately and also help to improve the verification accuracy of pore based fingerprint identification system. The matching of partial and full image pair is based on distance between two local binary pattern feature histogram. For that we use chi-square formula to get the best result. Future work would involve making the fingerprint enhancement technique more efficient and effective for partial fingerprint identification. It also provide the fundamental issues of fingerprint permanence and improve the more accuracy of fingerprint recognition algorithms. Partial fingerprint identification also need to verify with different database which consists of large data and address robust feature extraction methods in case of scars, warts.

## REFERENCES

- [1] S.Malathi, Dr.C.Meena “An Efficient Method for Partial Fingerprint Recognition based on Local Binary Pattern” IEEE International Conference on Communication Control and Computing Technologies, pages: 569-572, Oct 2010.
- [2] S.Malathi, S.Uma maheswari, Dr.C.Meena “Fingerprint Pore Extraction Based On Marker Controlled Watershed Segmentation” in Proceedings of Second International Conference of Computer Automation and Engineering published by IEEE, pages: 337-340, February 2010 .
- [3] Timo Ojala, Matti Pietikinen, and Topi Menp “Multiresolution gray-scale and rotation invariant texture classification with local binary patterns” IEEE Transactions on Pattern Analysis and Machine Intelligence, pages: 971-987, 2002.
- [4] American National Standards for Biometrics (NIST), <http://fingerprint.nist.gov/standard/>, May/2009.
- [5] Abhishek Rawat “A hierarchical fingerprint matching system” July 2009.
- [6] Chu He, Timo Ahonen and Matti Pietikäinen “A Bayesian Local Binary Pattern Texture Descriptor” IEEE International Conference on Pattern Recognition, pages: 1-4, Dec 2008.
- [7] S. Mil'shtein, A. Pillai, A. Shendye, C. Liessner, and M. Baier “Fingerprint Recognition Algorithms for Partial and Full Fingerprints” IEEE Conference on Technologies for Homeland Security, pages: 449-452, May 2008.

# A Novel Acknowledgement based Intrusion Detection System for MANETs

Parveen Pathan<sup>1</sup>, V. Jhansi Lakshmi<sup>2</sup>

<sup>1</sup> M. Tech (CSE), MVR College of Engineering and Technology, A.P., India.

<sup>2</sup>Asst. Professor, Dept. of Computer Science & Engineering, MVR College of Engineering and Technology, A.P., India.

**Abstract:** In Mobile Ad Hoc Networks(MANETs), a set of interacting nodes should cooperatively implement the routing functions to enable end-to-end communication along dynamic paths composed by multi-hop wireless links. Several multi-hop routing protocols have been proposed for ad hoc networks, and most popular ones include: Dynamic Source Routing (DSR), Optimized Link-State Routing (OLSR), Ad Hoc On-Demand Distance Vector (AODV) and Destination- Sequenced Distance-Vector (DSDV). Most of these protocols rely on the assumption of a trustworthy cooperation among all participating nodes; unfortunately, this may not be a realistic assumption in real hosts. Malicious hosts could exploit the weakness of MANET to launch various kinds of attacks. Node mobility on ad hoc network cannot be restricted. As results, many Intrusion Detection System(IDS) solutions have been proposed for the wired network, which they are defined on strategic points such as switches, gateways, and routers, can not be implemented on the MANET. Thus, the wired network IDS characteristics must be modified prior to be implemented in the ad hoc network. Thus an IDS should be added to enhance the security level of MANETs. If MANET can detect the attackers as soon as they enter the network, we will be able to completely eliminate the potential vulnerabilities caused by compromised nodes at the first time. IDSs usually act as the second layer in MANETs. This paper presents an novel IDS for MANETs which is based on acknowledgements.

**Keywords:** ACK, Collision, Digital signature, IDS, MANET.

## I. INTRODUCTION

Mobile Adhoc Networks (MANETs) is collection of wireless mobile nodes that are free to move in any directions at any speed. Mobile hosts are equipped with the wireless transmitter and a receiver that communicate directly with each other or forward message through other nodes. One of the major advantages of the mobile networks is to allow different nodes for data communications and still maintain their mobility. However, this communication is limited to the range of different transmitters. It means that two hosts cannot communicate with each other when the distance between the two hosts is beyond the communication range of their own. MANET solves this problem by allowing intermediate hosts to relay data transmissions. This is achieved by dividing MANET into two types of networks such as single-hop and multihop[1]. In a single-hop network, all the nodes within the same radio range communicate directly with each other. But in a multihop network, the nodes rely on other intermediate nodes to transmit if the end point node is out of their radio communication range [2].

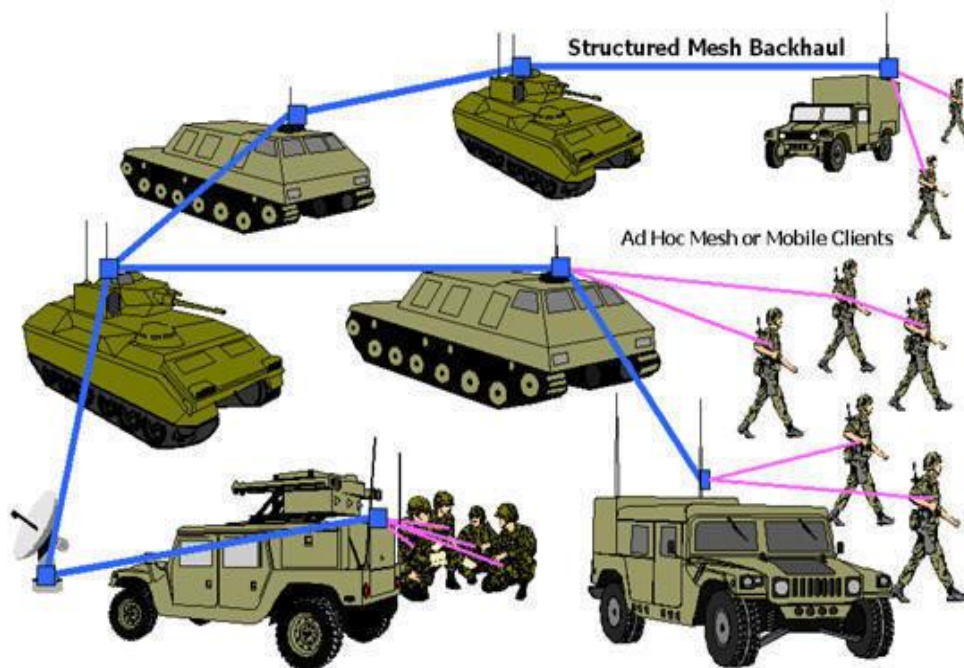


Fig. 1: An example Mobile Ad Hoc Network

MANET is capable of operating a self-maintaining and self-organizing network without the need of any fixed infrastructure. Ad hoc networks does not require expensive base stations of infrastructure dependent network (single-hop wireless networks)[3]. As MANETs have different characteristics from the wired networks and even from single-hop wireless networks, there are more number of new challenges interrelated to security issues that need to be addressed. Initially, MANET was initially designed for military applications, but, in recent years, has found new usage. For example, search and rescue mission, data collection, virtual classes and conferences where computers, laptops, PDA or other mobile devices are in wireless communication. Since ad hoc network is being used wide spread, security has become a very important issue. In general, MANETs are vulnerable based on the basic characteristics such as changing topology, open medium, absence of infrastructure, restricted power supply, and scalability. In such case, Intrusion detection can be defined as the process of monitoring activities in a system which can be a computer or a network. The mechanism that performs this task is known an Intrusion Detection System (IDS) [4].

## II. RELATED WORK

In [5], the authors suggested dynamic source routing protocol for the mobile adhoc networks. Because in the MANETs the mobile hosts are randomly moved. Due to the limited range of transmission one mobile host needs other mobile node to forward the data packets. The dynamic source routing protocol adjusts quickly to routing changes when node movement is frequent. But it requires little overhead during the frequent node movement. In [1], the authors proposed an Acknowledgment-based Approach to detect the routing misbehavior of the mobile adhoc networks. TWOACK is necessary to work on the routing protocols such as Dynamic Source Routing (DSR). The main idea of the two ACK method is when a node forwards a data packet, effectively through the next hop, the next-hop link of the destination node will send back a special two- hop ACK called 2ACK to specify that the data packet has been received successfully. In [6], the authors proposed a command filtering framework to allow or reject the human-issued commands so that unwanted executions are never performed. In this concept instead of using the client- server model the peer-to-peer (P2P) communication between mobile robots is used.

In [7], the authors proposed Collaborative Security Architecture for detecting the Black hole attack in the mobile adhoc networks. In this technique, if the node forwards the data packet to the watchdog node identifies whether the next node also forwards the data packet. If the next node does not forwards that data packet the watchdog node makes it is as the misbehavior node. In [8], the authors proposed Intrusion detection system for the MANETs. In the absence of the fixed infrastructure to provide communications, MANET is an attractive technology for some applications like environmental monitoring, conferencing, military applications. In [9], the authors suggested a model to detect the node misbehavior in the mobile adhoc networks. Based on

the Sequential Probability Ratio Test, the authors develop a model to describe how nodes can differentiate between the routes that include misbehaving nodes and routes that do not. For the detection of the misbehaving hosts in the infected routes a centralized and a localized approach is used. In [10], the authors suggested secure routing and the intrusion detection system in the adhoc networks. The authors present a proof-of-concept implementation of a secure routing protocol based on AODV over IPv6 for the Intrusion Detection and Response system for ad-hoc networks.

### III. PROPOSED WORK

#### 1. Problem Definition

Our proposed method is designed to tackle false misbehavior and receiver collision.

##### Receiver Collisions

Node A sends Packet 1 to node B, it tries to overhear if node B forwarded that packet to another node C; meanwhile, node X is forwarding Packet 2 to the node C. In such case, node A overhears that the node B has successfully forwarded Packet 1 to node C but failed to detect that the node C did not receive this packet due to a collision between Packet 1 and Packet 2 at node C. This is shown in figure 2.

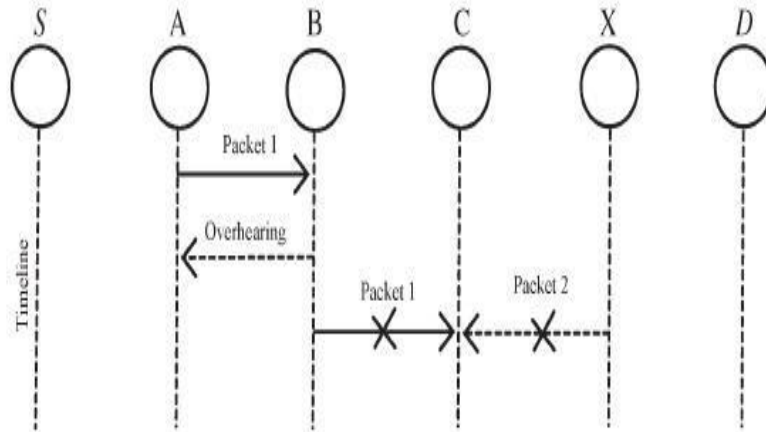


Fig. 2: Receiver Collision

##### False Misbehavior Report

Node A successfully overheard that the node B forwarded Packet 1 to node C, node A still reported node B as misbehaving. Due to the open medium and remote distribution of typical MANETs, the attackers can easily capture and compromise one or two nodes to achieve this false misbehavior report attack. This is shown in figure 3.

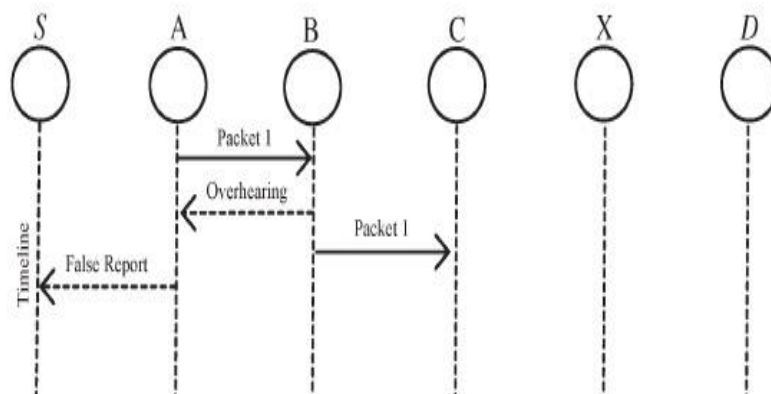


Fig. 3: False Misbehavior Report

Our proposed work is consisted of three major components, namely, ACK, secure ACK, and misbehavior report authentication(MRA).

## 2. ACK

ACK is essentially associate end-to-end acknowledgment scheme used in our work. It acts as a district of the hybrid scheme in this work, attending to scale back network overhead once no network misconduct is detected. In Figure 4, in ACK mode, node S initial sends out associate ACK information packet  $P_{sad1}$  to the destination node D. If all the intermediate nodes on the route between the nodes S and D square measure cooperative and node D with success receives  $P_{sad1}$ , the node D is needed to remand associate ACK acknowledgment packet  $P_{sak1}$  on a similar route however in a very reverse order. Inside a predefined fundamental quantity, if the node S receives  $P_{sak1}$ , then the packet transmission from node S to the node D is winning. Otherwise, node S can switch to S-ACK mode by causing out an associate S-ACK information packet to sight the misbehaving nodes within the network route.

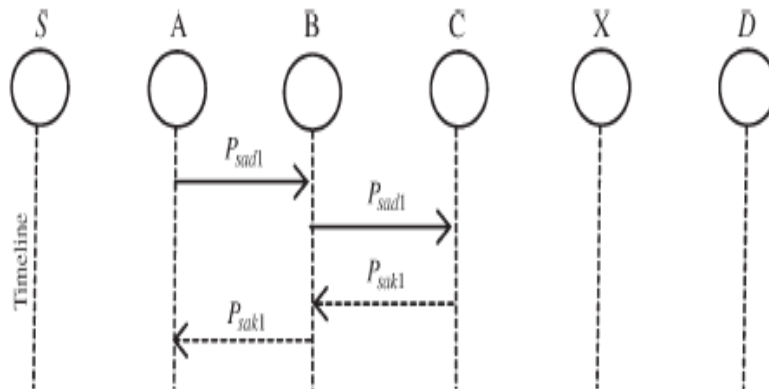


Fig. 4: ACK scheme

## 3. S- ACK

S-ACK scheme is an improved version of the TWOACK scheme. The principle is to let each three consecutive nodes work in a group to detect the misbehaving nodes. For each three consecutive nodes in the network route, the third node is required to send the S-ACK acknowledgement packet to the first node. The intention of introducing the S- ACK mode is to detect misbehaving nodes in the presence of receiver collision.

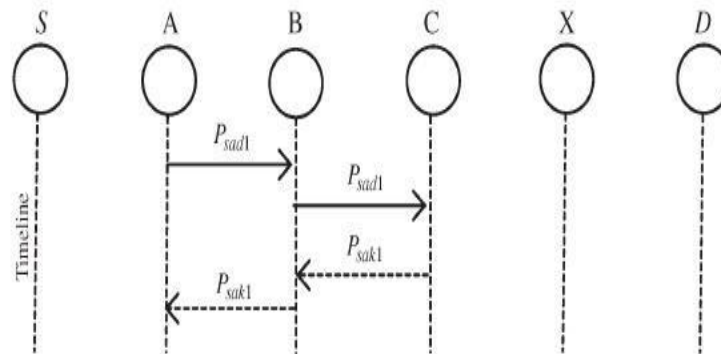


Fig. 5: Secure Acknowledgement

## 4. MRA

Unlike the TWOACK IDS, where the source node immediately trusts the misbehavior report, our work requires the source node to switch to MRA mode and confirm this misbehavior report. This is a vital step to detect such false misbehavior. The MRA field is designed to resolve the weakness of the Watchdog when it fails to detect misbehaving nodes with the presence of the false misbehavior. The false misbehavior report can be generated by the malicious attackers to falsely report innocent nodes as malicious. The core of the MRA field is to authenticate whether the destination node has received the reported missing packet through a different network route. To initiate the MRA mode, the source node first searches its local knowledge base and then seeks for an alternative route to the destination host. If there is no other that exists, then the source node starts a DSR routing request to find another route.

## 5. Digital Signature

Our proposed work is an acknowledgment-based IDS. They all rely on the acknowledgment packets to detect misbehaviors in the network. Thus, it is extremely important to ensure that all ACK packets are authentic and untainted. In order to ensure the integrity of the detection system, our work requires all acknowledgment packets to be digitally signed before they are sent out and verified until they are accepted.

## IV. CONCLUSION

MANET is a collection of wireless mobile nodes forming a network without the need of existing infrastructure. There are various challenges that are faced in the MANET environment. These are mostly due to the lack of the resources of these networks. They are usually set up in situations of emergency, for temporary operations or in a case if there are no resources to set up elaborate networks. The solutions for traditional networks are usually not sufficient to provide efficient Ad-hoc operations. The wireless nature of network communication and lack of any security infrastructure raise several security problems. This paper focuses on the acknowledgment based IDS for MANETs. The proposed method provides higher malicious- behavior-detection rates in certain circumstances while does not greatly affect the network performances.

## REFERENCES

- [1] K. Liu, J. Deng, P. K. Varshney, and K. Balakrishnan, "An acknowledgment-based approach for the detection of routing misbehaviour in MANETs," *IEEE Trans. Mobile Comput.*, vol. 6, no. 5, pp. 536–550, May 2007.
- [2] EAACK – A Secure Intrusion Detection System for MANETs Elhadi M. Shakshuki, Senior Member, IEEE, Nan Kang and Tarek R. Sheltami, Member, IEEE
- [3] R. Akbani, T. Korkmaz, and G. V. S. Raju, "Mobile Ad hoc Network Security," in *Lecture Notes in Electrical Engineering*, vol. 127. New York: Springer-Verlag, 2012, pp. 659–666.
- [4] Investigating Intrusion and Detection Systems in MANET and Comparing IDSs for Detecting Misbehaving Nodes Marjan Kuchaki Rafsan, Ali Movaghar and Faroukh Koroupi, *World Academic of Science Engineering and Technology* 44 2008.
- [5] D. Johnson and D. Maltz, "Dynamic Source Routing in ad hoc wireless networks," in *Mobile Computing*. Norwell, MA: Kluwer, 1996, ch. 5, pp. 153–181.
- [6] J.-S. Lee, "A Petri net design of command filters for semiautonomous mobile sensor networks," *IEEE Trans. Ind. Electron.*, vol. 55, no. 4, pp. 1835–1841, Apr. 2008.
- [7] A. Patcha and A. Mishra, "Collaborative security architecture for black hole attack prevention in mobile ad hoc networks," in *Proc. Radio Wireless Conf.*, 2003, pp. 75–78.
- [8] B. Sun, "Intrusion detection in mobile ad hoc networks," Ph.D. dissertation, Texas A&M Univ., College Station, TX, 2004.
- [9] N. Kang, E. Shakshuki, and T. Sheltami, "Detecting misbehaving nodes in MANETs," in *Proc. 12th Int. Conf. iiWAS*, Paris, France, Nov. 8–10, 2010, pp. 216–222
- [10] A. Patwardhan, J. Parker, A. Joshi, M. Iorga, and T. Karygiannis, "Secure routing and intrusion detection in ad hoc networks," in *Proc. 3rd Int. Conf. Pervasive Comput. Commun.*, 2005, pp. 191–199.



# International Journal of Modern Engineering Research (IJMER)

Volume : 4 Issue : 9 (Version-3)

ISSN : 2249-6645

September- 2014

## Contents :

- |  |       |
|--|-------|
| <b>A Novel Switch Mechanism for Load Balancing in Public Cloud</b><br><i>Kalathoti Rambabu, M. Chandra Sekhar</i>  | 01-05 |
| <b>Methodology used for improving overall equipment effectiveness by Implementing Total Productive Maintenance in plastic pipe manufacturing industries</b><br><i>Dashrath kumar, Er. Dinesh Kumar, Er. Rohit Rawat</i>                            | 06-12 |
| <b>Design and Fabrication of Vapour Absorption Refrigeration System [Libr-H2O]</b><br><i>Mohd Aziz Ur Rahaman, Md. Abdul Raheem Junaidi, Naveed Ahmed, Mohd. Rizwan</i>  | 13-18 |
| <b>An Adaptive Routing Algorithm for Communication Networks using Back Pressure Technique</b><br><i>Khasimpeera Mohammed, K. Kalpana</i>   | 19-23 |
| <b>Heat Ventilation &amp; Air- Conditioning System with Self-Tuning Fuzzy PI Controller</b><br><i>Mir Munawar Ali, Mohd Aamer Khan, Mohammed Shafi, Mohd Abdul Omer Khan, Md Azam Ali Farooky, Syed Azam, Syed Khasim, Shaik Wasei Eizaz Ahmed</i> | 24-35 |
| <b>A Chord based Service Discovery Approach for Peer- to- Peer Networks</b><br><i>Yaminipurnatilak Jakka, A. Sudarsan Reddy</i>  | 36-40 |
| <b>An Efficient top- k Query Processing in Distributed Wireless Sensor Networks</b><br><i>Shaik Shabeena, K Suresh Babu</i>  | 41-45 |
| <b>Simulation of gas turbine blade for enhancement of efficiency of gas turbine using ANSYS</b><br><i>Rahul Rao, M. N. Pandey</i>  | 46-51 |
| <b>FPGA Implementation of Efficient Viterbi Decoder for Multi-Carrier Systems</b><br><i>K. Rajendar, K. Bapayya</i>  | 52-59 |
| <b>A multi-Agent Architecture for a Co-Modal Transport System</b><br><i>Nesrine Zoghlami, Karma Jeribi, Christophe Merlo, Hayfa Zgaya, Slim Hammadi</i>  | 60-78 |

## A Novel Switch Mechanism for Load Balancing in Public Cloud

Kalathoti Rambabu<sup>1</sup>, M. Chandra Sekhar<sup>2</sup>

<sup>1</sup> M. Tech (CSE), MVR College of Engineering and Technology, A.P., India.

<sup>2</sup>Asst. Professor, Dept. of Computer Science & Engineering, MVR College of Engineering and Technology, A.P., India.

**Abstract:** In cloud computing environment, one of the core design principles is dynamic scalability, which guarantees cloud storage service to handle the growing amounts of application data in a flexible manner or to be readily enlarged. By integrating several private and public cloud services, the hybrid clouds can effectively provide dynamic scalability of service and data migration. A load balancing is a method of dividing computing loads among numerous hardware resources. Due to unpredictable job arrival pattern and the capacities of the nodes in cloud differ for the load balancing problem. In this load control is very crucial to improve system performance and maintenance. This paper presents a switch mechanism for load balancing in cloud computing. The load balancing model given in this work is aimed at the public cloud which has numerous nodes with distributed computing resources in many different geographical areas. Thus, this model divides the public cloud environment into several cloud partitions. When the cloud environment is very large and complex, these divisions simplify the load balancing. The cloud environment has a main controller that chooses the suitable partitions for arriving jobs while the balancer for each cloud partition chooses the best load balancing strategy.

**Keywords:** Cloud computing, Load balancing, Public cloud, Switch mechanism.

### I. INTRODUCTION

Cloud Computing[1][2] is a concept that has many systems interconnected through a real time network like internet. Cloud computing enables convenient, dynamic, on-demand, and reliable use of the distributed computing resources. The cloud computing model has five main characteristics on demand service, resource pooling, broad network access, flexibility, measured service. Cloud computing is efficient and scalable but to maintain the stability and to process many jobs in the cloud computing environment is a very difficult problem. The job arrival pattern cannot be predicted and the capacities of each host in the cloud environment differ. Hence for balancing the usage of the internet and related resources has increased widely. Due to this there is tremendous increase in overall workload. So there is uneven distribution of this workload which results in severe server overloading and may crash. In such the load, it is crucial to control the workloads to improve system performance and maintain stability.

The load on every cloud is variable and dependent on several factors [3]. To handle this problem of imbalance of load in the cloud and to increase its working efficiency, this work tries to implement a switch mechanism for load balancing. Good load balancing makes cloud computing more efficient and also improves the user satisfaction. This paper is aimed at the public cloud which has numerous hosts. A system having the main controller, balancers, servers and a client is implemented in this work. It introduces a switch mechanism for balancing load to choose different strategies for different situations. The proposed work divides the public cloud into cloud partitions and applies different strategies to balance the load on cloud. Our work helps to avoid overloading of servers and improve response times. The basic designs of the system and algorithms to implement it are described in this paper. The following are the goals of Load Balancing:

- To improve the performance substantially.
- To have a backup plan in case the system fails even partially.
- To maintain the system stability.
- To accommodate future modification in the system.

## **II. RELATED WORK**

In [4], the authors propose a binary tree structure that is used to partition the simulation area into sub-domains. The characteristics of this fast adaptive balancing technique is to be adjusted the workload between the processors from local areas to global areas. According to the difference in the workload, the arrangements of the cells are obtained. But the main workload concentrates on certain cells so that the procedure of adjusting the vertices of the network grid can be very long because of the local workload can be considered. This problem can be avoided by the fast load balancing adaptive technique. In [5], the authors propose a method named honeybee behavior inspired the load balancing algorithm. Here in this work well load balance across the virtual machines for maximizing the throughput. The load balancing cloud computing model can be achieved by modeling the foraging behavior of the honey bees. This algorithm is derived from the behavior of the honey bees that uses the method to find and reap food. In bee hives, there is a class of bees named as the scout bees and the another type was the forager bees .The scout bee which forage for the food sources, when they find the food, they come back to the beehive to advertise this news by using a dance called “vibration” dance. The purpose of this vibration dance, gives the idea of the quality and quantity of the food and also its distance from the beehive.

In [6], the authors propose a dynamic file migration load balancing method based on the distributed architecture. Considered the large file system there were various problems like dynamic file migration, algorithm based only on the centralized system and so on. So these problems are to be avoided by the introduction of the method called self acting load balancing algorithm (SALB).In the parallel file system the information is transferred between the memory and the storage devices so that the data management is an important role of the parallel file system. In [7], the authors propose an efficient cell selection scheme and two heat diffusion based method called local and global diffusion. Considered the distributed virtual environments there were various numbers of users and the load accessing by the concurrent users can cause severe problem. This can be avoided by this method. According to the heat diffusion method, the virtual environment is divided in to large number of square cells and each square cell having objects. The working of the heat diffusion method is in such a way that every node in the cell sends load to its neighboring nodes in every iteration and the transfer was the difference between the current node to that of the neighboring node. In [8], the authors addressed the concept of overlay networks for the interconnection of the machines that makes the backbone of an online environment. Virtual online world that makes the opportunities to the world for better technological advancements as well as developments. So the proposed network model that makes better feasibility and load balancing to the dynamic virtual environments. This proposed system developed Hyper verse architecture, that can be responsible for the proper hosting of the virtual environment. There were self organized load balancing technique by which the world surface is subdivided in to small cells, and it is managed by the public server. In this cells various hotspots so that the absolute mass of the object in the cell can be calculated by using the public server.

## **III. PROPOSED WORK**

### **1. System Model**

In our proposed load balancing model the public cloud is partitioned based on their geographical locations. Figure 1, shows the schematic representation of a partitioned public cloud. This proposed model divides the public cloud into several cloud partitions. When the environment is very large and complex, then these divisions simplify the load balancing technique. The cloud has a main controller that chooses the suitable partitions for arriving jobs while the balancer for each cloud partition chooses the best load balancing strategy. Load balancing is based on this partitioning of the public cloud. When the jobs arrive, then the job controller selects a best partition and the jobs are processed by the servers present in that partition. This selection of best partition is done by a central module called as main controller and the distribution of jobs among the servers is done by the balancers present in every partition. Figure 2 shows main controller collecting status info from balancer and apps server. Algorithm 1 shows best partitioning search to select best partitions among the available partitions.

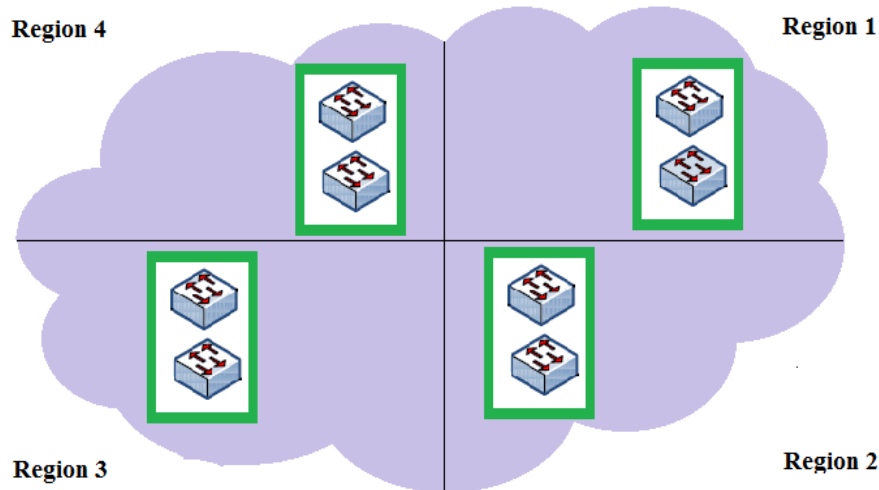


Fig. 1: Cloud Partitioning

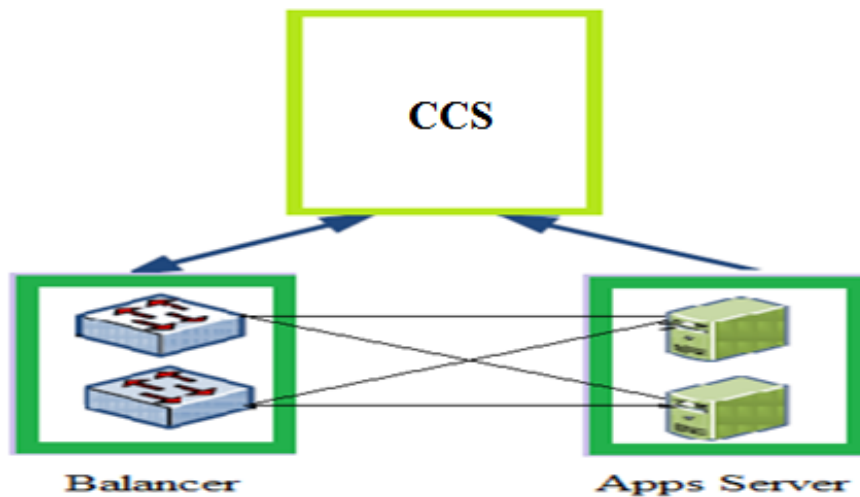


Fig. 2: Main controller (CCS) collecting status info from balancer and apps server.

The main controller decides the sub partition to be selected in the public cloud. The goal of the controller is to interact with the balancers and application servers (or nodes) and collect necessary status information of the system. The interaction between main controller and Balancer is a two-way interaction and that of between a controller and an Apps server is a one-way interaction. Based on the collected information and necessary calculations made, then a geographically nearest partition is selected. This selection of geographically nearest partition is to minimize and avoid the cost incurred on moving the jobs to a distant partition.

**Algorithm 1: Best Partitioning Search**

```

begin
while job do
searchBestPartition (job);
if partitionState == idle k partitionState == normal then
Send Job to Partition;
else
search for another Partition;
end if
end while
end
    
```

## 2. Assigning jobs to the cloud partition

After creating the cloud partitions, then load balancing the procedure begins as follows: The job arrives and then the partitions manager decides in which partition the job has to be executed and check is there any requirement for creation of new partition if required new partition is created or else in the existing partition the job is submitted. Then the job distributor decides how to assign the jobs to the individual nodes in that given partition. The choice of using the load balancing technique may depend on the job distributors. Even multiple strategies could be combined and used for favorable situations. Figure 3 shows the job assignment strategy.

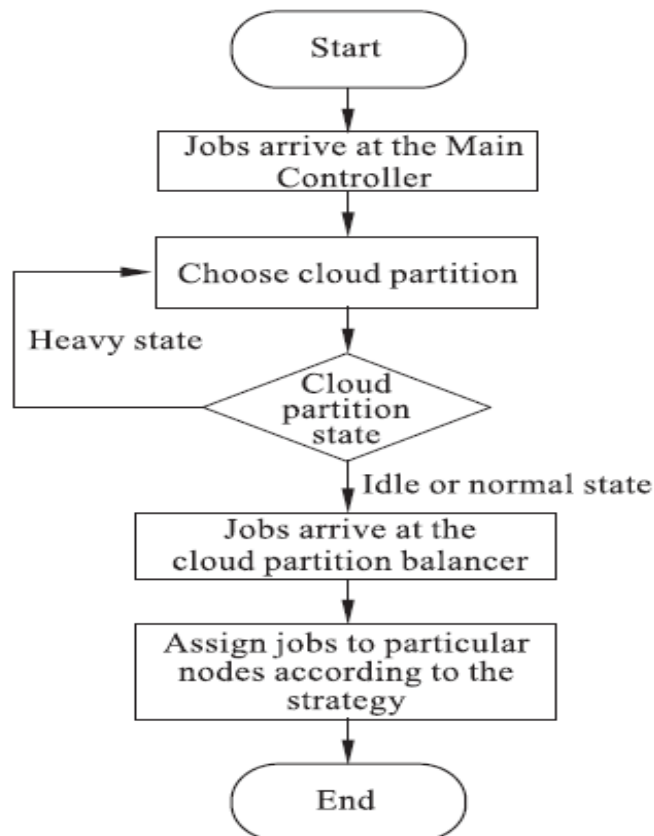


Fig. 3: Job assignment strategy

## 3. Assigning Jobs To The Nodes In The Cloud Partition

Cloud partition job distributor gathers load information from every node to calculate the cloud partition status. This calculation of each node's load status is very essential. The first task is to evaluate the load degree of each node. The node load degree is related to various static and dynamic parameters. The static parameters include the number of processing units, the memory size, the CPU processing speeds etc. Dynamic parameters are the memory utilization ratio, the CPU utilization ratio, the network bandwidth, etc. Based on the parameters the jobs are assigned to the nodes in the selected partitions. The Load Degree (LD) of a given node in any cloud partition is calculated from following equation:

$$LD(N) = \sum_{i=1}^m X_i * F_i$$

Here, N=Current Node,  $F_i$  are the parameter either static or dynamic where  $F_i(1 \leq i \leq m)$ ,  $m$  represents the total number of parameter.  $X_i$  are weights that may differ for different kinds of job for all  $(1 \leq i \leq n)$ . Average Load Degree (LD) of the cloud partition will be calculated as:

$$Avg\_LD = \sum_{i=1}^n LD (N_i) / n$$

According to the calculation of load degree for the given node three load status of the node are defined as follows:

**IDLE:** When  $LD (N)=0$

**NORMAL:**  $0 < LD (N) \leq High\_LD$

**OVERLOADED:**  $High\_LD < LD (N)$

Any cloud partition having the status=HEAVY is not selected by the balancing manager and likewise any given node having the Load Degree (LD) =OVERLOADED is not eligible for the processing. Only cloud partition having IDLE or NORMAL load status and the node having IDLE or NORMAL load degree are selected for scheduling and load balancing.

#### IV. CONCLUSION

Load balancing in the cloud environment differs from classical thinking on load balancing architecture and implementation by using commodity servers to perform the load balancing. This provides for new opportunities and economies-of-scale, and also presenting its own unique set of challenges. This paper proposes load balancing model based on the cloud partitioning concept. This model uses the switch mechanism depending upon the load status at the cloud partition when the request is made. Switch mechanism based load balancing allows choosing different strategies in different situations. This load balancing model applies to the public cloud to improve efficiency in the public cloud environment.

#### REFERENCES

- [1] P.T.Jaeger, J.Lin, and M. grimes, Cloud computing and information policy: Computing in a policy cloud? Journal of Information Technology and politics, 2009.
- [2] B.P.Rimal, E.Choi, and I.Lumb. A taxonomy and survey of Cloud Computing Systems. in Networked Computing and Advanced Information Management, International Conference. 2009.
- [3] Z. Chaczko, Venkatesh Mahadevan, Shahrzad Aslanzadeh, Christopher Mcdermid. "Availability and Load Balancing in Cloud Computing" 2011 International Conference on Computer and Software Modeling.
- [4] Dongliang Zhang, Changjun Jiang, Shu Li, "A fast adaptive load balancing method for parallel particle-based simulations", Simulation Modelling Practice and Theory 17 (2009) 1032–1042.
- [5] Dhinesh Babu L.D, P. VenkataKrishna, "Honey bee behaviour inspired load balancing of tasks in cloud computing environments", Applied Soft Computing 13 (2013) 2292–2303.
- [6] Bin Dong, Xiuqiao Li, Qimeng Wu, Limin Xiao, Li Ruan, "A dynamic and adaptive load balancing strategy for parallel file system with large-scale I/O servers", J. Parallel Distribution Computing. 72 (2012) 1254–1268.
- [7] Yunhua Deng, Rynson W.H. Lau, "Heat diffusion based dynamic load balancing for distributed virtual environments", in: Proceedings of the 17th ACM Symposium on Virtual Reality Software and Technology, ACM, 2010, pp. 203–210.
- [8] Markus Esch, Eric Tobias, "Decentralized scale-free network construction and load balancing in Massive Multiuser Virtual Environments", in: Collaborative Computing: Networking, Applications and Worksharing, Collaborate Com, 2010, 6th International Conference on, IEEE, 2010, pp. 1–10.

## Methodology used for improving overall equipment effectiveness by Implementing Total Productive Maintenance in plastic pipe manufacturing industries

Dashrath kumar<sup>1</sup>, Er. Dinesh Kumar<sup>2</sup>, Er. Rohit Rawat<sup>3</sup>

<sup>1</sup>final year student M. Tech. Mechanical Engg. J.C.D.C.M. College of Engg. Sirsa Haryana

<sup>2</sup>Associate Professor, Mechanical Engineering Department, J.C.D.M. College of Engg. Sirsa, Haryana

<sup>3</sup>Assistant Professor, Mechanical Engineering Department, Smalkha group of institution, Smalkha, Panipat, Haryana

**Abstract:** The global marketplace is highly competitive and organizations who want to survive long-term, have to continuously improve, change and adapt in response to market demands. Improvements in a company's performance should focus on cost cutting, increasing productivity levels, quality and guaranteeing deliveries in order to satisfy customers. Total Productive Maintenance (TPM) is one method, which can be used to achieve these goals. TPM is an approach to equipment management that involves employees from both production and maintenance departments. Its purpose is to eliminate major production losses by introducing a program of continuous and systematic improvements to production equipment.

### I. Total Productive Maintenance

In today's industrial scenario huge losses/wastage occur in the manufacturing shop floor. This waste is due to operators, maintenance personal, process, tooling problems and non-availability of components in time etc. Other forms of waste includes idle machines, idle manpower, break down machine, rejected parts etc are all examples of waste. The quality related waste are of significant importance as they matter the company in terms of time, material and the hard earned reputation of the company. There are also other invisible wastes like operating the machines below the rated speed, start up loss, break down of the machines and bottle necks in process. Zero oriented concepts such as zero tolerance for waste, defects, break down and zero accidents are becoming a pre-requisite in the manufacturing and assembly industry. In this situation, a revolutionary concept of TPM has been adopted in many industries across the world to address the above said problems.

TPM is a unique Japanese philosophy, which has been developed based on the Productive Maintenance concepts and methodologies. This concept was first introduced by M/s Nippon Denso Co. Ltd. of Japan, a supplier of M/s Toyota Motor Company, Japan in the year 1971. Total Productive Maintenance is an innovative approach to maintenance that optimizes equipment effectiveness, eliminates breakdowns and promotes autonomous maintenance by operators through day-to-day activities involving total workforce.

A strategic approach to improve the performance of maintenance activities is to effectively adapt and implement strategic TPM initiatives in the manufacturing organizations. TPM brings maintenance into focus as a necessary and vitally important part of the business. The TPM initiative is targeted to enhance competitiveness of organizations and it encompasses a powerful structured approach to change the mind-set of employees thereby making a visible change in the work culture of an organization. TPM seeks to engage all levels and functions in an organization to maximize the overall effectiveness of production equipment. This method further tunes up existing processes and equipment by reducing mistakes and accidents.

TPM is a world class manufacturing (WCM) initiative that seeks to optimize the effectiveness of manufacturing equipment (Shirose, 1995). Whereas maintenance departments are the traditional center of preventive maintenance programs, TPM seeks to involve workers from all departments and levels, including the plant-floor to senior executives, to ensure effective equipment operation.

**TPM as the name suggests consists of three words:**

- (1) **Total.** This signifies to consider every aspect and involving everybody from top to bottom.
- (2) **Productive.** Emphasis on trying to do it while production goes on a minimize troubles for production.
- (3) **Maintenance.** Means keeping equipment autonomously by production operators in good position.

### **Goals of Total Productive Maintenance**

The goal of TPM focuses on improving corporate culture through improvement of human resources and plant equipment. The Japan Institutes of Plant Maintenance (JIPM) has put forward the five goals of TPM which are the minimum requirements for the TPM development.

- 1. Improving equipment effectiveness.**
- 2. Improving maintenance efficiency and effectiveness.**
- 3. Early equipment management and maintenance prevention.**
- 4. Training to improve the skills of all people involved.**
- 5. Involving operators in routine maintenance.**

### **Improving Equipment Effectiveness**

Equipment effectiveness is a measure of the value added to production through equipment. This goal is to increase equipment effectiveness so each piece of equipment can be operated to its full potential and maintained at that level. Nakajima describes in his book that TPM maximizes equipment effectiveness through two types of activity to insure that the equipment performs to design specifications which is the true focus of TPM

- **Quantitative:** It increases the equipment's total availability & improving its productivity within a given period of operating time.
- **Qualitative:** It reduces the number of defective products, stabilizing & improving quality.

Although the equipment must operate at its design speed, produce at the design rate, and produce a quality product at these speeds and rates, there are factors which might obscure efficient utilization of the equipment. Examining, identifying and eliminating all losses which obscure the efficiency of the equipment will increase the efficiency of the equipment

The concept of zero breakdowns and zero defects are inevitable to maximize equipment effectiveness. These equipment losses include: equipment downtime loss, performance loss, and defect loss. Various equipment losses can be quantitatively calculated through measuring equipment effectiveness that ties the '6 major losses' to three measurable.

## **II. Literature Review**

TPM is a unique Japanese philosophy, which has been developed based on the Productive Maintenance concepts and methodologies. This concept was first introduced by M/s Nippon Denso Co. Ltd. of Japan, a supplier of M/s Toyota Motor Company, Japan in the year 1971. *Nakajima (1989)* A major contributor of TPM has defined TPM as an innovative approach to maintenance that optimizes equipment effectiveness, eliminates breakdowns, and promotes autonomous maintenance by operators through day-to-day activities involving the total workforce. TPM is not a maintenance specific policy; it is a culture, a philosophy and a new attitude toward maintenance. He suggests that equipments should be operated at 100 percent capacity 100 percent of the time. *Pirsig et al. (1996)* emphasizes upon seven unique broad elements and four main themes in any TPM implementation program. The key themes in the TPM implementation program include training, decentralization, maintenance prevention and multi-skilling, while the broad elements include asset strategy, empowerment, resource planning and scheduling, systems and procedures, measurement, continuous improvement and processes. Have proposed developed the eight-step approach to the implementation of TPM involving system, measurement, autonomous maintenance, housekeeping, continuous improvement, culture, training, and plant design. *Maier et al. (1998)* consider preventive maintenance, teamwork shop floor employee competencies, measurement and information availability work environment, work documentation, and extent of operator involvement in maintenance activities as factors reflecting TPM implementation. The basic practices of TPM are often called the pillars or elements of TPM. The entire edifice of TPM is built and stands, on eight pillars *Noon et al. (2000)* explained TPM seeks to maximize equipment effectiveness throughout the lifetime of the equipment. It strives to maintain the equipment in optimum condition in order to prevent unexpected breakdown, speed losses, and quality defects occurring from process activities. There are three ultimate goals of TPM: zero defects, zero accident, and zero breakdowns *Marco Castro (2013)* Total Productive Maintenance (TPM) is one of the World Class Manufacturing tools that seeks to manage assets by involving everyone in the manufacturing organization. The financial and productivity benefits of implementing TPM are significant. Many approaches have been proposed regarding TPM implementation procedures, of which logically sequenced implementation procedure is an identified success factor, yet the majority of TPM implementation attempts fail to achieve their intended goals.

### III. Methodology

#### Overall Equipment Effectiveness

Overall Equipment Effectiveness has been developed by the JIPM. OEE is regarded as an important measurement for assessing the performance of equipment. The method distinguishes the six big loss types, and three key performance measurements: availability, performance rate and quality rate that combines into one consolidated metric. The OEE can be used to help focus on improving the performance of machinery and associated processes by identifying those performance opportunities that will have the greatest impact to the bottom line. Improvements in changeovers, quality, machine reliability, working through breaks and more, can be measured and improved utilizing the OEE metric. It is the ratio of actual equipment output to its theoretical maximum output. OEE can be viewed as the percent of time that equipment would need to run at its maximum speed in order to attain the actual output of that tool or machine. It is calculated using the following formula.

$$OEE = \text{Availability} \times \text{Performance Rate} \times \text{Quality Rate}$$

To find the overall equipment efficiency of the plastic Industry, identifying the six major losses of the machines was the first stride by organizing under three key factors. And then data pertinent to those losses was collected for randomly selected machineries. The major losses that are identified and the OEE of the selected machineries presented as follows.

#### Calculating Overall Equipment Effectiveness

Some of the data pertinent to the above loss are difficult to obtain, since the company doesn't apply the overall equipment efficiency concepts in evaluating the performance of the machines at the individual level. It has been attempted to gather some relevant data to estimate the OEE of the typical machinery.

#### Availability

The availability is the ratio of time needed for operating the equipment to the time actually consumed for operation and it is expressed as:

$$\text{Availability} = \frac{\text{Actual Running Time}}{\text{Scheduled Running Time}} \times 100$$

Whereas Actual Running Time = Scheduled running time – Unplanned stoppages.

Unplanned stoppage means the period during which the line is stopped due to equipment failure, setup, adjustment, and change over and so forth.

So that:-

$$\text{Availability} = \frac{\text{Scheduled running time} - \text{Unplanned stoppages}}{\text{Scheduled running time}} \times 100$$

#### Performance Rate

The performance rate is the ratio between actual average production and standard production. This factor indicates the ratio of the actual output and the targeted output. Actual output is the actual performance of the operation and is less than the targeted output due to rough running of the equipment, jams and equipment wear. Hence, it is expressed as:

$$\begin{aligned} \text{Performance Rate} &= \frac{\text{Actual average production}}{\text{Standard production}} \times 100 \\ &= \frac{\text{Total production in cycle period}}{\text{No. of working days in a cycle period}} \end{aligned}$$

#### Quality Rate

This is percentage of good parts out of total produced sometimes called "yield". Quality losses refer to the situation when the line is producing, but there are quality losses due to in-progress production and warm up rejects. We can express a formula for quality like this:

$$\text{Quality Rate} = \frac{\text{No. of Products Processed} - \text{No. of Products rejected}}{\text{No. of Products Processed}} \times 100$$

#### IV. Case Study

##### About the Company

Shiv Plastic Pvt. Limited Company Are a Certified Company Situated In Fatehabad Industrial Area. Company Are Manufacturing Plastic Polythene Pipes Of Different Sizes According To The Demand Of Customers And Uses In Different Area. The Material Are Supplied To Company From Delhi. The Product Are Supplied In Different Area.

The Different Diameter From 5 Inches To 12 Inches Pipes Are Manufacturing.

Sr. no.	Dia. in Inches	Dia. In cm	Dia. In mm
1.	5	13	130
2.	6	15	150
3.	7	18	180
4.	8	20	200
5.	9	23	230
6.	10	25	250
7.	11	28	280
8.	12	30	300

**Dia. of pipes to manufacturing in industry**

##### Sample of Monthly Production of Pipes Before TPM ( May 2013 To Sept. 2013)

S. No	Month	Production(Quintal)
1	May	2200
2	June	2190
3	July	2150
4	August	2170
5	September	2100

##### Production and Wastage Before

##### TPM ( May 2013 to September 2013)

Months	Production (Quintal)	Waste (Quintal)	%
May	2200	250	11.36
June	2190	239	10.91
July	2150	235	10.93
August	2170	235	10.82
September	2100	230	10.95

#### V. Calculating Overall Equipment Effectiveness before TPM

$$\text{Availability} = \frac{\text{Scheduled running time} - \text{Unplanned stoppages}}{\text{Scheduled running time}} \times 100$$

Scheduled Running Time of Extruder & Electrical control machine  
(8am to 6 pm) = 10 hours (600 min's)

Unplanned Stoppages 3 to 4 Times = 45 min

Scheduled Running Time for 1 Month = 30 days = 30 × 10 = 300 hours (18000 min's)

Unplanned Stoppages for 1 month = 45 × 30 = 1350 min's

$$\text{Availability} = \frac{\text{Scheduled running time} - \text{Unplanned stoppages}}{\text{Scheduled running time}} \times 100$$

$$\text{Availability} = \frac{18000 - 1350}{18000} \times 100 = 92.50\%$$

**Performance Rate Without Implement TPM (From May 2013 To September 2013 )**

The performance rate is the ratio between actual average production and standard production. This factor indicates the ratio of the actual output and the targeted output. Actual output is the actual performance of the operation and is less than the targeted output due to rough running of the equipment, jams and equipment wear. Hence, it is expressed as:

$$\begin{aligned}
 \text{Performance Rate} &= \frac{\text{Actual average production}}{\text{Standard production}} \times 100 \\
 &= \frac{\text{Actual average production}}{\frac{\text{Total production in a cycle period}}{\text{No. of working days in a cycle period}}}
 \end{aligned}$$

Total pipe manufactured in five months ( cycle period) = 10810 Quintal  
 No. of working days in five months (cycle period) = 150  
 Standard production = 75 Quintal per day

$$\text{Actual average production} = \frac{10810}{150} = 72.066 \text{ Quintal per day}$$

$$\text{Performance Rate} = \frac{72.066}{75} \times 100 = 96.088$$

**Quality Rate ( From May 2013 To September 2013 )**

This is percentage of good parts out of total produced sometimes called “yield”. Quality losses refer to the situation when the line is producing, but there are quality losses due to in-progress production and warm up rejects. We can express a formula for quality like this:

$$\text{Quality Rate} = \frac{\text{No. of Products Processed} - \text{No. of Products rejected}}{\text{No. of Products Processed}} \times 100$$

Output for 1 day = 75 Quintal (10hours)  
 Waste for 1 day = 7.9 Quintal  
 Output for 1 month = 2250 Quintal  
 Waste for 1 month = 237 Quintal

$$\text{Quality Rate} = \frac{2250 - 237}{2250} \times 100 = 89.466\%$$

From the above the quality rate of the Extruder And Electrical Control machine is 89.466%  
 Therefore, the Overall Equipment Efficiency of the machine is obtained by multiplying the above three factors and the result is

$$.925 \times .96 \times .894 \times 100 = 79.38 \%$$

The calculated Overall Equipment Efficiency of the machines is 79.38 % before TPM.

**The major losses that are identified**

1. Equipment failure loss
2. Setup and adjustment loss
3. Startup loss
4. Minor stoppage and idling loss:
5. Speed Loss
6. Quality Defect and rework loss

**VI. Calculating Overall Equipment Effectiveness After TPM**

**Sample of Monthly Production of Pipes After TPM ( Dec. 2013 To April 2014 )**

S. No	Month	Production(Tones)
1	December	2240
2	January	2250
3	February	2160
4	March	2240
5	April	2220

**Production and Wastage After TPM( Dec 2013 to April 2014)**

Months	Production (Tones)	Waste (Tones)	%
December	2240	195	8.7
January	2250	190	8.4
February	2160	170	7.8
March	2240	170	7.5
April	2220	165	7.4

Scheduled Running Time of Extruder & Electrical control machine  
(8am to 6 pm) = 10 hours (600 min's)

Unplanned Stoppages 2 to 3 Times = 35 min

Scheduled Running Time for 1 Month = 30 days = 30 × 10 = 300 hours (18000 min's)

Unplanned Stoppages for 1 month = 35 × 30 = 1050 min's

$$\text{Availability} = \frac{\text{Scheduled running time} - \text{Unplanned stoppages}}{\text{Scheduled running time}} \times 100$$

$$\text{Availability} = \frac{18000 - 1050}{18000} \times 100 = 94.166\%$$

**Performance Rate With Implementation TPM (From Dec. 2013 To April 2014 )**

The performance rate is the ratio between actual average production and standard production. This factor indicates the ratio of the actual output and the targeted output. Actual output is the actual performance of the operation and is less than the targeted output due to rough running of the equipment, jams and equipment wear. Hence, it is expressed as:

$$\text{Performance Rate} = \frac{\text{Actual average production}}{\text{Standard production}} \times 100$$

$$\text{Actual average production} = \frac{\text{Total production in a cycle period}}{\text{No. of working days in a cycle period}}$$

Total pipe manufactured in five months ( cycle period) = 11110 Quintal

No. of working days in five months ( cycle period) = 150

Standard production = 75 Quintal per day

$$\text{Actual average production} = \frac{11110}{150} = 74.066 \text{ Quintal per day}$$

$$\text{Performance Rate} = \frac{74.066}{75} \times 100 = 98.755$$

**Quality Rate ( From Dec. 2013 To April 2014 )**

This is percentage of good parts out of total produced sometimes called “yield”. Quality losses refer to the situation when the line is producing, but there are quality losses due to in-progress production and warm up rejects. We can express a formula for quality like this:

$$\text{Quality Rate} = \frac{\text{No. of Products Processed} - \text{No. of Products rejected}}{\text{No. of Products Processed}} \times 100$$

Output for 1 day = 75 Quintal (10hours)

Waste for 1 day = 5.9 Quintal

Output for 1 month = 2250 Quintal

Waste for 1 month = 178 Quintal

$$\text{Quality Rate} = \frac{2250 - 178}{2250} \times 100 = 92.088\%$$

From the above the quality rate of the Extruder And Electrical Control machine is 92.088%

Therefore, the Overall Equipment Efficiency of the machine is obtained by multiplying the above three factors and the result is

$$.941 \times .987 \times .920 \times 100 = 85.44 \%$$

**The calculated Overall Equipment Efficiency of the machines is 85.44%.**

## **VII. Conclusion**

The main objective of this paper understand TPM concept and to generate awareness among the budding technologies about TPM. During research in Shiv plastic Pvt. limited we have compare before implementing TPM and after implementing TPM data and distort major problems by TPM based corrective action plan we have reduce 60% problems improve OEE. TPM methodology not only increases the effectiveness of the manufacturing system but also increase the effectiveness of the entire organization through mandatory participation and continuously improve Productivity, quality, cost, Delivery, safety health and Morale.

## **REFERENCES**

- [1.] Ravikant V et al. (2013), "International Journal of Advanced Engineering Sciences and Technologies", Vol. 6 No. 2, pp. 270 – 276.
- [2.] Wakjira and Ajit Pal Singh, (2012), "Total productive maintenance: A case study in manufacturing industry", Global Journal of Researches in Engineering, Vol 12, pp 25-31.
- [3.] Ahuja and Khamba (2008), "Strategies and success factors for overcoming challenges in TPM implementation in Indian manufacturing industry", Journal of Quality in Maintenance Engineering, Vol. 14 No. 2, pp. 123-147.
- [4.] Ahuja & Khamba, (2008), "Strategies and success factors in TPM", Vol. 14 No. 2, pp. 123-147.
- [5.] Ahuja & Khamba, (2007), "An evaluation of TPM implementation initiatives in an Indian manufacturing", Journal of Quality in Maintenance Engineering, Vol. 13 No. 4, pp. 338-352.

## Design and Fabrication of Vapour Absorption Refrigeration System [LiBr-H<sub>2</sub>O]

Mohd Aziz Ur Rahaman<sup>1</sup>, Md. Abdul Raheem Junaidi<sup>2</sup>, Naveed Ahmed<sup>3</sup>,  
Mohd. Rizwan<sup>4</sup>

<sup>1,2,3,4</sup>(Mechanical Engineering Department, Osmania University, India)

**Abstract:** Most of the energies are utilized by the industries due to depletion of fossil fuels and increasing the fuel price to exploit the maximum presented energy from the waste heat source. The industry which utilizes steam turbine exhaust carries a considerable amount of thermal energy. This energy can be set in to positive use as a heat source for vapour absorption system to serves as cooling system. This paper illustrates the thermal and fiscal advantages of using single effect lithium bromide water absorption by means of waste heat. The objective of this work is to hypothetical design of lithium bromide water absorption Refrigeration system using waste heat from any industry steam turbine exhaust. The various parts of the vapour absorption system are absorber, solution heat exchanger, evaporator, condenser and generator. Energy consumption and energy savings in terms of energy and fuels are calculated. The Overall heat transfer coefficient, effectiveness and COP of the heat exchanger are measured. The energy and global warming crises have drawn rehabilitated benefit to thermally driven cooling systems from the air conditioning and process cooling fraternities. The lithium bromide-water absorption refrigerator is one of the favorites due to the following specific reasons it can be thermally driven by gas, solar energy, and geothermal energy as well as waste heat, which help to substantially reduce Carbon dioxide emission its use of water as a refrigerant it is quiet, durable and cheap to maintain, being nearly void of high speed moving parts its vacuumed operation renders it amenable to scale up applications. LiBr-H<sub>2</sub>O absorption refrigerator enjoy cooling capacities ranging from small residential to large scale commercial or even industrial cooling needs. The coefficient of performance (COP) varies to a small extent (0.65-0.75) with the heat source and the cooling water temperatures.

**Keywords:** Fabrication, Vapour absorption, Refrigeration, LiBr-H<sub>2</sub>O absorption refrigerator, waste heat.

### I. INTRODUCTION

The working fluid in an absorption refrigeration system is a binary solution consisting of refrigerant and absorbent. In Fig. 1(a), two evacuated vessels are connected to each other. The left vessel contains liquid refrigerant while the right vessel contains a binary solution of absorbent/refrigerant. The solution in the right vessel will absorb refrigerant vapor from the left vessel causing pressure to reduce. While the refrigerant vapor is being absorbed, the temperature of the remaining refrigerant will reduce as a result of its vaporization. This causes a refrigeration effect to occur inside the left vessel. At the same time, solution inside the right vessel becomes more dilute because of the higher content of refrigerant absorbed. This is called the "absorption process". Normally, the absorption process is an exothermic process, therefore, it must reject heat out to the surrounding in order to maintain its absorption capability.

Whenever the solution cannot continue with the absorption process because of saturation of the refrigerant, the refrigerant must be separated out from the diluted solution. Heat is normally the key for this separation process. It is applied to the right vessel in order to dry the refrigerant from the solution as shown in Fig. 1(b). The refrigerant vapor will be condensed by transferring heat to the surroundings. With these processes, the refrigeration effect can be produced by using heat energy. However, the cooling effect cannot be produced continuously as the process cannot be done simultaneously. Therefore, an absorption refrigeration cycle is a combination.

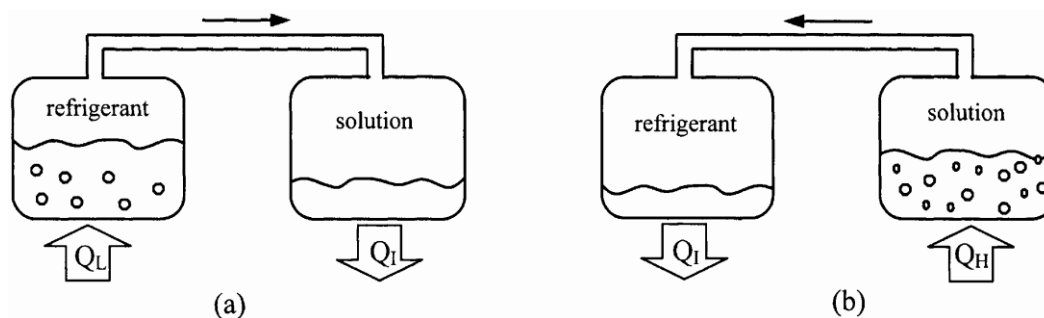


Fig. 1(a): Absorption process occurs in right vessel causing cooling effect in the other;

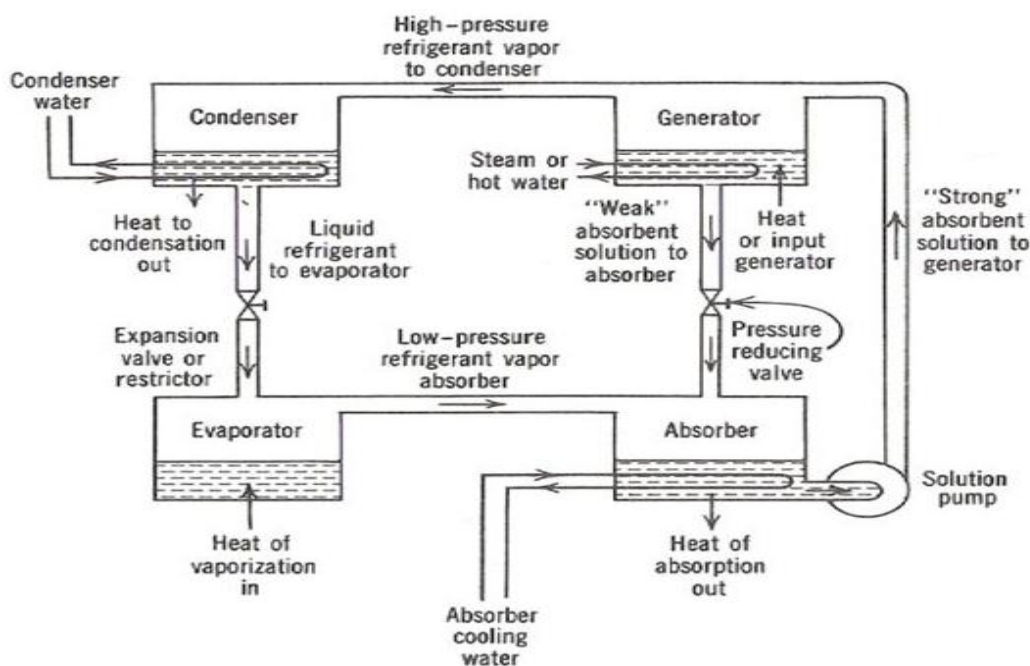


Fig. 1(b): Refrigerant. Fig. 2: Schematic diagram of absorption refrigeration system

Separation process occurs in the right vessel as a result of additional heat from outside heat source. of these two processes as shown in Figure As the separation process occurs at a higher pressure than the absorption process, a circulation pump is required to circulate the solution. The work input for the pump is negligible relative to the heat input at the generator, therefore, the pump work is often neglected for the purposes of analysis.

## II. METHODOLOGY

To design a single stage vapour absorption refrigeration system based on H<sub>2</sub>O-LiBr has a refrigeration capacity of 175 (0.05)watts. The system operates at an evaporator temperature of 5 degree centigrade (P<sub>sat</sub>=8.72mbar) and a condensing temperature of 30 degree centigrade (P<sub>sat</sub>=32.3 mbar). The concentration of solution at the exit of absorber and generator are 0.35 and 0.45, respectively. Assume 100 percent effectiveness for the solution pump, exit condition of refrigerant at evaporator and condenser to be saturated and the condition of the solution at the exit of absorber and generator to be at equilibrium. Enthalpy of strong solution at the inlet to the absorber may be obtained from the equilibrium solution data.

Required:

- The mass flow rates of refrigerant, weak and strong solutions
- Heat transfer rates at the absorber, evaporator, condenser, generator and solution pump.
- System COP and second law efficiency, and
- Solution pump work (density of solution = 1200 kg/m<sup>3</sup>).

In order to proceed with the design, firstly we need to calculate the composition with the help of stoichiometric formulae. The composition of water-lithium bromide solutions can be expressed either in mass fraction ( $\xi$ ) or mole fraction ( $x$ ). For water-lithium bromide solutions, the mass fraction  $\xi$  is defined as the ratio of mass of anhydrous lithium bromide to the total mass of solution, i.e.,

$$\text{Concentration}(\xi) = \frac{\text{mass of anhydrous lithium bromide}}{\text{mass of total solution}}$$

The composition can also be expressed in terms of mole fraction of lithium bromide as:

$$\text{No of moles}(X) = \frac{\text{number of moles of anhydrous lithium bromide}}{\text{number of moles of total solution}}$$

where  $M_L$  (= 86.8 kg/kmol) and  $M_W$  (= 18.0 kg/kmol) are the molecular weights of anhydrous lithium bromide and water respectively.

Specification of the system:

Size of the evaporator tank	: 15*30 cm.
Capacity of the evaporator(cooling Effect)	: 0.05 Tr (tonnage of refrigeration).
Size and capacity of the condenser	: 5 metres and 189.924 kW.
Size and capacity of the generator	: 3 litres and 221.54 kW.
Size and capacity of the absorber	: 3 litres and 206.75 kW.
Mass flow of refrigerant across the System	: 0.076 g/s.

Now after obtaining all the required parameters calculating its coefficient of performance. The COP of the system is given by:

$$\text{COP} = \frac{Q_e}{Q_g + W_p} \approx \frac{Q_e}{Q_g}$$

In order to find the steady-state performance of the system from the above set of equations, one needs to know the operating temperatures, weak and strong solution concentrations, effectiveness of solution heat exchanger and the refrigeration capacity. It is generally assumed that the solution at the exit of absorber and generator is at equilibrium so that the equilibrium P-T- $\xi$  and h-T- $\xi$  charts can be used for evaluating solution property data. The effectiveness of solution heat exchanger,  $\epsilon_{HX}$  is given by:

$$\epsilon_{HX} = \frac{(T_7 - T_6)}{(T_8 - T_6)}$$

From the above equation the temperature of the weak solution entering the generator ( $T_7$ ) can be obtained since  $T_6$  is almost equal to  $T_5$  and  $T_8$  is equal to the generator temperature  $T_g$ . The temperature of superheated water vapour at state 1 may be assumed to be equal to the strong solution temperature  $T_8$ .

Coefficient of performance:-

$$\begin{aligned} \text{System COP (neglecting pump work)} &= Q_e/Q_g = \mathbf{0.789} \\ \text{Second law efficiency} &= \text{COP}/\text{COP}_{\text{Carnot}} \\ \text{COP}_{\text{Carnot}} &= [T_c/(T_c - T_e)][(T_g - T_a)/T_g] = \mathbf{1.129} \\ \therefore \text{Second law efficiency} &= \mathbf{0.6983 * 100 = 69.83 \%} \end{aligned}$$

### **III. FABRICATION**

The primary components of the refrigeration system are:

#### **1. Generator**

According to the requirements specified in the design segment, we purchased a 3 litre, mild steel cylinder (it is usually used to carry refrigerants). this cylinder was purchased from gobind refrigerator & air conditioning equipments, balnagar.

Operations performed:

Drilling : Drilling of four holes of dia 1.5cm at the specifies spots for the inlet and outlets and one hole of dia 2.5 cms for the connection of thermocouple was performed on a vertical drilling machine.

Welding: Arc welding was done to weld four 1.5cms and one 2.5 cms mild steel, internally threaded nuts which get mated with the bronze adapters for inlet and outlet connections and one for the thermocouple.

#### **2. Absorber**

Another 3 litre, mild steel cylinder similar to the generator is used for the purpose of absorber. It was purchased along with the generator.

Operations performed:

Drilling: Drilling of three holes of dia 1.5cm at the specifies spots for the inlet and outles was performed on a vertical drilling machine.

Welding: Arc welding was done to weld four 1.5cms mild steel, internally threaded nuts which get mated with the bronze adapters for inlet and outlet connections and

#### **3. Condensor**

As specified in the design segment, assuming the natural convection coefficient (h) to be 10W/mK and theoretical mass flow rate(m) to be  $8 \times 10^{-5}$  kg/sec, the calculated length for a 1/4<sup>th</sup> inch mild steel was five meters. The pipe was bent at into several turns with the help of 180degrees bending tool to make it compact and also to enhance the drop in pressure which eliminates the requirements of any throttling device such as a capillary tube.

#### **4. Evapourator**

A 6mm thick glass container (24x15x6 cms) was ordered n purchased from a glass works shop at r.no 3 BANJARA HILLS. This container is used as an evaporator cabin which is filled with water and the water is expected to be cooled to 10 degrees centigrade as a result of the refrigeration cycle.

The same 1/4<sup>th</sup> inch mild steel tube is wounded in the form of a coil and sent through this evaporator cabin.

#### **5. Pump**

A special purpose 20w dc pump used in air-conditioning equipment is used in this cycle. The purpose of this device is to pump the solution (strong in water) from the absorber to the generator. This is the only mechanical device being used in the whole system. An adaptor is provided along with this pump to convert the 220v AC power input to 24V DC supply to the pump.

#### **6. Frame**

All the components are attached to a frame made of 18mm thick plywood frame shown below.

The generator is clamped by two 6inch mild steel strips with the help of 1 inch screws firmly.

The absorber is also clamped with a single similar 6 inch mild steel strip which is screwed to the frame and a support at the bottom.

The condenser is similarly fixed to frame and the frame is cut behind the condenser to enhance the convection heat transfer from the condenser.

The evaporator is supported at its base with a wooden frame.

The pump is screwed to the frame with two small screws.

The heating coil is fixed to the frame below the generator.

#### **7. Pipes**

The pipe used through out the system is 1/4 th inch, mild steel pipe. The length of total pipe used for the refrigeration system was 10 mts. The piping was done with assistance from the technician at NATIONAL PIPE WORKS, AFZAL GUNJ.

### **8. Valves, gauges and connecting adapters**

One stainless steel steam valve is used at the outlet of generator to control the mass flow rate of steam coming out of the generator. Three ball valves, one each for the three outlets of generators is used. Out of these three, one is used to control the flow of weak solution (weak in water) from the generator to the absorber, second one is to control the flow of solution coming from the pump and the third one is used for initial filling of water-lithium bromide solution into the generator.

Two gauges, one pressure gauge (range 760mm of Hg vacuum to 0mm of Hg) and one temperature gauge (thermocouple range 0-200 degree centigrade) are mounted on the generator to check the state of steam before allowing it to flow through the system.

All the connections are made with the help of bronze connecting adapters of 1/4 inch dia and provided with brass washers on both sides. All these connections are sealed using Teflon and to ensure it remains leak proof.

All of these valves, gauges and connectors were purchased from UNIQUE CONTROL SYSTEMS, RANIGUNJ.



**Fig. 3: Schematic arrangement of refrigeration system**

## **IV. DESIGN IMPROVEMENT**

### **a). Design of energy supplying network to the generator**

The prime motive behind this project was to utilize low grade thermal energy which is released by many industries and manufacturing units that go unused. This energy should be tapped and supplied to the generator. A proper system should be designed for this purpose.

Also the solar energy should be properly supplied as an input to the generator to provide refrigeration and air conditioning for domestic purposes.

### **b). Design Of Solution Heat Exchanger**

The efficiency of the system is greatly affected by the enthalpy of solution entering the generator and temperature of the solution entering the absorber. Thus a proper heat exchanger is necessary for enhancement of this refrigeration system.

### **c). Design Of A Water Cooled Condenser**

A properly designed water cooled condenser will reduce the size of the refrigeration system and make it compact, easy to transport and efficient.

### **d). Design of Generator and Absorber**

Since the system is operating under low pressure, the cylinders for generator and absorber can be properly selected so that mass of the system is greatly reduced and making the system cost effective.

## **V. CONCLUSION**

A simple vapor absorption system was designed and fabricated to analyze the performance of the system. The system is tested with heat input from an electric heating element of 500 watts capacity for a pressure of 32.5 mbar. The COP is found to be 0.698 and the increase from the designed value is because of

higher generator temperature. A more efficient thermal system should have higher COP and lower total entropy generation.

Comparison between actual and calculated values shows that heat loss from the generator greatly affects the system performance. The cooling capacity is limited because of limitations temperature and need of rectification which is absent in the current system. Further analysis to this system should involve the entropy generation to identify and quantify performance degradation of the system. The COP can be increased further by using a heat exchanger between the absorber and generator as well as between the condenser and pressure reducing valve. The various components of 0.05TR H<sub>2</sub>O-LiBr vapour absorption system were fabricated using mild steel due to the corrosive nature of water on copper, brass etc.

The thermodynamic analysis of absorption system using LiBr-H<sub>2</sub>O as working fluid has been presented. The irreversibility rate in generator is found to be the highest while it is found to be the lowest in the condenser and absorber. It is found that the irreversibility rate in the generator is more because of increase rate of heat transfer in the generator, also the exergy losses are more in generator because of heat of mixing in the solution, which is not present in pure refrigerant/fluids.

Results show that as expected the COP of the system increases minutely as the generator temperature is increased but the exergy efficiency of the system drops with the increase in generator temperature. It is also found that the COP of the system increases with increase in evaporator temperature this largely depends on the enthalpy difference between the chilled water at inlet and outlet of evaporator. However, it is reverse in case of exergy efficiency. The results with respect to exergy losses in each component and exergy efficiency are very important for the optimization of absorption system. These results are helpful for designers to bring changes in the actual system for optimum performance and less wastage of energy.

#### REFERENCES

- [1]. Ziegler, F., Recent developments and future prospects of sorption heat pump system. International Journal of Thermal Science, Vol. 38, (1999),pp.191-208.
- [2]. J.D Killon,; S.Garimella.(2001): A critical review of models coupled heat and mass transfer in falling film absorption, 24, pp.755-797.
- [3]. G.A. Florides,; S.A. Kalogiroua,; S.A. Tassoub,; L.C. Wrobelb. (2003):Design and construction of a LiBr–water absorption machine, 44(15),pp.2483-2508.
- [4]. D.A. Kouremenos, K.A. Antonopoulos and E. Rogdakis, 'Hour Simulation of Solar H<sub>2</sub>O-LiBr Absorption Heat Transformers in Athens', Solar and Wind Technology, Vol. 7, N°2/3, pp. 111-118, 19, 1990.
- [5]. Eisa, M. A. R., Devotta, S., and Holland, F. A. Thermodynamic design data for absorption heat pump systems operating on water lithium bromide: Part I: cooling. Applied Energy, 1986, 24, 287–301.
- [6]. Mr. S. S. Mali , Prof.M.M.Wagh, Prof. N. N. Shinde, " Review Of Design Of Single Effect Solar Powered Vapour Absorption Air Conditioning System " International Journal Of Advance Research In Science And Engineering, Vol. No.2, Issue No.7, July, 2013, Pp 4 -52.
- [7]. G. Ali Mansori And Vinod Patel, "Thermodynamic Basis For The Choice Of Working Fluids For Solar Absorption Cooling Systems " Solar Energy, Volume 2 , Issue 6, 1979, Pp. 483-491.
- [8]. Micallef, D. And Micallef, C, "Mathematical Model Of Vapour Absorption Refrigeration Unit" Int.J Simul Model 9, 2 , 2010, Pp 86-97.
- [9]. Anil Sharma, Bimal Kumar Mishra, Abhinav Dinesh, Ashok Misra, "Configuration Of A 2 Kw Capacity Absorption Refrigeration System Driven By Low Grade Energy Source" International Journal Of Metallurgical & Materials Science And Engineering (Ijmmse) Vol. 2 Issue 4 Dec - 2012 1-10, Pp 1-9.
- [10]. Desai AD, Bannur PV. Design, fabrication and testing of heat recovery system from diesel engine exhaust. J Inst Engrs 2001; 82:111–8.
- [11]. ASHARE, 'Handbook of Fundamentals', 1985.

## An Adaptive Routing Algorithm for Communication Networks using Back Pressure Technique

Khasimpeera Mohammed<sup>1</sup>, K. Kalpana<sup>2</sup>

<sup>1</sup> M. Tech (CSE), MVR College of Engineering and Technology, A.P., India.

<sup>2</sup> Asst. Professor, Dept. of Computer Science & Engineering, MVR College of Engineering and Technology, A.P., India.

**Abstract:** The basic idea of backpressure techniques is to prioritize transmissions over links that have the highest queue differentials. Backpressure method effectively makes packets flow through the network as though pulled by gravity towards the destination end, which has the smallest queue size of zero. Under high traffic conditions, this method works very well, and backpressure is able to fully utilize the available network resources in a highly dynamic fashion. Under low traffic conditions, however, because many other hosts may also have a small or zero queue size, there is inefficiency in terms of an increase in delay, as packets may loop or take a long time to make their way to the destination end. In this paper we use the concept of shadow queues. Each node has to maintain some counters, called as shadow queues, per destination. This is very similar to the idea of maintaining a routing table (for routing purpose) per destination. Using the concept of shadow queues, we partially decouple routing and the scheduling. A shadow network is maintained to update a probabilistic routing table that packets use upon arrival at a node. The same shadow network, with back-pressure technique, is used to activate transmissions between nodes. The routing algorithm is designed to minimize the average number of hops used by the packets in the network. This idea, along with the scheduling and routing decoupling, leads to delay reduction compared with the traditional back-pressure algorithm.

**Keywords:** Back pressure, Packets, Routing, Shadow queue.

### I. INTRODUCTION

The back pressure method first proposed in [1] has recently shown a great potential for solving a number of issues in the wireless multi-hop networks. The central idea of back-pressure scheduling model is that contention among the links should be resolved by scheduling the link which has the largest product of the queue differential backlog between its endpoints and the transmission rate at which the link can be served. In a perfectly time-slotted medium access mechanism such as TDMA (Time Division Multiple Access), this will result into optimal throughput of flows while guaranteeing the queue stability (ingress traffic to a queue never exceeds its egress traffic). The utility maximization framework initially proposed in [2] shows that injection rates of the flows should be chosen such that aggregate utility of the flows is to be maximized. Here the utility of flow represents a desirable effect on the entire network achieved by a particular rate of the flow. It was shown in [3] [4] that the backpressure scheduling and utility based rate control together can solve the global problem of the network utility maximization.

The fundamental challenge with back pressure method is that solution of the underlying scheduling strategy is NP-hard [5]. Also, since it was proposed for a centralized, time slotted, and synchronized system, a distributed implementation which can achieve even a closer approximation is very difficult to develop. Recently, [6] have attempted to incorporate backpressure technique based scheduling in random medium access protocols such as CSMA/CA. These protocols try to approximate the performance of the ideal back pressure scheduler by prioritizing the frame transmissions according to differential backlogs of the queues. Here, every node in the network maintains a per destination queue (PDQ) and the packets destined to a particular destination host are stored in the PDQ of that destination host until further forwarding decisions are made. Now, nodes share their PDQ information with their neighboring nodes, and this information is utilized by every node to calculate the differential backlogs of its PDQs. The differential backlog of a PDQ at a node is equal to the size of the PDQ minus the size of the PDQ of its upstream neighbor towards the destination end. To emulate the back pressure scheduling, the packets of the PDQ which has the highest differential backlog (highest back-pressure) in the neighborhood are given the higher chances for the transmission. This way, the likelihood that the packets are transmitted from a particular PDQ at a node is proportional to its differential

backlog compared to the differential backlogs of PDQs of all nodes in the neighborhood. This prioritization quickly moves the traffic from long back logged queues to the shorter queues achieving an improved throughput and a better overall stability of queues.

## II. RELATED WORK

The first theoretical work on backpressure scheduling technique is the classic result in [1], proving that this queue-differential based scheduling method is throughput optimal (i.e., it can stabilize any feasible rate vector in a network). Since then, researchers have combined the basic backpressure technique with utility optimization to provide a comprehensive approach to the stochastic network optimization [7], [8]. In [9], the authors present a method whereby only one real queue is maintained for each neighbor node, along with virtual counters and shadow queues for all destinations, and show that this yields delay improvements. In [10], a novel variant of the backpressure scheduling technique is proposed which uses head of line packet delay instead of the queue lengths as the basis of the backpressure weight calculation for each link or commodity, also yielding enhanced delay performance. However, these works both assume the existence of the static fixed routes.

In [11] and [12], the authors present two works on backpressure routing aimed specifically for cluster-based intermittently connected networks. In [11], the authors develop a two phase routing method, combining the backpressure routing with source routing for the cluster-based networks, separating intra cluster routing from inter-cluster routing. They show that this scheme results in large queues at only a subset of the nodes, yielding smaller delays than conventional backpressure technique. In [12], the authors implement the above-mentioned algorithm in a real experimental network and show that the delay improvements empirically. The key difference of these works from our proposed work is that we do not make any assumption about the intermittently connected network being organized in a cluster based hierarchy and we require no previous knowledge of nodes mobility.

## III. PROPOSED WORK

### 1. Throughput Optimal Backpressure Algorithm

This algorithm works on wireless networks. This back pressure algorithm should be depending on one main procedure. The main procedure is the destination queue procedure by using these procedure only we can reducing the poor delay of the time and the distance every node at the time of routing file in between the two or more locations predestination queues maintaining the two phases:

- routing algorithm
- scheduling algorithm.

In this system says distance is very high and time is very high. So may draw backs will be occurred at the time of working on the routing algorithm that's why we are implementing a new algorithm. Scheduling algorithm combined with the routing algorithm. Our scheduling algorithm says what to providing the schedule for prepress of the over come to draw backs that's why we are using the round robin algorithm and shortest path routing algorithm. In this algorithm providing quality of services to the end users depending on the service only routing will be decide it is best routing or the bad routing . QOS may be depends 4 phases: Bandwidth, frequency, time, distance. In any network depends on QOS. Bandwidth and frequency is very high and time distance is low QOS is very high. At each link the algorithm assigns a weight to each possible destination node that is called back pressure. Define the back pressure at link (n,j) for destination node d at slot t to be:

$$w_{n,j}^d(t) = Q_{nd}(t) - Q_{jd}(t)$$

where  $Q_{nd}(t)$  denotes the number of packets at node n denoted for node d at the beginning of time-slot t. Under this notation,  $Q_{nn}(t) = 0, \forall t$ . Assign a weight  $w_{nj}$  to each link (n, j), where  $w_{nj}$  is defined to be the maximum back pressure overall possible destinations. i.e.

$$w_{nj}(t) = \max_d w_{nj}^d(t)$$

### 2. Min Resource Routing

The back-pressure algorithm explores all paths in the entire network and, as a result, may choose paths that are unnecessarily long, which may even contain some loops, thus leading to poor performance. We address this problem by introducing a cost function that measures the total amount of the resources used by all flows in the network. Specially, we add up the traffic loads on all links in the network and use this as our cost function. The goal then is to minimize this cost subject to the network capacity constraints. Given a set of packet arrival rates that lie within the capacity area, our goal is to find the routes for the flows so that we use as few resources as possible in the network. Thus, we formulate the following optimization problem:

$$\begin{aligned} & \min \sum_{(nj) \in L} \mu_{nj} \\ & \text{s.t.} \sum_{f \in F} x_f I\{b(f) = n, e(f) = d\} + \sum_{(ln) \in L} \mu_{ln}^d \leq \sum_{(nj) \in L} \mu_{nj}^d \\ & \forall d \in N, n \in N \\ & \{\mu_{nj}\}(n, j) \in L \end{aligned}$$

Figure 1 illustrates how the M-back pressure algorithm works in a simple wireline network. All links in the network can be activate simultaneously without interfering with each other. Note that the backlog difference of route 1 is 6 and the backlog difference of the route 2 is 4. Because the backlog difference of the route 2 is smaller than M, the route 2 is blocked at current traffic load. The M-back-pressure algorithm will automatically choose the route 1, which is shorter. Therefore, a proper M can avoid the long routes in when the traffic is not close to capacity.

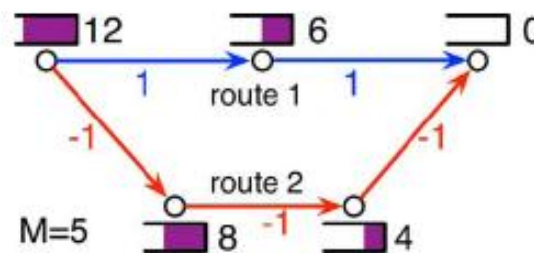


Fig. 1: Link weights under the M-back-pressure algorithm.

### 3. Shadow Queue Algorithm

In addition to the real queues, each node n also maintains a counter, which is known as shadow queue,  $p_{nd}$  for each destination d. Unlike the real queues, the counters are much easier to maintain even if the number of counters at each node grows linearly with the size of the overall network. The shadow queues are updated based on the movement of the fictitious entities called as shadow packets in the network. The movement of the fictitious packets can be thought of as an exchange of the control messages for the purposes of the routing and schedule. Just like the real packets, shadow packets arrive from outside the network and eventually exit the network. The back-pressure for destination on link (n j) is taken to be as follows:

$$w_{nj}^d[t] = p_{nd}[t] - p_{jd}[t] - M$$

The evolution of the shadow queue  $p_{nd}[t]$  is

$$\begin{aligned} p_{nd}[t+1] = & p_{nd}[t] - \sum_{j:(nj) \in L} I_{\{dn \wedge t=d\}} u_{nj}[t] + \\ & \sum_{l:(ln) \in L} I_{\{d \wedge t=d\}} u_{ln}[t] + \sum_{f \in F} I_{\{b(f)=n, e(f)=d\}} a_f[t] \end{aligned}$$

Where  $u_{nj}[t]$  is the number of shadow packets transmitted over the link (n j) in time t.  $d_{nj}[t]$  is the destination node that has the max weight on the link (n j).  $a_f[t]$  is the number of shadow packets generated in time t for flow f.

#### 4. Adaptive Routing Algorithm

When a packet arrived at a node, then it use routed as follows: Let  $\sigma_{nj}^d[t]$  is the number of shadow packets from node n to the node j for destination d during time t. Let  $\hat{\sigma}_{nj}^d$  denote an estimate of the expected value of  $\sigma_{nj}^d[t]$  at time t. At each time slot t, the following sequence of operations occurs at each node . A packet arriving at node n for destination d is inserted in the real queue  $q_{nj}$  for next-hop neighbor j with probability:

$$P_{nj}^d[t] = \frac{\hat{\sigma}_{nj}^d[t]}{\sum_{k:(nk) \in L} \hat{\sigma}_{nk}^d[t]}$$

Packets waiting at link (n j) are transmitted over the link when that link is scheduled as shown in figure 2.

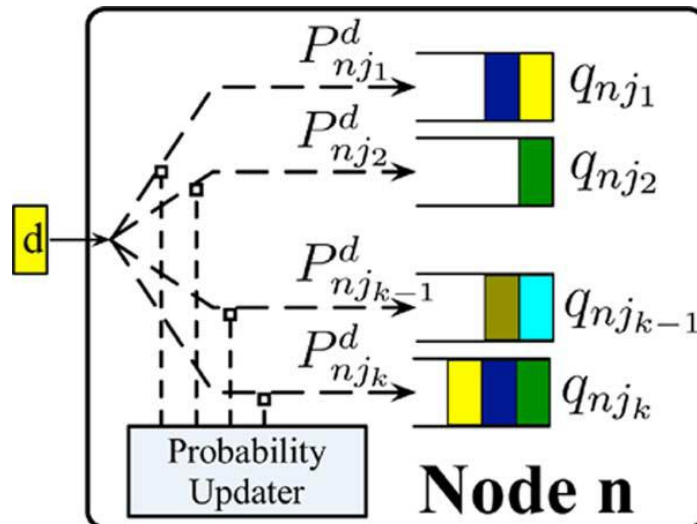


Fig. 2: Probabilistic splitting algorithm at node

#### IV. CONCLUSION

ackpressure scheduling and routing, in which packets are preferentially transmitted over communication links with high queue differentials, offers the promise of throughput-optimal operation for a wide range of the communication networks. However, when the traffic load is very low, due to the corresponding low queue occupancy, then the backpressure scheduling/routing experiences long delays. This is particularly of concern in the intermittent encounter-based mobile networks which are already delay-limited due to the sparse and highly dynamic network connectivity. While state of the art mechanisms for such networks have proposed the use of the redundant transmissions to improve the delay, they do not work well when the traffic load is high. We decouple (to a certain degree) routing and scheduling in the network through the use of the probabilistic routing tables and the so-called shadow queues. We use the same number of shadow queues as the back-pressure technique, but the number of real queues is very small (per neighbor). The new idea here is to perform the routing via probabilistic splitting, which allows the dramatic reduction in the number of the real queues. Finally, an important observation in this work is that the partial "decoupling" of the shadow back-pressure and real packet transmission allows us to activate more links than a regular back-pressure method would. This idea appears to be essential to reduce the delays in the routing case.

## REFERENCES

- [1] L. Tassiulas and A. Ephremides, "Stability properties of constrained queueing systems and scheduling policies for maximum throughput in multihop radio networks," dec 1990, pp. 2130 –2132 vol.4.
- [2] F. Kelly, A. Maulloo, and D. Tan, "Rate control in communication networks: shadow prices, proportional fairness and stability," in *Journal of the Operational Research Society*, vol. 49, 1998.
- [3] L. Chen, S. H. Low, M. Chiang, and J. C. Doyle, "Cross-layer congestion control, routing and scheduling design in ad hoc wireless networks," in *INFOCOM 2006. 25th IEEE International Conference on Computer Communications. Proceedings, 2006*, pp. 1 –13.
- [4] A. Eryilmaz and R. Srikant, "Joint congestion control, routing, and mac for stability and fairness in wireless networks," *Selected Areas in Communications, IEEE Journal on*, vol. 24, no. 8, pp. 1514 –1524, 2006.
- [5] M. J. N. Georgiadis Leonidas and L. Tassiulas, "Resource allocation and cross-layer control in wireless networks," in *Foundations and Trends in Networking*, 2006.
- [6] U. Akyol, M. Andrews, P. Gupta, J. Hobby, I. Saniee, and A. Stolyar, "Joint scheduling and congestion control in mobile ad-hoc networks," april 2008, pp. 619 –627.
- [7] X. Lin, N. Shroff, and R. Srikant, "A tutorial on cross-layer optimization in wireless networks," *IEEE Journal on Selected Areas in Communications*, vol. 24, no. 8, 2006.
- [8] M. J. Neely, "Stochastic network optimization with application to communication and queueing systems," *Synthesis Lectures on Communication Networks*, vol. 3, no. 1, 2010.
- [9] L. Bui, R. Srikant, and A. Stolyar, "Novel architectures and algorithms for delay reduction in back-pressure scheduling and routing," *IEEE INFOCOM 2009*.
- [10] B. Ji, C. Joo, and N. Shroff, "Delay-based back-pressure scheduling in multi-hop wireless networks," *IEEE INFOCOM*, 2011.
- [11] J. Ryu, L. Ying, and S. Shakkottai, "Back-pressure routing for intermittently connected networks," *IEEE INFOCOM 2010*.
- [12] J. Ryu, V. Bhargava, N. Paine, and S. Shakkottai, "Back-pressure routing and rate control for icns," *ACM Mobicom*, 2010.

## Heat Ventilation & Air- Conditioning System with Self-Tuning Fuzzy PI Controller

Mir Munawar Ali<sup>1</sup>, Mohd Aamer Khan<sup>2</sup>, Mohammed Shafi<sup>3</sup>, Mohd Abdul Omer Khan<sup>4</sup>, Md Azam Ali Farooky<sup>5</sup>, Syed Azam<sup>6</sup>, Syed Khasim<sup>7</sup>, Shaik Wasei Eizaz Ahmed<sup>8</sup>

<sup>1</sup> Associate Professor, Department of Electrical and Electronics Engineering, Deccan College of Engineering & Technology, Hyderabad, INDIA

<sup>2,3,4,5,6,7,8.</sup> Student, Department of Mechanical Engineering, Sreyas Institute of Engineering & Technology, Nizam Institute of Engineering & Technology, Hyderabad, INDIA

**Abstract:** In this paper, a Self-tuning Fuzzy PI controller is used for the supply air pressure Control loop for Heating, Ventilation and Air-Conditioning (HVAC) system. The modern H. V. A. Cussing direct digital control methods have provided useful performance data from the building occupants. The self-tuning Fuzzy PI controller (STFPIC) adjusts the output scaling factor on-line by fuzzy rules in accordance to the current trend of the control process. This research work has got the integration and application of these fundamental sources of information, using some modern and novel techniques. In Comparison to PID and Adaptive Neuro-Fuzzy (ANF) Controllers, the simulation results show that STFPIC performances are better under normal conditions as well as extreme conditions where in the HVAC system encounters large variations. The cost and scalability of the set techniques can be positively influenced by the recent technological advancement in computing power, sensors and data bases.

### I. Introduction

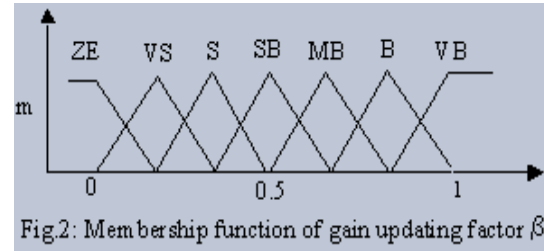
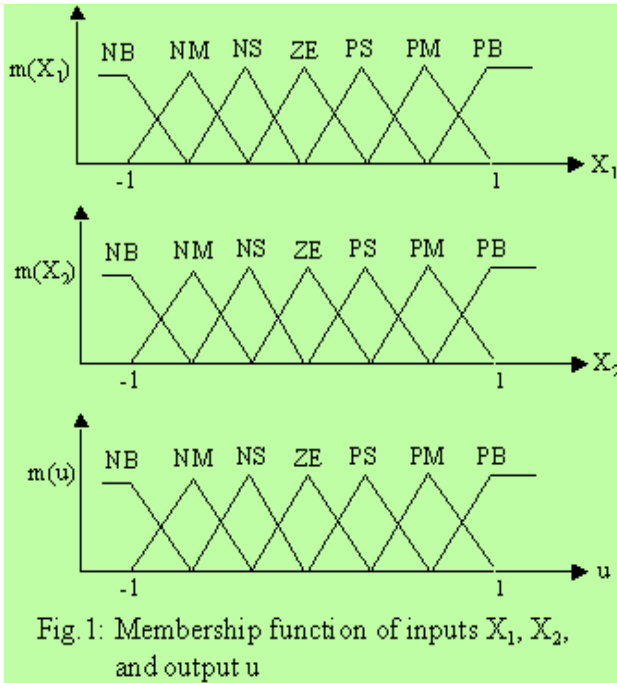
Heating, Ventilation and Air-Conditioning (HVAC) systems require control of environmental variables such as pressure, temperature, humidity etc. In this system, the supply air pressure is regulated by the speed of a supply air fan. Increasing the fan speed will increase supply air pressure, and vice versa. In the large commercial buildings modern Direct Digital Control (D.D.C.) systems are becoming more favorable with the use of new sophisticated hardware. The H.V.A.C System components are used together and monitored remotely from a central location positions. The general trend in the design and commissioning of new commercial buildings includes the new types of these systems. It has been reported that fuzzy logic controller is very suitable for non-linear system and even with unknown structure. The tuning procedure can be a time-consuming, expensive and difficult task. This problem can be easily eliminated by using self-tuning scheme for fuzzy PI / PID controller. The conventional PID controllers are widely used in industry due to their simplicity in arithmetic, ease of using, good robustness, high reliability, stabilization and zero steady state error. But HVAC system is a non-linear and time variant system. It is difficult to achieve desired tracking control performance since tuning and self-adapting adjusting parameters on line are a scabrous problem of PID controller. In the first part of this paper Self-tuning Fuzzy Logic Controller is described. The second part described the implementation of the PI type Self-tuning Fuzzy Logic Controller on a HVAC system. In the last part simulation results are presented to compare with the well-tuned PID controller and Adaptive Neuro-Fuzzy (ANF) controller.

### II. Development of pi-Type self-Tuning Fuzzy controller

The basic function of the rule base is to represent in a structured way the control policy of an experienced process operator and/or control engineer in the form of a set of production rules such as: If{process state}then{control output} Considered a set of desired input-output data pairs:

$$[X_1^{(1)}, X_2^{(1)}; U^{(1)}], [X_1^{(2)}, X_2^{(2)}; U^{(2)}] \dots \dots \dots (1)$$

Where  $X_1$  and  $X_2$  are inputs and  $u$  is the output.  
Here considered error( $e$ )as $X_1$  and change of error( $\Delta e$ )as $X_2$ .



The task here is to generate a set of fuzzy rules from the desired input-output pairs of equation(1) through following steps[20]:

Divide the input and output spaces into fuzzy regions.

Assumed the domain interval so  $x_1, x_2$  and  $u$  are  $[x_1^-, x_1^+]$ ,  $[x_2^-, x_2^+]$  and  $[u^-, u^+]$  respectively.

Fig.1 shows each domain interval divided into 7 equal regions, denoted by NB (negative big), NM (negative medium), NS (negative small), ZE (zero), PS (positive small), PM (positive medium) and PB (positive big) and assigns each region a fuzzy membership function. The shape of each membership function is triangular.

$\Delta e$		NB	NM	NS	ZE	PS	PM	PB
NB		NB	NB	NB	NM	NS	NS	ZE
NM		NB	NM	NM	NM	NS	ZE	PS
NS		NB	NM	NS	NS	ZE	PS	PM
ZE		NB	NM	NS	ZE	PS	PM	PB
PS		NM	NS	ZE	PS	PS	PM	PB
PM		NS	ZE	PS	PM	PM	PM	PB
PB		ZE	PS	PS	PM	PB	PB	PB

Table 1: Fuzzy rules for computation of  $u$

$\Delta e$		NB	NM	NS	ZE	PS	PM	PB
NB		VB	VB	VB	VB	B	MB	SB
NM		VB	VB	VB	B	MB	SB	S
NS		VB	VB	B	MB	SB	S	VS
ZE		VB	B	MB	SB	S	VS	ZE
PS		B	MB	SB	S	VS	ZE	ZE
PM		MB	SB	S	VS	ZE	ZE	ZE
PB		SB	S	VS	ZE	ZE	ZE	ZE

Table 2: The rule base for determination of  $\beta$

The term set so  $f_e, \Delta e$  and  $u$  contains the same linguistic expressions for the magnitude part of the linguistic values ,i.e.,

$$LE = L \square E = LU = \{NB, NM, NS, ZE, PS, PM, PB\}$$

As shown in Fig. 1 and represents the rule base in the table format as shown in Table 1. The cell defined by the intersection of the first row and the first column represents a rule such as, If  $e(k)$  is NM and  $\Delta e(k)$  is PS then  $u(k)$  is NS. The fuzzy controller is developed using this 49 fuzzy if-then rules as shown in Table 1.

Similar like fuzzy controller, using symmetrical triangle calculate membership functions of (i)e, Δe, u(as shown in Fig.1) and (ii)gain updating factor(β) (as shown in Fig.2)for self-tuning mechanism. An additional logic for addition at the output of controller is incorporated for PI controller. Because the discrete-time version equation of PI controller is

$$u(k) = K_p e(k) + K_I \sum e(k);$$

$$u(k) = u(k) - u(k-1);$$

or

$$u(k) = \Delta u(k) + u(k-1),$$

Where Δu(k) is the change of control output and u(k) is the total control output.

Fig.3 shows that the output scaling-factor (SF) of the fuzzy controller is modified by a self-tuning mechanism, which is marked by bold rectangular portion in the figure. Then based on the knowledge of process control or by trial and error method choose suitable SF's for inputs and output. The relationship as follows for PI self-tuning fuzzy controller scheme.

$$N_e = N_{\Delta e}, N_{\Delta e} = N_e \Delta e \text{ and } N_u = (\beta N_u) \Delta u$$

Where  $N_e$  and  $N_{\Delta e}$  are input scaling factor of error and change of error respectively and  $N_u$  is output scaling factor. There after apart from fuzzy PI controller rule determination, also determines the rule base for gain updating factor, in the similar way like, if e is E and Δe is ΔE then β is β.

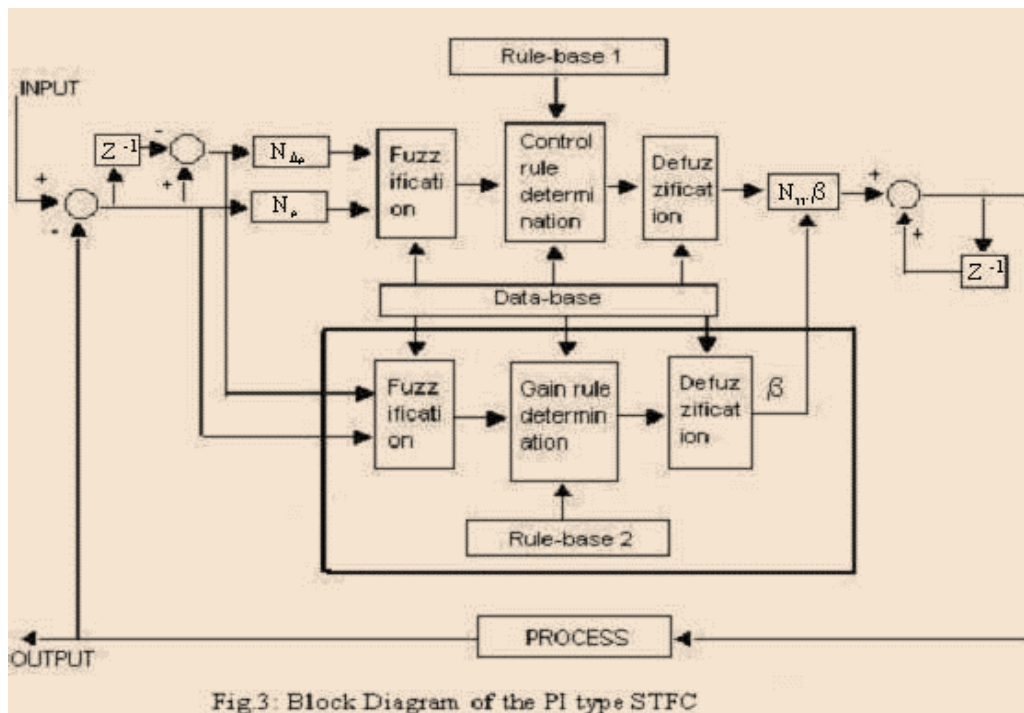
A structure of which is shown in Table2, though it may vary. Further modification of the rule base for β may be required, depending on the type of response the control system designer wishes to achieve. As shown in Fig.3, when this β is multiplied with the fuzzy controller gain  $N_u$ , gives the overall gain of STFPI. It is very important to note that the rule base for computation of β will always be dependent on the choice of the rule base for the controller.

Choice of Scaling Factor (gain): The scaling factors also known as gains, which describe the particular input normalization and output demormalizations, plays an important role similar to that of the gain coefficients in a conventional controller.

For example, a fuzzy controller can be represented as

$$N_u u(k) = F(N_e e(k), N_{\Delta e} \Delta e(k)),$$

Where  $N_e$ ,  $N_{\Delta e}$  and  $N_u$  are the scaling factors for e, Δe and u respectively, and F is a non-linear function representing the fuzzy controller. Same gain principle is used in the design of self-tuning fuzzy controller.



### III. Simulation results

A typical cooling only HVAC system is shown in Fig.8. In the system, the outside air is mixed with the building return air. Then the mixed air (supply air) is sucked through the cooling coil via a filter by an apply air fan. The cooled air is then supplied to different zones as shown in the figure. In this HVAC system, the supply air pressure is regulated by the speed of a supply air fan. Increasing the fan speed will increase the supply air pressure, and vice versa. The dynamics of the control signal feeding to the fan Variable Speed Drive to the supply air pressure can be modeled as a second order plus dead time plant.

#### A. Performance Analysis of the STFPIIC

Study as well as analysis is made if the performance of STFPIIC is applied under normal condition and changing of HVAC process model.

Under Normal Condition: The transfer function of the supply Air pressure loop under normal condition is obtained as

$$G(s) = 0.81e^{-2s} / (0.97s+1)(0.1s+1)$$

Where gain(K)=0.81,  $\tau_1=0.97$ ,  $\tau_2 = 0.1$  and deadtime( $\delta$ ) = 2sec.

For this process scaling factors are set at  $N_e = 0.9$ ,  $N_{\Delta e} = 5$  and  $N_u = 2.5$ .

#### Under HVAC Process Parameters Variation:

1) When

gain(K)=0.81,  $\tau_1=0.2$ ,  $\tau_2=2$  and deadtime( $\delta$ )=2sec., then the transfer function of the supply air pressure loop is obtained as

$$G(s) = 0.81e^{-2s} / (0.2s+1)(2s+1).$$

For this process scaling factors are set at  $N_e = 0.9$ ,  $N_{\Delta e} = 15$  and  $N_u = 0.3$ .

2) When gain(K)=1.2,  $\tau_1=0.97$ ,  $\tau_2 = 0.1$  and deadtime ( $\delta$ )=3sec., then the transfer function of the supply air pressure loop is obtained as

$$G(s) = 1.2e^{-3s} / (0.97s+1) (0.1s+1).$$

For this process scaling factors are set at  $N_e=0.9$ ,  $N_{\Delta e}=3$  and  $N_u=1$ .

3) When gain(K)=1.2,  $\tau_1=0.97$ ,  $\tau_2 = 0.1$  and deadtime ( $\delta$ )=4sec., then the transfer function of the supply air pressure loop is obtained as

$$G(s) = 1.2e^{-4s} / (0.97s+1)(0.1s+1).$$

For this process scaling factors are set at  $N_e = 0.9$ ,  $N_{\Delta e}=3$  and  $N_u = 1$ .

The Fig.4, Fig.5, Fig.6, Fig.7 and Table3 are shown that the supply air pressure loop of HVAC works satisfactorily both under normal and as well as under model variations. Table3 refers that both the rise time and settling time is very much satisfactory. Peak over shoots are also shown negligible when STFPIIC is used.

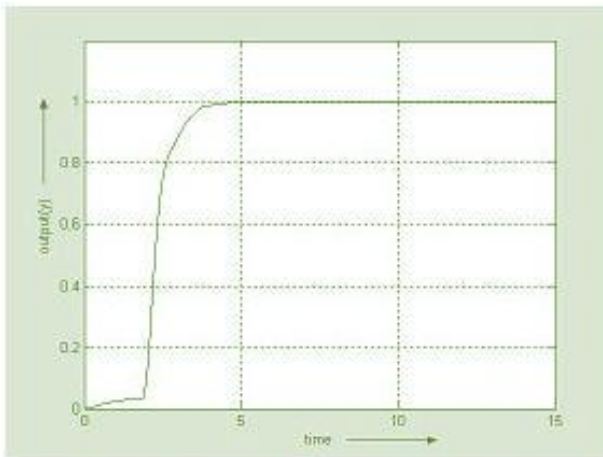


Fig.4: Performance of the transfer function  

$$\frac{0.81 e^{-2s}}{(0.97s + 1)(0.1s + 1)}$$

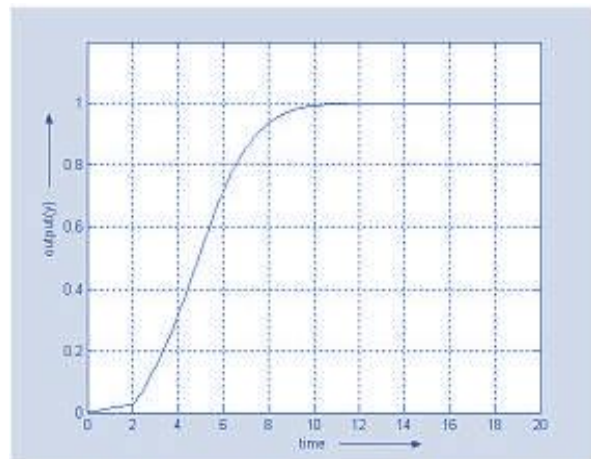


Fig.5: Performance of the transfer function  

$$\frac{0.81 e^{-2s}}{(0.2s + 1)(2s + 1)}$$

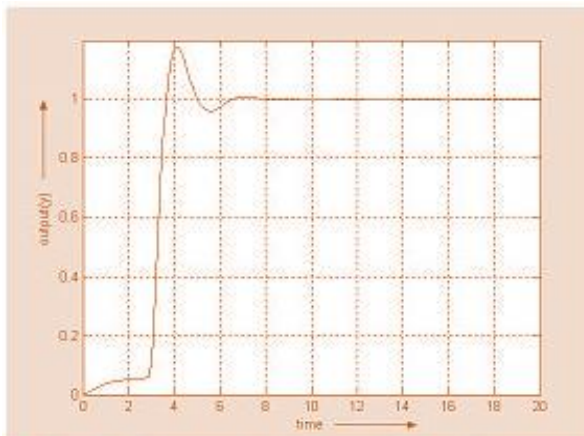


Fig.6: Performance of the transfer function  

$$\frac{1.2 e^{-3s}}{(0.97s + 1)(0.1s + 1)}$$

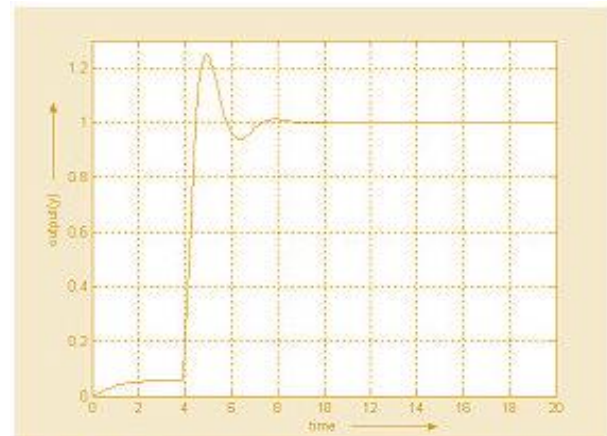


Fig.7: Performance of the transfer function  

$$\frac{1.2 e^{-4s}}{(0.97s + 1)(0.1s + 1)}$$

**B. Comparison of Practical Performance with Existing Methods.**

In order to demonstrate the effectiveness and robustness, the performance of the proposed STFPI has been compared with those of existing methods, the Bi, Cai’s PID controller and Jian, Cai’s ANF controller[22] for supply air pressure loop control. The comparison has been done under changing process model. The results are provided in Table 4. For the application of STFPI, substantial improvements have been observed in settling time and also in peak overshoot for all the transfer function of the air supply model compare to ANF and PID controller. Furthermore, it is more important that when the process encounters large parameter variations, the method provided presents much robustness as shown in Table 4.

Transfer Function of the Supply Air Pressure Loop	Controller Type	Peak Overshoot (Mp %)	Settling Time (t <sub>s</sub> , sec.)
$\frac{0.81 e^{-2s}}{(0.97s+1)(0.1s+1)}$	PID	3.9	6.7
	ANF	3.5	7.5
	STFPIC	0.0	3.6
$\frac{0.81 e^{-2s}}{(0.2s+1)(2s+1)}$	PID	17.9	16.2
	ANF	0.9	10.6
	STFPIC	0.088	8.9
$\frac{1.2 e^{-3s}}{(0.97s+1)(0.1s+1)}$	PID	63	37
	ANF	56	19
	STFPIC	17.6	6
$\frac{1.2 e^{-4s}}{(0.97s+1)(0.1s+1)}$	PID	100	>120
	ANF	59	32
	STFPIC	25	6.9

Table 4: Control index of PID, ANF (with secondary loop) and STFPIC under normal and different model variations

Transfer Function of the Supply Air Pressure Loop	Rise Time (t <sub>r</sub> , sec.)	Settling Time (t <sub>s</sub> , sec.)	Peak Overshoot (Mp %)	IAE	ITAE
$\frac{0.81 e^{-2s}}{(0.97s+1)(0.1s+1)}$	3.3	3.6	0.00	2.40	2.91
$\frac{0.81 e^{-2s}}{(0.2s+1)(2s+1)}$	8.2	8.9	0.088	5.05	14.29
$\frac{1.2 e^{-3s}}{(0.97s+1)(0.1s+1)}$	3.5	6.0	17.61	3.38	6.00
$\frac{1.2 e^{-4s}}{(0.97s+1)(0.1s+1)}$	6.6	6.9	25.04	4.33	9.83

Table 3: Performance analysis of STFPIC for different HVAC – Supply Air Pressure Loop

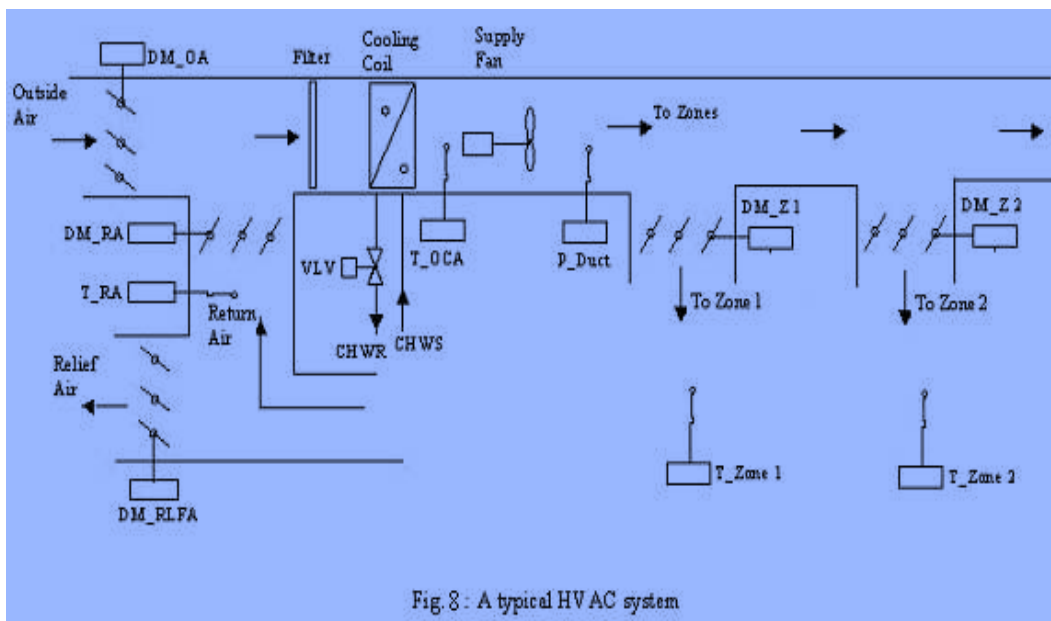


Fig. 8: A typical HVAC system

#### IV. Application of Fuzzy Control for Optimal Operation of Complex Chilling Systems

##### 4.1 Requirements for the design of the fuzzy control system

The fuzzy control system is needed to ensure supply of the required cooling power during the operating time of the building by the lowest cost and the shortest system operating time with a low range of set point error for the supply temperature. The concept of knowledge engineering by measurement and analysis of system behavior is necessary, since no expert knowledge has existed for the formulation of the fuzzy rules. Measurement of two physical values of the system is necessary, in order to consider system behavior. These process values are: the outdoor air temperature  $T_{out}$ , which partially presents the thermal behavior of the building, and the user net return temperature ( $T_{r-un}$ ), which contains the total cooling load alternation of the building. These requirements focus on three different fuzzy controllers for the different components of the chilling system. The design data for fuzzy controllers has been organized in various tables for the assistance of membership function values of various input variables to a mamdani type fuzzy inference system (FIS).

**Table 5: FUZZY CONTROLLER’S TEMPERATURE DISTRIBUTION DESIGN DATA.**

SUPPLY TEMPERATURE (HE <sub>1</sub> ) °C	SUPPLY TEMPERATURE (HE <sub>2</sub> ) °C	EXTERNAL TEMPERATURE T <sub>out</sub> (K) °C
4.2	31.1	29.7
5.8	31.2	30.1
6.3	31.5	33
6.9	31.9	34
7.3	33.2	35
8.2	33.4	37
13	33.5	39
14	34.5	42
15	35.4	54

Here, HE2 and HE1 are the respective heat exchangers for evaporator and condenser and Tout is the outdoor air temperature. The fuzzy controller’s set point error difference design data is as shown in table 4.3. Here error (e1) and error (e2) gives the difference between the SP (set point value) & MV (measured value) for condenser and evaporator. Tr-un gives the user net return temperature due to individual zone and internal load (occupants, equipment, computers etc). Tr-un gives the difference between user net return temperature and set point temperature. Tout gives the difference between user net return temperature and outdoor air temperature and d Tout/ dt gives the difference between outdoor air temperature by K<sup>th</sup> cycle and K-1<sup>TH</sup> cycle. The assessment of refrigeration is made from the coefficient of performance (COP). It depends upon evaporator temperature Te and condensing temperature Tc.

$$COP_{Carnot} = \frac{T_e}{(T_c - T_e)}$$

COP in industry calculated for type of compressor:

$$COP = \frac{\text{Cooling effect (kW)}}{\text{Power input to compressor (kW)}}$$

**4.2 Thermal analysis of the building and chilling system**

The aim of the thermal analysis of the building is to find measure able information for the needed current cooling load. Alternation for internal cooling load of computers and machines could not be exactly registered or measured. It has been proven by measurement of current cooling power of the building as shown in fig.2 that there is not a significant correlation between T out and the current cooling power. Also, at higher internal load, there is a heat transmission to the outdoor air space, if Tout is lower than 33°C. The current cooling power will increase, if Tout gets higher than 33°C. Al though the equipment and computers are on service for 24 hours a day, there is a big alternation of cooling power. In the summertime, when the Tout increases to about 45°C, the current cooling power will be more influenced by Tout. So Tout can be used for fore casting the maximum cooling power. Additional information is necessary, in order to analyze the thermal behavior of the building. This information is gained by measuring the user net return temperature (Tr-un). Any change of total cooling load will influence Tr-un and is an important input for the fuzzy controller.

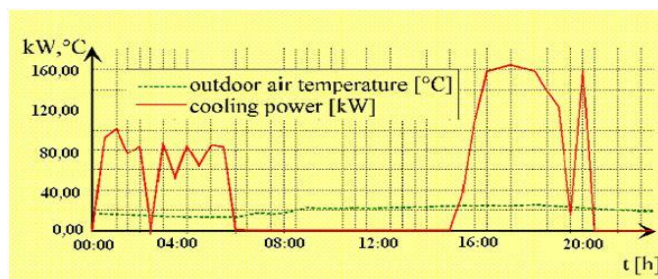


Fig.9: Alternation of current cooling power and outdoor air temperature.

#### 4.3 Description of the Chilling System

The chilling system described here supplies chill water to the air conditioning systems (AC-systems) installed in basement at Ansal Highway Plaza, Jalandhar (Punjab), India as shown in fig.1. These search conditions are ensured by the AC systems by supplying conditioned air to the building. The amount of cooling power for the building is the sum of internal cooling load (produced by occupants, equipment and computers) and the external cooling load, which depends on outdoor air temperature ( $T_{out}$ ) and sun radiation through the windows. The compression cooling method is made use of by the cooling machines installed here.

The principle of a compression cooling machine can be described in two thermodynamically processes. In the first step of the cooling process, the heat energy will be transferred from the system to the heat exchanger (evaporator) of the cooling machine, and therefore the liquid gas will evaporate by absorbing the heating energy. After the compression of the heated gas, in the second part of the process, the gas condenses again by cooling the gas through the air cooling system. In that step of the process, the heat transfer is from the condensation system to the outdoor air space. The process is continuous, and based on the second law of the thermodynamics. The vapour compression chiller system consists of following components.

(a) Compressor: It acts as a reclaiming agent.

(b) Condenser and Evaporator: These acts as a heat exchangers.

(c) Expansion Device: It acts as a throttling device to expand the liquid refrigerant.

(d) Refrigerant: It acts as a working fluid which absorbs heat from the fluid to be cooled and rejects heat to the atmosphere, through evaporation and condensation.

The schematic of a vapour compression chiller system is as shown in fig.10.

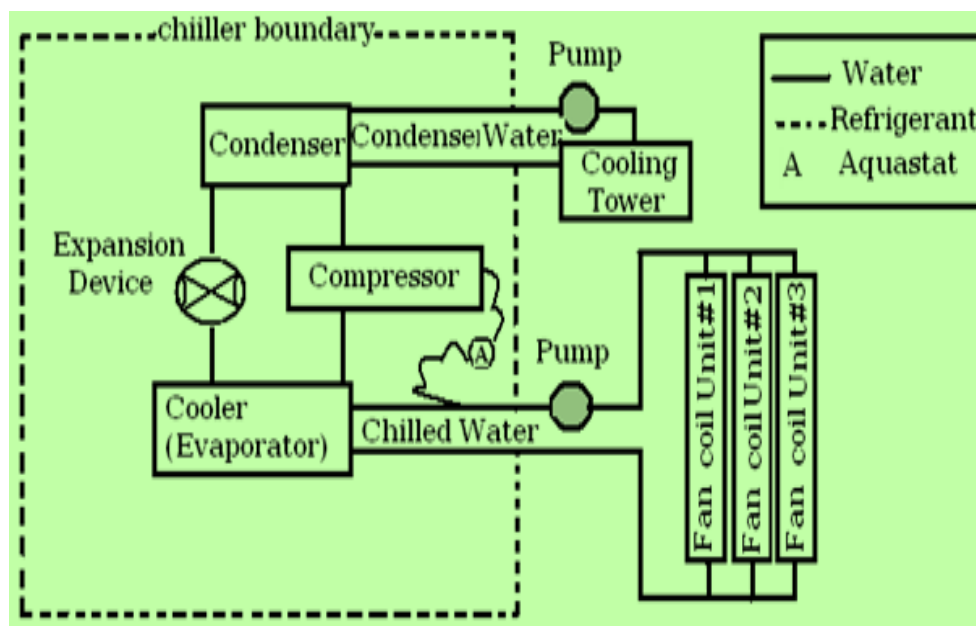


Fig.10: Schematic of a water-cooled chiller system.

During the operation of the cooling machines, the air cooling systems will be used and the condensation energy of the cooling machine is transferred to the outdoor air space. If the outdoor air temperature is much lower than user net return temperature on heat exchanger one, the air cooling system should serve as a free cooling system and replace the cooling machine.

#### 4.4 Fuzzy controller1 for operation of the cooling load storage system.

The optimum start point for the discharge of the cooling load storage system depends on the maximum cooling power needed, which can differ every day. For calculation of maximum cooling power,  $T_{out}$  must be processed by the fuzzy controller, since the maximum cooling power in the summer time will be influenced extremely by  $T_{out}$ . A feed back of current cooling power calculated by Fuzzy control Block2 is also necessary, in order to estimate the maximum cooling power. If the peak of a maximum cooling power is estimated by the fuzzy controller, then this will be compensated by optimally discharging the cooling load storage system parallel to the cooling machines.

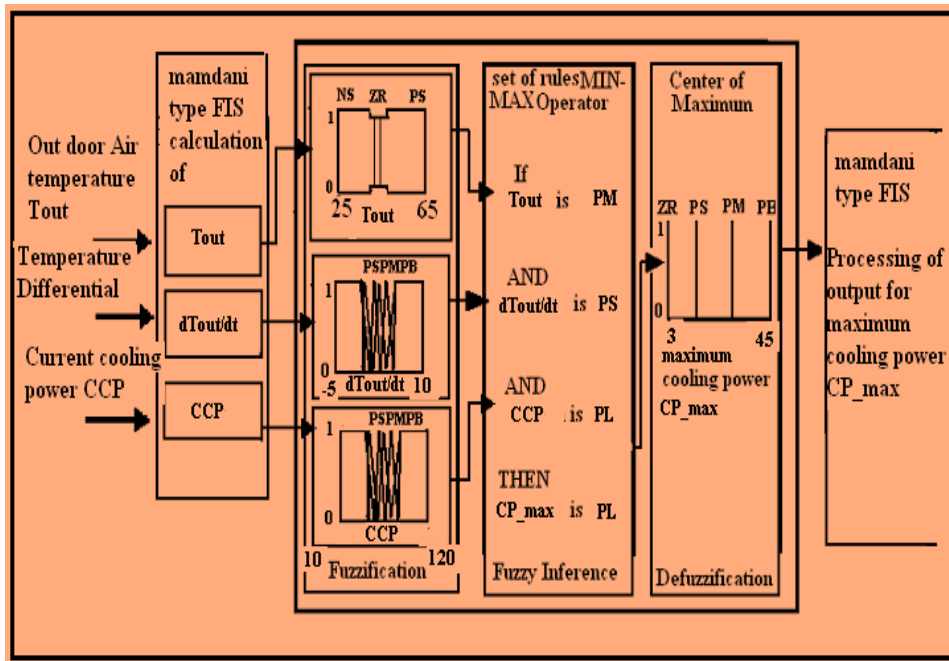


Fig.11:Fuzzycontroller 1 foroptimallydischargingcooling load storage system.

Theinputvariablesofthecontroller 1are:

- (1)Outdoor air temperature Tout
- (2)Differential of T out
- (3) Current cooling power of the cooling machines.

For the fuzzification of the Tout, we have following system knowledge. Observation of the system has shown that above Toutof45°C, a second cooling machine is necessary, in order to meet demand for increasing cooling load. There fore the fuzzification will be around Tout45° C with only three fuzzy sets. The second fuzzy variable is calculated by eqn(4.1)

$$D \text{ Tout}/dt=(\text{Tout}(k)-\text{Tout}(k-1)) \tag{4.1}$$

With Tout(k)=outdoor air temperature by K<sup>th</sup> cycle  
 Tout( k-1)=outdoor air temperature by K-1<sup>TH</sup> cycle.

The third input variable is the output K value1<sup>TH</sup>ofthe Fuzzy controller2, and represents the current cooling power. The output of the fuzzy controller1 is the estimated maximum cooling power CP-max. The membership function used for the fuzzy variables are available as P, Z, trapezmf, trimf andS- functions. For the defuzzification,"Centre of maximum "has been supported by the Mamdani type FIS (Fuzzy Inference System) Fig.4shows the P membership function as calculated byequation4.2

$$X=\text{MAX}\{0, \text{MIN}[1,B/(B-C) - AB(1/(B-C) (K-A))]\} \tag{4.2}$$

With° =degree of membership  
 X=process variable as input variable  
 A,B and C=parameters for the membership functions in value of the input variable, e.g.°C

**Membership function P type :**

The rule viewerforfuzzycontroller 1 isasshowninFig.12

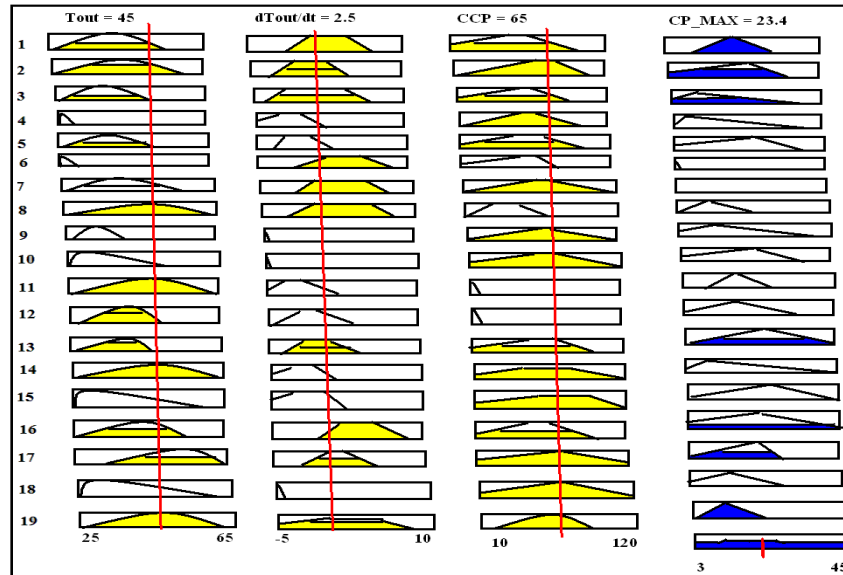


Fig.12: Rule viewer for fuzzy controller

#### 4.5 Fuzzy controller 2 for the operation of the cooling machines

The fuzzy controller 2 (FC-2) is the important part of the optimization control system, so that the cooling potential of the outdoor air is used, before starting any cooling machine. If "e1" is zero, or negative, then the capacity of free cooling system is enough for the required cooling power. The output signal of FC-2 will be zero. In other cases, FC-2 is responsible for the operation of the cooling machines. This controller consists of 3 input variables as following:

- (1) Setpoint error "e1" at the exchanger 1
- (2) Setpoint error "e2" at the exchanger 2
- (3) Difference between user net return temperature ( $T_{r-un}$ ) and T set point.

The input variable 1, is calculated as the difference between user net set point temperature ( $T_{set\ point}$ ), and output temperature of the heat exchanger (THE1) according to equation 4.3.

$$e1 = T_{set\ point} - T_{HE1} \quad (4.3)$$

For this variable, only three sets are necessary, in order to define if, e1 is NS, ZR or PS. The range of e1 is between +1k and -1k. The second input variable is calculated as the difference between ( $T_{set\ point}$ ), and output temperature of heat exchanger 2 (THE2) according to equation 4.4

$$e2 = T_{set\ point} - T_{HE2} \quad (4.4)$$

The third input variable is determined by equation 3.5

$$Tr-un = Tr-un - T_{set\ point} \quad (4.5)$$

Calculation of  $Tr-un$  is necessary, because  $T_{set\ point}$  is variable, and therefore  $Tr-un$  contains the real information about the cooling load of the building.

As soon as the first variable of the controller "e1" reaches the values of PS or ZR, this indicates that the capacity of FC-system is enough to cover the demanded cooling power, and the output signal for cooling machines is zero. In cases, where the capacity of the free cooling system is not enough, "e" will have values of NS, so that output of the controller will be determined by other rules. In that case the third input variable  $Tr-un$  is more weighted for the output value of the controller, because  $Tr-un$  represents the real alternation of the cooling load of the building. As shown in fig.5, the mamdani type fuzzy inference system (FIS) consists of calculation of input variables such as supply temperature HE1 set point error e1, supply temperature HE2 set point error e2 and user net return temperature  $Tr-un$ , then through the process of fuzzification, fuzzy inference

and defuzzification. The processing of output for current cooling power (CCP) takes place in mamdani type fuzzy inference system (FIS).

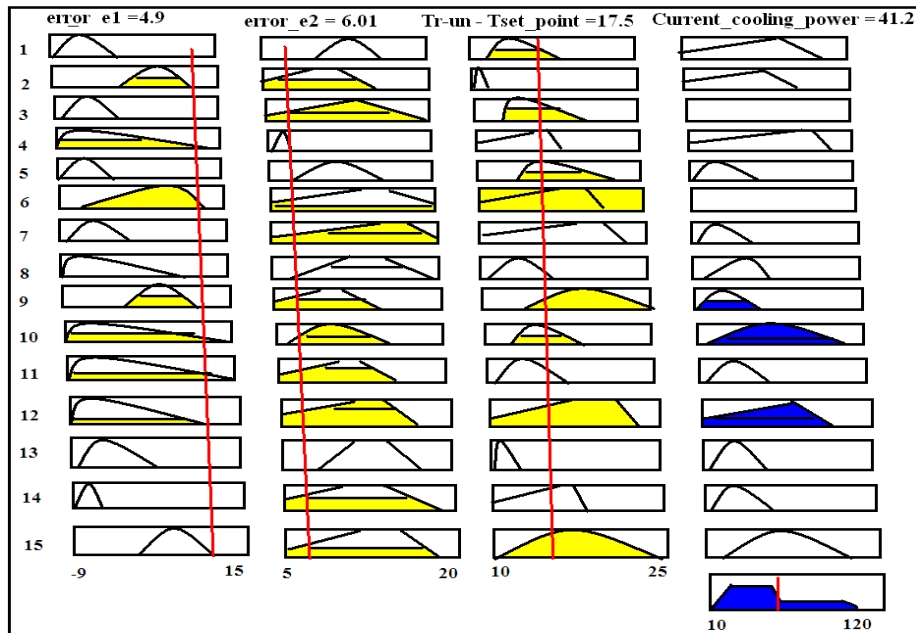


Fig.13: Fuzzy controller2 for optimal operation of cooling machines.

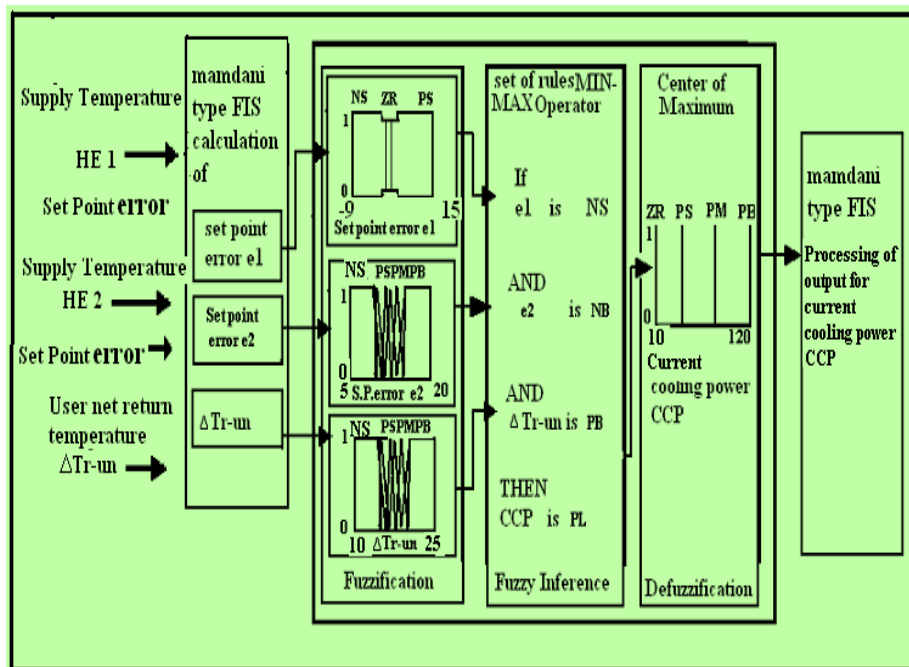


Fig.14: Rule view er for fuzzy controller.

### V. Conclusion

From the above elucidation, the process of controlling using fuzzy PI Controller can be clearly understood, as the basic process of fuzzy control by using variables which come across in HVAC System operation is meticulously depicted.

The different types of fuzzies and its operations are explained in the above paragraphs with its applications. These applications are very helpful to know the importance of fuzzy. The variations of the controlling processes are explained with the help of graphs.

## REFERENCES

- [1] T. Takagi and M. Sugeno, "Fuzzy identification of systems and its applications to modeling and control," *IEEE Trans. Syst., Man, Cybern.* vol. 15, 1985.
- [2] W. Pedrycz, "An identification algorithm in fuzzy relational systems," *Fuzzy Sets Syst.*, vol. 13, pp. 153 – 167, 1984.
- [3] W. Pedrycz and J. V. de Oliveira, "Optimization of fuzzy models," *IEEE Trans. Syst., Man, Cyber.*, vol. 26, no.4, Feb.1996.
- [4] R. Alcalá, J. Casillas, O. Cordon, A. Gonzalez, and F. Herrera, "A genetic rule weighting and selection process for fuzzy control of heating, ventilation and air conditioning systems," *Engineering application of Artificial Intelligence* 28 (2005) 279 – 296.
- [5] Qiang Xiong, Wen-Jian Cai and Ming He, "A practical decentralized PID auto-tuning method for TITO systems under closed-loop control," *International Journal of Innovative Computing, Information and Control*, vol.2, No.2, April.2006.
- [6] Qing-Gao Wang, Chang-Chieh Hang, Yong Zhang and Qiang Bi, "Multivariable Controller Auto-Tuning with its Application in HVAC Systems," *Proceedings of the American Control Conference*, California, June.1999.
- [7] R.K.Mudi and N.R.Pal, "A robust self-tuning scheme for PI and PDtype fuzzy controllers," *IEEE trans. on fuzzy sys.* vol. 7, no. 1, Feb.1997. [18] Qiang Bi, Wenjian Cai and et al, "Advanced controller auto-tuning and its application in HVAC systems," *Control Engineering Practice*, 2000.
- [8] D. Dirankov, H. Hellendorn and M. Reintrank, "An introduction to Fuzzy Control," New York: Springer-Verlag, 1993.
- [9] K. Ogata, "Modern Control Engineering," Englewood Cliffs, NJ: Prentice-Hall, 1970.
- [10] W. Jian and C. Wenjian, "Development of an adaptive neuro-fuzzy method for supply air pressure control in HVAC system," *Syst., Man, Cybern., IEEE*, 2000.
- [11] Z. R. Radakovic, V. M. Milosevic, S. B. Radakovic, "Application of temperature fuzzy controller in an indirect resistance furnace," *Applied Energy*. 73 (2002) 167-182.
- [12] H.R.Benerji, *Fuzzy Logic Controllers*, in: R. R. Yager, L. A. Zadeh (Eds.), "An introduction to Fuzzy logic application in intelligent systems," Kluwer, Boston, MA, 1992.
- [13] H. J. Zimmermann, "Fuzzy sets theory and its applications." Kluwer, Nijhoa, Boston, Dordrecht, Lancaster, 1984. Singapore: World Scientific,1993.
- [14] Kim J-H, Kim K-C, Chong EKP, "Fuzzy pre compensated PID controllers," *IEEE Trans. Con. Syst. Technology*, 1994: 2(4).
- [15] Cho Hyun-Joon, Cho Kwang-Bo, Wang Bo- Hyeun, "Fuzzy-PID hybrid control: automatic rule generation using genetic algorithm," *Fuzzy sets and systems*, 1997, 92(3), 305-316.
- [16] Wu Zhi Qiao, Masaharu Mizumoto, *Fuzzy sets and systems* 78 (1996), 23-35.
- [17] M. Sugeno, "Industrial applications of Fuzzy Control," Amsterdam, Netherlands: Elsevier,1985.
- [18] M. Sugeno and K. Tanaka, "Successive identification of a fuzzy model and its application to prediction of a complex system," *Fuzzy Sets Syst.*, vol. 42, pp. 315 – 334, 1991.
- [19] M. Sugeno and T. Yasukawa, "A fuzzy-logic-based approach to qualitative modeling," *IEEE Trans. Fuzzy Syst.*, vol. 1, pp. 7 – 31, Feb.1993.
- [20] R. M. Tong, "The construction and evaluation of fuzzy models," in *advances in Fuzzy Set Theory and applications* ed. M. M. Gupta et. al., North Holland, 1979.
- [21] R. Palm, "Sliding mode fuzzy control", in *Proc. Fuzz IEEE*, San Diego, CA, 1992, pp. 519-526.

## A Chord based Service Discovery Approach for Peer- to- Peer Networks

Yaminipurnatilak Jakka<sup>1</sup>, A. Sudarsan Reddy<sup>2</sup>

<sup>1</sup> M. Tech (CSE), Vasireddy Venkatadri Institute of Technology, Guntur, A.P., India.

<sup>2</sup> Assoc. Professor, Dept. of Information Technology, Vasireddy Venkatadri Institute of Technology, Guntur, A.P., India

**Abstract:** The limitations of client- server systems become evident in the large scale distributed environments. Peer to peer (P2P) networks can be used for improving communication process, optimizing resources discovery/localization, facilitating distributed information exchange. P2P applications need to discover and locate efficiently the node that provides the requested and targeted service. This paper proposes an approach called Chord4S, a Chord-based decentralized service discovery approach that supports service description distribution and discovery in a P2P manner. The main aim of designing Chord4S approach is to largely improve the availability of service descriptions in volatile environments by distributing descriptions of functionally equivalent services to different successor nodes. Two main features of Chord4S approach are to support service discovery with wildcard(s) and QoS awareness. Furthermore, Chord4S approach extends Chord's original routing protocol to support the discovery of multiple functionally equivalent services at different successor nodes with one query, which is necessary for negotiation of a Service Level Agreement and selection of optimal service providers.

**Keywords:** Chord, Decentralized approach, P2P network, Service discovery.

### I. INTRODUCTION

Peer-to-Peer (P2P) systems (figure 1) are distributed systems without (or with a minimal) the need of centralized control or hierarchical organization, where each node is equivalent in term of functionality. P2P refers to a class of systems and applications that employ the distributed resources to perform a critical function such as resources localization in a decentralized manner. The main challenge in peer to peer computing is to design and implement a robust distributed system composed of distributed and the heterogeneous peer nodes, located in unrelated administrative domains. In a typical P2P system, the participants can be “domestic” or “enterprise” terminal nodes connected to the Internet. Peer-to-Peer computing is a very controversial topic. Many experts believe that there is not much new in peer to peer networks. There are several definitions of P2P systems that are being used by the peer to peer community. As defined in [1], “P2P allows file sharing or computer resources and services by direct exchange between the systems”, or “allows the use of devices on the Internet periphery in a non client capacity”. Also, it could be defined through 3 key requirements: a) they have an operational computer of server quality, b) they have a DNS independent addressing system” and c) they are able to scope with variable connectivity. Also, as defined in [2]: peer to peer is a class of applications that takes advantage of resources-storage, cycle, content, human presence-availability at the edges of Internet. Because accessing to these decentralized resources means operating in an environment with unstable connectivity and unpredictable IP addresses. P2P nodes must operate outside the DNS system and have significant or total autonomy from central servers [1].

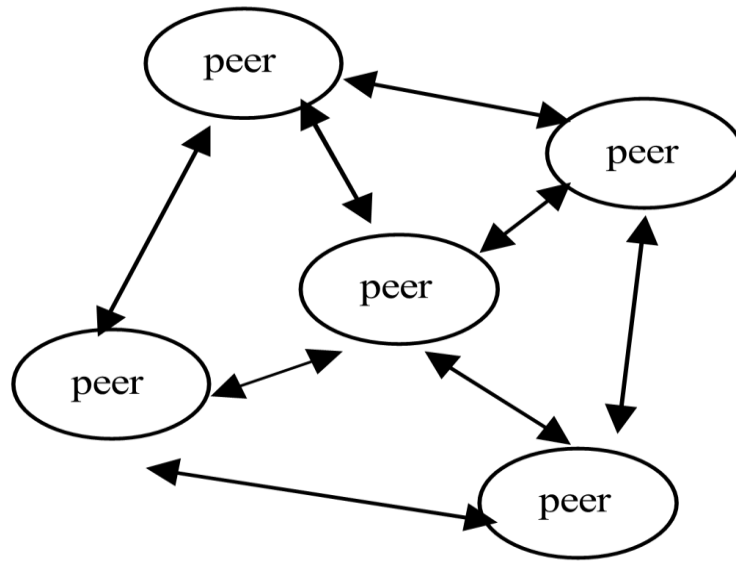


Fig. 1: Decentralized peer- to- peer Network

Naturally, a P2P-based decentralized service discovery approach consists of a set of distributed nodes that form a structured peer to peer overlay network. Upon registration, the description of a service is distributed to a relevant node to be stored in the repository. A service query can be submitted to any node, and this node, if does not store the required service description, it is able to route the query to an appropriate node for resolution. Descriptions of matched services are retrieved and returned to the service consumer as the result of the service query. This paper proposes an approach called Chord4S, a Chord-based decentralized service discovery approach that supports service description distribution and discovery in a peer to peer manner. Chord is selected because it is well recognized for its flexibility and scalability and is considered suitable in large scale service computing environments. Chord4S takes advantages of the basic principles of Chord approach for nodes organization, data distribution and query routing. The main aim of designing Chord4S approach is to largely improve the availability of service descriptions in volatile environments by distributing descriptions of functionally equivalent services to different successor nodes. In case a node fails, a service consumer is still able to find functionally equivalent services that are stored at other successor nodes.

## II. RELATED WORK

The centralized client/server model has been adopted for service discovery in service oriented computing. These traditional service discovery approaches of the web services technology are based on the Universal Description, Discovery, and Integration (UDDI) [3]. The UDDI Version 3.0.2 Specification [3] describes the Web services, data structures and the behaviours of all instances of a UDDI registry. Extension for a query federation of UDDI registries within Web Service environment is depicted in [4]. The search space is enlarged and the opportunity for the service consumers to discover more services that satisfy their requirements is increased, as this allows queries for businesses or services to be forwarded transparently to those extended UDDI nodes within the federation. In [5], the authors describe an interoperable model of distributed UDDI. This model divides UDDI servers into three types: normal server, super domain server and root server. Philosophy of the Domain Name System (DNS) is adopted here. Super domain servers, which are managed by the root server, are further used to maintain normal servers. This model is exposed to the same threats that domain name system faces, e.g., Distributed Denial of Service (DDoS) attack, as it is based on concept of DNS. In [6], the authors proposed a Web Service Crawler Engine to address the performance issue caused because of huge number of UDDI registries. Required web services can be efficiently discovered from a repository by the service consumers, as the crawler in the engine crawls accessible UDDI registries and gathers information in a centralized repository.

Decentralized service discovery is considered as a promising approach to addressing the problems caused by the centralized infrastructures. In particular, some preliminary research has been conducted to utilize peer to peer computing for service discovery [7]. In [8], the authors presents an enhanced Skip Graph, Service Index, using WSDL-S as the semantic description language. Skip Graph is built by extracting semantic attributes of the web services as indexing keys. It consists of a set of increasingly sparse doubly-linked lists

ordered by levels starting at level zero. In [9], the authors propose distributed web service discovery architecture. It is based on the distributed shared space concept and intelligent search among a subset of spaces. Publishing of the Web service descriptions as well as to submit requests to discover the Web service of user's interests is allowed. Integration of several applications running on different resource specific devices is also supported. In [10], the authors propose a Chord based structured peer-to-peer framework for Web service discovery in which Web services are located based on both service functionality and process behavior. Process behavior of the Web services is represented with finite automata and these finite automata are used for publishing and querying the Web services within the system. In [11], the authors propose the approach based on the concept that service providers themselves should take the responsibility to maintain their own service descriptions in the decentralized environment. To group peer nodes by service categories to form islands on the Chord ring, the decentralized service directory infrastructure is built with hashing descriptive strings into the identifiers. In [12], the authors present PSWD, a distributed web service discovery architecture based on an extended Chord algorithm called XChord [7]. In PSWD, XML is used to describe the web service descriptions and to express the service request.

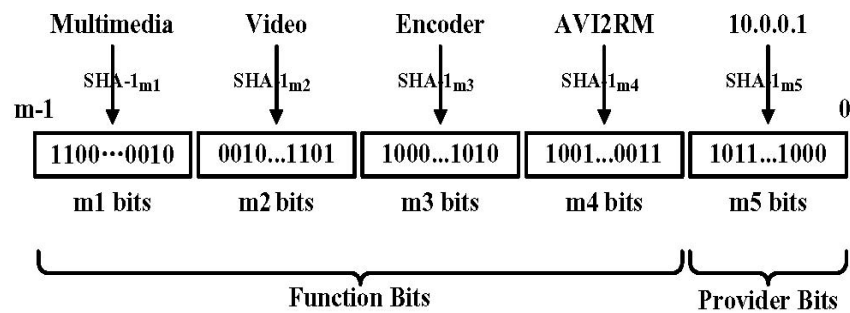
### III. PROPOSED WORK

#### 1. Chord4S Service Description

The service description supported by Chord4S approach consists of three main parts:

- Service identifier
- QoS specification
- Syntax specification.

The service identifiers are the identifications of the services as the basis for routing the query messages. A service identifier for Chord4S is divided into 2 parts, function bits and provider bits. The function bits are used to refer to the functionality of the service while the provider bits are utilized to describe provider specific information. When hashing a service description to generate the service identifier, Chord4S approach allocates certain bits of a service identifier for the function descriptions and the rest for provider bits. A sample of service identifier consisting of 5 layers is presented in figure 2.



$$\begin{aligned}
 \text{Service identifier}_m &= \text{hash}_{m_1}(\text{"Multimedia"}) \\
 &\quad + \text{hash}_{m_2}(\text{"Video"}) \\
 &\quad + \text{hash}_{m_3}(\text{"Encoder"}) \\
 &\quad + \text{hash}_{m_4}(\text{"AVI2RM"}) \\
 &\quad + \text{hash}_{m_5}(\text{"10.0.0.1"}) \\
 &\quad (m_1 + m_2 + m_3 + m_4 + m_5 = m)
 \end{aligned}$$

**Note:** Here "+" executes connection of bits.

Fig. 2: Service identifier generated from hierarchical service description

The QoS specification in Chord4S specifies the quality of the service that the service provider can offer. Chord4S approach allows service providers to publish their services with quality specifications attached as advertisements. However, the quality specifications are not involved in the generation of the service

identifier. After finding a service description that matches its functional requirements according to the Chord4S service identifier, the service consumer can look over the attached quality specification. Chord4S approach supports 3 types of QoS attributes, defined as follows: Numeric, Boolean and enumerated. The syntax specification for Chord4S describes the syntax of the service, e.g., the names and data types of the input and output parameters.

### 2. Chord4S Service Publication

There are two traditional approaches to address the data availability issue in traditional chord approach: replication (i.e., storage of multiple copies of a service description at different nodes) and redundancy (i.e., storage of redundant information along with the service description). Chord4S approach improves data availability by distributing descriptions of functionally equivalent services to different nodes. In this way, a failed node would just have limited impact on the data availability. A service consumer has the opportunity to locate the functionally equivalent services from those available network nodes. Consider a Chord4S- based overlay network consisting of  $n$  network nodes, let the length of the service identifier be  $m$  and the maximum number of functionally equivalent services be  $k$ . The length of the service provider bits  $x$  should be carefully calculated to achieve even service description distribution. Obviously, a smallest virtual segment should be capable of accommodating all the functionally equivalent services, as shown in constraint (1) below:

$$2^x \geq k - 1 \tag{1}$$

Hence,

$$x \geq \log_2(k - 1) \tag{2}$$

To allocate enough bits for service provider bits, constraint (3) below should be satisfied:

$$2^x \geq k - 1 \cdot \frac{2^m}{n} \tag{3}$$

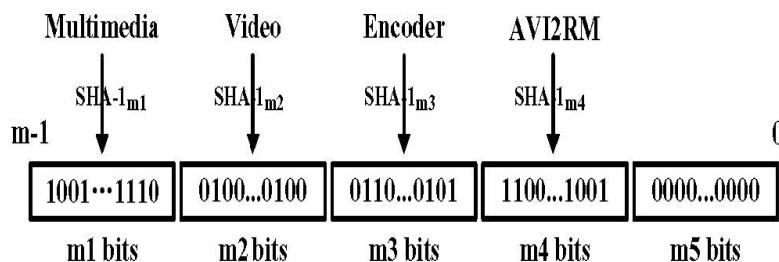
Hence,

$$x \geq \log_2\left(\frac{k - 1}{n} \cdot 2^m\right) \tag{4}$$

With constraints (2) and (4) satisfied, the descriptions of functionally equivalent services can be evenly distributed in a virtual segment which means that all of them are distributed to different successor nodes.

### 3. Chord4S Service Query

Chord4S approach supports 2 types of query: service- specific queries and queries with wildcard(s). A service-specific query contains complete details of the service description and is used to look up a specific service. In a system that allows four-layered function bits in the service descriptions, “Multimedia.Video.Encoder.AVI2RM” is a typical example of the service-specific query. The generation of target service identifier for the query “Multimedia.Video.Encoder.AVI2RM” is given in figure 3 as an example.



$$\begin{aligned} \text{Target Service Identifier}_m &= \text{hash}_{m1}(\text{“Multimedia”}) \\ &+ \text{hash}_{m2}(\text{“Video”}) \\ &+ \text{hash}_{m3}(\text{“Encoder”}) \\ &+ \text{hash}_{m4}(\text{“AVI2RM”}) \\ &+ (0000\dots0000)_{m5} \end{aligned}$$

Fig. 3: Generation of target service identifier.

When solving a query with wildcards, it is actually looking up a virtual segment composed by the nodes succeeding service descriptions that fall into the target service category. The generation of the target service identifier—or more specifically target service category identifier—for a query with wildcards is similar to that for a service specific query. The difference is that the layers corresponding to the wildcards will be stuffed with 0s.

#### IV. CONCLUSION

Peer-to-Peer systems are based on the concept of resources localization and mutualisation in a dynamic context. In specific environment such as mobile networks, characterized by high variability and dynamicity of the network conditions and performances, where network nodes can join and leave the network dynamically, resources reliability and availability constitute a critical issue. Traditional service discovery approaches using centralized registries can easily suffer from problems such as performance bottleneck and vulnerability to failures in large scalable service networks, thus functioning abnormally. To address these issues, this paper proposes a peer-to-peer-based decentralized service discovery approach called as Chord4S. Chord4S utilizes the data distribution and lookup capabilities of the popular Chord approach to distribute and discover services in a decentralized manner. Chord4S approach supports QoS-aware service discovery and also supports service discovery with wildcards.

#### REFERENCES

- [1] Peer-to-Peer Working Group, Bidirectional Peer-to-Peer communication with interposing Firewalls and NATs, White Paper, 2001.
- [2] R. Steinmetz and K. Wehrle, peer to peer Systems and applications, (Eds) Springer LNCS 3485, 2006.
- [3] L. Clement, A. Hately, C. von Riegen, and T. Rogers, “UDDI Version 3.0.2,” OASIS, [http://www.uddi.org/pubs/uddi\\_v3.htm](http://www.uddi.org/pubs/uddi_v3.htm), 2004.
- [4] P. Rompothong and T. Senivongse, “A Query Federation of UDDI Registries,” Proc. First Int’l Symp. Information and Comm. Technologies, pp. 561-566, 2003
- [5] L. Wu, Y. He, D. Wu, and J. Cui, “A Novel Interoperable Model of Distributed UDDI,” Proc Int’l Conf. Networking, Architecture, and Storage (NAS ’08), pp. 153-154, 2008.
- [6] J. Beatty, G. Kakivaya, D. Kemp, T. Kuehnel, B. Lovering, B. Roe, C. St.John, J. Schlimmer, G. Simonet, D. Walter, J. Weast, Y. Yarmosh, and P. Yendluri, “Web Services Dynamic Discovery (WS-Discovery) <http://specs.xmlsoap.org/ws/2005/04/discovery/ws-discovery.pdf>, 2005.
- [7] Qiang He, Member, IEEE, Jun Yan, Yun Yang, Ryszard Kowalczyk, and Hai Jin, Senior Member, IEEE, “A Decentralized Service Discovery Approach on Peer-to-Peer Networks”, IEEE Transaction on Services Computing, VOL. 6, NO. 1, JANUARY-MARCH 2013.
- [8] G. Zhou, J. Yu, R. Chen, and H. Zhang, “Scalable Web Service Discovery on P2P Overlay Network,” Proc IEEE Int’l Conf. Services Computing (SCC ’07), pp. 122-129, 2007.
- [9] B. Sapkota, D. Roman, S.R. Kruk, and D. Fensel, “Distributed Web Service Discovery Architecture,” Proc. Advanced Int’l Conf. Telecomm. and Int’l Conf. Internet and Web Applications and Services, p. 136, 2006.
- [10] F. Emekci, O.D. Sahin, D. Agrawal, and A.E. Abbadi, “A Peer-to-Peer Framework for Web Service Discovery with Ranking,” Proc. IEEE Int’l Conf. Web Services (ICWS ’04), pp. 192-199, 2004.
- [11] T.H.-T. Hu and A. Seneviratne, “Autonomic Peer-to-Peer Service Directory,” IEICE Trans. Information System, vol. E88-D, no. 12, pp. 2630-2639, 2005.
- [12] Y. Li, F. Zou, Z. Wu, and F. Ma, “PWS: A Scalable Web Service Discovery Architecture Based on Peer-to-Peer Overlay Network,” Proc. Sixth Asia-Pacific Web Conf. Advanced Web Technologies and Applications (APWeb ’04), pp. 291-300, 2004.

## An Efficient top- k Query Processing in Distributed Wireless Sensor Networks

Shaik Shabeena<sup>1</sup>, K Suresh Babu<sup>2</sup>

<sup>1</sup> M. Tech (CSE), Vasireddy Venkatadri Institute of Technology, Guntur, A.P., India.

<sup>2</sup> Assoc. Professor, Dept. of Computer Science & Engineering, Vasireddy Venkatadri Institute of Technology, Guntur, A.P., India

**Abstract:** Wireless Sensor Networks (WSNs) are usually defined as large-scale, ad-hoc, multi-hop and wireless unpartitioned networks of homogeneous, small, static nodes deployed in an area of interest. Applications of sensor networks include monitoring volcano activity, building structures or natural habitat monitoring. In this paper, we present the problem of processing probabilistic top-k queries in a distributed wireless sensor networks. The basic problem in top-k query processing is that, a single method cannot be used as a solution to the problem of top-k query processing because there are many types of top-k query processing. The method has to be based on the situation, the classification and the type of database and the query model. Here we develop three algorithms, namely, sufficient set-based (SSB), necessary set-based (NSB), and boundary-based (BB), for inter- cluster query processing with bounded rounds of communications. Moreover, in responding to dynamic changes of data distribution in the overall network, we develop an adaptive algorithm that dynamically switches among the three proposed algorithms to minimize the transmission cost.

**Keywords:** BB, NSB, SSB, Top- k query, WSN.

### I. INTRODUCTION

A wireless Sensor Network (WSN) consists of number of nodes that is used in different applications such as military, health care, commerce, etc. Usually a sensor node is used for sensing precision to monitor environmental conditions. This will be varies in sensing precision. Every sensor node will be varying in the sensing quality. So, whatever the values i.e. raw sensor readings that are collected from sensor is of data uncertainty and energy consumption. In order to remove the data uncertainty many approaches has been used, but that gives inefficient results. A data uncertainty is removed by placing more sensor nodes and as well as by calculating the probability i.e. aggregate probability.

In many application domains, top-k query is a fundamental query to search for the most important objects according to the object ranking. Being different from those studies of top- k query in the centralized databases, in this paper we focus on the top-k query optimization in resource-constrained wireless sensor networks (WSNs). Technological advances have enabled the deployment of the large-scale sensor networks consisting of thousands of inexpensive sensor nodes in an ad-hoc fashion for a variety of environmental monitoring and surveillance purposes. During this course, a large volume of sensed data are needed to be aggregated within the sensor network to respond to user queries. The WSN thus is treated as a virtual database by the database community [1]. However, query processing in sensor networks is essentially different from it in traditional databases due to the unique characteristics imposed on sensors, e.g., slow processing capability, limited storage, and energy-limited batteries, etc. [2], which can be seen from several aspects. Firstly, to prolong network lifetime, the energy consumption is an optimization objective in sensor networks, because the battery-powered sensor nodes will quickly become inoperative due to the large quantity of energy consumption, and the network lifetime is closely tied to the energy consumption rate of the sensors. Secondly, a WSN that senses the data periodically can be viewed as a distributed stream system [3]. However, this special distributed stream system is different from the general distributed stream system because it is more expensive to obtain the sensed information from the sensors far away from the base station than those nearby. Finally, for query processing in sensor networks, minimizing not only the total energy consumption but also the maximum energy consumption among the sensors is the optimization objective. Hence, how to evaluate queries effectively and efficiently in sensor networks poses great challenges.

## II. RELATED WORK

In recent years, many works have been done. Here we review representative work in the areas of 1) top-k Query processing in WSNs, and 2) top-k query processing on the uncertain data. An extensive number of research works in this area has appeared in the literature [4], [5], [6]. Due to the limited energy budget available at sensors, the primary issue is how to develop energy-efficient methods to reduce communication and energy costs in the networks. TAG [4] is one of the first studies in this research area. By exploring the semantics of aggregate operators (e.g., sum, avg, and top-k), in-network processing approach is adopted to suppress the redundant data transmissions in wireless sensor networks. Moreover, continuous top-k queries for sensor networks have been studied in [7] and [8]. In addition, a distributed threshold join algorithm has been developed for the top- k queries [5]. These studies, considering no uncertain data, have a different focus from our present study.

For uncertain databases, two interesting top-k definitions (i.e., U-Topk and U-kRanks) and like methods are proposed [9]. U-Topk returns a list of k- tuples that has the highest probability to be in the top-k list over all possible worlds. U-k- Ranks returns a list of k tuples such that the ith record has the highest probability to be the ith best record in all possible worlds. In [10], PT-Topk query, which returns the set of the tuples with a probability of at least p to be in the top-k lists in the possible worlds, is studied. Inspired by the concept of dominate set in the top-k query, a method which avoids unfolding all possible worlds is given. Besides, a sampling method is developed to quickly compute an approximation with quality guarantee to the answer set by drawing a small sample of the uncertain data. In [11], the expected rank of each tuple across all possible worlds serves as the ranking function for finding the final result. In [12], U-Topk and U-kRank queries are improved by exploiting their stop conditions. In [13], all existing top-k semantics have been unified by using some generating functions. Recently, a study on processing top-k queries over a distributed uncertain database is reported in [14].

## III. PROPOSED WORK

### 1. Sufficient and Necessary sets

In this section We introduce the notion of sufficient set and necessary set for distributed processing of probabilistic top-k queries in cluster-based wireless sensor networks. These two concepts have very nice properties and can facilitate localized data pruning in clusters.

Given an uncertain data set  $T_i$  in the cluster  $C_i$ , if there exists a tuple  $t_{sb} \in T_i$  (called sufficient boundary) such that the tuples ranked lower than  $t_{sb}$  are useless for the query processing at the base station, then the sufficient set of  $T_i$ , denoted as  $S(T)$ , is a subset of  $T_i$  as specified below:

$$S(T_i) = \{t | f(t) \geq f(t_{sb})\}$$

where  $f$  is a given scoring function for ranking. Note that a sufficient boundary may not exist for a given data set. Given a local data set  $T_i$  in the cluster  $C_i$ , assume that  $A_i$  is the set of locally known candidate tuples for the final answer and  $t_{nb}$  (called necessary boundary) is the lowest ranked tuple in  $A_i$ . The necessary set of  $T_i$ , denoted as  $N(T_i)$ , is

$$N(T_i) = \{t | t \in T_i, f(t) < f(t_{nb})\}$$

Using the notion of sufficient and necessary sets as a basis, we propose 3 distributed algorithms for processing probabilistic top-k queries in wireless sensor networks, namely 1) Sufficient Set-based method; 2) Necessary Set-based method; and 3) Boundary-based method.

### 2. Sufficient Set-Based (SSB) Algorithm

After collecting data tuples from its cluster,  $c_i$  computes the  $S(T_i)$  from the locally collected tuples and sends it to the base station. If a sufficient set cannot be obtained, then all the tuples are transmitted to the base station. After receiving the transmitted data tuples from all the cluster heads, they compute final answer.

Algorithm 1: SSB ALGORITHM

AT CLUSTER HEAD ( $c_i$ ):

1. **if**  $S(T_i)$  exists

$S(T_i) \leftarrow \{x | x \leq f_{SB}(T_i) \wedge x \in T_i\}$

$Y_i \leftarrow S(T_i)$

**Else**

$Y_i \leftarrow T_i$

- Now,  $Y_i$  is delivered to the base station.

**AT BASESTATION:**

- It receive the tuples  $Y_i$  from the cluster head. ( $1 \leq i \leq N$ )

$T' \leftarrow \bigcup_{1 \leq i \leq N} Y_i$

Where,  $x$  is the tuples  $c_i$  is the cluster head  $S(T_i)$  is the sufficient set  $T_i$  is the records collected from the sensor  $N$  is the number of clusters in the zone  $C_i$  is the cluster  $Y_i$  is the sufficient boundary for SSB.  $T'$  is the aggregation of data sets received from the clusters

**3. Necessary Set-Based (NSB) Algorithm**

After receiving all the necessary sets, the received tuples are merged into a table in a base station and finds the necessary boundary called the global boundary (GB)). If GB is ranked higher than the highest ranked necessary boundary, all the necessary data have delivered to the base station. Otherwise, it entering the second phase, it sends the GB back to the  $c_i$ , which return the supplementary data tuples ranked between its local necessary boundary and GB. Then, the base station computes the final answer.

Algorithm 2: NSB ALGORITHM

**AT CLUSTER HEAD:**

- Compute the necessary boundary  $NB(T_i)$ ,

$N(T_i) \leftarrow \{x | x \leq f_{NB}(T_i) \wedge x \in T_i\}$

- Deliver  $N(T_i)$  to the base station

- if cluster head receive GB from the base station then

$N'(T_i) \leftarrow \{x | x \leq f_{GB} \wedge x \in [T_i - N(T_i)]\}$  Now,  $N'(T_i)$  is send to the base station.

end if

**AT BASESTATION:**

- It receives the tuples  $N(T_i)$  from the cluster head.

$(1 \leq i \leq N) T' \leftarrow \bigcup_{1 \leq i \leq N} N(T_i)$

- Now, it will calculate the global boundary.

- if global boundary GB is less than that of  $NB(T_i)$ , then

It calculate the final necessary boundary

else

It will broadcast GB to  $c_i$  and once again it collects necessary tuples

$T' \leftarrow \bigcup_{1 \leq i \leq N} N'(T_i)$

end if

Where,  $x$  is the tuples  $c_i$  is the cluster head  $N(T_i)$  is the necessary set  $NB(T_i)$  is the necessary boundary  $T_i$  is the records collected from the sensor  $N$  is the number of clusters in the zone  $T'$  is the aggregation of data sets received from the clusters

**4. Boundary-Based (BB) Algorithm**

The boundary-based method first delivers the local knowledge in clusters, in the form of NB and SB, to the base station in order to provide a refined global data pruning among clusters. It is done instead of directly delivering data tuples to the base station.

Algorithm 3: BB Algorithm

**AT CLUSTER HEAD:**

1. Calculate the Necessary Boundary (NB) and Sufficient Boundary (SB) and send it to the base station.
2. Base station receive Global Boundary (GB)
3.  $Y_i \leftarrow \{x | x \leq f_{GB} \times C [T_i - N(T_i)]\}$
4. Now,  $Y_i$  is delivered to the base station.

**AT BASESTATION:**

1. It will receive the NB and SB from cluster heads ( $c_i$ ),
2. Now, base station computes the (Sufficient Boundary<sub>high</sub> and Necessary Boundary<sub>low</sub> ).
3. if  $SB_{high} < NB_{low}$  , then  $SB_{high} \rightarrow GB$   
else  
     $NB_{low} \rightarrow GB$
4. Now, broadcast the global boundary to each  
     $C_i T' \leftarrow \cup_{1 \leq i \leq N} Y(T_i)$

Where,  $x$  is the tuple  $c_i$  is the cluster head  $S(T_i)$  is the sufficient set  $N(T_i)$  is the necessary set  $T_i$  is the records collected from the sensor  $N$  is the number of clusters in the zone  $Y_i$  is the sufficient boundary for  $SSB$   $T'$  is the aggregation of data sets received from the clusters

**5. Cost Analysis**

We perform a cost analysis on data transmission of the three proposed methods by using adaptive algorithm. Adaptive Algorithm: The performance of the data transmission using proposed method is affected by factors such as the skewness of data distribution among clusters which may change continuously over time. A cost-based adaptive algorithm that is used dynamically Sufficient Set Based, Necessary Set Based, and Boundary Based as the data distribution within the network changes.

Algorithm 4: Adaptive Algorithm

```
Count=0 ;
ZSSB , ZNSB , ZBB =0 Where R is varied window size.
Then estimate the cost of CSSB, CNSB, CBB
ZSSB ← ZSSB + CSSB
ZNSB ← ZNSB + CNSB
ZBB ← ZBB + CBB
if count ≥ R then
if ZSSB = min{ ZSSB , ZNSB , ZBB } then
switch to SSB
end if
if ZNSB = min{ ZSSB , ZNSB , ZBB } then
switch to NSB
end if
if ZBB = min{ ZSSB , ZNSB , ZBB } then
switch to SSB
end if
end if
```

**IV. CONCLUSION**

Motivated by many applications, top- $k$  query is a fundamental operation in the modern database systems. Technological advances have enabled the deployment of several large-scale sensor networks for environmental monitoring and surveillance purposes, efficient processing of top- $k$  query in such networks poses great challenges due to the unique characteristics of sensor nodes and a vast amount of data generated by sensor networks. This work supports in-network top- $k$  query process over uncertain data in the distributed wireless sensor network. We develop the notion of the sufficient set and necessary set for efficient in-network

pruning of uncertain data in a distributed setting. This notion, along with its nice properties, provides a theoretical basis for the distributed query processing methods. Based on the notion of sufficient sets and necessary sets, we propose a suite of algorithms for in-network processing of PT-Topk queries in a two-tier hierarchical sensor network. These methods exploit individual and combined strengths of sufficient and necessary sets in query processing. We propose a cost-based adaptive algorithm that dynamically switches among the three proposed algorithms based on their estimated costs.

## REFERENCES

- [1] S. Madden, M. J. Franklin, J. M. Hellerstein, W. Hong. TAG: a tiny aggregation service for ad hoc sensor networks. ACM SIGOPS Operating Systems Review, Vol.36, pp.131–146, 2002.
- [2] G. J. Pottie, W. J. Kaiser Wireless Integrated Network Sensors. Communication of ACM, Vol.43 No.5, pp.51–58, 2000.
- [3] B. Babcock and C. Olston. Distributed top-k monitoring. Proc. of ACM SIGMOD, ACM, pp.28–39, 2003.
- [4] P. Cao and Z. Wang, “Efficient Top-k Query Calculation in Distributed Networks,” Proc. 23rd Ann. ACM Symp.Principles of Distributed Computing (PODC), pp. 206-215, 2004.
- [5] M. Ye, X. Liu, W.-C. Lee, and D.L. Lee, “Probabilistic Top-k Query Processing in Distributed Sensor Networks,” Proc. IEEE Int’l Conf. Data Eng. (ICDE ’10), 2010.
- [6] D. Zeinalipour-Yazti, Z. Vagena, D. Gunopulos, V. Kalogeraki, V.Tsotras, M. Vlachos, N. Koudas, and D. Srivastava, “The Threshold Join Algorithm for Top-k Queries in Distributed Sensor Networks,” Proc. Second Int’l Workshop Data Management for SensorNetworks (DMSN ’05), pp. 61-66, 2005
- [7] Q. Han, S. Mehrotra, and N. Venkatasubramanian, “Energy Efficient Data Collection in Distributed Sensor Environments,” Proc. 24th Int’lConf.Distributed Computing Systems (ICDCS’04), pp. 590-597, 2004.
- [8] M.Wu, J.Xu, X. Tang, and W.-C. Lee, “Top-k Monitoring in Wireless Sensor Networks,” IEEE Trans. Knowledge and Data Eng., vol. 19, no. 7, pp. 962-976, July 2007.
- [9] M.A. Soliman, I.F. Ilyas, and K.C. Chang, “Top-k Query Processing in Uncertain Databases,” Proc. Int’l Conf.
- [10] M. Hua, J. Pei, W. Zhang, and X. Lin, “Ranking Queries on Uncertain Data: A Probabilistic Threshold Approach,” Proc. ACM SIGMOD Int’l Conf. Management of Data (SIGMOD ’08), 2008.
- [11] C. Jin, K. Yi, L. Chen, J.X. Yu, and X. Lin, “Sliding-Window Top-k Queries on Uncertain Streams,” Proc. Int’l Conf. Very Large Data Bases (VLDB ’08), 2008.
- [12] D. Wang, J. Xu, J. Liu, and F. Wang, “Mobile Filtering for Error-Bounded Data Collection in Sensor Networks,” Proc. 28th Int’l Conf. Distributed Computing Systems (ICDCS ’08), pp. 530-537, 2008.
- [13] K. Yi, F. Li, G. Kollios, and D. Srivastava, “Efficient Processing of Top-k Queries in Uncertain Databases with X-Relations,” IEEE pp. 1669 1682, Dec.2008.
- [14] F. Li, K. Yi, and J. Jestes, “Ranking Distributed Probabilistic Data,” Proc. 35th SIGMOD Int’l Conf. Management of Data (SIGMOD ’09), 2009.

## Simulation of gas turbine blade for enhancement of efficiency of gas turbine using ANSYS

Rahul Rao<sup>1</sup>, M. N. Pandey<sup>2</sup>

<sup>1</sup>Department of mechanical engineering, Nit Patna/ Nit Patna, India

<sup>2</sup>Department of mechanical engineering, Nit Patna/ Nit Patna, India

**Abstract:** As day by day population of the world is increasing and our resources are frequently reducing hence to meet this demand of the world of energy we have to move to a device which have a maximum efficiency for the condition turbo-machinery are better suited machines having a good efficiency, in which a Gas turbine is best example of turbo- machinery Turbine is the part of gas turbine which provide the power to compressor to run or provide power to external source from where energy can be extracted by attaching alternator in the shaft of Gas turbine. As in earlier a lot of work have been done by the researcher to increase the efficiency and standard of Gas turbine by the method of film cooling, coating, and curvature of blade to protect the blade from high temperature of 1200 C° inside the Gas turbine to increase the life of blade without considering about the efficiency of the engine As in this work is to enhancement of efficiency of Gas turbine. Gas turbine blade is very important component of engine as they are attached to both turbine or compressor and turbine provide energy to compressor hence the turbine blade are more important component to enhance the efficiency which will be analyzed on the basis of blade height area of fluid flow , area of blade thickness and angles . This simulation is based on the define value of temperature pressure density of fluid and solid used in blade construction will be meshed in ANSYS and calculation on the basis of FEM and the result from this calculation over the temperature and fluid flow inside the gas turbine of different number of blade is studied will be compare to reach high efficiency point. By determent these value output is formulated on graph chart and will be studied and result obtain

**Keywords:** Cp specific heat, C camber length, LE Leading edge ,TE trailing edge , (C/S) Solidity, R1 inlet of blade , Pitch Cord Ratio (S/C),S2 inlet of shroud ,S1 inlet of hub ,T temperature ,kg/s mass flow rate

### I. INTRODUCTION

Velocity of gases increases or decreases due to blade attached to its components' turbine, compressor or several other devices such as regenerator economizer etc. Gas turbine is classified into three categories by number of shaft. Gas turbine is a machine which has a shape of a long cylinder attached with tricone at the end. They have higher efficiency or power /weight ratio compared to other turbo-machinery or internal combustion engines. Gas turbine has very few moving parts which mean they are more reliable than other turbo machine. Gas turbines are easier and cheaper when it is installed in a power plant. For the instalment of Gas turbine in power plant , installation can be completed in a period of about 400 days which is less than nuclear power plant takes 1900 days, coal plant takes 1200 days .This is factor by gas turbine is getting more attention in some nation. They are easily operated and provide power to industries by the help of generator attached to the shaft of Gas turbine and are also providing power to boats aircraft cars etc and are replacing other cycle engine as they are more economical. Siemens turbines are of about 90 % efficiency and total efficiency of this turbine is 45 % is utilized by the industries or other respective field. By combining two different type of turbine the efficiency can be increased. Gas turbine efficiency is based on brayton cycle and is calculated on this value of assumption. Gas turbine has compressor, turbine and combustion chamber attached to shaft. The main part of turbine and compressor are blade attached to them , blades are attached in compressor and turbine in opposite direction to each other , hence blade is major part of Gas turbine engine as by changing blade geometry efficiency can be increased in the engine.

### II. Blades

Blades are attached to hub in meridian manner to withstand heat and forces, stress. Turbines are of also two types radial and axial turbine .Compressor and external machine for output get power from turbine only

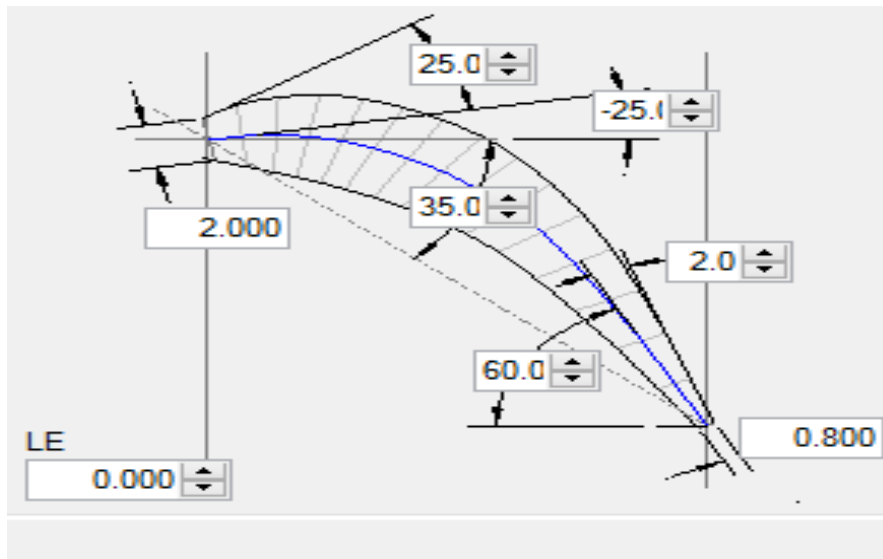


Fig 1 Sketch of blade of type 1

The blades of gas turbine are attached to compressor and turbine. The blades are part of Gas turbines which are providing gas. They receive all the time heat in spite of that blade have to produce power to compressor or turbine for outcome by exerting a high stress on their part. Blade of turbine can be divided on the basis of leading and trailing edge geometry in the form of

1< Edge, 2< Ellipse shape , 3< Cut of type

### III. Methodology 1

Design of turbine blade with having LE Pitch = 7.46518 mm and TE Pitch(S) = 7.70221 mm and Airfoil Area = 131.637 mm<sup>2</sup>, Camber Length = 43.3695 , Cord Length (C) = 39.2005 , Meridional Length (M) = 31.144mm, Stagger Angle = 37.4°, Solidity (C/S) = 5.08951° Pitch Cord Ratio (S/C) = 0.196483 LE Thickness = 1.94059 mm, TE Thickness = 0.800947 mm and these are the value of size for this turbine blade and for this thesis many blade design were model to check the correct value to suit the turbine After modulating a 2 dimensional model of blade of length 40 mm then a height of according to shaft diameter blade length were made and the blade design of 3 model were drafted in cad

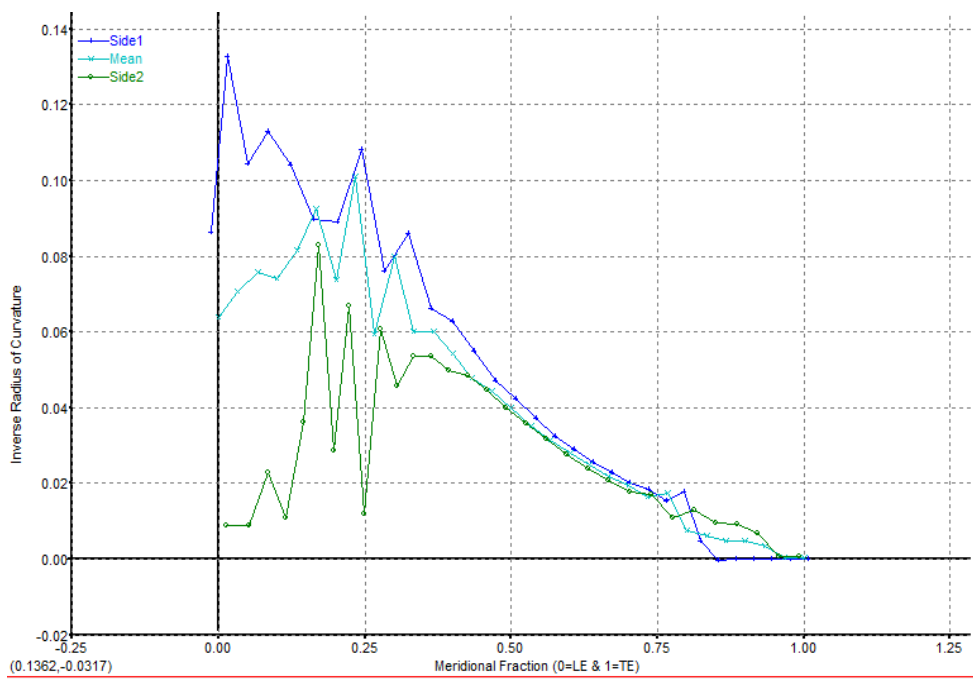


Fig 2 the graph variation of radius at two side of blade

On the basis of graph of figure 2 showing blade location thickness aerofoil area the blade model is design for this report after designing of blade then they are ready to attached in turbine then they are attached in shaft so that they can for series of blade in circular manner

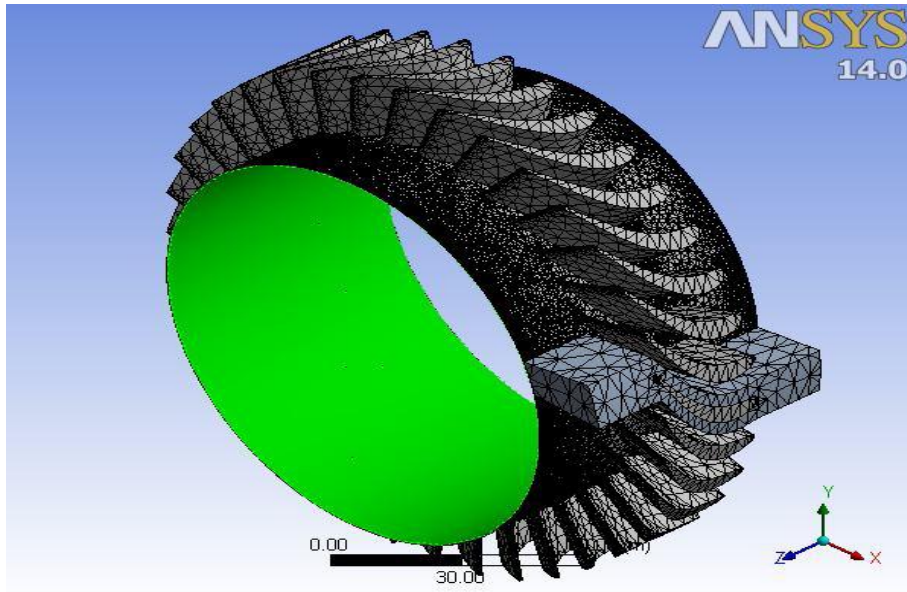


Fig3.12 showing mesh model of turbine blade attached to hub

Meshing is the first pre processing stage in ANSYS analysis. Meshes are done on the model to substitute the values of input parameter. Meshing in thesis is done by defining this model in to geometry and then the fluid flow region of one blade is define as body is symmetry not necessary define all the blade, by meshing fluid flow and heat transfer are based on differential equation, in order to analyze fluids and heat flow nodal point are split into hexahedral mesh. Continuity equation all around nodes of model will be put in the entire flow region by creating mesh

domain	Nodes	element
R1	15916	13378
S1	12880	11286
S2	4480	3654
Total	33276	28309

Table 3.1

#### IV. Methodology 2

The blade which is generated in CAD transported to software ansys of fluent where the flow of fluid will be analyzed and design of blade with hub of turbine for 3D design is processed for solving first step is to check the mesh quality and the model is again meshed for solution

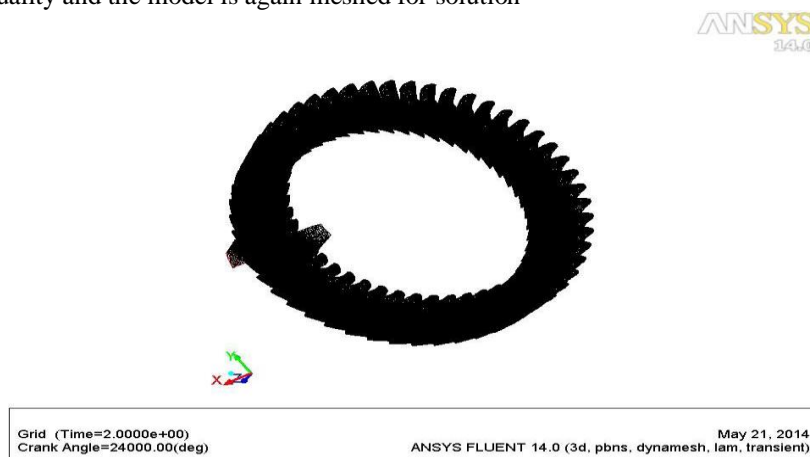


Figure 4.1 mesh design of turbine blade

Fluid which will flow in the Gas turbine is define and the and the radius and height is according to hub diameter is set and all this solution are based on Navier stroke equation by keeping gravitation force on the blade and the fluid which are flowing are acetylene air acetone etc are define for analysis with their density thermal conductivity and many other input are define to solve the result the blades are calculated in the dynamic mode and mesh is again update which are based on

- Smoothing:** This enables to calculate the mesh of blade on the basis of diffusion method
- Layering:** Layer of mesh are added or removed the cell by moving toward adjacent layer
- Remeshing:** by this model is again meshed For setting up reference quality for computing the result geometry reference value are specified taking hub as value from where value is calculated area  $1\text{m}^2$  , density  $1.252\text{kg/m}^3$  enthalpy 0 length  $39.37\text{ mm}$  temperature =  $300\text{ k}$  with value  $1\text{ m/s}$  and specific heat  $C_p = 1.4$

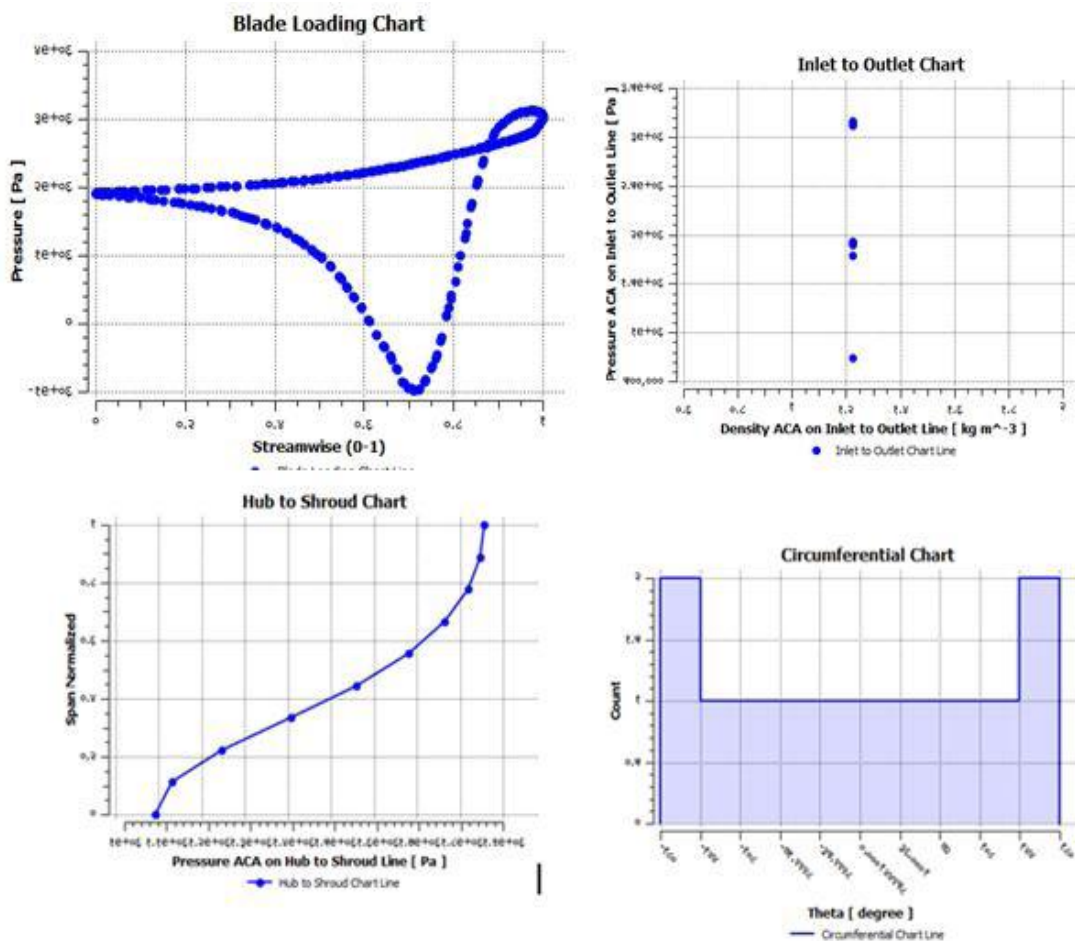
Then the parameters are set to solve the equation by the following way

- Gradient is set on the basis of heat pressure square cell
- Pressure equation set to calculate pressure at nodes or element of blades
- Momentum is second order upwind
- Energy is second order upwind

All these formulation is based on first order equation For up and down in the value in calculation the relaxation of 0.3 in pressure,  $1\text{kg/m}^3$  in density, energy 1 moment 0.7 is taken into consideration for calculation For solution to be in perfect result the iteration is set to max 27 in a interval of 1 and Force value area analyses then value are calculated on each nodes of geometry by meshing and the area of blade inflow are calculated

### V. Result

**FLUID FLOW ANALYSIS OF BLADES** Fig result of analysis of fluid flow for blade type 1 In this report more than 30 type of blade were analysed and according to them the value are obtained but only two types blade results



It is mention. Pressure at the blade were calculated and shown on the Graph and density variation according to area mention

**FORCE REPORT**

Domain Name: Default Domain  
Global Length = 2.3664E-02  
Minimum Extent = 2.0757E-02  
Maximum Extent = 5.0000E-02  
Density = 1.1850E+00  
Dynamic Viscosity= 1.8310E-05  
Velocity = 0.0000E+00

These are values which are obtained by the analysis of fluid forces at point of blade hub shroud etc  
**Figure 5 density and pressure effect on blade**

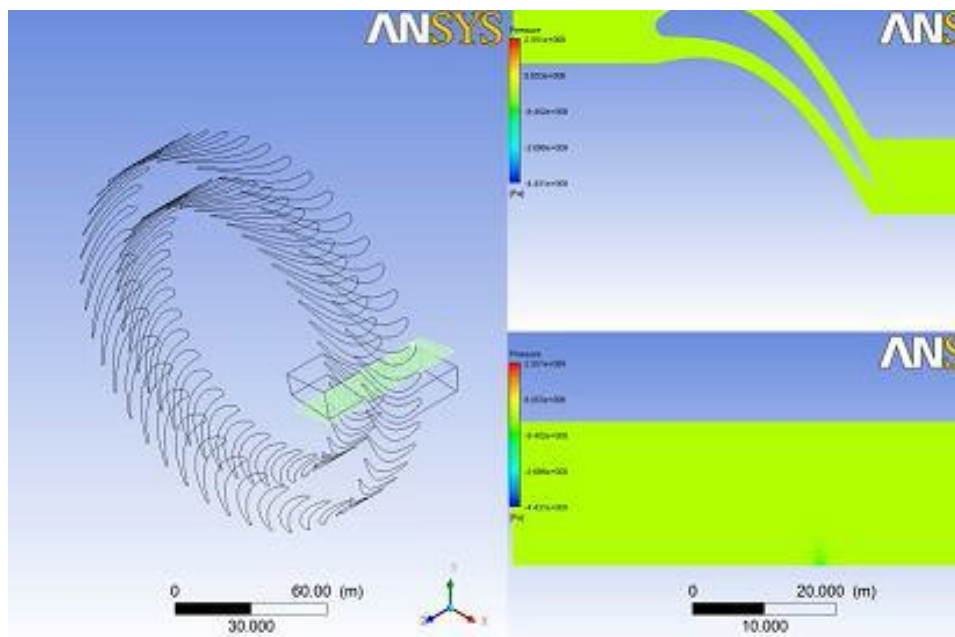
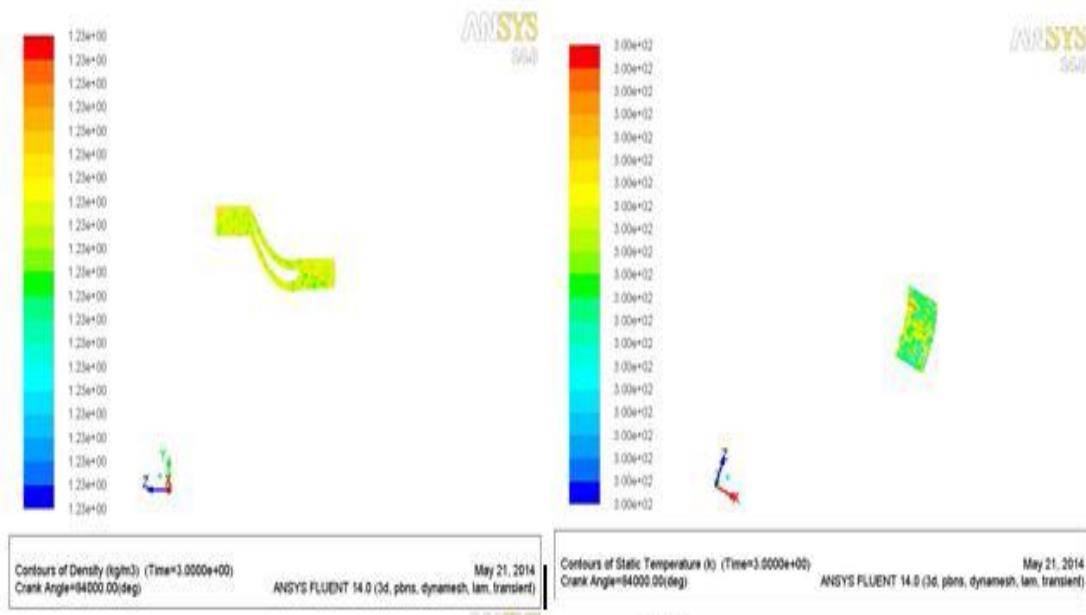


**Figure 5 variation of fluid while flowing over blade**

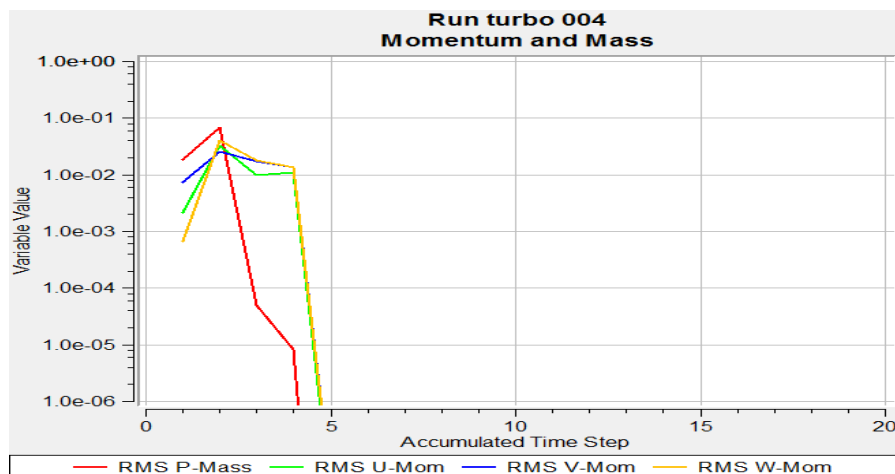


Figure 5 variation pressures, velocity internal energy

## VI. Conclusion

On the basis of result obtained from more than 30 types of blade at temperature from 22 °C to 2000 °C of blade having shroud for leading edge and trailing edge different size and shape and the camber length increasing and decreasing value. Flow analysis for blade having blade without shroud results are best but life of blade are shorter than but it will increase the efficiency of blade as flow of fluid inside the turbine having 42 number of blade the pressure are less at leading edge comparisons than trailing edge and less interference of fluid takes place can also enhance the efficiency of turbine. The heating effect of blade is same for all materials are based on density of blade material INCONES 165 having density 8400 Kg/m<sup>3</sup> is good. The value will also increase when density of material will increase. Shroud will reduce the flow of fluid inside the turbine. Temperature does not show any type variations on the blade geometry until its operating condition or melting point incone165 is best. Forces on the turbine with 42 blades have an effect of maximum 5.00575 E 002 and minimum 2.00575 E 02 and dynamic viscosity is also better for more than or less than 42 blades of turbine. Value obtained for 42 number of blade having leading and trailing edge square cut is also less than the elliptical shape blade. On the basis of this report the number of 42 blade of turbine having elliptical leading edge and trailing edge the result output of turbine efficiency is better than other.

## VII. Future Aspect

With the invention of different type of material having high melting point and thermal conductivities and different density the blade of turbine can be further studied, as the use of turbine is increasing in the industries to because of increasing have maximum efficiency as resources are diminishing day by day.

## REFERENCE

- [1] cohen-gfc-rogers-hih-saravanamuttoo (1996) ,gas turbine theory .Longman group London
- [2] Tony Giampaolo Gas Turbine Handbook: Principles and Practices 3rd Edition , MSME, PE
- [3] Ganesan V, Gas Turbine third edition 2010 Mcgraw Hill New Delhi
- [4] Eifel M, Caspary V, Hönen H, Jeschke 2011 Experimental and Numerical Analysis of Gas Turbine Blades With Different Internal Cooling Geometries by ASME January 2011, Vol. 133 / 011018-1
- [5] Krishnakanth I p.v , narasa g., raju2 prasadr d v , r. sairinu 2013 structural & thermal analysis of gas turbine blade by using f.e.m (ijsret) volume 2 issue 2 pp 060-065 may 2013
- [6] Gómez-Mancilla J. C. . Palacios-Pineda L. M Y. López-Grijalba; Gutiérrez-Suárez O 2011 Preliminary Analysis for Worn Out Gas Turbine Blade-Vane Components Related to Resonant Mode Frequencies and Fatigue Life Consumption 13th World Congress in Mechanism and Machine Science, Guanajuato, México, 19-25 June,
- [7] baheri islami , b. a. jubran 2011 the effect of turbulence intensity on film cooling of gas turbine blade from trenced shaped holes. / by springer -verlag 2011]
- [8] Rao nageswara paregouda shridhar 2013. cfd simulation on gas turbine blade and effect of hole shape on leading edge film cooling effectiveness by(ijmer) vol. 3, issue. 4, jul - aug. 2013 pp-2066-2072
- [9] Poor blade curvature - a contributor in the loss of performance in the compressor unit of gas turbine systems chigbo a. mgbemene journal of energy technologies and policy issn 2224-3232 (paper) (online) vol.2, no.4, 2012
- [10] girish modgil, william a. crossley2, dongbin 2011 design optimization of a high pressure turbine blade using generalized polynomial chaos may 19 -24, Orlando, Florida, USA
- [11] yaşar kahraman \*, sedat iriç, imdat taymaz 2012 modeling of residual stresses in tbc coated gas turbine blades the online journal of science and technology- April 2012, volume 2, issue 2.

## FPGA Implementation of Efficient Viterbi Decoder for Multi-Carrier Systems

K. Rajendar<sup>1</sup>, K. Bapayya<sup>2</sup>

<sup>1</sup>M.Tech., VLSI-SD Student, ECE Dept., CVR College of Engineering, Hyderabad, India

<sup>2</sup>Asst. Prof., ECE Dept., CVR College of Engineering, Hyderabad, India

**Abstract:** In this paper, we concern with designing and implementing a Convolutional encoder and Adaptive Viterbi Decoder (AVD) which are the essential blocks in digital communication system using FPGA technology. Convolutional coding is a coding scheme used in communication systems for error correction employed in applications like deep space communications and wireless communications. It provides an alternative approach to block codes for transmission over a noisy channel. The block codes can be applied only for the blocks of data where as the Convolutional coding has an advantage that it can be applied to both continuous data stream and blocks of data. The Viterbi decoder with PNPH (Permutation Network based Path History) management unit which is a special path management unit for faster decoding speed with less routing area. The proposed architecture can be realized by an Adaptive Viterbi Decoder having constraint length,  $K$  of 3 and a code rate ( $k/n$ ) of  $1/2$  using Verilog HDL. Simulation is done using Xilinx ISE 12.4i design software and it is targeted into Xilinx Virtex-5, XC5VLX110T FPGA.

**Keywords:** Convolutional Encoder, Viterbi Decoder, Trellis, PNPH Unit, Virtex-5, Verilog HDL, FPGA.

### I. Introduction

Nowadays most of the digital communication systems are employed with Convolutionally encoded data in channel to compensate Additive White Gaussian Noise (AWGN), Fading of the channel, Quantization noise and other data degradation effects. Error detection and error correction is important for reliable communication; error detection techniques are much simpler than Forward Error Correction (FEC). But error detection techniques have certain disadvantages. Error detection pre-supposes the existence of an Automatic Repeat Request (ARQ) feature which acknowledges for the retransmission of data blocks, segments or packets in which errors have been detected.

Convolutional encoding with Viterbi decoding is a powerful FEC technique that is particularly suited to a channel in which the transmitted signal is corrupted mainly by AWGN. It operates on data stream and has memory that uses previous bits to encode. It is simple and has good performance with low implementation cost. The Viterbi Algorithm (VA) was proposed in 1967 by Andrew Viterbi and is used for decoding a bitstream that has been encoded using FEC code. The Convolutional encoder adds redundancy to a continuous stream of input data by using a linear shift register. Adaptive Viterbi decoder is very efficient and robust. The main advantage of Adaptive Viterbi Decoder is it has fixed decoding time and also it suites for hardware decoding implementation. The implementation requires the exponential increase in the area and power consumption to achieve increased decoding accuracy.

Most of the Viterbi decoders in the market are a parameterizable Intelligent Property (IP) core with an efficient algorithm for decoding of one convolutionally-encoded sequence only and this is mostly used in the field of satellite and radio communications. In addition, the cost for the convolutional encoder and Viterbi decoder are expensive for a specified design because of the patent issue. Therefore, to realize an adaptive Convolutional encoder and Viterbi decoder on a Field Programmable Gate Array (FPGA) board is very demanding especially for Multi-Carrier Systems like Orthogonal Frequency Division Multiplexing (OFDM).

The general block diagram of Viterbi decoder communication system is shown in Figure 1.

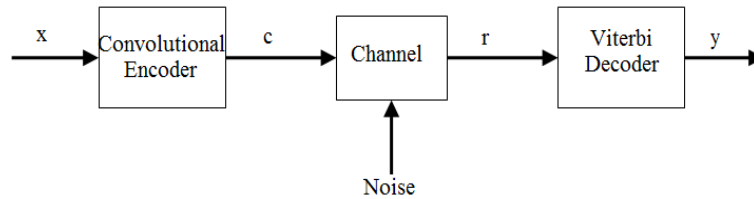


Figure 1: Block diagram of Viterbi decoder communication system

The remainders of this paper are organized as follows. In section II, The important terms and its definitions used in this paper are discussed. In section III, The analysis and FPGA design of (2,1,3) Convolutional encoder are presented. Section IV discusses about the Viterbi Decoder. Section V shows the Results and its discussions based on Xilinx ISE (Integrated Software Environment) 12.4 version tool. In Section VI, The hardware implementation of Convolutional encoder with Viterbi decoder on Xilinx Virtex-5, XUPV5LX110 FPGA board. The paper is concluded in Section VII.

## II. Important Terms And Its Definitions

The following terms are important to the understanding of Convolutional coding and Viterbi decoding.

- 1. Hard-decision/soft-decision decoding:** Hard-decision decoding means that the demodulator is quantized to two levels: zero and one. If you derive more than two quantization levels from the demodulator, then the decoder is soft-decision decoding.
- 2. Code rate  $R(=k/n)$ :** Number of bits into Convolutional encoder ( $k$ )/ number of bits in output symbol( $n$ ) which corresponds not only current input bit, but also previous ( $K-1$ ) ones.
- 3. Constraint length ( $K$ ):** It denotes the “length” of the Convolutional encoder, i.e., no of  $k$ -bit stages are available to feed the combinatorial logic that produces the output symbols.
- 4. Branch Metric:** Difference between the received sequence and the branch word is called the Branch metric.
- 5. Path Metric:** Branch metric accumulates to form Path metric.

## III. Convolutional Encoder

The Convolutional encoder is basically a Finite State Machine (FSM). It converts the single bit input into two or more bits for every clock pulse according to the generator polynomial. The generator polynomial gives the connections of the encoder to the modulo-2 adder. In the generator polynomial logic ‘1’ indicates the connection between the stages and logic ‘0’ indicates no connection between the stages. The convolutional encoder can be represented by  $(n,k,K)$  where ‘ $k$ ’ is the number of input bits , ‘ $n$ ’ is the number of output bits and ‘ $K$ ’ is the constraint length that depends up on the number of flip flops used for convolutional encoder. The code rate of a convolutional encoder is defined as ratio of number of input bits to number of output bits. The convolutional encoder with a code rate of  $\frac{1}{2}$  and Constraint length of 3 is shown in Fig. 2.

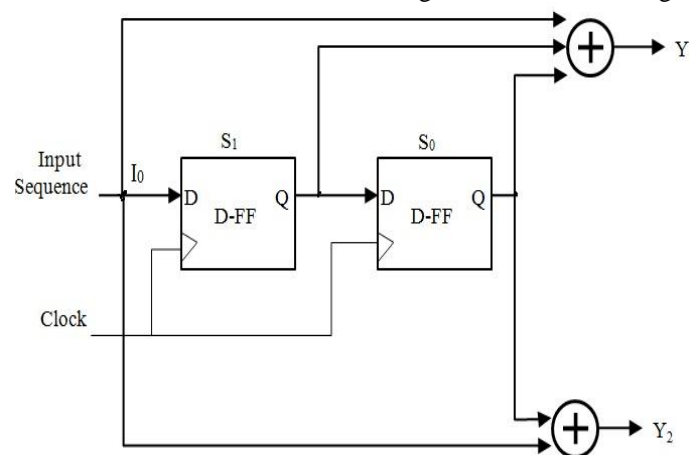


Figure 2: (2,1,3) Convolutional encoder

The Convolutional encoder can be represented by using state table, state diagram and trellis diagram. The state is defined by using the shift register contents of encoder. In state table output symbol is a function of input symbol and state. The state diagram shows the transition between different states. The Trellis diagram is the description of state diagram of encoder by a time line i.e. to represent each time unit with a separate state diagram. The state diagram and the trellis diagram of  $\frac{1}{2}$  rate convolutional encoder in Figure 2 is shown in Figure 3(a) and 3(b) respectively.

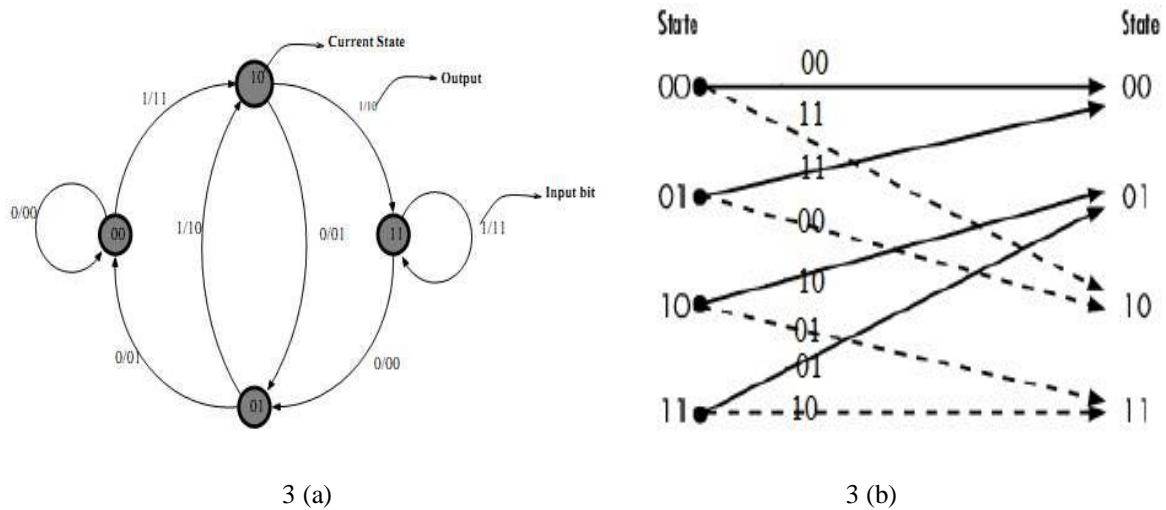


Figure 3: (a) State diagram (b) Trellis diagram

The Trellis diagram is used to find out accumulated distances (called as path metric in viterbi decoder) from the received sequence to get the same transmitted sequence.

#### IV. Viterbi Decoder

When a sequence of data is received from the channel, it is required to estimate the original sequence that has been sent. The process of identifying original message sequence from the received data can be done using the diagram called "trellis". A Viterbi decoder uses the Viterbi algorithm for decoding a bit stream that has been encoded using Forward Error Correction based on a convolutional code. Figure 4 shows the block diagram of Viterbi decoder.

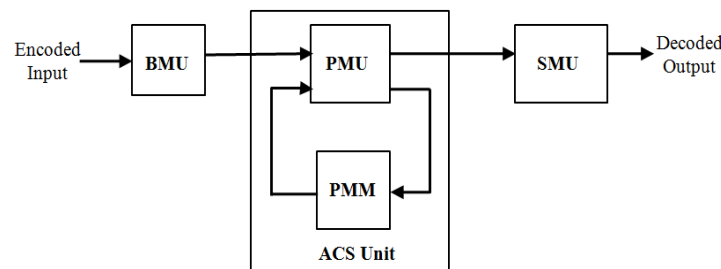


Figure 4: Block diagram of Viterbi decoder

The Viterbi Decoder consists of following functional parts

- a). Branch Metric Unit (BMU)
- b). Add Compare Select Unit (ACSU)
- c). Survivor Memory Management Unit (SMU).

##### a) Branch Metric Unit:

The first unit is called branch metric unit, the received data symbols are compared to the ideal outputs of the encoder from the transmitter and branch metric is calculated. Hamming distance or the Euclidean distance is used for branch metric computation. It is typically a smallest unit of the Viterbi decoder. Its complexity increases exponentially with reciprocal of the coding rate. It is non critical block with respect to area and throughput.

In the hard-decision decoding, the path through trellis is determined by using Hamming distance measure. Thus, most optimal path through trellis is path with minimum Hamming distance. The Hamming distance can be defined as the number of bits that are different between the observed symbol at decoder and the

sent symbol from encoder. Furthermore, the hard decision decoding applies one bit quantization on the received bits.

The Soft-decision decoding is applied for maximum likelihood decoding, when the data is transmitted over the Gaussian channel. On the contrary to hard decision decoding, the soft-decision decoding uses multi-bit quantization for the received bits, and Euclidean distance as a distance measure instead of hamming distance. A 3-bit quantization results in an 8-array output. An implementation of the BMU block is shown in Figure 5.

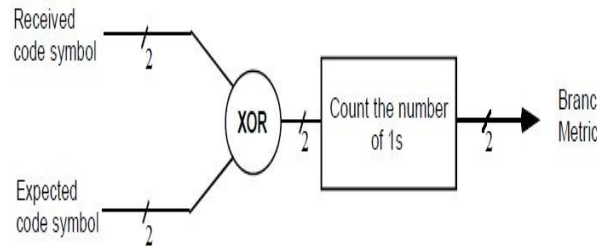


Figure 5: Branch metric computation block

**b) Add Compare and Select Unit:**

The hardware architecture of the ACS module is shown in Figure 6. Path Metric (PM) of the node/state is found by adding the partial path metric from the previous stage and the present stage branch metrics. Since there are two possible ways to reach any node/state two path metrics are obtained. These two are compared to select the one with the least path metric.

The path with the better metric is chosen and stored as the new path metric for current state, while generating a decision bit.

Mathematically,

$$\text{If } BM(i;p) + PM(i;p) < BM(j;p) + PM(j;p) \\ \text{Then } Dec(p)=0, PM(p)=PM(i)+BM(i;p)$$

$$\text{Else} \\ Dec(p)=1, PM(p)=PM(j)+BM(j;p)$$

Where BM is Branch Metric, PM is Path Metric and Dec is Decision bit.

The decision bit indicates what branch was chosen. Because each state can be achieved from the earlier stage, the decision value is represented by one bit. If the bit is '1' the path selected is coming from the lower state from those two possible states in the trellis diagram, and if the decision bit is '0' the path selected is coming from the upper state. As the ACS unit needs the results from the calculations of the previous steps, it forms a feedback loop with the path metric memory unit, where the results are stored.

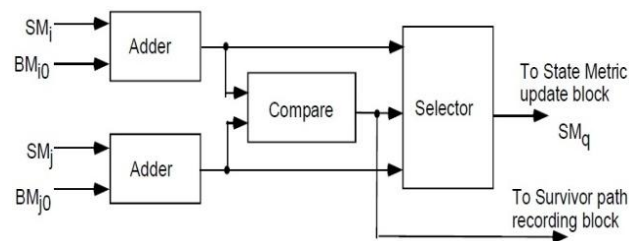


Figure 6: ACS (Add Compare select) module

**c) Survivor Memory management Unit:**

The Survivor Memory management Unit (SMU) stores the decisions of the ACS unit and uses them to compute the decoded output. The Trace-Back (TB) technique and the Register-Exchange (RE) approaches are two major techniques used for the path history management. The Trace Back unit takes up less area but require much more time than the Register Exchange method. A relatively new approach called Permutation Network based Path History (PNPH) unit implements directly the trellis diagram of the given Convolutional code to trace the survivor path back sequentially.

The resulting circuit has smaller routing area than register-exchange technique and has faster decoding speed than trace-back method regardless of the constraint length.

**Permutation network based path history (PNPH) unit:**

The Permutation Network based Path History (PNPH) unit for a convolutional code is a 5L-stage permutation network with each stage containing 1-to-2k demultiplexers, where each Demux corresponds to each node of the trellis diagram and is associated with a K-bit register and a 2k-input OR gate. The K bit register is used to store the decision bits associated with the state node and to determine the partial survivor path associated with the node.

Thus, each registers demultiplexer pair determines the part of the survivor path associated its corresponding state node. The connection between two adjacent stages of the interconnection network is defined by the next function of the state diagram of the underlying encoder. New decision-bit values for each state calculated by Add-Compare-Select (ACS) enter into the rightmost end of corresponding shift register. The PNPH unit for the convolutional code (2, 1, 3) shown in Figure 7.

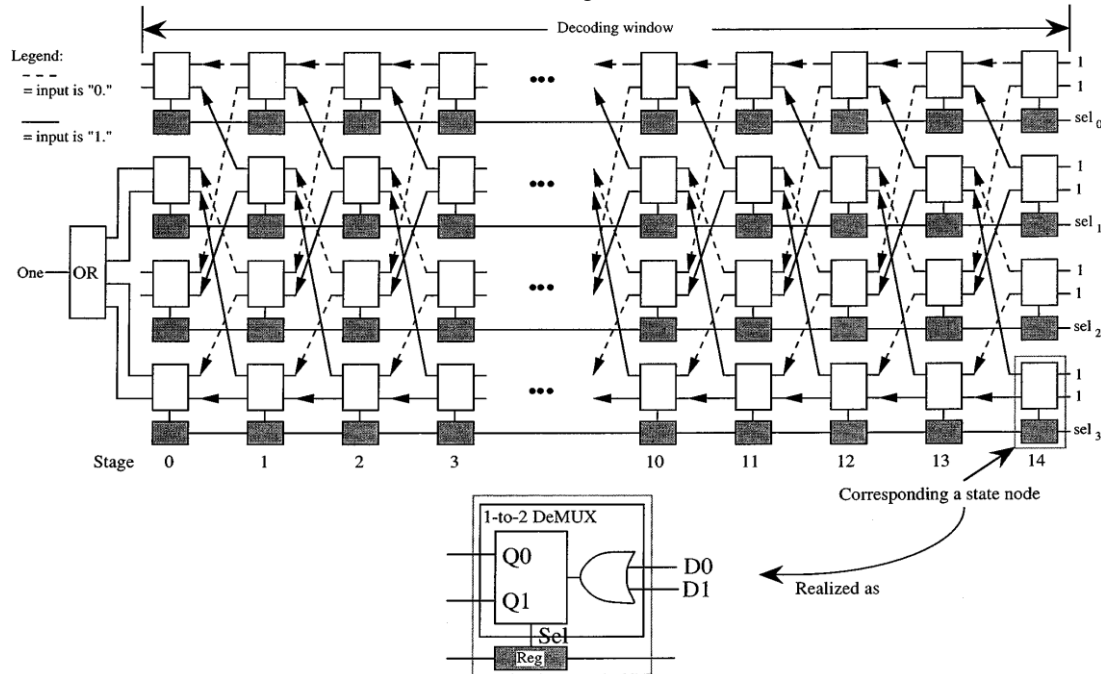


Figure 7: PNPH Unit for the convolutional code (2,1,3)

**V. Results And Discussions**

**1). RTL Schematic:**

The RTL schematic of Convolutional encoder with Viterbi decoder is shown in Figure 8.

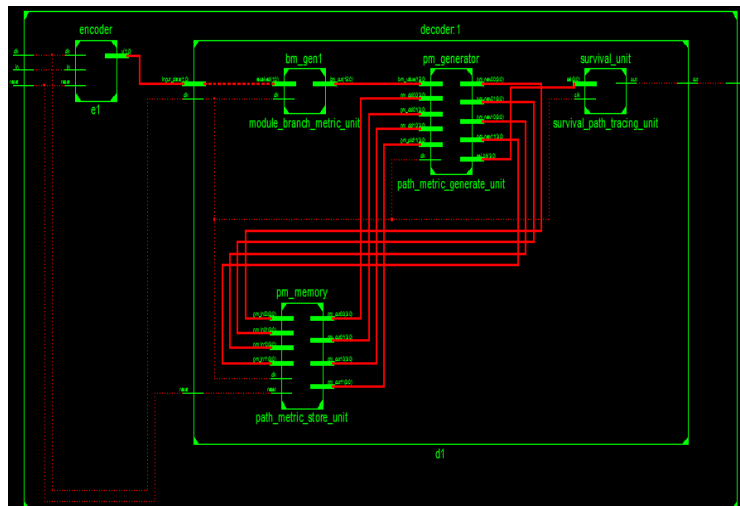


Figure 8: RTL schematic of Convolutional encoder with Viterbi Decoder

2). Simulation Results:

i) Convolutional Encoder:

The simulation results of Convolutional encoder with constraint length of  $K=3$  and code rate of  $r=1/2$  is shown in Figure 9.

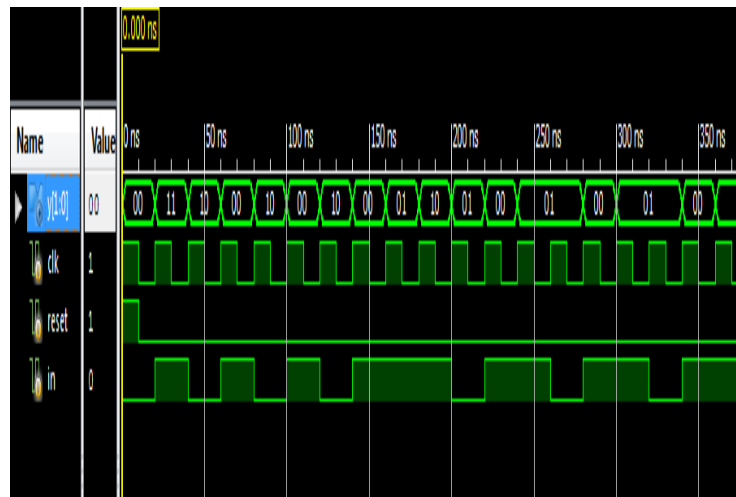


Figure 9: Simulation results of Convolutional encoder

ii) Viterbi Decoder:

The simulation results of Viterbi decoder is shown in Figure 10.



Figure 10: Simulation results of Viterbi Decoder

The simulation results of overall Convolutional encoder with Viterbi Decoder is shown in Figure 11.

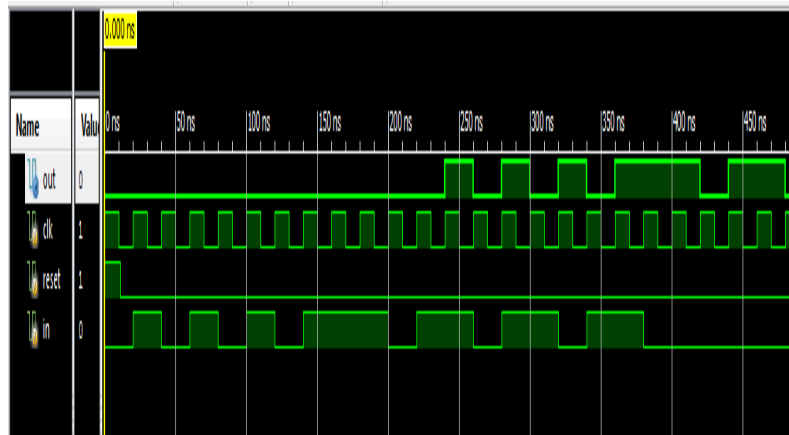


Figure 11: Simulation results of overall Convolutional encoder with Viterbi Decoder

The simulation results of overall Convolutional encoder and Viterbi Decoder with noise is shown in Figure 12.

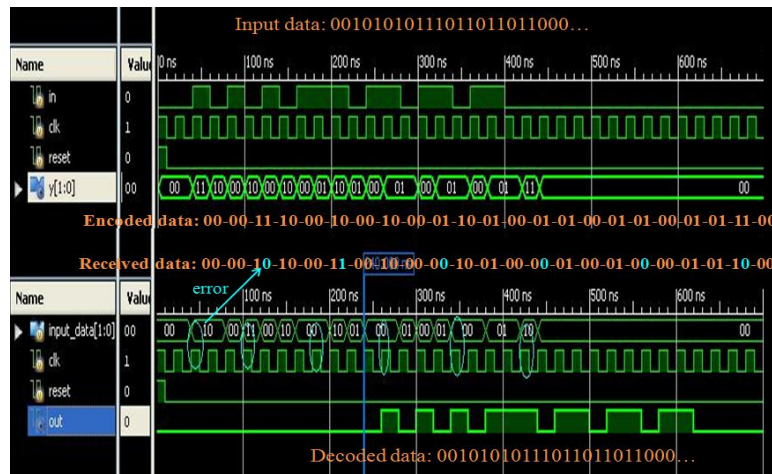


Figure 12: Simulation results of Viterbi Decoder with noise

### VI. FPGA Prototyping

The design of Convolutional encoder and Viterbi decoder is verified on Xilinx Virtex-5, XUPV5LX110T FPGA board by using Xilinx iMPACT device configuration tool. The output of Convolutional encoder with Viterbi decoder on Xilinx Virtex-5, XUPV5LX110T FPGA board with bouncing pattern of LEDs indicating respective outputs is also shown in Figure 13.

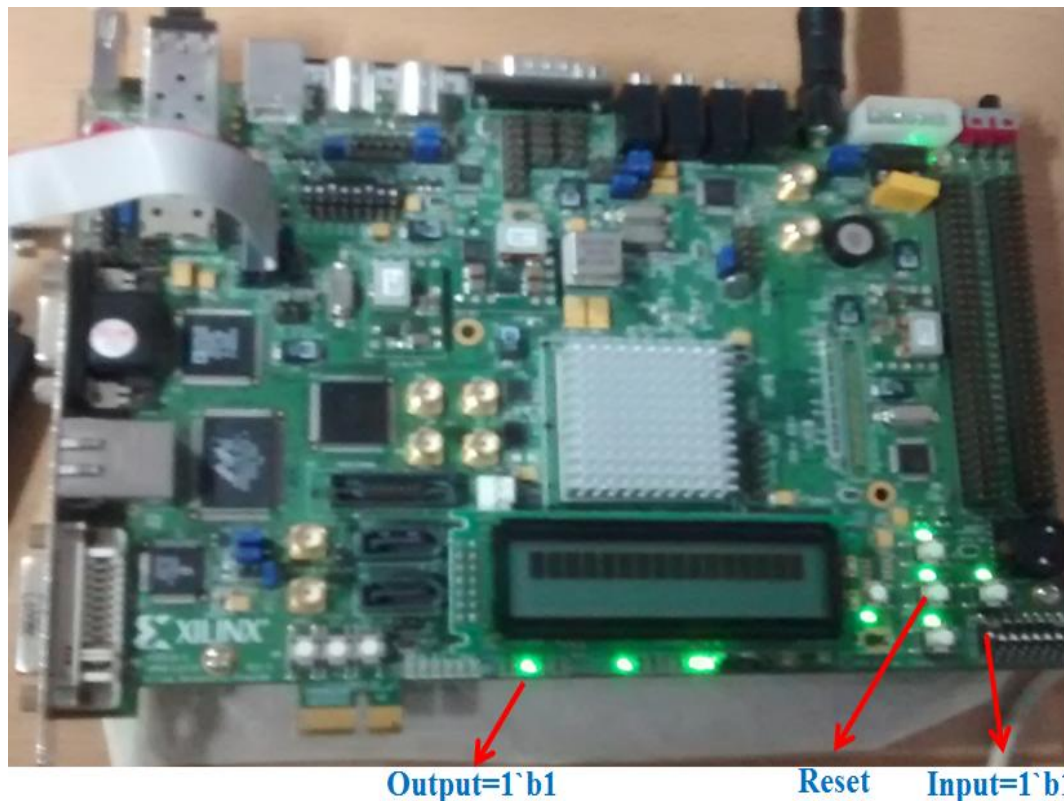


Figure 13: Output of Convolutional encoder with Viterbi decoder on Xilinx Virtex-5, XUPV5LX110T FPGA board

### VII. Conclusion

In this paper, we have presented the design and implementation of the Convolutional encoder and Viterbi Decoder with constraint length of  $K=3$  and code rate of  $r=1/2$ .

The Convolutional encoder and Viterbi decoder with PNPH unit is successfully designed in Xilinx ISE Design suite 12.4 platform with Verilog HDL. The design is simulated for functionality by using Xilinx ISE simulator tool, and Implemented on Xilinx Virtex-5, XUPV5LX110T FPGA board. The synthesized Convolutional encoder with Viterbi decoder has 96 slice LUT's, 78 slice registers and 1-buffer. The timing analysis results show that the critical path is 6.016 ns, i.e. the maximum clock frequency of 166.223 MHz.

As an extension to this work, we can implement Folded PNPH unit to improve the decoding speed and also we can think of reconfigurable architecture for implementing Convolutional encoders with different code rates simultaneously.

#### REFERENCES

- [1] Ming-Bo Lin, "New path history management circuits for viterbi decoders," in IEEE transactions on communications, vol 48, no.10, october 2000.
- [2] A. J. Viterbi, "Error Bounds for Convolutional Codes and an Asymptotically Optimum Decoding Algorithm," IEEE Trans. on Information Theory, Vol. IT-13, pp. 260-269, April 1967.
- [3] Anh Dinh, Ralph mason and Joe toth, "High speed v.32 Trellis encoder & decoder implementation using FPGA," in IEEE transactions on communications, 1999.
- [4] Samirkumar Ranpara, "On a Viterbi decoder design for low power dissipation," towards his master's thesis submitted to virginia polytechnic institute and state university.
- [5] M. Kivioja, J. Isoaho and L.Vanska, "Design and implementation of Viterbi decoder with FPGAs," Journal of VLSI Signal Processing Systems for Signal, Image, and Video Technology, Kluwer Academic Publishers, vol. 21, no. 1, pp. 5-14, May 1999.
- [6] M. Kling, "Channel Coding Application for CDMA2000 implemented in a FPGA with a Soft Processor Core," Linköping University, Department of Electrical Engineering, 2005.
- [7] W. Chen, "RTL Implementation of Viterbi Decoder," Linköping University, Department of Electrical Engineering, June 2006.
- [8] V.Kavinilavu1, S. Salivahanan, V. S. Kanchana Bhaaskaran2, Samiappa Sakthikumaran, B. Brindha and C. Vinoth, "Implementation of Convolutional Encoder and Viterbi Decoder using Verilog Hdl" in IEEE tran. On inform theory, 2011.
- [9] Hema.S, Suresh Babu.V and Ramesh.P, "FPGA Implementation of Viterbi decoder", proceedings of the 6<sup>th</sup> WSEAS ICEHWOC, Feb. 2007.
- [10] Yan Sun, Zhizhong Ding "FPGA Design and Implementation of a Convolutional Encoder and a Viterbi Decoder Based on 802.11a for OFDM", Wireless Engineering and Technology, 2012, 3, 125-131.
- [11] B. Sklar, "Digital Communications, Fundamentals and Applications", Second Edition, New Delhi, Pearson Education, 2004.
- [12] Chip Fleming, "A tutorial on Convolutional coding with viterbi decoding".

## Amulti-Agent Architecture for a Co-Modal Transport System

Nesrine Zoghlami<sup>1</sup>, Karma Jeribi<sup>2</sup>, Christophe Merlo<sup>3</sup>, Hayfa Zgaya<sup>4</sup>,  
Slim Hammadi<sup>5</sup>  
<sup>1,3,4</sup>ESTIA Bidart, France  
<sup>2</sup>Ecole Centrale Lille, France  
<sup>5</sup>ILIS Lille, France

**Abstract:** Improving the co-modal transport and introducing systems for traveler information is becoming more and more urgent in our society in order to guarantee a high level of mobility in the long term. The goal of this research is to develop a distributed co-modal transport system that takes into account all possible means of transport including carpooling, vehicles on service and public transport and satisfies traveler's queries, constraints and preferences. The main contribution of this work is to propose an innovative multi-agent approach to solve problems in wide co-modal transport networks. First, we propose a multi-agent architecture to model the system. Then we use a method to construct a co-modal transport network representation by categorizing the transport services and using transfer links and a distributed algorithm in order to resolve the shortest paths problem. We test our model and algorithms based on a case study in Lille, France. The experiments results on theoretical graphs as well as on real transport networks are very promising.

**Keywords:** Co-modal transport, Co-modal Transfer Point, Distributed Shortest paths, Multi-agent Systems, Optimization.

### I. INTRODUCTION

Nowadays, the daily mobility of passenger has become a very important problem in our society. Also, the spatial dispersion of habitat and activities contribute to a considerable growth of the use of cars and traffic. Private vehicle remains the most popular and the preferred mean of transport thanks to its flexibility, efficiency, speed and comfort. In fact, statistics show that in 2008, the private car is the dominant mean of transport by 60% of urban travel while the others means like walking, public transport, bicycle and motorcycle represent recursively 27%, 9%, 2% and 2% [1], [2]. Traffic congestion acts directly on the economy, causes an increase of pollution, and reduces citizens' comfort. According to the "Agency for the environment of the European union", transport represents 23,8% of the total greenhouse gases emissions and 27.9% of total CO2 emissions [3].

Different policy options exist in order to deal with the transport problem such as the resort to other solutions that complete the classic public transport like transport on demand, vehicle-sharing services (carpooling, car sharing) and cycling (free use bicycles for example). These solutions are complementary and respond to each specific need. In fact, combining the different private and public transport means might be more effective.

The idea of combining different transport modes is supported by the European commission of transport since 2006. The new notion of co-modality was introduced in the transport policy as the optimum combination of modes of transport chain [4]. With this approach, we don't seek anymore to oppose transport modes one to another but rather to find an optimum solution exploiting the domains of relevance of the various transport modes and their combinations.

The co-modal approach, in the same way as its predecessor, the "multimodal" approach, consists on developing infrastructures and taking measures and actions that will ensure optimum combination of individual transport modes i.e. enabling them to be combined effectively in terms of economic efficiency (i.e. providing the most cost effective combination), environmental efficiency (the least polluting combination), service efficiency (level of service provided), financial efficiency (best use of society's resources), etc [5]. It refers to the "use of different modes on their own or in combination".

In the research community, many projects were devoted to transport systems that recommend travelers a combination of transport means door to door journeys [6], [7], [8], [9].

Knowing that our target is to satisfy transport user demands, respecting user's preferences, we propose in this paper a distributed vehicle-sharing services system. This system combines all possible means of transport including private cars, vehicles on service and public transport, which remains a remarkable solution for the environment and the streets obstruction. The adopted method combines the optimization methods and the multi-agent system. It is a distributed co-modal approach based on a multi-agent system. The resolution of the co-modal transport problem is divided into two parts. First, a co-modal approach is applied to a transfer graph in order to compute the shortest paths in terms of time and then an evolutionary optimization approach in terms of total cost, time and gas emission volume is adopted, taking into account passenger constraints and preferences. In this paper, only the first part of optimization is considered.

So, some related works and researches will be introduced in section 2 following by the problem description in section 3. Section 4 describes the multi-agent system organization for the co-modal system. In our multi-agent system, the notion of roles is applied and especially for one special agent. The different roles of this agent are described in section 5. Then, the distributed co-modal graphs are described in section 6 with some definitions of co-modal graphs and a special distributed graph: the transfer graph. We present then in the next section our approach and our algorithms in order to resolve the transfer graph and applied by the "Super Agent". We end the paper with a simulation example and a conclusion and some prospects in respectively section 8 and 9.

## II. RELATED WORKS

Recently, the transport sector is under pressure across the world. Overloaded roads lead to both economical and ecological problems. This engendered the rise of Intelligent Transportation Systems (ITS). An ITS is a transportation system that aims to alleviate and minimize the transport congestion problems using different information and communication technologies (geo-localization, GPS, mobile technologies...)[10]. As an integral important part of intelligent transport system, Advanced Travelers Information Systems (ATIS) provides travelers all the pre-trip and real-time information through a dynamic transportation network. An ATIS must have the ability to model not only mono-modal itineraries but also co-modal ones including both private and public transport services. Multimodal and co-modal transport models and optimization algorithms attract many researchers' interests. In France, [11] and [12] proposed systems that optimize in real time user itineraries in term of cost and travelling time for the multimodal common transport and [13] enriched the system by adding co-modal transport in case of perturbation. [14] proposed a transfer graph approach for multimodal transport problems. An hybrid approach using the Dijkstra's algorithm and Ant colony optimization was applied. In other works, [15] proposed a parallel algorithm for solving the Time Dependent Multimodal Transport Problem (TDMP) in very large transport networks. [16] proposed a public transportation domain ontology that considers different concepts related to the best and more relevant planning for the passenger. In the United States, different multimodal trip planner for mobile devices were developed [17], [18],[19]. Also, a distributed solution integrating different trip planning systems into a distributed system was presented by [20]. In Germany, many researchers were interested by extending networks from single mode to multimodal like [21] and [22]. Mentz company [23] developed a personal travel companion. This system focuses on personalized multimodal journey planning, mobile multimodal trip management and smart-phone-based pedestrian orientation and guidance in complex public transport transfer buildings. We can cite another application, the RUHRPILOT. It is a multimodal trip planner for the "Rhur" area in Germany. Public transport schedules from 15 cities are combined with each other to cover the whole geographical area and also a dynamic car routing is offered [24]. [25] proposed a switch point approach to model multimodal transport networks. In the Netherlands, [26], developed a personal intelligent travel assistant for public transport. [27] proposed a multimodal transport network model for advanced traveler information systems that simultaneously consider private and public transport modes. A co-modal travel planner, combining both private and public modes of transport was introduced in Stockholm, Sweden [28]. In other countries, Zografos [29]

described an algorithm for itinerary planning based on dynamic programming. Su [30] developed a multimodal trip planning system for intercity transportation in Taiwan. Also, in India a multimodal transport system for Hyderabad city was proposed by [31].

All the researches described above deal with traveler information systems in multimodal networks. We can remark that there is a small difference between the different descriptions of multimodal networks. For some researches, multimodal transport concerns the different modes of public transport (bus, subway, train...). Others consider that multimodal transport includes both of private (car, bike...) and public transport. The term of co-modality is not commonly used since it is a new notion. Based on all these researches, we propose a distributed co-modal transport system that satisfies the traveler's demands and plans their trips in real time. It respects the new notion of co-modality and combines all possible means and services of transport including private cars thanks to the carpooling service, vehicles on service (carsharing, bikes) and public transport. We model co-modal transport networks and categorize networks into different services.

### III. PROBLEM DESCRIPTION

The main concern of our system is to combine all the existing transport services in order to satisfy the users by providing optimized co-modal itineraries and respecting their priorities criteria.

As shown in Fig.1, a transport user can use a medium of communication (e.g. laptop, PDA, smartphone) in order to express his demand and provide a departure and arrival points and the correspondent earlier and later schedules. In a short time interval, many transport users can formulate simultaneously a set of requests. So the system should find feasible decompositions in terms of independent sub-itineraries called Routes recognizing similarities. For a given Route, we can have several possibilities with different vehicles which are available to ensure this Route through the same time window. All these identified Routes constitute our co-modal graph and we have to recognize the different possibilities of RoutesCombinations to compose each itinerary demand. The problem is how to choose the most effective RouteCombination to a given user, taking into account his constraints and preferences in terms of total cost, total travelling time and total greenhouse gas volume for example.



Figure 1 Global system description

At a time  $t$ , our problem is defined by:

- $N$  requests formulated through a short interval of time  $\Delta_\epsilon \sim$  milliseconds.  $I_t$  is the set of these requests. In fact, the system catches simultaneously all travellers queries expressed through  $\Delta_\epsilon$ .
- $I_k(d_k, a_k, W_k) \in I_t$  is an itinerary request formulated by a user  $k$  at a time  $t$  from a departure point  $d_k$  to an arrival point  $a_k$  through a time window  $W_k = [td_k, ta_k]$ ;  $td_k$  and  $ta_k$  correspond respectively to the earliest (minimum departure time from  $d_k$ ) and the latest (maximum arrival time to  $a_k$ ) possible schedules with  $t \leq td_k < ta_k$ ;

- $R_g(d_g, a_g, W_g)$  is a *Route* identified to respond to a part of the total itinerary requests  $I_k \in I_t$ .

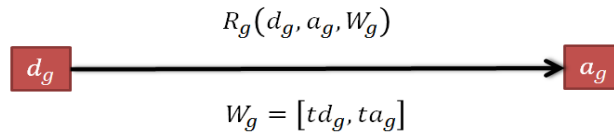


Figure 2 Route  $R_g(d_g, a_g, W_g)$

A junction or a succession of different routes  $R_g(d_g, a_g, W_g)$  composes a possible solution for one request.  $RC_{k,p}$  is a possible *RouteCombination* identified to respond to the request  $I_k(d_k, a_k, W_k) \in I_t$ .

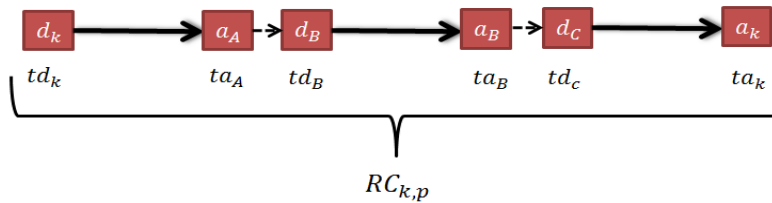


Figure 3 Route combination  $RC_{k,p}$

- For one *Route*  $R_g(d_g, a_g, W_g)$ , we need a mean of transport available to move from the departure point  $d_g$  to the arrival point  $a_g$  through a time window  $W_g = [tg_d, tg_a]$  with  $tg_d$  and  $tg_a$  correspond respectively to the possible earliest departure time to leave  $d_g$  and the possible latest arrival time to attend  $a_g$ .
- $R_t$  is the set of all identified *Routes* to response to  $I_t$ .
- $(RC)_k = \{RC_{k,p}, p \in [1..P]\}$  is the set of all possible *RouteCombinations* identified to answer to the request  $I_k(d_k, a_k, W_k) \in I_t$ . P is the total number of these *RouteCombinations*.
- Let CR be the total number of the optimization criteria. We focus on three criteria (CR = 3): Total Cost, Total Travel time and Gas emission. When a user k formulates his itinerary request  $I_k$ , he has also to mention his priorities criteria.
- A *Route*  $R_g(d_g, a_g, W_g)$  can be ensured by more than one vehicle. We note  $V_h^{R_g}$  the vehicle  $V_h$  that ensures the *Route*  $R_g(d_g, a_g, W_g)$  at the time t with  $1 \leq h \leq H$ , H is the total number of the vehicles  $V_h^{R_g}$  available for the *Route*  $R_{g,t}$ . Each vehicle  $V_h^{R_g}$  ( $1 \leq h \leq H$ ) is characterized by a value for each criterion  $Cr_i$  (dynamic character obtained by  $V_h^{R_g} \cdot Cr_i$ ).
- A vehicle  $V_h^{R_g}$  ( $1 \leq h \leq H$ ) has a departure time and a single value per criterion. We distinguish in this paper three types of vehicles : private vehicles used for the carpooling services, free use vehicles (e.g. Free use bicycles “VLIB”, free use cars “AUTOLIB”) and the multimodal transport vehicles (Bus, Metro...)

According to the problem described above, we pass from the multimodal network to the co-modal network. In fact, our system is a co-modal system that combines different means of transport services like the public transport service, carpooling and free use vehicle services. In order to resolve the co-modal transport problem, we choose to combine optimization algorithms with the multi-agent systems and apply a distributed co-modal approach based on multi-agent system and distributed co-modal graphs.

#### IV. MULTI-AGENT SYSTEM ARCHITECTURE FOR A DISTRIBUTED CO-MODAL TRANSPORT SYSTEM

The agent computing paradigm is one of the powerful technologies for the development of distributed complex systems [32]. The agent technology has found a growing success in different areas thanks to the inherent distribution which allows for a natural decomposition of the system into multiple agents. These agents interact with each other to achieve a desired global goal [33]. Since transport systems are usually geographically distributed in dynamic changes

environments, the transport domain is well suited for an agent-based approach [34]. Each agent is composed of states, different types of knowledge (environmental, social and personal), messages, behavior rules and a perception function. Thanks to the behavior rule, the agent can modify its state according to current states, knowledge and received messages in order to reach the collective goal [35]. A set of rules and behaviors can define a role. An agent can though have different roles. From a role to another, the agent changes its capabilities and behaviors [36].

According to the problem described above, we propose a multi-agent system based on the coordination of several kinds of software. The architecture of the proposed multi-agent system is described below (Fig.4).

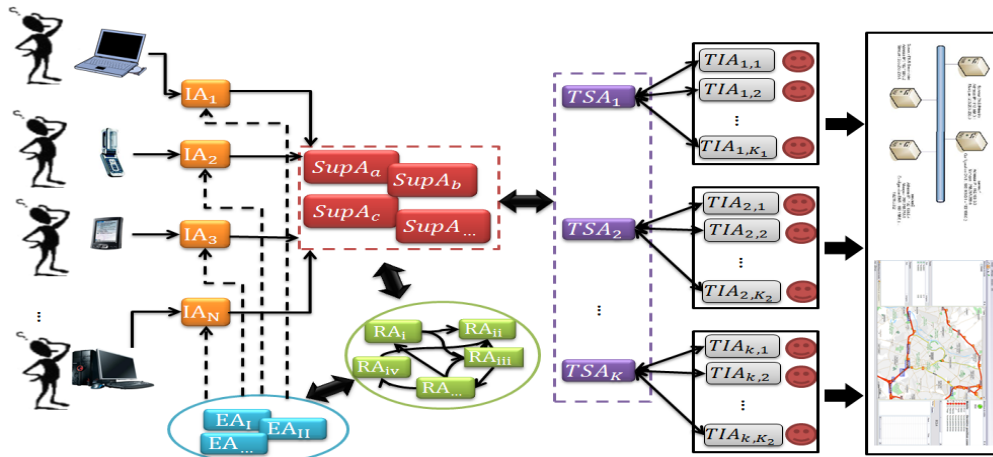


Figure 4 Multi-Agent system architecture

In our system, we consider  $K$  transport services and  $K_i$  transport operators associated to the transport service  $i$  ( $i \in [1..K]$ ). We associate an agent to each transport service and an agent to each transport operator. A *transport Service Agent* ( $TSA_i, 1 \leq i \leq K$ ) is responsible for a set of Transport Information Agent ( $TIA_{i,j}, 1 \leq j \leq K_i$ ). Each  $TIA_{i,j}$  is able to respond to an itinerary request  $(x, y, W_{x,y})$  by a shortest path  $RC_{x,y}^{*i,j}$  that allows to go from  $x$  to  $y$  on a transport network of the operator  $j$  associated to the service  $i$ .

For a global request  $I_k(d_k, a_k, W_k) \in I_t$ , an *Interface Agent* ( $IA$ ) interacts with a system user allowing him to formulate his request choosing his preferences and constraints and displays at the end the correspondent results. When an  $IA$  handles a user request, it sends it to a *SuperAgent* ( $SupA$ ). It is an agent with different important roles. Firstly, this agent asks the  $TSA$ s for a search domain and all the transport operators that will be involved in the itinerary research. We assume that the  $SupA$  has a global view of all the  $TSA$ s that define the environment. The  $SupA$  cooperates then with the set of  $TIA$ s identified by the  $TSA$ s and starts by constructing a co-modal graph. The  $SupA$  decomposes this complex graph into a special graph called “Transfer graph” and a co-modal approach is applied. After a first computing of the shortest paths in terms of time, the  $SupA$  generates all possible RouteCombinations from simultaneous itinerary requests thanks to the *Route Agents* ( $RA$ ). All the roles and the tasks executed by the  $SupA$  are detailed in the next sections.

The  $RA$  represents a generated chromosome scheme called VeSAR for an identified useful  $RouteR_g(d_g, a_g, W_g)$  in order to assign concerned users to possible vehicles. As soon as each  $RA$  assigns persons to vehicles, updating the number of passengers in carpooling vehicles and the number of available vehicles of free use vehicle service, it computes all values criteria of each vehicle for each assignment. A multi-agent coalition [37], [38] is then created regrouping all  $RAs$  corresponding to a possible Routecombination for a given itinerary. Therefore, we have as many coalitions as combinations knowing that an  $RA$  can belong to many different coalitions according to combinations overlapping. Coalitions appear and disappear dynamically according to requests receptions and responses.

The chromosome scheme generation and the assignment were explained in previous works [39], [40]. Then, the generated data is transferred to an *Evaluator Agent* ( $EA$ ) who decides

of the best Combinations thanks to its interaction with the autonomous *RAs*. The EA computes the best Combination Route for each itinerary demand and sends it to the correspondent *IA*.

### V. DIFFERENT ROLES OF THE SUPER AGENT

We focus in this paper on the distributed co-modal approach applied by the *SupA*. As explained in the previous section, we consider that each agent can have one or more different roles. In fact, the *SupA* have three roles.

The goal of the first role is to define the domain search. The *SupA* executes two tasks. The first task is to locate all the departure and arrival points of all the requests and identify through the correspondent TSAs. The second task is to send the requests to the identified TSAs. Thanks to the Domain Search Selection Algorithm (DSSA) [41], all the TSAs will provide to the *SupA* the list of TIAs that are interested to respond to the requests. Then, the *SupA* begins its second role of the identification of the different Routes and the determination of the first shortest paths. For the first goal, it sends the requests to the identified TIAs. It receives then all the possible *Routes* that could be solutions or part of the solutions to the requests. The second goal of the second role is to determine the preliminary optimized Routes that will construct later the solutions to the requests. The *SupA* constructs a co-modal graph with the different Routes. This graph may be very complex and hard to resolve. So we adopt a new approach based on a special form of graph that we called transfer graph. The *SupA* executes then a Distributed Shortest Path Algorithm (DSRA) in order to solve the transfer graph and to compute the shortest paths in terms of travel time. This approach is explained in the next sections. Until this step, no person is affected to any Route or vehicle. Also, we want to provide to the users a set of optimized itineraries in terms of three criteria: the travel time, the gas emission and the travel cost. In order to complete the approach, the *SupA* have to switch to its third role and generate the *RAs*. In fact, after the application of the DSRA, each Route is represented by a *RA* which is a special chromosome *VeSAR*. The chromosome *VeSAR* is a matrix where rows correspond to Persons (transport users) and columns correspond to different identified vehicles  $V_h^{R_g}$  where  $1 \leq h \leq H$  which are available to transport these persons through the same time window  $W_g$  to serve the route  $R_g(d_g, a_g, W_g)$ .

Each element of the matrix is an assignment of the person  $P_{cp}$  to the vehicle  $V_{ch}$  as follows:

- 1 : if  $P_p$  is assigned to  $V_h$
- CH[p,h]=\* : if  $P_p$  can be assigned to  $V_h$
- x : if  $P_p$  can not be assigned to  $V_h$

A person cannot be assigned more than one time to a several vehicles and cannot be assigned to a vehicle if his preferences or constraints exile this assignment. For example, when a person can't drive an AUTOLIB, we take into account this constraint in the assignment process: the assignment of this person to this AUTOLIB is x (i.e. non-assignment). For example, we have three simultaneous itineraries requests at  $t=9:15$  whose correspondent possible Routes Combinations are generated. We suppose here that the route  $R_2(x, y, W_2)$  belongs to at least a possible Route Combination of three users with  $W_2=[9h30,10h45]$ . For this identified Route (sub-itinerary), we have a *VeSAR* instance where rows correspond to all users concerned by this Route through the same time window and columns to all transport vehicles available to go from departure point to arrival point of this route also through this same time window with:

- User 1 ( $P_6$ ) : does not like carpooling,
- User 2 ( $P_3$ ): does not like public transport,
- User 3 ( $P_{25}$ ): can't drive a Vlib.

The life cycle of a *VeSAR* starts with (pre-assignment):

$R(x, y, [9h30,10h45])$	$V_{13}(2,3)$	Vlib(12)	$V_4(1,4)$	Bus <sub>9</sub>	Autolib(8)
$P_6$	x	*	X	*	*
$P_3$	*	*	*	x	*
$P_{25}$	*	x	*	*	*

A possible assignment can be:

R(x, y, [9h30,10h45])	V <sub>13</sub> (0,3)	Vlib(12)	V <sub>4</sub> (1,4)	Bus <sub>9</sub>	Autolib(8)
P <sub>6</sub>	x	*	x	1	*
P <sub>3</sub>	1	*	*	x	*
P <sub>25</sub>	1	x	*	*	*

While, the system continue to identify the best Route Combination thanks to the application of genetic operators and the RAs coalition, the *SupA* keeps in mind all these Routes. It will be help full for the coalition of RAs to consult the *SupA* and its knowledge since it can optimize the number of messages and negotiation between the different RAs. In this paper, we don't explain in detail the RAs coalition and the Negotiation protocol but we focus on the distributed co-modal approach used in order to compute the shortest paths in the co-modal graph. So the second role of the *SupA* is detailed in the next sections.

## VI. DISTRIBUTED CO-MODAL GRAPHS

### Co-modal Graph

Let  $G(N, E, M)$  denotes a co-modal graph or co-modal network, where  $N = \{n_1, \dots, n_j\}$  is a set of vertices and  $J$  is the total number of vertices,  $E = \{e_1, \dots, e_L\}$  is a set of edges,  $L$  is the total number of edges and  $M = \{m_1, \dots, m_K\}$  is a set of transport services (e.g. Public transport, Carsharing or Carpooling),  $K$  is the total number of transport services. An edge  $e_l \in E$  with  $l \in \{1..L\}$  can be identified by  $(n_p, n_q)_{m_r}$ , where  $n_p, n_q \in N$  and  $m_r \in M$  with  $p, q \in \{1..J\}$  and  $r \in \{1..K\}$ . The  $e_l$  expresses that it is possible to go from vertex  $n_p$  to  $n_q$  by using transport service  $m_r$ . A value  $D_{e_l} = D(n_p, n_q)_{m_r}$  is associated to each edge  $e_l$ , indicating the weight and the cost of including the edge in the solution.

**Definition 1:** A graph  $G(N, E, M)$  is said to be comodal if there is at least two transport services  $m_i, m_j \in M$  where  $(n_p, n_q)_{m_i}, (n_{p'}, n_{q'})_{m_j} \in E, m_i \neq m_j$  with  $i, j \in \{1..K\}$  and  $n_p, n_{p'}, n_q, n_{q'} \in N, p, p', q, q' \in \{1..J\}$ . It is possible to have  $n_q = n_{p'}$  and also  $n_p = n_{p'}$  and  $n_q = n_{q'}$  with  $p, p', q, q' \in \{1..J\}$ . If there is only one transport service in the graph, the graph is said to be uni-service.

Given a co-modal graph  $G(N, E, M)$ , a path or a routecombination  $RC_{n_1, n_l} = (n_1 \rightarrow n_l)$  is a sequence of edges between a pair of vertices  $n_1$  and  $n_l$  with  $((n_1, n_2)_{m_1}, \dots, (n_{l-1}, n_l)_{m_k})$  where  $\forall l \in \{1, \dots, J\}, n_j \in N, (n_j, n_{j+1})_{m_i} \in E, m_i \in M$  and  $i \in \{1..K\}$ .

So, a path  $RC_{n_1, n_l} = (e_1, e_2, \dots, e_l)$  is said to be comodal if  $\exists e_p, e_q \in E, e_p = (n_p, n_{p'})_{m_i}, e_q = (n_q, n_{q'})_{m_j}, m_i \neq m_j, i \neq j$  and  $i, j \in \{1..L\}$ . If there is only one service involved in the routecombination, the routecombination is said to be uni-service.

**Definition 2:** Given a routecombination  $RC_{n_i, n_j} = (n_i \rightarrow n_j)$  or an edge  $(n_i, n_j)_{m_k}, i, j \in \{1..L\}$  and  $\in \{1..K\}$ , a time window is defined as a time interval  $[t_{n_i}, t_{n_j}]$  where  $t_{n_i}$  denotes the departure time from vertex  $n_i$  and  $t_{n_j}$  the arrival time at  $n_j$ .

**Definition 3:** Since each edge represent a route assured by a transport service, the cost of edges is considered to be time-dependent.  $\forall e_i \in E$  we can have  $D_{e_i}(t_j) \neq D_{e_i}(t_k)$ . Our graph  $G(N, E, M)$  becomes a dynamic comodal graph.

### Transfer Graph

The authors of [Ayed et al. 2010] proposed a new approach based on transfer graph in order to solve a time-dependent multimodal transport problems while a transfer graph is composed of a set of uni-modal graphs. In our case, we adopt this approach with a transfer graph described by a set of uni-service networks and a set of arcs connecting them. It is defined by  $G_T(C, TR)$  where  $C = \{C_1, C_2, \dots, C_k\}$  is the set of uni-service networks called components and  $TR$  is the set of virtual edges which interconnect them. Each component  $C_i = (N_i, E_i, M_i, PTC_i)$  is such that  $\forall i, j \in \{1, \dots, K\}, M_i \neq M_j$ . Besides,  $N = \cup_{i \in \{1, \dots, K\}} N_i, E = \cup_{i \in \{1, \dots, K\}} E_i, M = \cup_{i \in \{1, \dots, K\}} M_i$  and

$TR = \{(n_i, n_j) \text{ such as } n_i \in C_i, n_j \in C_j, n_i = n_j\}$  where  $(n_i, n_j)$  represents a transfer from service transport  $m_i$  to another service transport  $m_j$  ( $m_i, m_j \in M$ ) at the *co-modal transfer point*  $n_i$  (or  $n_j$ ).  $n_i \in PTC_i, n_j \in PTC_j, i, j \in \{1..K\}$  are called *Co-modal Transfer Point* and symbolized the same location. So, we have  $PTC_i = \{n_i \in C_j \setminus \exists n_j \in C_j \text{ with } n_i = n_j, i, j \in \{1, \dots, K\}\}$ .

Figure 5 illustrates an example of a transfer graph  $G_T(C, TR)$  where  $C = \{C_1, C_2, C_3\}$ ,  $C_1, C_2$  and  $C_3$  are three components connected by four transfers. Each component  $C_i = (N_i, E_i, M_i, PTC_i)$  represents just one transport service.  $C_1$  represents the multimodal public transport service,  $C_2$  represents the carpooling service and finally  $C_3$  corresponds to the free use vehicles. The vertices  $a, c, b$  and  $d$  are *co-modal transfer points*.  $a, c, b \in PTC_1; a, c, d \in PTC_2$  and  $b, d \in PTC_3$ .  $TR = \{(a, a), (b, b), (c, c), (d, d)\}$  Each component contains edge belonging to only one transport service. In this example, we can go from  $d_k$  to  $d_a$  using only the public transport  $RC_{d_k, a_k} = (d_k, c)_{C_1}, (c, b)_{C_1}, (b, a_k)_{C_1}$ . Another possibility is the Route combination  $RC_{d_k, a_k} = (d_k, d)_{C_2}, (d, e)_{C_3}, (e, a_k)_{C_3}$ .

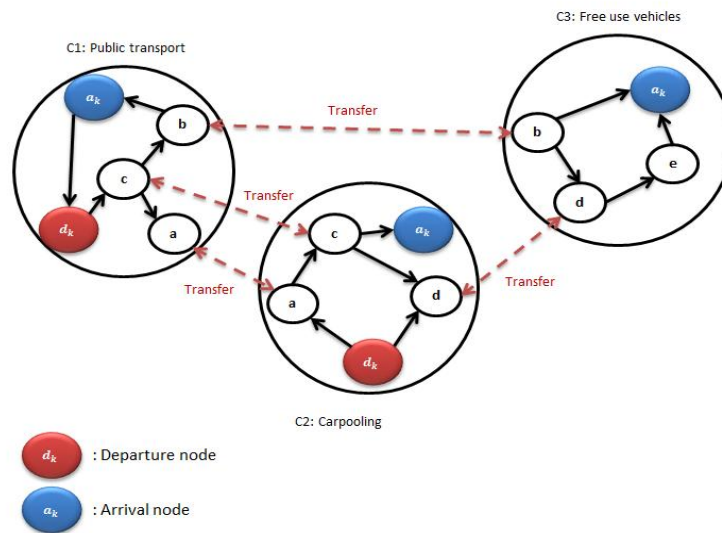


Figure 5 Example of transfer graph

The transfer graph represents and adapts to the distributed nature of real word transport information providers since it separates and keeps all transport modes in different uni-modal or uni-service networks.

So, each uni-modal network is independent and can be easily changed or updated without requiring any further recalculation [42], [43].

In this graph, we distinct two path's types: inter-components and intra-components. An inter-component path is considered as any path which connects two vertices  $x, y \in N$ , where at least two edges belong to two distinct components. However, an intra-component path with  $C_i$  is a path which connects two vertices  $x, y \in N_i$  whose edges belong to only one component  $C_i$ . It is possible to have several route combinations  $RC_{x,y}^i$  which connect  $x$  and  $y$  in the component  $C_i$ .

An intra-component can be one of the following categories:

- $RC_{d_k, a_k}^i$  is the shortest path which starts at source vertex  $d_k$  and ends at target vertex  $a_k$  within  $C_i$ .
- $RC_{d_k, PTC_i}^i$  is the set of shortest paths which start at source vertex  $d_k$  and end at a *Co-modal Transfer Point*  $PTC_i$  within  $C_i$ .
- $RC_{PTC_i, PTC_j}^i$  is the set of shortest paths which start at any *Co-modal Transfer Point*  $PTC_i$  and end at  $PTC_j$  within  $C_i$ .
- $RC_{PTC_i, a_k}^i$  is the set of shortest paths which start at any *Co-modal Transfer point*  $PTC_i$  and ends at target vertex  $a_k$  within  $C_i \in C$ .

The transfer graph  $G_T = (C, TR)$  has to be solved by computing the different intra-component paths:  $RC_{d_k, a_k}^i, RC_{d_k, PTC_i}^i, RC_{PTC_i, PTC_j}^i, RC_{PTC_i, a_k}^i$  for all components  $C_i \in C$ .

### VII. SOLVING THE TRANSFER GRAPH

The *SupA* has to compute  $RC_{d_k, a_k}^{*i}$ ,  $RC_{a_k, PTC_i}^{*i}$ ,  $RC_{PTC_i, PTC_j}^{*i}$ ,  $RC_{PTC_i, a_k}^{*i}$  for all the component  $C_i \in C$  knowing that each  $C_i$  is represented by a  $TSA_i$ ,  $1 \leq i \leq K$ .

Each transport service  $C_i$  can be provided thanks to different operators. Each transport operator's information system (TOIS) is composed of a local database (DB) describing the different means of available transport that it manage (Metro, Bus, Tramway, with stations, timetables, carsharing available with stations and cars for carpooling...) and of an Itinerary Calculating Algorithm (ICA) which uses these local data to search optimal itineraries for users requests. To integrate the co-modal information from the different heterogeneous Transport Operator's Information Systems (TOIS), we proceed to applications integration. This integration tries to take advantage of the current multi-modal or mono-modal information systems and make the TOIS cooperate to calculate multi-modal route. For this reason, each service or each component  $C_i = (N_i, E_i, M_i, PTC_i)$  is composed of different classes  $C_{i,j}$  with  $1 \leq j \leq K_i$ ,  $K_i$  is the total number of operators related to the component  $C_i$ .

**Definition 4:** A class in a distributed system refers to an autonomous subsystem. A class possesses its independent resources [44].

Each class  $C_{i,j}$  is represented by a graph  $G_{i,j}(N_{i,j}, E_{i,j})$  with  $N_{i,j}$  and  $E_{i,j}$  are respectively the set of vertices and edges related to the operator  $j$  of the service  $C_i$ . A vertex  $n_{i,j}$  can be even a public transport's station, carsharing station or a departure or arrival point for a carpooling service. Also, an edge  $e_{i,j}$  represents a *Route* using a transport mode managed by the operator  $C_{i,j}$  with  $1 \leq j \leq K_i$ .

The graph  $C_i = (N_i, E_i, M_i, PTC_i)$  is a supergraph that allows more than one edge between a pair of vertices. For example, if  $x$  and  $y$  are intersections of class  $C_{i,l}$  and  $C_{i,j}$  (i.e.,  $x \in N_{i,l}$ ,  $x \in N_{i,j}$ ,  $y \in N_{i,l}$ ,  $y \in N_{i,j}$ ),  $(x, y)_{i,l} \in E_{i,l}$  and  $(x, y)_{i,j} \in E_{i,j}$  with  $1 \leq l, j \leq K_i$ , then there are two edges  $(x, y)_{i,l}$  and  $(x, y)_{i,j}$  between vertices  $x$  and  $y$  in  $C_i = (N_i, E_i, M_i, PTC_i)$  and each edge has a label  $D((x, y)_{i,l})$  and  $D((x, y)_{i,j})$ , respectively.

Since the component represented by  $C_i = (N_i, E_i, M_i, PTC_i)$  is a distributed system in which local classes maintain their own data and there is not an aggregate central database,  $C_i = (N_i, E_i, M_i, PTC_i)$  is actually a virtual graph and not stored with the central computing server. The distributed shortest path problem is defined as a problem for the central computing server to find the shortest inter-class route between any two vertices in  $C_i = (N_i, E_i, M_i, PTC_i)$  based on some local information provided by individual classes.

In the case of one operator, a shortest path can be resolved using the following non-distributed Dijkstra's Algorithm or another shortest path algorithm.

We consider a system represented by a graph  $G(N, E)$  with vertex set  $N$  and edge set  $E$ . The graph may contain cycles. Also, the graph is assumed to be simple meaning that there is no edge from a vertex to itself (no loops) and between any two vertices there is at most one edge. There is a label,  $D(n_1, n_2)$  for an edge  $(n_1, n_2)$  representing the length of the edge. Dijkstra's algorithm identifies the shortest route between two nodes, A (source) and B (destination), as follows.

---

#### The non-distributed Dijkstra Algorithm

---

**Step 1:** Let vertex set  $R = \{A\}$ ; let  $N = N \setminus \{A\}$ .

**Step 2:** Iteratively **do until** node  $B \in R$ :  
Identify a smallest label  $D(j, k)$  such that  
 $j \in R$  and  $k \in N$

**Step 3:** Let  $R = R \cup \{k\}$ ,  $N = N \setminus \{k\}$

---

This algorithm is used to find the shortest intra-class route within a class that is a non-distributed subsystem. But for the central computing server of a distributed system, Dijkstra's algorithm does not guarantee the optimal result since the central computing server does not have complete data. So the adopted approach used by Wang and Kaempke [Wang et al 2004] will organize the local information about the intersections into a non-distributed graph. So the

shortest route identified by Dijkstra's algorithm in this graph forms a trace of the shortest route in the original distributed system.

The approach begins by constructing a graph of intersections and the shortest route on it can be calculated by Dijkstra's algorithm and can be easily extended to the original distributed system  $C_i = (N_i, E_i, M_i, PTC_i)$ .

Let  $RC_{m,n}^{*i,j}$  be the shortest route linking  $m$  to  $n$  in class  $C_{i,j}$ . Also, let  $I(m,n) = \{j \mid m, n \in C_{i,j}\}$  denote an index set of classes containing both vertices  $n$  and  $m$ . The following procedure formally defines the complete intersection graph  $G_{cint}$ .

**Definition 5:** Let  $G_{cint}$  denotes the intersection graph. A vertex  $n \in G_{cint}$  if and only if  $n$  is an intersection vertex in  $(N_i, E_i, M_i, PTC_i)$ . There is an edge between vertices  $m$  and  $n$  in  $G_{cint}$  if and only if  $n$  and  $m$  are clannish.

Each edge  $(n, m)$  has two labels,  $RC_{m,n}^{*i}$  and  $rec(m, n)$ , so that:

$$RC_{m,n}^{*i} = \min_{j \in I(m,n)} (RC_{m,n}^{*i,j}) \text{ and } rec(m, n) = j \text{ if } RC_{m,n}^{*i} = RC_{m,n}^{*i,j} \text{ for some } j \in I(m, n).$$

Label  $RC_{m,n}^{*i}$  on edge  $(m, n)$  in  $G_{cint}$  represents the shortest distance between vertices  $m$  and  $n$  by using the resource of only one class.  $RC_{m,n}^{*i}$  is the length of the shortest intra-class route between  $m$  and  $n$ . Label  $rec(m, n)$  indicates the class associated with  $RC_{m,n}^{*i}$ .

To compute the shortest route between  $d_k$  and  $a_k$  in the time window  $W_k$ , we need to extend the complete intersection graph by including  $d_k$  and  $a_k$  in the graph. This graph is called the virtual extended intersection graph, denoted as  $G_{veint}(d_k, a_k, W_k)$ .

**Definition 6:** Let the virtual extended intersection graph  $G_{veint}(d_k, a_k, W_k)$  contains all vertices of  $G_{cint}$  plus the departure and arrival vertices  $d_k$  and  $a_k$  (if they are not in  $G_{cint}$ )

$G_{veint}(d_k, a_k, W_k)$  contains all the edges of  $G_{cint}$  and the following: an edge between  $d_k$  and each of its clannish vertices and an edge between  $a_k$  and each of its clannish vertices.

The distributed Shortest Route Algorithm using all the definitions described below, is described as following.

---

**Distributed Shortest Route Algorithm (DSRA)**

---

**Step 1:** Construct the complete intersection graph  $G_{cint}$

**Step 2:** Construct the extended virtual complete intersection graph  $G_{veint}(d_k, a_k, W_k)$ .

**Step 3:** Compute the shortest route  $RC_{d_k, a_k}^* = (d_k = n_0, n_1, \dots, n_n = a_k)$  using a Shortest Route Algorithm (SRA).

**Step 4:** For each pair of vertices on the shortest route  $RC_{d_k, a_k}^* = (d_k = n_0, n_1, \dots, n_n = a_k)$  call relative class to the edge  $(n_k, n_{k+1})$  to fill in the details of the intra-class route associated.

---

We consider that:

$\varphi_{d_k, j}(td_k)$  denotes the earliest arrival time to the vertex  $j$  leaving from the depart vertex  $d_k$  at the time  $td_k$ .

$pred_{td_k}(j)$  defines the predecessor vertex  $j$  at  $td_k$ .

The algorithm that computes the shortest route  $RC_{d_k, a_k}^*$  is described as following:

---

**Shortest Route Algorithm (SRA)**

---

**1. Initialization**

$$\varphi_{d_k, d_k}(td_k) = td_k$$

$$\varphi_{d_k, l}(td_k) = \infty, \quad pred_{td_k}(l) = \infty \text{ et } rec(l) = \infty, \quad \forall l \in N_i - \{d_k\}$$

$$pred_{td_k}(d_k) = d_k \text{ and } N_{current} = \{d_k\}$$

**2. Node Selection**

Let the node  $l$  with  $\min_{j \in N_{current}} (\varphi_{d_k, j}(td_k))$

**3. Exploration of possible successors**

$$\forall j \in N^+(l) \text{ do}$$


---

---

$If((\varphi_{d_k,j}(td_k) > \varphi_{ij}(\varphi_{d_k,l}(td_k))) \text{ and } (\varphi_{d_k,j}(td_k) < ta_k))$  Then  
 $\varphi_{d_k,j}(td_k) = \varphi_{ij}(\varphi_{d_k,l}(td_k))$   
 $pred_{td_k}(j) = l$   
 $rec(j) = \text{Class Index}$   
 If  $j \notin N_{current}$  then  $N_{current} = \{j\} \cup N_{current}$   
 4. If  $N_{current} = \emptyset$  then end of the algorithm else go to the step  
 2.

---

After the computing of each shortest paths we obtain a Shortest Path Transfer graph defined as following:

**Definition 7:** Given a transfer graph  $G_T(t) = (C, TR)$ , we define a Shortest Path Transfer graph as  $G_F = (N_f, E_f)$ , where  $N_f = \cup_{C_i \in C} PTC_i \cup \{d_k, a_k\}$  and  $E_f = \cup RC_{d_k, a_k}^* \cup RC_{d_k, PTC_i}^* \cup RC_{PTC_i, PTC_j}^* \cup RC_{PTC_i, a_k}^*, \forall C_i \in C$

### VIII. SIMULATIONS

Our application is the result of a significant and sustained work by our research team in the French High School EcoleCentrale (LAGIS – EC-Lille) to implement a distributed co-modal transport system. In order to explain in detail and evaluate the solution proposed in this paper and validate the distributed co-modal approach for the vehicle sharing services system we applied the methodology proposed on two examples for transport requests.

We are developing our system, with JADE platform (Java Agent Development platform). JADE is a middleware which permits a flexible implementation of multi-agents systems; it offers an efficient transport of ACL (Agent Communication Language) messages for agents communication which complies with FIPA specifications.

We chose a part from the transport network in the region of Lille (Fig.6) and we collected data from the different existing transport services.

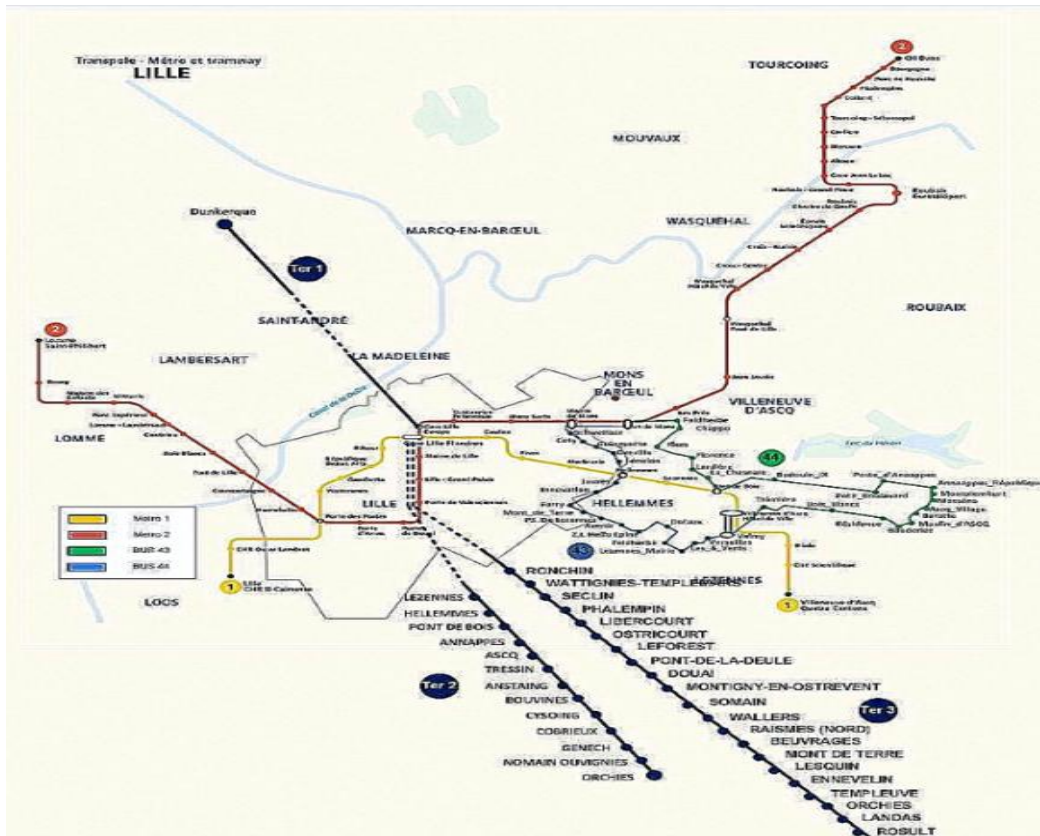


Figure 6 Transport network for simulations

The data include three transport services which are public transport, carpooling and vehicles on service. For the public transport service, we collected data from three operators: Transpole, SNCF and BCDLigne. The carpooling service is assured by one operator. We also have one operator Vville for bikes' service and Lilas for carsharing service.

In order to illustrate our approach, we propose two examples of simulation. For the first example, we consider just one request in order to explain the co-modal approach: We consider one request  $I_1$  at  $t=7:45$  am going from Dunkerque to Lezennes in the window time [8, 9:15]. The user has no preference in terms of transport modes.

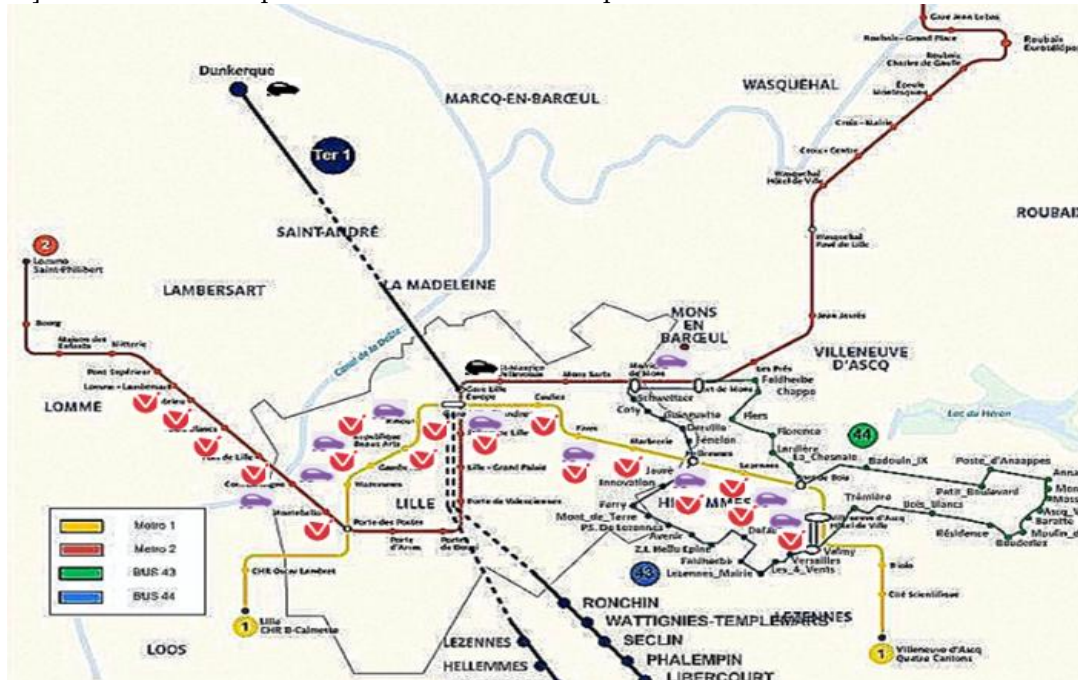


Figure 7 Transport network for the first example

For the second example, we consider six itinerary requests at  $t=7$  am:

- $I_1$ (Dunkerque, Villeneuve d'Ascq Hotel de Ville, [7:30, 9h30]). Transport service preferences: Public transport and carpooling. Criteria priority: Cost, time, Greenhouse gases emission;
- $I_2$ (CHRB Calmette, Orchies, [7:20, 10:30]). Transport service preferences: Public Transport and carsharing. Criteria priority: Time, Greenhouse gases emission, cost
- $I_3$ (Dunkerque, CHDron, [7:30, 9:30]) : Transport service preferences: Public transport and carpooling. Criteria priority: Cost, time, Greenhouse gases emission;
- $I_4$ (Cormontaigne, Ascq\_Village, [8:45, 10]) : Transport service preferences: All the proposed services. Criteria priority: time, cost, greenhouse gases emission;
- $I_5$ (Boulogne Ville, Port de Douai, [6, 9:15]) : Transport service preferences: Public transport. Criteria priority: time, cost, greenhouse gases emission;
- $I_6$ (Lezennes, C.H.R Oscar Lambret, [7, 9]) : Transport service preferences: Public transport, carpooling. Criteria priority: greenhouse gases emission, time, cost;

**Identification of the TIAs**

The IAs receive these itinerary requests and send it to the *SupA*. This agent locates all the departure and arrival points and asks all the TSAs for a domain search. In our case, we consider that we have three TSAs:  $TSA_1$  for the Public transport service,  $TSA_2$  for the carpooling service and  $TSA_3$  for the free vehicle services (free use vehicles). Each TSA sends to the *SupA* the list of TIAs identified for each request. In fact, each TSA executes a Domain Search Selection Algorithm (DSSA) in order to identify the operators that could respond to the request. The Fig. 8 and 9 show the results sent by the TSAs to the *SupA* for the two examples. The operators that will intervene in order to respond to the user's requests are:

Example 1:

- TIA<sub>1,1</sub>: Transpole
- TIA<sub>1,2</sub>: SNCF
- TIA<sub>2,2</sub>: VLille
- TIA<sub>3,1</sub>: Carpooling

```

MainProject (3) [Java Application] C:\Program Files (x86)\Java\jre7_32\bin\javaw.exe (1)
Requête de domaine de recherche pour la requête: 0
Covoiturage || CovoiturageFR || 7:30 || 9:30 || 0
VeloPartage || VLille || 7:30 || 9:30 || 0
Bus_44_1 || Transpole || 7:30 || 9:30 || 0
Metro2_vers_CH_Dron || Transpole || 7:30 || 9:30 || 0
Ter1_Dunkerque_LilleEurope || SNCF || 7:30 || 9:30 || 0
Metro2_vers_St_Philbert || Transpole || 7:30 || 9:30 || 0
Bus_44_2 || Transpole || 7:30 || 9:30 || 0
Bus_43_1 || Transpole || 7:30 || 9:30 || 0
Metro1_vers_4_Cantons || Transpole || 7:30 || 9:30 || 0
Metro1_vers_CHRB_Calmette || Transpole || 7:30 || 9:30 || 0
Ter2_LilleFlandres_Orchies || SNCF || 7:30 || 9:30 || 0
Ter2_Orchies_LilleFlandres || SNCF || 7:30 || 9:30 || 0
Ter3_Valenciennes_LilleFlandres || SNCF || 7:30 || 9:30 || 0
Ter3_LilleFlandres_Valenciennes || SNCF || 7:30 || 9:30 || 0
Bus_43_2 || Transpole || 7:30 || 9:30 || 0
Ter1_LilleEurope_Dunkerque || SNCF || 7:30 || 9:30 || 0
    
```

Figure 8 Identification of the TIAs for the first example

Exemple 2:

- TIA<sub>1,1</sub>: Transpole
- TIA<sub>1,2</sub>: SNCF
- TIA<sub>1,3</sub>: Ligne BCD
- TIA<sub>2,1</sub>: Lilas
- TIA<sub>2,2</sub>: VLille
- TIA<sub>3,1</sub>: Carpooling

```

<terminated> MainProject (1) [Java Application] C:\Program Files (x86)\Java\jre7_32\bin\javaw.exe (1)
Requête de domaine de recherche pour la requête: 0
Covoiturage || CovoiturageFR || 7:30 || 9:30 || 0
Metro2_vers_CH_Dron || Transpole || 7:30 || 9:30 || 0
Ter1_Dunkerque_LilleEurope || SNCF || 7:30 || 9:30 || 0
Metro2_vers_St_Philbert || Transpole || 7:30 || 9:30 || 0
Bus_BoulogneVille_Dunkerque || LigneBCD || 7:30 || 9:30 || 0
Metro1_vers_4_Cantons || Transpole || 7:30 || 9:30 || 0
Metro1_vers_CHRB_Calmette || Transpole || 7:30 || 9:30 || 0
Ter2_Orchies_LilleFlandres || SNCF || 7:30 || 9:30 || 0
Ter3_Valenciennes_LilleFlandres || SNCF || 7:30 || 9:30 || 0
Bus_Dunkerque_BoulogneVille || LigneBCD || 7:30 || 9:30 || 0
Ter2_LilleFlandres_Orchies || SNCF || 7:30 || 9:30 || 0
Ter3_LilleFlandres_Valenciennes || SNCF || 7:30 || 9:30 || 0
Ter1_LilleEurope_Dunkerque || SNCF || 7:30 || 9:30 || 0
*****
Requête de domaine de recherche pour la requête: 1
Ter2_LilleFlandres_Orchies || SNCF || 7:20 || 10:30 || 1
Metro1_vers_4_Cantons || Transpole || 7:20 || 10:30 || 1
Ter2_Orchies_LilleFlandres || SNCF || 7:20 || 10:30 || 1
Metro2_vers_St_Philbert || Transpole || 7:20 || 10:30 || 1
Metro2_vers_CH_Dron || Transpole || 7:20 || 10:30 || 1
Ter3_LilleFlandres_Valenciennes || SNCF || 7:20 || 10:30 || 1
Ter3_Valenciennes_LilleFlandres || SNCF || 7:20 || 10:30 || 1
Metro1_vers_CHRB_Calmette || Transpole || 7:20 || 10:30 || 1
*****
Requête de domaine de recherche pour la requête: 2
Covoiturage || CovoiturageFR || 7:30 || 9:30 || 2
Metro2_vers_CH_Dron || Transpole || 7:30 || 9:30 || 2
Ter1_Dunkerque_LilleEurope || SNCF || 7:30 || 9:30 || 2
Bus_BoulogneVille_Dunkerque || LigneBCD || 7:30 || 9:30 || 2
Metro2_vers_St_Philbert || Transpole || 7:30 || 9:30 || 2
Bus_Dunkerque_BoulogneVille || LigneBCD || 7:30 || 9:30 || 2
Ter1_LilleEurope_Dunkerque || SNCF || 7:30 || 9:30 || 2
*****
<terminated> MainProject (1) [Java Application] C:\Program Files (x86)\Java\jre7_32\bin\javaw.exe (1)
Requete de domaine de recherche pour la requete: 3
VeloPartage || VLille || 8:45 || 10:0 || 3
Bus_43_1 || Transpole || 8:45 || 10:0 || 3
Metro2_vers_CH_Dron || Transpole || 8:45 || 10:0 || 3
Bus_43_2 || Transpole || 8:45 || 10:0 || 3
Bus_44_2 || Transpole || 8:45 || 10:0 || 3
Metro1_vers_4_Cantons || Transpole || 8:45 || 10:0 || 3
Metro1_vers_CHRB_Calmette || Transpole || 8:45 || 10:0 || 3
Metro2_vers_St_Philbert || Transpole || 8:45 || 10:0 || 3
*****
Requête de domaine de recherche pour la requête: 4
Metro2_vers_CH_Dron || Transpole || 6:0 || 9:15 || 4
Ter1_Dunkerque_LilleEurope || SNCF || 6:0 || 9:15 || 4
Bus_BoulogneVille_Dunkerque || LigneBCD || 6:0 || 9:15 || 4
Metro2_vers_St_Philbert || Transpole || 6:0 || 9:15 || 4
Bus_Dunkerque_BoulogneVille || LigneBCD || 6:0 || 9:15 || 4
*****
Requête de domaine de recherche pour la requête: 5
Metro1_vers_4_Cantons || Transpole || 7:0 || 9:0 || 5
Metro1_vers_CHRB_Calmette || Transpole || 7:0 || 9:0 || 5
Metro2_vers_CH_Dron || Transpole || 7:0 || 9:0 || 5
Metro2_vers_St_Philbert || Transpole || 7:0 || 9:0 || 5
*****
    
```

Figure 9 Identification of the TIAs for the second example

### Computation of shortest paths in the Transfer Graph

After the identification of transport operators list, the SupA sends all the requests to the correspondent agents (TIAs) and wait for the set of routes that could be part of the final itineraries. Once the SupA received all the routes from all the TIAs, it constructs the Transfer Graph and executes the DSRA algorithm in order to find the shortest paths.

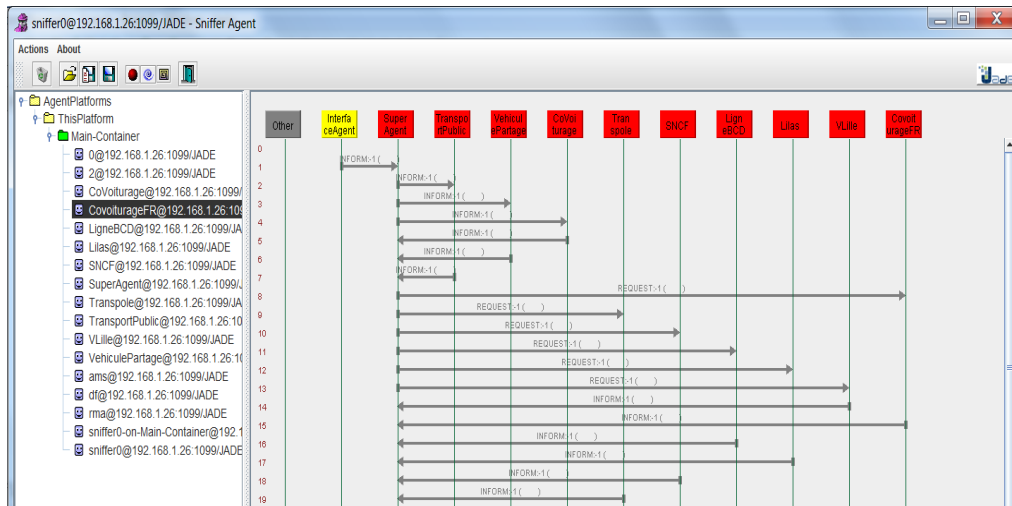


Figure 10 Communication between the different agents *supA*, *TSAs* et *TIAs*

For example 1, the transfer graph obtained is represented in the Fig.11:

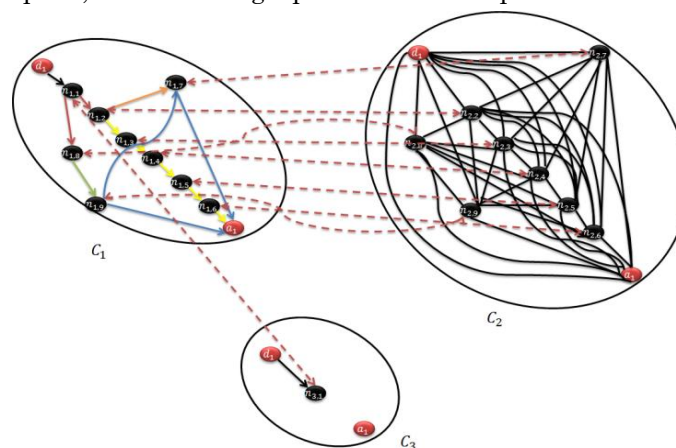


Figure 11 Transfer graph for example 1

The transfer graph is composed of three components  $C_1$ ,  $C_2$  et  $C_3$  related respectively to the public transport, free use vehicles and the carpooling services. In this transfer graph, we obtained nine Co-modal Transfer Points (PTCs):

Table 1 Liste of PTCs

$n_{1,1} = n_{3,1}$	Gare Lille Europe
$n_{1,2} = n_{2,2}$	Gare Lille Flandres
$n_{1,3} = n_{2,3}$	Caulier
$n_{1,4} = n_{2,4}$	Fives
$n_{1,5} = n_{2,5}$	Marbrerie
$n_{1,6} = n_{2,6}$	Hellemmes
$n_{1,7} = n_{2,7}$	Mont de Terre
$n_{1,8} = n_{2,8}$	Fort de Mons
$n_{1,9} = n_{2,9}$	Faidherbe

The DSRA is applied in this transfer graph in order to compute all the shortest paths. The computation of the shortest path between  $d_1$  and  $a_1$  is described in Fig.12 and Fig.13.

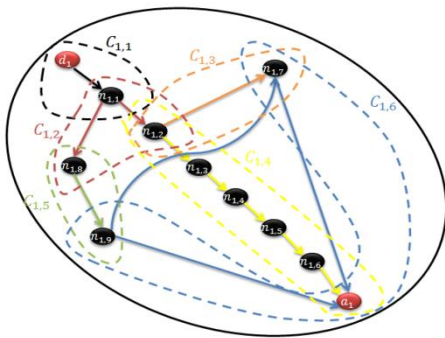


Figure 12 Classes of component  $C_1$

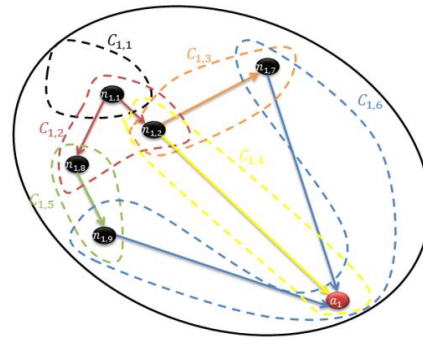


Figure 13 Intersection graph

The application of the DSRA begins by constructing the intersection graph which is composed of 6 classes. The shortest path obtained is:  $(d_1 \rightarrow n_{1,1} \rightarrow n_{1,2} \rightarrow a_1)$ .

The second example is more complex and it is difficult to represent the corresponding graphs. In fact, when constructing the Transfer Graph and after the computation of the shortest paths in each component, we obtained the following results:

**Table 2: Results obtained with the Transfer graph**

Component	$C_1$	$C_2$	$C_3$
Number of nodes	125	60	13
Number of Co-modal Transfer Points (PTC)	14	12	3
Number of edges	248	3540	2

**Table 3 Results obtained with the SPTG**

Component	$C_1$	$C_2$	$C_3$
Number of nodes	30	21	13
Number of Co-modal Transfer Points (PTC)	14	12	3
Number of edges	88	66	2

In these tables, we distinguished the number of nodes, co-modal transport points and edges in both of the Transfer Graph and the SPTG. All these parameters are compared in Fig.14 :

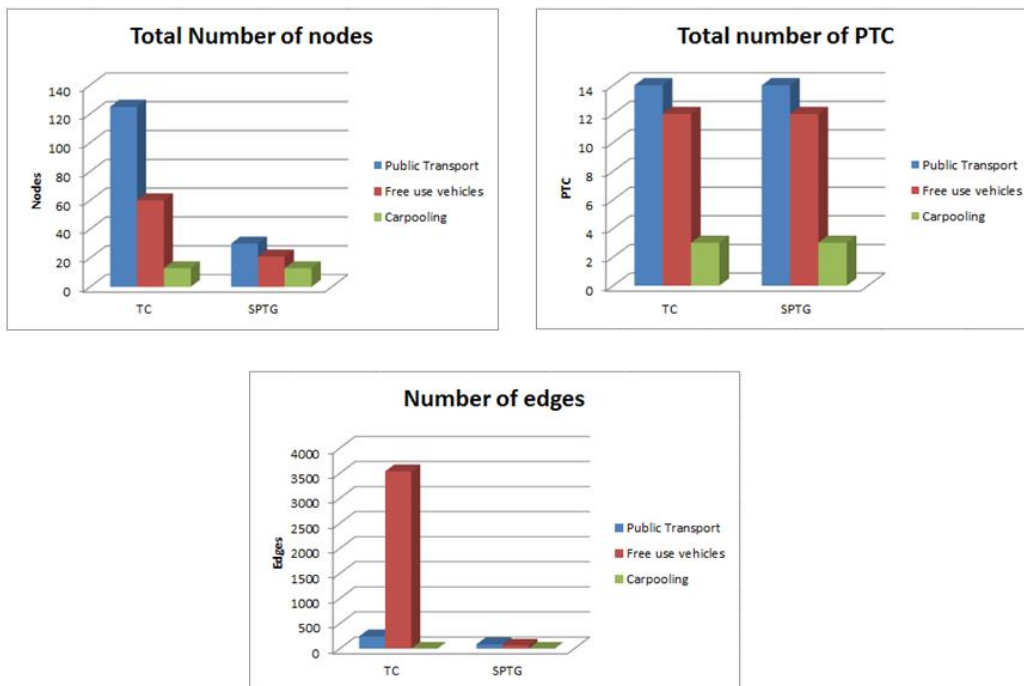


Figure 14 Comparison between the TC and the SPTG

In this figure, we can see a remarkable reduction of the number of nodes and specially the edges number and thereafter a reduction of routes. The number of Co-modal Transfer Point doesn't change since we compute the shortest paths between all the PTCs. The itineraries obtained for the six requests are presented in Fig.15:

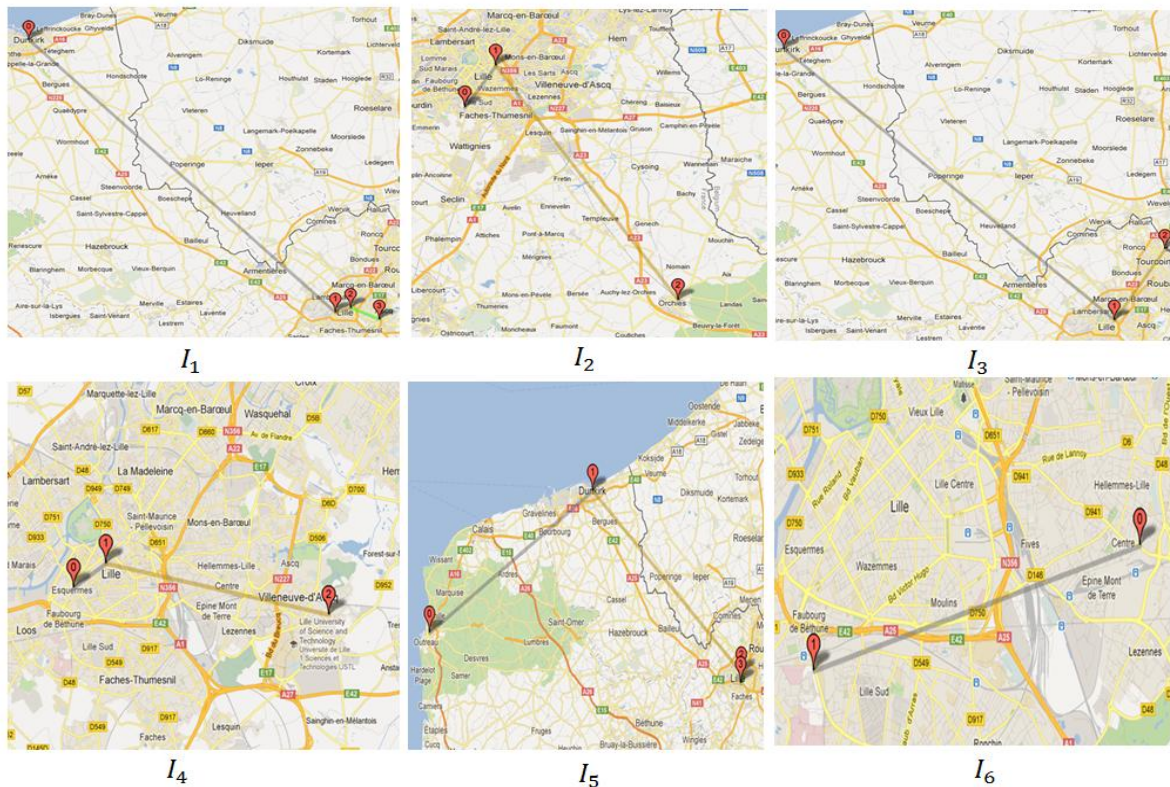


Figure 15 Final itineraries

This figure described the obtained results:

- For  $I_1$ : we obtained a co-modal itinerary with two transport services. Carpooling with the first route (Dunkerque, Port de Lille, [7:45, 8:35]), a subway line 2 with the second route (Port de Lille, Gare Lille Flandres, [8:35, 8:47]) and a subway line 1 with the third route (Gare Lille Flandres, Villeneuve d'Ascq Hotel de Ville, [8:48, 8:58])
- For  $I_2$ : the itinerary is multimodal thanks to one transport service : the public transport and two modes of transport. The first route (CHRB Calmette, Gare Lille Flandres, [7:22, 7:30]) is assured by the subway line 1 and the second route (Gare Lille Flandres, Orchies, [7:37, 7:59]) is assured by the train TER3.
- For  $I_3$ : we obtained a co-modal itinerary composed of two routes. The first route (Dunkerque, Port de Lille, [7:45, 8:35]) thanks to a carpooling car and the second route (Port de Lille, CH\_Dron, [8:36, 9:11]) thanks to the line 2 of the subway.
- For  $I_4$ : the itinerary is co-modal with two different transport services: free use vehicle (bike) for the first route (Cormontaigne, Massena, [8:45, 8:52]) and Public transport (Bus) for the last route (Massena, Ascq Village, [8:57, 8:59])
- For  $I_5$ : it is a mono-service itinerary (only public transport) but multimodal thanks to three transport operators. The first operator LigneBCD assured the first route (Boulogne ville, Dunkerque, [6:15, 7:35]). The second operator SNCF assured the route (Dunkerque, Gare Lille Europe, [8:21, 8:55]) and the operator Transpole assured the last route (Gare Lille Europe, Port de douai, [8:55, 9:00])
- For  $I_6$ : the itinerary is monomodal with just one route (Lezennes, CHR Oscar Lambret, [7:07, 7:21]) thanks to the line 1 of the subway.

In order to improve the impact of the number of requests and services, we make some tests. We vary the requests and the number of services and we compare the variation of the number of nodes, co-modal transport points and edges shown in Fig.16.

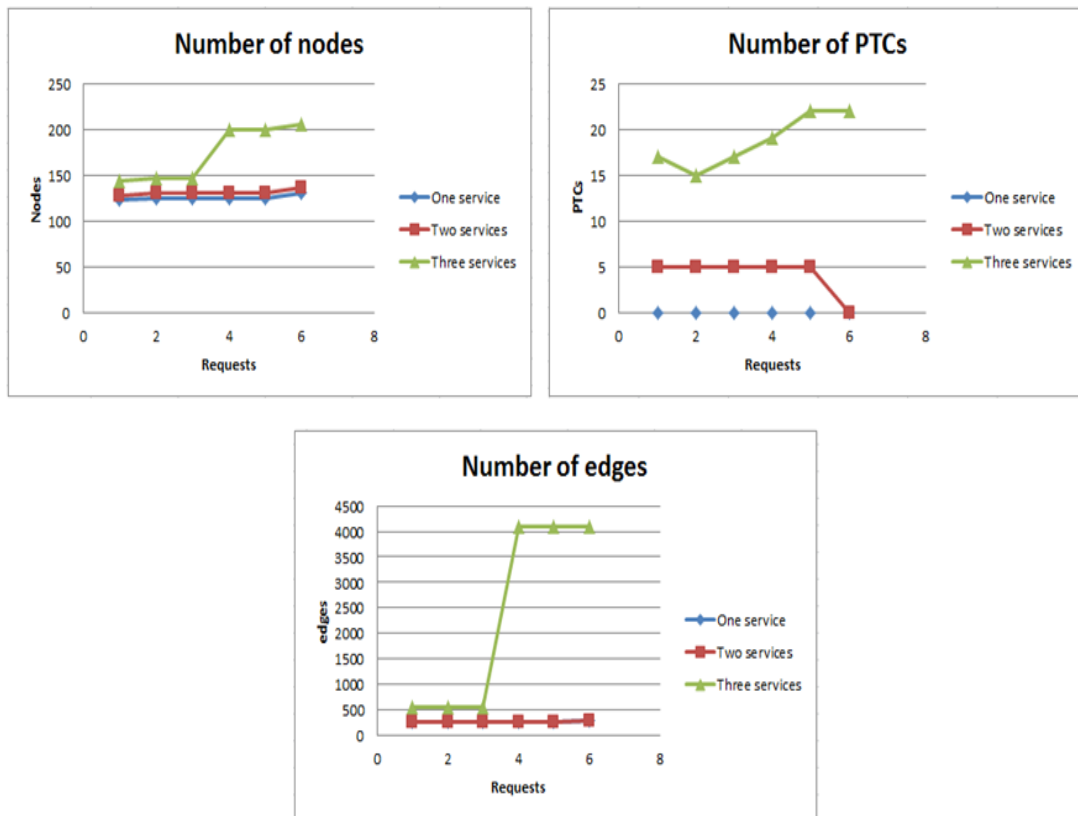


Figure 16 Variation of the number of nodes, PTCs and edges

We notice that in case of one transport service, the number of PTCs must be null. The number of edges increases in the case of including three transport services. We remark some constancy of the curves due to the similarity between the different requests. In fact, when the departure and arrival points are similar or near geographically, we obtain the same routes and so the same edges.

### IX. CONCLUSIONS

In this work, we proposed a distributed co-modal approach based on multi-agent system which aims to find an effective itinerary proposition to transport users including public transport, carsharing and carpooling. The system employs different optimization techniques. In fact, the developed Distributed Shortest Path Algorithm (DSRA) allows the system to simplify the resolution of shortest paths in term of time in a distributed system. Then, the system uses an evolutionary optimization approach in terms of total cost, time and gas emission volume taking into account user constraints and preferences. The employment of multi-agent system, the use of the co-modal and transfer graph and the rapid assignment process to a combinatorial problem thanks to an evolutionary method, make our adopted approach very interesting. The alliance of multi-agent systems and different optimization techniques is very important because with agent-based approaches we explore the ability to handle a large problem domain and a short time-scale of the domain while with the optimization techniques, we explore the ability to achieve system optimality or near optimality with a quality assurance. In future work, we intend to develop the evolutionary approach and the coalition of the RA generated by the SupA. We also aim to employ a genetic process generating more chromosome generations, in order to improve gradually generated solutions to find better solutions and to develop the protocol negotiation between the different RAs.

## REFERENCES

- [1] CLAVEL, R., MARIOTTO, M. AND ARSAC, B., 2008. L'autopartage en France et en Europe en 2008 –Etat des lieux et perspectives.
- [2] BALLEST, J.C. AND CLAVEL, R., 2007. Le covoiturage en France et en Europe-Etat des lieux et perspectives.
- [3] GENERAL COMMISSARIAT OF THE SUSTAINABLE DEVELOPMENT., 2011, Les comptes du transport en 2010, 48<sup>th</sup> report for the committee on transportation accounts nations.
- [4] THE EUROPEAN COMMISSION, 2010. European transport policy for 2010: time to decide. White paper.
- [5] GIANNOPOULOS, G.A., 2008. The application of co-modality in Greece : a critical appraisal of progress in the development of co-modal freight centers and logistics services. *Transition studies Review*, vol. 15, number 2.
- [6] ZOGRAFOS, K.G AND ANDROUTSOPOULOS, K.N, 2008. Algorithms for itinerary planning in multimodal transportation networks. *IEEE Transactions on Intelligent Transportation Systems*, vol. 9, pp 175-184.
- [7] CHANG, T.S, 2008. Best routes selection in international intermodal networks. *Computers and Operations Research Archive*, vol. 35, pp. 2877-2891.
- [8] LI, Q. AND KURT, C.E., 2000. GIS- based itinerary planning system for multimodal and fixed-route transit network. In proceedings of the MID-Continent Transportation Symposium, pp. 47-50, Iowa State.
- [9] ZILIASKOPOULOS, A. AND WARDELL, W., 2000. An intermodal optimum path algorithm for multimodal networks with dynamic arc travel times and switching delays. *European Journal of Operational Research*, vol. 125, no. 3, pp, 486-50
- [10] CALABRESE, F., COLONNA, M., Lovisolò, P., PARATA, D. AND RETTI, C., 2011. Real-Time Urban Monitoring Using Cell Phones: A case Study in Rome. ", *IEEE Transactions on Intelligent Transportation Systems*, vol. 12, No. 1.
- [11] KAMOUN, M.A, 2007. Conception d'un système d'information pour l'aide au déplacement multimodal: une approche multi-agents pour la recherche et la composition des itinéraires en ligne. PhD LAGIS/ EC- Lille FRE CNRS 3303, France.
- [12] ZIDI, K., 2006. Système interactif d'aide au déplacement multimodal (SIADM). ), PhD LAGIS/ EC- Lille FRE CNRS 3303, France.
- [13] FEKI, M. F., 2010. Optimisation distribuée pour la recherche des itinéraires multi-opérateurs dans un réseau de transport co-modal. PhD LAGIS/EC-Lille FRE CNRS 3303. France.
- [14] AYED, H., GALVEZ-FERNANDEZ, C., HABBAS, Z. AND KHADRAOUI, D., 2010. Solving time dependent multimodal transport problems using a transfer graph model. *Computers & Industrial Engineering*.
- [15] AYED, H., KHADRAOUI, D., AND GALVEZ-FERNANDEZ, C., 2011, A parallel algorithm for solving time dependent multimodal transport problem. 14<sup>th</sup> International IEEE Conference on Intelligent Transportation Systems, Washington, DC, USA, October 5-7, 2011.
- [16] HOUDA, M., KHEMAJA, M., OLIVEIRA, K., AND ABED, M., A public transportation ontology to support user travel planning. *IEEE International Conference on Research Challenges In Information Science*, Nice, France, 2010.
- [17] JARIYASUNANT, J., WORK, D.B, KERKEZ, B., SENGUPTA, R., GLASER, S. AND BAYEN, A. Mobile transit trip planning with real time data. *Transportation Research Board Annual Meeting*, Washington DC, 2010.
- [18] LI, L., ZHANG, H., WANG, X., LU, W. AND MU, Z, 2010. Urban Transit Coordination Using an Artificial Transportation System. *IEEE Transactions on Intelligent Transportation Systems*, vol. 11, Issue 4.
- [19] ZHANG, L., LI, J.Q., AND ZHOU, K. Design and Implementation of a traveler information tool with integrated real-time transit information and multi-modal trip planning. *Transportation Research Board Annual Meeting*, Washington, DC, 2011.
- [20] PENG, Z.R. AND KIM, E., 2008 A standard-based integration framework of distributed transit trip planning systems. *Journal of the Intelligent Transportation Systems*, vol 12, pp13-19.
- [21] SCHULTES, D.,. Route planning in road networks. PhD Thesis of Karlsruhe Institute of Technology, 2008.
- [22] PAJOR, T. Multi-modal route planning, Master thesis of Karlsruhe Institute of Technology, 2009.
- [23] REHRL, K., BRUNTSCH, S., MENTZ, H.J., 2007. Assisting multimodal travelers: Design and prototypical implementation of a personal travel companion, vol 8, No 1, pp 31-42.
- [24] THE EUROPEAN COMMISSION AND SEVENTH FRAMEWORK PROGRAMME COOPERATION. I-travel. Theme 7 Transport, Horizontal activities for implementation of the transport programme,2007-2013.

- [25] LIU, L. AND MENG, L, 2009. Algorithms of multi-modal route planning based on the concept of switch point. 6<sup>th</sup> International Symposium on LBS & TeleCartography, Nottingham, UK, 2009.
- [26] ROTHKRANTZ, L., DATCU, D. AND BEELEN, M., 2005; Personal intelligent travel assistant: a distributed approach. International Conference on Artificial Intelligence, June 2005.
- [27] ZHANG, J., LIAO, F., ARENTZE, T. AND TIMMERMANS, H., 2011. A multimodal transport network model for advanced traveler information systems. Ambient Intelligence at the services of info-mobility and Critical Transportation networks (ARTIFACT), Proceeding Computer Science, 5, pp 912-919.
- [28] SIRLAND, J., 2009. Green and ITS: An overview of innovations for a sustainable transport system in Stockholm. Editorial:sweco ITS, 2009.
- [29] ZOGRAFOS, K.G AND ANDROUTSOPOULOS, K.N, 2008. Algorithms for itinerary planning in multimodal transportation networks. IEEE Transactions on Intelligent Transportation Systems, vol. 9, pp 175-184.
- [30] SU, J.M., CHANG, C.H. AND HO W.C., 2008. Development of trip planning systems on public transit in Taiwan, IEEE International Conference on Networking, Sensing and Control, Hainan, China, pp 791-795.
- [31] KUMAR, J.SINGH, V. AND REDDY, D., 2005. Advanced traveler information system for Hyderabad city. IEEE Transactions on Intelligent Transportation Systems, vol 6, issue 1, pp 26-37.
- [32] ZAMBONELLI, F. AND VAN DYKE PARUNAK, H., 2003. Signs of a revolution in computer science and software engineering. In proceedings of the 3<sup>rd</sup> International Workshop Engineering Societies in the Agent World, vol. 2577, pp 13-28.
- [33] CHEN, B. AND CHENG, H. H., 2010. : A Review of the Applications of Agent Technology in Traffic and Transportation Systems. IEEE Transactions on Intelligent Transportation Systems, vol. 11, Issue. 2, pp. 485-497.
- [34] WANG, F. Y., 2005. : Agent-based control for networked traffic management systems. IEEE Intelligent Systems., vol. 20, no. 5, pp. 92-96.
- [35] ADAM, E., GRISLIN-LE-STRUGEON, E., MANDIAU, R., 2008, Flexible hierarchical organization of role based agents. Second IEEE International Conference on Self-Adaptive and Self-Organizing Systems Workshops, pp. 186-191.
- [36] CABRI, G., FERRARI, L., LEONARDI, L., 2004. Agent Role-based Collaboration and Coordination : a Survey About Existing Approaches. IEEE International Conference on Systems, Man and Cybernetics, Vol 6, pp 5473-5478.
- [37] YANG, J. AND LUO, Z., 2007. Coalition formation mechanism in multi-agent systems based on genetic algorithms. Journal of Applied Soft Computing, vol. 7, Issue 2, pp 561-568.
- [38] GENIN, T. AND AKNINE, S., 2010. Coalition Formation Strategies for self-Interested Agents in Task oriented Domains. In proceedings of the 2010 IEEE/ WIC/ ACM International Conference on Web Intelligence and Intelligent Agent technology.
- [39] JERIBI, K., ZGAYA, H. AND HAMMADI S., 2009. Multi-agent Based Evolutionary Method to Optimize Vehicle Sharing Services. International Conference WSEAS, Tenerife, Canary Islands, Spain.
- [40] JERIBI, K., MEJRI, H., ZGAYA, H. AND HAMMADI S., 2011. Vehicle Sharing Services Optimization Based on Multi-agent Approach. ,” 18<sup>th</sup> World Congress of the International Federation of Automatic Control (IFAC) Milano 2011.
- [41] JERIBI, K., ZGAYA, H., ZOGHLAMI, N., HAMMADI, S., 2011 (b). Distributed Architecture for a Co-modal Transport System. IEEE International Conference on Systems, Man and Cybernetics, Anchorage, Alaska.
- [42] FEKI, M. F., 2010. Optimisation distribuée pour la recherche des itinéraires multi-opérateurs dans un réseau de transport co-modal. PhD LAGIS/EC-Lille FRE CNRS 3303. France.
- [43] WANG, J. AND KAEMPKE, T., 2004. Shortest Route Computation in Distributed Systems. Computers & Operations Research, Vol. 31, Issue 10, pp 1621-1633.
- [44] WANG, F. Y., 2005. : Agent-based control for networked traffic management systems. IEEE Intelligent Systems., vol. 20, no. 5, pp. 92-96.



# International Journal of Modern Engineering Research (IJMER)

Volume : 4 Issue : 9 (Version-4)

ISSN : 2249-6645

September- 2014

## Contents :

<b>Simulation and Static Analysis of an Off-Road Vehicle Roll Cage</b> <i>R. Bhandari, P. Birajdar, A. Dafedar, S. Bammani, A. Pereira</i>	01-08
<b>Tensile and Impact Properties of Natural Fiber Hybrid Composite Materials</b> <i>Sathish. S, Kumaresan. M, Karthi. N, Dhilip kumar. T</i>	09-12
<b>Automotive Applications of Welding Technology – A Study</b> <i>Devarasiddappa. D</i>	13-19
<b>A Study on Risk Assessment in Construction Projects</b> <i>K. Jayasudha, Dr. B. Vidivelli</i>	20-23
<b>Credit Card Fraud Detection System: A Survey</b> <i>Dinesh L. Talekar , K. P. Adhiya</i>	24-31
<b>Seismic Vulnerability of RC Building With and Without Soft Storey Effect Using Pushover Analysis</b> <i>Harsha G, Syed Ahamed Raza</i>	32-47
<b>Decoupled Inverter Fed - Open end Winding Induction Motor Drive for Three Level Voltage SPWM Strategy</b> <i>Bukya. Balaji, B. Venkateswarlu, D. Jagan</i>	48-60
<b>Transient Stability Assessment and Enhancement in Power System</b> <i>Aysha P. A, Anna Baby</i>	61-65
<b>On Some Partial Orderings for Bimatrices</b> <i>G. Ramesh, N. Anbarasi</i>	66-74
<b>Novel Direct Switching Power Control Method of UPFC by Using Matrix Converter Based On SVPWM Techniques</b> <i>B. Venkateswarlu, D. Jagan, A. Karunakar, CH. Renuka</i>	75-90

## Simulation and Static Analysis of an Off-Road Vehicle Roll Cage

R. Bhandari<sup>1</sup>, P. Birajdar<sup>2</sup>, A. Dafedar<sup>3</sup>, S. Bammani<sup>4</sup>, A. Pereira<sup>5</sup>

<sup>1,2,3,4,5</sup> Department of Mechanical Engineering, N. K. Orchid College of Engineering and Technology, Gat No.16, Solapur-Tuljapur Road, Tale-Hipparaga, Solapur 413002, India

**Abstract:** The SAE-BAJA competition is arranged every year with a purpose to have teams of engineering students design, build and race a prototype of a four-wheel, one passenger, off-road vehicle. The most important aspect of the vehicle design is the frame. The frame contains the operator, engine, brake system, fuel system and steering mechanism, it must be of adequate strength to protect the operator in the event of a rollover or impact. The roll cage must be constructed of steel tubing, with minimum dimensional and strength requirements dictated by Society of Automotive Engineers (SAE). Increased concern about the roll cage has created the importance of simulation and analysis thereby predicting failure modes of the frame. In the present paper, we have used ANSYS to investigate the response of the frame under various impacts. We considered a direct frontal impact and side impact that results in a 4g horizontal loading, a rollover impact of 3g deceleration value, bump impact and front torsional impact analysis with 3g deceleration value. The impact loading is simulated by restricting displacements at certain locations, and applying discrete forces at various points on the frame where the weight is concentrated. Throughout the analysis of roll cage more emphasis was given on obtaining a allowable factor of safety and designed according to it.

**Keywords:** roll cage; frontal impact; side impact; rollover impact; ANSYS.

### I. Introduction

A frame of a vehicle plays the most important role in safety of the passenger. The frame contains the operator, engine, brake system, fuel system, and steering mechanism, and must be of adequate strength to protect the operator in the event of a rollover or impact. The passenger cabin must have the capacity to resist all the forces exerted upon it. This can be achieved either by using high strength material or better cross sections against the applied load. But the most feasible way to balance the dry mass of roll-cage with the optimum number of members is done by triangulation method. The roll cage must be constructed of steel tubing, with minimum dimensional and strength requirements dictated by SAE. The SAE BAJA vehicle development manual also restricts us about the vehicle weight, shape and size, and dimensions [1-3].

Circular cross-section is employed for the roll cage development as it helps to overcome difficulties like increment in dimension, rise in the overall weight and decrease in fuel efficiency. It's always a perfect one to resist the twisting and the rolling effects, therefore is preferred for torsional rigidity.

#### a) Design objective of roll cage are:

- 1) Provide full safety to the driver, by obtaining required strength and torsional rigidity, while reducing weight through diligent tubing selection.
- 2) Design for manufacturability, as well as cost reduction, to ensure both material and manufacturing costs are competitive with other SAE vehicles.
- 3) Improve driver comfort by providing more lateral space and leg room in the driver compartment.
- 4) Maintain ease of serviceability by ensuring that roll cage members do not interfere with other subsystems [4-6].

This roll cage is developed in ANSYS Multiphysics Menu by plotting the keypoints, lines and arcs. The element type selected for it is PIPE 16, a uniaxial element with tension, torsion and bending capabilities. The element has six degrees of freedom at two nodes: translations in the nodal x, y and z directions and rotations about the nodal x, y and z axes. The real constants involved in the pre-processing of PIPE 16 element are its outer diameter and thickness value. The material used for the roll cage is AISI 1018 with Young's Modulus 210 GPa; yield strength is 365.5 MPa and Poisson's ratio 0.29. The density of material is 8000 kg/m<sup>3</sup> with hardness (Brinell) of 126 HB [7].

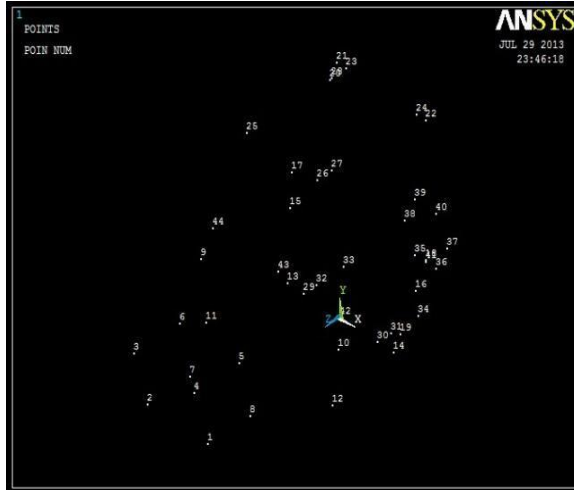


Figure 1. Modelling of keypoints

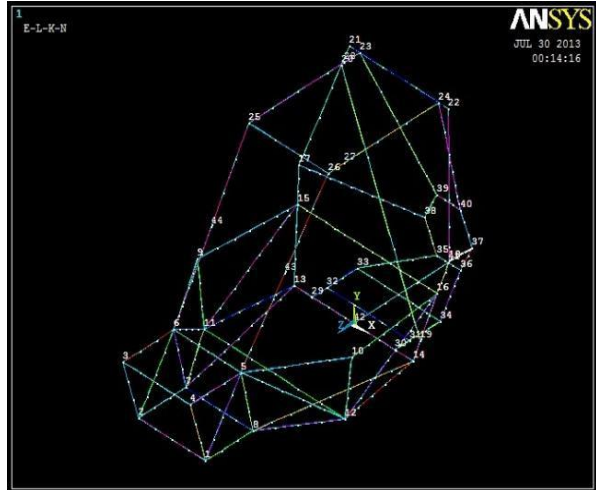


Figure 2. Modelling of lines

## II. Meshing And Analytical Calculations

### a) Meshing constraints and calculations

As the roll cage was developed by plotting keypoints, lines and splines, so every member of the roll cage is considered to be properly constrained at every joint. For boundary conditions for frontal impact test, the roll cage is to be fixed from the rear side and the front member will come across the applied load. In the similar way, for side impact test, one side of the roll cage elements are fixed while the other side will be applied with load. For rollover impact test, the lower elements of the roll cage are fixed. For bump impact test and torsional impact test, the roll cage is to be fixed from the rear side. The load will be distributed among the number of joints framed by front members in the opposite direction to the frame, i.e. in X axis.

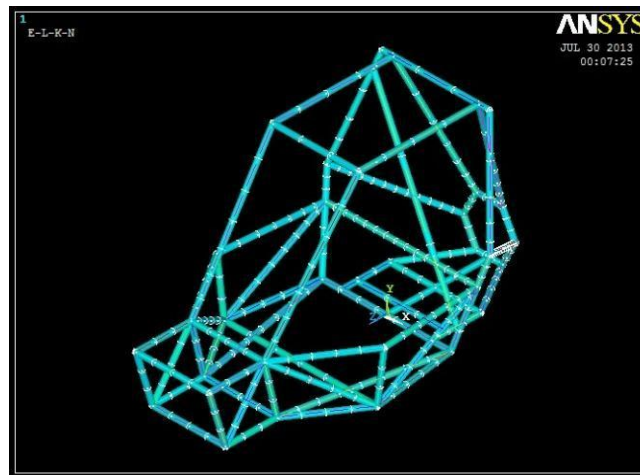


Figure 3. Meshed model with element shape

### b) Analytical calculation for determining impact on roll cage

To properly analyze the impact force, we need to find the deceleration of the vehicle after impact. To approximate the worst case scenario that the vehicle will undergo, momentum equations were used to determine the deceleration of the vehicle. The vehicle was considered to be at maximum speed of 60 km/hr having total weight of 400 kg and according to different scenarios the conditions of head on impacts, oblique collisions, and inelastic or partially elastic collisions were employed with a crash pulse consideration of 0.1s.

The forces which were impacted on the roll cage were decelerations of 4g & 3g and it is calculated as follows:-

Assume gravitational force =  $9.8 \text{ m/s}^2 \approx 10 \text{ m/s}^2$

$g = \text{mass of the vehicle} \times \text{gravitational force acting on the vehicle}$   
 $= 400 \times 10$   
 $= 4000 \text{ N}$

Therefore,  $4g = 16000 \text{ N}$  &  $3g = 12000 \text{ N}$ .

### III. Impact Analysis Using Ansys

#### a) Frontal Impact Analysis

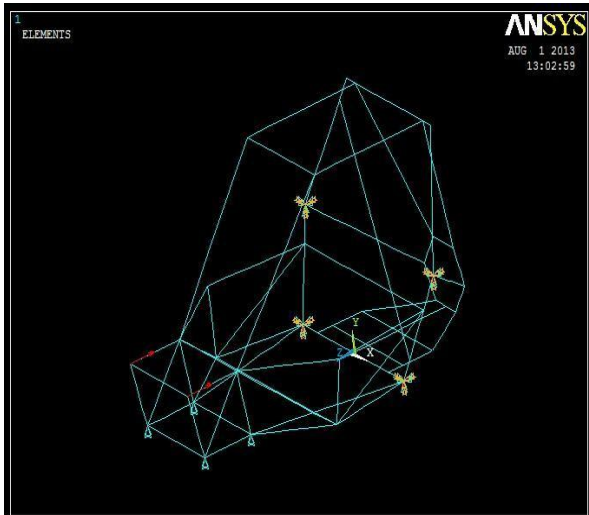


Figure 4. Frontal impact load application

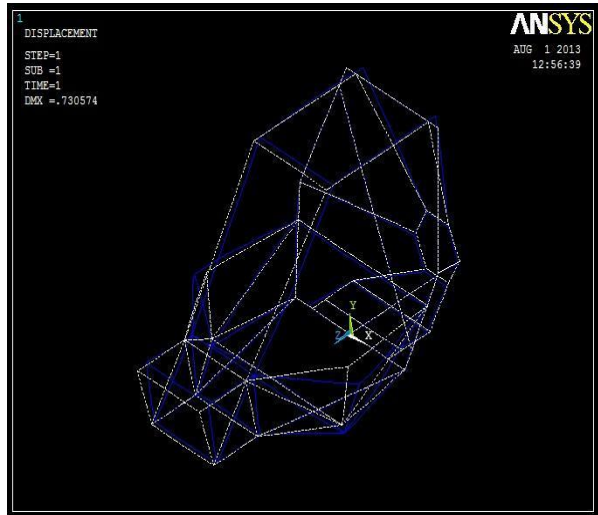


Figure 5. Deformation plot

It is the impact wherein there is a possibility of vehicle crashing into another vehicle head on during the race (Sharma and Purohit, 2012). The deceleration value for frontal impact is  $4g$ . This is equivalent to a loading force of  $16000 \text{ N}$ . The load is applied on two nodes at front as depicted by red arrows in (Fig. 4). Thus, the force gets divided into two parts i.e.  $8000 \text{ N}$  on each node. The value recorded for the deformed shape is  $0.73 \text{ mm}$  (Fig. 6) which abides by the safety regulations and standards of SAE BAJA competition. (Fig. 7) shows the Von Mises stress plot, where the maximum stress is observed at the front members ( $68.673 \text{ MPa}$ ) where the load is applied. The driver cabin members are shown in yellow and green colors which clearly depicts the safety of driver cabin even when loaded with such high force.

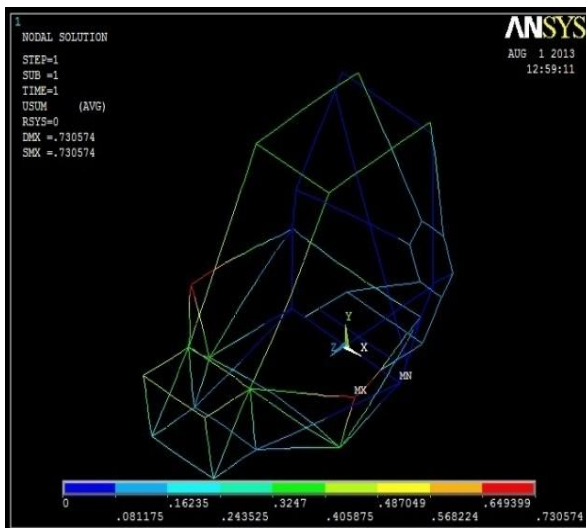


Figure 6. Nodal solution plot

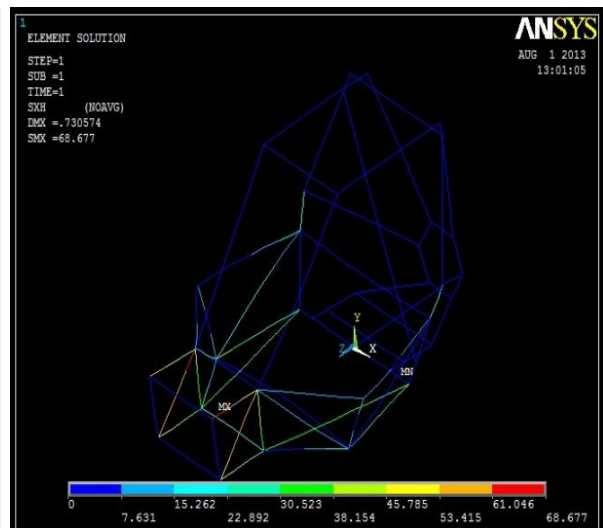


Figure 7. Von Mises stress plot.

b) Side Impact Analysis

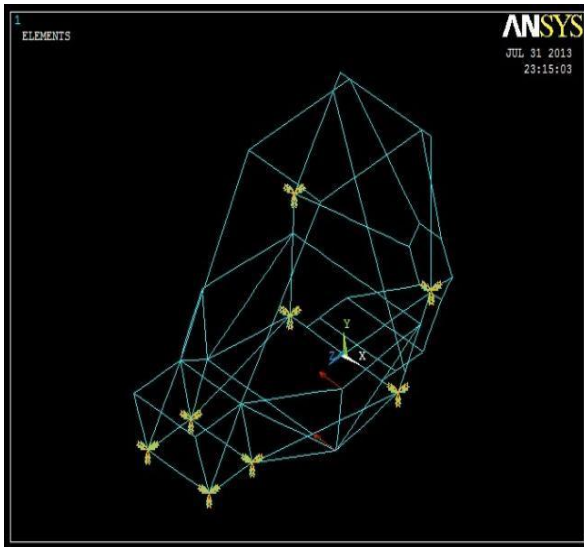


Figure 8. Side impact load application

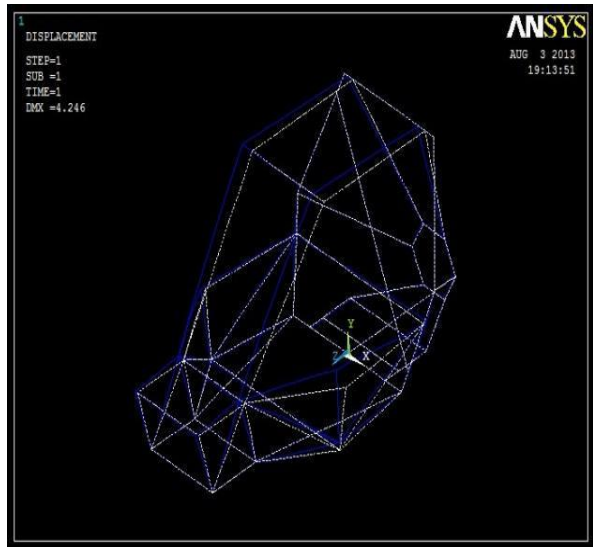


Figure 9. Deformation plot

The side impact analysis is carried out as there is a possibility of collision with another vehicle from either direction. Thus, the stresses acting on the side members of the roll cage are analyzed. The deceleration value for side impact is 4g. This is equivalent to a loading force of 16000 N. The load is applied on two nodes as shown in (Fig. 8). Thus, the force on each node is 8000N. The nodal solution shows a deformation of 4.246 mm in colored contour same as the deformation plot as depicted in (Fig. 10). The Von Mises stresses came out to be 99.453 MPa which is inside the permissible range of the material (Fig. 11). The driver cabin members are shown with green colours which reflect the safety of driver cabin even when such a high load is introduced.

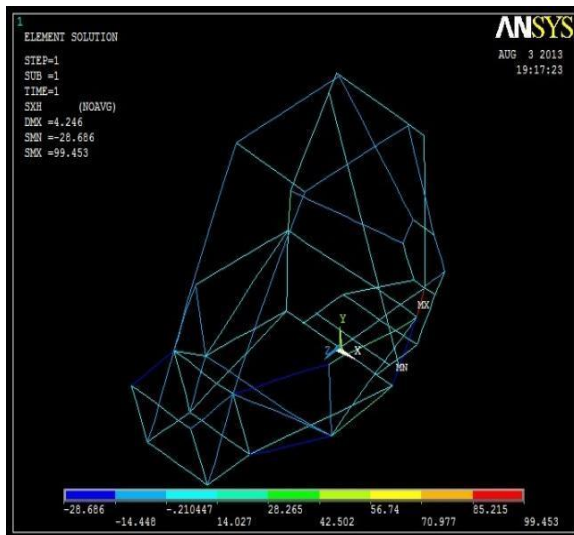


Figure 10. Nodal Displacement plot

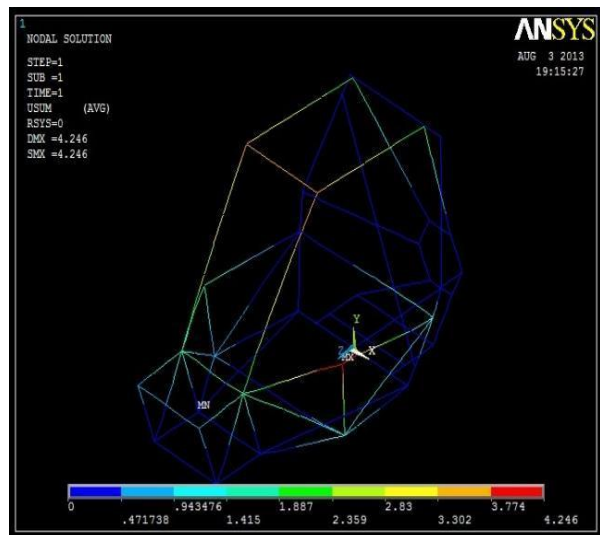


Figure 11. Von Mises stress plot

c) Rollover Impact Analysis

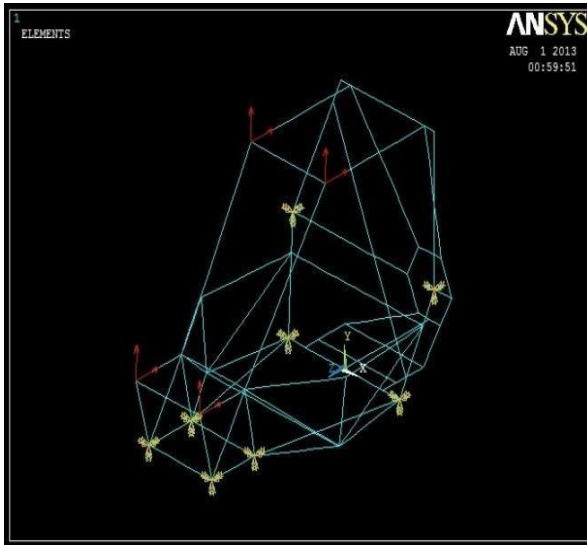


Figure 12. Rollover impact load application

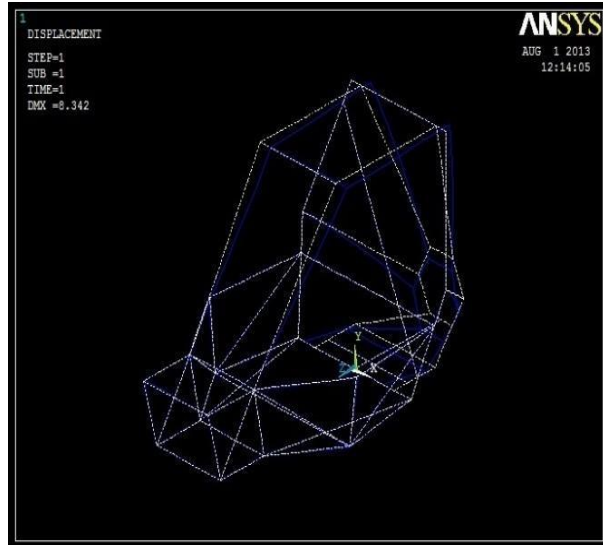


Figure 13. Deformation plot

The rollover impact analysis is carried out by considering the stresses induced on the members of the roll cage when the vehicle topples down from a slope with an angle of  $45^\circ$ . In this impact, the upper and rear members of the vehicle will bear the force. The deceleration value for rollover impact is 3g. This is equivalent to a loading force of 12000 N. The number of nodes on which the load is applied is 4 (Fig. 12). Thus 3000 N was applied on each node. The maximum deformation is 8.342 mm in the members of the vehicle as shown in (Fig. 14). The Von Mises stress induced on the members is shown in (Fig. 15). The maximum stress i.e. 139.69 MPa was observed at the upper members of the vehicle which is well below the permissible range.

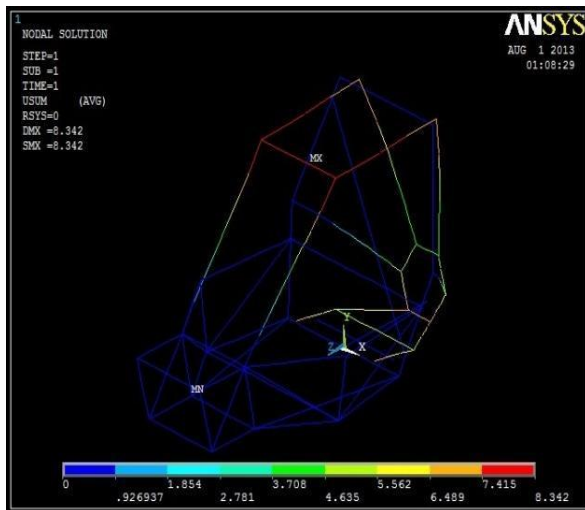


Figure 14. Nodal solution plot

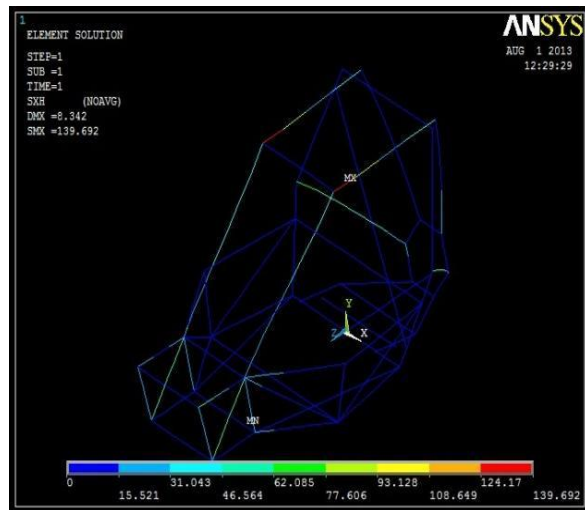


Figure 15. Von Mises stress plot

d) Two Wheel Bump Impact Analysis

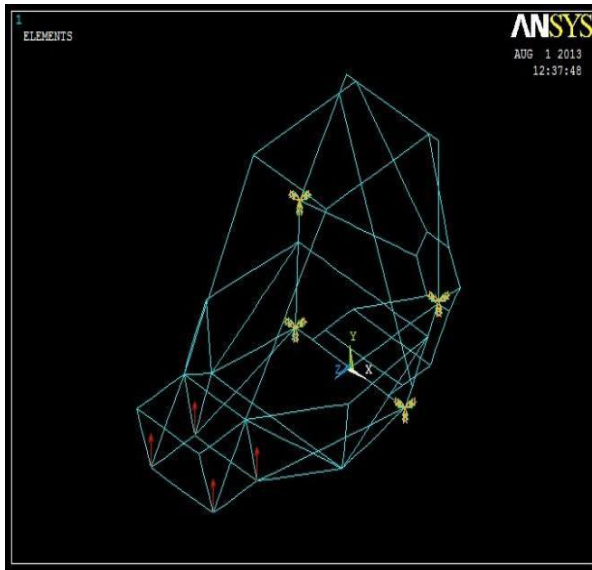


Figure 16. Bump impact load application

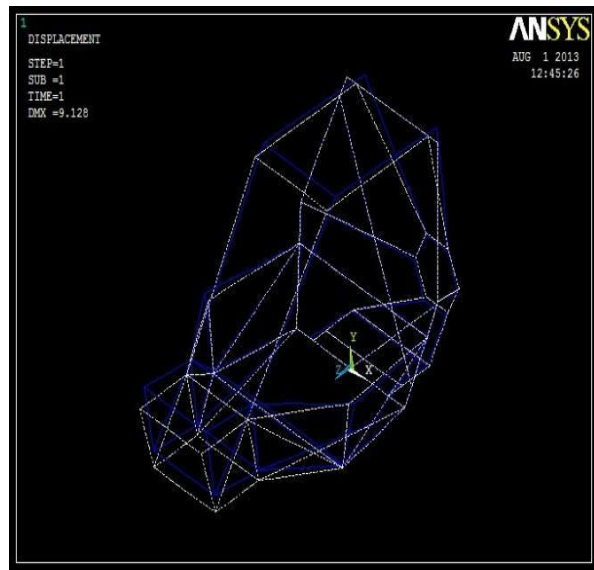


Figure 17. Deformation plot

During the SAE-BAJA competition, the vehicle has to travel on uneven tracks. There are times when the vehicle moving along an upward slope travels about a curved projectile in air before landing on its wheels. The lower frontal part of the vehicle is the initial member which faces this impact. Once the front tyres touch the surface, the suspension system absorbs the initial forces exerted on it. A time comes when the suspension system are compressed to its maximum extent and act like solid member of the vehicle. The rest of the load is transferred to the roll cage members of the vehicle [9]. In order to ensure the safety of the driver, we determine this impact force using ANSYS.

The deceleration value for bump analysis was taken as 3g i.e. 12000N. The force was applied on the frontal four suspension pick up points (Fig. 16). The load applied on each node was 3000 N. The deformation value is 9.128 mm which abides by the safety regulations and standards of SAE BAJA competition (Fig. 18). The Von Mises stress is plotted in (Fig. 19) showing the individual stresses in the members. The maximum stress as observed was found out to be 190.79 MPa which is within the permissible limit of the materials yield strength.

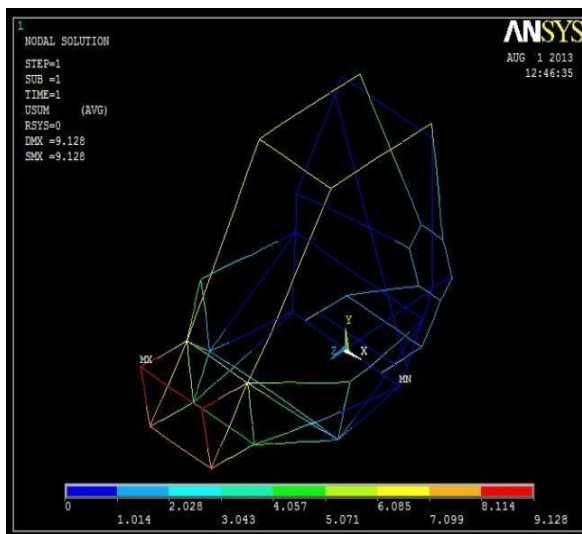


Figure 18. Nodal solution plot

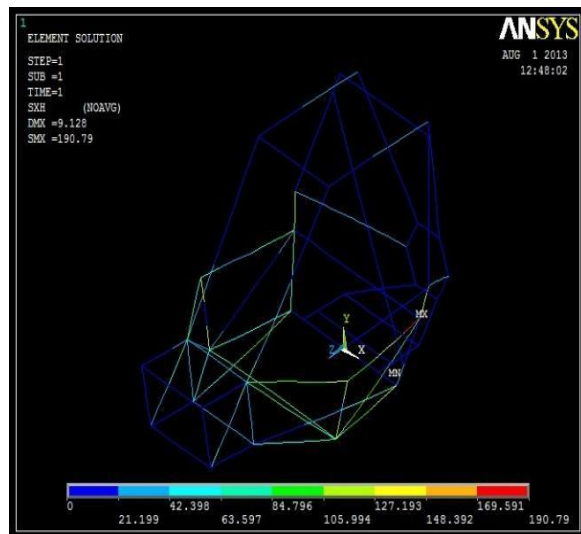


Figure 19. Von Mises stress plot

e) Front Torsional Impact Analysis

This impact is analyzed taking into consideration the torsional forces acting on the frontal elements of the vehicle. This type of force is exerted on the vehicle when it traverses on an uneven road. The two tyres on the front axle experience a moment. The torque is applied to one tyre and reacted by the other one (Fig. 20). These forces are equal and opposite. The deceleration value for this impact is 3g i.e. 12000 N. But as these act in opposite direction, the number of nodes for application of force is 2. The amount of force per node is 6000 N.

The deformed value after analysis is 9.476 mm as shown in (Fig. 22). The maximum Von Mises stress in this analysis came out to be 90.117 MPa which lies within the permissible range of the material (Fig. 23).

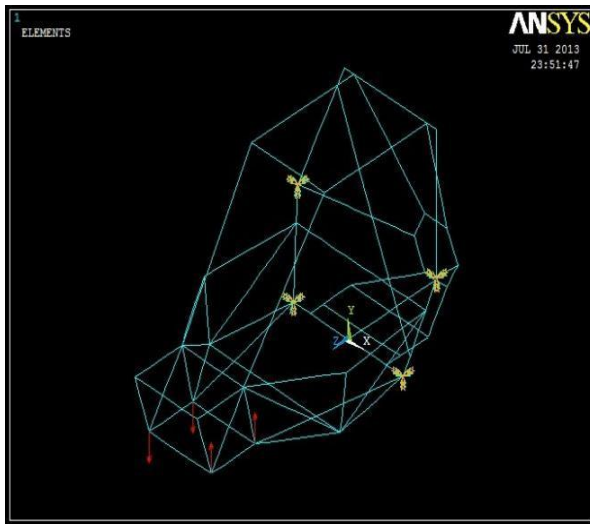


Figure 20. Torsional impact load

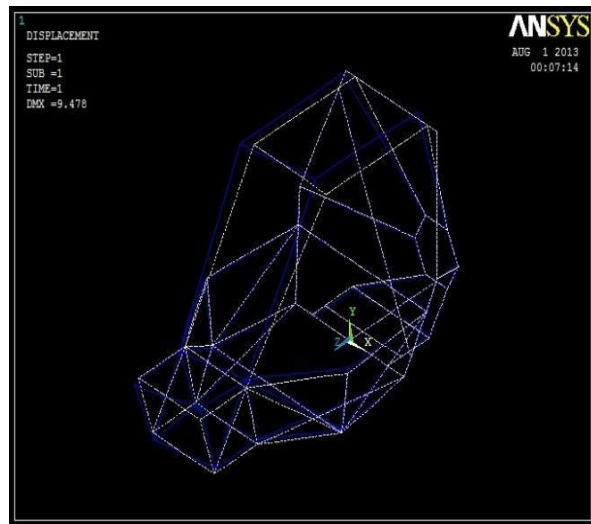


Figure 21. Deformation plot application

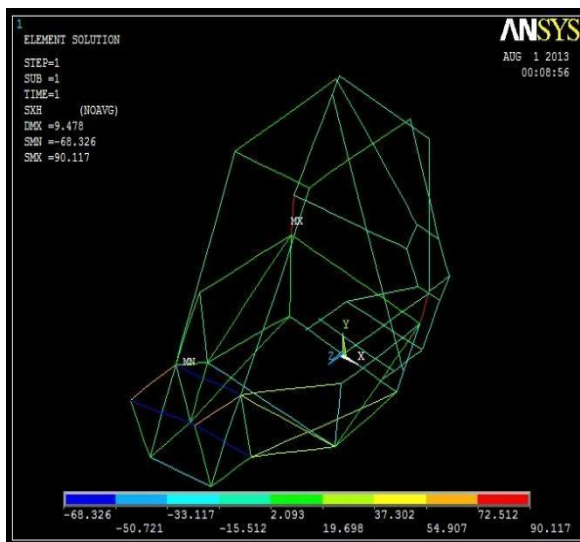


Figure 22. Nodal solution plot

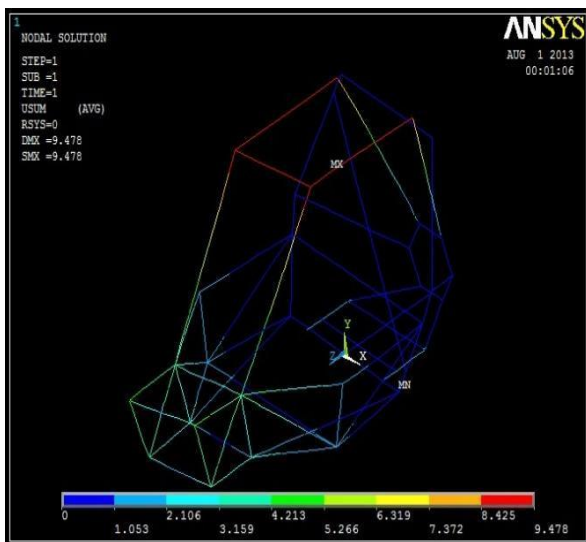


Figure 23. Von Mises stress plot

IV. Results And Discussion

Stress plots and deformations of critical elements undergoing different loads during the impact tests were analyzed using ANSYS. This project helps us to understand the vital components of designing. As mentioned above the yield strength of the material which we are using is 365.5 MPa. The maximum stress values of various impact tests have been determined and we can easily find the factor of safety of the vehicle. Safety is of utmost concern in every respect; for the driver, crew & environment. Considerable factor of safety

(FOS) or design factors is applied to the roll cage design to minimize the risk of failure & possible resulting injury. This FOS value implies the safe value of applied loads and deformations. The following table shows the various loading conditions, deformations, maximum stress values and factor of safety for various test conditions.

*Table 1. Analysis results of impact tests.*

Factor of Safety (FOS)	Von Mises stress (MPa)	Maximum Deformation (mm)	Number of Nodes	Loading force (N)	Type of impact test
5.322	68.673	0.73	2	16,000	Front
3.675	99.453	4.246	2	16,000	Side
2.616	139.69	8.342	4	12,000	Roll-over
1.915	190.79	9.128	4	12,000	Bump
4.157	90.117	9.476	2	12,000	Torsional

## V. Conclusion

The use of finite element analysis was invaluable to the design and analysis of the frame for SAE-BAJA off-road vehicle. The analysis was helpful in finding out the maximum deformation, Von Mises stress and the factor of safety for five different impact tests namely frontal impact, side impact, rollover impact, bump impact and torsional impact. The findings from the finite element analysis and the actual failure will allow future designers to integrate a solution to this problem into their design from the beginning.

## REFERENCES

- [1]. BAJA SAE INDIA Rulebook. 2013. <http://www.bajasaecindia.org/downloads.html>.
- [2]. Milliken, D., Kasprak, E., Metz, L. and Milliken W. (2003). *Race Car Vehicle Dynamics: Problems, Answers and Experiments*. Society of Automotive Engineers, Inc.
- [3]. Gillespie, T., (2001). *Fundamentals of Vehicle Dynamics*, Society of Automotive Engineers, Inc.
- [4]. Fenton, J., (1996). *Handbook of Vehicle Design Analysis*, Society of Automotive Engineers, Inc.
- [5]. Erjavec, J., (2009). *Automotive Technology: A Systems Approach*. Delmar Cengage Learning.
- [6]. Huang, M., (2002). *Vehicle crash mechanics*. CRC press.
- [7]. Dave, H.K., Desai, K.P. and Raval, H.K. 2008. Investigations on prediction of MRR and surface roughness on electro-discharge machine using regression analysis and artificial neural network programming. Proceedings of the World Congress on Engineering and Computer Science, pp. 123-128.
- [8]. Ezugwu, E.O. 2007. Improvements in the machining of aero-engine alloys using self-propelled rotary tooling technique. Journal of Materials Processing Technology, 185: 60-71.
- [9]. Hascalik, A., Caydas, U. and Gurun, H. 2007. Effect of traverse speed on abrasive waterjet machining of Ti-6Al-4V alloy. Materials and Design, 28: 1953-1957.
- [10]. Kansal, H.K., Singh, S. and Kumar, P. 2005. Parametric optimization of powder mixed electrical discharge machining by response surface methodology. Journal of Materials Processing Technology, 169: 427-436.
- [11]. Sharma, V. and Purohit, D. 2012. Simulation of an Off-road Vehicle Roll Cage: A Static Analysis. International Journal of Engineering Research and Applications, 4(2): 126-128.
- [12]. Kao, J.Y. and Tarn, Y.S. 1997. A neural-network approach for the on-line monitoring of the electrical discharge machining process. Journal of Materials Processing Technology, 69: 112-119.
- [13]. Khan, M.A.R., Rahman, M.M., Kadirgama, K. and Bakar, R.A. 2012. Artificial neural network model for material removal rate of Ti-15-3 in electrical discharge machining. Energy Education Science and Technology Part A: Energy Science and Research, 29(2): 1025-1038.
- [14]. Rahman, M., Wong, Y.S. and Zareena, A.R. 2003. Machinability of titanium alloys. JSME International Journal Series C: Mechanical Systems, Machine Elements and Manufacturing, 46: 107-115.
- [15]. Rahman, M.M., Khan, M.A.R., Kadirgama, K., Maleque, M.A. and Bakar, R.A. 2011a. Parametric optimization in EDM of Ti-6Al-4V using copper tungsten electrode and positive polarity: A statistical approach. Mathematical Methods and Techniques in Engineering and Environmental Science, pp. 23-29.
- [16]. Rahman, M.M., Khan, M.A.R., Kadirgama, K., Noor, M.M. and Bakar, R.A. 2011b. Optimization of machining parameters on tool wear rate of Ti-6Al-4V through EDM using copper tungsten electrode: A statistical approach. Advanced Materials Research, 152-153: 1595-1602.
- [17]. Razak, N.H., Rahman, M.M. and Kadirgama, K. 2012. Investigation of machined surface in end-milling operation of Hastelloy C-2000 using coated-carbide insert. Advanced Science Letters, 13: 300-305
- [18]. Wu, C.F.J. 2002. Experiments planning, analysis and parameter design optimization. 2nd ed. New York: John Wiley.

## Tensile and Impact Properties of Natural Fiber Hybrid Composite Materials

Sathish. S<sup>1</sup>, Kumaresan. M<sup>2</sup>, Karthi. N<sup>3</sup>, Dhillip kumar. T<sup>4</sup>

<sup>1,2,3&4</sup>Department of Mechanical Engineering, Sri Krishna College of Engineering and Technology, Tamilnadu, Coimbatore-641008, India

**Abstract:** This paper is a review on the tensile and impact properties of natural fiber hybrid composites. Natural fibers are having good mechanical properties, high specific strength, low cost, bio-degradable and easily can recyclable through thermal methods. In this paper two different hybrid composites were manufactured by compression molding and properties of tensile and impact results are conducted as per ASTM standards. In this project three different fibers such as sisal, jute and glass with thermosets epoxy resin used with weight ratio of fiber to resin as 15:15:70. Results showed that sisal/glass hybrid composite has more tensile and impact strength while comparing to sisal/jute hybrid composite.

**Keywords:** Tensile, Impact, Sisal, Jute, Glass and Epoxy

### I. INTRODUCTION

Increasing environmental concerns and depletion of petroleum resources calls for new green ecofriendly materials. Among various natural polymers, cellulosic natural fibers are envisioned as the most suitable ways to solve these problems especially environment related issues. The potential of cellulosic fibers as reinforcement in composite materials have been well recognized since many centuries ago. The term 'composite' has been used in material science refers to a material made up of a matrix containing reinforcing agents. The beginning of composite materials may have been the bricks, fashioned by the ancient Egyptians from mud and straw. Nearly 70 years ago, a number of technical products and other commodity materials were derived from natural resources e.g., textile ropes, canvas and paper were made of local natural fibers such as flax and hemp. Emergence of polymers in the beginning of the nineteenth century inculcated the new era of research based on exploring the viability of natural fibers and their applications in more diversified fields. At the same time, interest in synthetic fibers due to its superior dimensional properties, gained attention and slowly replaced the natural fibers in major avenues. With the passage of time, the accumulation of the hazardous synthetic byproducts and waste, started polluting the environment and once again led the scientists towards natural fibers due to their distinct advantages. Thus, the renewed interest in the natural fibers resulted in a large number of modifications in order to bring it equivalent and even superior to synthetic fibers. After tremendous changes in the quality of natural fibers, they emerged as a substitute for the traditional building materials including lumber steel, Portland cement and lime. Considering the high performance standard of composite materials in terms of durability, maintenance and cost effectiveness, applications of natural fiber reinforced composites as construction material, have done wonders and are environment friendly material for the future.

### II. REASON OF NATURAL FIBER REINFORCED COMPOSITES

Many shortcomings due to high density and poor recycling properties were seen in glass fiber reinforced plastics. Moreover, glass fiber dust produced during processing triggers allergic skin irritation. The possible substitution of glass fiber by natural fiber in exterior application raised the question about mechanical properties of the material, flammability and effect of weathering. Natural fibers offer several advantages over glass fibers:

- Plant fibers are renewable and their availability is unlimited.
- When natural fiber reinforced plastics are subjected to combustion or landfill at the end of their life cycle, the released amount of carbon dioxide is less with respect to that assimilated during its life cycle.
- Natural fibers are less abrasive and can be easily processed as compared to glass fiber.
- Natural fiber reinforced plastic, consisting of biodegradable polymer matrix are environment friendly and can be composted easily.

### III. EXPERIMENTAL METHODOLOGY

#### 1. Selection of Materials

In this project we have used the glass as synthetic fiber and sisal and jute are as natural fiber reinforced plastics. The hybrid composites are used to find out the tensile and impact properties. The sisal/jute and sisal/glass reinforced epoxy are thus used as hybrid composites. The purpose of using E-glass fiber with sisal fiber is to improve the mechanical properties of natural fiber.

#### 2. Chemical Treatment

The sisal and jute fibers are immersed in distilled water for 24 hrs separately and then dried in direct sun light. After that it is immersed in NaOH solution for 24 hrs and then it is dried. After that it was kept in hot air oven for 6 hrs for remove air bubbles. The sodium hydroxide alkali treatment effectively used for improves the adhesive bond between fiber and matrix.

#### 3. Manufacturing Method

There are various methods to fabricate the composites. They are hand lay-up process, pultrusion process, filament winding process, resin transfer molding, sheet molding compound, reaction injection molding. Here we use the compression molding process for the fabrication of hybrid composites.

##### 3.1 Compression Molding Method

- With the dies apart, the prepared polymer 'dough' is placed into the cavity.
- With the die closed, the article is formed and the small amount of flashing on each side will be removed later.
- When the die is closed, heat and pressure are maintained until the condensation polymerization process is completed.
- The hot compression molding process is used to form components from phenolic, urea and melamine thermosetting polymers, as well as alkyl resins.

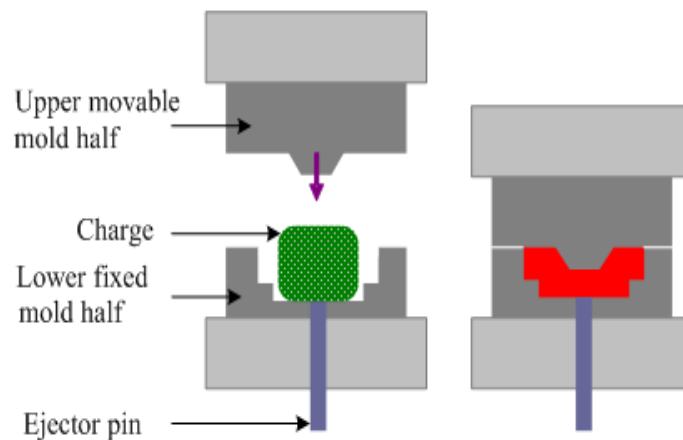


Fig 1. Compression Molding

### IV. EXPERIMENTAL TEST

The hybrid composite materials sisal-glass-epoxy and sisal-jute-epoxy are to be tested for their mechanical properties. Tensile test and Impact test are can be done on the samples produced from composites. Here, the samples cut to ASTM standards from the manufactured composites are tested to find out the values of tensile strength and impact strength. The tensile test for two sample pieces are performed by the universal testing machine Instron 1195 and impact test are performed using Izod impact testing machine.

#### 1. Universal Testing Machine

The tensile strength of a material is the maximum amount of tensile stress that it can take before failure. During the test a uni-axial load is applied through both the ends of the sample. The dimension of the sample is (250x25x3) mm. The tensile test is performed in the universal testing machine (UTM) Instron 1195 and results are analyzed to calculate the tensile strength of composite samples.

## 2. Izod Impact Testing Machine

The impact test is for the purpose of knowing the material's ability to resist the impact load and the service life of the material. The impact test designed to give information on how a sample of a known material will respond to a suddenly applied stress, e.g. shock. A method for determining behavior of material subjected to shock loading in bending, tension, or torsion. The Izod test is most commonly used to evaluate the relative toughness or impact toughness of materials and as such is often used in quality control applications where it is a fast and economical test. It is used more as a comparative test rather than a definitive test.

## V. RESULTS AND DISCUSSION

The samples of two different combinations tested for their tensile and impact strength showed better result with sisal/glass has lead in both tests.

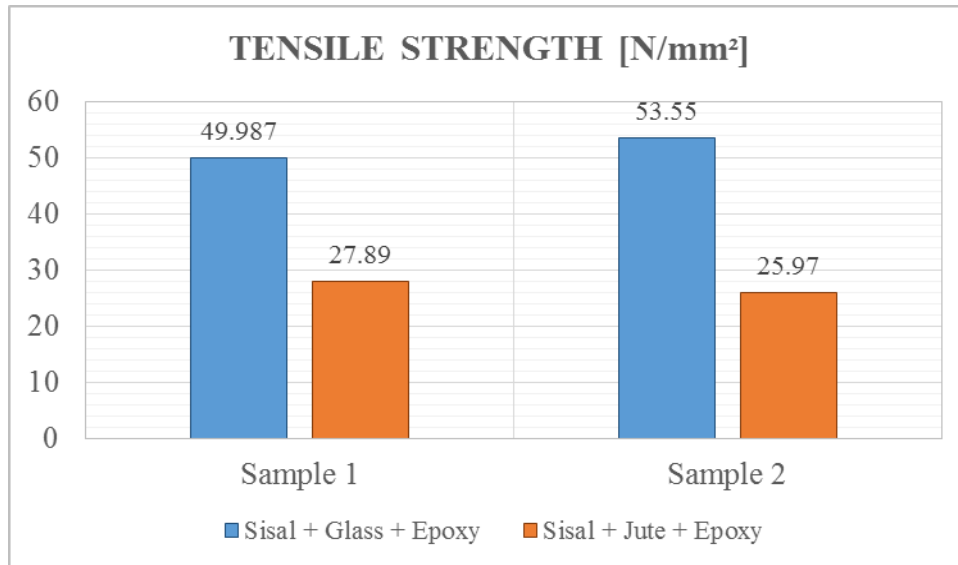


Fig 2. Result of Tensile Strength

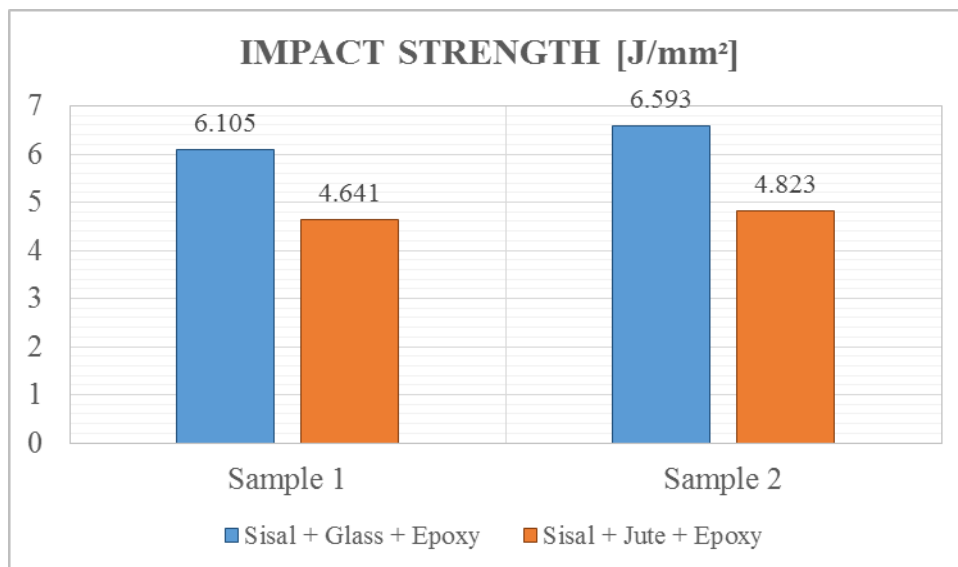


Fig 3. Result of Impact Strength

- For sisal/jute combination tensile strength of two samples are 27.89 N/mm<sup>2</sup> and 25.97 N/mm<sup>2</sup>.
- For sisal/glass combination tensile strength of two samples are 49.98 N/mm<sup>2</sup> and 53.55 N/mm<sup>2</sup>.
- For sisal/jute combination impact strength of two samples are 4.641 J/mm<sup>2</sup> and 4.823 J/mm<sup>2</sup>.
- For sisal/glass combination impact strength of two samples are 6.105 J/mm<sup>2</sup> and 6.593 J/mm<sup>2</sup>.

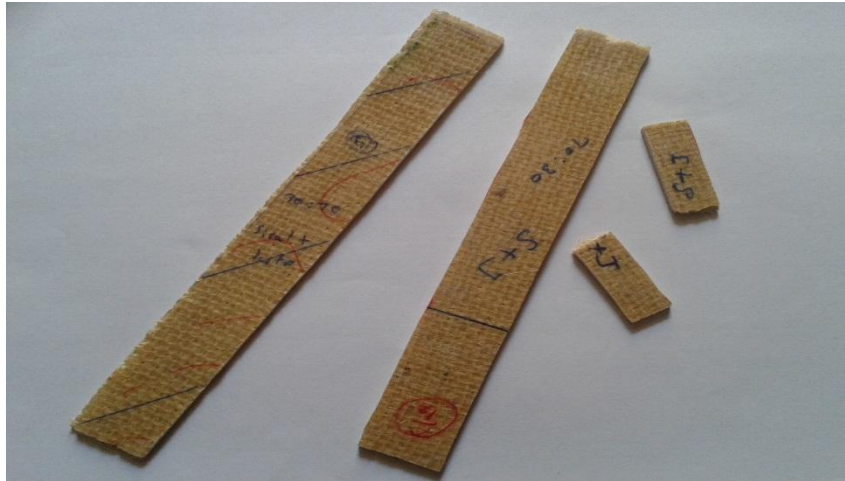


Fig 4. Sample after Tensile and Impact Test

## VI. CONCLUSION

- Treatment of sisal and jute with NaOH resulted in increase an adhesive strength and tensile strength.
- Tensile and impact properties were studied for two different hybrid composites such as sisal/glass and sisal/jute.
- Sisal/glass shows great tensile and impact strength with comparing to sisal/jute hybrid composite.
- Because naturally glass fiber has good specific strength and high elongation but it cannot recycle throughout.
- Sisal/jute hybrid composite can be easily recyclable and biodegradable. So it can be apply for similar applications.

## REFERENCES

- [1] Ku, H., Wang, H., Pattarachaiyakoop, N., Trada, M: A review on the tensile properties of natural fibre reinforced polymer composites, *Composites: Part B* (2011).
- [2] Robert M. Jones: *Mechanics of Composite Materials*, 2nd edition (1999).
- [3] A. N. Shah and S. C. Lakkad: *Mechanical Properties of Jute-Reinforced Plastics*, *Fibre Science and Technology*, 15 (1981) 41-46
- [4] D. Ray, B.K. Sarkara, A.K. Rana, N.R. Bose: The mechanical properties of vinyl ester resin matrix composites reinforced with alkali-treated jute fibres, *Composites: Part A* 32 (2001) 119-127
- [5] Hassan M.L., Rowell R.M., Fadl N.A., Yacoub S.F. and Chrisainsen A.W: Thermo plasticization of Bagasse. II. Dimensional Stability and Mechanical Properties of Esterified Bagasse Composite, *Journal of applied polymer science*, Volume 76, (2000): p. 575-586.
- [6] Murali Mohan Rao.K, Mohana Rao.K, Ratna Prasad. A.V: Fabrication and testing of natural fibre composites: Vakka, sisal, bamboo and banana, *Materials and Design* Vol.31, pp.508-513, 2010.
- [7] Girisha.C, Sanjeevamurthy, Gunti Rangasrinivas: Tensile Properties of Natural Fiber Reinforced PLA-Hybrid Composites, *International Journal of Modern Engineering Research*, Vol.2, pp-471-474, 2012.
- [8] K. John, S. Venkata Naidu: Chemical resistance studies of sisal/glass fiber hybrid composites, *Journal of Reinforced Plastic Composites*. 26(4) (2007) 373-376.
- [9] Jarukumjorn K, Supakarn Nitinnat: Effect of glass fiber hybridization on properties of sisal fiber-polypropylene composites, *Composites: Part B* 40(7) (2009) 623-7.
- [10] V.Nagaprasad Naidu, M.Ashok kumar, G.Ramachndrareddy, M.Mohan reddy: Tensile & flexural properties of sisal/glass fiber reinforced hybrid composites, *International Journal of Macromolecular Science* 1(1) (2011):19-22, ISSN-2249-8559.

## Automotive Applications of Welding Technology – A Study

Devarasiddappa. D

Department of Automobile Engineering, Rajiv Gandhi Govt. Polytechnic, Itanagar, Arunachal Pradesh, India

**Abstract:** Welding is invariably used in the automotive industries for joining variety of structural components and engine parts. The constant demand for new improved material requirement for automotive applications necessitates the development of innovative joining techniques. In this paper, the welding techniques commonly adapted in the automotive industries are discussed. Illustrative diagrams and specific automotive applications are included in the paper. The novel technique of joining dissimilar metals viz., magnetic pulse welding is also discussed. The latest update on medium frequency welding method used by auto manufacturers is also presented with its technical and operational merits.

**Keywords:** Automotive applications, Magnetic pulse welding, Medium frequency welding, Welding

### I. INTRODUCTION

Basically, welding is used to obtain permanent joint of two metals through localized application of suitable combination of temperature, pressure and metallurgical conditions. A wide variety of welding processes have been developed by different combinations of temperature and pressure. Welding is the principal means of fabricating and repairing of metal products and is used in every industry [1]. Amongst the major areas of applications, welding is extensively used in automotive industries. The most commonly used welding methods for automotive applications include resistance spot welding (RSW), resistance seam welding (RSEW), metal inert gas (MIG) welding, tungsten inert gas (TIG) welding, laser beam welding (LBW), friction welding (FW) and plasma arc welding (PAW). The advanced welding processes for automotive applications have been developed envisaging reduction in vehicle weight and increase in fuel efficiency [2]. In conventional welding methods, an additional material is always added to the weld joint that flows into the materials to be joined to produce an extremely strong bond. The added metal at each weld increases the vehicle weight which in turn decreases fuel economy. In this paper, welding techniques used in automotive applications viz., RSW, RSEM, FW, LBW are discussed. The advanced technique viz., magnetic pulse welding (MPW) process used to produce lighter weld components is also presented. The latest welding technology i.e. medium frequency welding (MFW) used in the automotive industries is also discussed in this paper.

### II. AUTOMOTIVE APPLICATIONS OF WELDING

A wide variety of automobile body components are joined together using welding techniques. The necessity for development of new welding techniques for automotive applications is ever growing to meet the new material combinations for auto body parts. The requirement for innovative welding processes is felt strongly in the recent days with automotive manufactures focusing on lighter yet strong and fuel efficient vehicles employing light weight alternative materials. The most commonly used welding techniques in automotives applications are explained in the following sections.

#### 2.1 Resistance spot welding

The conventional steel body of a car, on an average, contains 4500 spot weld joints. Resistance spot welding is the principle joining method used in automotive industries and has been for many years. In this method the joint is produced by the heat generated due to the resistance of work pieces to the flow of current and application of pressure [3]. The weld is limited to the spots on overlapped work pieces and hence not continuous. The pointed copper electrodes conduct the welding current to the work spot and also serve to apply pressure to form the strong joint as shown in the Fig. 1.

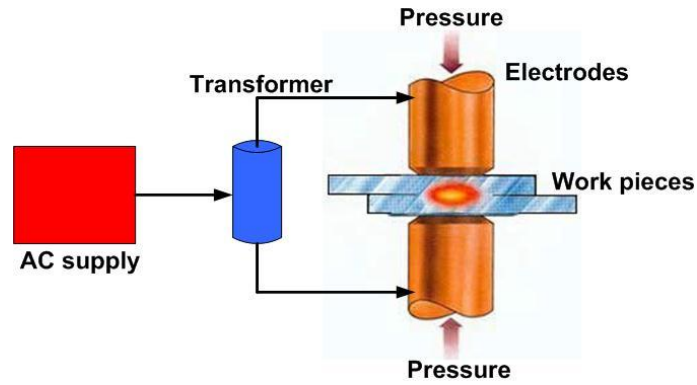


Fig. 1 Resistance spot welding

RSW is automated and used in the form of robotic spot welding in automotive industries to weld the sheet metals to form car body. Industrial robots spot welding the car body in production line is shown in the photograph given in Fig. 2.



Fig. 2 Industrial robots welding car body  
(Source: Rexroth- Bosh group) [4]

### 2.2 Resistance seam welding

In this type of resistance welding, the joint is produced progressively along the length of the weld. This gives a continuous and leak tight joint in sheet metals. The weld may be made with overlapping or continuous work pieces. In automobile industries, this welding process is used to produce leak proof fuel tanks. The principle of RSEW is depicted in the Fig. 3. This process provides high welding speeds, but its applicability is limited by component shape and wheel access. A seam welding process in operation is shown in Fig. 4.

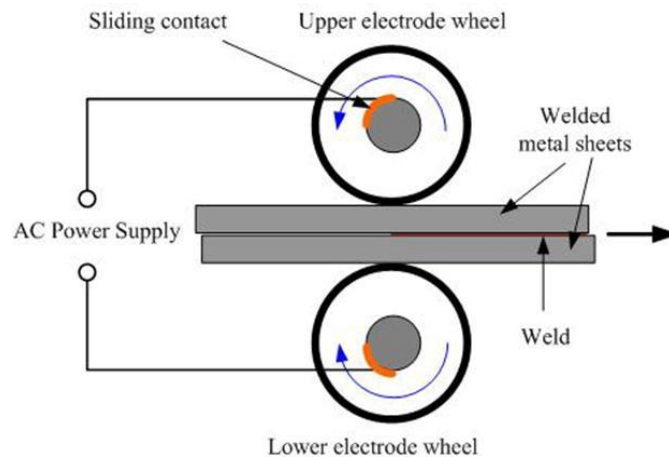


Fig. 3 Principle of resistance seam welding



Fig. 4 RSEW producing continuous joint

### 2.3 Friction welding

In solid state welding the joint is produced by the application of pressure without significant melting any of the work parts. Friction welding is a form of solid state welding where the heat is obtained from the mechanically induced sliding motion between the parts to be welded [5]. The weld parts are held together under pressure. Generally, the frictional heat is generated by rotating one part against the other. When certain temperature is reached, the rotational motion is seized and the pressure applied welds the parts together. The two shafts joined by FW process is depicted in Fig. 5. This welding process can be controlled by regulating the time, rotational speed and pressure.

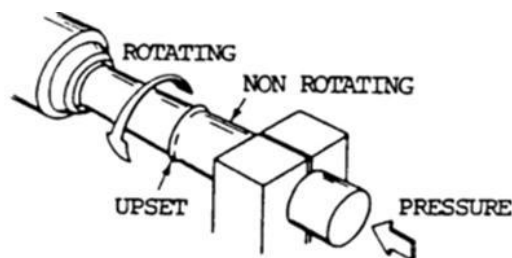


Fig. 5 Shafts joined by friction welding process

The metallic materials possessing certain degrees of plasticity at high temperature and thermal stability can easily be friction welded. Although all common engineering alloys can be friction welded, cast iron is an exception. In automotive industries, the FW is used to fabricate a wide range of components including half shafts, axle cases, steering columns, hydraulic cylinders, pistons rods and engine valves etc. The Fig. 6 shows few friction welded automotive components.



Fig. 6 Friction welded automotive components  
(Engine valves and tie rod)

## 2.4 Laser beam welding

The application of laser technology for welding the high volume automotive components has gained popularity because of its distinct advantages. The main benefits include good flexibility, improved productivity with substantial saving on maintenance and energy cost while producing a strong weld. The LBW process uses the heat generated when a focused laser beam impinges on the joint. Metal sheets having thickness in the range 0.2 to 6mm can easily be laser welded. Majority of the automotive industries employ cross flow CO<sub>2</sub> laser system in the power range of 3 to 5 kW [6]. The schematic arrangement of components of a typical laser welding system is depicted in the Fig. 7.

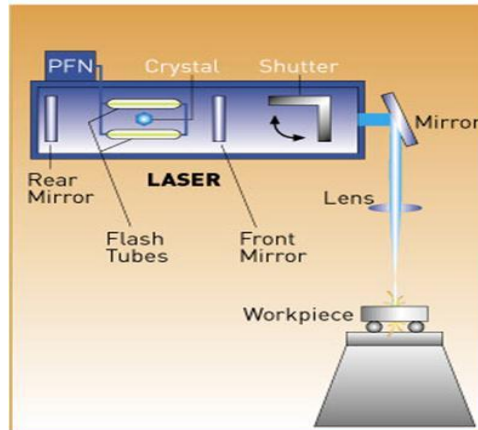


Fig. 7 Diagram of laser beam welding (Source: Oguzhan Yılmaz )

The laser beam directed on the workstation is focused on the parts to be welded using the copper mirrors. It is a non contact process and well suited for automated applications. The process parameters such as laser power, speed and focused spot size determine the weld depth and width. A beam from one laser source can easily be switched to several workstations allowing optimum utilization of laser for different welding functions. This inherent flexibility of LBW satisfies high volume automotive production requirement for different part geometries without extensive set up. The Fig. 8 shows welding of low carbon steel sheet using CO<sub>2</sub> laser system.



Fig. 8 Laser beam welding of low carbon steel sheet

Joining automatic transmission components found particularly suited for LBW. The components produced from powder metallurgy (PM) process are increasingly used in the automotives. The performance of PM components is characterized by combination of finished density, composition of alloying elements and part microstructure. These factors provide greater flexibility to determine weldability of PM components. The density is reported to have pronounced influence on performance and weldability [7]. The other automotive applications LBW include welding of roof to the side panels of car body structure. A continuous water tight joint with better accuracy can be obtained as less material is displaced. Also, post treatment of the weld is not necessary [8]. The evaluation of laser beam process for joining hinges to the reinforcement structure of car door is presented by Quintino et al., [9, 10]. The CO<sub>2</sub> laser equipment giving output power of 6 kW was used

in the evaluation. The surface finish of the parts affected porosity formation with LBW, hence improved surface finish can overcome this problem.

### 2.5 Medium frequency welding

The medium frequency welding is a type of resistance welding and latest offering from Bosch-Rexroth Ltd, Great Britain. The Fig. 9 depicts the basic working principle of MFW. In this welding process, the three-phase 50 Hz alternating current (AC) is rectified and supplied to an inverter. The inverter converts the current to a frequency of 1000 Hz (medium frequency) and is fed to a transformer, usually integrated into the welding gun [4]. Hence the welding current available is always direct current (DC). The technical and operational merits of MFW are listed in the Table 1.

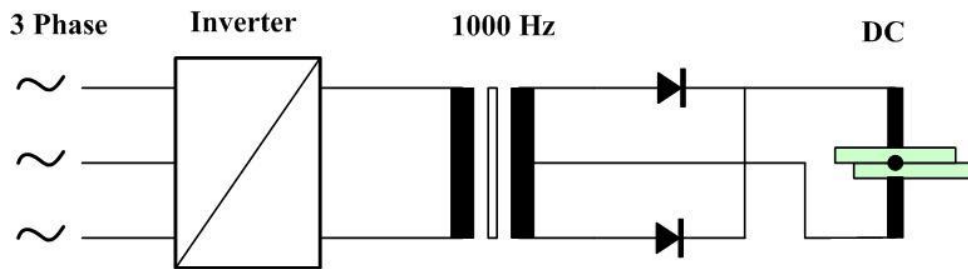


Fig. 9 Working principle of MFW

Table 2 Technical and operational advantages of MFW

Sl. No.	Merit	Description
1	Reduced bill	It is less demanding on electrical distribution network since it draws current from all the three phases. This in turn results reduced electricity charges.
2	More tolerant	The welding current is supplied thorough an inverter and hence the process is more tolerant of mains disturbances.
3	Higher operating efficiency	As much as 25 % power savings can be achieved against single phase AC system. The transformers used are more compact and lighter. Most suitable for robotic applications. Hence robots can be made smaller and less power is expended in moving welding gun.
4	Faster welding	Due to reduced or no current fluctuations weld times are approximately 15 % shorter and can be controlled to millisecond. This gives 20 times more accuracy than 50 Hz AC supply. Since there is no resistance in the welding arm, the arm lengths and tip characteristics do not affect weld times. The enhanced tip life results in considerable savings on tip dressing and consumables.
5	Cleaner weld	It gives high quality weld with peak voltage is almost same as RMS voltage. No splash or sparks are present in the weld.
6	More material choices	The process is controllable to high accuracy. Difficult to weld materials such as high strength steel, aluminium, laminated steels, polymer composites, coated steels etc can be welded easily.

### 2.6 Magnetic pulse welding

The demand for lighter and fuel efficient vehicles has increased in the recent days. The automotive manufactures strive to produce lighter components. This helps to make existing cars more fuel efficient and meet the requirement of alternative fuel powered vehicles viz. fuel-cell powered cars and hybrid gas/electric vehicles. The use of lighter material like aluminum and development of new manufacturing processes using less steel in weld can help to achieve the above goal. The additional material deposited on weld joint as in conventional welding process increases the weight of the welded component. The MPW is a novel technology developed by Dana Corporation, USA for bonding aluminium and steel (dissimilar metals) without using additional metal at the weld joint [2]. In this method, the pre-shaped aluminum and steel tubular stock are subjected to high pressure using precision machined die cavities. This process is called hydro-forming and results in more precise fitting of structural components requiring very little fill material in the subsequent welding steps.

The hydro-formed components are then fitted together loosely. A rapidly switching magnetic field produced by an inductor (either internally or externally) causes one of the metallic components to form quickly and impact the other stationary metal part with sufficient velocity and force to create a weld. This requires high end machines to produce proper welds in complex geometric designs. The MPW process enhances manufacturing productivity due to reduction in production steps, materials, equipments and personnel expenses. The vehicle frame welded with MPW process is reported to be two-thirds lighter resulting in 8-10% improvement in fuel efficiency. This further reduces air pollution. The reduced energy consumption and shielded gases further aid to decrease air pollution. The MPW process is more efficiently used to produce automobile parts such as frames, side rails, cradles, stampings, space frames, and bumper reinforcements (Fig. 10).



Fig. 10 Automobile components (frames) produced by MPW process  
(Source: Dana Corporation, USA)

With the commercialization of MPW process, it is possible to weld dissimilar metals (bimetallic welding) most effectively. This helps to design new geometries for automobile transmissions and undercarriage systems using different combinations of lighter materials to enhance fuel economy and cost savings.

### **III. Conclusions**

The automotive application of permanent joining methods is discussed with illustrative diagrams. The resistance welding techniques namely spot and seam welding are presented with specific applications. The solid state welding method viz. the friction welding is also discussed. The need for innovative and cost effective welding methodologies to meet the growing requirement of lighter and fuel efficient vehicles is highlighted. The technological advancement in the metal joining in the context of auto industry is presented. The working aspect of medium frequency welding is briefed with its distinct merits. The magnetic pulse welding-a breakthrough in metal joining technique is also explained. The following points concluded from this above study.

- The automotive manufacturers focused on producing lighter yet strong and fuel efficient vehicles using new improved alternative materials. This necessitated most efficient welding techniques that produce lighter weld joints without adding additional material.
- The commercial implementation of magnetic pulse welding can prove advantageous for automotive industries to manufacture lighter and fuel efficient cars.
- The advancement in laser beam welding and medium frequency welding allows evolving new geometries for automobile transmissions and undercarriage systems using new combinations of materials, particularly made from powder metallurgy process.

### **Acknowledgements**

The author acknowledges the financial support extended by his parent institute under the NE-QIP scheme of AICTE in the publication of this paper. The author also acknowledges the valuable feedback/suggestion of the anonymous reviewers.

**REFERENCES**

- [1] H. Hayashi, Development of high strength steel sheets and practical application to auto body parts, *Journal of Materials and Manufacturing, Society of Automotive Engineers*, 104 (5), 1995, 560-569.
- [2] B. Durand, Magnetic pulse welding process to decrease vehicle weight and increase fuel efficiency, *Research and Data for Status Report*, 95-02-0055, 2001, 271-274.
- [3] [www.ewf.be/iab](http://www.ewf.be/iab), accessed on 03-May-13.
- [4] [www.boschrexroth.co.uk/automotive](http://www.boschrexroth.co.uk/automotive), accessed on 03-May-13
- [5] C. J. Dawes and W. M. Thomas, Friction Stir Process Welds Aluminum Alloys, *Welding Journal*, 75, 1996, 41-45.
- [6] A. H. Jack, Jr. Frank, R. Manley and D. E. Nelson, Fusion Welding P/M Components for Automotive Applications, *Proc. SAE International Congress, Detroit, MI., March 1-5, 1993.*
- [7] A. H. Jack and W. Jeter. Laser welding of P/M for automotive applications, *Proc. SAE International Congress and Exposition, Detroit, Michigan, USA, February 28 - March 3, 1994.*
- [8] T. Holt, New applications in high power laser welding. *Welding & Metal Fabrication*, 63(6), 1995, 230–234.
- [9] L. Quintino, P. Villica, P. Rodrigues and L. Bordalo, Laser beam welding for automobile hinges, *Welding Research Supplement*, 11(1), 2001, 261-267.
- [10] D. Havrilla and T. Weber, Laser welding takes the lead, *Lasers & Optronics*, 1(1), 1991, 30-35.

## A Study on Risk Assessment in Construction Projects

K. Jayasudha<sup>1</sup>, Dr. B. Vidivelli<sup>2</sup>

<sup>1</sup> Research Scholar, Department of Civil and Structural Engineering, Annamalai University, Chidambaram.

<sup>2</sup> Professor, Department of Civil and Structural Engineering, Annamalai University, Chidambaram

**Abstract:** Risks are very common in construction sector. Risk management includes identifying risks, assessing risks either quantitatively or qualitatively, choosing the appropriate method for handling the risks, and then monitoring and documenting risks. By identifying risks in an early stage of planning and assessing their relative importance, project managers can identify methods used to reduce risks and allocate the best people to mitigate them. Thus, this research focuses on risk identification, as opposed to other processes of risk management. "Brain-storming sessions" is the most popular method used frequently to identify the risks in projects as deduced from a questionnaire survey from participants in large construction projects. Time and cost management need to be fully integrated with the identification process. Time constraints and project managers with sufficient experience are critical when identifying the level of risk for large and/or complex projects. The most considerable types of risk in construction projects are financial risks, construction risks, and demand or product risks.

**Keywords:** Risk, Risk identification techniques, Risk management, and Construction Projects.

### I. INTRODUCTION

Construction companies and firms, such as the government, consultants and contractors, normally face different kinds of risks (e.g., environmental, physical, political, social and economic risks) during construction. However, most of them do not predict risks when they are considering bids and tenders. Construction risk is generally perceived as events that influence project objectives, i.e., cost, time and quality. In project management terms, the most serious effects of risk can be summarised as follows:

1. Failure to keep within the cost estimate.
2. Failure to achieve the required completion date.
3. Failure to achieve the required quality and operational requirements.

This study aims to better understand the risk identification process and other risk processes. Risk identification is the first process in risk management. Therefore, this study focuses on risk identification because it is important to know how the players in the construction industry handle risk identification. Without having any perspective on or approach for risk identification, construction participants cannot make appropriate decisions in other risk management processes. This study evaluates risk identification by better understanding the processes and guidelines related to the risks in large and infrastructure construction projects, so that project risk management can be more effective. It has already been recognised that a clear understanding of the risks born by each participant leads to better risk allocation. The objective of this study is to find means of identifying risk management and other processes that can be utilised and to make new suggestions on the use of these risk management methods. It is of particular interest to find the means to manage risks that are the most effectively managed with the co-operation of several project participants.

### II. Methodology

To achieve the objectives of this research, questionnaires were deemed to be the most effective tool for gathering information. These questions helped identify any projects that should definitely not be undertaken by the parties and those which, although risky, should be examined further after a more rigorous examination of the potential sources of risk. The questionnaire was designed based on the knowledge of government, consultant, or contractor in large or infrastructure construction projects; the questions were meant to identify their method of risk identification and possible effects of those risks.

The general methodology of this study relies largely on the survey questionnaire which will be collected from the various multi project construction contractors and project manager of different sizes by mail

or by personnel meeting. A thorough literature review was initially conducted to identify the risk factors that affect the performance of construction industry as a whole. This study has adopted the more general and broad definition of risk as presented by Shen et al (2001) on china's construction joint ventures and more risk factors from other literature. Also some interviews with industrial practitioners were conducted to produce to check of questionnaires.

### III. QUESTIONNAIRE STRUCTURE AND DESIGN

. The questionnaire was tested with a pilot survey for clarity, ease of use, value of the information that could be gathered. The questionnaire survey is divided into two parts. The first part consists of general information like type of company, experience, value of their project etc., and the second part consists of the construction risk factors for evaluation.

Risk factor for this study classified into eight categories, namely: financial risk, legal risk, management risk, market risk, policy & political risk, technical risk, environmental risk, social risk.

The survey questionnaire survey is designed to probe the cross-sectional behavioral pattern of construction risks construction industry. The questionnaire was prepared for the pilot survey was formulated by seeing the relevant literatures in the area of construction risk. The interviewer was free to ask additional questions that focused on issues arising during the course of the interview. The freedom to follow the interviewee, to ask for clarifications, and to focus on the specify projects, risk practices and knowledge, made the interviews insightful

#### 3.1 Risk Rating

A Likert scale of 1-5 was used in the questionnaire. A Likert scale is a type of psychometric response scale questionnaire, and is the most widely used scale in survey research. When responding to a Likert questionnaire item, respondents specify their level of agreement to a statement. The scale is named after Rensis Likert, who published a report describing its use. The respondents were required to indicate the relative critically/effectiveness of each of the probability of risk factors and their impact to the management.

#### 3.2 Design of Survey

The respondents were requested to judge the significance or "expected loss" of each risk. There are many criteria that respondents may need to consider. One alternative approach adopted by previous researches is to consider two attributes for each risk: the probability level of risk occurrence, denoted by  $\alpha$ ; and the degree of impact or the level of loss if the risk occurs denoted by  $\beta$ . The same type of evaluation is followed in this study also. Therefore, risk significance, denoted as RS, can be described as the function of the two attributes  $RS=f(\alpha, \beta)$ .

By applying this approach, the respondents were asked to respond to the two attributes for each risk. For considering  $\alpha$ , the respondents were required to judge the probability level of risk occurrence by selecting one from among five levels namely, very small, small, normal, large and very large. For considering  $\beta$ , the respondents were required to judge the degree of impact if the risk concerned occurs, by selecting one from among five grades namely, very low, low, and medium, high and very high.

#### 3.3 Analysis of Survey

To assess the relative significance among risks, previous literatures study suggests establishing a risk significance index by calculating the significance score for each risk. For calculating the significance score is to multiply the probability of occurrence by the degree of impact Thus, the significance score of each risk assessed by each respondent can be obtained through the model

$$S_p^i = \alpha_j^i \beta_j^i$$

Where  $S_i$  = significance score assessed by respondent j for risk i;  $\alpha_j^i$  = probability of occurrence of risk i, assessed by respondent j; and  $\beta_j^i$  = degree of impact of risk i, assessed by respondent j. By averaging scores from all responses, it is possible to get an average significance score for each risk, and this average score is called the risk index score and is used to rank among all risks. The model for the calculation of risk index score can be written

$$RS^i = \frac{\sum_{j=1}^T S_j^i}{T}$$

Where  $RS^i$  = index score for risk  $i$ ; and  $S^j$  = significance score assessed by respondent  $j$  for risk  $I$  and  $T$ =Total number of responses. To calculate  $S'$ , the five scales for 0 and (3, this will be converted into numerical (Likert scale) scales.

### **3.4 Pilot Survey**

A pilot questionnaire survey and follow-up interviews with local contractors was conducted. The purpose was to identify the factors out of the 68 factors that applied overseas could also apply to the construction industry. The small number interviews and the structure of the questionnaire in die pilot study does not allow for statistical analysis.

Responses to the interviews have been used to identify consistent themes, common practices, and insight provided by active and influential project participants that would provide additional guidance and assistance to the research team.

The survey results formed the basis of modifying the questionnaire for the subsequent full-scale survey. The pilot study attempts to short-list locally relevant factors. The criteria for a shortlisting are that the chosen factors are relevant in the local construction industry. As a result, only important and relevant factors can be chosen for inclusion in the full-scale survey in the second phase research.

## **IV. Risk Identification And Risk Identification Technique**

The risk identification phase as being either one of the most important stages within the risk management process, the risk identification phase into three categories.

1. The Risk identification conducted only by a risk analyst and based exclusively in his practice, knowledge and capacity.
2. The Risk identification was conducted through the interview of the risk analyst with one or many members of the project staff in order to analyze the reviewed data and the project life cycle based on the knowledge and expert of the people interviewed.
3. The Risk identification in which the risk analyst guides one or many work groups applying the risk identification techniques.

### **4.1 Risk Identification Techniques**

1. **Brainstorming** – An idea generation group technique is divided in two phases. (i) idea generation phase, in which participant generate as more ideas as possible (ii) idea selection phase, the ideas are filtered, remaining only those approved by the entire group
2. **Delphi Technique** – Delphi is a technique to obtain an opinion consensus about future events from a group of experts. It is supported by structured knowledge, experience and creativity from an expert
3. **Interview/ Expert judgment** – Unstructured, semi structured or structured interviews individually or collectively conducted with a set of experienced project members, specialist or project
4. **Checklist** – It consists of a list of item that are marked as yes or no , could be used by an individual project team members, a group or in an interview.
5. **Influence Diagram** – It is a graphical representation containing nodes representing the decision variables of a problem. A traditional influence diagram is formed by three types of nodes: utility, decision and informational. The causal relationship occurs between utility and chance nodes and represents a probabilistic dependence.
6. **Flowchart** – Graphical tool that shows the steps of a process. This technique is applied for a better comprehension of the risks or the elements interrelation
7. **Cause-and-Effect Diagrams** – These are also called Ishikawa diagrams or fishbone diagram, illustrate how various factor might be linked to potential problems or effects. The diagram is designed by listing the effect on the right sides and the causes on the left sides. There are categorized for each effect, and the main causes must be grouped according to these categories .

## **V. Conclusions**

This paper is based on a literature review on the risk assessment methods. The risk assessments approaches are applied in various areas and the problems solve. It was found that the currently used methods for risk assessment are Brainstorming, checklist, Flowchart, Delphi method, Risk significant index method. Each method of risk assessment has their limitation therefore this paper attempt to formulate integrated risk assessment tools. It was observed that currently used risk assessment methods can be integrated into new approach that can aid the decision makers applying the risk assessment effectively. The specifications for

identifying project risk that have been particularised for construction projects have been presented from diverse points of view (from government, consultants and contractors) and construction companies and firms that may be helping the process of dealing with the project in the planning and construction phases. The process can also be adapted to identify the level of risk for a particular project.

The brain-storming sessions and analysis of historical data for similar projects were found to be the most preferred methods of risk identification in the construction industry. The risks associated with construction projects included financial risks (project funding problem), construction risks and demand/product risks. These risks commonly prevent the completion of construction project objectives.

### REFERENCES

- [1] R.C.Walke et al. "An approach to risk quantification in construction projects" International Journal of Engineering Science and Technology Vol. 3 No. 9 September 2011 .pp 6846-6855.
- [2] L. Y. Shen,<sup>1</sup> George W. C. Wu,<sup>2</sup> and Catherine S. K. Ng<sup>3</sup>. Risk assessment for construction joint venture in chinaJournal of construction Engineering and management Vol. 127 No. 1 January/ February 2001 pp. 76-81.
- [3] Wenzhe Tang<sup>1</sup>; Maoshan Qiang<sup>2</sup>; Colin F. Duffield<sup>3</sup>; David M. Young<sup>4</sup>; and Youmei Lu<sup>5</sup>. Risk management in the Chinese construction industry. Journal of construction Engineering and Management ASCE/ DECEMBER 2007
- [4] Dr Patrick. X.W. Zou<sup>1</sup>, Dr Guomin Zhang<sup>2</sup> and Professor Jia-Yuan Wang<sup>3</sup> 1 and 2: Faculty of Built Environment, University of New South Wales, Sydney 2052, Australia;3: College of Architecture and Civil Engineering, Shenzhen University, Shenzhen, P.R. China. Identified Key Risks in Construction Projects: Life Cycle and Stake Holder Perspectives.
- [5] Akintoye A.S and MacLeod, M.J. (1997). Risk analysis and management in construction, International Journal of project Management. Vol 15, February 1997, pages 31-38.
- [6] Ossama A.Abdou (Asst.Prof. Dept. of Civil and Arch. Engg.Drexel University) Managing Construction Journal of Architectural Engineering, Vol 2, No.1 March 1996, pp. 3- 10.
- [7] Matins Claudia Garrido, Morano Cassia Andra Ruotolo, Fereira Miguel Luiz Riberio and Haddad Assed Naked. Risk Identification Techniques Knowledge and Application in the Brazilian Construction Vol. 2(11), pp. 242-252, November2011
- [8] Chapman R.J. (2001) The Controlling Influences on Effective Risk Identification and Assessment for Construction Design Management, International Journal of Project Management. Vol 19.Issue 3, pp. 147-160.
- [9] Al-Bahar, J.F. and Crandall, K.C. (1990). Systematic risk management approach for construction project. Journal of Construction Engineering and Management, 116(3): 533–546.
- [10] Artto, K.A. (1999). Development of World-Class Practices in Project Companies. In The Future of Project Management, Project Management Institute Research Series. Newtown Square, PA: Project Management Institute (PMI), 127–137.
- [11] Kendrick, T. (2009). Identifying and Managing Project Risk: Essential Tools for Failure-Proofing Your Project. 2nd Edition. New York: AMACOM Div. American Management Association.
- [12] Project Management Institute. (2004). A Guide to the Project Management Body of Knowledge. Newtown Square, Pennsylvania: PMI.

## Credit Card Fraud Detection System: A Survey

Dinesh L. Talekar<sup>1</sup>, K. P. Adhiya<sup>2</sup>

<sup>1,2</sup> Department of Computer Engineering, SSBT COET, Bambhori, Jalgaon (M.S.), India

**Abstract:** The credit card has become the most popular mode of payment for both online as well as regular purchase, in cases of fraud associated with it are also rising. Credit card frauds are increasing day by day regardless of the various techniques developed for its detection. Fraudsters are so expert that they generate new ways for committing fraudulent transactions each day which demands constant innovation for its detection techniques. Most of the techniques based on Artificial Intelligence, Fuzzy logic, neural network, logistic regression, naïve Bayesian, Machine learning, Sequence Alignment, decision tree, Bayesian network, meta learning, Genetic Programming etc., these are evolved in detecting various credit card fraudulent transactions. This paper presents a survey of various techniques used in credit card fraud detection mechanisms.

**Keywords:** Credit Card Fraud, Hidden Markov Model (HMM), Fraud Detection, Password, Security question.

### I. INTRODUCTION

While performing online transaction using a credit card issued by bank, the transaction may be either Online Purchase or transfer. The online purchase can be done using the credit or debit card issued by the bank or the card based purchase can be categorized into two types Physical Card and Virtual Card. In both the cases if the card or card details are stolen the fraudster can easily carry out fraud transactions which will result in substantial loss to card holder or bank. In the case of Online Fund Transfer a user makes use of details such as Login Id, Password and transaction password. Again here if the details of the account is wrong then, as a result, it will give rise to fraud transaction. Credit card fraud is a wide-ranging term for theft and fraud committed using a credit

Card or any similar Payment mechanism as a fraudulent source of funds in a transaction. The target may be to obtain goods Without paying money, or to obtain unauthorized funds from an account. The fraud begins with either the theft of the physical card or the compromise of data associated with the account, it include the card account number or other information that would routinely and necessarily be available to a merchant during a legal transaction. The compromise can occur by many common routes and can usually be conducted without tipping off the card holder or the merchant at least until the account is ultimately used for fraud. A store clerk

copying sales receipts for later use is a simple example. The speedy growth of credit card use on the Internet has made database security lapses particularly costly; in some cases, millions of accounts have been determined. Stolen cards can be reported emergently by cardholders, but a determined account can be cached by a thief for weeks or months before any miss use, making it difficult to identify the source of the determined.

Popularity of online shopping is growing day to day. Credit card is the easy way to do online shopping. According to an ACNielsen study conducted in 2005 one-tenth of the world's population is shopping online in same study it is also mentioned that credit cards are most popular mode of online payment. In US it is found that total number of credit cards from the four credit card network (Master Card, VISA, Discover, and American Express) is 609 million and 1.28 billion credit cards from above four primary credit card networks plus some other networks (Store, Oil Company and other). If consider the statistics of credit cards in India, it is found that total number of credit cards In India at the end of December-31-2012 is about 18 to 18.9 million [1]. In case of multinational banks, the usage or average balance, per borrower for credit card holder has rise up from Rs. 61,758 in 2011 to Rs. 82,455 in 2012. in the same period, private bank customers' usage rise from Rs 39,368 to Rs. 47,370 [1]. As the number of credit card users increases world-wide, the opportunities for fraudster to steal credit card details and, subsequently, commit fraud are also grew up.

### II. MOTIVATION

Now a day the customers prefer the most accepted payment mode via credit card for the convenient way of paying bills, online shopping is easiest way. At the same time the fraud transaction risks using credit card is a main problem which should be avoided. So There are many data mining techniques available to avoid

these risks effectively. In existing research they modeled the sequence of operations in credit card transaction processing using a Hidden Markov Model (HMM) and shown how it can be used for the detection of frauds. To avoid computational complexity and to provide better accuracy in fraud detection in proposed work.

### III. LITERATURE SURVEY

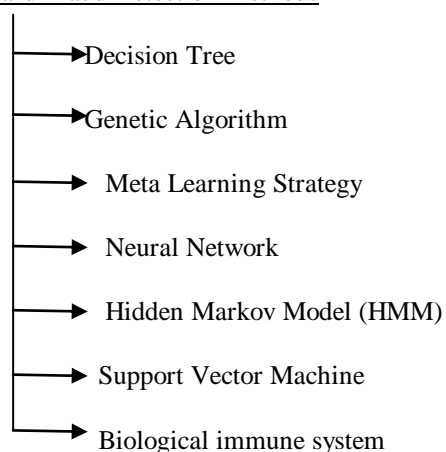
Abhinav Srivastava et al describe the “Credit card fraud detection method by using Hidden Markov Model (HMM)” [2]. In this method, they model the sequence of operations in credit card transaction processing using a Hidden Markov Model (HMM) and show how it can be used for the detection of fraud Transaction. An HMM is initially trained with the normal behavior of a cardholder.

S. Ghosh and Douglas L. Reilly et al describes the “Credit card fraud detection With Neural Network (NN)” [3]. In this method author use data from a credit card issuer, a neural network based credit card fraud detection system was trained on a large sample of labeled credit card account transactions and tested on a holdout data set that consisted of all account activity over a subsequent two-month of time. The neural network was trained on examples of fraud due to stolen cards, lost cards, application fraud, mail-order fraud, counterfeit fraud. The network detected significantly more fraud accounts (an order of magnitude more) with significantly fewer false positives (reduced by a factor of 20) over rule based fraud detection procedures.

### IV. VARIOUS TECHNIQUES FOR CREDIT CARD FRAUD DETECTION SYSTEM

In Credit Card Fraud Detection there are many methods, here we present survey of some most powerful method.

#### Credit Card Fraud Detection Methods



#### A) Decision Tree

Decision Tree algorithm is a data mining induction Techniques that recursively partitions a data set of records using depth-first greedy approach (Hunts et al, 1966) or breadth-first approach (Shafer et al, 1996) until all the data items belongs to a special class. A decision tree structure is made of root, leaf and internal nodes. The tree Structure is used in classifying unknown data records. So at each internal node of the tree, a decision of best split is made using impureness measures (Quinlan, 1993). The tree leaves are made up of the class labels which the data items have been group [5]. In this method a Credit Card Fraud Detection using algorithm for Decision Tree Learning. Although focus on the Information Gain based Decision Tree Learning in this technique estimating the best split of Purity Measures of Gini, Entropy and Information Gain Ratio to test the best classifier attribute. In this Technique simply find out the Fraudulent Customer/Merchant through Tracing Fake Mail and IP Address. Customer /merchant are suspicious if the mail is fake they are traced all information about the owner/sender through IP Address. It can find out the Location of the customer and Trace all details. Decision Tree is Powerful Technique in Data Mining Decision Tree is vital part of Credit card Fraud Detection [5].

## **B) Genetic Algorithm**

In this Technique fraud detected and fraud transactions are generated with the given sample data set. If this algorithm is applied into bank credit card fraud detection, the chance of fraud transactions can be predicted soon after credit card transactions is in process, and a series of anti-fraud strategies can be adopted to prevent banks from great losses before and reduce risks [6].

The Experiment process has four steps:

STEP1: Input group of data credit card transactions, every transaction record with n attributes, and standardize the data, get the sample finally, which includes the confidential information about the card holder.

STEP2: Compute the critical values, Calculate the Credit Card usage frequency count, Credit Card overdraft, current bank balance, Credit Card usage location, average daily spending.

STEP3: Generate critical values found after limited number of generations. Critical Fraud Detected, Monitor able Fraud Detected, Ordinary Fraud Detected etc. using Genetic algorithm.

STEP4: Generate fraud transactions using this algorithm. This is to analyze the feasibility of credit card fraud detection based on technique, then applies detection mining based on critical values into credit card fraud detection and proposes this detection procedures and its process [7].

The initial population is selected randomly from the sample space which has many populations. The fitness value is calculated in each population and is sorted out. In selection process is selected through tournament method. The Crossover is calculated using single point probability. Mutation mutates the new offspring using uniform probability measure. In elitism selection the best solution are passed to the further generation. The new population is generated and undergoes the same process it maximum number of generation is reached.

## **C) Meta Learning Strategy**

The meta-learning aims to filter the legitimate transactions from the fraudulent ones, and by quickly and accurately identifying the fraudulent transactions, fraud losses can be reduced. "Meta-learning" techniques introduced by Chan and Stolfo. There are two methods of combing algorithms that were introduced by Chan and Stolfo, the arbiter and the combiner strategies. Chan and Stolfo found that the combiner strategy performs more effectively than the arbiter strategy. Therefore, the combiner strategy is used. In the combiner strategy the attributes and correct classifications of credit card transaction instances are used to train multiple base classifiers. The predictions of the base classifiers are used as new attributes for the meta-level classifier. By combining the original attributes, the base classifier predictions, and the correct classification for each instance, a new "combined" dataset is created [8] which are used as the training data to generate the meta-level classifier. The predictions from the meta-level classifier are then used as the final predictions in the combiner strategy.

There are four main stages in the meta-learning process:

STAGE 1: Establishes the base classifiers using a training dataset that consists of 50% fraudulent transactions and 50% legitimate transactions [8]. This was done on a month by month basis for the first 8 months where all of the fraudulent transactions for the given month were matched with an equal number of randomly chosen legitimate transactions.

STAGE 2: The base classifiers are applied to a validation dataset to generate base predictions. The validation set consisted of all of the transactions. The predictions from the second stage are then combined with the validation dataset.

STAGE 3: Meta-algorithm is applied to this combined dataset to produce a meta-classifier.

STAGE 4: The forward predicting test stage, the meta- classifier is applied to the testing dataset to produce forward looking predictions [8].

#### **D) Neural Network**

Fraud detection using Neural network is totally based on the human brain working principal. Neural network technology has made a computer capable of think. As human brain learn through past experience and use its knowledge or experience in making the decision in daily life problem the same technique is applied with the credit card fraud detection technology. When a particular consumer uses its credit card, There is a fix pattern of credit card use, made by the way consumer uses its credit card. When credit card is being used by unauthorized user the neural network based fraud detection system check for the pattern used by the fraudster and matches with the pattern of the original card holder on which the neural network has been trained, if the pattern matches the neural network declare the authorize transaction. When a transaction arrives for authorization, it is characterized by a stream of authorization data fields that carry information identifying the cardholder (account number) and characteristics of the transaction (e.g., amount, merchant code). There are additional data fields that can be taken in a feed from the authorization system (e.g., time of day) [9]. The neural network is design to produce output in real value between 0 and 1 .If the neural network produce output that is below .6 or .7 then the transaction is ok and if the output is above .7 then the chance of being a transaction illegal increase [9]. In the design of neural network-based pattern recognition Systems, there is always a process of business History descriptors contain features characterizing the use of the card For transactions, the payments made to the account over Some immediately prior time interval. Other some descriptors can Include such factors as the date of issue (or most recent issue) of the credit card. This is important for the detection of NRI (non-receipt of issue) fraud [9].

#### **E) Hidden Markov Model (HMM)**

An HMM is a double embedded stochastic process with two hierarchy levels. It can be used to model complicated stochastic processes as compared to a traditional Markov model. An Hidden Markov Model has a finite set of states governed by a set of transition probabilities. In a particular state, observation or an outcome can be generated according to an associated probability distribution. So It is only the outcome and not the state that is visible to an external observer. HMM uses cardholder's spending behavior to detect fraud. In Implementation, three behavior of cardholder are taken into consideration.

- 1) Low spending behavior
- 2) Medium spending behavior
- 3) High spending behavior

Different cardholders has their different spending behavior (low, medium, high).Low spending behavior of any cardholder means cardholder spend low amount (L), medium spending behavior of any cardholder means cardholder spend medium amount (M), high spending behavior of any cardholder means cardholder spend high amount (H). These profiles are observation symbols [10].

Algorithm Steps:

Training Phase: Cluster creation

STEP 1: To Identify the profile of cardholder from their purchasing

STEP 2: The probability calculation depends on the amount of time that has elapsed since entry into the current state.

STEP 3: To construct the training sequence for training model

Detection Phase: Fraud detection

STEP 1: To Generate the observation symbol

STEP 2: To form new sequence by adding in existing sequence

STEP 3: To Calculate the probability difference and test the result with training phase

STEP 4: Finally, If both are same it will be a normal customer else there will be fraud signal will be provided.

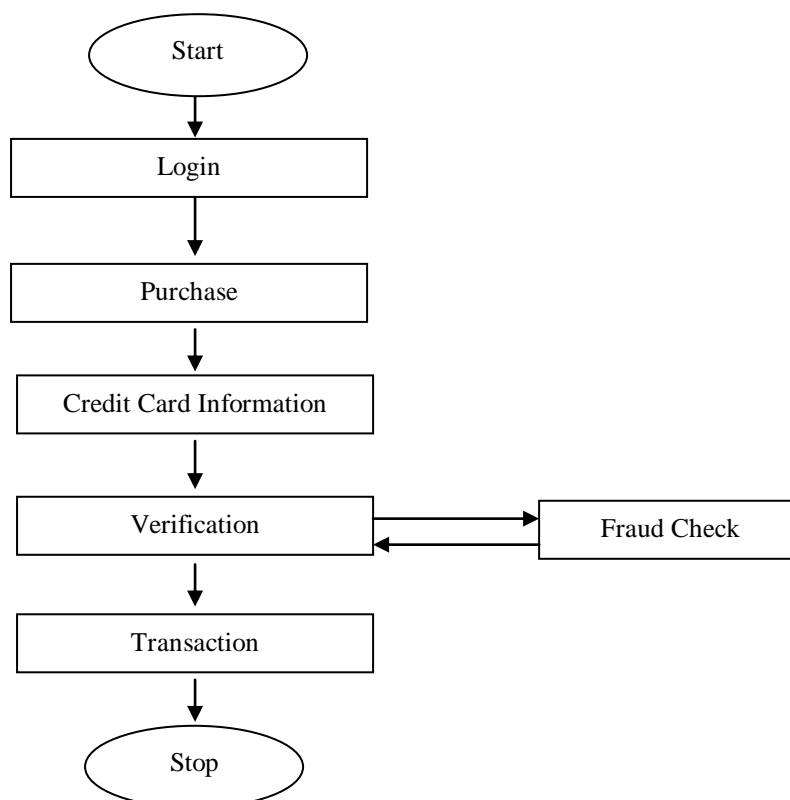


Fig: Flow chart for Credit Card Fraud Detection

In this Technique Clustering algorithm are used for creating three clusters and clusters represent observation symbols. Then calculate clustering probability of each cluster, which is percentage of number of transaction in each cluster to total number of transactions. Then calculate fraudulent Transaction.

But in this Proposed system no need to check the original user as we Maintain a log. We can find the most accurate detection using this technique. This reduces the tedious work of an employee in the bank. A one-time password (OTP) is a password that is valid for only one login session or transaction.

### F) Support Vector Machine

Support Vector Machines (SVMs) have developed from Statistical Learning Theory. It have been widely applied to fields such as handwriting digit, character and text recognition, and more recently to satellite image classification. SVMs, like ANN and other nonparametric classifiers have a reputation for being robust. SVMs function by nonlinearly projecting the training data in the input space to a feature space of higher dimension by use of a kernel function. This results in a linearly separable dataset that can be separated by a linear classifier. This process enables the classification of datasets which are usually nonlinearly separable in the input space. The functions used to project the data from input space to feature space are called kernels (or kernel machines) examples of which include polynomial, Gaussian (more commonly referred to as radial basis functions) and quadratic functions. Each function has unique parameters which have to be checked prior to classification and it also usually determined through a cross validation process [11].

The choice of a Kernel depends on the problem at hand because it depends on what we are trying to model. A polynomial kernel, allows us to model feature up to the order of the polynomial. And Radial functions allows to pick out circles (or hyper spheres) in contrast with the Linear kernel it allows only to pick out lines (or hyper planes).

Linear Kernel: The Linear kernel is the simplest kernel function. It is given by the inner product  $\langle x,y \rangle$  plus and constant  $c$  as optional. Kernel algorithms using a linear kernel are often equivalent to their non-kernel counterparts, that means. KPCA[11] with linear kernel is the same as standard PCA.

$$K(X,Y) = XT Y + C$$

Polynomial Kernel: The Polynomial kernel means it is a non-stationary kernel. Polynomial kernels are good for problems where as all the training data is normalized.

$$K(X,Y) = (\alpha XT Y + C)^d$$

The adjustable parameters are the constant term  $c$ , the slope  $\alpha$  and the polynomial degree  $d$ .

Here detail the proposed algorithm for classification of Fraud Transactions.

Step 1: Read the given data.

Step 2: Re-categorize the data in five groups as transaction month, date, day, amount of transaction & difference between successive transaction amounts.

Step 3: Make each transaction in the form of data as vector of five fields.

Step 4: Then make two separate groups of data named True & False transaction group (if false transaction data is not available add randomly generate data in this group).

Step 5: Select one of three kernels (Linear, Quadratic, and RBF)[11].

Step 6: Train SVM.

Step 7: Save the classifier.

Step 8: Read the current Transaction.

Step 9: Restart the process from step1 to step3 for current transaction data only.

Step 10: Replaced the saved classifier & currently generated vector in classifier.

Step 11: Admit the generated decision from the classifier.

Since there is no real data is available because of privacy maintained by respective banks. so for testing of implementation of algorithm author generated the data of true & false Transaction using different mean & variance & then mixed them with different probability. And used the MATLAB for the execution of the algorithm because of its rich sets of mathematical functions and also supporting the inbuilt functions for SVM. Finally author said these technique give near about 90 to 97 % accuracy but future improvement is needed[11].

### **G) Biological immune system (BIS)**

BIS is, a multilayered defense system comprising of cells and molecules which interact in various ways to detect and eliminate infectious agents (pathogens) from our body. BIS differentiates between self, (S), and (ii) nonself (NS) peptides and then assigns the right effectors to eliminate each pathogen. Similarly, detection system which sets apart fraudulent credit card transactions from genuine ones. The input for the system is financial transactions (i.e., source, destination and amount) in the form of a of e-commerce binary string. BIS in turn can be equated to a parallel adaptive information-system (IS) which works on the principle of simple and, localized rules. BIS interacts with pathogens in a localized fashion. Surfaces of BIS cells are covered with receptors, which chemically bind to (i) pathogens, and (ii) other immune system cells or molecules. Also BIS cells circulate around the body via the blood and lymph systems, to form a dynamic system of distributed detection and response. BIS has no centralized control, and hierarchical organization. Similarly, FDSCC detectors can be mobile agents that migrate across networks linking banks, financial institutions, etc.

BIS will comprise of two steps (i) detection and (ii) response. In step 1, detectors will be trained to discriminate between true and fraudulent transactions. In step 2, based on the training the FDSCC will classify a given transaction. It will help to memorize the rule for subsequent detection[12].

**Detectors**

The mobile detectors of System are analogous to the receptors on lymphocytes (B-cell receptor i.e. antibody or T-cell receptor). The receptors on lymphocytes bind to antigenic determinants (epitopes) on pathogens. Non-self detection results in the activation of the lymphocytes which trigger a series of reactions that can lead to elimination of the pathogens. A lymphocyte only activated when the number of its receptors binding to epitopes exceeds a threshold. Similarly, System detector matches the binary string inputs by using r-contiguous bit algorithm and confirms whether it is genuine or fraud transaction. The specificity of the detector is governed by the length of r-contiguous bits.

**Response**

BIS has a variety of response mechanism to eliminate different pathogens that attack the human body. One very important response (effector function) is mediated by soluble receptors called antibodies secreted by plasma cell (matured B lymphocytes). Antibody molecule has 2 parts variable region and constant region. Variable region binds to the pathogen and the constant region is responsible for the effector response. This is analogous to the System detector. Selection of effectors in System is determined by mathematical models[12].

BIS based anomaly detection and response system, which augments its performance through self learning. System will be an effective mechanism to detect and eliminate online credit card fraud transactions. This will help promote e-commerce as it will effectively minimize losses and other online credit card frauds.

**V. Result**

Comparison of Existing Methods

Authors	Year	Techniques / Algorithms	Results
Dr. R. Dhanapal	2012	Decision Tree/ Hunts Algorithm	Fraud detect by using Tracing Email and IP
Rinky D. Patel & Dheeraj Kumar Singh	2013	Genetic Algorithm	Optimizing the parametric fraud detection solution
Joseph Pun, Yuri Lawryshyn	2012	Meta Learning Strategy/ Meta Algorithm	Improvement in catch fraud than Neural Network
Raghavendra Patidar, Lokesh Sharma	2011	Neural Network/ Back Propagation Algorithm	Neural network-based pattern recognition.
Avinash Ingole, Dr. R. C. Thool	2013	HMM/ Clustering Algorithm	Fraud Detect using spending profile
Gajendra Singh, Ravindra Gupta	2012	Support Vector Machine	True Positive rate and false positive rate using MATLAB
Arunabha Mukhopadhyay, Sayali Mukherjee	2011	Artificial Immune System	By Matching Binary string Using detector and response

## V. CONCLUSION

Credit card fraud has become more and more rampant in recent years. To improve merchants' risk management level in an automatic and efficient way and building an accurate and easy handling credit card risk monitoring system is one of the key tasks for the merchant banks. One aim of this study is to identify the user model that best identifies fraud cases. There are many ways of detection of credit card fraud. If one of these or combination of algorithm is applied into bank credit card fraud detection system, Then the probability of fraud transactions can be predicted soon after credit card transactions by the banks. This paper gives contribution towards the effective ways of credit card fraudulent detection. In our paper we survey on seven existing Techniques for credit card fraud detection with comparing their results hence we conclude that out of these method HMM model is one of the best model because in HMM model fraud detect using Card holders spending behavior, but we need to improvement HMM in future.

## REFERENCES

- [1] Avinash Ingole, Dr. R. C. Thool, "Credit Card Fraud Detection Using Hidden Markov Model and Its Performance," *International Journal of Advanced Research In Computer Science and Software Engineering (IJARCSSE)*, vol. 3, 6 June 2013.
- [2] Srivastava, Abhinav, Kundu, Amlan, Sural, Shamik and Majumdar, Arun K., (2008) "Credit Card Fraud Detection Using Hidden Markov Model", *IEEE Transactions on Dependable and Secure Computing*, Vol. 5, No. 1, pp. 37-48.
- [3] S. Ghosh and D.L. Reilly, "Credit Card Fraud Detection with a Neural-Network," *Proc. 27th Hawaii Int'l Conf. System Sciences: Information Systems: Decision Support and Knowledge Based Systems*, vol. 3, pp. 621-630, 1994.
- [4] Pankaj Richhariya et al "A Survey on Financial Fraud Detection Methodologies" BITS, Bhopal," *International Journal of Computer Applications (0975 – 8887) Volume 45 No.22, May 2012.*
- [5] Dr R. Dhanapal, Gayathiri. P, "Credit Card Fraud Detection Using Decision Tree For Tracing Email And Ip," *International Journal of Computer Science Issues (IJCSI) Vol. 9, Issue 5, No 2, September 2012.*
- [6] K.RamaKalyani, D.UmaDevi "Fraud Detection of Credit Card Payment System by Genetic Algorithm", *International Journal of Scientific & Engineering Research Volume 3, Issue 7, July-2012.*
- [7] Rinky D. Patel, Dheeraj Kumar Singh "Credit Card Fraud Detection & Prevention of Fraud Using Genetic Algorithm", *International Journal of Soft Computing and Engineering (IJSCE) ISSN: 2231-2307, Volume-2, Issue-6, January 2013.*
- [8] Joseph Pun, Yuri Lawryshyn "Improving Credit Card Fraud Detection using a Meta-Classification Strategy", *International Journal of Computer Applications (0975 – 8887) Volume 56– No.10, October 2012.*
- [9] Raghavendra Patidar, Lokesh Sharma "Credit Card Fraud Detection Using Neural Network", *International Journal of Soft Computing and Engineering (IJSCE) ISSN: 2231-2307, Volume-1, Issue-NCIAI2011, June 2011.*
- [10] Avinash Ingole, Dr. R. C. Thool "Credit Card Fraud Detection Using Hidden Markov Model and Its Performance", *International Journal of Advanced Research in Computer Science and Software Engineering (IJARCSSE) ISSN: 2277 128X, Volume 3, Issue 6, June 2013.*
- [11] Gajendra Singh, Ravindra Gupta, Ashish Rastogi, Mahiraj D. S. Chandel, A. Riyaz "A Machine Learning Approach for Detection of Fraud based on SVM", *International Journal of Scientific Engineering and Technology (ISSN : 2277-1581), Volume No.1, Issue No.3, pg : 194-198 01 July 2012.*
- [12] Arunabha Mukhopadhyay, Sayali Mukherjee and Ambuj Mahanti, "Artificial Immune System for detecting online credit card frauds," *Research Front, www.csi-india.org, CSI Communications , December 2011.*

## Seismic Vulnerability of RC Building With and Without Soft Storey Effect Using Pushover Analysis

Harsha G<sup>1</sup>, Syed Ahamed Raza<sup>2</sup>

<sup>1</sup>Post Graduation Student (Structural Engineering), Ghousia College of Engineering, Ramanagaram, 562159, Affiliated to VTU, Karnataka, India.

<sup>2</sup>Assistant Professor, Department of Civil Engineering, Ghousia College of Engineering, Ramanagaram 562159, Affiliated to VTU, Karnataka, India.

**Abstract:** A soft storey is one which has less resistance to earthquake forces than the other storeys; Buildings containing soft stories are extremely vulnerable to earthquake collapses, since one floor is flexible compared to others. Vulnerability of buildings is important in causing risk to life hence special consideration is necessary for such soft storey RC buildings. In the present study, analytical investigation of a RC building by considering the effect of soft storey situated in seismic Zone-V of India, in accordance with IS 1893-2002 (part-1), is taken as an example and the various analytical approaches (linear static and nonlinear static analysis) are performed on the building to identify the seismic demand and also pushover analysis is performed to determine the performance levels, and Capacity spectrum of the considered, also Storey Shear is compared for 3 models by using Finite Element Software Package ETAB's 9.7.4 version.

**Key words:** Linear static analysis, non linear static analysis, Pushover analysis, , Performance levels, Capacity demand ,Performance point.

### I. Introduction

According to IS 189-2002 (part1) "A soft storey is one in which the lateral stiffness is less than 70 percent of that in the storey above or less than 80 percent of the average lateral stiffness of the three storeys above." Now a day's open storeys are unavoidable construction in practice for many practical reasons, a building may have larger public spaces such as lobbies, large meeting rooms or open-plan retail space. In urban locations, residential buildings sometimes have fewer walls at the ground level to allow for parking underneath the building, but these soft storey buildings has poor performance during past earthquakes. In the present study, seismic performance of 3D building frame was studied. Performance of R.C. frame was evaluated varying storey level and location of the soft storey. The main objective of the study was to investigate the behaviour of multi-storey, multi-bay soft storey and to evaluate their performance levels when subjected to earthquake loading.

#### 1.1 Current Practice

Currently, FEMA 356 (Pre standard and commentary for the seismic rehabilitation of buildings) and FEMA 440 (Improvement of Nonlinear Static Seismic Analysis Procedures).The focus is on anticipated recommendations to improve inelastic analysis procedures as currently documented in FEMA 356 and ATC 40 serve as the source documents for future design code. Based on performance-based design methodology, FEMA 356 specifies the following procedures in the design for an existing building to be retrofitted by energy dissipation dampers.

- Preliminary design, including sizing of the devices
- Device prototype testing
- Final design of the rehabilitated building to meet the target performance level.

For the performance-based design, a structural analysis is needed to obtain the building seismic performance. Although there are four analysis procedures specified in FEMA 356 Prestandard, the linear static procedure is the most efficient for preliminary design purpose. To account for the damping from adding VED's, FEMA 356 specifies a damping modification factor to reduce the seismic effect (pseudo lateral load in a given horizontal direction) on the structure.

## II. Methods of Seismic Evaluation

There are different methods of analysis provides different degrees of accuracy. Currently seismic evaluation of buildings can be divided into two categories:

- a. Qualitative method
- b. Analytical method

The Qualitative methods are based on the available background information on the structures, past performance of the similar structures under severe earthquakes, visual inspection report and some non-destructive test results, etc.

### Analytical Methods

Analysis methods are broadly classified as linear static, linear dynamic, nonlinear static and nonlinear dynamic methods.

#### 2.1 Linear Static Analysis (Equivalent Static Analysis)

In linear static procedures the building is modelled as an equivalent single degree of freedom (SDOF) system with a linear static stiffness and an equivalent viscous damping. The seismic input is modelled by an equivalent lateral force with the objective to produce the same stresses and strains as the earthquake it represents.

This procedure does not in and require dynamic analysis, however, it accounts for the dynamics of building in an approximate manner. The static method is a simplest one; it requires less computational effort and is based on formulae given in code of practice. First, the design Base Shear is computed for the whole building and it is then distributed along the height of buildings. The lateral forces at each floor level, thus obtained are distributed to individual lateral load resisting elements. The procedure generally used for the Equivalent static analysis is explained below:

(i) Determination of fundamental natural period

( $T_a$ ) of the buildings  $T_a = 0.075 * h^{0.075}$  Moment resisting RC frame building without brick infill wall.

$T_a = 0.085 * h^{0.075}$  Moment resisting steel frame building without brick infill walls.

$T_a = 0.09 * h / \sqrt{d}$  All other buildings, including moment resisting RC frame building with brick infill walls.

Where,

h - Is the height of the building in meters

d- Is the base dimension of building at plinth level in m, along the considered direction of lateral force.

(ii) Determination of base shear (VB) of the building

$$VB = Ah \times W$$

Where,

$Ah = Z * I * S_a / 2Rg$  is the design, horizontal seismic coefficient, which depends on the seismic zone. Factor (Z), importance factor (I), response, reduction factor (R) and the average response acceleration coefficients ( $S_a/g$ ).  $S_a/g$  in turn depends on the nature of foundation soil (rock, medium or soft soil sites), natural period and the damping of the structure.

(iii) Distribution of design base shear

The design Base Shear VB thus obtained shall be distributed along the height of the building as per the following expression:

Where,  $Q_i$  is the design lateral force,

$W_i$  is the seismic weight,

$H_i$  is the height of the  $i^{\text{th}}$  floor measured from the base and n is the number of stories in the building.

#### 2.2 Nonlinear static Analysis (Pushover Analysis)

The pushover analysis of a structure is a static non-linear analysis under permanent vertical loads and gradually increasing lateral loads. The load is incrementally increased in accordance with a certain predefined pattern. The analysis is carried out up to failure, thus it enables determination of collapse load and ductility capacity. On a building frame, plastic rotation is monitored, and a plot of the total Base Shear versus Displacement in a structure is obtained by this analysis that would indicate any premature failure or weakness.

#### 2.3 Performance Objectives

A performance objective has two essential parts - a damage state and a level of seismic hazard. Seismic performance is described by designating the maximum allowable damage state (performance level) for an identified seismic hazard (earthquake ground motion). A performance objective may include consideration of damage states for several levels of ground motion and would then be termed a dual or multiple-level performance objective.

The target performance objective is split into Structural Performance Level (SP-n, where n is the designated number) and Non-structural Performance Level (NP-n, where n is the designated letter). These may

be specified independently; however the combination of the two determines the overall Building Performance level shown in Fig 1. Structural Performance Levels is shown in the Table 1:

TABLE 1: Structural Performance Levels

PERFORMANCE LEVELS	STRUCTURAL PERFORMANCE	NON-STRUCTURAL PERFORMANCE
<b>Operational (O)</b>	Very light damage. No permanent drift Substantially original strength and stiffness.	Negligible damage.
<b>Immediate Occupancy (IO)</b>	Light damage. No permanent drift, Substantially original strength & stiffness. Minor cracking. Elevators can be restarted. Fire protection operable.	Power and other utilities are available. Equipment's and content secure may not operate due to mechanical.
<b>Life Safety (LS)</b>	Moderate damage. Some permanent drift. Residual strength & stiffness in all stories. Gravity elements function. Building may be beyond economical repair.	Falling hazard. mitigated But extensive system damage.
<b>Collapse Prevention (CP)</b>	Severe damage. Large permanent Drifts. Little residual strength & Stiffness, Gravity elements function. Some exits blocked, Building near Collapse.	Extensive damage

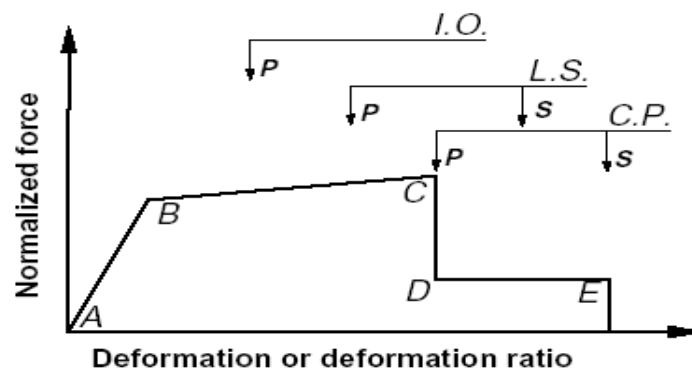


Fig 1: force deformation for performance levels

The owner, architect, and structural engineer then decide upon the desired condition of the structure after a range of ground shakings, or Building Performance Level. The Building Performance Level is a function of the post event conditions of the structural and non - structural components of the structure.

### III. Purpose of Pushover Analysis

The purpose of pushover analysis is to evaluate the expected performance of structural systems by estimating performance of a structural system by estimating its strength and deformation demands in design of earthquakes by means of static inelastic analysis and comparing these demands to available capacities at the performance levels of interest. The evaluation is based on an assessment of important performance parameters, including global drift, inter-storey drift, inelastic element deformations (either absolute or normalized with respect to a yield value), deformations between elements, and element connection forces (for elements and connections that cannot sustain inelastic deformations). The inelastic static pushover analysis can be viewed as a method for predicting seismic force and deformation demands, which accounts in an approximate manner for the redistribution of internal forces that no longer can be resisted within the elastic range of structural behaviour. The pushover is expected to provide information on many response characteristics that cannot be obtained from an elastic static or dynamic analysis.

Table 5: Performance levels for G+5 Building Model in longitudinal direction PUSHX. The above Table 5 indicates the range of overall performance level of G+5 storey building model in PUSH X direction which lies in between A to IO.

The above Table 6 indicates the range of overall performance level of G+11 storey building model in PUSH X direction which lies in between A to IO.

**Performance Point of the Building using Capacity Spectrum Method**

Performance point can be obtained by superimposing capacity spectrum and demand spectrum and the intersection point of these two curves is performance point. Fig 8 shows superimposing demand spectrum and capacity spectrum.

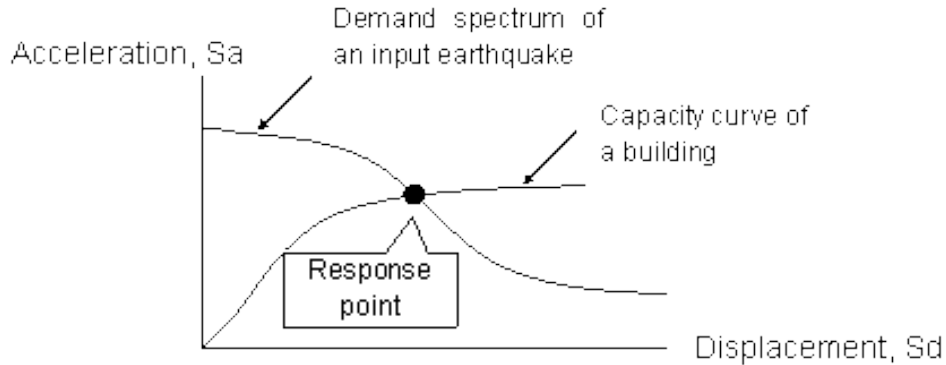


Fig 2: Performance Point of the Building using Capacity Spectrum Method

**IV. Descriptions Of The Building Considered**

The structure used in this study is a building of reinforced concrete of 10 storeys with 6 bays along longitudinal direction and 6 bays along transverse direction (Fig.2, Fig.3 and Fig.4.). The beams are of sections 0.3m x 0.6m and the columns are of sections 0.5m x 0.5m and the height of first storey is 3.5m and other stories are 3m with the thickness of the slab is 125mm. Live load on the roof slab is 1.5 kN/m<sup>2</sup> and live load on each floor is 3 kN/m<sup>2</sup> finishes is 2 kN/m<sup>2</sup> on roof and 1.75 kN/m<sup>2</sup> on each floor. Concrete cube compressive strength,  $f_{ck} = 25 \text{ N/mm}^2$  (M25). Characteristic strength of reinforcing steel,  $f_y = 415 \text{ N/mm}^2$  (Fe415). Modulus of Elasticity of concrete,  $E = 25 \text{ kN/mm}^2$ . Unit weight of concrete = 25 kN/m<sup>3</sup>. Model-1; Without soft storey

Model-2; With first storey as soft storey

Model-3; With middle storey as soft storey

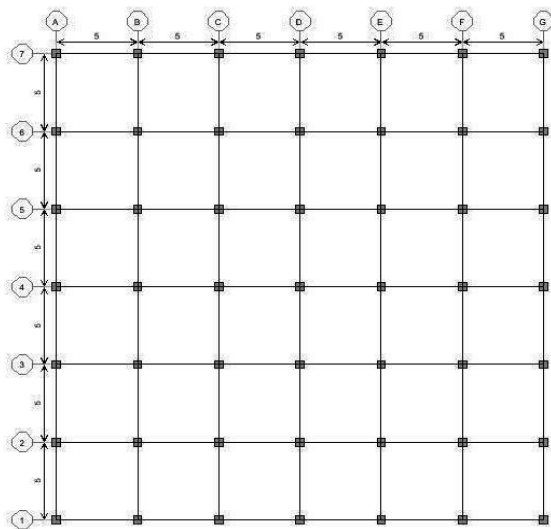


Figure2: Plan of 10 Storey Building Modelled (from ETABS 9.7.4)

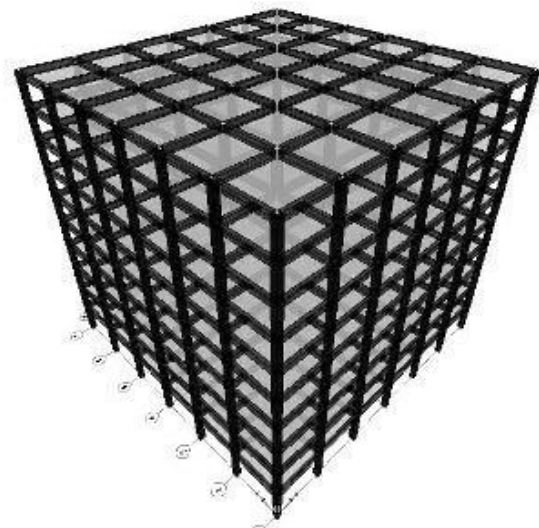


Figure3: 3D view of 10 Storey Building Model-1

4.0 RESULTS AND DISCUSSION

4.1 Storey drift

Table2: Data for Storey drift for 10 storey building in longitudinal direction EQX

MODEL 1		MODEL 2		MODEL 3	
STOREY NUMBER	STOREY DRIFT in m	STOREY NUMBER	STOREY DRIFT in m	STOREY NUMBER	STOREY DRIFT in m
10	0.000148	10	0.000141	10	0.000147
9	0.000246	9	0.000235	9	0.000244
8	0.00033	8	0.000315	8	0.000328
7	0.000395	7	0.000377	7	0.000403
6	0.000443	6	0.000423	6	0.000511
5	0.000476	5	0.000454	5	0.00053
4	0.000496	4	0.000475	4	0.000486
3	0.000505	3	0.000496	3	0.000483
2	0.000502	2	0.000557	2	0.000478
1	0.000395	1	0.000443	1	0.000376

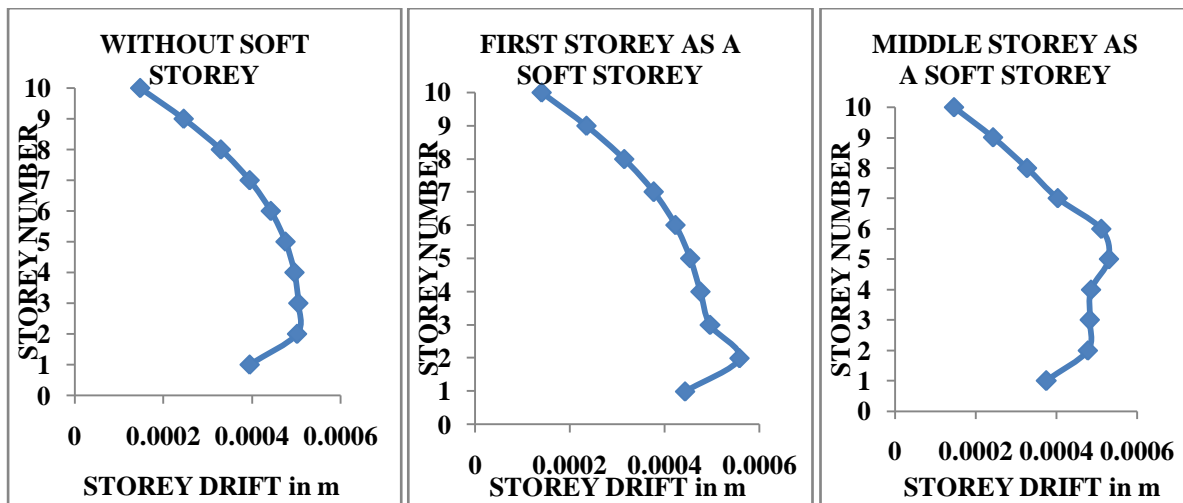


Figure: 5 Storey drift for Model-1 along EQX, Figure:6 Storey drift for Model-2 along EQX, Figure:7 Storey drift for Model-3 along EQX

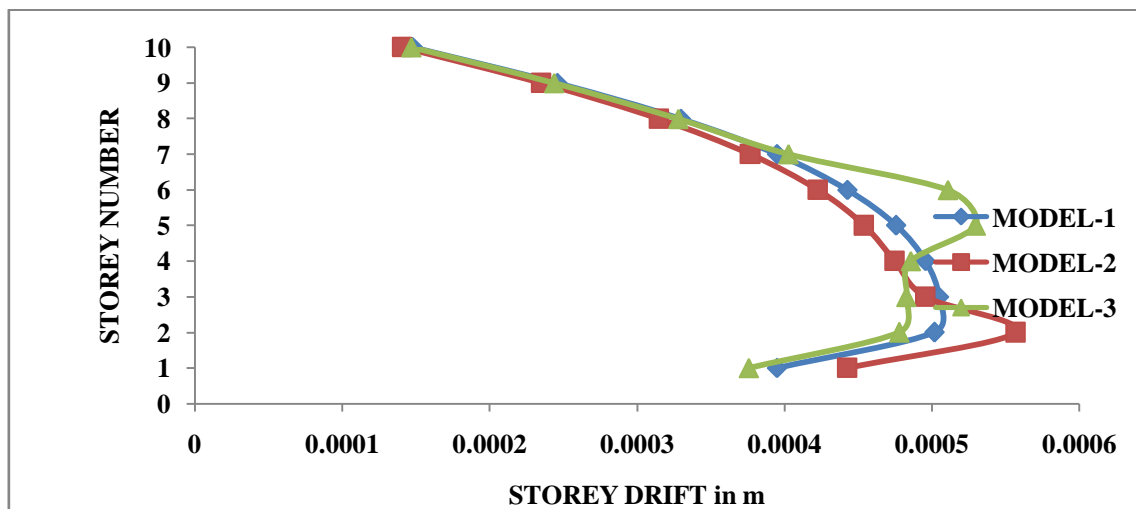


Figure:8 Storey drift comparison for Model-1, Model-2, Model-3 along EQX

Table3: Data for Storey drift for 10 storey building in longitudinal direction PUSH X

MODEL1		MODEL 2		MODEL 3	
STOREY NUMBER	STOREY DRIFT in m	STOREY NUMBER	STOREY DRIFT in m	STOREY NUMBER	STOREY DRIFT in m
10	0.001933	10	0.001797	10	0.001818
9	0.004767	9	0.004497	9	0.004632
8	0.008695	8	0.008333	8	0.008653
7	0.012847	7	0.01246	7	0.013007
6	0.016387	6	0.016007	6	0.016856
5	0.019181	5	0.018355	5	0.01882
4	0.019609	4	0.019039	4	0.018558
3	0.017371	3	0.017755	3	0.01658
2	0.013402	2	0.014228	2	0.012633
1	0.006034	1	0.006584	1	0.005659

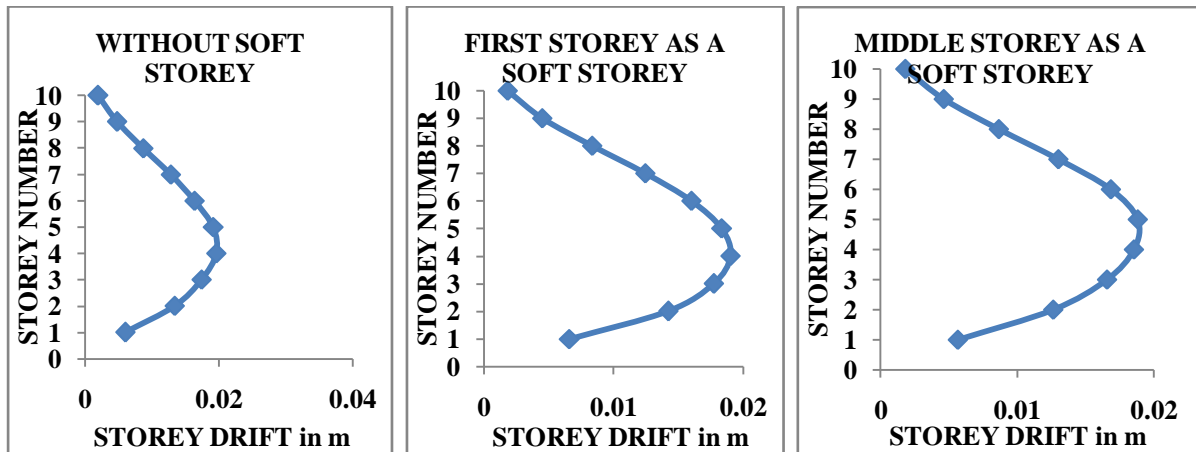


Figure:9 Storey drift for Model-1 along PUSH X, Figure:10 Storey drift for Model-2 along PUSH X, Figure:11 Storey drift for Model-3 along PUSH X

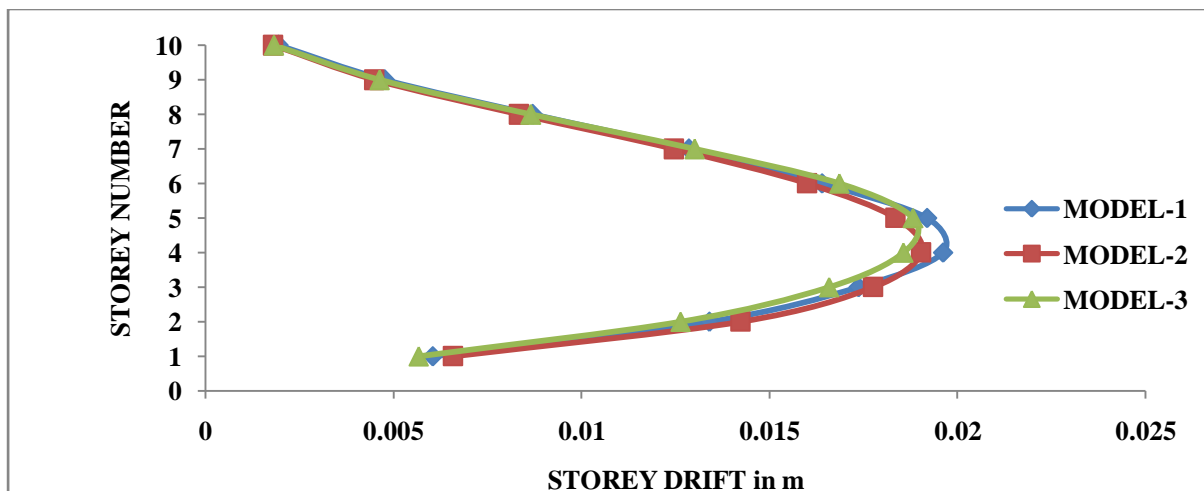


Figure:12 Storey drift comparison for Model-1, Model-2, Model-3 along PUSH X

4.2 Storey shear

Table4: Data for Storey shear for 10 storey building in longitudinal direction EQX

MODEL 1		MODEL 2		MODEL 3	
STOREY NUMBER	STOREY SHEAR in Kn	STOREY NUMBER	STOREY SHEAR in Kn	STOREY NUMBER	STOREY SHEAR in Kn
1	1383.57	1	1315.85	1	1315.85
2	1378.77	2	1312.89	2	1311.11
3	1362.37	3	1299.28	3	1294.92
4	1327.32	4	1265.86	4	1260.33
5	1266.66	5	1208	5	1200.44
6	1173.37	6	1119.04	6	1141.16
7	1040.48	7	992.3	7	1027.06
8	861	8	821.13	8	849.89
9	627.94	9	598.86	9	619.84
10	334.31	10	318.83	10	329.99

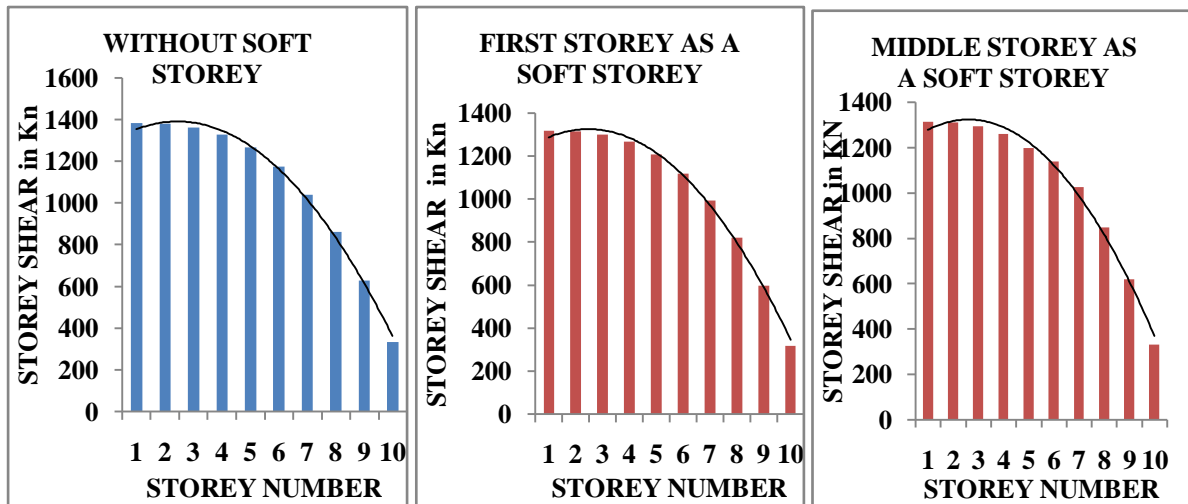


Figure:13 Storey shear for Model-1 along EQX, Figure:14 Storey shear for Model-2 along EQX, Figure:15 Storey shear for Model-3 along EQX

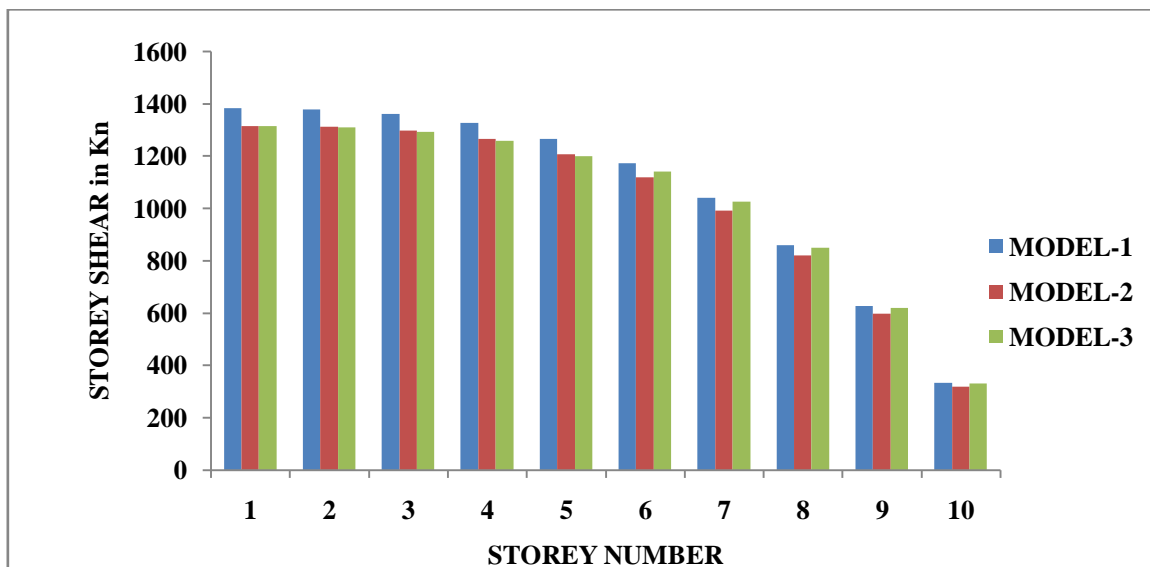


Figure:16 Storey shear comparison for Model-1, Model-2, Model-3 along EQX

Table5: Data for Storey shear for 10 storey building in longitudinal direction PUSH X

MODEL1		MODEL 2		MODEL 3	
STOREY NUMBER	STOREY SHEAR in kN	STOREY NUMBER	STOREY SHEAR in kN	STOREY NUMBER	STOREY SHEAR in kN
1	2407.77	1	3491.07	1	4985.76
2	2399.41	2	3483.2	2	4967.79
3	2370.86	3	3447.1	3	4906.44
4	2309.88	4	3358.43	4	4775.38
5	2204.3	5	3204.93	5	4548.47
6	2041.97	6	2968.9	6	4323.84
7	1810.71	7	2632.67	7	3891.52
8	1498.37	8	2178.54	8	3220.24
9	1092.78	9	1588.83	9	2348.56
10	581.78	10	845.87	10	1250.34

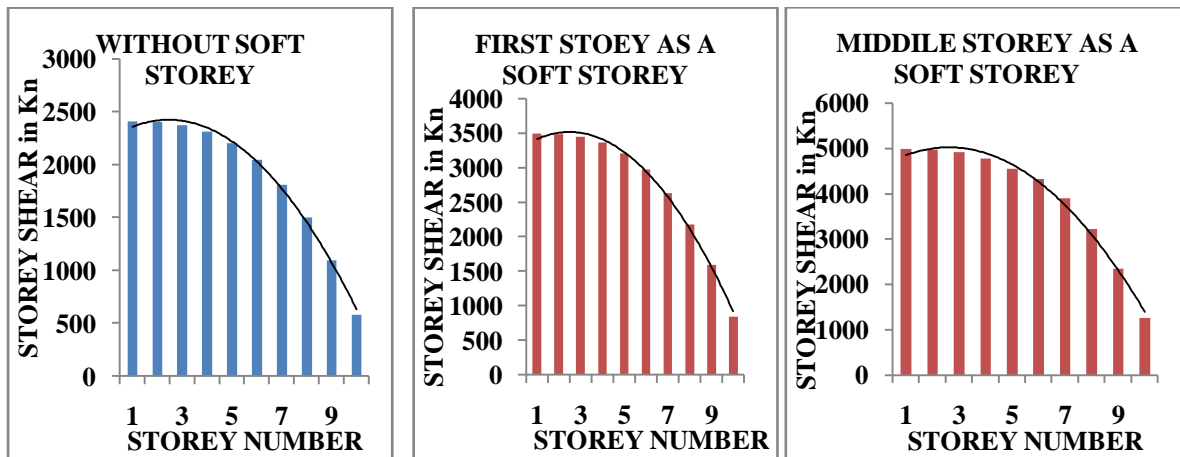


Figure:17 Storey shear for Model-1 along PUSH X, Figure:18 Storey shear for Model-2 along PUSH X, Figure:19 Storey shear for Model-3 along PUSH X

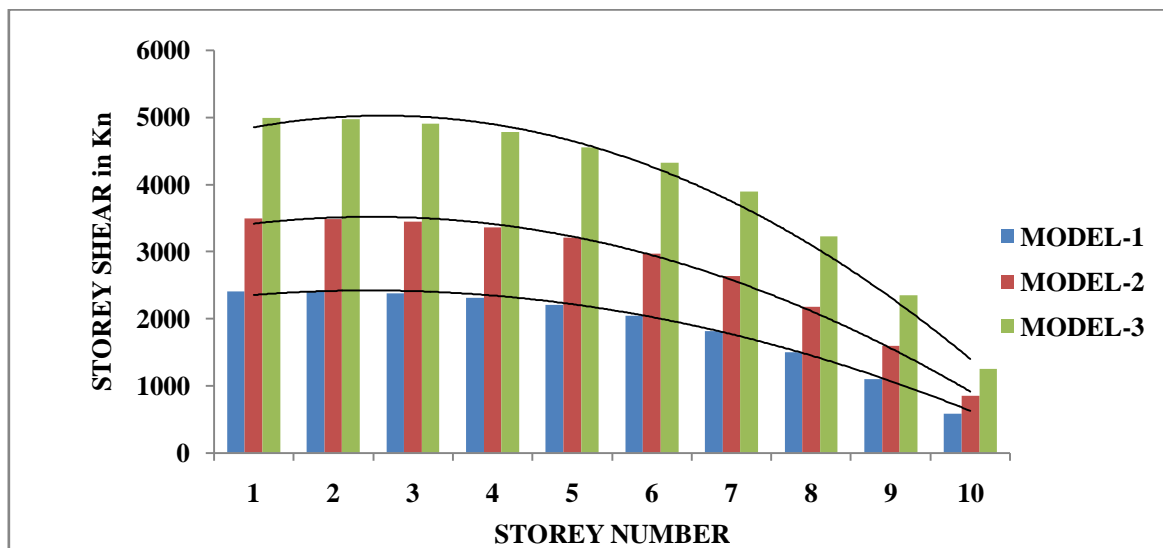


Figure: 20 Storey shear comparison for Model-1, Model-2, Model-3 along PUSH X

Table6: Data for Storey drift for 10 storey building in longitudinal direction EQX & PUSH X

STOREY DRIFT COMPARISON						
STOREY	MODEL-1		MODEL-2		MODEL-3	
	EQX	PUSH X	EQX	PUSH X	EQX	PUSH X
1	0.000148	0.001933	0.000141	0.001797	0.000147	0.001818
2	0.000246	0.004767	0.000235	0.004497	0.000244	0.004632
3	0.00033	0.008695	0.000315	0.008333	0.000328	0.008653
4	0.000395	0.012847	0.000377	0.01246	0.000403	0.013007
5	0.000443	0.016387	0.000423	0.016007	0.000511	0.016856
6	0.000476	0.019181	0.000454	0.018355	0.00053	0.01882
7	0.000496	0.019609	0.000475	0.019039	0.000486	0.018558
8	0.000505	0.017371	0.000496	0.017755	0.000483	0.01658
9	0.000502	0.013402	0.000557	0.014228	0.000478	0.012633
10	0.000395	0.006034	0.000443	0.006584	0.000376	0.005659

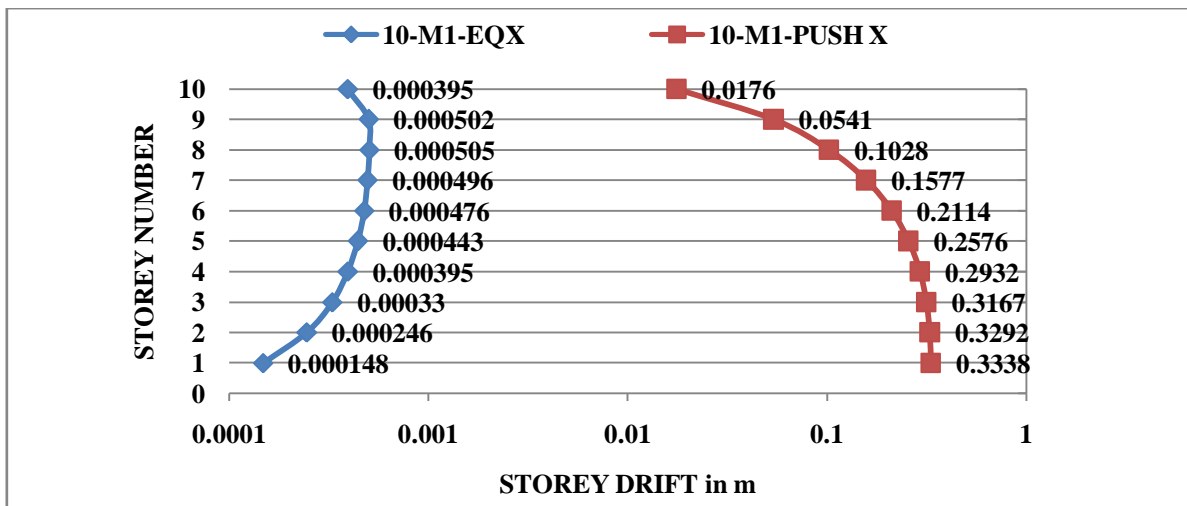


Figure: 20 Storey drift comparison for Model-1 along EQX and PUSH X

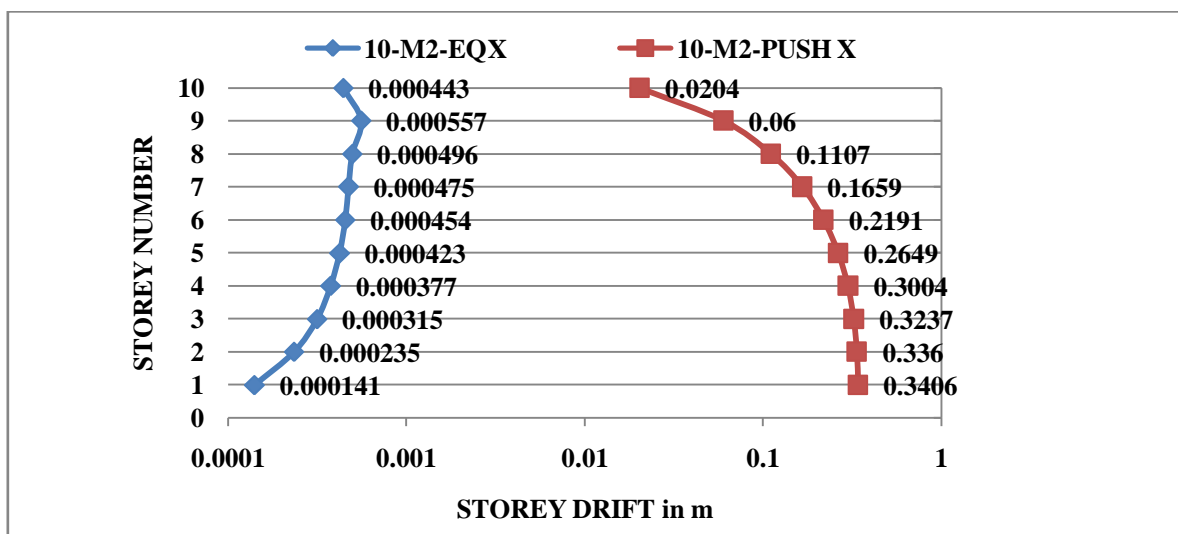


Figure: 21 Storey drift comparison for Model-2 along EQX and PUSH X

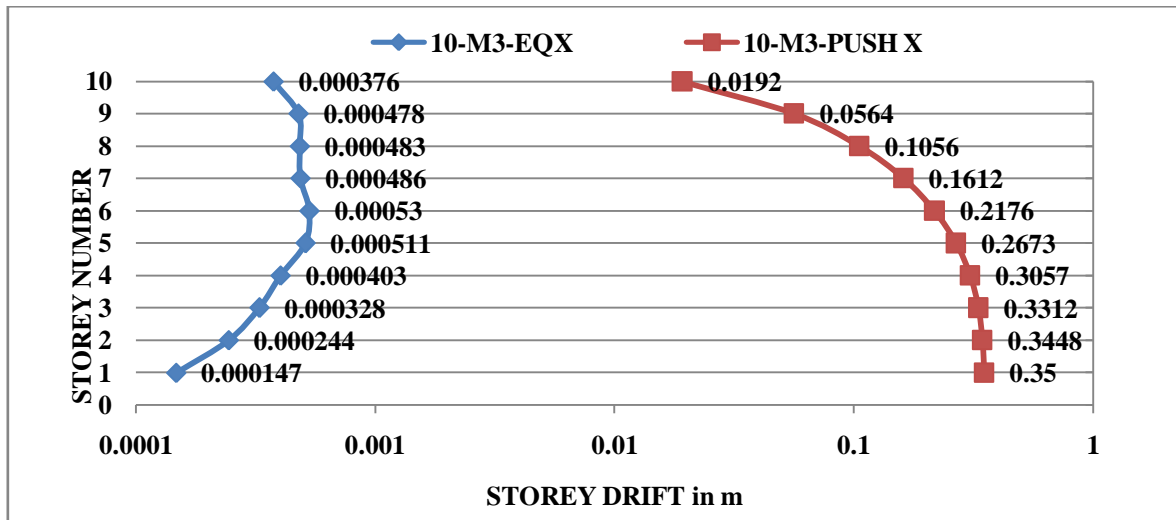


Figure: 22 Storey drift comparison for Model-3 along EQX and PUSH X

Table7: Data for Storey shear for 10 storey building in longitudinal direction EQX & PUSH X

STOREY SHEAR COMPARISON						
STOREY	MODEL-1		MODEL-2		MODEL-3	
	EQX	PUSH X	EQX	PUSH X	EQX	PUSH X
1	1383.57	2407.77	1315.85	3491.07	1315.85	4985.76
2	1378.77	2399.41	1312.89	3483.2	1311.11	4967.79
3	1362.37	2370.86	1299.28	3447.1	1294.92	4906.44
4	1327.32	2309.88	1265.86	3358.43	1260.33	4775.38
5	1266.66	2204.3	1208	3204.93	1200.44	4548.47
6	1173.37	2041.97	1119.04	2968.9	1141.16	4323.84
7	1040.48	1810.71	992.3	2632.67	1027.06	3891.52
8	861	1498.37	821.13	2178.54	849.89	3220.24
9	627.94	1092.78	598.86	1588.83	619.84	2348.56
10	334.31	581.78	318.83	845.87	329.99	1250.34

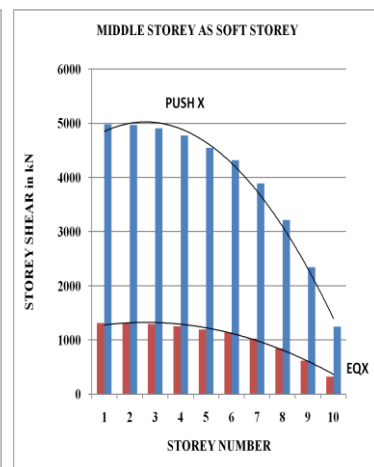
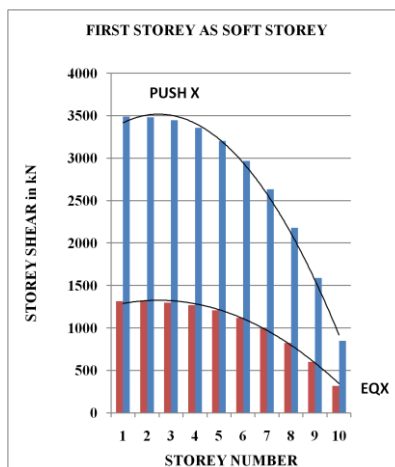
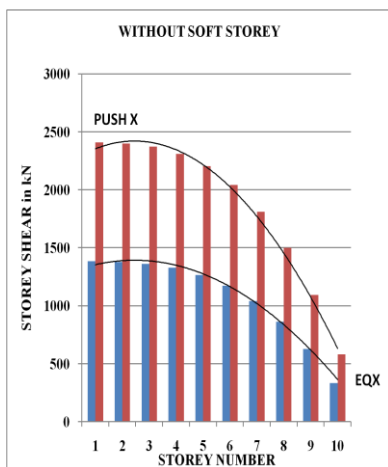


Figure:23 Storey shear comparison for Model-1 along EQX and PUSH X, Figure:24 Storey shear comparison for Model-2 along EQX and PUSH X, Figure:25 Storey shear comparison for Model-3 along EQX and PUSH X

4.3 Pushover curve

Table8: Data for Pushover curve for 10 storey building Model-1

Step	Displacement	Base Force
0	2.62E-05	0
1	0.0246	2839.8311
2	0.0408	3968.291
3	0.046	4107.5303
4	0.1084	4682.0269
5	0.2441	5418.3188
6	0.3595	5906.5449
7	0.3595	5358.1396
8	0.3615	5423.0996
9	0.3338	2407.7725

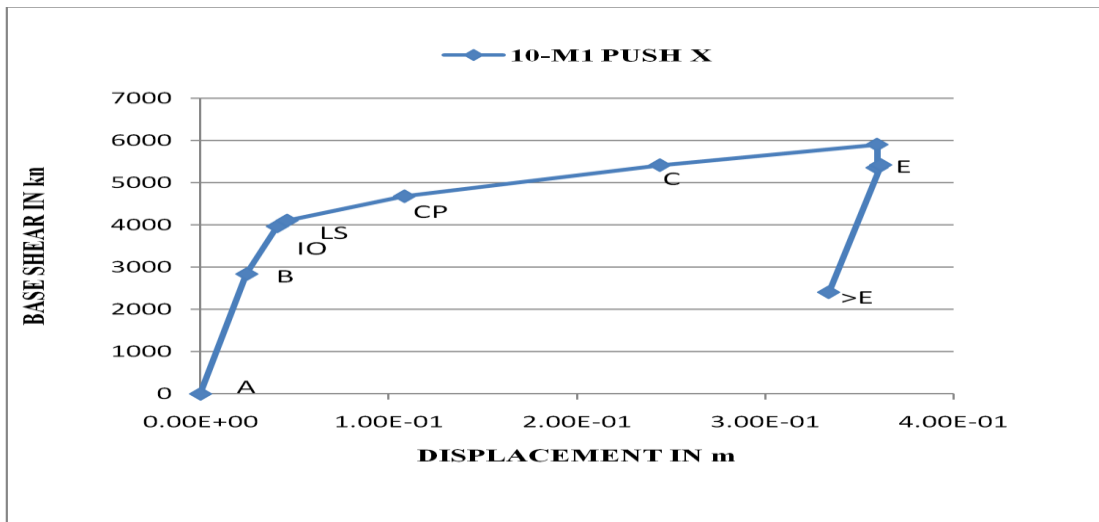


Figure:26 Pushover curve for Model-1

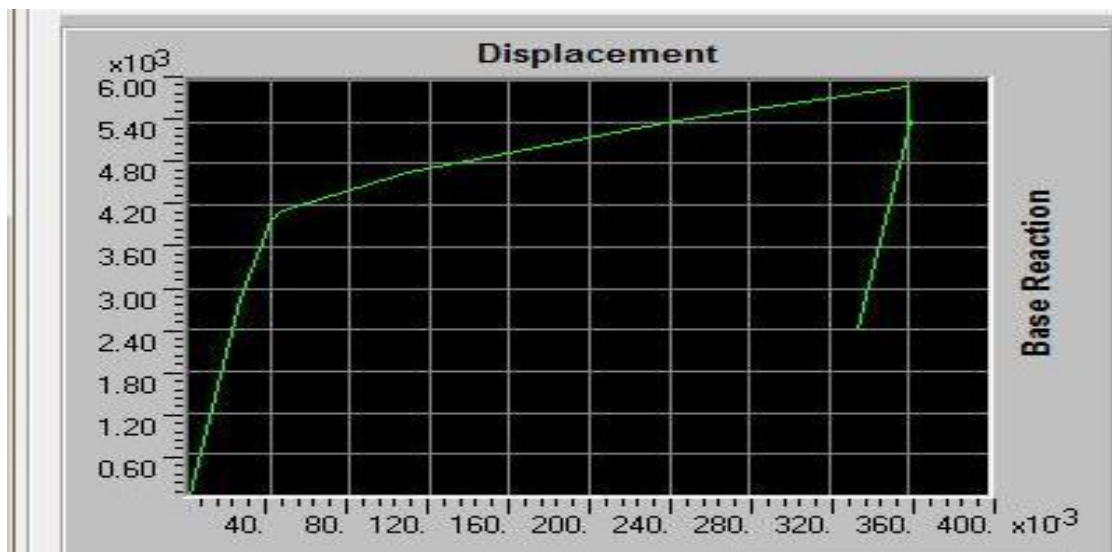


Figure: 27 Pushover curve for Model-1 from ETAB 9.7.4

Table9: Data for Pushover curve for 10 storey building Model-2

Step	Displacement	Base Force
0	2.58E-05	0
1	0.0236	2602.5703
2	0.0364	3563.0684
3	0.0437	3832.4939
4	0.0787	4295.6494
5	0.2109	5130.2783
6	0.3347	5679.7065
7	0.3601	5780.4019
8	0.3406	3491.0718

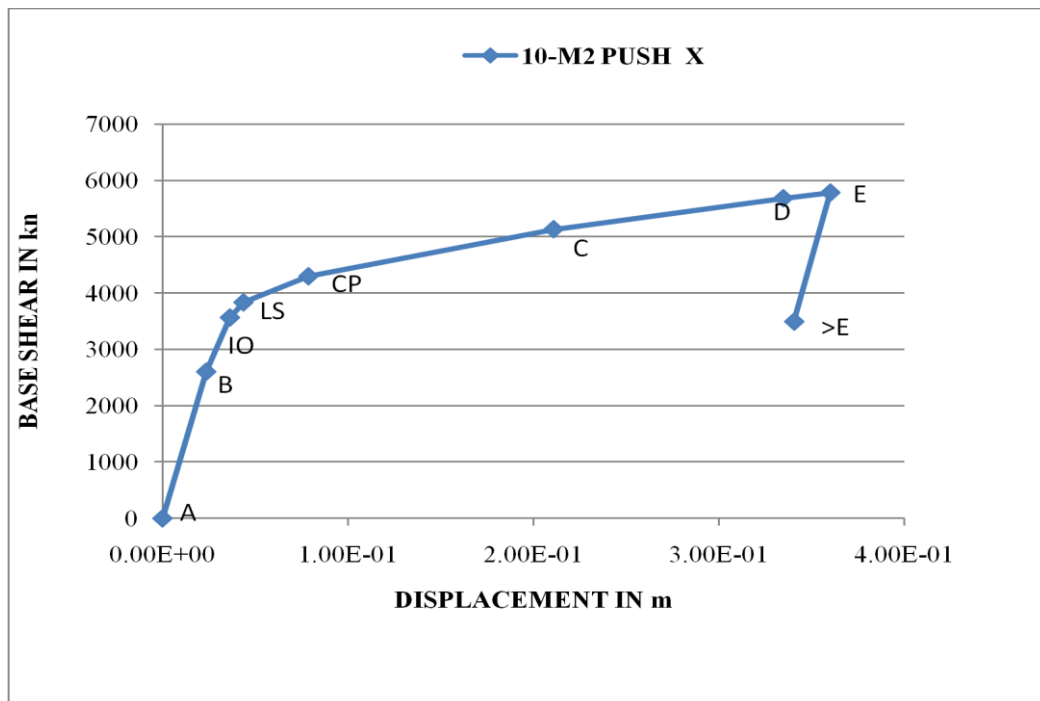


Figure: 28 Pushover curve for Model-2

Table10: Data for Pushover curve for 10 storey building Model-3

Step	Displacement	Base Force	A-B
0	2.46E-05	0	4241
1	0.0254	2770.2466	3933
2	0.0397	3704.5022	3846
3	0.0444	3876.3352	3618
4	0.1666	4772.3354	3506
5	0.2909	5356.1021	3486
6	0.3539	5606.5405	3486
7	0.35	4985.7607	4244

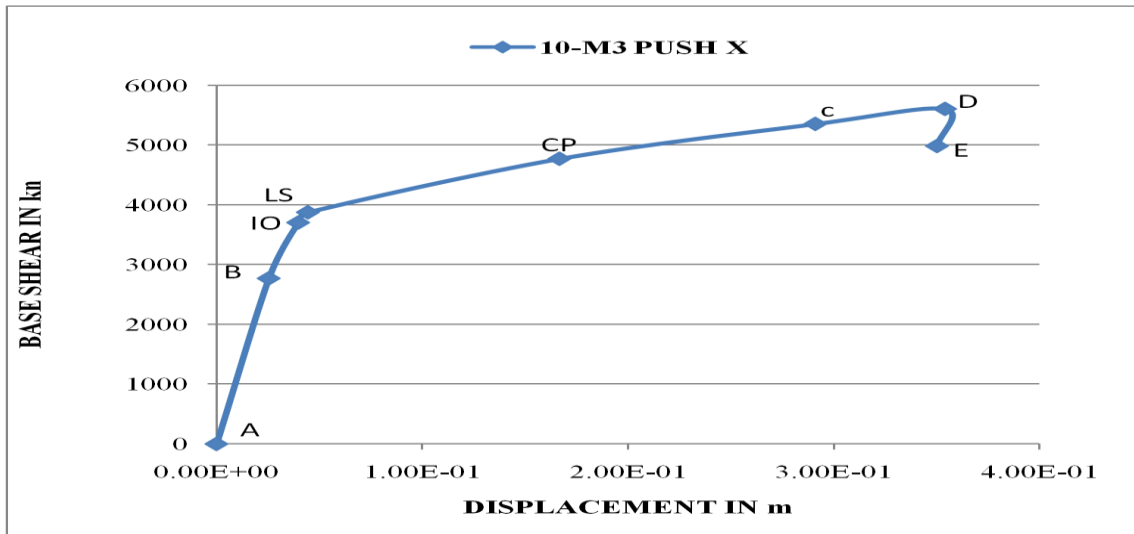


Figure:29 Pushover curve for Model-3

4.4 Performance points

Table 10: Data for Spectral displacement and Spectral acceleration for capacity curve and demand curve for 10 storey building Model-1

Step	Sd(C)	Sa(C)	Sd(D)	Sa(D)
0	0	0	0.128	0.312
1	0.019	0.046	0.128	0.312
2	0.032	0.063	0.115	0.23
3	0.036	0.065	0.111	0.202
4	0.089	0.075	0.129	0.109
5	0.198	0.09	0.172	0.078
6	0.286	0.1	0.198	0.069
7	0.287	0.091	0.199	0.063
8	0.288	0.092	0.199	0.063

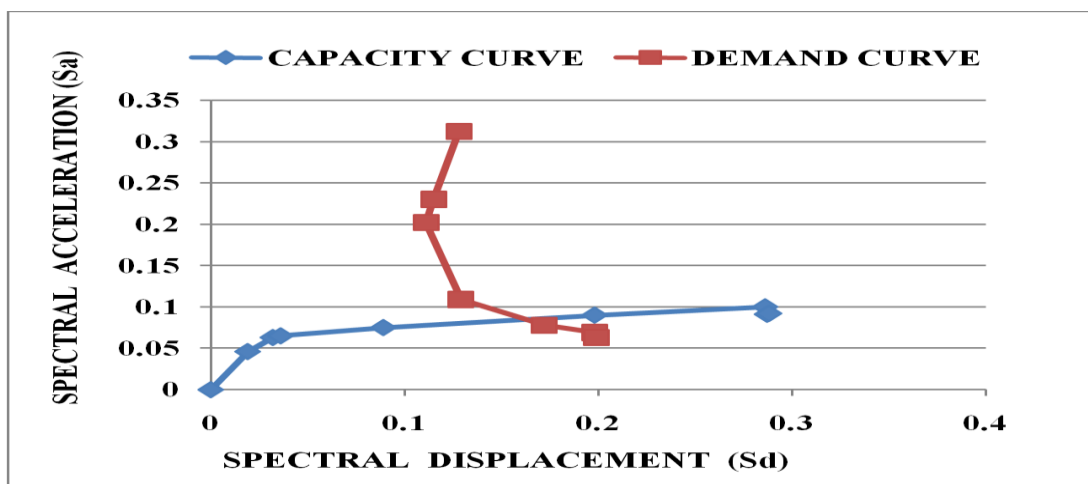


Figure: 30 Performance point for Model-1

Table 11: Data for Spectral displacement and Spectral acceleration for capacity curve and demand curve for 10 storey building Model-2

Step	Sd(C)	Sa(C)	Sd(D)	Sa(D)
0	0	0	0.131	0.304
1	0.018	0.042	0.131	0.304
2	0.028	0.057	0.119	0.239
3	0.035	0.061	0.114	0.201
4	0.065	0.068	0.12	0.126
5	0.174	0.085	0.168	0.082
6	0.27	0.096	0.197	0.07
7	0.289	0.098	0.202	0.068

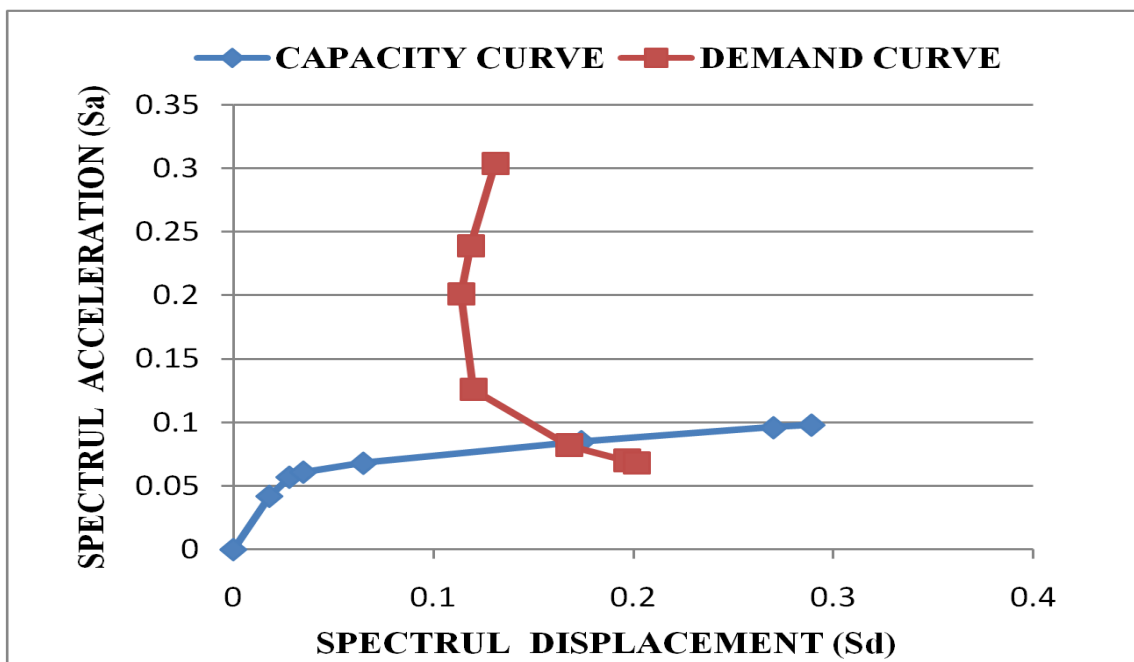


Figure:31 Performance point for Model-2

Table 12: Data for Spectral displacement and Spectral acceleration for capacity curve and demand curve for 10 storey building Model-3

Step	Sd(C)	Sa(C)	Sd(D)	Sa(D)
0	0	0	0.127	0.313
1	0.019	0.048	0.127	0.313
2	0.031	0.064	0.114	0.236
3	0.035	0.067	0.112	0.216
4	0.137	0.084	0.149	0.091
5	0.236	0.096	0.182	0.074
6	0.284	0.102	0.195	0.07

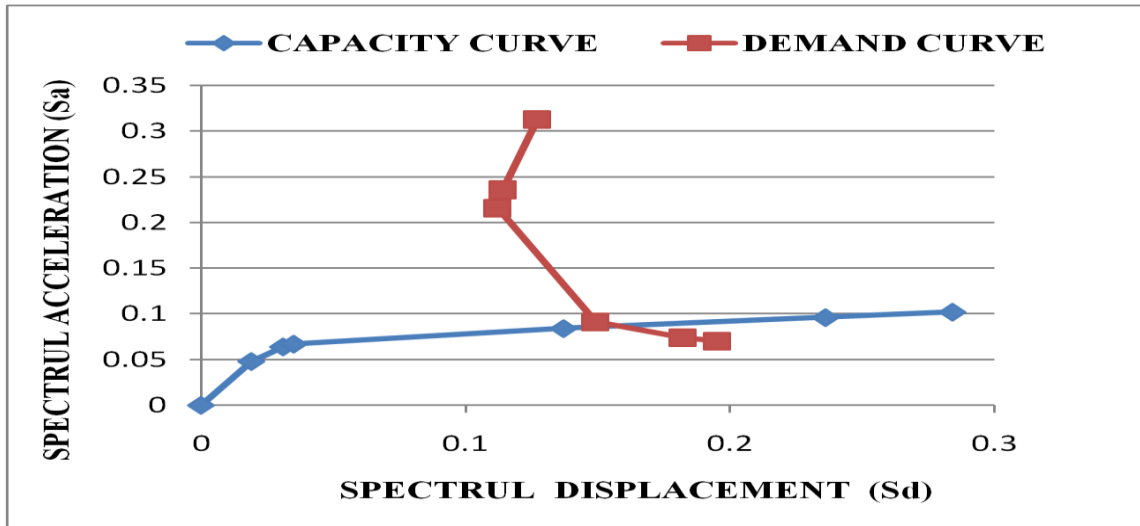


Figure:32 Performance point for Model-3

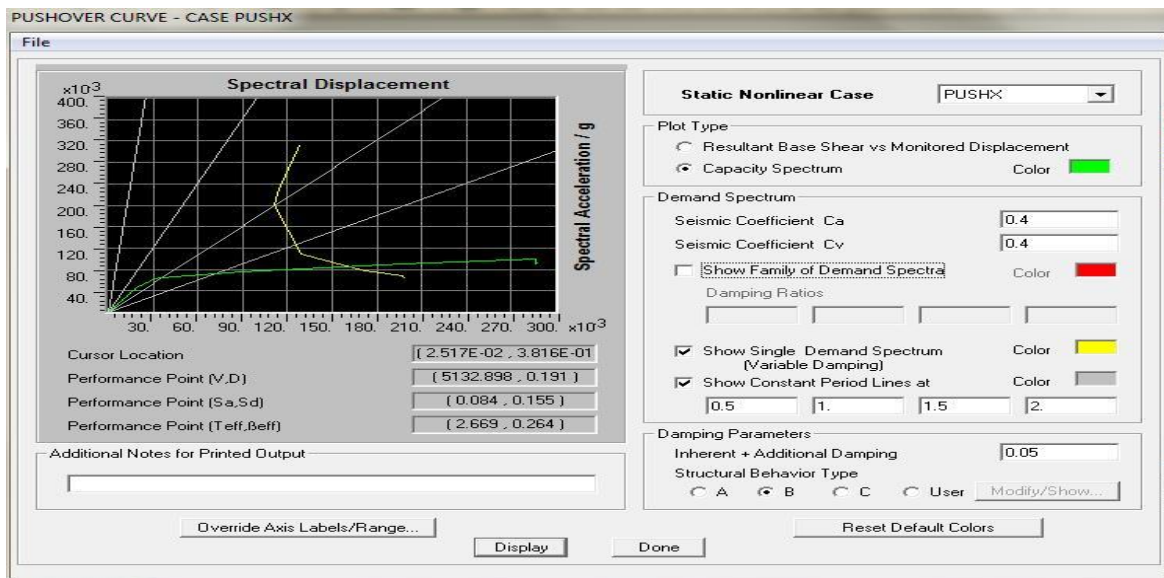


Figure:33 Performance point for Model-1 from ETAB 9.7.4

4.5 Performance levels

Table13: Data for Performance levels for 10 storey building Model-1

Step	Displacement	Base Force	A-B	B-IO	IO-LS	LS-CP	CP-C	C-D	D-E	>E	TOTAL
0	2.62E-05	0	4338	2	0	0	0	0	0	0	4340
1	0.0246	2839.8311	4010	330	0	0	0	0	0	0	4340
2	0.0408	3968.291	3884	456	0	0	0	0	0	0	4340
3	0.046	4107.5303	3717	480	143	0	0	0	0	0	4340
4	0.1084	4682.0269	3609	163	232	336	0	0	0	0	4340
5	0.2441	5418.3188	3542	126	154	488	0	30	0	0	4340
6	0.3595	5906.5449	3542	126	154	476	0	0	42	0	4340
7	0.3595	5358.1396	3542	126	154	466	0	10	42	0	4340
8	0.3615	5423.0996	3542	126	154	466	0	0	52	0	4340
9	0.3338	2407.7725	4340	0	0	0	0	0	0	0	4340

Table14: Data for Performance levels for 10 storey building Model-2

<i>Displacement</i>	<i>Base Force</i>	<i>A-B</i>	<i>B-IO</i>	<i>IO-LS</i>	<i>LS-CP</i>	<i>CP-C</i>	<i>C-D</i>	<i>D-E</i>	<i>&gt;E</i>	<i>TOTAL</i>
2.58E-05	0	4241	3	0	0	0	0	0	0	4244
0.0236	2602.5703	3977	267	0	0	0	0	0	0	4244
0.0364	3563.0684	3861	383	0	0	0	0	0	0	4244
0.0437	3832.4939	3734	510	0	0	0	0	0	0	4244
0.0787	4295.6494	3566	198	234	246	0	0	0	0	4244
0.2109	5130.2783	3488	163	131	462	0	0	0	0	4244
0.3347	5679.7065	3472	151	106	488	0	27	0	0	4244
0.3601	5780.4019	3472	151	106	480	0	0	35	0	4244
0.3406	3491.0718	4244	0	0	0	0	0	0	0	4244

Table15: Data for Performance levels for 10 storey building Model-3

<i>Step</i>	<i>Displacement</i>	<i>Base Force</i>	<i>A-B</i>	<i>B-IO</i>	<i>IO-LS</i>	<i>LS-CP</i>	<i>CP-C</i>	<i>C-D</i>	<i>D-E</i>	<i>&gt;E</i>	<i>TOTAL</i>
0	2.46E-05	0	4241	3	0	0	0	0	0	0	4244
1	0.0254	2770.2466	3933	311	0	0	0	0	0	0	4244
2	0.0397	3704.5022	3846	398	0	0	0	0	0	0	4244
3	0.0444	3876.3352	3618	208	418	0	0	0	0	0	4244
4	0.1666	4772.3354	3506	174	168	396	0	0	0	0	4244
5	0.2909	5356.1021	3486	127	176	448	0	7	0	0	4244
6	0.3539	5606.5405	3486	127	176	428	0	3	24	0	4244
7	0.35	4985.7607	4244	0	0	0	0	0	0	0	4244

### V. Conclusion

1. The results obtained in terms of pushover demand, capacity spectrum gave an insight into the real behaviour of structures.
2. The model with soft storey having greater storey drift rather than the model without soft storey.
3. The overall performance level for G+9 storey Building Models were found between B-IO.
4. The performance point is determined for G+9 storey Building Model-1 in PUSH X direction at  $S_a = 0.084, S_d = 0.155$ .
5. Storey Shear obtained from pushover analysis is much more greater than storey shear obtained from equivalent static analysis as shown in Table:7
6. Pushover curve is obtained by plotting displacement along X axis and base shear along Y axis which gives the non linear behaviour of considered model as shown in fig.27
7. Capacity of building is determined by capacity spectrum analysis.

### REFERENCES

#### Journal Papers:

- [1] Applied Technology Council (ATC-40) (1996) prepared a report on Seismic evaluation and retrofit of concrete buildings sponsored by California Safety Commission.
- [2] Ashraf Habibullah and Stephen Pyle, (Published in Structure Magazine, Winter, 1998)“Practical Three Dimensional Nonlinear Static Pushover Analysis”.
- [3] Federal Emergency Management Agency (FEMA 273) NEHRP GUIDELINES (1997) developed a set of technically sound, nationally applicable guidelines (with commentary) for the seismic rehabilitation of buildings.
- [4] Federal emergency management agency (FEMA 356), Nov 2000, is a report on Prestandard and commentary for the seismic rehabilitation of buildings prepared by American society of civil engineers.
- [5] IS 1893-2002(Part-1), “Criteria for Earthquake resistant design of structures”, General provisions and buildings, Bureau of Indian Standards, New Delhi.
- [6] Mrugesh D. Shah and Sumant, B. Patel, “Non-linear static Analysis of R.C. Frames”, (2011).
- [7] L. Teresa Guevara-Perez, Journal paper on “Soft Story” and “Weak Story” in Earthquake Resistant Design: A Multidisciplinary Approach
- [8] Amit V. Khandve, International Journal on “ Seismic Response of RC Frame Buildings with Soft Storeys”
- [9] Susanta Banerjee , International Journal on “Inelastic Seismic Analysis of Reinforced Concrete Frame Building with Soft Storey “
- [10] M.R. Amin ,prepared a journal on “Effect of soft storey on multistoried reinforced concrete building frame”

## Decoupled Inverter Fed - Open end Winding Induction Motor Drive for Three Level Voltage SPWM Strategy

Bukya. Balaji<sup>1</sup>, B. Venkateswarlu<sup>2</sup>, D. Jagan<sup>3</sup>

<sup>1,2</sup> Associate Professor/<sup>3</sup> Assistant Professor /Sri Sai Educational Society's Group of Institutions/JNTUH/T.S/INDIA

**Abstract:** An open-end winding induction motor, fed by two 2-level inverters connected at either end produces space vector locations, identical to those of a conventional 3-level inverter. In this paper, two switching algorithms are proposed to implement space vector PWM for the dual inverter scheme. The proposed algorithms do not employ any look-up tables. The time consuming task of sector identification is altogether avoided in both these algorithms. The proposed algorithms employ only the instantaneous reference phase voltages for the implementation of the space vector PWM. An equal switching duty for both the inverters is also ensured with one of the proposed PWM strategies. Also, it is observed that the speed torque and voltages in motor phases is significantly reduced with the proposed PWM strategies.

### I. Introduction

Three-level inversion has been extensively researched in the past and several circuit topologies were suggested. Of these topologies, the neutral point clamped topology [1], the flying capacitor topology [2] and the H-bridge topology [3] have become popular. Recently, a circuit configuration to obtain three-level inversion by cascading two 2-level inverters has also been suggested [7]. Stemmler's pioneering work has shown that three-level inversion can be achieved by the open-end winding connection of an induction motor with two two-level inverters feeding the motor from either end [4]. In this work [4], sine-triangular modulation technique is employed for the control of inverters. Various derivatives of this power circuit and/or the associated PWM schemes are also reported in the recent past [6]-[14]. The inverters may be controlled with space vector modulation technique as it improves the DC-bus utilization compared to the sine-triangle modulation technique. A space vector modulation technique for the open-end winding topology has been suggested in [6]. In this work [6], the implementation of space vector modulation requires sector identification, which is a time consuming task. Further, this switching scheme employs lookup tables, enhancing the memory requirement with a typical Digital implementation.

In this paper, two space vector modulation techniques are suggested, which obviate the need for the sector identification. Also these PWM schemes do not employ any look-up table, thus reducing the memory requirement.

This section gives a general background and review of the paper or work done by other engineers in the field. It should be well supported by citations. Moreover, the citations are served as a guide for those who want to learn more about the field.

Fig.1 shows the basic open-end winding induction motor drive operated with a single power supply. The symbols  $v_{BO}$ ,  $v_{AO}$ , and  $v_{CO}$  denote the pole voltages of the inverter-1. Similarly, the symbols  $v_{A'O}$  and  $v_{B'O}$  denote the pole voltages of inverter-2. The space vector locations from individual inverters are shown in Fig.2. The numbers 1 to 8 denote the states assumed by inverter-1 and the numbers 1' through 8' denote the states assumed by inverter-2 (Fig.2).

Table-1 summarizes the switching state of the switching devices for both the inverters in all the states. In Table-1, a '+' indicates that the top switch in a leg of a given inverter is turned on and a '-' indicates that the bottom switch in a leg of a given inverter is turned on.

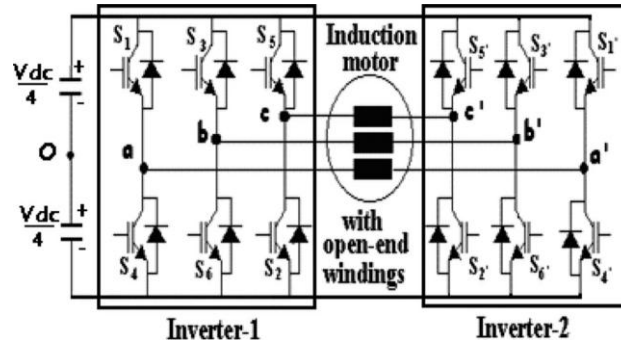


Fig1: The primitive open end winding induction motor drive

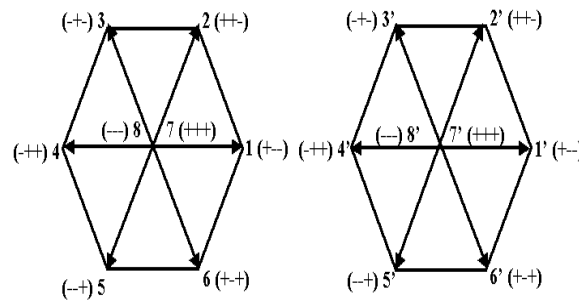


Fig 2: Space vector locations of inverter-1 (Left) and inverter-2 (Right)

As each inverter is capable of assuming 8 states independently of the other, a total of 64 space vector combinations are possible with this circuit configuration. The space vector locations for all space vector combinations of the two inverters are shown in Fig.3. In Fig.3,  $|OA|$  represents the DC-link voltage of individual inverters, and is equal to  $V_{dc}/2$  while  $|OG|$  represents the DC-link voltage of an equivalent single inverter drive, and is equal to  $V_{dc}$ .

Fig.1 shows the basic open-end winding induction motor drive. It cannot be operated with a single power supply, due to the presence of zero-sequence voltages (common-mode voltages) [5], [6]. Consequently, a high zero-sequence current would flow through the motor phase windings, which is deleterious to the switching devices and the motor itself. To suppress the zero-sequence components in the motor phases, each inverter is operated with an isolated dc- power supply as shown in Fig.4. From the Fig.4, when isolated DC power supplies are used for individual inverters, the zero-sequence current cannot flow as it is denied a path. Consequently, the zero-sequence voltage appears across the points 'O' and 'O'''. The zero-sequence voltage resulting from each of the 64 space vector combinations is reproduced in from [6] to facilitate an easy reference.

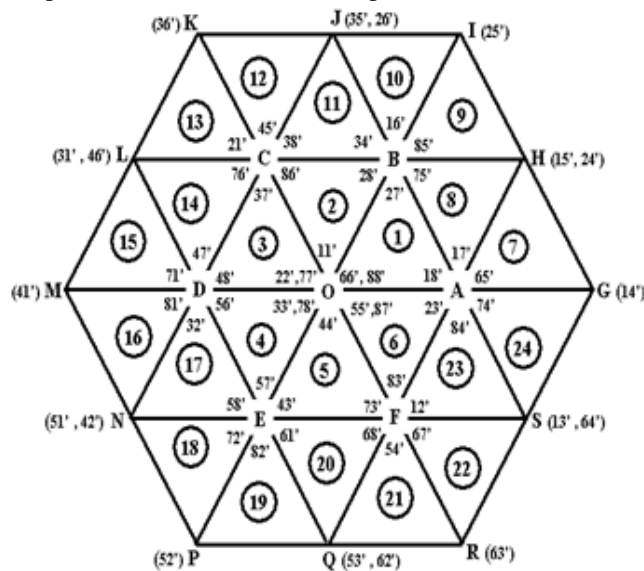


Fig 3: Resultant space vector combinations in the dual-inverter scheme

In Fig.5, the vector OT represents the reference vector (also called the reference sample), with its tip situated in sector-7 (Fig.3). This vector is to be synthesized in the average sense by switching the space vector combinations situated in the closest proximity (the combinations situated at the vertices A, G and H in the present case) using the space vector modulation technique. In the work reported in reference [7], the reference vector OT is transformed to OT' in the core hexagon ABCDEF by using an appropriate coordinate transformation, which shifts the point A to point O. In the core hexagon, the switching timings of the active vectors OA, OB and the switching time of the null vector situated at O to synthesize the transformed reference vector OT' are evaluated. The switching algorithm described in reference [5] is employed to evaluate these timings. These timings are then employed to produce the actual reference vector OT situated in sector-7 by switching amongst the switching.

Table – 1: Switching states of the individual inverters

State of Inverter-1	Switches turned on	State of Inverter-2	Switches turned on
1 (+ - -)	S <sub>6</sub> , S <sub>1</sub> , S <sub>2</sub>	1' (+ - -)	S <sub>6</sub> , S <sub>1</sub> , S <sub>2</sub> '
2 ( + + -)	S <sub>1</sub> , S <sub>2</sub> , S <sub>3</sub>	2' ( + + -)	S <sub>1</sub> ', S <sub>2</sub> ', S <sub>3</sub> '
3 ( - + -)	S <sub>2</sub> , S <sub>3</sub> , S <sub>4</sub>	3' ( - + -)	S <sub>2</sub> ', S <sub>3</sub> ', S <sub>4</sub> '
4 ( - + +)	S <sub>3</sub> , S <sub>4</sub> , S <sub>5</sub>	4' ( - + +)	S <sub>3</sub> ', S <sub>4</sub> ', S <sub>5</sub> '
5 ( - - +)	S <sub>4</sub> , S <sub>5</sub> , S <sub>6</sub>	5' ( - - +)	S <sub>4</sub> ', S <sub>5</sub> ', S <sub>6</sub> '
6 ( + - +)	S <sub>5</sub> , S <sub>6</sub> , S <sub>1</sub>	6' ( + - +)	S <sub>5</sub> ', S <sub>6</sub> ', S <sub>1</sub> '
7 ( + + +)	S <sub>1</sub> , S <sub>3</sub> , S <sub>5</sub>	7' ( + + +)	S <sub>1</sub> ', S <sub>3</sub> ', S <sub>5</sub> '
8 ( - - -)	S <sub>2</sub> , S <sub>4</sub> , S <sub>6</sub>	8' ( - - -)	S <sub>2</sub> ', S <sub>4</sub> ', S <sub>6</sub> '

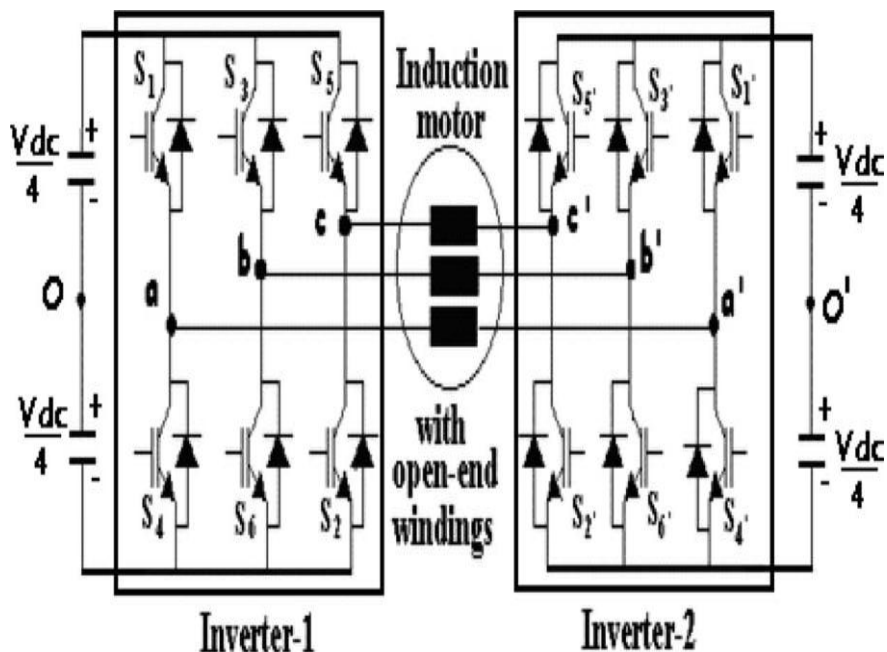
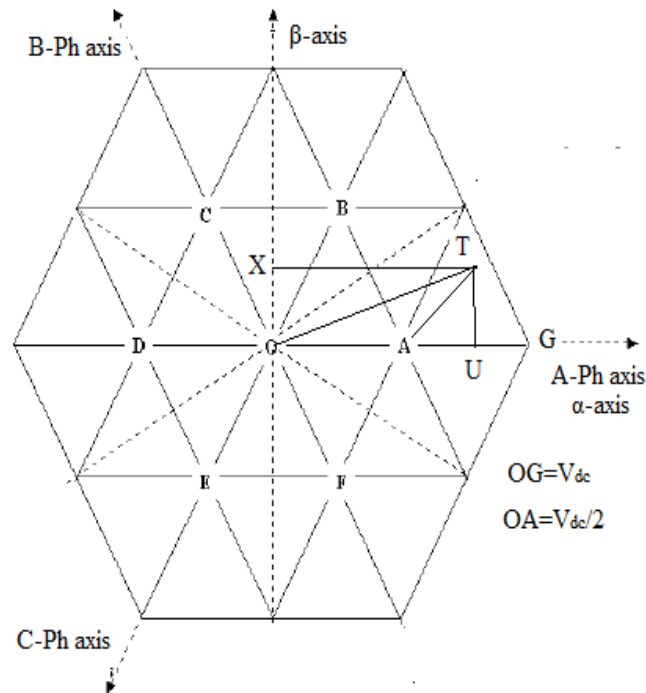


Fig 4: A dual-inverter fed open-end winding induction motor drive with isolated power supplies



**Fig 5: Principle of biasing inverter PWM strategy**

## II. Simulation Of The Proposed Scheme

The Simulation is carried out using MATLAB and the results are verified by implementing the decoupled scheme through dual two level inverters on a 1kW Open end winding Induction motor drive.

The proposed Scheme involves two, two level Inverters which are collectively feeding the open ended winding of the induction motor by proportionately dividing the reference voltage among themselves. Here lies an important difference between the proposed method and the one used in the conventional SVPWM scheme.

In the present case the pole voltages are separately consumed from each inverter which is enabled to realize half of the reference voltage and then difference among of both these pole voltages is captured which serves as a phase component and is thus fed to the induction motor phases. Where as in the equivalent conventional scheme (i.e. a scheme in which a single two level inverter feeds a motor), the pole voltages of the inverter are initially converted into phase voltages and then these are fed to the three phases of the induction motor.

The block representation of the proposed scheme and that of a conventional SVPWM scheme is as shown in. The powerful block represented in both these schemes is used to carry out the FFT analysis.

When the induction motor is fed from the corresponding phase voltages then the output phase currents and the torque & speed parameters are separately consumed from which the current harmonics are analyzed with each other.

The d-q model of a three phase Induction motor in a stationary frame is represented as shown in the Fig (6) from which the proposed scheme is analyzed.

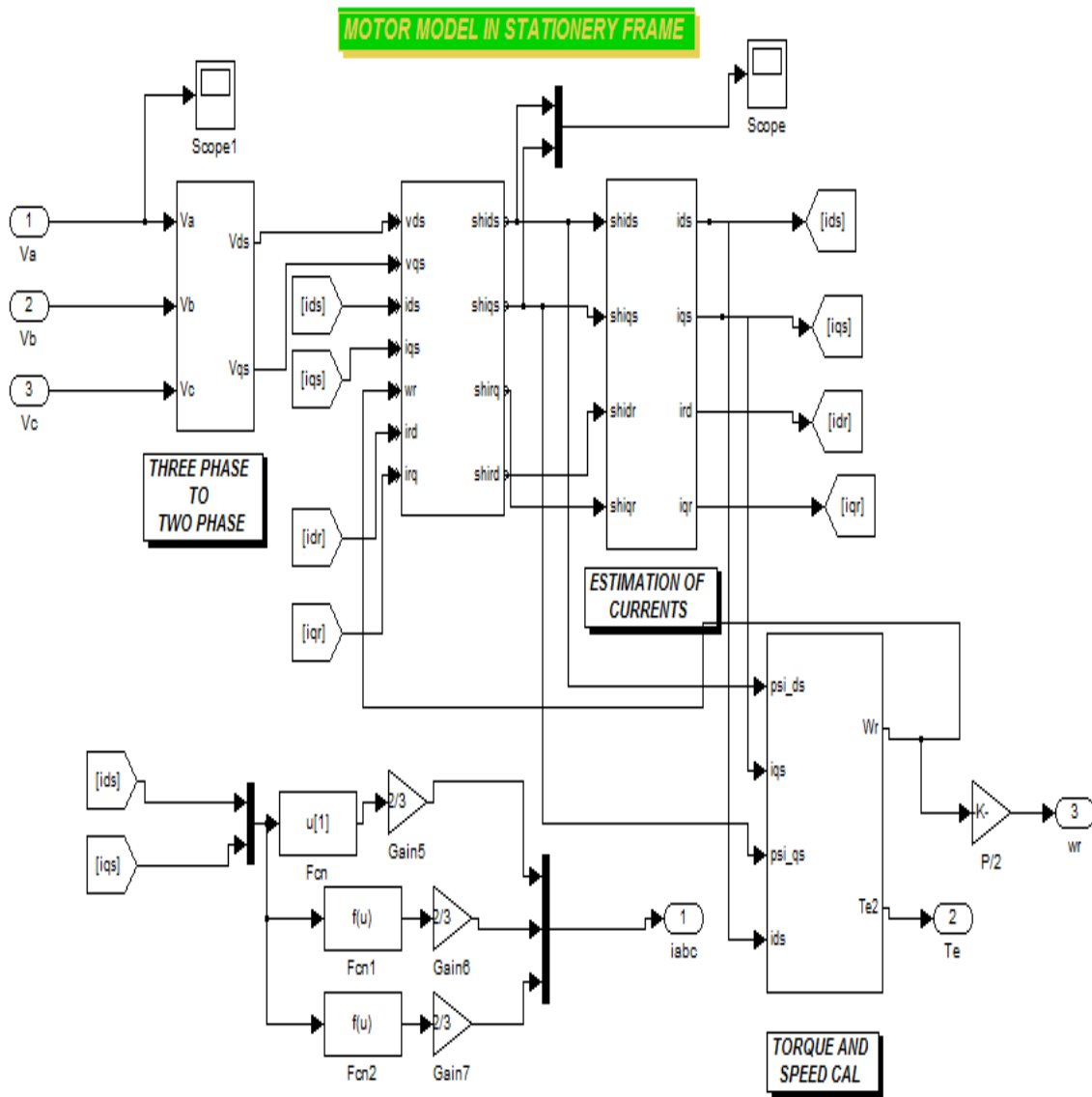


Fig 6 : Proposed model of the Induction motor

### III. Generation Of Gating Pulses

The Gating pulses for both the inverters are generated by a m-file program separately and the corresponding pole voltages are obtained for the respective inverters and the difference in these pole voltages are fed to the three phases of a 1kW open end winding Induction Motor.

The input motor parameters are initialized accordingly and are provided to the motor before they are fed from the inverters.

The generation of gating pulses is accomplished by the proposed scheme whose diagrammatical representation is as shown in the figure (7), where three reference sinusoidal signals with a phase difference of  $120^\circ$  are used which are instantly converted to two phases from three phase to two phase transformation or by using functional block (embedded with transformation commands within).

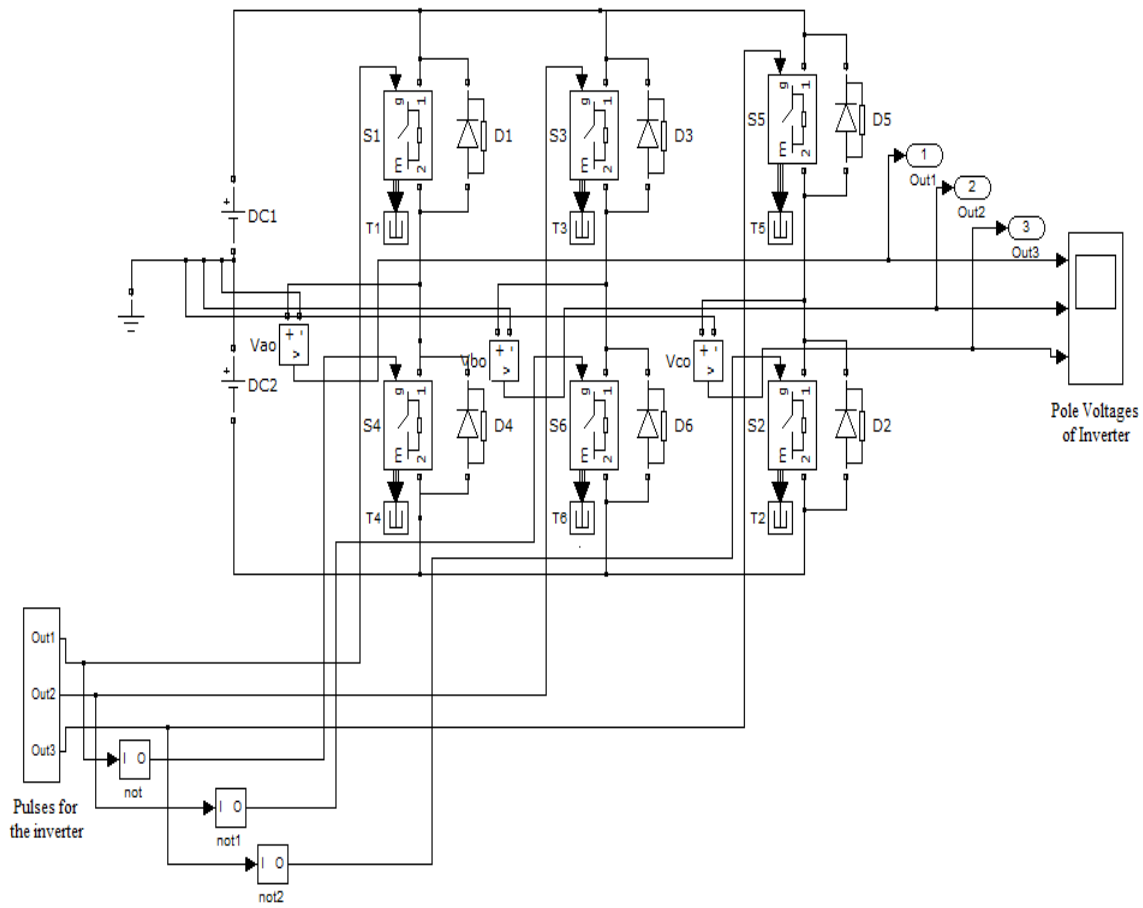


**Fig 7: Generated gating signals fed to the inverter.**

Then with the use of “Cartesian to polar” block the magnitude and the phase parameters are separated and are fed to “MATLAB fcn” block along with the timing factor. This block is the one where an “M-file program” is embedded for the generation of gating pulses which takes into account the magnitude, angle of the reference vector and its time.

Thus the three gating signals are generated from a M-file program and these are meant to be fed to the top switches of each of the inverter’s leg and the bottom switches are fed with the gating signals which are negotiated (reversed) from the former, which accompanies a fact that either one of the switch (top/bottom) is turned-on in one instant. Hence with this method all the six gating signals are generated and fed to the appropriate switches of the inverter as shown in figure (7).

#### IV. Simulation Results

The gating pulses are thus generated by the use of a m-file program separately for both the inverters and from the present scheme of generation it is designed ought to get the gating pulses along with the sector number for the prescribed inverter. So a diagrammatical representation of these pulses and their respective sector number is as shown in the figure (8)

These Gating pulses generated by use of the program stands to be common for both the cases i.e. for a dual two level inverter scheme and for a conventional single inverter scheme.

In the Dual inverter scheme the m-file program for the other inverter will be designed in such a way that the other inverter realizes the other half reference vector whose phase will be shifted 180° from the original reference vector (as discussed in chapter 3).The gating pulses generated from the proposed scheme will be negotiated and all these six pulses will be provided for the switches of Inverter as shown in Fig (9)

These gating pulses from the propose generating schemes are fed to inverter-1 and inverter- 2 and their corresponding pole voltages are as shown in fig (10) respectively.

The difference in these pole voltages is obtained and the resultant is given to the three phase of open end winding induction motor. The voltage difference thus captured is shown in figure (11).

A similar procedure is followed in the case of a conventional Single inverter scheme for the generation of gating pulses. Thus the so obtained pole voltages from the single two level inverter are converted to phase voltages and are then fed to the Induction motor. The simulated pole voltages and the converted neutralized phase voltages are shown in the Fig's (12) and (13) respectively.

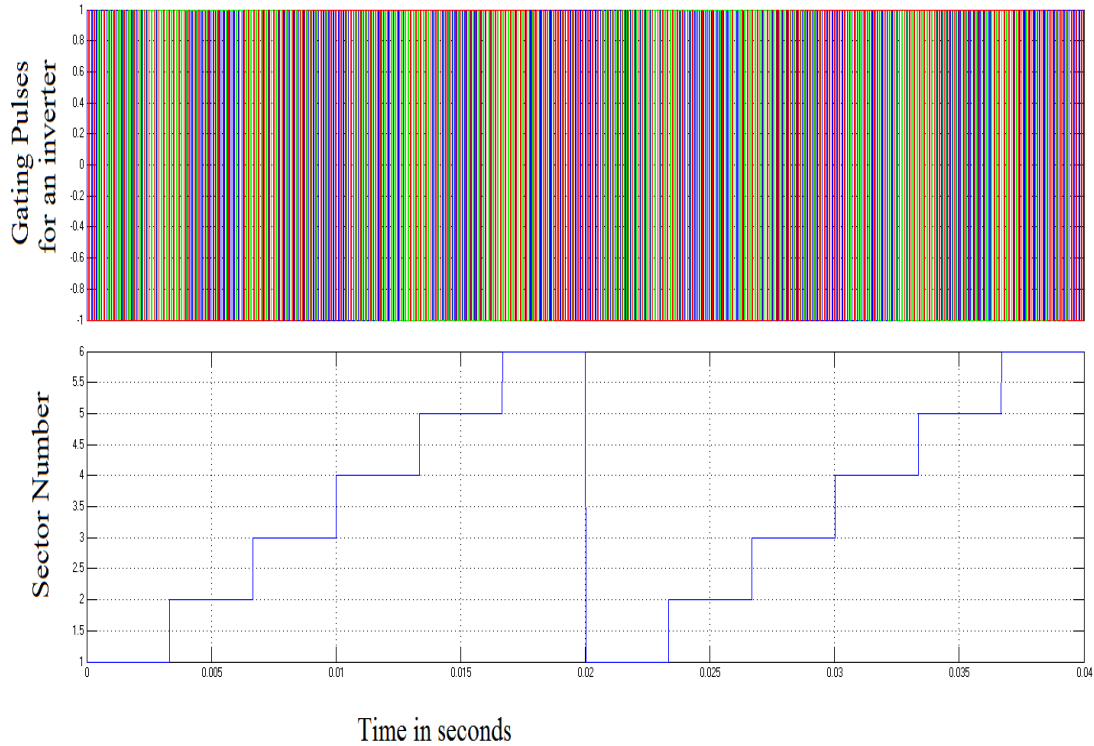


Fig 8: Combined Gating Pulses for all the sectors of an Inverter

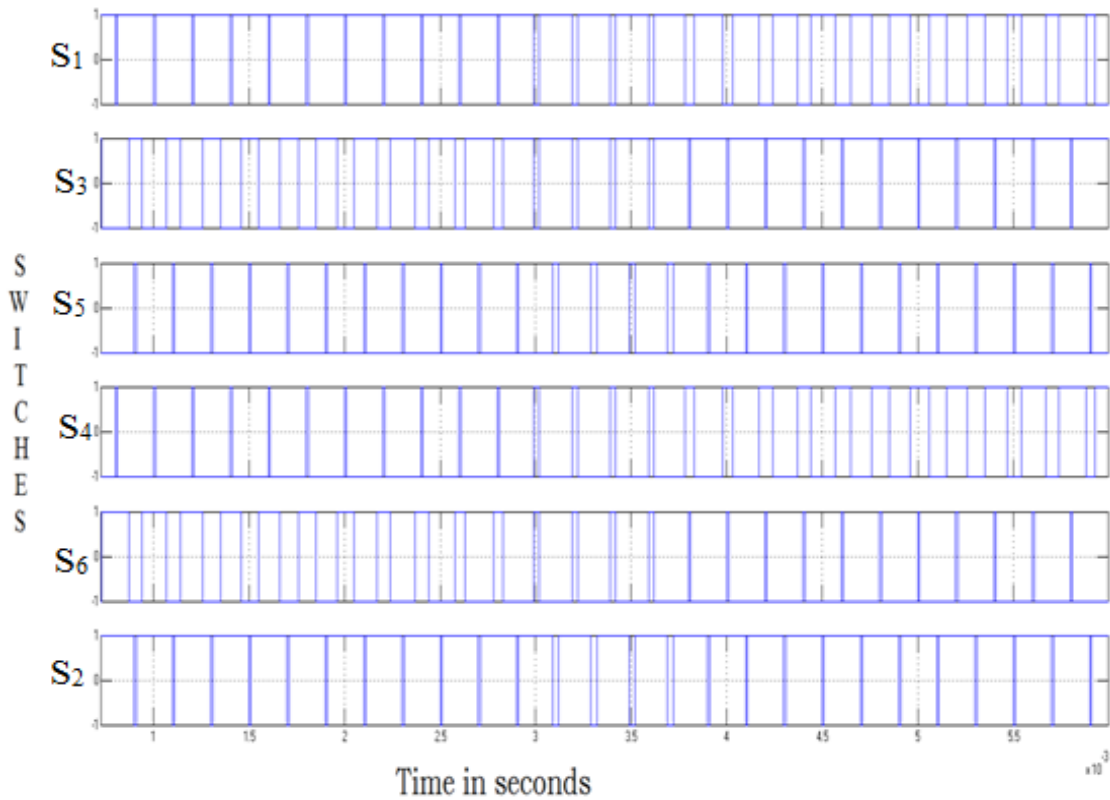
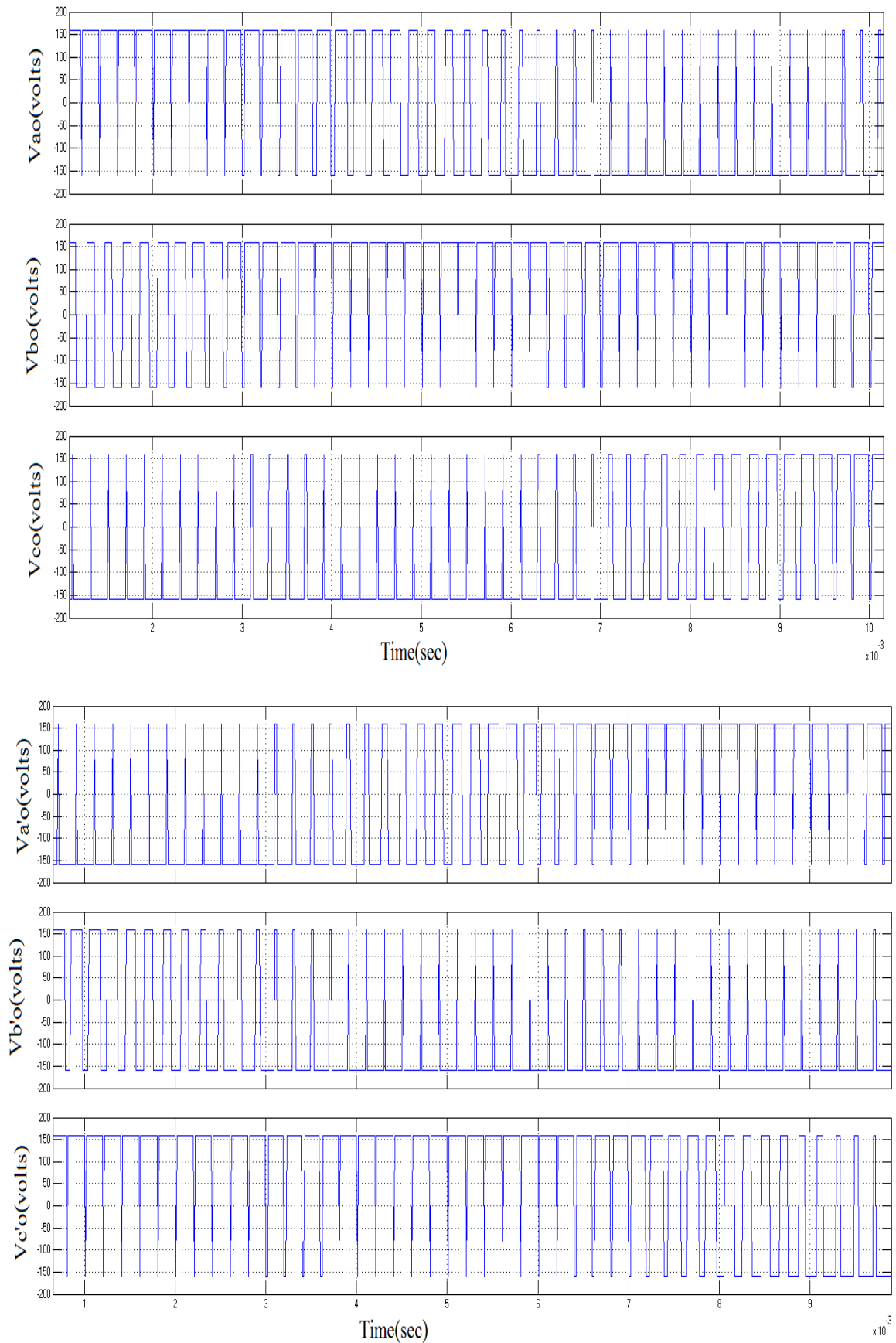


Fig 9: Gating Pulses For the Inverter



**Fig 10: Pole Voltages for Inverter-1(top trace) and Inverter-2(bottom trace).**

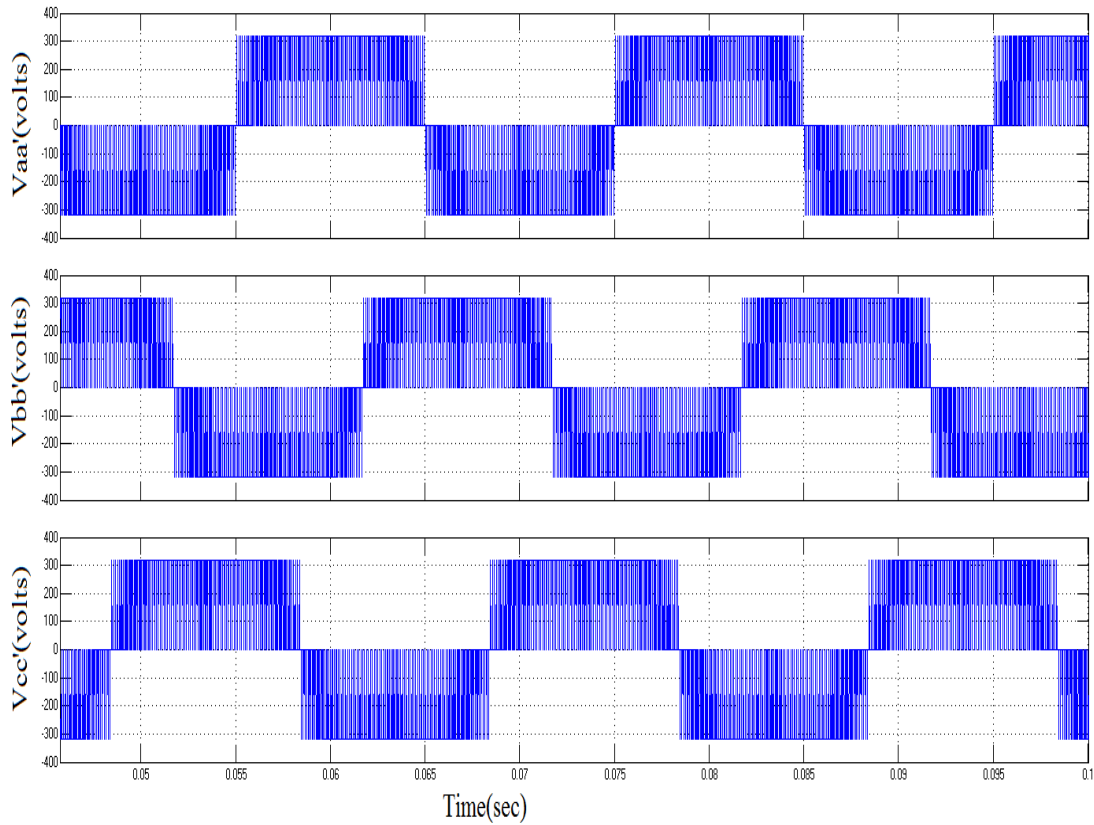


Fig 11: Difference in the pole voltages from both the inverters

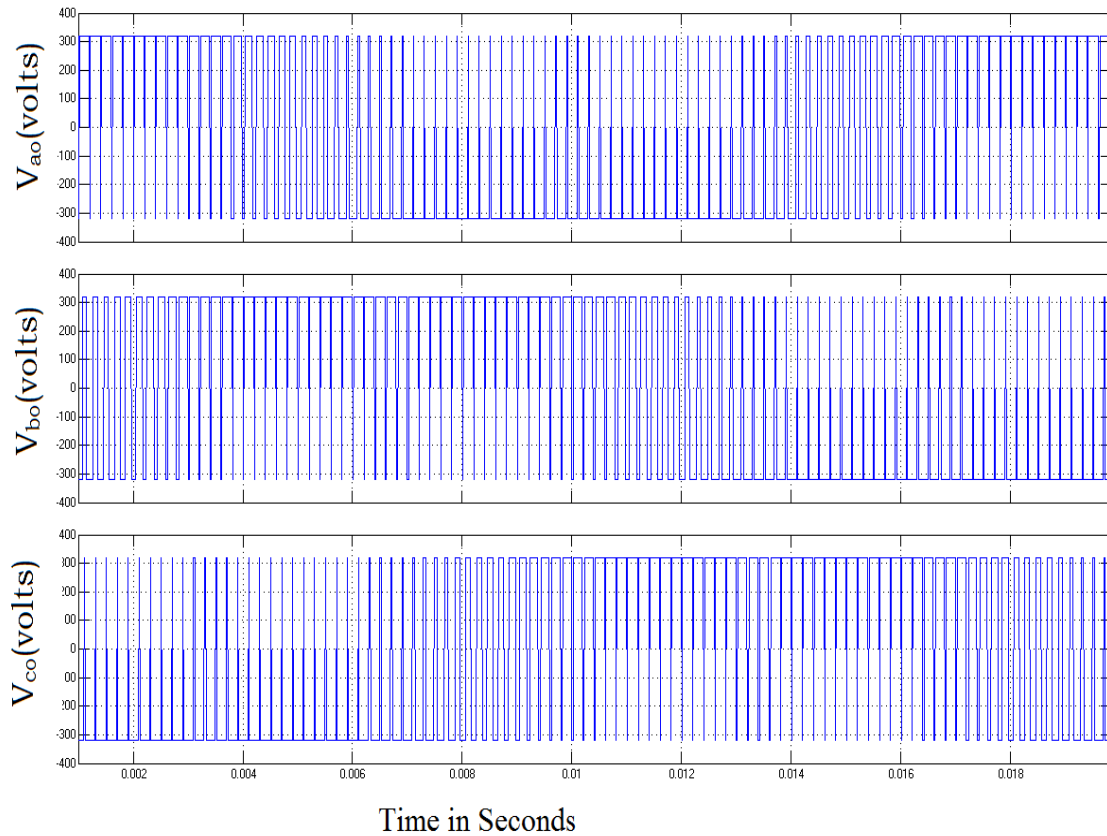


Fig 12: Pole Voltages of a conventional Single two level inverter

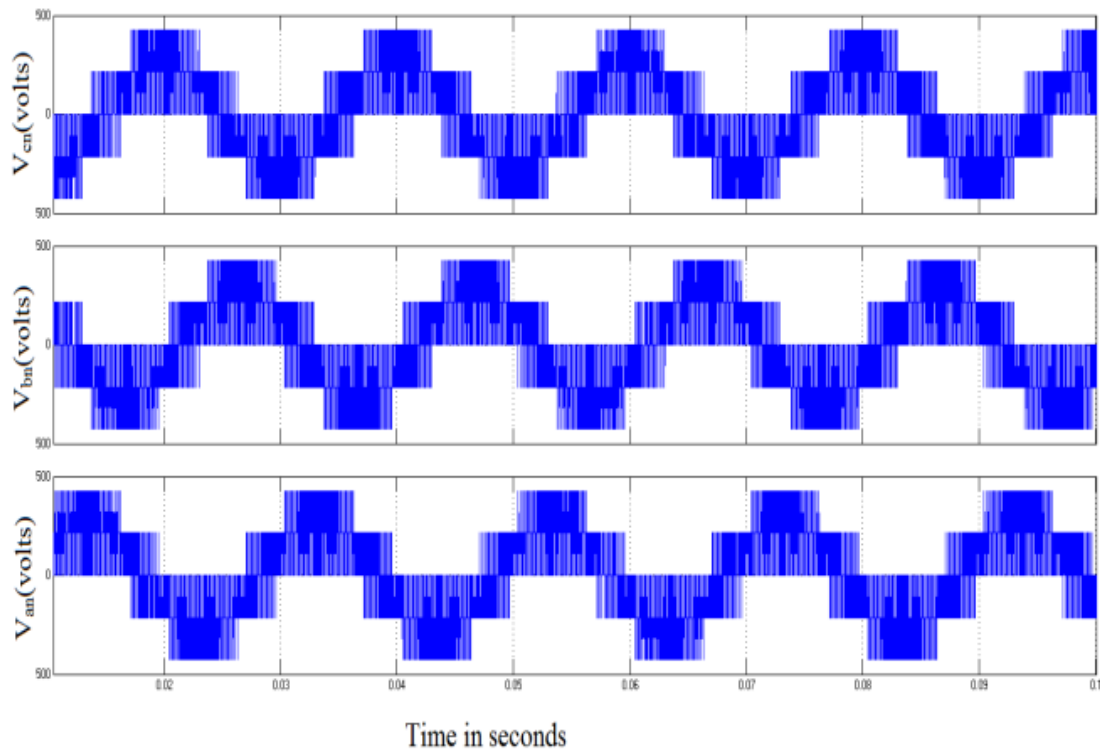
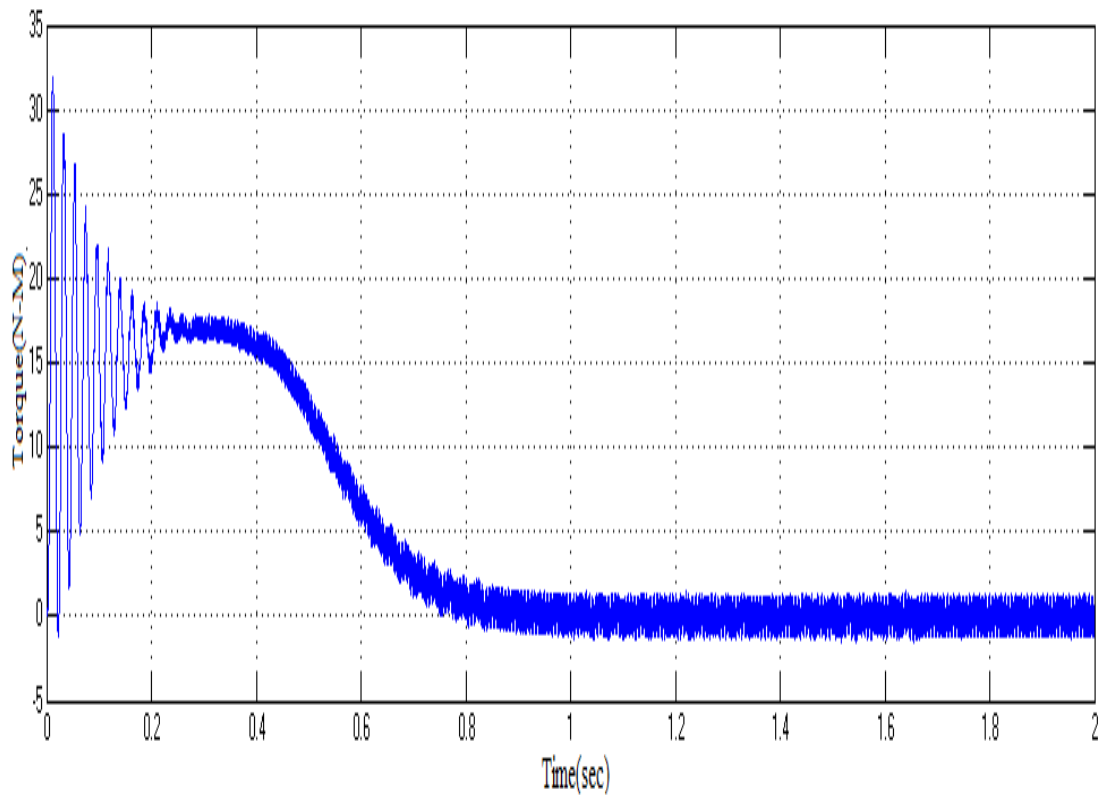
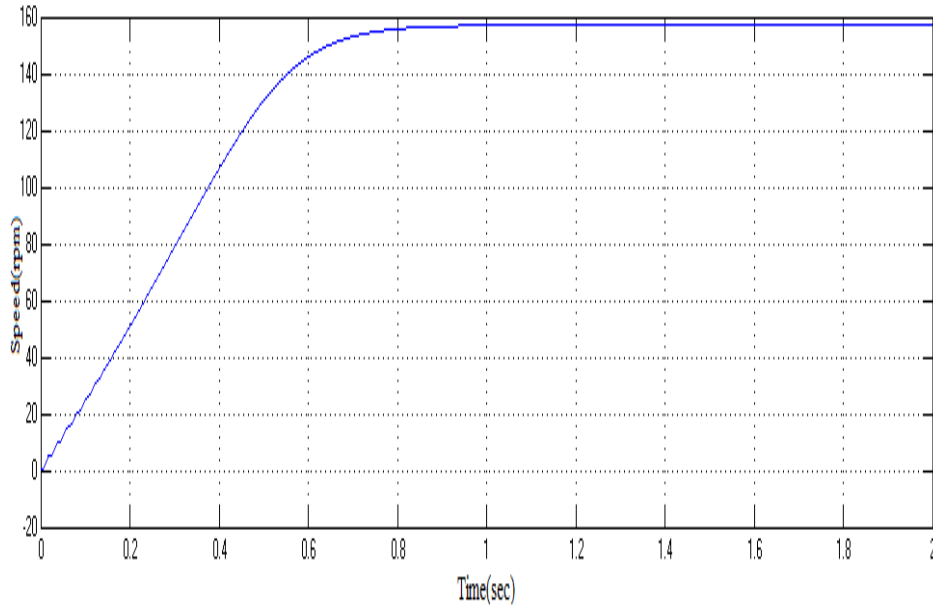


Fig 13 Converted pole to neutralize phase voltages from a Inverter





**Fig 14: Torque and Speed of the induction motor for modulation index 0.75**

Fundamental (50Hz) = 1.951 , THD= 10.84%

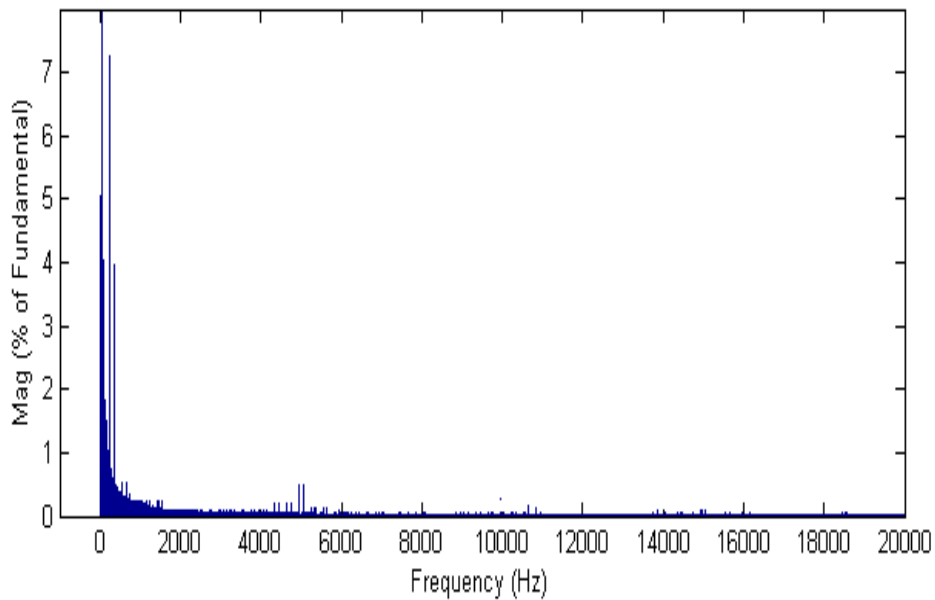


**Fig 15: %THD of Induction motor drive for a modulation index of 0.75**

S.No	Operating Frequency	Modulation Index	Biasing Inverter PWM Fed Induction Motor Drive
			Phase Current(I <sub>a</sub> )
			% THD
1	50	0.1	13.25
2	50	0.21	13.01
3	50	0.45	12.17
4	50	0.75	9.84
5	50	0.85	8.28

## V. Conclusion

In this project a dual two-level inverter capable of generating three level output voltage using the PWM switching scheme is simulated using MATLAB/SIMULINK. With the biasing inverter PWM strategy the reference space vector is synthesized in the average sense by switching amongst the vector combinations available at the nearest three vertices. The time consuming process of sector identification and the Look-up tables are not needed with the proposed PWM strategy. The rms value of this harmonic content is decreasing with the increase in the modulation index of the dual-inverter feeding with the open-end winding induction motor. The higher modulation index range of 0.85 the harmonic content in the phase currents is low.

## REFERENCES

- [1] R.M. Green and J.T. Boys, "Implementation of Pulse width Modulated Inverter Modulation Strategies", IEEE Trans. on Ind. Appl. Vol. IA-18, No.2, Mar/Apr.1982, pp.138 - 145.
- [2] Leon M.Tolbert, Fang Zheng Peng and Thomas G. Habetler, "Multilevel Converters for Large Electric Drives," IEEE Trans. on Industry Appl. vol.35, no.1, Jan/Feb 1999, pp.36 - 44.
- [3] J. Rodriguez, J. S. Lai, and F. Z. Peng, "Multilevel Inverters: A Survey of topologies, Controls, and Applications," IEEE Trans. on Ind. Electronics, Vol 49, No.4, August 2002, pp.724 - 738.
- [4] Muhammad H. Rashid, "Power Electronics Circuits, Devices and applications", Pearson Education publications, 2009, Third edition.
- [5] J. Holtz, "Pulse width modulation- A survey", IEEE Trans. on Industrial Electronics, Vol. 30, No. 5, Dec 1992, pp. 410-420.
- [6] Vladimir Blasko, "Analysis of a Hybrid PWM based on Modified Space-Vector and Triangle-Comparison Methods", IEEE Trans. on Ind. Appl., Vol.33, No.3, May/June, 1997, pp. 756-764.
- [7] G.Narayanan, Di Zhao and Harish K.krishnamurthy, "Space vector based hybrid PWM technique for reduced current ripple", on Ind. Electronics, Vol.55, No.4, April 2008, pp.1614 - 1627.
- [8] V.T.Somasekhar, K.Gopakumar, A.Pittet and V.T.Ranganathan, "PWM inverter switching strategy for a dual two-level inverter fed open end winding induction motor drive with a switched neutral", IEE Proc. Of Electr. Power Appl., vol.149, No.2, March 2002, pp.152-160.
- [9] M. R. Baiju, K. K. Mohapatra, R. S. Kanchan and K. Gopakumar, "A Dual Two-level Inverter Scheme with common Mode Voltage Elimination for an Induction Motor Drive", IEEE Trans. on Power Electronics. Vol.19, No.3, May 2004, pp.794-805.
- [10] Somasekhar, V.T., and Srinivas, S.: 'Switching algorithms for a dual inverter fed open-end winding induction motor drive'. Conf. Proc. IEEE-IICPE, Mumbai, India, 2004.
- [11] Akira Nabae, Isao Takahashi and Hirofumi Akagi, "A Neutral-Point Clamped PWM Inverter", IEEE-Trans. on Ind. Appl. Vol. IA-17, No.5, Sep/Oct 1981, pp.518-523.
- [12] A.M.Hava, R.J.Kerkman and T.Lipo, "A high-performance generalized discontinuous PWM algorithm", IEEE Trans. on Ind. Appl., Vol.34, Spt/Oct.1998, pp. 1059-1071.
- [13] V.T.Somasekhar, S.Srinivas & K.Kranti Kumar, "Effect of Zero-Vector Placement in a Dual-Inverter fed Open-end winding Induction Motor Drive with a Decoupled Space Vector PWM Strategy" IEEE Trans. On Indus. Electronics, Vol.55, No.6, June-2008, pp.2497-2505.
- [14] S.Srinivas and V.T.Somasekhar, "A New Alternate-Inverter PWM Switching Strategy for reducing the Common-mode Voltages for a Dual-Inverter fed Open-end winding Induction motor Drive", Conf. Proc. IPEC-2005, Niigata, Japan, pp.1460-1465.
- [15] E.G. Shivakumar, K.Gopakumar, S.K. Sinha, Andre Pittet, V.T. Ranganathan, "Space Vector Control of Dual Inverter Fed Open-end Winding Induction Motor Drive", EPE Journal, Vol.12, No.1, Feb 2002, pp.9 -18.
- [16] R.S.Kanchan, P.N.Tekwani, M.R.Baiju, K.Gopakumar and A.Pittet, "Three-level inverter configuration with common-mode voltage elimination for induction motor drive", IEE Proc. of Electr. Power Appl., Vol.152, No.2, March-2005, pp. 261-270.
- [17] D. G. Holmes, "The significance of Zero-Space Vector placement for Carrier-based PWM schemes", IEEE Trans. on Ind. Appl., vol.32, No.5, Sept-Oct 1996, pp. 1122-1129.
- [18] K.Basu, J.S.Siva Prasad and G.Narayanan, "Minimization of torque ripple in PWM AC Drives", IEEE-Trans. on Ind. Electronics, Vol. 56, No.2, February 2009, pp.553 - 558.
- [19] Dae-Woong Chung, Joohn-Sheok Kim and Seung-Ki Sul, "Unified Voltage Modulation Technique for Real-Time Three-Phase Power Conversion", IEEE-Trans. on Ind. Appl, Vol.34, No.2, March/April 1998, pp.374-380.
- [20] Y. Kawabata, M. Nasu, T. Nomototo, E. C. Ejiogu, and T. Kawabata, "High efficiency and low acoustic noise drive system using open-end winding AC motor and two space-vector-modulated inverters," IEEE Trans. Ind. Electron., vol. 49, no. 4, pp. 783-789, Aug. 2002.

## BIOGRAPHIES



**B. Balaji** received the B. Tech degree in Electronics & Communication Engineering from JBIET college in JNTU Hyderabad and his Masters degree from NCET College-Kakinada in 2003 and 2009 respectively. He is currently working as Associate Professor in Sri Sai Educational Society's Group of Institutions His interests are multi-level inverters, PWM Switching Strategies, Multi-level inversion realized through Open-end winding Induction motor drives, AC drives etc.



**B. Venkateswarlu** received the B. Tech degree in Electrical Engineering from KMCET college in JNTU Hyderabad and his Masters degree from CMR College-hyd in 2006 and 2010 respectively. He is currently working as Associate Professor in Sri Sai Educational Society's Group of Institutions His interests are multi-level inverters, PWM Switching Strategies, Multi-level inversion realized through Open-end winding Induction motor drives, AC drives etc.



**D. Jagan** received the B. Tech degree in Electrical Engineering from vathsalya college in JNTU Hyderabad, T.S and his Masters degree from RGM College-Nandyala, A.P in 2010 and 2013 respectively. He is currently working as Assistant Professor in Sri Sai Educational Society's Group of Institutions. His current interests are multilevel inversion with open-end induction motors, AC drives and PWM strategies.

# Transient Stability Assessment and Enhancement in Power System

Aysha P. A<sup>1</sup>, Anna Baby<sup>2</sup>

<sup>1,2</sup> Department of Electrical and Electronics, ASIET Kalady, India

**Abstract:** Power system is subjected to sudden changes in load levels. Stability is an important concept which determines the stable operation of power system. For the improvement of transient stability the general methods adopted are fast acting exciters, circuit breakers and reduction in system transfer reactance. The modern trend is to employ FACTS devices in the existing system for effective utilization of existing transmission resources. The critical clearing time is a measure to assess transient instability. Using PSAT, the critical clearing time (CCT) corresponding to various faults are calculated. The most critical faults were identified using this calculation. The CCT for the critical faults were found to change with change in operating point. The CCT values are predicted using Artificial Neural Network (ANN) to study the training effects of ANN. TCSC is selected as the FACTS device for transient stability enhancement. Particle Swarm Optimization method is used to find the optimal position of TCSC using the objective function real power loss minimization. The result shows that the technique effectively increases the transient stability of the system.

**Keywords:** Artificial Neural Network, Critical Clearing Time, Particle Swarm Optimization.

## I. INTRODUCTION

Power system networks grow rapidly and continuously with a large number of interconnections. The complicated structure of such network has exposed the system to various contingencies that could lead to system instabilities: steady-state, dynamic or transient. Transient stability analysis is important in evaluating the network's ability to regain an acceptable state of equilibrium after being subjected to either large or small disturbances [1]. The stability characteristic of a power system is analysed from the nature of the set of differential equations when subjected to disturbances [8].

An electric power system is a network of electrical components used to supply, transmit and use power. With the wide access of renewable energy, power system is becoming increasingly complicated, and thus the calculation of transient stability limits is more significant. The development and use of accurate methods to predict the transient stability is crucial in preventing such conditions and therefore of special interest in the field of power system protection and planning. The critical clearing time (CCT) of three-phase fault is an important parameter which shows the transient stability limit of power system. CCT can be used as the indicator to transient stability assessment and artificial neural network is currently a research topic in the field of power system security. The critical faults of a power system can be identified using CCT. Thyristor Controlled Series Capacitor (TCSC) is one of the most effective FACTS devices which are increasingly used nowadays in stressed transmission systems. TCSC can enhance the stability, improve the dynamic characteristics of power system, and increase the transfer capability of the transmission system by reducing the transfer reactance between the buses at which the line is connected. However the effectiveness of TCSCs depends importantly on their locations and sizes in power system. The prediction, identification and avoidance of transient instability points play a significant role in power systems planning and operation.

## II. SYSTEM OVERVIEW

Power System Analysis Toolbox (PSAT) was used for the transient stability analysis of the test system. PSAT is an open source Matlab package for analysis and design of small to medium size electric power systems[17]. PSAT includes power flow, continuation power flow, optimal power flow, small-signal stability analysis, and time-domain simulation, as well as several static and dynamic models, including non conventional loads, synchronous and asynchronous machines, regulators, and FACTS. PSAT is also provided with a complete set of user-friendly graphical interfaces and a Simulink-based editor of one-line network diagrams.

For the transient stability study, we consider New England 10-machine 39-bus test system. The single line diagram of the test system is shown in figure below:

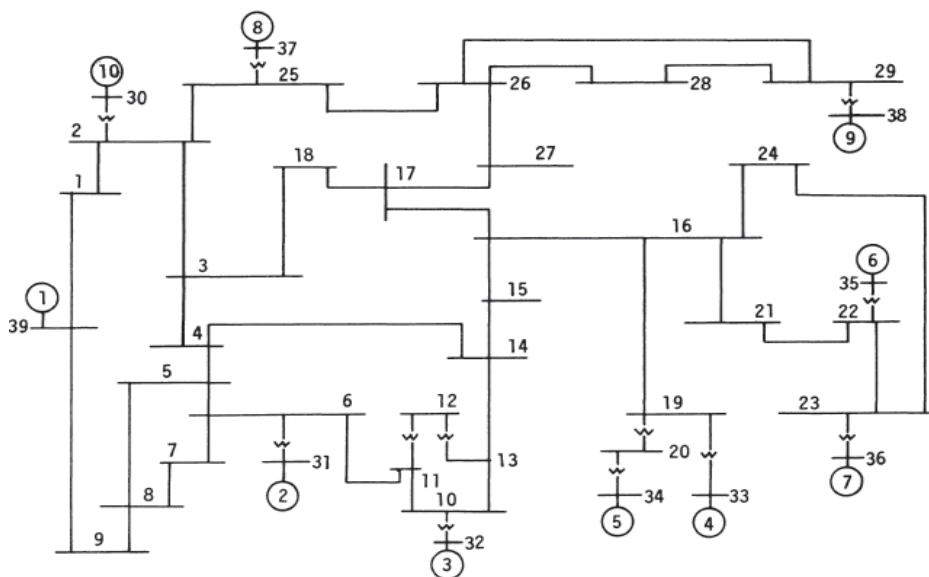


Figure 1: Single line diagram of IEEE 39 bus system

The IEEE 39 Bus (New England) power system is an equivalent power system of subsystems of the New England area and Canada. It consists of 39 Buses of which 10 Buses are generator Buses, 12 transformers, 10 generators, 34 transmission lines, and 19 loads.

Static data for the New England 39 bus test system along with dynamic data for its generators as well as their exciters and AVRs can be found in Ref. [5]. In PSAT, the synchronous machines are initiated after power flow computations. A PV or a slack generator is required to impose the desired voltage and active power at the machine bus. The voltage ratings of all system equipments in kV need to be specified in PSAT.

### III. TRANSIENT STABILITY ASSESSMENT

If the relationship between system operating conditions and system stability is reached, by training neural network, the network model should be used to assess online transient stability. For on-line transient stability assessment, CCT is chosen as an accurate indicator of transient stability margin. The fast calculation of CCT is also necessary for on-line stability assessment.

Application of Artificial Neural Network (ANN) to the above-mentioned problem has attained increasing importance mainly due to the efficiency of present day computers. Moreover real-time use of conventional methods in an energy management center can be difficult due to their significant large computational times. One of the main features, which can be attributed to ANN, is its ability to learn nonlinear problem offline with

selective training, which can lead to sufficiently accurate online response. The ability of ANN to understand and properly classify such a problem of highly non-linear relationship has been established in most of the papers and the significant consideration is that once trained effectively ANN can classify new data much faster than it would be possible with analytical model.

The neurons are assumed to be arranged in layers, and the neurons in the same layer behave in the same manner. All the neurons in a layer usually have the same activation function. The neuron in one layer can be connected to neuron in another layer. The arrangement of neurons into layers and the connection pattern within and between layers is known as network architecture. The architecture of a developed network consists of input layer, one hidden layer, and one output layer.

Time domain simulation method is used in this work to assess the transient stability of the power system because it is the most reliable, mature and accurate method compared to other method. The differential equations to be solved in transient stability analysis are non-linear ordinary equations with known initial values.

In this work, the dynamic performance of the system during disturbances is based on observation of the rotor angle of generators via a time domain simulation method. Three-phase faults are created at various locations in the systems at any one time. In this aspect, the power system goes through pre-fault, fault-on, and post-fault stages. When a three-phase fault occurs at any line in the system, a breaker will operate and the respective line will be disconnected at the fault clearing time(FCT) which is set at 10 ms. If the relative rotor angles remain stable after a fault is cleared, it implies that the power system is stable, but, if the relative angles go out of step after a fault is cleared, it means that the system is unstable. The time step for the time domain simulations is set at 0.01 seconds. The time frame of interest in transient stability studies is usually limited to 3 to 5 seconds following the disturbance. It may be extended to 10 seconds for very large systems. All the rotor angles data collected from all the contingencies are then applied to calculate the CCT.

Simulations were carried out using the PSAT software in which the output data were collected and CCT calculated using the MATLAB program.

The generation and load data presented in Ref.[30] was employed as the given initial operating point. Three-phase short-circuit ground fault, the severest fault among the fault types, was applied to each bus in the test systems. All contingencies were cleared by tripping the faulted line, and their CCTs were calculated. There are 46 lines in the system. Each of these lines can be tripped to clear the faults at two buses between which the lines are connected. Hence there are 92 three phase contingency cases in total. Of these 92 cases, there are 22 islanding cases. The islanding cases corresponds to tripping of the lines 2-30, 10-32, 16-19, 19-33, 19-20, 20-34, 22-35, 23-36, 25-37, 29-38 and 6-31.

In the next step, 75 operating points were generated in the vicinity of the given initial operating point by randomly changing +10% to -10% of each generator bus's terminal voltage magnitude and generated active power, +10% to -10% of each load bus's active power demand and reactive power demand. There are nine synchronous machines (one machine act as swing bus) and 17 load buses (two loads connected to generator buses) in the test systems, thus there were  $52(9*2 + 17*2)$  input attributes in each case. Output attribute was the CCT corresponding to all three phase faults. The dimension of dataset  $75 * 122$  (52 inputs and 70 outputs).

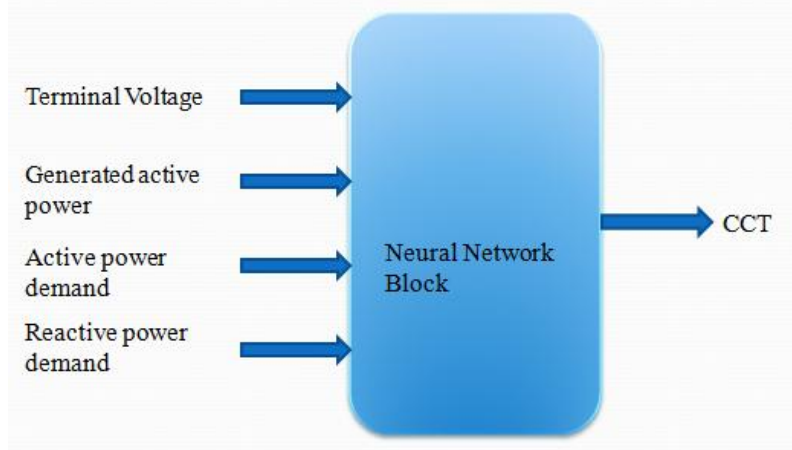


Figure 2: Neural network block diagram

#### IV. OPTIMAL PLACEMENT OF TCSC USING PSO

To improve the performance of the power system, proper location and parameter setting of FACTS controllers is required. For the optimal utilization and cost of FACTS controllers, optimization can be done based on one of the following without violating the power system constraints:

- a) Reduction in total system real power loss
- b) Increase in Available Transfer Capability

In the last two decades, researchers have been using various algorithms like GA, PSO, HSA for solving the optimal power flow problems and for finding the impact of FACTS on the performance of a power system. Generally in power flow studies, the FACTS devices, such as SVC and TCSC, are usually modelled as controllable impedance and the devices like STATCOM and UPFC are modelled as controllable sources.

PSO is an optimization tool and a population based search procedure in which individuals called particles change their position with time. It was observed that a flock of birds stochastically find food present in an area. Similar to seeking food, the solution to an optimization problem is found out from a solution space with a population based search in which the particles, like birds, change their positions with time.

Inspired initially by flocking birds, Particle Swarm Optimization (PSO) is another form of Evolutionary Computation and is stochastic in nature much like Genetic Algorithms [17]. Instead of a constantly dying and mutating GA population we have a set number of particles that fly through the hyperspace of the problem. A minimization (or maximization) of the problem topology is found both by a particle remembering its own past best position and the entire group's (or flock's, or swarm's) best overall position.

TCSC is the best FACTS device for transient stability improvement. Transient stability assessment in IEEE-39 bus system using Artificial Neural Network shows that the severe faults in the system changes as the operating point varies. So we are positioning the TCSC so as to improve the CCT of these severe faults. The goal of transient stability improvement under contingency condition is to minimize the real power losses by optimal positioning of TCSC and its corresponding parameter.

Objective Function:

$$MinF = \sum_{i=1}^{Ng} P_{gi} - \sum_{j=1}^{Nl} P_{lj}$$

subject to the constraints

Limit of Bus Voltages :  $V_{imin} \leq V_i \leq V_{imax}$

Power Flow Limits :  $S_{ijmin} \leq S_{ij} \leq S_{ijmax}$

CCT limits :  $CCT_i \geq CCT_{imin}$

Particle Swarm Optimisation program is done with the real power loss minimisation as the objective function. The critical CCT values for the first operating point before optimisation is shown:

Tripped line	Faulted bus	CCT
4	2	0.07
4	25	0.07
30	27	0.09
39	25	0.09
39	26	0.05
41	26	0.09
42	26	0.01
42	28	0.01
43	26	0.01
43	29	0.01
44	28	0.01
44	28	0.01

Table 1: CCT values before TCSC placement.

The optimal placement of TCSC is obtained as the following:

$P_{loss} = 0.4431$ , TCSC Location = 31, TCSC compensation = 31.0544 %.

The CCT values after placement of TCSC is shown in the table below.

Line	Bus	CCT
4	2	0.17
4	25	0.17
30	27	0.19
39	25	0.19
39	26	0.17
41	26	0.19
42	26	0.11
42	28	0.12
43	26	0.11
43	29	0.12
44	28	0.11
44	28	0.12

Table 2: CCT values after TCSC placement.

After placing TCSC, the CCT values are observed to be greater than 0.1 sec for all the critical contingencies.

## V. CONCLUSION

Neural network computation of CCT in the IEEE 39 bus system is done. The most critical faults in a system can be identified using ANN by training it with the previous data. If ANN can be trained using minimum number of inputs this method will be useful for the operators to initiate the necessary control actions to operate the power system with maximum reliability.

It is well established that enhancing the real power supplying ability of a power system is an effective means to improve voltage stability. So schemes for the enhancement of real power is initiated after assessing the critical faults using ANN. Optimal Placement of TCSC for transient stability improvement using PSO is done using P-loss minimization as the objective function for various operating points. The algorithm is easy to implement and is able to find the optimal solution with regard to global best position and size of TCSC. The result seemed to be quite promising when tested on IEEE 39-bus system and can be used in a practical system to find the optimal location of TCSC's for transient stability enhancement.

## REFERENCES

- [1] Pavella M, Ernst D, Ruiz-Vega D. "Transient stability of power systems", Kluwer Academic Publishers; 2000.p.6.
- [2] Olwegard A, Walve K, Waglund G, Frank H, Toresng S. "Improvement of transmission capacity by thyristor controlled reactive power", Trans Power Apparatus Syst, VOL.8,NO.10,May 1981.
- [3] Poubek P, Kundur PS, Taylor CW. The anatomy of a power grid black-out, IEEE Power Energy Magazine, Volume 22, Issue 9, Sep 2006 358 ISSN 2278-7763.
- [4] Wehenkel L, Pavella M, Preventive vs. emergency control of power systems, International Conference on Electrical Energy Systems (ICEES 2011), 3-5 Jan 2011.
- [5] Ernst D, Wehenkel L, Pavella M. What is the likely future of real-time transient stability? ,IEEE power energy society power systems conference and exposition, 3-5 Feb 2009.
- [6] Miranda V, Fidalgo JN, Peas Lopes JA, Almeida LB."Real time preventive action for transient stability enhancement with a hybrid neural network optimization approach", IEEE Transactions On Power Systems, VOL. 26,NO.2, February 2011.
- [7] Fidalgo JN, Peas Lopes JA, Miranda V. " Neural network applied to preventive control measures for the dynamic security of isolated power systems with renewable.", IEEE Transactions On Power Systems, VOL. 11,NO.4, 1811-6 ,April 2006.

## On Some Partial Orderings for Bimatrices

G. Ramesh<sup>1</sup>, N. Anbarasi<sup>2</sup>

<sup>1</sup> Associate Professor of Mathematics, Govt Arts College (Auto), Kumbakonam

<sup>2</sup> Assistant Professor of Mathematics, Arasu Engineering College, Kumbakonam

**Abstract:** The usual star, left-star, right-star, plus order, minus order and Lowner ordering have been generalized to bimatrices. Also it is shown that all these orderings are partial orderings in bimatrices. The relationship between star partial order and minus partial order of bimatrices and their squares are examined.

**Keywords:** Star partial order, left-star partial order, right-star partial order, plus order, minus order and lowner order.

**AMS Classification:** 15A09, 15A15, 15A57

### I. Introduction And Preliminaries

Let  $\mathbb{C}_{m \times n}$  be the set of  $m \times n$  complex bimatrices. The symbols  $A_B^*$ ,  $\mathcal{R}(A_B)$  and  $r(A_B)$  denote the conjugate transpose, range space and rank subtractivity of  $A_B \in \mathbb{C}_{m \times n}$  respectively. Further,  $A_B^\dagger \in \mathbb{C}_{n \times m}$  stand for the Moore-Penrose inverse of  $A_B$  [10], that is the unique bimatrix satisfying the equations,

$$A_B A_B^\dagger A_B = A_B, A_B^\dagger A_B A_B^\dagger = A_B^\dagger, A_B A_B^\dagger = (A_B A_B^\dagger)^*, A_B^\dagger A_B = (A_B^\dagger A_B)^* \quad (1.1)$$

and  $I_{Bn}$  be the identity bimatrix of order  $n$ . Moreover,  $\mathbb{C}_n^{EP}$ ,  $\mathbb{C}_n^H$  and  $\mathbb{C}_n^{\geq}$  denote the subsets of  $\mathbb{C}_{n \times n}$  consisting of EP, Hermitian, and Hermitian non-negative definite bimatrices respectively.

That is,

$$\begin{aligned} \mathbb{C}_n^{EP} &= \{A_B \in \mathbb{C}_{n \times n} : R(A_B) = R(A_B^*) \Rightarrow R(A_1) = R(A_1^*) \text{ and } R(A_2) = R(A_2^*)\} \\ \mathbb{C}_n^H &= \{A_B \in \mathbb{C}_{n \times n} : A_B = A_B^* \Rightarrow A_1 = A_1^* \text{ and } A_2 = A_2^*\} \text{ and} \\ \mathbb{C}_n^{\geq} &= \{A_B \in \mathbb{C}_{n \times n} : A_B = L_B L_B^* \Rightarrow A_1 = L_1 L_1^* ; A_2 = L_2 L_2^* \text{ for some } L_B = L_1 \cup L_2 \in \mathbb{C}_{n \times p}\} \end{aligned}$$

In this paper, the usual star, left-star, right-star, plus order, minus order and Lowner order have been generalized to bimatrices. Also it is shown that all these orderings are partial orderings in bimatrices. The relationship between star partial order and minus partial order of bimatrices and their squares are examined.

#### Definition 1.1

The star ordering for bimatrices is defined by,

$$\left. \begin{aligned} A_B \leq^* B_B &\Leftrightarrow A_B^* A_B = A_B^* B_B \text{ that is, } A_1^* A_1 = A_1^* B_1 ; A_2^* A_2 = A_2^* B_2 \\ &\text{and } A_B A_B^* = B_B A_B^* \text{ that is, } A_1 A_1^* = B_1 A_1^* ; A_2 A_2^* = B_2 A_2^* \end{aligned} \right\} \quad (1.2)$$

and can alternatively be specified as,

$$\left. \begin{aligned} A_B \leq^* B_B &\Leftrightarrow A_B^\dagger A_B = A_B^\dagger B_B \text{ that is, } A_1^\dagger A_1 = A_1^\dagger B_1 ; A_2^\dagger A_2 = A_2^\dagger B_2 \\ &\text{and } A_B A_B^\dagger = B_B A_B^\dagger \text{ that is, } A_1 A_1^\dagger = B_1 A_1^\dagger ; A_2 A_2^\dagger = B_2 A_2^\dagger \end{aligned} \right\} \quad (1.3)$$

#### Example 1.2

Consider the bimatrices

$$A_B = \begin{pmatrix} 1 & 1 \\ 0 & 0 \end{pmatrix} \cup \begin{pmatrix} 2 & 2 \\ 0 & 0 \end{pmatrix}$$

$$\text{and } B_B = \begin{pmatrix} 1 & 1 \\ 1 & -1 \end{pmatrix} \cup \begin{pmatrix} 2 & \\ & -2 \end{pmatrix}$$

$$\Rightarrow A_B \leq^* B_B$$

**Definition 1.3**

The left - star ordering for bimatrices is defined by,

$$\left. \begin{aligned} A_B * \leq B_B &\Leftrightarrow A_B^* A_B = A_B^* B_B \text{ that is, } A_1^* A_1 = A_1^* B_1 ; A_2^* A_2 = A_2^* B_2 \\ \text{and } \mathcal{R}(A_B) &\subseteq \mathcal{R}(B_B) \text{ that is, } \mathcal{R}(A_1) \subseteq \mathcal{R}(B_1) ; \mathcal{R}(A_2) \subseteq \mathcal{R}(B_2) \end{aligned} \right\} \quad (1.4)$$

**Definition 1.4**

The right - star ordering for bimatrices is defined by,

$$\left. \begin{aligned} A_B \leq^* B_B &\Leftrightarrow A_B A_B^* = B_B A_B^* \text{ that is, } A_1 A_1^* = B_1 A_1^* ; A_2 A_2^* = B_2 A_2^* \\ \text{and } \mathcal{R}(A_B^*) &\subseteq \mathcal{R}(B_B^*) \text{ that is, } \mathcal{R}(A_1^*) \subseteq \mathcal{R}(B_1^*) ; \mathcal{R}(A_2^*) \subseteq \mathcal{R}(B_2^*) \end{aligned} \right\} \quad (1.5)$$

**Definition 1.5**

The plus - order for bimatrices is defined as,  $A_B < B_B$  whenever  $A_B^\dagger A_B = A_B^\dagger B_B$  and  $A_B A_B^\dagger = B_B A_B^\dagger$ , for some reflexive generalized inverse  $A_B^\dagger$  of  $A_B$ . (satisfying both  $A_B A_B^\dagger A_B = A_B$  and  $A_B^\dagger A_B A_B^\dagger = A_B^\dagger$ ).

**Definition 1.6**

The minus (rank Subtractivity) ordering is defined for bimatrices as,

$$\left. \begin{aligned} A_B \leq^- B_B &\Leftrightarrow r(B_B - A_B) = r(B_B) - r(A_B) \text{ that is, } r(B_1 - A_1) = r(B_1) - r(A_1) \text{ and} \\ r(B_2 - A_2) &= r(B_2) - r(A_2) \end{aligned} \right\} \quad (1.6)$$

or as,

$$A_B \leq^- B_B \Leftrightarrow A_B B_B^\dagger B_B = A_B, B_B B_B^\dagger A_B = A_B \text{ and } A_B B_B^\dagger A_B = A_B \quad (1.7)$$

**Note 1.7**

i) It can be shown that,  $A_B < B_B \Leftrightarrow r(B_B - A_B) = r(B_B) - r(A_B)$  and so the plus order is equivalent to rank subtractivity.

ii) From (1.4) and (1.5) it is seen that  $A_B \leq^* B_B \Leftrightarrow A_B^* \leq^* B_B^*$

**Definition 1.8**

The Lowner partial ordering denoted by  $\leq_L$ , for Which  $A_B, B_B \in \mathbb{C}_{n \times n}$  is defined by

$$A_B \leq_L B_B \Leftrightarrow B_B - A_B \in \mathbb{C}_n^{\geq}$$

**Result 1.9**

Show that, the relation  $\leq$  is a partial ordering.

**Proof**

(1)  $A_B \leq A_B \Rightarrow A_1 \leq A_1$  and  $A_2 \leq A_2$  holds trivially.

(2) If  $A_B^* A_B = A_B^* B_B$  and  $\mathcal{R}(B_B) \subseteq \mathcal{R}(A_B)$  then

$$\begin{aligned} A_B &= A_1 \cup A_2 \\ &= A_1^{\dagger*} A_1^* A_1 \cup A_2^{\dagger*} A_2^* A_2 \\ &= A_1^{\dagger*} A_1^* B_1 \cup A_2^{\dagger*} A_2^* B_2 \\ &= (A_1 A_1^\dagger)^* B_1 \cup (A_2 A_2^\dagger)^* B_2 \\ &= B_1 \cup B_2 \end{aligned}$$

$$A_B = B_B$$

(3) If  $A_B^* A_B = A_B^* B_B$  and  $B_B^* B_B = B_B^* C_B$  hold along with  $\mathcal{R}(A_B) \subseteq \mathcal{R}(B_B)$  and  $\mathcal{R}(B_B) \subseteq \mathcal{R}(C_B)$ , then

$$\begin{aligned} A_B^* A_B &= A_B^* B_B \\ &= A_1^* B_1 \cup A_2^* B_2 \\ &= A_1^* B_1^{\dagger*} B_1^* B_1 \cup A_2^* B_2^{\dagger*} B_2^* B_2 \\ &= A_1^* B_1^{\dagger*} B_1^* C_1 \cup A_2^* B_2^{\dagger*} B_2^* C_2 \\ &= (B_1 B_1^{\dagger} A_1)^* C_1 \cup (B_2 B_2^{\dagger} A_2)^* C_2 \\ &= A_1^* C_1 \cup A_2^* C_2 \end{aligned}$$

$$A_B^* A_B = A_B^* C_B \text{ and } \mathcal{R}(A_B) \subseteq \mathcal{R}(C_B)$$

Similarly, it can be verified that all the orderings are partial orderings.

**Lemma 1.10 [1]**

Let  $A, B \in \mathbb{C}_{m \times n}$  and let  $a = r(A) < r(B) = b$ . Then  $A \leq^* B$  if and only if there exist  $U \in \mathbb{C}_{m \times b}, V \in \mathbb{C}_{n \times b}$  satisfying  $U^*U = I_b = V^*V$ , for which

$$A = U \begin{pmatrix} D_1 & 0 \\ 0 & 0 \end{pmatrix} V^* \text{ and } B = U \begin{pmatrix} D_1 & 0 \\ 0 & D_2 \end{pmatrix} V^* \tag{1.8}$$

where  $D_1$  and  $D_2$  are positive definite diagonal matrices of degree  $a$  and  $b - a$ , respectively. For  $A, B \in \mathbb{C}_n^H$ , the matrix  $U$  in (1.8) may be replaced by  $V$ , but then  $D_1$  and  $D_2$  represent any nonsingular real diagonal matrices.

**Lemma 1.11[1]**

Let  $A, B \in \mathbb{C}_{m \times n}$  and let  $a = r(A) < r(B) = b$ . Then  $A \leq^- B$  if only if there exist  $U \in \mathbb{C}_{m \times b}, V \in \mathbb{C}_{n \times b}$ , satisfying  $U^*U = I_b = V^*V$ , for which

$$A = U \begin{pmatrix} D_1 & 0 \\ 0 & 0 \end{pmatrix} V \text{ and } B = U \begin{pmatrix} D_1 + R D_2 S & R D_2 \\ D_2 S & D_2 \end{pmatrix} V^* \tag{1.9}$$

Where  $D_1$  and  $D_2$  are positive definite diagonal matrices of degree  $a$  and  $b - a$ , while  $R \in \mathbb{C}_{a \times b - a}$  and  $S \in \mathbb{C}_{b - a \times a}$  are arbitrary. For  $A, B \in \mathbb{C}_n^H$  the matrices  $U$  and  $S$  in (1.9) may be replaced by  $V$  and  $R^*$  respectively, but then  $D_1$  and  $D_2$  represent any nonsingular real diagonal matrices.

**Lemma 1.12**

Let  $A_B, B_B \in \mathbb{C}_n^H$  be star-ordered as  $A_B \leq^* B_B$ . Then  $A_B \leq_L B_B$  if and only if  $\gamma(A_B) = \gamma(B_B)$ , Where  $\gamma(\cdot)$  denotes the number of negative eigenvalues of a given bimatrix.

**Proof**

**Case (i)**

Let  $r(A_B) = r(B_B)$  that is,  $r(A_1) = r(B_1)$  and  $r(A_2) = r(B_2)$ .

The result is trivial.

**Case (ii)**

Let  $r(A_B) < r(B_B)$  that is,  $r(A_1) < r(B_1)$  and  $r(A_2) < r(B_2)$  Lemma (1.1) ensures that if  $A_B \leq^* B_B$ , then

$$\begin{aligned} B_B - A_B &= (B_1 \cup B_2) - (A_1 \cup A_2) \\ &= (B_1 - A_1) \cup (B_2 - A_2) \\ &= \left[ U_1 \begin{pmatrix} D_{11} & 0 \\ 0 & D_{12} \end{pmatrix} V_1^* - U_1 \begin{pmatrix} D_{11} & 0 \\ 0 & 0 \end{pmatrix} V_1^* \right] \cup \left[ U_2 \begin{pmatrix} D_{21} & 0 \\ 0 & D_{22} \end{pmatrix} V_2^* - U_2 \begin{pmatrix} D_{21} & 0 \\ 0 & 0 \end{pmatrix} V_2^* \right] \end{aligned}$$

$$\begin{aligned}
 &= (U_1 \cup U_2) \begin{pmatrix} D_{11} \cup D_{12} & 0 \\ 0 & D_{12} \cup D_{22} \end{pmatrix} (V_1^* \cup V_2^*) - (U_1 \cup U_2) \begin{pmatrix} D_{11} \cup D_{21} & 0 \\ 0 & 0 \end{pmatrix} (V_1^* \cup V_2^*) \\
 &= U_B \begin{pmatrix} D_{B1} & 0 \\ 0 & D_{B2} \end{pmatrix} V_B^* - U_B \begin{pmatrix} D_{B1} & 0 \\ 0 & 0 \end{pmatrix} V_B^* \\
 B_B - A_B &= U_B \begin{pmatrix} 0 & 0 \\ 0 & D_{B2} \end{pmatrix} V_B^*
 \end{aligned}$$

Hence it is seen that the order  $A_B \leq^L B_B$  is equivalent to the non-negative definiteness of  $D_{B2}$ , that is,  $\gamma(D_2) = 0$ . Consequently, the result follows by noting that  $\gamma(A_B) = \gamma(D_{B1})$  and  $\gamma(B_B) = \gamma(D_{B1}) + \gamma(D_{B2})$ .

## II. Star Partial Ordering

Theorem (3) of Baksalary and Pukel sheim [3] asserts that, for any  $A, B \in \mathbb{C}_n^{\geq}$ ,

$$A \leq^* B \Leftrightarrow A^2 \leq^* B^2 \Rightarrow A B = B A \tag{2.1}$$

This result is revisited here with the emphasis laid on the question which from among four implications comprised in (2.1) continues to be valid for bimatrices not necessarily being bihermitian non negative definite.

### Theorem 2.1

$$\text{Let } A_B \in \mathbb{C}_n^{EP} \text{ and } B_B \in \mathbb{C}_{n \times n}. \text{ Then } A_B \leq^* B_B \Rightarrow A_B^2 \leq^* B_B^2 \text{ and } A_B B_B = B_B A_B \tag{2.2}$$

#### Proof

$$\text{Since } A_B = A_1 \cup A_2 \in \mathbb{C}_n^{EP} \Leftrightarrow A_B A_B^\dagger = A_B^\dagger A_B$$

$$\text{That is, } A_1 A_1^\dagger = A_1^\dagger A_1 \text{ and } A_2 A_2^\dagger = A_2^\dagger A_2$$

$$\begin{aligned}
 \text{Now, } A_B^2 A_B^\dagger &= A_1^2 A_1^\dagger \cup A_2^2 A_2^\dagger \\
 &= A_1 (A_1 A_1^\dagger) \cup A_2 (A_2 A_2^\dagger) \\
 &= A_1 \cup A_2
 \end{aligned}$$

$$A_B^2 A_B^\dagger = A_B$$

$$\begin{aligned}
 \text{Also, } A_B^\dagger A_B^2 &= A_1^\dagger A_1^2 \cup A_2^\dagger A_2^2 \\
 &= (A_1^\dagger A_1) A_1 \cup (A_2^\dagger A_2) A_2 \\
 &= A_1 \cup A_2
 \end{aligned}$$

$$A_B^\dagger A_B^2 = A_B$$

$$\Rightarrow A_B^2 A_B^\dagger = A_B^\dagger A_B^2$$

$$\begin{aligned}
 \text{And } (A_B^2)^\dagger &= (A_1^2 \cup A_2^2)^\dagger \\
 &= (A_1 A_1)^\dagger \cup (A_2 A_2)^\dagger \\
 &= A_1^\dagger A_1^\dagger \cup A_2^\dagger A_2^\dagger \\
 &= (A_1^\dagger \cup A_2^\dagger)^2
 \end{aligned}$$

$$(A_B^2)^\dagger = (A_B^\dagger)^2$$

Consequently, in view of (1.3),

$$\begin{aligned}
 A_B B_B &= A_1 B_1 \cup A_2 B_2 \\
 &= A_1^2 A_1^\dagger B_1 \cup A_2^2 A_2^\dagger B_2 \\
 &= A_1^2 A_1^\dagger A_1 \cup A_2^2 A_2^\dagger A_2
 \end{aligned}$$

$$A_B B_B = A_B^2$$

$$\text{And } B_B A_B = B_1 A_1 \cup B_2 A_2$$

$$= B_1 A_1^\dagger A_1^2 \cup B_2 A_2^\dagger A_2^2$$

$$= B_1 A_1^\dagger A_1^2 \cup A_2 A_2^\dagger A_2^2$$

$$B_B A_B = A_B^2$$

$$\Rightarrow A_B B_B = B_B A_B = A_B^2$$

Moreover,

$$(A_B^2)^\dagger B_B^2 = (A_1^2 \cup A_2^2)^\dagger (B_1^2 \cup B_2^2)$$

$$= (A_1^2)^\dagger B_1^2 \cup (A_2^2)^\dagger B_2^2$$

$$= (A_1^2)^\dagger A_1^2 \cup (A_2^2)^\dagger A_2^2$$

$$= (A_1^2 \cup A_2^2)^\dagger (A_1^2 \cup A_2^2)$$

$$(A_B^2)^\dagger B_B^2 = (A_B^2)^\dagger A_B^2$$

$$\text{and } B_B^2 (A_B^2)^\dagger = B_1^2 (A_1^2)^\dagger \cup B_2^2 (A_2^2)^\dagger$$

$$= B_1 A_1 (A_1^\dagger)^2 \cup B_2 A_2 (A_2^\dagger)^2$$

$$= A_1^2 (A_1^\dagger)^\dagger \cup A_2^2 (A_2^\dagger)^\dagger$$

$$B_B^2 (A_B^2)^\dagger = A_B^2 (A_B^2)^\dagger$$

$$\Rightarrow A_B^2 \leq^* B_B^2$$

**Note 2.2**

Implication 2.2 is not reversible.

**Example 2.3**

Consider the bimatrices,

$$A_B = \begin{pmatrix} 1 & 1 \\ 0 & 0 \end{pmatrix} \cup \begin{pmatrix} 2 & 2 \\ 0 & 0 \end{pmatrix} \text{ and } B_B = \begin{pmatrix} 1 & 1 \\ 1 & -1 \end{pmatrix} \cup \begin{pmatrix} 2 & 2 \\ 2 & -2 \end{pmatrix}$$

In which the order  $A_B \leq^* B_B$  does not entail either of the conditions  $A_B^2 \leq^* B_B^2$ ,  $A_B B_B = B_B A_B$ .

On the otherhand, if  $A_B = \begin{pmatrix} 1 & 0 \\ 0 & 0 \end{pmatrix} \cup \begin{pmatrix} 2 & 0 \\ 0 & 0 \end{pmatrix}$  and  $B_B = \begin{pmatrix} 0 & 1 \\ 1 & 0 \end{pmatrix} \cup \begin{pmatrix} 0 & 2 \\ 2 & 0 \end{pmatrix}$  then  $A_B^2 \leq^* B_B^2$ , but  $A_B^* A_B \neq A_B^* B_B$  and  $A_B B_B \neq B_B A_B$ .

This showing that even for bihermitian matrices the star order between  $A_B^2$  and  $B_B^2$  and does not entail the star order between  $A_B$  and  $B_B$  and the commutativity of these bimatrices which are the other two implications contained in (2.1).

It is pointed out that the two conditions on the right-hand side of (2.2) are insufficient for  $A_B \leq^* B_B$ . When there is no restriction on  $A_B$ , a similar conclusion is obtained in the case of combining the two orders  $A_B \leq^* B_B$  and  $A_B^2 \leq^* B_B^2$ . The bimatrices,

$$A_B = \begin{pmatrix} 0 & 1 \\ 0 & 0 \end{pmatrix} \cup \begin{pmatrix} 0 & 2 \\ 0 & 0 \end{pmatrix} \text{ and } B_B = \begin{pmatrix} 0 & 1 \\ 1 & 0 \end{pmatrix} \cup \begin{pmatrix} 0 & 2 \\ 2 & 0 \end{pmatrix}$$

and their squares are star ordered, but  $A_B B_B \neq B_B A_B$ . However, the combination of the order  $A_B \leq^* B_B$  with the commutativity condition appears sufficient for  $A_B^2 \leq^* B_B^2$  for all quadratic bimatrices.

**Theorem 2.4**

Let  $A_B, B_B \in \mathbb{C}_{n \times n}$ . Then  $A_B \leq^* B_B$  and  $A_B B_B = B_B A_B \Rightarrow A_B^2 \leq^* B_B^2$

**Proof**

On account of (1.2), it follows that if  $A_B \leq^* B_B$  and  $A_B B_B = B_B A_B$  then,

$$\begin{aligned} (A_B^2)^* B_B^2 &= (A_1^2 \cup A_2^2)^* (B_1^2 \cup B_2^2) \\ &= [(A_1^2)^* \cup (A_2^2)^*] (B_1^2 \cup B_2^2) \\ &= (A_1^2)^* B_1^2 \cup (A_2^2)^* B_2^2 \\ &= A_1^* (A_1^* A_1) B_1 \cup A_2^* (A_2^* A_2) B_2 \\ &= (A_1^*)^2 A_1 B_1 \cup (A_2^*)^2 A_2 B_2 \\ &= A_1^* (A_1^* B_1) A_1 \cup A_2^* (A_2^* B_2) A_2 \\ &= (A_1^2)^* A_1^2 \cup (A_2^2)^* A_2^2 \\ (A_B^2)^* B_B^2 &= (A_B^2)^* A_B^2 \\ \text{and } B_B^2 (A_B^2)^* &= (B_1^2 \cup B_2^2) (A_1^2 \cup A_2^2)^* \\ &= B_1^2 (A_1^2)^* \cup B_2^2 (A_2^2)^* \\ &= B_1 (B_1 A_1^*) A_1^* \cup B_2 (B_2 A_2^*) A_2^* \\ &= B_1 (A_1 A_1^*) A_1^* \cup B_2 (A_2 A_2^*) A_2^* \\ &= A_1 (B_1 A_1^*) A_1^* \cup A_2 (B_2 A_2^*) A_2^* \\ &= A_1 (A_1 A_1^*) A_1^* \cup A_2 (A_2 A_2^*) A_2^* \\ &= A_1^2 (A_1 A_1^*)^* \cup A_2^2 (A_2 A_2^*)^* \\ &= A_1^2 (A_1^2)^* \cup A_2^2 (A_2^2)^* \\ B_B^2 (A_B^2)^* &= A_B^2 (A_B^2)^* \end{aligned}$$

**III. Minus Partial Ordering**

Baksalary and Pukelsheim [3, Theorem 2] showed that for  $B \in \mathbb{C}_n^{\geq}$ , the following three implications hold.

$$A \leq^- B \text{ and } A^2 \leq^- B^2 \implies AB = BA \tag{3.1}$$

$$A \leq^- B \text{ and } AB = BA \implies A^2 \leq^- B^2 \tag{3.2}$$

$$A^2 \leq^- B^2 \text{ and } AB = BA \implies A \leq^- B \tag{3.3}$$

Now, we extend these implications for bimatrices also by the following theorems.

**Theorem 3.1**

For any  $A_B, B_B \in \mathbb{C}_{n \times n}$  if  $A_B \leq^- B_B$  and  $A_B B_B = B_B A_B$  then  $A_B^2 \leq^- B_B^2$

**Proof**

First notice that,

$$A_B \leq^- B_B \text{ and } A_B B_B = B_B A_B \tag{3.4}$$

$$\implies A_B B_B = A_1 B_1 \cup A_2 B_2 = A_1^2 \cup A_2^2 = B_1 A_1 \cup B_2 A_2 = B_B A_B \tag{3.5}$$

On account of 1.7, it follows that,

$$\begin{aligned} A_B B_B &= A_1 B_1 \cup A_2 B_2 \\ &= A_1 B_1^\dagger A_1 B_1 \cup A_2 B_2^\dagger A_2 B_2 \\ &= A_1 B_1^\dagger B_1 A_1 \cup A_2 B_2^\dagger B_2 A_2 \\ &= A_1 A_1 \cup A_2 A_2 \end{aligned}$$

$$\begin{aligned}
 &= A_1^2 \cup A_2^2 \\
 A_B B_B &= A_B^2 \\
 B_B A_B &= B_1 A_1 \cup B_2 A_2 \\
 &= B_1 A_1 B_1^\dagger A_1 \cup B_2 A_2 B_2^\dagger A_2 \\
 &= A_1 (B_1 B_1^\dagger A_1) \cup A_2 (B_2 B_2^\dagger A_2) \\
 &= A_1 A_1 \cup A_2 A_2 \\
 &= A_1^2 \cup A_2^2 \\
 B_B A_B &= A_B^2 \\
 \Rightarrow A_B B_B &= A_B^2 = B_B A_B
 \end{aligned}$$

The conditions on the right hand sides of (1.7) and (3.5) lead to the equalities,

$$\begin{aligned}
 B_B^2 (B_B^2)^\dagger A_B^2 &= (B_1^2 \cup B_2^2) (B_1^2 \cup B_2^2)^\dagger (A_1^2 \cup A_2^2) \\
 &= B_1^2 (B_1^2)^\dagger A_1^2 \cup B_2^2 (B_2^2)^\dagger A_2^2 \\
 &= B_1^2 (B_1^2)^\dagger B_1^2 B_1^\dagger A_1 \cup B_2^2 (B_2^2)^\dagger B_2^2 B_2^\dagger A_2 \\
 &= B_1^2 B_1^\dagger A_1 \cup B_2^2 B_2^\dagger A_2 \\
 &= B_1 A_1 \cup B_2 A_2 \\
 &= B_B A_B \\
 \Rightarrow B_B^2 (B_B^2)^\dagger A_B^2 &= A_B^2 \\
 A_B^2 (B_B^2)^\dagger B_B^2 &= A_1^2 (B_1^2)^\dagger B_1^2 \cup A_2^2 (B_2^2)^\dagger B_2^2 \\
 &= A_1 B_1 (B_1^2)^\dagger B_1^2 \cup A_2 B_2 (B_2^2)^\dagger B_2^2 \\
 &= A_1 B_1^\dagger B_1^2 (B_1^2)^\dagger B_1^2 \cup A_2 B_2^\dagger B_2^2 (B_2^2)^\dagger B_2^2 \\
 &= A_1 B_1^\dagger B_1^2 \cup A_2 B_2^\dagger B_2^2 \\
 &= A_1 B_1 \cup A_2 B_2 \\
 &= A_B B_B \\
 \Rightarrow A_B^2 (B_B^2)^\dagger B_B^2 &= A_B^2 \\
 \text{(iii) } A_B^2 (B_B^2)^\dagger A_B^2 &= A_1^2 (B_1^2)^\dagger A_1^2 \cup A_2^2 (B_2^2)^\dagger A_2^2 \\
 &= A_1 B_1 (B_1^2)^\dagger B_1 A_1 \cup A_2 B_2 (B_2^2)^\dagger B_2 A_2 \\
 &= A_1 B_1^\dagger B_1^2 B_1^\dagger A_1 \cup A_2 B_2^\dagger B_2^2 B_2^\dagger A_2 \\
 &= A_1 (B_1^\dagger B_1) (B_1 B_1^\dagger) A_1 \cup A_2 (B_2^\dagger B_2) (B_2 B_2^\dagger) A_2 \\
 &= A_1^2 \cup A_2^2 \\
 A_B^2 (B_B^2)^\dagger A_B^2 &= A_B^2
 \end{aligned}$$

According to (1.7), which shows that

$$A_B^2 \leq^- B_B^2$$

**Lemma 3.2**

Let  $A_B \in \mathbb{C}_n^{EP}$ . If the Moore – Penrose inverse  $B_B^\dagger$  of some  $B_B \in \mathbb{C}_n^H$  is a generalized inverse of a bimatrix  $A_B$ , that is,  $A_B B_B^\dagger A_B = A_B$ , Then  $A_B \in \mathbb{C}_n^H$ .

**Proof**

It is mentioned that,  $A_B \in \mathbb{C}_n^{EP}$  if and only if,  $A_B A_B^\dagger = A_B^\dagger A_B$

Then, on the other hand

$$\begin{aligned} A_B A_B^\dagger B_B^\dagger A_B^* &= A_1 A_1^\dagger B_1 A_1^* \cup A_2 A_2^\dagger B_2 A_2^* \\ &= (A_1 B_1 A_1 A_1^\dagger)^* \cup (A_2 B_2 A_2 A_2^\dagger)^* \\ &= (A_1 A_1^\dagger)^* \cup (A_2 A_2^\dagger)^* \\ &= A_1 A_1^\dagger \cup A_2 A_2^\dagger \\ A_B A_B^\dagger B_B^\dagger A_B^* &= A_B^\dagger A_B \end{aligned} \tag{3.6}$$

Further, 
$$\begin{aligned} A_B A_B^\dagger B_B^\dagger A_B^* &= A_1 A_1^\dagger B_1^\dagger A_1^* \cup A_2 A_2^\dagger B_2^\dagger A_2^* \\ &= A_1^\dagger A_1^* \cup A_2^\dagger A_2^* \end{aligned}$$

$$A_B A_B^\dagger B_B^\dagger A_B^* = A_B^\dagger A_B^*$$

Comparing (3.6) with (3.7) we get

$$A_B^\dagger A_B = A_B^\dagger A_B^*$$

Pre-multiplying by  $A_B$ ,

$$\begin{aligned} A_B A_B^\dagger A_B &= A_B A_B^\dagger A_B^* \\ \Rightarrow (A_1 A_1^\dagger A_1) \cup (A_2 A_2^\dagger A_2) &= A_1 A_1^\dagger A_1^* \cup A_2 A_2^\dagger A_2^* \\ A_1 \cup A_2 &= A_1^* \cup A_2^* \\ A_B &= A_B^* \\ \Rightarrow A_B &\in \mathbb{C}_n^H \end{aligned}$$

**Theorem 3.3**

$$\text{Let } A_B \in \mathbb{C}_n^{EP} \text{ and } B_B \in \mathbb{C}_n^H. \text{ Then } A \leq^- B \text{ and } A^2 \leq_L B^2 \Leftrightarrow A_B \leq^* B_B \tag{3.8}$$

**Proof**

Without loss of generality,  $A_B$  may be assumed to be Hermitian.

From (1.6) it is clear that and that  $r(A_B) \leq r(B_B)$  and that the equality holds only in the trivial case when  $A_B = B_B$ .

Therefore, assume that  $a = r(A_B) < r(B_B) = b$  that is  $r(A_1) = r(A_2) = a$  and  $r(B_1) = r(B_2) = b$

If  $A_B \leq^* B_B$ , then the fact that  $A_B, B_B \in \mathbb{C}_n^H$  enables representing these bimatrices in the forms described in the second part of Lemma(1.10).

Hence the  $\Leftarrow$  part of (3.8) follows.

For the proof of the converse implication observe that, on account of the first two equalities in (1.7)

$$\begin{aligned} A_B^2 \leq_L B_B^2 &\Leftrightarrow B_B^\dagger A_B^2 B_B^\dagger \leq_L B_B^\dagger B_B^2 B_B^\dagger \\ &\Leftrightarrow B_B^\dagger A_B^\dagger (B_B^\dagger A_B)^\dagger \leq_L B_B^\dagger B_B^\dagger \end{aligned} \tag{3.9}$$

By conditions (1.1), the Moore-Penrose inverse of a hermitian bimatrix  $B_B$  of the form specified in the second part of Lemma (1.11) admits the representation

$$B_B^\dagger = V_B \begin{pmatrix} D_{B_1}^{-1} & -D_{B_1}^{-1} R_B \\ -R_B^* D_{B_1}^{-1} & D_{B_2}^{-1} + R_B^* D_{B_1}^{-1} R_B \end{pmatrix} V_B^*$$

and hence

$$\begin{aligned}
 B_B^\dagger A_B (B_B^\dagger A_B)^* &= V_B \begin{pmatrix} I_{Ba} & 0 \\ -R_B^* & 0 \end{pmatrix} \begin{pmatrix} I_{Ba} & -R_B \\ 0 & 0 \end{pmatrix} V_B^* \\
 &= V_B \begin{pmatrix} I_{Ba} & -R_B \\ -R_B^* & R_B^* R_B \end{pmatrix} V_B^*
 \end{aligned}
 \tag{3.10}$$

Since the bimatrix  $B_B^\dagger B_B (= B_B B_B^\dagger)$  represents the orthogonal projector onto  $\mathcal{R}(B_B) = \mathcal{R}(V_B)$ , it may be expressed as  $V_B V_B^*$ .

Consequently, in view of (3.10)

$$B_B^\dagger B_B - B_B^\dagger A_B (B_B^\dagger A_B)^* = V_B \begin{pmatrix} 0 & R_B \\ R_B^* & I_{B(b-a)} - R_B^* R_B \end{pmatrix} V_B^*
 \tag{3.11}$$

On the account of (3.9), equality (3.11) shows that supplementing the minus order  $A_B \leq^- B_B$  by Lower order  $A_B^2 \leq_L B_B^2$  forces to be 0.

Then the bimatrix  $B_B$  characterized in lemma (1.11) takes the form described in lemma (1.1), thus leading to the conclusion that

$$A_B \leq^* B_B$$

### REFERENCES

- [1] Jerzy.K. Baksalary, Jan Hauke, Xiaoji Liu, Sanyang Liu, ‘Relationships between partial orders of matrices and their powers’ *Linear Algebra and its Applications* 379 (2004) 277-287.
- [2] J.K. Baksalary, S.K. Mitra, ‘Left-star and right-star partial orderings’, *Linear Algebra Applications*, 149 (1991) 73-89.
- [3] Jerzy.K. Baksalary, Oskar Haria Baksalary, Xiaoji Liu, ‘Further properties of the star, left-star, minus partial orderings’ *Linear Algebra and its Applications* 375 (2003) 83-94.
- [4] J.K. Baksalary, F. Pukelshiom, G.P.H. Styan, ‘some properties of matrix partial orderings’, *Linear Algebra Applications*, 119 (1989) 57-85.
- [5] Jerzy.K. Baksalary, Sujit Kumar Mitra, ‘Left-star and right-star and partial orderings’. Elsevier Science Publishing Co.,Inc.,1991 (73-89).
- [6] M.P. Drazin, ‘Natural structures on semi groups with involution *Bull. Amer. Hath. Soc.* 84 (1978) 139-141.
- [7] R.E.Hartwig, ‘How to partially order regular elements’, *Math. Japan.*25 (1980) 1-13.
- [8] R.E. Hartwig, G.P.H. Styan, ‘on some characterizations of the star partial ordering for matrices and rank subtractivity’, *Linear Algebra Applications* 82 (1986) 145-161.
- [9] K.S.S. Nambooripal, ‘The natural partial order on a regular semi group’ *Proc. Edinburgh Math. Soc.* 23 (1980) (249-260).
- [10] Ramesh.G,Anbarasi.N, ‘ On inverses and Generalized inverses of Bimatrices’, *International Journal of Research in Engineering and Technology*, Vol.2, Issue 8, Aug 2014,PP(77-90)

## Novel Direct Switching Power Control Method of UPFC by Using Matrix Converter Based On SVPWM Techniques

B. Venkateswarlu<sup>1</sup>, D. Jagan<sup>2</sup>, A. Karunakar<sup>3</sup>, CH. Renuka<sup>4</sup>.

<sup>1,2,3</sup> Assistant Professor/<sup>4</sup> PG Student /Sri Sai Educational Society's Group of Institutions/JNTUH/T.S/ INDIA.

**Abstract:** This paper presents a direct Switching power control for three-phase matrix converters operating as unified power flow controllers (UPFCs). Matrix converters (MCs) allow the direct ac/ac power conversion without dc energy storage links; therefore, the MC-based UPFC (MC-UPFC) has reduced volume and cost, reduced capacitor power losses, together with higher reliability. Theoretical principles of direct Switching power control based on sliding mode control techniques are established for an MC-UPFC dynamic model including the input filter. As a result, line active and reactive power, together with ac supply reactive power, can be directly controlled by selecting an appropriate matrix converter switching state guaranteeing good steady-state and dynamic responses. Experimental results of DSPC controllers for MC-UPFC show decoupled active and reactive power control, zero steady-state tracking error, and fast response times. Compared to an MC-UPFC using active and reactive power linear controllers based on a modified Venturing high-frequency PWM modulator, the experimental results of the advanced DSPC-MC guarantee faster responses without overshoot and no steady state error, presenting no cross-coupling in dynamic and steady-state responses.

**Index Terms:** Direct Switching Power Control, matrix converter (MC), unified power-flow controller (UPFC).

### I. Introduction

In the last few years, electricity market deregulation, together with growing economic, environmental, and social concerns, has increased the difficulty to burn fossil fuels, and to obtain new licenses to build transmission lines (rights-of-way) and high-power facilities. This situation started the growth of decentralized electricity generation (using renewable energy resources).

Unified Power-Flow Controllers (UPFC) enable the operation of power transmission networks near their maximum ratings, by enforcing power flow through well-defined lines. These days, UPFCs are one of the most versatile and powerful flexible ac transmission systems (FACTS) devices.

The UPFC results from the combination of a static synchronous compensator (STATCOM) and a static synchronous series compensator (SSSC) that shares a common dc capacitor link.

The existence of a dc capacitor bank originates additional losses, decreases the converter lifetime, and increases its weight, cost, and volume. These converters are capable of performing the same ac/ac conversion, allowing bidirectional power flow, guaranteeing near sinusoidal input and output currents, voltages with variable amplitude, and adjustable power factor. These minimum energy storage ac/ac converters have the capability to allow independent reactive control on the UPFC shunt and series converter sides, while guaranteeing that the active power exchanged on the UPFC series connection is always supplied/absorbed by the shunt connection.

Recent nonlinear approaches enabled better tuning of PI controller parameters. Still, there is room to further improve the dynamic response of UPFCs, using nonlinear robust controllers. In the last few years, direct power control techniques have been used in many power applications, due to their simplicity and good performance. In this project, a matrix converter- based UPFC is proposed, using a direct Switching power control approach (DSPC-MC) based on an MC-UPFC dynamic model (Section II).

In order to design UPFCs, presenting robust behavior to parameter variations and to disturbances, the proposed DSPC-MC control method, in Section III, is based on sliding mode-control techniques, allowing the real-time selection of adequate matrix vectors to control input and output electrical power. Sliding mode-based DSPC-MC controllers can guarantee zero steady-state errors and no overshoots, good tracking performance, and fast dynamic responses, while being simpler to implement and requiring less processing power, when compared to proportional-integral (PI) linear controllers obtained from linear active and reactive power models of UPFC using a modified Aventura high-frequency PWM modulator.

The dynamic and steady-state behavior of the proposed DSPC-MC P, Q control method is evaluated and discussed using detailed simulations and experimental implementation (Sections IV and V). Simulation and experimental results obtained with the nonlinear DSPC for matrix converter-based UPFC technology show decoupled series active and shunt/series reactive power control, zero steady state error tracking, and fast response times, presenting faultless dynamic and steady state responses.

## II. Modeling of the UPFC Power System

### A. General Architecture

A simplified power transmission network using the proposed matrix converter UPFC is presented in Fig. 1, where  $a_0$  and are, respectively, the sending-end and receiving-end sinusoidal voltages of the and generators feeding load. The matrix converter is connected to transmission line 2, represented as a series inductance with series resistance through coupling transformers and .Fig. 2 shows the simplified three-phase equivalent circuit of the matrix UPFC transmission system model. For system modeling, the power sources and the coupling transformers are all considered ideal. Also, the matrix converter is considered ideal and represented as a controllable voltage source, with amplitude and phase . In the equivalent circuit, is the load bus voltage? The DSPC-MC controller will treat the simplified elements as disturbances. Considering a symmetrical and balanced three-phase system and applying Kirchhoff laws to the three-phase equivalent circuit (Fig. 2), the ac line currents are obtained in coordinates

$$\frac{dI_d}{dt} = \omega I_q - \frac{R_2}{L_2} I_d + \frac{1}{L_2} (V_{Ld} - V_{R0d}) \quad (1)$$

$$\frac{dI_q}{dt} = -\omega I_d - \frac{R_2}{L_2} I_q + \frac{1}{L_2} (V_{Lq} - V_{R0q}). \quad (2)$$

The active and reactive power of end generator are given in dq coordinates by

$$\begin{bmatrix} P \\ Q \end{bmatrix} = \begin{bmatrix} V_d & V_q \\ V_q & -V_d \end{bmatrix} \begin{bmatrix} I_d \\ I_q \end{bmatrix}. \quad (3)$$

The active and reactive power P and Q are given by (4) and (5) respectively

$$P = V_d I_d \quad (4)$$

$$Q = -V_d I_q. \quad (5)$$

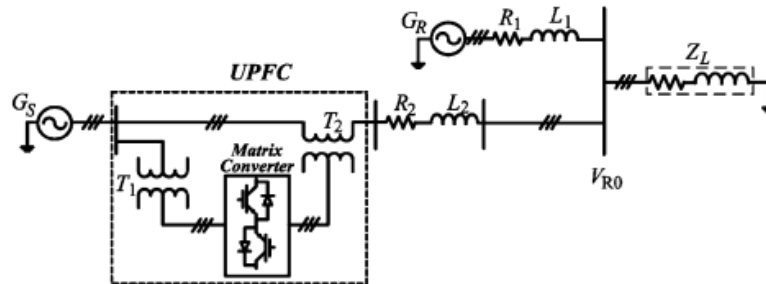


Fig. 1 Transmission network with matrix converter UPFC

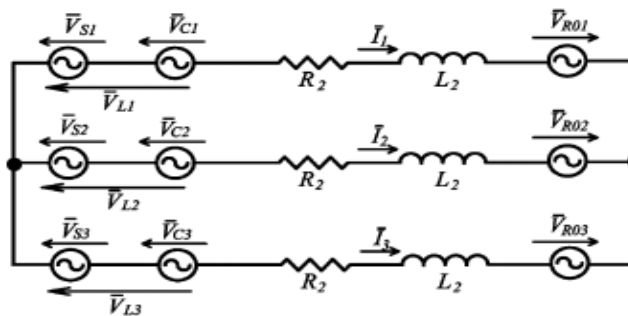


Fig.2. Three-phase equivalent circuit of the matrix UPFC and transmission line

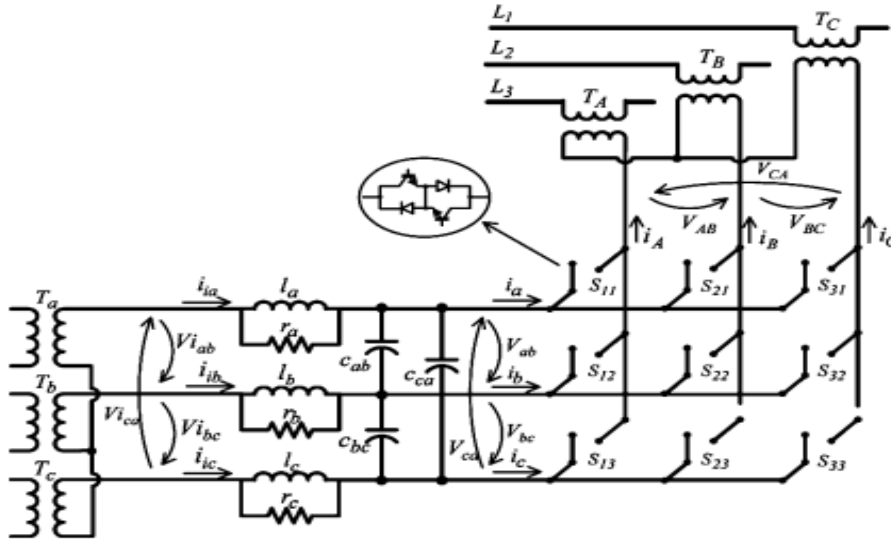


Fig. 3. Transmission network with matrix converter UPFC

**B. Matrix Converter Output Voltage and Input Current Vectors**

A diagram of the UPFC system (Fig. 3) includes the three-phase shunt input transformer (with windings  $T_a, T_b, T_c$ ), the three-phase series output transformer (with windings  $L_A, L_B, L_C$ ) and the three-phase matrix converter, represented as an array of nine bidirectional switches with turn-on and turn-off capability, allowing the connection of each one of three output phases directly to any one of the three input phases. The three-phase input filter is required to re-establish a voltage-source boundary to the matrix converter, enabling smooth input currents. Applying coordinates to the input filter state variables presented in Fig. 3 and neglecting the effects of the damping resistors, the following equations are obtained.

Where  $V, i$  represent, respectively, input voltages and input currents in dq components (at the shunt transformer secondary) and  $V, i$  are the matrix converter voltages and input currents in components, respectively.

Assuming ideal semiconductors, each matrix converter bidirectional switch can assume two possible states: “ $S_{kj}=1$ ” if the switch is closed or “ $S_{kj}=0$ ” if the switch is open.

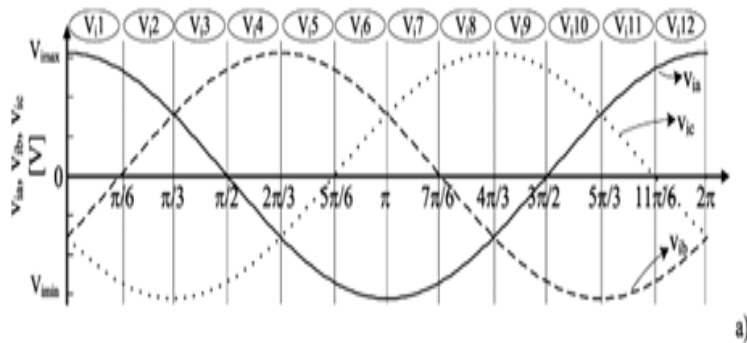


Fig. 4. (a) Input voltages and their corresponding sector

switch is open. The nine matrix converter switches can be represented as a  $3 \times 3$  matrix (7)

$$\begin{cases} \frac{di_{id}}{dt} = \omega i_{iq} - \frac{1}{2l} V_d - \frac{1}{2\sqrt{3}l} V_q + \frac{1}{l} V_{id} \\ \frac{di_{iq}}{dt} = -\omega i_{id} + \frac{1}{2\sqrt{3}l} V_d - \frac{1}{2l} V_q + \frac{1}{l} V_{iq} \\ \frac{dV_d}{dt} = \omega V_q - \frac{1}{2\sqrt{3}C} i_{iq} + \frac{1}{2C} i_{id} - \frac{1}{2C} i_d + \frac{1}{2\sqrt{3}C} i_q \\ \frac{dV_q}{dt} = -\omega V_d + \frac{1}{2\sqrt{3}C} i_{id} + \frac{1}{2C} i_{iq} - \frac{1}{2\sqrt{3}C} i_d - \frac{1}{2C} i_q \end{cases} \quad (6)$$

$$\mathbf{S} = \begin{bmatrix} S_{11} & S_{12} & S_{13} \\ S_{21} & S_{22} & S_{23} \\ S_{31} & S_{32} & S_{33} \end{bmatrix}. \quad (7)$$

The relationship between load and input voltages can be expressed as

$$[v_A \ v_B \ v_C]^T = \mathbf{S}[v_a \ v_b \ v_c]^T. \quad (8)$$

The input phase currents can be related to the output phase currents (9), using the transpose of matrix (9)

$$[i_a \ i_b \ i_c]^T = \mathbf{S}^T[i_A \ i_B \ i_C]^T. \quad (9)$$

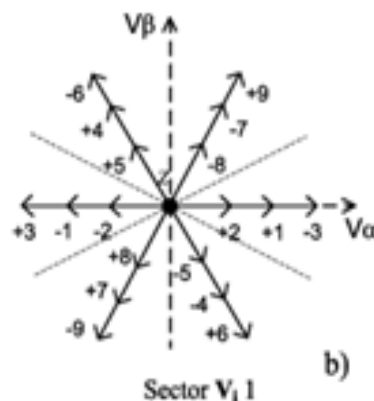
From the 27 possible switching patterns, time-variant vectors can be obtained (Table I) representing the matrix output voltages and input currents coordinates, and plotted in the frame [Fig. 4(b)].

The active and reactive power DSPC-MC will select one of these 27 vectors at any given time instant.

### III. Direct Power Control of MC-UPFC

#### A. Line Active and Reactive Power Sliding Surfaces

The DSPC controllers for line power flow are here derived based on the sliding mode control theory. From



#### (b) Output voltage state-space vectors when the input voltages are located at sector.

Fig. 2, in steady state, is imposed by source . From (1) and (2), the transmission-line currents can be considered as state variables with first-order dynamics dependent on the sources and time constant of impedance . Therefore, transmission-line active and reactive powers present first-order dynamics and have a strong relative degree of one [25], since from the control viewpoint, its first time derivative already contains the control variable (the strong relative degree generally represents the number of times the control output variable must be differentiated until a control input appears explicitly in the dynamics) [26]–[29].

From the sliding mode control theory, robust sliding surfaces to control the and variables with a relatively strong degree of one can be obtained considering proportionality to a linear combination of the errors of between the power references and the actual transmitted powers , respectively the state variables [29]. Therefore, define the active power error and the reactive power error as the difference

**TABLE I**  
Switching Combinations and Output Voltage / Input Current State-Space Vectors

	$v_{AB}$	$v_{BC}$	$v_{CA}$	$i_a$	$i_b$	$i_c$	$V_o$	$\delta_o$	$I_i$	$\mu_i$	
<b>I</b>	1g	$v_{ab}$	$v_{bc}$	$v_{ca}$	$i_A$	$i_B$	$i_C$	$v_i$	$\delta_i$	$i_o$	$\mu_o$
	2g	$-v_{ca}$	$-v_{bc}$	$-v_{ab}$	$i_A$	$i_C$	$i_B$	$-v_i$	$-\delta_i+4\pi/3$	$i_o$	$-\mu_o$
	3g	$-v_{ab}$	$-v_{ca}$	$-v_{bc}$	$i_B$	$i_A$	$i_C$	$-v_i$	$-\delta_i$	$i_o$	$-\mu_o+2\pi/3$
	4g	$v_{bc}$	$v_{ca}$	$v_{ab}$	$i_C$	$i_A$	$i_B$	$v_i$	$\delta_i+4\pi/3$	$i_o$	$\mu_o+2\pi/3$
	5g	$v_{ca}$	$v_{ab}$	$v_{bc}$	$i_B$	$i_C$	$i_A$	$v_i$	$\delta_i+2\pi/3$	$i_o$	$\mu_o+4\pi/3$
	6g	$-v_{bc}$	$-v_{ab}$	$-v_{ca}$	$i_C$	$i_B$	$i_A$	$-v_i$	$-\delta_i+2\pi/3$	$i_o$	$-\mu_o+4\pi/3$
	+1	$v_{ab}$	0	$-v_{ab}$	$i_A$	$-i_A$	0	$\frac{2}{\sqrt{3}}v_{ab}$	$\pi/6$	$\frac{2}{\sqrt{3}}i_A$	$-\pi/6$
	-1	$-v_{ab}$	0	$v_{ab}$	$-i_A$	$i_A$	0	$-\frac{2}{\sqrt{3}}v_{ab}$	$\pi/6$	$-\frac{2}{\sqrt{3}}i_A$	$-\pi/6$
	+2	$v_{bc}$	0	$-v_{bc}$	0	$i_A$	$-i_A$	$\frac{2}{\sqrt{3}}v_{bc}$	$\pi/6$	$\frac{2}{\sqrt{3}}i_A$	$\pi/2$
	-2	$-v_{bc}$	0	$v_{bc}$	0	$-i_A$	$i_A$	$-\frac{2}{\sqrt{3}}v_{bc}$	$\pi/6$	$-\frac{2}{\sqrt{3}}i_A$	$\pi/2$
	+3	$v_{ca}$	0	$-v_{ca}$	$-i_A$	0	$i_A$	$\frac{2}{\sqrt{3}}v_{ca}$	$\pi/6$	$\frac{2}{\sqrt{3}}i_A$	$7\pi/6$
	-3	$-v_{ca}$	0	$v_{ca}$	$i_A$	0	$-i_A$	$-\frac{2}{\sqrt{3}}v_{ca}$	$\pi/6$	$-\frac{2}{\sqrt{3}}i_A$	$7\pi/6$
	+4	$-v_{ab}$	$v_{ab}$	0	$i_B$	$-i_B$	0	$\frac{2}{\sqrt{3}}v_{ab}$	$5\pi/6$	$\frac{2}{\sqrt{3}}i_B$	$-\pi/6$
	-4	$v_{ab}$	$-v_{ab}$	0	$-i_B$	$i_B$	0	$-\frac{2}{\sqrt{3}}v_{ab}$	$5\pi/6$	$-\frac{2}{\sqrt{3}}i_B$	$-\pi/6$
<b>II</b>	+5	$-v_{bc}$	$v_{bc}$	0	0	$i_B$	$-i_B$	$\frac{2}{\sqrt{3}}v_{bc}$	$5\pi/6$	$\frac{2}{\sqrt{3}}i_B$	$\pi/2$
	-5	$v_{bc}$	$-v_{bc}$	0	0	$-i_B$	$i_B$	$-\frac{2}{\sqrt{3}}v_{bc}$	$5\pi/6$	$-\frac{2}{\sqrt{3}}i_B$	$\pi/2$
	+6	$-v_{ca}$	$v_{ca}$	0	$-i_B$	0	$i_B$	$\frac{2}{\sqrt{3}}v_{ca}$	$5\pi/6$	$\frac{2}{\sqrt{3}}i_B$	$7\pi/6$
	-6	$v_{ca}$	$-v_{ca}$	0	$i_B$	0	$-i_B$	$-\frac{2}{\sqrt{3}}v_{ca}$	$5\pi/6$	$-\frac{2}{\sqrt{3}}i_B$	$7\pi/6$
	+7	0	$v_{ab}$	$v_{ab}$	$i_C$	$-i_C$	0	$\frac{2}{\sqrt{3}}v_{ab}$	$3\pi/2$	$\frac{2}{\sqrt{3}}i_C$	$-\pi/6$
	-7	0	$v_{ab}$	$v_{ab}$	$-i_C$	$i_C$	0	$-\frac{2}{\sqrt{3}}v_{ab}$	$3\pi/2$	$-\frac{2}{\sqrt{3}}i_C$	$-\pi/6$
	+8	0	$-v_{bc}$	$v_{bc}$	0	$i_C$	$-i_C$	$\frac{2}{\sqrt{3}}v_{bc}$	$3\pi/2$	$\frac{2}{\sqrt{3}}i_C$	$\pi/2$
	-8	0	$v_{bc}$	$-v_{bc}$	0	$-i_C$	$i_C$	$-\frac{2}{\sqrt{3}}v_{bc}$	$3\pi/2$	$-\frac{2}{\sqrt{3}}i_C$	$\pi/2$
	+9	0	$-v_{ca}$	$v_{ca}$	$-i_C$	0	$i_C$	$\frac{2}{\sqrt{3}}v_{ca}$	$3\pi/2$	$\frac{2}{\sqrt{3}}i_C$	$7\pi/6$
	-9	0	$v_{ca}$	$-v_{ca}$	$i_C$	0	$-i_C$	$-\frac{2}{\sqrt{3}}v_{ca}$	$3\pi/2$	$-\frac{2}{\sqrt{3}}i_C$	$7\pi/6$
<b>III</b>	$z_a$	0	0	0	0	0	0	0	-	0	-
	$z_b$	0	0	0	0	0	0	0	-	0	-
	$z_c$	0	0	0	0	0	0	0	-	0	-

$$e_P = P_{ref} - P \tag{10}$$

$$e_Q = Q_{ref} - Q. \tag{11}$$

Then, the robust sliding surfaces must be proportional to these errors, being zero after reaching sliding mode

$$S_P(e_P, t) = k_P(P_{ref} - P) = 0 \tag{12}$$

$$S_Q(e_Q, t) = k_Q(Q_{ref} - Q) = 0. \tag{13}$$

The proportional gains and are chosen to impose appropriate switching frequencies

**B. Line Active and Reactive Power Direct Switching Laws**

The DPC uses a nonlinear law, based on the errors and to select in real time the matrix converter switching states (vectors). Since there are no modulators and/or pole zero-based approaches, high control speed is possible. To guarantee stability for active power and reactive power controllers, the sliding-mode stability conditions (14) and (15) must be verified

$$S_P(e_P, t) \dot{\bar{S}}_P(e_P, t) < 0 \tag{14}$$

$$S_Q(e_Q, t) \dot{\bar{S}}_Q(e_Q, t) < 0. \tag{15}$$

According to (12) and (14), the criteria to choose the matrix vector should be

1. If  $S_P(e_P, t) > 0 \Rightarrow \dot{\bar{S}}_P(e_P, t) < 0 \Rightarrow P < P_{ref}$ ,  
then choose a vector suitable to increase  $P$ .
2. If  $S_P(e_P, t) < 0 \Rightarrow \dot{\bar{S}}_P(e_P, t) > 0 \Rightarrow P > P_{ref}$ ,  
then choose a vector suitable to decrease  $P$ .
3. If  $S_P(e_P, t) = 0$ ,

To designs the DSPC control system, the six vectors of group I will not be used, since they require extra algorithms to calculate their time-varying phase [14]. From group II, the variable amplitude vectors, only the 12 highest amplitude voltage vectors are certain to be able to guarantee the previously discussed required levels of and needed to fulfill the reaching conditions. The lowest amplitude voltages vectors, or the three null vectors of group III, could be used for near zero errors. If the control errors and are quantized using two hysteresis comparators, each with three levels (and ), nine output voltage error combinations are obtained. If a two-level comparator is used to control the shunt reactive power, as discussed in next subsection, 18 error combinations will be defined, enabling the selection of 18 vectors. Since the three zero vectors have a minor influence on the shunt reactive power control, selecting one out 18 vectors is adequate. As an example, consider the case of and Then, and imply that and . According to Table I, output voltage vectors depend on the input voltages (sending voltage), so to choose the adequate output voltage vector, it is necessary to know the input voltages location [Fig. 4(a)]. Suppose now that the input voltages are in sector [Fig. 4(b)], then the vector to be applied should be 9 or 7. The final choice between these two depends on the matrix reactive power controller result , discussed in the next subsection. Using the same reasoning for the remaining eight active and reactive power error combinations and generalizing it for all other input voltage sectors, Table II is obtained. These P, Q controllers were designed based on control laws not dependent on system parameters, but only on the errors of the controlled output to ensure robustness to parameter variations or operating conditions and allow system order reduction, minimizing response times [26].

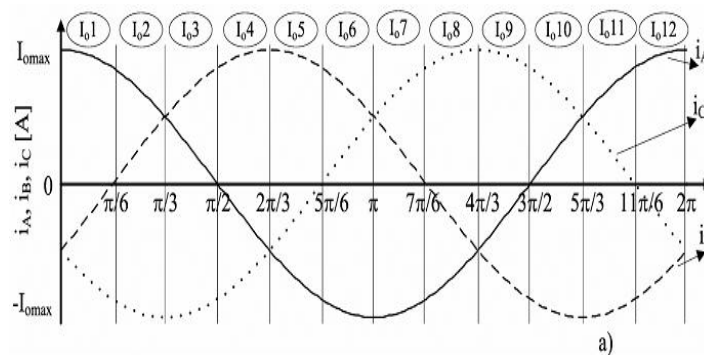


Fig.5: (a) Output currents and their corresponding sector.

**C. Direct Control of Matrix Converters Input Reactive Power**

In addition, the matrix converter UPFC can be controlled to ensure a minimum or a certain desired reactive power at the matrix converter input. Similar to the previous considerations, since the voltage source input filter (Fig. 3) dynamics (6) has a strong relative degree of two [25], then a suitable sliding surface (19) will be a linear combination of the desired reactive power error and its first-order time derivative [29] (19) The time derivative can be approximated by a discrete time difference, as has been chosen to obtain a suitable switching frequency, since as stated before, this sliding surface

$$S_{Q_i}(e_{Q_i}, t) = (Q_{i_{ref}} - Q_i) + K_{Q_i} \frac{d}{dt} (Q_{i_{ref}} - Q_i).$$

$$\begin{aligned} \dot{S}_{Q_i}(e_{Q_i}, t) = \\ V_{id} \left( \frac{di_{iq}}{dt} + K_{Q_i} \frac{d^2 i_{iq}}{dt^2} \right) = V_{id} \left( -\omega i_{id} + \frac{1}{2\sqrt{3}l} V_d - \frac{1}{2l} V_q \right) + \\ V_{id} K_{Q_i} \left( -\omega^2 i_{iq} + \frac{\omega}{l} V_d + \frac{\omega}{\sqrt{3}l} V_q - \frac{\omega}{l} V_{id} - \frac{i_{iq}}{3lC} + \frac{i_q}{3lC} \right). \end{aligned}$$

The sliding mode is reached when vectors applied to the converter have the necessary current amplitude to satisfy stability conditions, such as (15). Therefore, to choose the most adequate vector in the chosen reference frame, it is necessary to know the output currents location since the input current depends on the output currents (Table I). Considering that the  $\alpha$ -axis location is synchronous with the input voltage (i.e., reference frame depends on the input voltage location), the sign of the matrix reactive power can be determined by knowing the location of the input voltages and the location of the output currents (Fig. 5).

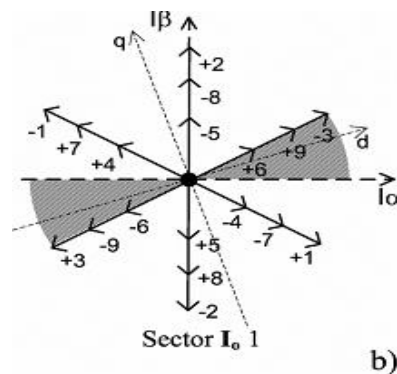


Fig. 5. (a) Output currents and their corresponding sector.

1. If  $S_{Q_i}(e_{Q_i}, t) > 0 \Rightarrow \dot{S}_{Q_i}(e_{Q_i}, t) < 0$ , then select vector with current  $i_q < 0$  to increase  $Q_i$
2. If  $S_{Q_i}(e_{Q_i}, t) < 0 \Rightarrow \dot{S}_{Q_i}(e_{Q_i}, t) > 0$ , then select vector with current  $i_q > 0$  to decrease  $Q_i$ .

Considering the previous example, with the input voltage at sector and sliding surfaces signals and both vectors or would be suitable to control the line active and reactive powers errors (Fig. 4). However, at sector, these vectors have a different effect on the value: if has a suitable amplitude, vector leads to while vector originates. So, vector should be chosen if the input reactive power sliding surface is quantized as 1, while vector 7 should be chosen when is quantized as 1. When the active and reactive power errors are quantized as zero, 0 and 0, the null vectors of group III, or the lowest amplitude voltages vectors at sector at Fig. 4(b) could be used. These vectors do not produce significant effects on the line active and reactive power values, but the lowest amplitude voltage vectors have a high influence on the control of matrix reactive power. From Fig. 5(b), only the highest amplitude current vectors of sector should be chosen: vector 1 if is quantized as 1, or vector 2 if is quantized as 2.

#### IV. Implementation Of The DSPC-MC As UPFC

As shown in the block diagram (Fig. 6), the control of the instantaneous active and reactive powers requires the measurement of voltages and output currents necessary to calculate and sliding surfaces. The output current measurement is also used to determine the location of the input currents component. The control of the matrix converter input reactive power requires the input currents measurement to calculate. At each time instant, the most suitable matrix vector is chosen upon the discrete values of the sliding surfaces, using tables derived from Tables II and III for all voltage sectors.

**TABLE II**  
State-Space Vectors Selection for Different Error Combinations

$C_\alpha$	$C_\beta$	Sector					
		$V_i 12; 1$	$V_i 2; 3$	$V_i 4; 5$	$V_i 6; 7$	$V_i 8; 9$	$V_i 10; 11$
-1	+1	-9; +7	-9; +8	+8; -7	-7; +9	+9; -8	-8; +7
-1	0	+3; -1	+3; -2	-2; +1	+1; -3	-3; +2	+2; -1
-1	-1	-6; +4	-6; +5	+5; -4	-4; +6	+6; -5	-5; +4
0	+1	-9; +7; +6; -4	-9; +8; +6; -5	+8; -7; -5; +4	-7; +9; +4; -6	+9; -8; -6; +5	-8; +7; +5; -4
0	0	$Z_a; Z_b; Z_c;$ -8; +2; -5; +8; -2; +5	$Z_a; Z_b; Z_c;$ -7; +1; -4; +7; -1; +4	$Z_a; Z_b; Z_c;$ +9; -3; +6; -9; +3; -6	$Z_a; Z_b; Z_c;$ -8; +2; -5; +8; -2; +5	$Z_a; Z_b; Z_c;$ -7; +1; -4; +7; -1; +4	$Z_a; Z_b; Z_c;$ -9; +3; -6; +9; -3; +6
0	-1	-6; +4; +9; -7	+5; -6; -8; +9	+5; -4; -8; +7	-4; +6; +7; -9	+6; -5; -9; +8	-5; +4; +8; -7
+1	+1	+6; -4	+6; -5	-5; +4	+4; -6	-6; +5	+5; -4
+1	0	-3; +1	+2; -3	-1; +2	+3; -1	-2; +3	+1; -2
+1	-1	+9; -7	+9; -8	+7; -8	+7; -9	-9; +8	+8; -7

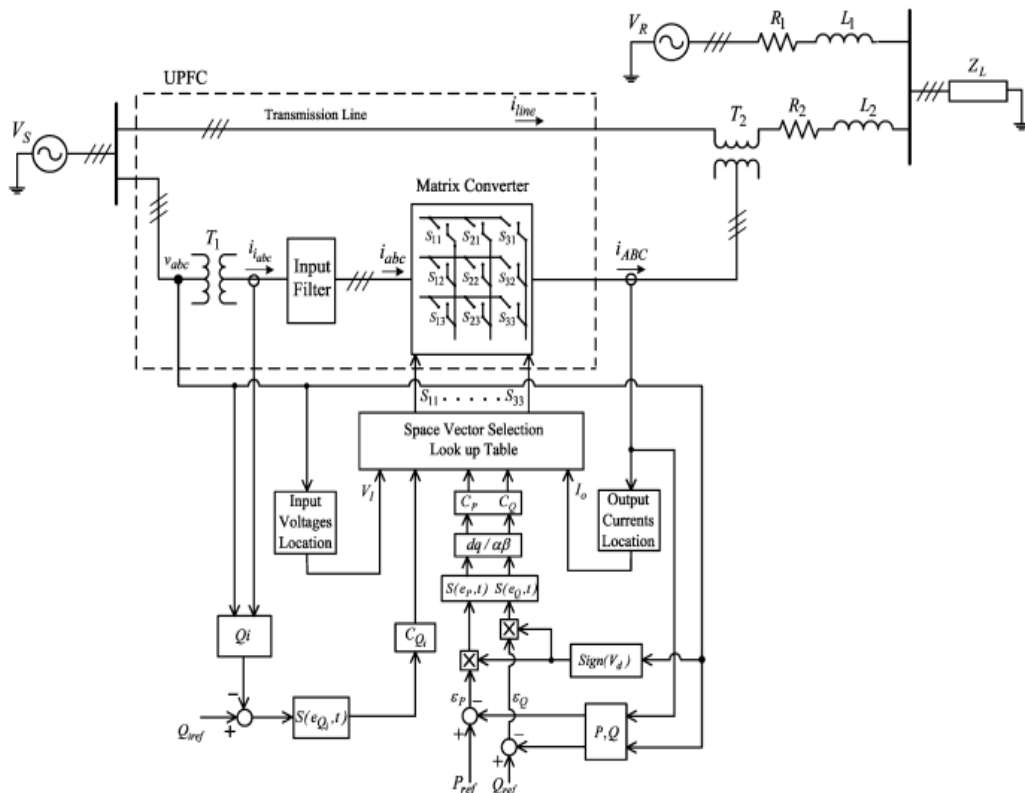


Fig. 6. Control scheme of direct power control of the three-phase matrix converter operating as a UPFC.

**A. Simulation Modeling**

The performance of the proposed direct control system was evaluated with a detailed simulation model using the\*-MATLAB/Simulink Sim Power Systems to represent the matrix converter, transformers, sources and transmission lines, and Simulink blocks to simulate the control system. Ideal switches were considered to simulate matrix converter semiconductors minimizing simulation times.



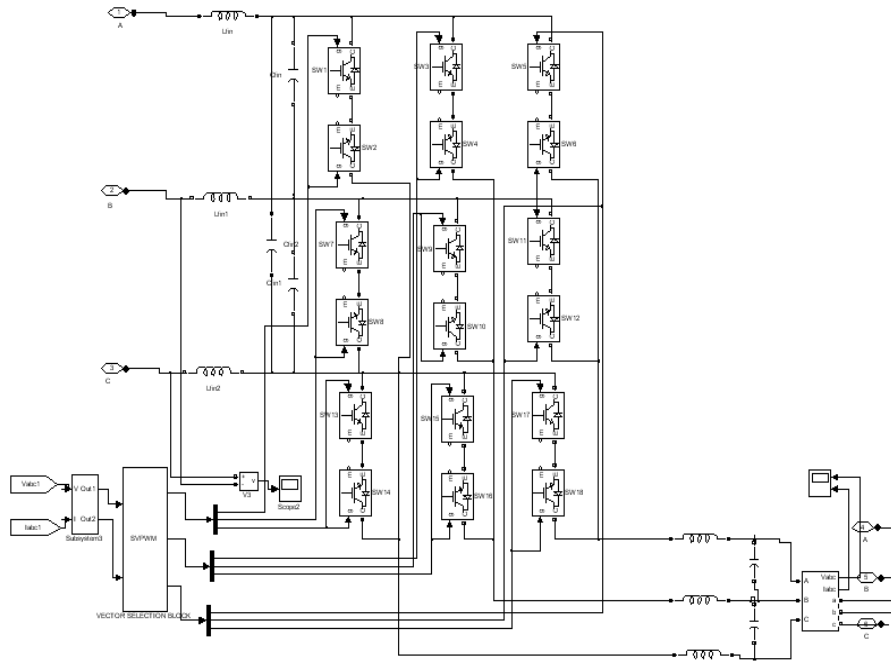


Fig 9; Modeling of matrix convertor

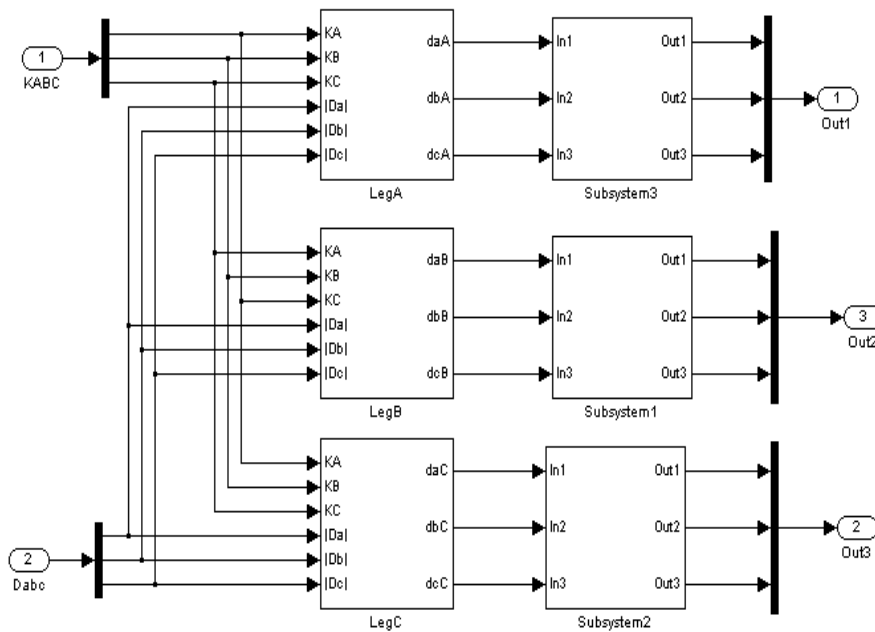


Fig 10; Modeling of vector selection block

The simulation power spectral density of transmission line and matrix converter current respectively, Fig. 5.3 shows that the main harmonics are nearly 30 db below the 50-Hz fundamental for the line current, and 22 db below the 50-Hz fundamental for the matrix converter current. The power spectral density shows switching frequencies mainly below 2.5 kHz as expected. Simulation results confirm the performance of the proposed controllers, showing no cross-coupling, no steady-state error (only switching ripples), and fast response times for different changes of power references. DSPC active and reactive power step response and line currents results were compared to active and reactive power linear PI controllers [11] using a Aventurine high-frequency PWM modulator [17], working at 5.0-khz switching frequency.

Simulation results for 0.4 p.u. And 0.2 p.u. Show cross-coupling between active and reactive power control, which introduces a slowly decaying error in the response. Longer response times are also present, when compared to DSPC simulation results presented showing the claimed DSPC faster dynamic.

Response to step active and reactive power reference change To test the DSPC controller ability to operate at lower switching frequencies, the DSPC gains were lowered and the input filter parameters were changed accordingly (5.9 mH) to lower the switching frequency to nearly 1.4 kHz. The results also show fast response without cross coupling between active and reactive power's This confirms the DSPC-MC robustness to input filter parameter variation, the ability to operate at low switching frequencies, and insensitivity to switching non linearity.

### B. Simulation Results

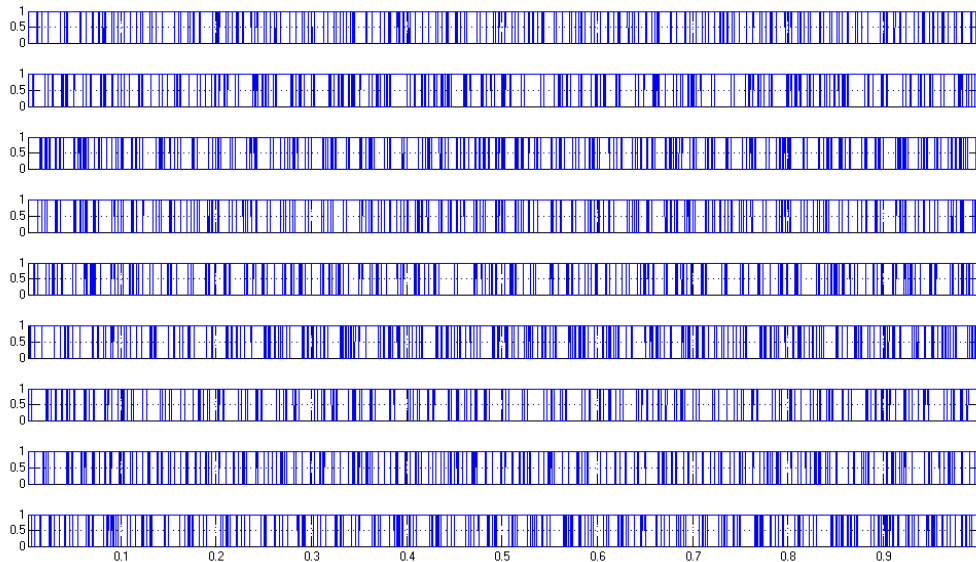


Fig 11: SVPWM Pulse wave forms

In SVPWM Pulse wave forms as shown Fig 11 the pulse gives to nine bi-directional on matrix converter and it works the switches turn ON & turn OFF

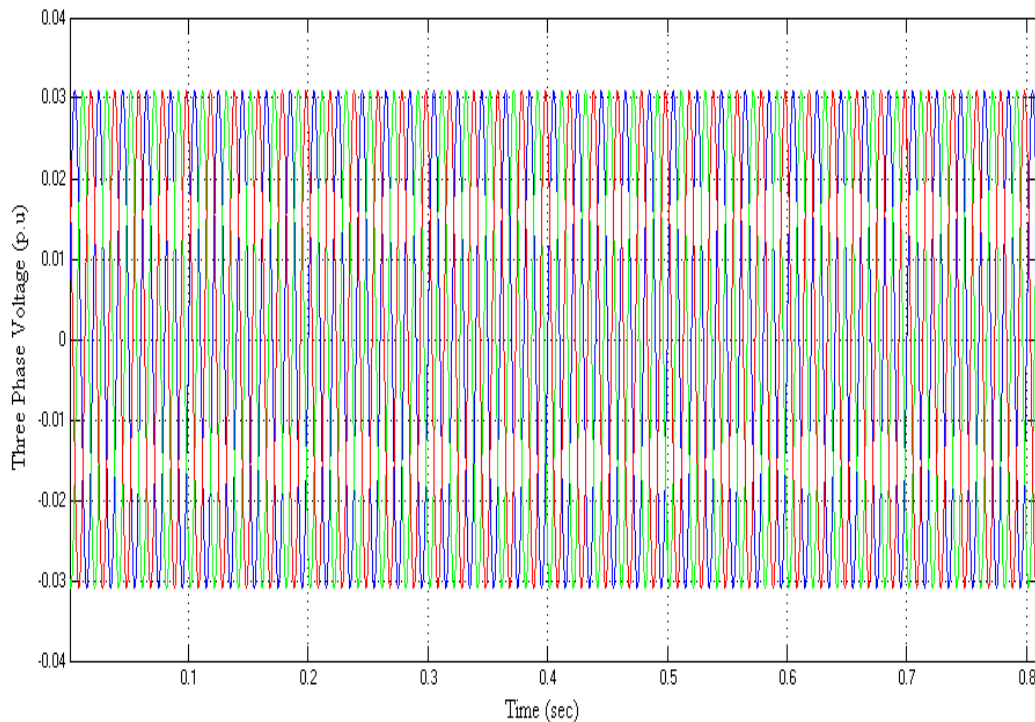


Fig 12: Output 3-Phase Voltage of UPFC without Matrix Converter.

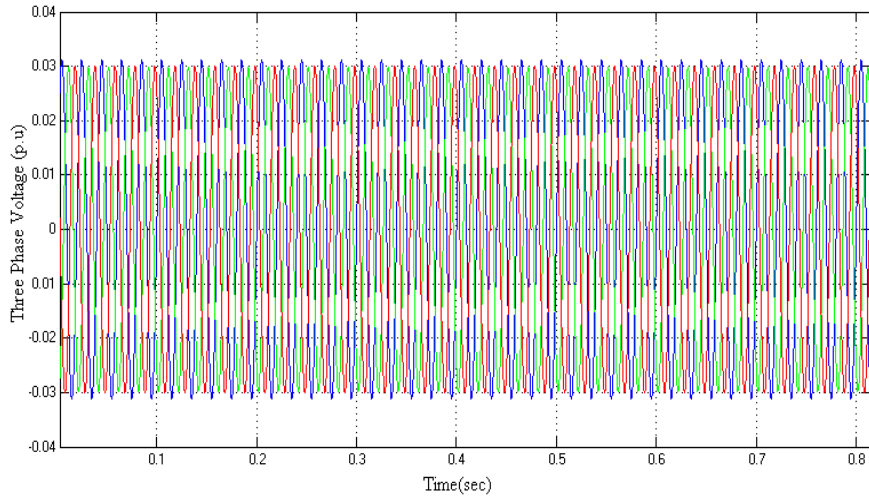


Fig 13: Output 3-Phase Voltage of UPFC with Matrix Converter

In Output 3-Phase Voltage of UPFC with and without Matrix Converter as shown in above (fig 12&13) those are output wave forms do not change why because all the loads connected are parallels

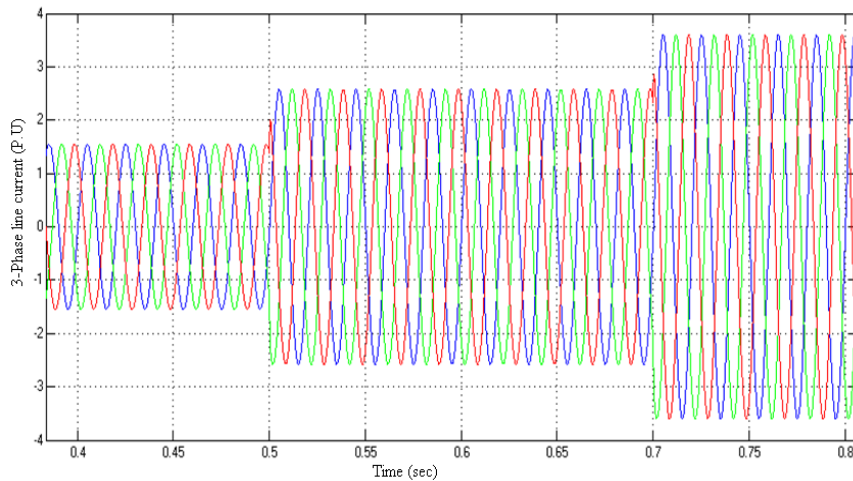


Fig 14: Output 3-Phase Line Current of UPFC without Matrix Converter.

In 3-Phase line current ( $i_A, i_B, i_C$ ) as shown in above (fig 14) the current will be increased with respect to time and doesn't control the output current in without Matrix converter of UPFC.

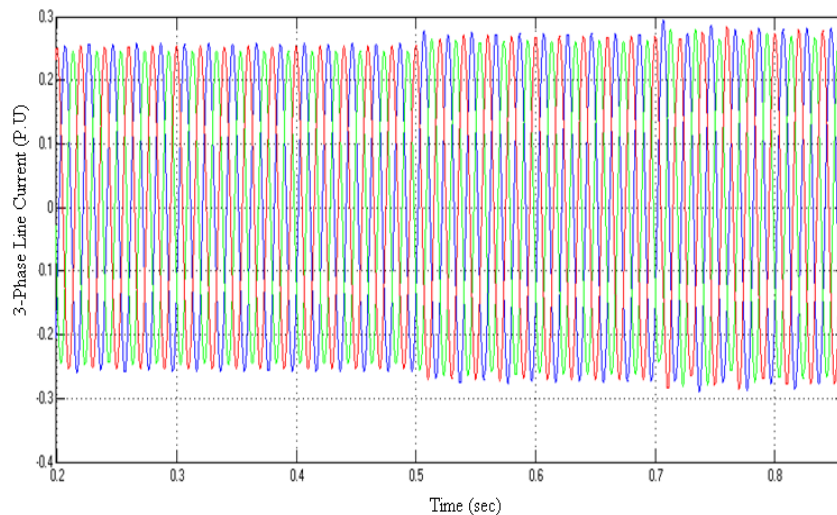


Fig 15: Output 3-Phase Line Current of UPFC with Matrix Converter.

In 3-Phase line current ( $i_A, i_B, i_C$ ) as shown in above (fig 15) the current will be increased with respect to time and we can control the output current with Matrix converter of UPFC

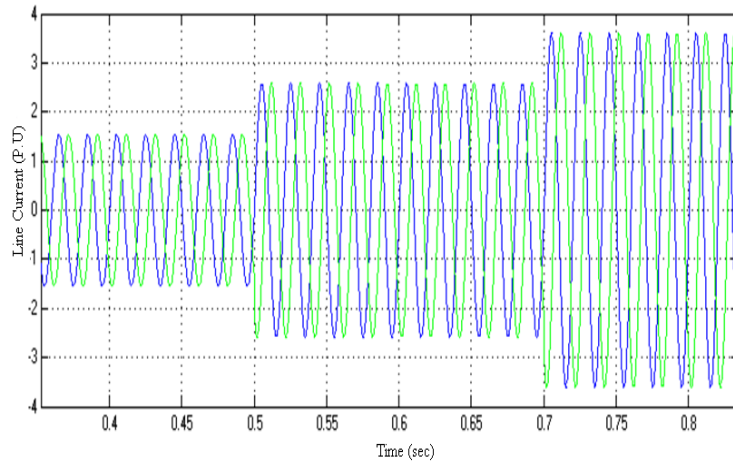


Fig 16: Output Line Current ( $i_A, i_B$ ) of UPFC without Matrix Converter.

In line current ( $i_A, i_B$ ) as shown in above (fig 16) the current will be increased with respect to time and doesn't control the current in without Matrix converter of UPFC

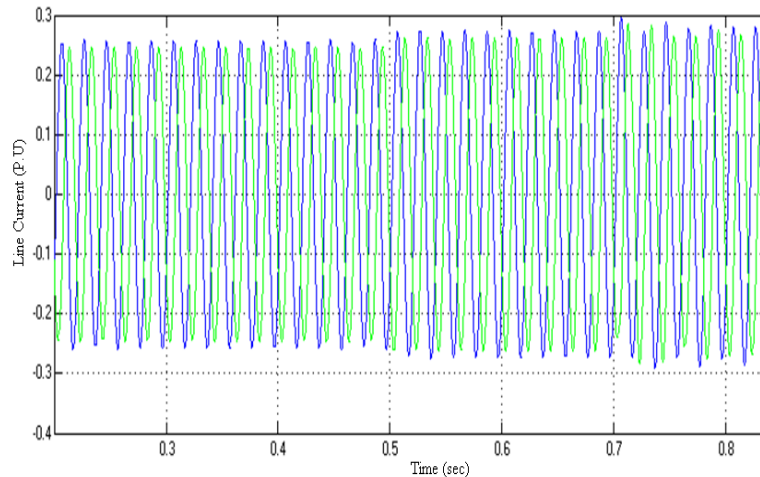


Fig 17: Output Line Current ( $i_A, i_B$ ) of UPFC with Matrix Converter.

In line current ( $i_A, i_B$ ) as shown in above (fig 17) the current will be increased with respect to time and we can control the output current with Matrix converter of UPFC

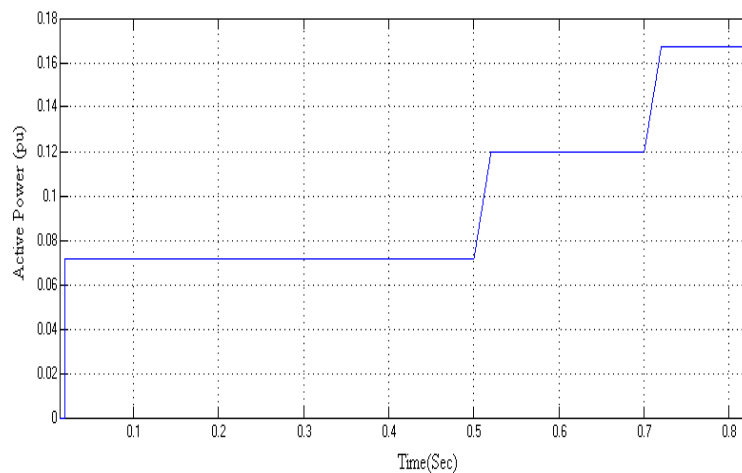


Fig 18: Magnitude of output Active Power without Matrix Converter.

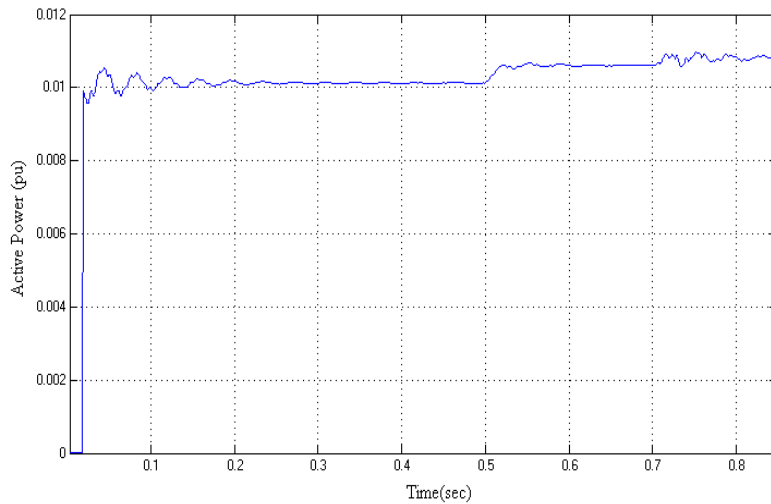


Fig 19: Magnitude of output Active Power with Matrix Converter.

The magnitude of output active power of UPFC without Matrix Converter as shown in above (fig 18) gets reached to the not steadystate with more time where as with matrix converter the active power as shown in above (fig 19) gets reached the steadystate with less time.

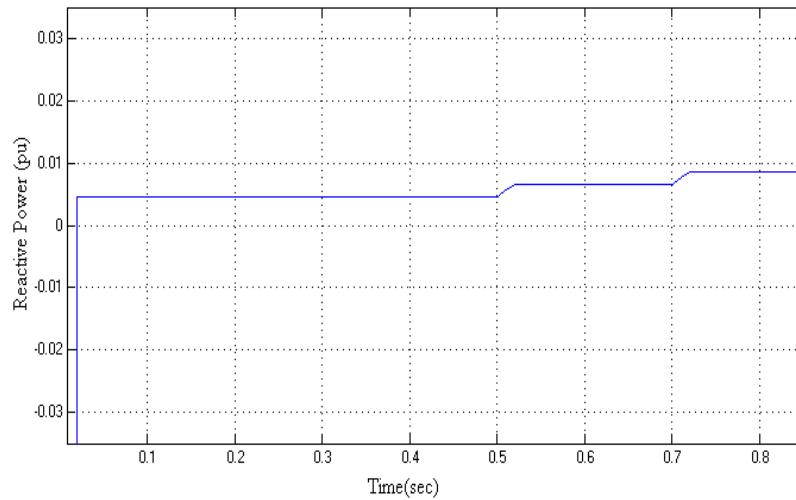


Fig 20: Magnitude of output Reactive Power without Matrix Converter.

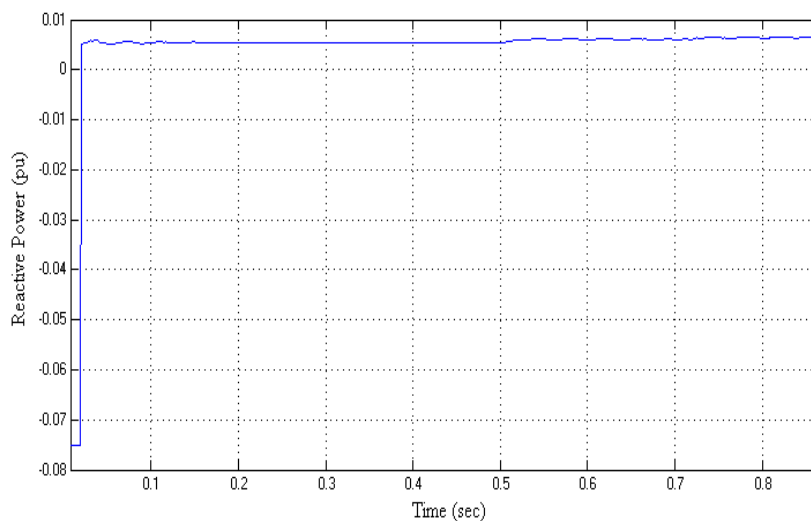


Fig 21: Magnitude of output Reactive Power with Matrix Converter.

The magnitude of output reactive power of UPFC without Matrix Converter as shown in above (fig 20) gets reached to the not steadystate and controlabul where as with matrix converter the active power as shown in above (fig 21) gets reached the steadystate and controlabul.

## V. Conclusion

This paper derived advanced nonlinear direct power controllers, based on sliding mode control techniques, for matrix converters connected to power transmission lines as UPFCs. Presented simulation and experimental results show that active and reactive power flow can be advantageously controlled by using the proposed DSPC. Results show no steady-state errors, no cross-coupling, insensitivity to no modeled dynamics and fast response times, thus confirming the expected performance of the presented nonlinear DSPC methodology. The obtained DSPC-MC results were compared to PI linear active and reactive power controllers using a modified Venturing.

## REFERENCES

- [1] N. Hingorani and L. Gyugyi, *Understanding FACTS—Concepts and Technology of Flexible AC Transmission Systems*. Piscataway, NJ: IEEE Press/Wiley, 2000.
- [2] L. Gyugyi, “Unified power flow control concept for flexible AC transmission systems,” *Proc. Inst. Elect. Eng. C*, vol. 139, no. 4, Jul. 1992.
- [3] L. Gyugyi, C. Schauder, S. Williams, T. Rietman, D. Torgerson, and A. Edris, “The unified power flow controller: A new approach to power transmission control,” *IEEE Trans. Power Del.*, vol. 10, no. 2, pp. 1085–1097, Apr. 1995.
- [4] C. Schauder, L. Gyugyi, M. Lund, D. Hamai, T. Rietman, D. Torgerson, and A. Edris, “Operation of the unified power flow controller (UPFC) under practical constraints,” *IEEE Trans. Power Del.*, vol. 13, no. 2, pp. 630–639, Apr. 1998.
- [5] T. Ma, “P-Q decoupled control schemes using fuzzy neural networks for the unified power flow controller,” in *Electr. Power Energy Syst.*. New York: Elsevier, Dec. 2007, vol. 29, pp. 748–748.
- [6] L. Liu, P. Zhu, Y. Kang, and J. Chen, “Power-flow control performance analysis of a unified power-flow controller in a novel control scheme,” *IEEE Trans. Power Del.*, vol. 22, no. 3, pp. 1613–1619, Jul. 2007.
- [7] F. Gao and M. Iravani, “Dynamic model of a space vector modulated matrix converter,” *IEEE Trans. Power Del.*, vol. 22, no. 3, pp. 1696–1750, Jul. 2007.
- [8] B. Geethalakshmi and P. Dananjayan, “Investigation of performance of UPFC without DC link capacitor,” in *Elect. Power Energy Res.*. New York: Elsevier, 2008, pp. 284–294, 736-746.
- [9] X. Jiang, X. Fang, J. Chow, A. Edris, E. Uzunovic, M. Parisi, and L. Hopkins, “A novel approach for modeling voltage-sourced converterbased FACTS controllers,” *IEEE Trans. Power Del.*, vol. 23, no. 4, pp. 2591–2598, Oct. 2008.
- [10] R. Strzelecki, A. Noculak, H. Tunia, and K. Sozanski, “UPFC with matrix converter,” presented at the EPE Conf., Graz, Austria, Sep. 2001.
- [11] J. Monteiro, J. Silva, S. Pinto, and J. Palma, “Unified power flow controllers without DC bus: Designing controllers for the matrix converter solution,” presented at the Int. Conf. Electrical Engineering, Coimbra, Portugal, 2005.
- [12] A. Dasgupta, P. Tripathy, and P. Sensarma, “Matrix converter as UPFC for transmission line compensation,” in *Proc. 7th Int. Conf. Power Electronics, Exco, Daegu, Korea*, Oct. 2007, pp. 1050–1055.
- [13] P. Wheeler, J. Rodriguez, J. Clare, L. Empringham, and A. Weinstein, “Matrix converters: A technology review,” *IEEE Trans. Ind. Electron.*, vol. 49, no. 2, pp. 276–288, Apr. 2002.
- [14] S. Pinto, “Conversores matriciais trifásicos: generalização do comando vectorial directo,” Ph.D. dissertation, Instituto Superior Técnico Universidade Técnica de Lisboa, Lisbon, Portugal, Jul. 2003.
- [15] T. Podlesak, D. Katsis, P. Wheeler, J. Clare, L. Empringham, and M. Bland, “A 150-kVAVector-controlled matrix converter induction motor drive,” *IEEE Trans. Ind. Appl.*, vol. 41, no. 3, pp. 841–847, May/Jun. 2005.

## BIOGRAPHIES



B. Venkateswarlu received the B.Tech degree in Electrical Engineering from KMCET college in JNTU Hyderabad and his Masters degree from CMR College-hyd in 2006 and 2010 respectively. He is currently working as Assistant Professor in Sri Sai Educational Society’s Group of Institutions. His interests are Direct Switching Power Control Method of UPFC by Using Matrix Converter Based on SVPWM Techniques, power system, power electronics etc.



D.Jagan received the B.Tech degree in Electrical Engineering from vathsalya college in JNTU Hyderabad,-T.S and his Masters degree from RGM College-Nandyala ,A.P in 2010 and 2013 respectively. He is currently working as Assistant Professor in Sri Sai Educational Society's Group of Institutions. His current interests are Direct Switching Power Control Method of UPFC by Using Matrix Converter Based on SVPWM Techniques, power system, power electronics etc.



A.Karunakar received the B.Tech degree in Electrical Engineering from vathsalya college in JNTU Hyderabad,-T.S and his Masters degree from DARE College-Khammam ,T S in 2010 and 2013 respectively. He is currently working as Assistant Professor in Sri Sai Educational Society's Group of Institutions. His current interests are Direct Switching Power Control Method of UPFC by Using Matrix Converter Based on SVPWM Techniques, power system, power electronics etc.



CH.Renuka is born in 1989 in India. She is graduated from MITS college JNTU Hyderabad in 2011. Presently she is doing Post graduation in Electrical Power Systems Specialization at Sri Sai Educational Society's Group of Institutions JNTUH, She is current interests are Direct Switching Power Control Method of UPFC by Using Matrix Converter Based on SVPWM Techniques, power system, power electronics etc.



# International Journal of Modern Engineering Research (IJMER)

Volume : 4 Issue : 9 (Version-5)

ISSN : 2249-6645

September- 2014

## Contents :

- |   |       |
|---|-------|
| <b>Testing Model Of Development Organic Farming Dragon Fruit Based Market Research</b><br><i>Kustiawati Ningsih, Halimatus Sakdiyah, Herman Felani</i>  | 01-09 |
| <b>Synthesis and Characterization of Mn, Ce Co-Doped CDS Nanoparticles Synthesized Via Co-Precipitation Method</b><br><i>M. Sreenivas, G. S. Harish, P. Sreedhara Reddy</i>   | 10-16 |
| <b>An Experimental Investigation on Strength Characteristics of Concrete with Partial Replacement of Silica Fume and Metakaolin with Cement on M-30 Grade of Concrete</b><br><i>Mohammad Imteyazuddin , Prof. Syed Arafath</i>      | 17-25 |
| <b>Design and Implementation of VLSI Architecture for Image Scaling Processor</b><br><i>Bukya. Balaji, Yarra. Naresh</i>  | 26-34 |
| <b>An insight on transparent antennas</b><br><i>Pushpa U. S, Smita Chopde</i>   | 35-41 |
| <b>The Effect of Design Parameters of an Integrated Linear Electromagnetic Motor, At the Process of Pulling Away Anchor, From Its Breakaway Stage</b><br><i>Dr. Ginady G. Ugarov, Dr. Vladimir Iv. Moshkin, Dr. Amer Kh. Massad</i> | 42-49 |
| <b>Thermal Analysis of Clay Pot in Pot Refrigerator</b><br><i>Harish. H. G, Y. T. Krishne Gowda</i>   | 50-55 |
| <b>Effects of applied voltage and flow rates of ozone generator fed by dry air and O2 on the coaxial wire-cylinder reactor by varying various electrodes parameters</b><br><i>Hamid. H. Murbat</i>                                  | 56-60 |
| <b>A Review of Routing Protocols for Wireless Sensor Network</b><br><i>Vikas Chaudhary, Aasiya Khatoon, Nalin Chaudhary</i>   | 61-66 |

## Testing Model Of Development Organic Farming Dragon Fruit Based Market Research

Kustiawati Ningsih<sup>1</sup>, Halimatus Sakdiyah<sup>2</sup>, Herman Felani<sup>3</sup>

<sup>1,3</sup>Agribusiness Study Program, Faculty Of Agriculture, University of Islam Madura, INDONESIA

<sup>2</sup>Fakulty Of Economics, University of Islam Madura, INDONESIA

<sup>1</sup>[ningsihkustiawati@yahoo.com](mailto:ningsihkustiawati@yahoo.com), <sup>2</sup>[hsfeum@yahoo.com](mailto:hsfeum@yahoo.com), <sup>3</sup>[felani.here@yahoo.com](mailto:felani.here@yahoo.com)

**Abstract:** This study aims to test the model of the development of organic farming dragon fruit which has been obtained in previous studies. This follow-up study to test the model that has been obtained, through a comprehensive marketing research by analyzing the factors which influence consumers purchasing organic dragon fruit. Object of the research in Pamekasan, The method used is the analysis of factors that influence consumer buying decisions in determining organic dragon fruit. The data used is the 60 respondents, the number of variables studied were 23 variables, factor analysis is based on 22 variables that can be further analyzed. One variable ignored because the value of the MSA is less than 0.5, the results showed that of the 22 variables were analyzed. The results showed that of the 22 variables analyzed, there are 8 factors that influence consumers to buy organic dragon fruit, while the results of the 8 factors analyzed are: [1] Psychological (eigen value = 5,025), [2] The product (eigen value = 3,015), [3] Social (eigen value = 2,186), [4] Distribution (eigen value = 1.640), [5] Price (eigen value = 1.354), [6] Promotion (eigen value = 1,286), [7] Individuals (eigen value = 1,196), [8] Service (eigen value = 1.115), overall there are 3 of the most dominant factor affecting the marketing of organic dragon fruit, is the first factor of the product, the second is the social factor and the third factor is the price.

**Keywords:** marketing research, organic farming dragon fruit, factor analysis

### I. INTRODUCTION

Based on the model of the development of organic farming through the dragon fruit QSPM matrix method that has been obtained, priorities resulting organic agriculture development strategy that optimizes the dragon fruit quality control on products and existing markets (STAS = 5.607) as shown in Figure 1. So that further research needs to be done is to optimize the cultivation practices of organic farming dragon fruit thoroughly and improve product quality. Therefore, the need for an understanding of the concepts of technical and non-technical agriculture by the farmers so that they can ensure the process will go well as expected.

Marketing of organic dragon fruit is still in the traditional markets that need to be expanded. Therefore, the expansion of the market can still be done, especially for supermarkets located in the city of Pamekasan. Before expanding market, as manufacturers must know and analyze the factors that influence consumer decisions in the purchase of organic dragon fruit.

Research related to the analysis of the factors that influence consumer decisions in the purchase of a product has been done. One of the research is less common genital Indrayani et al (2013) about the factors that influence the consumer's decision to purchase dairy products Ultra High Temperature (UHT), The results showed that the results of data analysis showed the factors that influence consumer buying UHT milk is the selling price, the price of rival products, flavor, nutritional composition, addition of these results it can be seen that the dominant independent variable which determines the purchasing decisions in buying products UHT milk in Supermarkets Persada is a dairy flavor factor. Other research is Haliana study (2012) on the analysis of the factors that influence consumer decisions in the purchase decision making instant noodles brand Indomie. The results showed that based on the results of tests performed found that all the factors of both the cultural, social, personal and psychological influence on product purchase decision Indomie Instant Noodles Brand. However, of the four most dominant factors are the cultural factors with a correlation value of 0.466 making purchasing decisions.

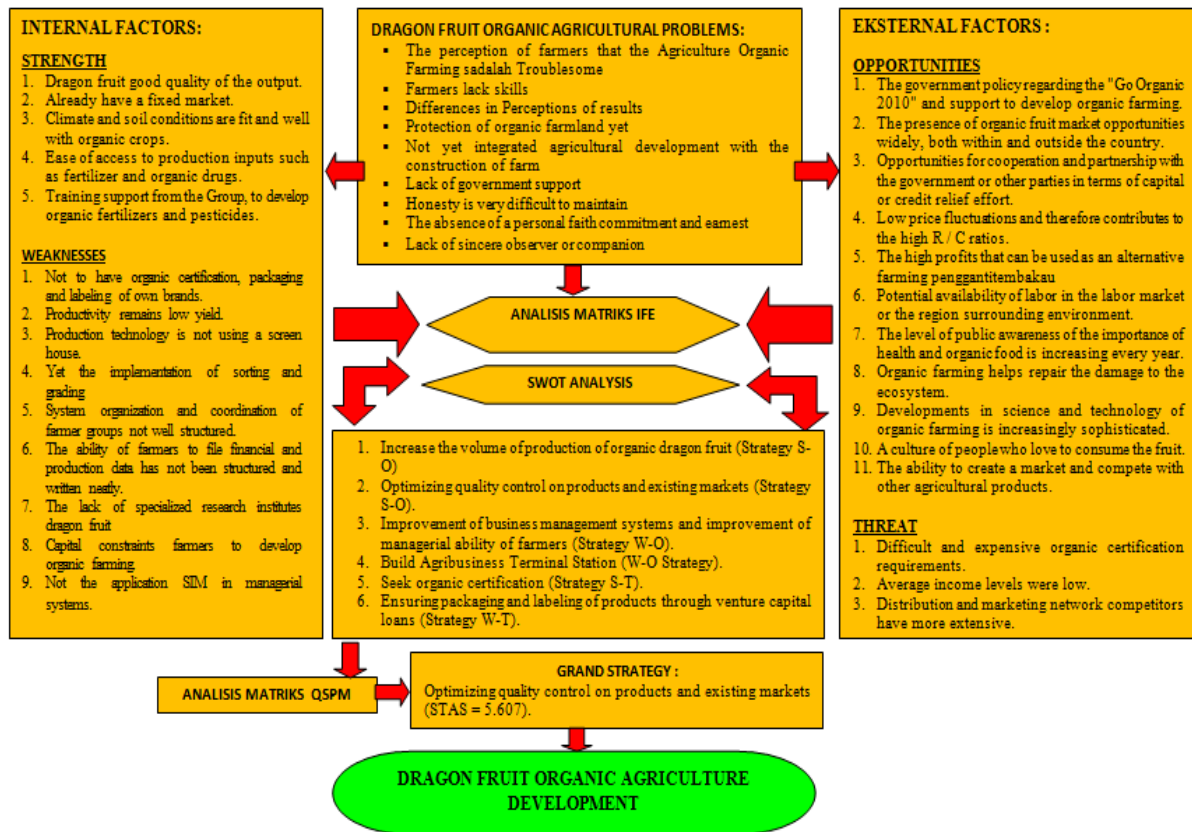


Figure 1. Model Development of Organic Farming Dragon Fruit

Based on the results of research that has been done some research, it can be seen that very many factors that influence the behavior or background for a consumer in making a purchase decision for a product whether it be a product that is tangible or intangible (service). Research of others will be used as a tool to test models of development of organic agriculture researcher dragon fruit is obtained in the first year of study.

## II. RESEARCH METHODS

### 2.1. Location and time study

The research was conducted in the village of the District ban Blumbungan Pamekasan with 50 asl altitude, ± 6.4 hectares of land area. The region selected by purposive sampling because the organic dragon fruit production centers in Pamekasan, this study was conducted in April 2014 until July 2014.

### 2.2. Types and sources of data

The data used in this study consisted of primary and secondary data, namely:

- **Primary data**

Primary data is data obtained directly from the field to conduct direct interviews with relevant parties in this case the Department of Agriculture, Office of Information Agriculture and Forestry Extension, Organic Farmers, Growers Semi Organic, Conventional Farmers, Local Community Leader, Initiator of Organic Farming, consumer / Market Participants Organic Products.

- **Secondary Data**

Secondary data were obtained by collecting written sources or documents from the Office of the Village, District, Department of Agriculture, and from a variety of library books that no connection with this research.

### 2.3. Population, sample and research instrument

The population in this study are those related to the development of organic farming. Determination of the number of samples is not restricted but saw the development of research on information obtained through the questionnaire, interview and observation were performed. The sample interviewed are:

- Farmers who carry out the dragon fruit cultivation in semi organic and still tolerate the use of fertilizers /pesticides synthetic.
- Conventional farmers in the cultivation process still relies on seeds, fertilizers and synthetic pesticides.
- Prominent initiators / pioneers of organic farming
- Local leaders of local
- Government officials from the Department of Agriculture, Office of Information Agriculture and Forestry Extension, and the District.
- Consumer / organic dragon fruit market participants Blumbungan.

#### 2.4. Methods of data analysis

Data analysis methods used is factor analysis. Factor analysis equation or formula is as follows:

$$X_i = A_{i1}F_1 + A_{i2}F_2 + A_{i3}F_3 + A_{i4}F_4 + \dots + V_iU_i \dots \dots \dots (1)$$

Where :

- $F_i$  = standardized variables to  $i$
- $A_{i1}$  = regresidari coefficient to the variable  $i$  on unique factor to  $i$
- $V_i$  = standardized regression coefficient of variable  $i$  on factors unique to the  $i$ th
- $F$  = common factor
- $U_i$  = unique variable to variable to  $i$
- $M$  = number of common factors

Details common factor can be formulated as follows:

$$F_i = W_{i1}X_1 + W_{i2}X_2 + W_{i3}X_3 + \dots + W_{ik}X_k \dots \dots \dots (2)$$

Where:

- $F_i$  = Factor to estimate  $i$
- $W_i$  = Weighting factor or factor score coefficients
- $X_k$  = Number of variables

The main principle is the correlation factor analysis, the assumptions associated with statistical correlation methods:

- a. Large correlation or correlation between variables must be sufficiently strong independet.
- b. Large partial correlation, the correlation between two variables by assuming other variables remain.
- c. Testing a correlation matrix is measured by the amount of Barlett Test Of Spercicity or with Measure Sampling Adequacy (MSA).

Having obtained samples and test assumptions are met, then the next step is to make the process of factor analysis. The process includes:

- a. Examine variables that will be analyzed.
- b. Test variables have been determined, using the Bartlett Test of Spercicity and MSA.
- c. Core process of factor analysis, namely factoring, or decrease one or more factors of the variables that have passed the test of the previous variables.
- d. Doing the rotation or rotation factor to the form factor. The purpose of the rotation to clarify the variables that go into a particular factor.
- e. Interpretation or factors that have been formed, which is considered to represent the member variables of these factors.
- f. Validation of the results of factors to determine whether the factors that have a valid form.

The first stage in the analysis was to assess which factors are variables that are considered eligible for inclusion in subsequent analyzes. The test is performed by entering all variables that exist, then the variables tested. Logic test if a variable does have a tendency to cluster and form a factor, the variable will have a fairly high correlation with other variables, but on the contrary, if the variables with weak correlations on the other variables, it will be less likely to be clustered in certain factors.

KMO test and Bartlett Test, has some things that KMO numbers should be above 0.5 and significant must be below 0.05, whereas the MSA test numbers should be at 0 to 1, with the following criteria:

- MSA = 1, the variable can be predicted without error by the other variables.
- MSA > 0.5, and the predicted variables can still be analyzed further.
- MSA < 0.5, variables can not be predicted and could not be analyzed further, or excluded from other variables.

### III. RESULTS AND DISCUSSION

After the field data obtained, we then do a factor analysis method based on a predetermined, while the discussion phase of this study as follows:

#### 3.1. Factor analysis

Data processing of the factor analysis are as follows:

##### 1. Determining the variables to be analyzed.

Variables to be analyzed in this study were 23 variables, 23 variables are then tested by factor analysis.

##### 2. Test variables have been determined

23 variables were tested then performed factor analysis to test the value of KMO, Bartlett Test and MSA (*measures of sampling adequacy*). MSA value must be above 0.5.

Table I. *KMO and Bartlett's Test*

Kaiser-Meyer-Olkin Measure of Sampling Adequacy	.651
Bartlett's Test of Sphericity	Approx Chi Square
	1115.563
	Df
	139
	Sig.
	.000

From Table 1 above, it can be seen that the number of KMO and Bartlett Test worth 0.651 with a significance level of 0.000. Therefore, the variables and the sample can be analyzed further.

Of the 23 variables tested, we then see the value of the MSA, If the MSA values below 0.5, then these variables can not be analyzed further. Of the 23 variables MSA smallest value is the income level of consumers of organic dragon fruit (Q17) with a value of 0.461 MSA, therefore, the income level of consumers of organic dragon fruit (Q17) were excluded from the factors because it has the smallest number of MSA.

After a variable level of income consumers of organic dragon fruit removed from the factor, then the next step is to retest the 22 remaining variables. To see this, it can be seen in the value of KMO and Bartlett's Test as well as the value of the MSA.

Table II. *KMO and Bartlett's Test*

Kaiser-Meyer-Olkin Measure of Sampling Adequacy	.665
Bartlett's Test of Sphericity	Approx Chi Square
	1064.343
	Df
	175
	Sig.
	.000

From Table 2 above it can be concluded that the value of KMO and Bartlett's Test increased from 0.651 into 0.665 with significant fixed rate (0.000). This is because there is a reduction in the variable with the smallest MSA figures, it can increase the value of existing MSA.

1. Organic Dragon Fruit flavor (Q1) = 0.763.
2. Organic Dragon Fruit Aroma (Q2) = 0.753.
3. Organic Dragon Fruit size (Q3) = 0.685.
4. Organic Dragon Fruit Leather (Q4) = 0.703.
5. Dragon Fruit Organic Resilience (Q5) = 0.649.
6. Organic Dragon Fruit Price (Q6) = 0.511.
7. Organic dragon fruit price suitability of the Health Benefits (Q7) = 0.557.
8. Organic Dragon Fruit Price Competition (Q8) = 0.625.
9. Promotion of Organic Pitaya (Q9) = 0.630.
10. Direct Marketing Organic Pitaya (Q10) = 0.614,
11. Affordability Location to Obtain Organic Pitaya (Q11) = 0.619.
12. Ease of Getting Organic Pitaya (Q12) = 0.639.
13. Seller Services Provided to Consumers (Q13) = 0.675.
14. Consumer Habits in Eating Organic Pitaya (Q14) = 0.685.
15. Healthy Lifestyle Trend (Q15) = 0.612.
16. Age Organic Dragon Fruit consumption (Q16) = 0.615.
17. Family Influence in Eating Organic Pitaya (Q17) = 0.596.
18. Influence Others in Eating Organic Pitaya (Q18) = 0.623.
19. Effect of Consuming role in Dragon Fruit Sellers (Q19) = 0.605.
20. Confidence Respondents in Eating Organic Pitaya (Q20) = 0.739.

- 21. Respondents Perception in Eating Dragon Fruit (Q21) = 0.686.
  - 22. Experience in Eating Dragon Fruit Respondents (Q22) = 0.633.
- Thus the value of the MSA are all above 0.5, so it can be analyzed further.

**3. Doing factoring and rotation**

The next stage to extract the set of variables that already exist, to form one or several factors. In doing this extraction, the method used was *Principal Component Analysis*, formed after eight factors to determine the spread of the 22 variable factors, then the process is carried out using varimax rotation.

**Table III. Communalities**

	Initial	Extraction
Q1	1.000	.675
Q2	1.000	.704
Q3	1.000	.710
Q4	1.000	.630
Q5	1.000	.445
Q6	1.000	.652
Q7	1.000	.583
Q8	1.000	.460
Q9	1.000	.454
Q10	1.000	.623
Q11	1.000	.725
Q12	1.000	.758
Q13	1.000	.605
Q14	1.000	.725
Q15	1.000	.545
Q16	1.000	.534
Q18	1.000	.613
Q19	1.000	.563
Q20	1.000	.584
Q21	1.000	.637
Q22	1.000	.786
Q23	1.000	.753

Table 3 above shows that the variables Organic Dragon Fruit Flavour (Q1) resulted in approximately 67.5% of variance of the variables Q1, Organic Dragon Fruit Aroma variables (Q2) generates approximately 70.4% variance of the variables Q2, variable Size / Shape Organic Pitaya (Q3) resulted in 71.10% of variance of the variable Q3, Organic Dragon Fruit Leather variable (Q4) generates approximately 63.00% of the variance variable Q4, variable Dragon Fruit Organic Power Save (Q5) generates approximately 44.5% of the variance variable Q5, Organic Dragon Fruit Price variable (Q6) resulted in approximately 65.2% of the variance variable Q6, Suitability variable price Organic Dragon fruit on Health Benefits (Q7) generates approximately 58.3% of the variance variable Q7, variables Organic Dragon Fruit Price Competition (Q8) generates approximately 46.00% of the variance variable Q8, Organic Dragon Fruit Promotion variable (Q9) resulted in approximately 45.4% of the variance variable Q9, variable Direct Marketing Organic Pitaya (Q10) produces approximately 62.3% variance of the variable Q10.

Affordability location to obtain organic pitaya (Q11) produces approximately 72.5% variance of the variables Q11, variables ease of getting organic pitaya (q12) generates approximately 75.8% variance of the variables Q12, variable seller services provided to consumers (q13) generates approximately 60.5% variance of the variables Q13, consumers eating habits variables in organic pitaya (Q14) produces approximately 72.5% variance of the variables Q14, Healthy Lifestyle Trend variable (Q15) produces approximately 72.5% variance of the variables Q15, Age variable in Eating Organic Pitaya (Q16) produces approximately 53.4% variance of the variables Q16, The influence of family variables in Eating Organic Pitaya (Q18) produces approximately 61.3% variance of the variables Q18, Others Influence variables in Eating Organic Pitaya (Q19) produces approximately 56.3% variance of the variables Q19, The influence of variables in Eating Dragon Fruit Sellers (Q20) produces approximately 58.4% variance of the variables Q20, Respondents Confidence variable in Eating Organic Pitaya (Q21) produces approximately 63.7% variance of the variables Q21, Respondents perception variables in Eating Dragon Fruit (Q22) produces approximately 78.6% of the variance of variables and variable Q22 Respondents experience in Eating Dragon Fruit (Q23) produces approximately 75.3% variance of the variable Q23.

Table IV. Total Variance Explained

Component	Initial Eigenvalues			Extraction Sums of Squared Loadings		
	Total	% of Variance	Cumulative %	Total	% of Variance	Cumulative %
1	5.025	17.624	17.624	5.025	17.624	17.624
2	3.015	11.819	29.443	3.015	11.819	29.443
3	2.186	8.126	37.569	2.186	8.126	37.569
4	1.640	6.100	43.669	1.640	6.100	43.669
5	1.354	5.010	48.679	1.354	5.010	48.679
6	1.286	5.673	54.352	1.286	5.673	54.352
7	1.196	4.497	58.849	1.196	4.497	58.849
8	1.115	4.165	63.014	1.115	4.165	63.014
9	.883	4.584	67.598			
10	.894	3.245	70.843			
11	.899	3.225	74.068			
12	.825	3.087	77.155			
13	.807	3.005	80.160			
14	.607	2.175	82.335			
15	.576	2.103	84.438			
16	.565	2.065	86.503			
17	.510	2.716	89.219			
18	.455	2.603	91.822			
19	.447	2.856	94.678			
20	.394	1.098	95.776			
21	.378	1.435	97.211			
22	.289	1.087	98.298			
23	.275	1.702	100.000			

From table 4, it can be seen that there are 22 factors that go into factor analysis, but in the above table are only 8 factors formed, therefore researchers only limiting factor 8.

Table V. Component matrix (a)

	Component							
	1	2	3	4	5	6	7	8
Q1	.483	.354	-.357	-.219	-.230	-.147	-.156	-.053
Q2	.576	.225	-.389	-.246	-.086	-.117	.037	.100
Q3	.375	.386	-.405	-.305	-.038	-.129	-.010	-.167
Q4	.389	.087	-.086	-.137	.403	-.198	-.265	.357
Q5	.426	.255	-.257	-.001	-.236	.109	-.028	-.175
Q6	.247	.450	.119	.327	.315	.253	.125	.028
Q7	.389	.337	.098	-.164	-.237	.075	.354	-.153
Q8	.157	.396	.286	.002	-.197	-0.370	.200	.005
Q9	.254	.335	.278	.187	-.389	.198	.187	.006
Q10	.302	.199	.275	.121	-.374	.269	.260	.110
Q11	.486	.269	.155	.130	.009	-.278	-.300	-.152
Q12	.386	.178	.285	.050	.200	-.175	-.210	-.378
Q13	.126	.375	-.019	.392	.165	.109	-.279	.295
Q14	.427	.100	-.125	-.135	.198	.385	.257	-.326
Q15	.296	.495	.096	.267	.100	.125	-.193	.075
Q16	.486	.069	-.297	-.059	.157	.034	-.156	-.109
Q18	.486	-.287	.069	-.098	.332	-.068	.107	.223
Q19	.486	-.300	.106	.099	-.065	.126	.268	.105
Q20	.368	-.237	.076	.300	-.247	-.020	.298	-.103
Q21	.287	-.230	.065	-.356	-.202	-.026	.346	-.102
Q22	.352	-.157	.325	-.163	-.199	.226	-.239	.376
Q23	.349	-.148	.259	-.149	-.079	.220	-.236	.350

After it is known that eight factors are the most optimal amount, then the component matrix table shows the distribution of the 22 variables on the eight factors formed. While the figures in the table is the factor loading, which indicates the magnitude of the correlation of a variable with a factor of 1 to 8 process will determine which variable will enter the factor which, carried by a large ratio of the correlation of each row.

For example, Organic dragon fruit flavors (Q1) has some correlation, namely:

1. Correlation between Q1 denganfaktor 1 is 0.483 (pretty, but weak as below 0.5).
2. Correlation between Q1 by a factor of 2 is 0.354 (weak, below 0.5).
3. Correlation between Q1 by a factor of 3 is -0.357 (very weak, below 0.5)
4. Correlation between Q1 by a factor of 4 is -0.219 (very weak, below 0.5).
5. Correlation between Q1 by a factor of 5 is -0.230 (very weak, below 0.5).
6. Correlation between Q1 by a factor of 6 is -0.147 (very weak, below 0.5).
7. Correlation between Q1 by a factor of 7 is -0.156 (very weak, below 0.5).
8. Correlation between Q1 by a factor of 8 is -0.053 (very weak, below 0.5).

According *Singgih Santoro (2004)*, that the distribution of the variable component matrix shows that there is the form factor. While the figures in the table is the factor loading matrix component shows a large correlation between a variable with factors there. Rotated component matrix shows the distribution of the more real variables, Table 6 below shows the change in the value of the variable.

Table VI. *Rotated component matrix*

	Component							
	1	2	3	4	5	6	7	8
Q1	.052	.736	.032	.033	.068	.151	-.052	-.015
Q2	.147	.775	.004	.024	.078	-.003	.230	.060
Q3	-.139	.738	-.025	.086	.070	-.058	.176	.003
Q4	-.025	.730	.006	.127	.046	-.015	.310	.230
Q5	.209	.490	-.003	.109	.169	.087	-.179	.200
Q6	-.070	-.020	-.100	.627	.168	.089	.148	.200
Q7	-.030	.347	.079	-.039	.490	.082	.015	.353
Q8	-.162	.078	.110	.227	.497	-.024	.059	-.045
Q9	-.010	-.012	.067	.290	.068	.425	.010	.258
Q10	.078	.099	.069	.046	.215	.570	.027	-.356
Q11	.036	.235	.065	.678	.170	.153	.004	-.125
Q12	.012	.068	.139	.705	.040	.225	.039	.160
Q13	.036	.097	-.020	.292	-.005	.010	.008	.692
Q14	.427	.100	-.125	-.135	.198	.385	.257	-.326
Q15	-.036	.169	.026	.648	.150	.183	-.060	.046
Q16	.260	.118	.047	.169	-.210	.479	.116	.189
Q18	.286	.030	.587	.010	-.049	.060	.300	.049
Q19	.440	-.017	.468	-.067	.200	.100	.065	.055
Q20	.258	-.098	.479	-.098	.347	.107	.100	.107
Q21	.658	.046	.185	.137	.159	-.103	.010	-.182
Q22	.725	.040	.069	-.119	.039	.176	.120	.096
Q23	.649	.030	.257	-.120	.028	.150	.115	.086

From Table 6 above, can be explained for example we take the variable organic dragon fruit flavors (Q1), the greatest factor loading is on factor 2 with the value of 0.736, it means organic dragon fruit flavors are at a factor of 2. Therefore the 22 variables above, reduced to eight factors, namely:

1. The first factor consists of: *Consumer Habits in Eating Organic Dragon Fruit, Respondent Confidence in Eating Organic Dragon Fruit, Respondents Perception in Eating Organic Dragon Fruit, Respondents experience in Eating Organic Dragon Fruit.*
2. The second factor consists of: *Organic Dragon Fruit Flavour, Aroma Organic Pitaya, Dragon Fruit Size Organic, Organic Skin Pitaya, Dragon Fruit Organic Resilience.*
3. The third factor consists of: *The influence of the family in Eating Organic Dragon Fruit, Influence Others in Eating Organic Dragon Fruit, Influence Sellers in Eating Organic Dragon Fruit.*
4. The fourth factor consists of: *dragon fruit price Organic, Healthy Lifestyle Trend, Affordability Location to Obtain Organic Pitaya, Dragon Fruit Organic Ease of Getting.*
5. The fifth factor consists of: *dragon fruit price Conformance to the Health Benefits of Organic, Organic Dragon Fruit Price Competition.*
6. The sixth factor consists of: *Promotion of Organic Pitaya, Dragon Fruit Organic Direct Marketing.*
7. Seventh factor consisted of: *age in Eating Organic Dragon Fruit.*
8. Eighth factor consists of: *Services provided by the Seller to the Customer.*

According *Singgih Santoro (2004)*, that the distribution of the variable component matrix shows that there is the form factor. While the figures in the table is the factor loading matrix component shows a large correlation between a variable with factors there. Rotated component matrix shows the distribution of the more real variables, Table 7 below shows the change in the value of the variable.

**Table VII. Component transformation matrix**

Component	1	2	3	4	5	6	7	8
1	.426	.450	.279	.170	.210	.291	.290	.185
2	-.447	.505	.204	.494	.305	.118	-.149	.090
3	-.230	-.526	.525	.050	.410	.300	.039	-.063
4	.470	-.308	-.486	.476	.122	.100	-.105	-.098
5	-.225	-.190	-.053	.285	.552	.150	.524	.295
6	.104	-.120	-.296	.337	.168	-.028	-.426	.489
7	-.025	-.129	-.279	-.296	.497	-.269	.415	.385
8	-.029	.018	.153	.225	.119	-.498	.359	-.560

From table 7 above, can be explained that the diagonal factor of 1 to 8 was obtained (0.426; 0.505; 0.525; 0.476; 0.552, -0.28, 0.415, -0.560). Number with a minus sign (-) indicates the direction of the correlation, while the diagonal which shows a figure below 0.5 which indicates the presence of other components contained in each of the factors that have a higher correlation. Therefore, there are three factors whose value is above 0.5, namely: a factor of 2 (0.505), factor 3 (0.525), and a factor of 5 (0.552).

**3.2. Interpretation of factors that have formed**

If factor and rotation has been performed, the next step is to interpret the factors that have been formed. This is done in order to represent the member variables of these factors. Giving the name of each factor is determined based on the variables in it (Hasan & Saputro, 2007). Based on the results of these studies it is known that psychological factors, products, social, distribution, pricing, promotion, and greatly affect the individual consumer.

Important part of the consumer buying process is Psychological Factors, Kotler (2000) states that the consumer into buying a product can be affected by several things: motivation, perception, experience and confidence. Based on the analysis of these factors can be concluded that consumers in buying organic dragon fruit has a variety of reasons but the determining factor of consumer psychology into their buying decisions determining the dragon fruit.

**IV. CONCLUSION**

Based on the above analysis of marketing research are modeling the factors that influence consumers in deciding to buy organic dragon fruit, so it can be concluded that there are eight most influential factor for determining consumers to buy organic dragon fruit, namely:

- Psychological factors consist of the variable: Consumer Habits in Eating Organic Pitaya (FL = 0.427), Respondent Confidence in Eating Organic Pitaya (FL = 0.658), Respondents Perception in Eating Organic Pitaya (FL = 0.725), the Respondents Consuming Experience Organic Dragon Fruit (FL = 0.649).
- Product factors consists of several variables: Organic Dragon Fruit Flavour (FL = 0.736), Dragon Fruit Aroma Organics (FL = 0.775), Organic Dragon Fruit Size (FL = 0.738), Organic Dragon Fruit Leather (FL = 0.730), Resilience Dragon Fruit organic (FL = 0.490).
- Social factors consists of several variables: The influence of the family in Eating Organic Pitaya (FL = 0.587), Influence of Others in Eating Organic Pitaya (FL = 0.468), Effect of Seller in Eating Organic Pitaya (FL = 0.479).
- Distribution factor consists of several variables that include: Organic Dragon Fruit Price (FL = 0.627), Healthy Lifestyle Trend (FL = 0.648), Affordability Location to Obtain Organic Pitaya (FL = 0.678), Ease of Getting Organic Pitaya (FL = 0.705).
- Price factor consists of several variables that include: Dragon Fruit Organic Conformity Price on Health Benefits (FL = 0.490), Organic Dragon Fruit Price Competition (FL = 0.497).
- Factors Promotion consists of several variables that include: Promotion of Organic Organic Pitaya (FL = 0.425), Direct Marketing Organic Organic Pitaya (FL = 0.570).
- Individual factors consist of variables: age in Eating Organic Pitaya (FL = 0.479).
- Service consists of variable factors: Services provided by the Seller to the Customer (FL = 0.692).

## REFERENCES

- [1]. Kadir, Abdul, 2002, *Organic Farming, Alternative Pananggulangan Crisis of Modern Agriculture Towards Sustainable Agriculture*, Philosophy of Science Papers
- [2]. Kotler, Philips. 2000, *Marketing Management: Analysis, Planning, Implementation and Control*. Salemba Four. Jakarta.
- [3]. Lehman. (1997), *Organic farming has a bright prospect. Scientific Magazine universe University General Sudirman (PKA)*. Vol (1), no. 1.
- [4]. Rangkuti, Freddy. 2001, *SWOT Analysis Technique Dissecting the Business Case. Reorientation of Strategic Planning Concepts for the 21st Century Facing*, PT. Scholastic Press. Jakarta.
- [5]. Rosalinda, Linda, 2009, *Business Development Strategy Analysis of Organic Vegetables at Farmers Group Sugih Farmers in Zone Agropolitan Karehkel Village, District Leuwi Liang, Bogor Regency*. Thesis. Department of Management. Faculty of Economics and Management. Bogor Agricultural University. Bogor.
- [6]. Santoso, Singgih. 2004, *Complete Guide to Mastering SPSS 17*. Elex Media Komputindo. Jakarta.
- [7]. Saptana, et al, 2007, *The Sustainable Agriculture Development Through Business Partnership*, *Journal of Agricultural Research*, 26 (4), 2007, <http://www.pustaka.deptan.go.id>
- [8]. Sitorus, Felix, 2006, *The Cultural Ecology Paradigm for the Development of Rice Agriculture*, *Agricultural Policy Analysis Journal* Volume 4 Number 3, 167 -184, Bogor Agricultural University. Bogor.
- [9]. Suryana, Achmad, 2005, *The Sustainable Agriculture Development Mainstay of National Development, Sustainable Agriculture Systems*. Seminar Paper to Support National Development February 15, 2005 at the University of March Solo, <http://pse.litbang.deptan.go.id> Department of Agriculture. 2004 Four Years Go Organic Directorate General BPPHP 2010. <http://agribisnis.deptan.go.id> [March 3, 2010]
- [10]. Sutanto, Rachman, 2002, *Towards Organic Farming and Sustainable Agriculture Alternative*, Canisius Publisher, Yogyakarta.
- [11]. Suwanto, Andreas Avelinus. 2008, *Analysis of Development of Organic Agriculture in Magelang District (Case Study in District Sawangan)*. Thesis. Master of Environmental Science Program. Graduate Program. Diponegoro University. Semarang.
- [12]. Law of the Republic of Indonesia No. 4 of 2006 on the Ratification of the International Treaty On Plant Genetic Resources For Food And Agriculture (*Agreement Concerning the Plant Genetic Resources for Food and Agriculture*).
- [13]. Winangun, Y.W. 2005, *Character Building Successful Organic Farmers in the Age of Globalization*. Canisius, Yogyakarta.
- [14]. Winarno, F.G, A. K. Seta, and Surono. 2002, *Organic Agriculture and Food Systems and Certification*. M-BRIO PRESS, Bogor.

## Synthesis and Characterization of Mn, Ce Co-Doped CdS Nanoparticles Synthesized Via Co-Precipitation Method

M. Sreenivas<sup>1</sup>, G. S. Harish<sup>2</sup>, P. Sreedhara Reddy<sup>3</sup>

<sup>1,2,3</sup>Department of Physics, Sri Venkateswara University, Tirupati, Andhra Pradesh-517502, India

**Abstract:** Mn, Ce co-doped CdS nanoparticles were prepared by chemical co-precipitation method at room temperature. The prepared samples were characterized by X-ray diffraction (XRD), scanning electron microscopy (SEM), energy dispersive analysis of X-rays (EDAX), photoluminescence (PL) and high resolution Raman spectroscopic techniques. X-ray diffraction studies showed that the diameter of the particles was around 10-12 nm. Broadened XRD peaks revealed the formation of nanoparticles with wurtzite structure. The Raman spectra of undoped and Mn, Ce ions co-doped CdS nanoparticles showed longitudinal optical mode. Compared with the 1LO and 2LO Raman modes (296 and 590  $\text{cm}^{-1}$ ) of undoped CdS nanoparticles, the Raman modes of Mn, Ce co-doped CdS nanoparticles were slightly shifted towards lower frequency. PL spectra of the samples showed remarkable enhancement in the intensity upon doping.

**Keywords:** Chemical synthesis, Nanoparticles, Photoluminescence, Raman spectra, XRD

### I. INTRODUCTION

The Nanomaterials doped with optically active luminescence centers create new opportunities for luminescence research and also for the application of nanometer-scale structured materials. Doped II–VI semiconductors like ZnS:Cu, CdS:Mn, etc have been intensively investigated with new luminescence centers [1–3]. Cadmium sulfide is an important semiconducting material that has attracted much interest owing to their unique electronic and optical properties, and their potential applications in solar energy conversion, photoconducting cells, non-linear optics and heterogeneous photocatalysis [4, 5]. The extended life time of charge carriers as observed in Mn doped CdS, for example, could be advantageous to improve the performance of solar energy conversion systems. When doping with Mn, for example, the photoinduced electrons in the conduction band of CdS are transferred to the Mn  $^4T_1$  state, which temporarily traps the electrons and prevents recombination with holes or oxidized electrolyte species [7]. Mn<sup>2+</sup> doped CdS NPs are interesting because of the fact that Mn<sup>2+</sup> ions provide good traps for the excited electrons, which give rise to their potential use in nonlinear optics, electronic and optoelectronic devices [8-10]. Many literatures from different groups have reported the optical properties of various doped nanocrystals and the potential application of these luminescent materials. Today, various transition metal ions and rare-earth ions as impurities doped in CdS nanocrystalline materials have many interesting optical properties [11-15].

Previous works have shown that large quantities of nanomaterials were prepared by various methods artificially. Optoelectronic properties, particle sizes, and morphologies of nanomaterials have a close relation to preparation conditions. Appropriate preparation methods should be utilized according to the demands for different applications. Nanocrystalline CdS, CdTe, CdSe, ZnSe and PbS have been synthesized by a variety of methods including precipitation, sputtering, electrochemical deposition and inverse micelles. A reduction in the particle size strongly influences the crystallinity, melting point and structural stability. In the present work, Ce and Mn co-doped CdS nanoparticles were prepared via cost effective, facile chemical co-precipitation method at room temperature and the structural, morphological, chemical composition and luminescent properties of these nanoparticles were investigated.

### II. EXPERIMENTAL

All the chemicals used were of analytical reagent grade and used without further purification. Undoped CdS, cerium (Ce) (2 at.%) and manganese (Mn) (0, 2, 4 and 6 at.%) co-doped CdS nanoparticles were prepared by a simple chemical co-precipitation method with biocompatible polyvinylpyrrolidone (PVP) as a capping agent. The reactants were CdCl<sub>2</sub>, CeCl<sub>3</sub>.7H<sub>2</sub>O (2at. %), MnSO<sub>4</sub>.H<sub>2</sub>O, Na<sub>2</sub>S and polyvinylpyrrolidone (PVP). Ultrapure de-ionized water was used as the reaction medium in all the synthesis steps. In a typical

synthesis, desired molar proportions of CdCl<sub>2</sub>, CeCl<sub>3</sub>·7H<sub>2</sub>O (2at.%) and MnSO<sub>4</sub>·H<sub>2</sub>O (0,2,4 and 6 at.%) each in 50 ml were dissolved in ultrapure de-ionized water. An appropriate amount of capping agent PVP was added to control the growth of the nanoparticles during the reaction. Later stirring the solution for 60 min, Na<sub>2</sub>S solution was drop wisely added to the solution at room temperature under constant stirring which was continued for four hours to get fine precipitation. The obtained precipitate was washed with de-ionized water several times. Finally, the powders were vacuum dried for 3 hours at 80 °C to obtain Ce, Mn co-doped CdS nanoparticles. Undoped CdS nanoparticles were synthesized by the same procedure.

### III. CHARACTERIZATION

The as synthesized nanopowders were characterized by studying the structure, composition, surface morphology and optical properties. The X-ray diffraction patterns of the samples were collected on a Rigaku D X-ray diffractometer using Cu-K $\alpha$  radiation ( $\lambda=1.5406\text{\AA}$ ). The morphology and elemental composition of the prepared samples were analyzed through EDAX using Oxford Inca Penta FeTX3 EDS instrument attached to a Carl Zeiss EVO MA 15 scanning electron microscope. Photoluminescence spectra was recorded in the wavelength range of 400–650 nm using a PTI (Photon Technology International) Fluorimeter with a Xe-arc lamp of power 60 W and an excitation wavelength of 320 nm. Raman Spectroscopic studies of the as prepared samples were carried out using a LabRam HR800 Raman Spectrometer.

### IV. RESULTS AND DISCUSSION

#### 4.1. Structural Analysis

Fig. 1 represents the XRD patterns of undoped CdS and Ce, Mn co-doped CdS nanoparticles. The broadening of peaks indicates that particles are in the nanosize regime. The XRD pattern shows (100), (002), (101), (102), (110), (103) and (112) planes of wurtzite CdS corresponding to JCPDS File No. 41-1049. The planes (110), (103) and (112) clearly distinguish the wurtzite structure of the Mn doped CdS NPs. The intensity of the plane (102) is very low and this intensity increases as the doping concentration of Mn<sup>2+</sup> increases. The increased intensity of the plane (102) in doped CdS may be due to increased crystallinity in this plane on doping [16]. The low intensity in undoped system may be due to imperfection or due to the strain or low crystallinity in the crystals [16]. In the diffraction patterns, peak broadening is due to four factors: deformation of the lattice, crystalline domain size, crystalline faults and domain size distribution [16]. From the XRD spectra it was also observed that no diffraction peaks corresponding to the impurity phases were detected and this rule out Ce or Mn precipitation or secondary phases. The average particle size calculated by Debye Scherrer's equation [a] for Ce, Mn co-doped CdS nanoparticles lies in the range of 10-12 nm.

$$D = \frac{0.94\lambda}{\beta_{hkl} \cos \theta} \text{----- [a]}$$

Where, D is the average particle size and  $\beta_{hkl}$  is full width at half maximum of the XRD peak expressed in radians and  $\theta$  is the position of the diffraction peak. The average particle size of the samples was calculated by Debye Scherrer's equation [a].

#### 4.2. Morphological and Compositional Analysis

Fig. 2 shows the morphology of Ce, Mn co-doped CdS nanoparticles. Figures 2(a), 2(b), 2(c), 2(d) and 2(e) show the SEM images of pure CdS, CdS: Ce<sub>x</sub>, Mn<sub>y</sub> (x=2%, y=0%, 2% and 4%, 6%) respectively. SEM images showed the agglomerated nanoparticles of the prepared samples.

The chemical composition analysis of the Ce, Mn co-doped CdS nanoparticles was done using the EDAX technique. The EDAX spectra of the CdS: Ce, Mn nanoparticles shown in Fig. 3 confirms the effective doping of Ce and Mn. Figures 3(a), 3(b), 3(c), 3(d) and 3(e) shows the EDAX spectra of pure CdS, CdS: Ce<sub>x</sub>, Mn<sub>y</sub> (x=2%, y= 0%, 2%, 4%, 6%) respectively, confirmed that the samples were composed of Cd, Ce, Mn and S elements in desired composition and without any impurities.

#### 4.3. Photoluminescence Studies

Fig. 4 shows the PL spectra recorded at room temperature with an excitation wavelength of 390 nm for pure CdS, Ce (2%) and Mn (0, 2, 4 and 6 at. %) co-doped CdS nanoparticles. High intense peaks centered at 450 nm are assigned to band edge emission of CdS nanocrystallites. The peaks of the CdS nanocrystallites doped with Ce<sup>3+</sup> ions were almost the same as those of the pure CdS nanocrystallites. However, the fluorescence intensity of the CdS nanocrystallites doped with Ce<sup>3+</sup> ions is about 6 times of that of CdS

nanoparticles. The broad peak located around 605 nm may be arises from sulphur sites and the  $Mn^{2+}$  luminescence is caused by emission from the first excited state  ${}^4T_1$  to the ground state  ${}^6A_1$  [17-18]. An additional red-shifted emission feature is observed with increase in  $Mn^{2+}$  concentration.  $Mn^{2+}$  pairing has also been observed in  $Zn_2SiO_4:Mn^{2+}$  [19]. There are however a few reports on  $Mn^{2+}$  pairing in CdS: Mn nanoparticles and Chory et al.[20] were the only group reporting a red (640 nm) luminescence from CdS: Mn nanoparticles. Present studies show that, the enhanced luminescence properties of the PVP capped CdS: Ce, Mn nanoparticles that continued upto Mn (4 at.%) and a decrease in luminescence is observed at Mn (6 at.%). The red luminescence is attributed to  $Mn^{2+}$  pairing effect due to high concentration of  $Mn^{2+}$  and  $Ce^{3+}$  in CdS host lattice.

#### 4.4. Raman Spectroscopy

Raman spectra of the undoped and Ce (2 at. %) and Mn (0, 2, 4 and 6 at. %) co-doped CdS nanoparticles in the frequency range 200 - 700  $cm^{-1}$  are shown in Fig. 5. The Raman spectrum of bulk CdS exhibits the first longitudinal optical phonons (1LO) peak at 304  $cm^{-1}$  and the second longitudinal optical phonons (2LO) peak at 600  $cm^{-1}$ [21]. The Raman spectrum of undoped CdS nanoparticles exhibited strong but broad peaks at 296 and 590 $cm^{-1}$  corresponding to 1LO and 2LO optical phonons, respectively. The frequency shift of the Raman bands towards lower frequency could be due to large surface to volume ratio. In the case of large surface-to-volume ratio, surface scattering contributes more to the Raman signal than volume scattering. The frequency shifts of the 1LO and 2LO modes observed in the present samples may be attributed to a smaller size and larger surface-to-volume ratio compared with that of the undoped CdS. Another possible reason for the Raman shift is that the ionic radius of  $Ce^{3+}$  is higher than that of  $Cd^{2+}$ . Lattice defects are introduced or intrinsic host lattice defects are activated when  $Ce^{3+}$  and  $Mn^{2+}$  ions are incorporated. The  $Ce^{3+}$  and  $Mn^{2+}$  ions tend to occupy substitutional cationic sites resulting in host lattice defects. Further, no additional Raman modes due to Ce and Mn impurities were observed in Ce and Mn co-doped CdS nanoparticles. This revealed the absence of impurity phases in the prepared nanopowder samples.

### V. FIGURES

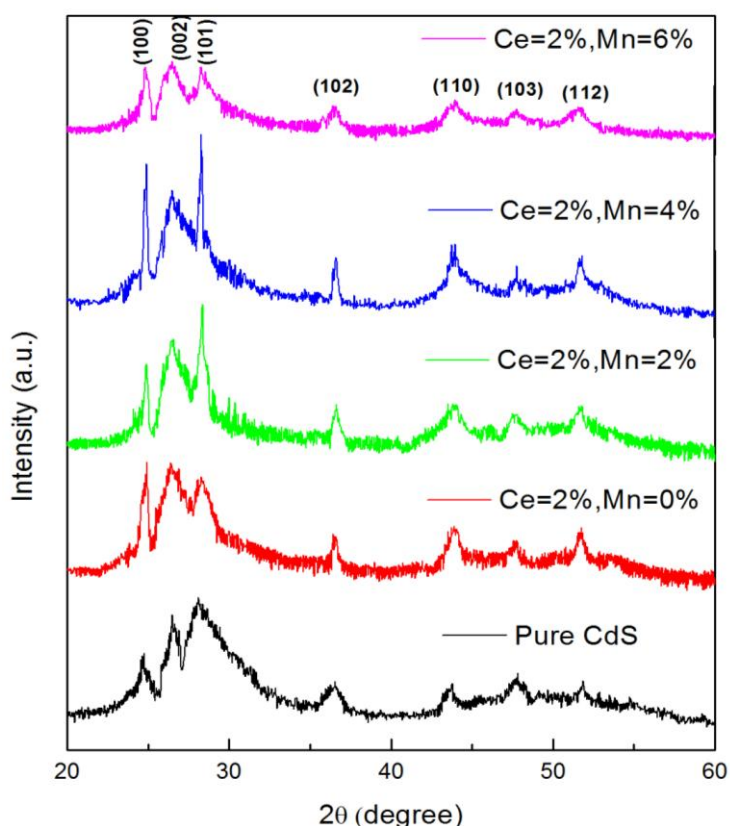


**Fig.1.** XRD patterns of undoped CdS and Ce, Mn co-doped CdS nanoparticles

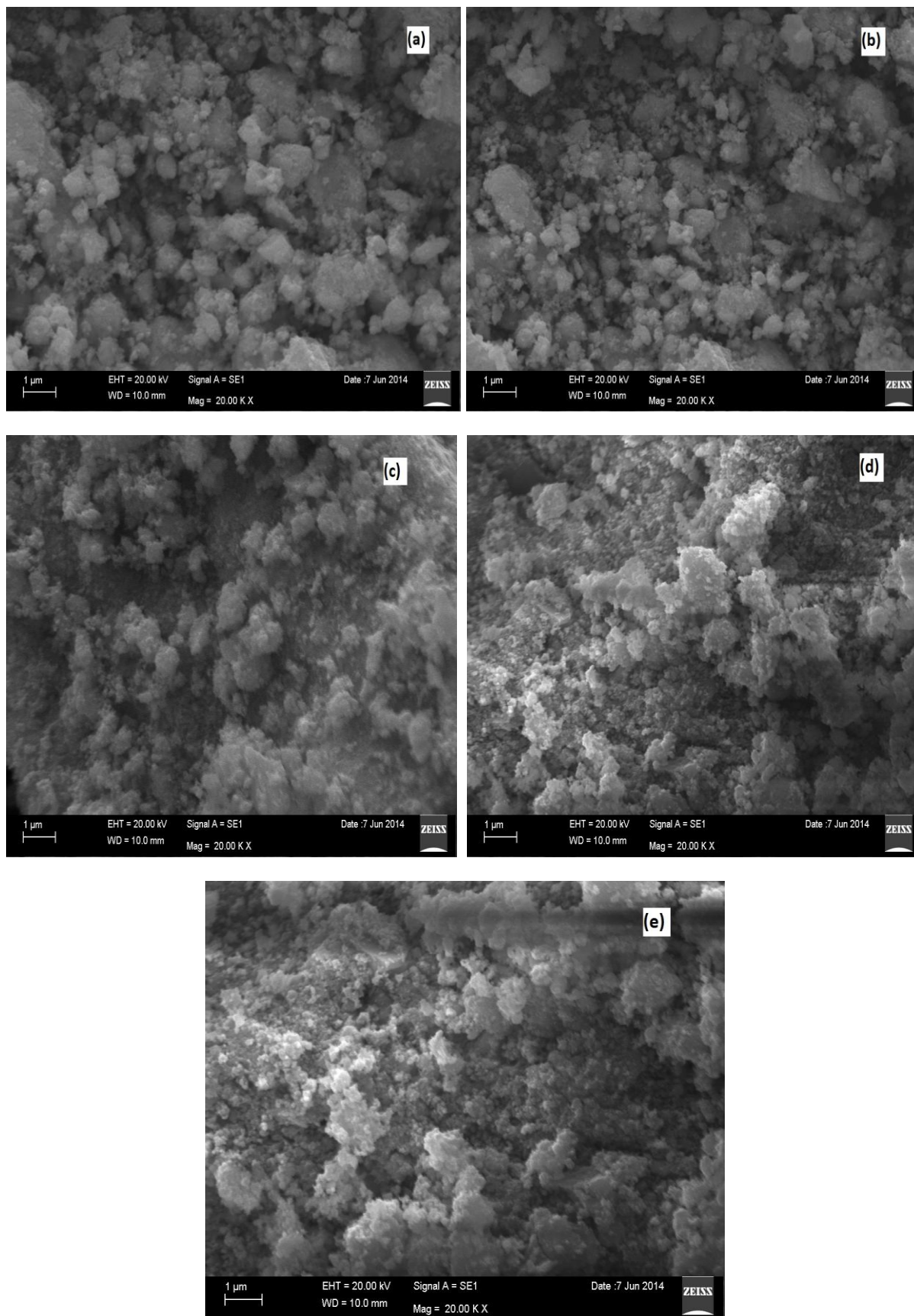


**Fig. 2.** SEM images of CdS: Ce, Mn nanoparticles. (a) Pure CdS, (b) Ce=2%, Mn=0%, (c) Ce=2%, Mn=2%, (d) Ce=2%, Mn=4% and (e) Ce=2%, Mn=6%

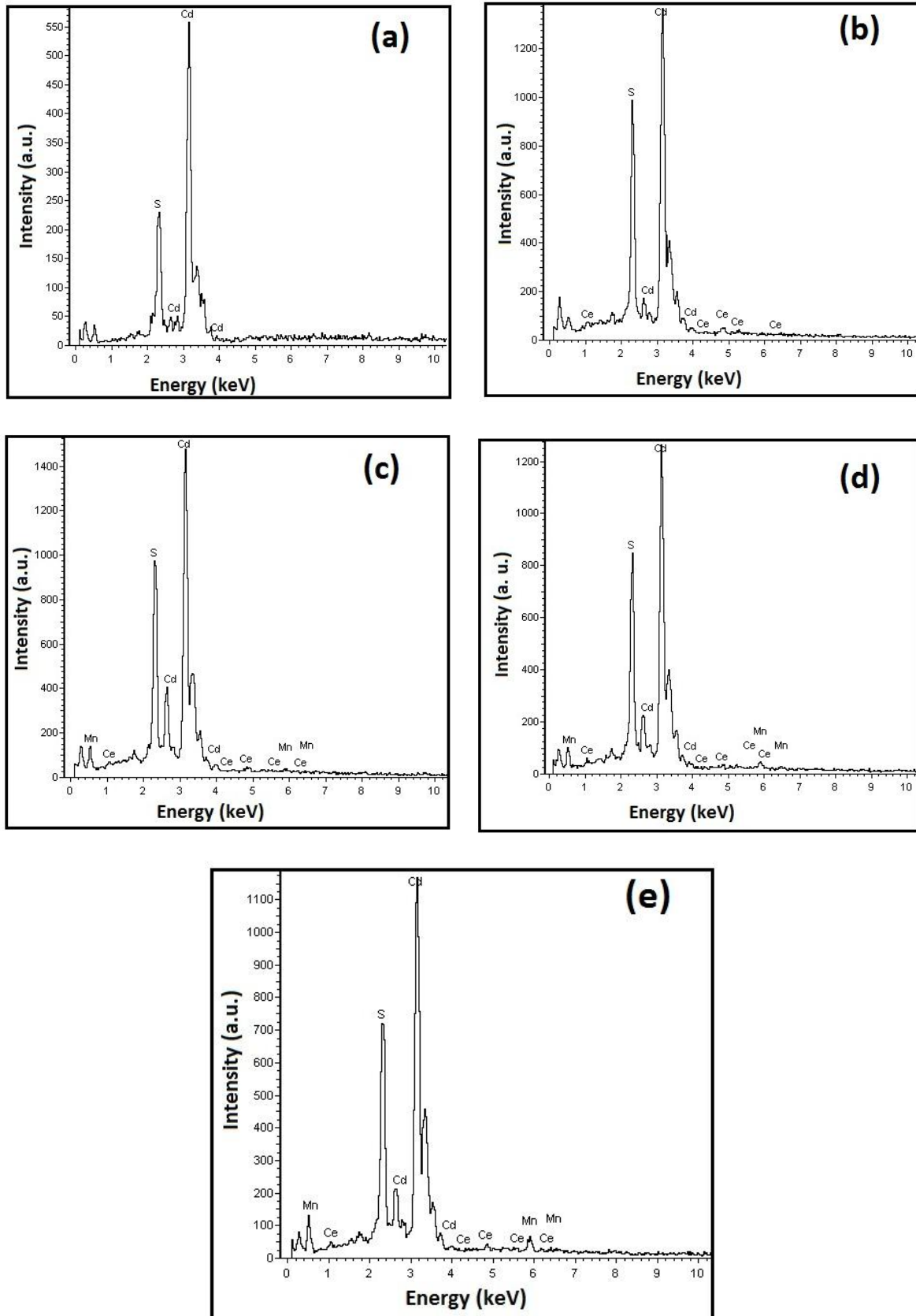


**Fig. 3.** Representative EDS spectrum of Ce, Mn co-doped CdS nanoparticles. (a) Pure CdS, (b) Ce=2%, Mn=0%, (c) Ce=2%, Mn=2%, (d) Ce=2%, Mn=4% and (e) Ce=2%, Mn=6%.

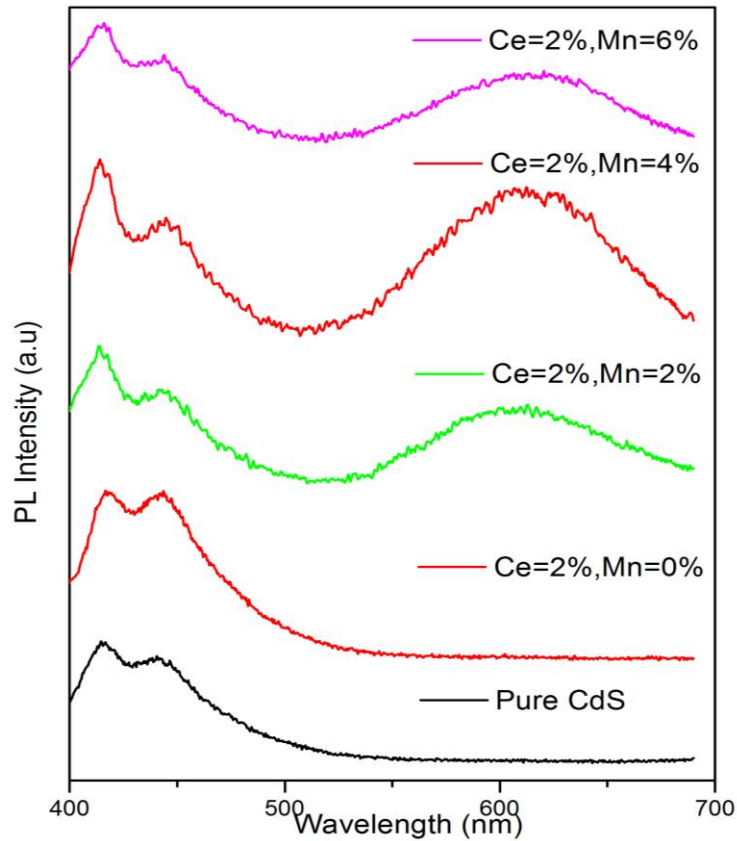


Fig. 4. Photoluminescence spectra of undoped and Ce, Mn co-doped CdS nanoparticles.

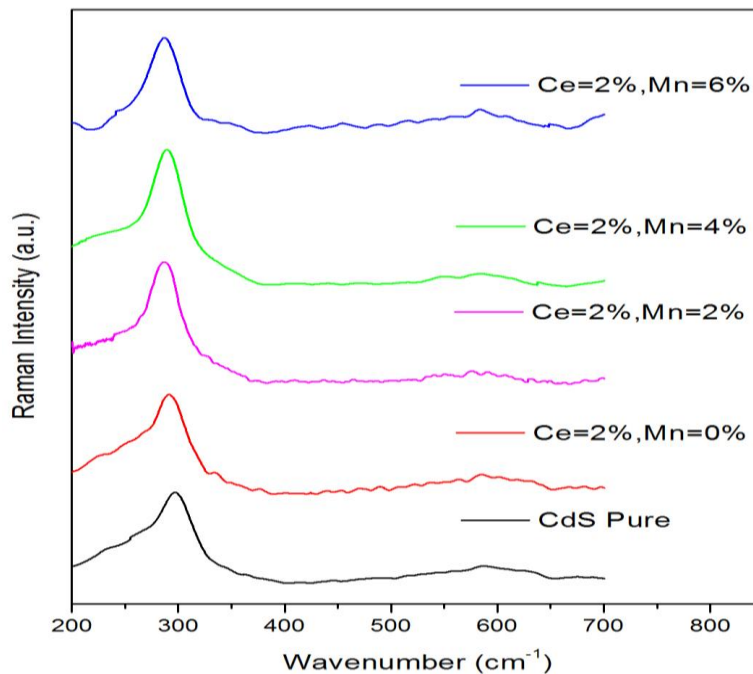


Fig. 5. Raman spectra of undoped CdS and Ce, Mn co-doped CdS nanoparticles

## VI. CONCLUSION

In summary, Ce and Mn co-doped CdS nanoparticles have been successfully synthesized by chemical co-precipitation method at room temperature. X-ray diffraction (XRD) measurements showed that the Ce, Mn co-doped CdS nanoparticles have a wurtzite structure. The morphology and composition of CdS: Ce, Mn

nanoparticles were successfully studied by scanning electron microscopy (SEM) and energy dispersive X-ray spectroscopy (EDAX) respectively. The luminescence peak of CdS nanoparticles is centered at 450 nm and is enhanced to 6 times by doping with Ce<sup>3+</sup> ions. The emission peaks of CdS: Ce, Mn nanoparticles are observed at 450 nm and broad emission peak around 610 nm are enhanced effectively that of undoped CdS nanoparticles with a red shift. Undoped CdS showed Raman peaks at 296 and 590 cm<sup>-1</sup> correspond to the 1LO mode and 2LO mode of the samples showed a slight red shift and asymmetric broadening indicating phonon confinement effects.

### Acknowledgements

One of the authors, Mr. G. S. Harish, is thankful to C.S.I.R., New Delhi, for awarding a Junior Research Fellowship.

### REFERENCES

- [1] W. Zhang, H.R. Lee, Synthesis and optical property of water-soluble ZnS:Cu quantum dots by use of thioglycolic acid, *Appl. Opt.* 49 (2010) 2566–2570.
- [2] A. Nag, S. Chakraborty, D.D. Sarma, To dope Mn<sup>2+</sup> in a semiconducting nanocrystal, *J. Am. Chem. Soc.* (2008) 10605–10611.
- [3] A. Nag, S. Sapra, C. Nagamani, A. Sharma, N. Pradhan, S.V. Bhat, D.D. Sarma, A study of Mn<sup>2+</sup> doping in CdS nanocrystals, *Chem. Mater.* 19 (2007) 3252–3259.
- [4] P. Verma, G.S. Manoj, A.C. Pandey, Organic capping-Effect and mechanism in Mn-doped CdS nanocomposites, *Physica B*, 405 (2010) 1253–1257.
- [5] G. Murugadoss, Synthesis of high quality and monodisperse CdS: Mn<sup>2+</sup>/ZnS and CdS:Mn<sup>2+</sup>/CdS core-shell nanoparticles, *Superlattices and Microstructures* 52 (2012) 1026–1042.
- [6] W. Lee, W.C. Kwak, S.K. Min, J.C. Lee, W. S. Chae, Y. M. Sung, S.H. Han, *Electrochem. Commun.* (2008) 1699–1702
- [7] M. Liu, Y. Du, L. Ma, D. Jing, L. Guo, Manganese doped cadmium sulfide nanocrystal for hydrogen production from water under visible light, *International Journal of Hydrogen Energy*, 37 (2012) 730-736
- [8] N.V. Hullavarad, S.S. Hullavarad, P.C. Karulkar, Review of Cadmium Sulfide CdS Nanotechnology: synthesis and Applications, *J. Nanosci. Nanotechnol.* 8 (2008) 3272-3299.
- [9] A. Nag, R. Cherian, P. Mahadevan, A.V. Gopal, A. Hazarika, A. Mohan, A. S. Vengurlekar, D. D. Sarma, Size-Dependent Tuning of Mn<sup>2+</sup> Emission in Mn<sup>2+</sup>-Doped CdS Nanocrystals: Bulk vs Surface, *J. Phys. Chem. C*, 114 (2010) 18323–18329.
- [10] M. A. White, A. L. Weaver, R. Beaulac, D. R. Gamelin, Electrochemically Controlled Auger Quenching of Mn<sup>2+</sup> Photoluminescence in Doped Semiconductor Nanocrystals, *ACS NANO*, 5, 5 (2011) 4158-4168.
- [11] S. Salimian, S.F. Shayesteh, Structural, Optical and Magnetic Properties of Mn-doped CdS diluted Magnetic Semiconductor Nanoparticles, *J Supercond Nov Magn.* 25 (2012) 2009–2014.
- [12] R. Xie, U. Kolb, J. Li, T. Basche, A. Mews, Synthesis and characterization of highly luminescent CdSe-core CdS/ZnO.5Cd0.5S/ZnS multishell nanocrystals, *J. Am. Chem. Soc.* 127 (2005) 7480–7488.
- [13] M. Amelia, R. Flamini, L. Latterini, Recovery of CdS nanocrystal defects through conjugation with proteins, *Langmuir* 26 (2010) 10129–10134.
- [14] H. Zhao, E.P. Douglas, Preparation of corona-embedded CdS nanoparticles, *Chem. Mater.* 14 (2002) 1418–1423.
- [15] Y. Yang, O. Chen, A. Angerhofer, Y.C. Cao, Radial-position controlled doping in CdS/ZnS core/shell nanocrystals, *J. Am. Chem. Soc.* (2006) 12428–12429.
- [16] B.D. Cullity, S.R. Stock, *Elementary of X-ray Diffraction*, 3<sup>rd</sup> ed., Prentice-Hall, Englewood Cliffs, NJ, 2001 Y. Wang, N. Herron, *J. Phys. Chem.* 95 (1991) 525-532.
- [17] C. Cheng, G. Xu, H. Zhang, H. Wang, J. Cao, H. Ji, Solvothermal synthesis and photoluminescence properties of single-crystal Mn<sup>2+</sup> doped CdS nanowires, *Materials Chemistry and Physics* 97 (2006) 448–451.
- [18] S. Liu, F. Liu, H. Guo, Z. Zhang, Z. Wang, Surface states induced photoluminescence from Mn<sup>2+</sup> doped CdS nanoparticles, *Solid State Communications* 115 (2000) 615–618.
- [19] N. Taghavinia, G. Lerondel, H. Makino, A. Parisini, A. Yamamoto, T. Yao, Y. Kawazoe, T. Goto, Structural and Optical Properties of Oxidized Porous Silicon Layers Activated by Zn<sub>2</sub>SiO<sub>4</sub> : Mn<sup>2+</sup>, *J. Electrochem. Soc.* 149 (2002) G251-G256.
- [20] C.B. Chory, C. Remenyi, C. Dem, M. Schmitt, W. Kiefer, C. Gould, C. Ruster, G. Schmidt, D.M. Hofmann, D. Pfistererd, G. Muller, Synthesis and characterization of manganese-doped CdS nanoparticles, *Phys. Chem. Chem. Phys.* 5 (2003) 1639-1643.
- [21] A.K. Gupta, R. Kripal, EPR and photoluminescence properties of Mn<sup>2+</sup> doped CdS nanoparticles synthesized via co-precipitation method, *Spectrochimica Acta Part A: Molecular and Biomolecular Spectroscopy* 96 (2012) 626–631.

## An Experimental Investigation on Strength Characteristics of Concrete with Partial Replacement of Silica Fume and Metakaolin with Cement on M-30 Grade of Concrete

Mohammad Inteyazuddin <sup>1</sup>, Prof. Syed Arafath <sup>2</sup>

<sup>1</sup>P.G Student of Structural Engineering, Department of Civil Engineering, K. B. N. College of Engineering Gulbarga-585104, India

<sup>2</sup>Department of Civil Engineering, V.T.U University, India

**Abstract:** One of the approaches in improving the durability of concrete is to use blended cement materials such as fly ash, silica fume, slag and more recently, metakaolin.. This study presents the results of different mechanical properties of concrete such as compressive strength, split tensile strength and flexural concrete by partially replacing cement with metakaolin and silica fume. The replacement of metakaolin is varied from 10%, 15%, 20% and 25% and silica fume from 6%, 8% and 10%. The property of concrete in fresh state, that is the workability is also studied during the present investigation. The optimum doses of silica fume and metakaolin in combination were found to be 6% and 15% (by weight) respectively, when used as part replacement of ordinary Portland cement.

**Keywords:** Silica fume, metakaolin, OPC, Compressive strength, Flexural strength, Split Tensile Strength, Load Deflection RC Beam

### I. INTRODUCTION

Recent societal shift toward sustainable consumption and growth applied to civil infrastructure systems requires the construction materials to be designed and used with utmost attention to their durability and long term response. A majority of design codes and specifications use the compressive strength of concrete as the main criterion for design of concrete structures. Mechanically properties which are functions of porosity could to some extent provide indications of the transport properties of concrete, however they are not valid criteria for overall durability performances. Major transport properties of concrete are permeation, diffusion and absorption through which the aggressive media penetrate into the bulk of concrete and may cause gradual degradation. Pozzolanic materials including silica fume, fly ash, slag, and metakaolin have been used in recent decades for developing high performance concrete with improved workability, strength and durability. The use of supplementary cementitious materials (SCMs) is fundamental in developing low cost construction materials for use in developing countries. Concrete is the most widely used and versatile building material which is generally used to resist compressive forces. By addition of some pozzolanic materials, the various properties of concrete viz, workability, durability, strength, resistance to cracks and permeability can be improved. Many modern concrete mixes are modified with addition of admixtures, which improve the microstructure as well as decrease the calcium hydroxide concentration by consuming it through a pozzolanic reaction. The subsequent modification of the microstructure of cement composites improves the mechanical properties, durability and increases the service-life properties. When fine pozzolana particles are dissipated in the paste, they generate a large number of nucleation sites for the precipitation of the hydration products. Therefore, this mechanism makes paste more homogeneous. This is due to the reaction between the amorphous silica of the pozzolanic and calcium hydroxide, produced during the cement hydration reactions (Sabir et al. 2001, Rojas and Cabrea 2002, Antonovich and Goberis 2003). In addition, the physical effect of the fine grains allows dense packing within the cement and reduces the wall effect in the transition zone between the paste and aggregate. This weaker zone is strengthened due to the higher bond development between these two phases, improving the concrete microstructure and properties. In general, the pozzolanic effect depends not only on the pozzolanic reaction, but also on the physical or filler effect of the smaller particles in the mixture. Therefore, the addition of pozzolanas to ordinary portland cement (OPC) increases its mechanical strength and durability as compared to the referral paste, because of the interface reinforcement. The physical action of the pozzolanas provides a denser, more homogeneous and uniform paste. Silica fume is a by product resulting from the reduction of high purity quartz with coal or coke and wood chips in an electric arc furnace during the production of silicon metal or silicon alloys. Silica fume is known to

improve both the mechanical characteristics and durability of concrete. The principle physical effect of silica fume in concrete is that of filler, which because of its fineness can fit into space between cement grains in the same way that sand fills the space between particles of coarse aggregates and cement grains fill the space between sand grains. As for chemical reaction of silica fume, because of high surface area and high content of amorphous silica in silica fume, this highly active pozzolan reacts more quickly than ordinary pozzolans. The use of silica fume in concrete has engineering potential and economic advantage. Metakaolin is another pozzolanic materials which is manufactured from selected kaolins, after refinement and calcination under specific conditions. It is a highly efficient pozzolana and reacts rapidly with the excess calcium hydroxide resulting from OPC hydration, via a pozzolanic reaction, to produce calcium silicate hydrates and calcium aluminosilicate hydrates. It is quite useful for improving concrete quality, by enhancing strength and reducing setting time, and may thus prove to be a promising material for manufacturing high performance concrete. Both the Silica fume and Metakaolin are useful pozzolanic materials. In the present work, the results of a study carried out to investigate the effects of combination of these two materials on strength and workability of concrete are presented. The referral concrete M<sub>30</sub> was made using 53 grade OPC and the other mixes were prepared by replacing part of OPC with Silica Fume and Metakaolin. The replacement levels were 0%, 6%, 8% and 10% (by weight) for Silca Fume and 0%, 15%, 20% and 25% (by weight) for Metakaolin.

## II. MATERIALS AND THEIR PROPERTIES

### 1. Materials:

**1.1. Cement:** Cement in general can be defined as a material which posses very good adhesive and cohesive properties which make it possible to bond with other material to form compact mass. As Shown in table 1.

Table 1

Physical properties of OPC.		Chemical Properties of OPC	
Properties	Chart Result	Properties	Chart Result
Fineness (Sp.Surface )	348 m <sup>2</sup> / Kg	% Soluble Silica	21.3
Specific gravity	3.15	% Alumina	5.2
Comp. Strength -7 days	16.25 MPa	% Iron Oxide	3.7
Comp. Strength – 28 days	25.0 MPa	% Lime	63.9
Initial setting Time	40 min	% Magnesia	0.7
Final Setting Time	205 min	% Insoluble Residue	0.9
Soundness (Le-Chatlier Exp.)*	1.0mm	% So <sub>3</sub>	2.2

**1.2. Fine Aggregate (FA):-** The aggregate which is passing through 4.75 mm sieve is known as fine aggregate. Locally available river sand which is free from organic impurities is used. Sand passing through 4.75 mm sieve and retained on 150 micron IS sieve is used in this investigation. For the casting, locally available river-sand, free from silt and organic matters was procured and used. The particle size of fine aggregate used in this study was such a way that it passed through 4.75 mm sieve conforming to zone II of IS:383-1970.

Table 2

The Physical Properties of Fine Aggregate	
Property	Value
Specific Gravity	2.65
Fineness Modulus	3.75
Bulk Density	15.90 kN/m <sup>3</sup>
Grading	Zone-II

**1.3. Coarse Aggregate (CA):-** The coarse aggregate used in the investigation is 20mm down size crushed aggregate and angular in shape.

Table 3

Physical Properties of Coarse Aggregate	
Property	Value
Specific Gravity	2.7
Bulk Density	16.05 kN/m <sup>3</sup>
Water absorption	0.66%
Flakiness index	13.88
Elongation index	21.24
Crushing value	2.42
Impact value	16.1

**1.4. Water (IS 456-2000):-** Water used for both mixing and curing should be free from injurious amount of deleterious materials. Potable water is generally considered satisfactory for mixing and curing concrete. In the present work potable tap water was used.

**1.5. Silica Fume:-** Silica fume is also referred to as micro silica or condensed silica fume, but the term ‘silica fume’ has become generally accepted. It is a by-product of the manufacture of silicon and ferrosilicon alloys from high-purity quartz and coal in a submerged-arc electric furnace. The escaping gaseous SiO oxidizes and condenses in the form of extremely fine spherical form of amorphous silica (SiO<sub>2</sub>); hence, the name silica fume. Physical & chemical properties as shown in table 4 and 5.

Table 4

Physical Properties of Silica Fume	
Colour	Varies from white or pale-grey to a dark grey.
Specific gravity	2.2
Specific surface Area	About 20000/kg approx. 10 times more than Portland cement
Particle size	Mostly fine spheres with a mean dia of 0.1 micron
Bulk loose density	230 – 300 kg/m <sup>3</sup>

Table 5

Chemical composition of Silica Fume	
Constituents	Percent
SiO <sub>2</sub>	90 – 96
Al <sub>2</sub> O <sub>3</sub>	0.5 – 0.8
Mgo	0.5 – 1.5
Fe <sub>2</sub> O <sub>3</sub>	0.2 - 0.8
CaO	0.1 – 0.5
Na <sub>2</sub> O <sub>2</sub>	0.2 – 0.7
K <sub>2</sub> O	0.4 – 1.0
C	0.5 – 1.4
S	0.1 - 0.4

**1.6. Metakaolin:** Metakaolin is another pozzolanic materials which is manufactured from selected kaolins, after refinement and calcination under specific conditions. The Metakaolin was sieved and the fraction passing 100µ IS sieve was used in the experiments. The physical and chemical properties of metakaolin shown in Table 6 and 7.

Table 6

Physical properties of Metakaolin	
Appearance	Off white powder
Specific gravity	2.4 – 2.6
Density	2640 kg/m <sup>3</sup>
Brightness	76%
Particle size	12µm
Residue on 375 mesh	Max 0.5%
fineness	15000 – 30000 m <sup>2</sup> /kg

Table 7

Typical Chemical Composition of Metakaolin	
Item	% by weight
SiO <sub>2</sub> (%)	51.52
Al <sub>2</sub> O <sub>3</sub>	40.18
Fe <sub>2</sub> O <sub>3</sub>	1.23
CaO	2.0
MgO	0.12
Na <sub>2</sub> O	0.08
K <sub>2</sub> O	0.53
Loss on ignition	0.91

## 2. Casting & Curing:

For each mix the standard size of (150mm x 150mm x 150mm) cube moulds, standard size of (100mm dia x 200mm height) cylinder moulds, standard size (100mm x 100mm x 500mm) prisms, modal RC beams of size (700mm x 150mm x 150mm) are casted. Cube, cylinder, prism and beam moulds are made up of cast iron for casting. Before pouring the fresh concrete into these moulds, an engine oil is applied in thin layers to the inner surfaces of moulds in order to prevent the sticking of concrete to mould. These specimens are allowed to set in the mould for 24 hours, after 24 hours these specimens are de-moulded and were kept under wet conditions by immersing them in water continuously for 7 and 28 days for cubes & Cylinders, 28 days for prisms, beams.

## III. RESULTS & DISCUSSIONS

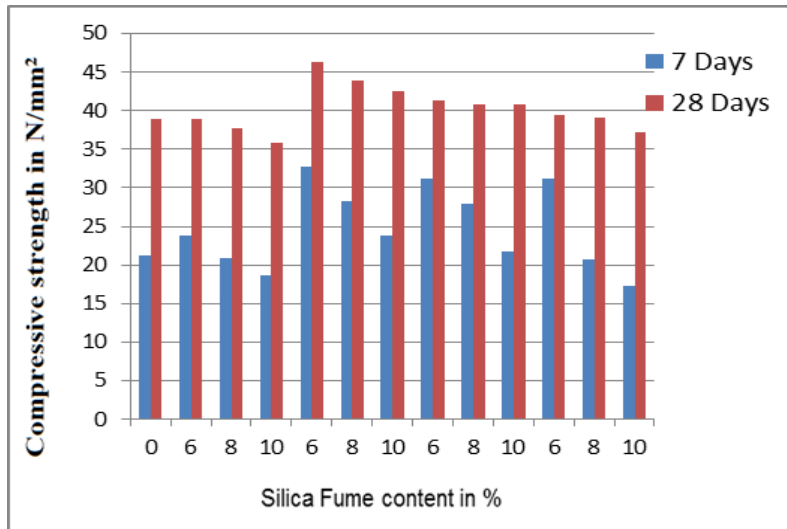
The compressive strength of the cubes, the split tensile strength of the cylinders, the flexural strength of the prisms, at different ages and different silica fume and metakaolin combination are presented in Table. The slump values and compaction factor of the different mixes are also included.

Table 8

Replacement level (%)		Slump in mm	Compaction Factor
Silica fume replacement (%)	Metakaolin replacement (%)		
0	0	58	0.80
6	10	61	0.82
8	10	66	0.84
10	10	63	0.83
6	15	59	0.91
8	15	61	0.87
10	15	62	0.90
6	20	54	0.81
8	20	57	0.82
10	20	57	0.82
6	25	52	0.80
8	25	51	0.81
10	25	53	0.81

Table 9

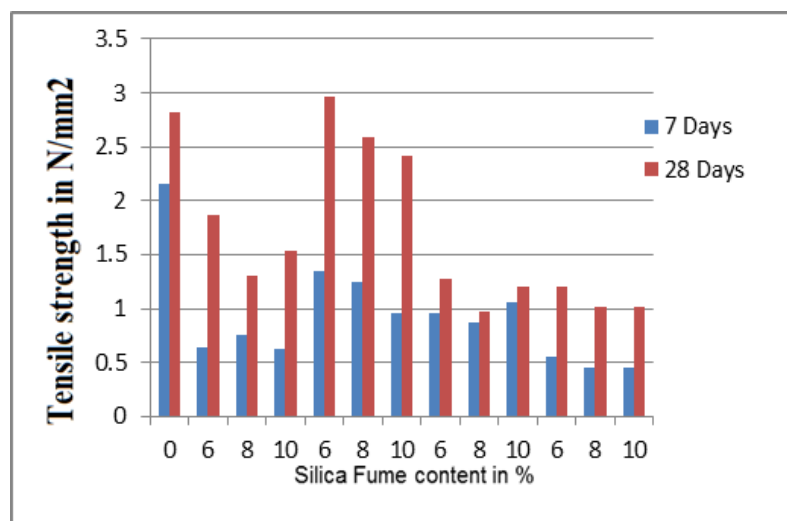
Replacement level (%)		Compressive Strength N/mm <sup>2</sup>	
Silica fume	Metakaolin	7 Days	28 Days
0	0	21.25	38.85
6	10	23.86	39.0
8	10	20.86	37.75
10	10	18.66	35.75
6	15	32.77	46.29
8	15	28.23	43.96
10	15	23.82	42.58
6	20	31.11	41.34
8	20	27.88	40.80
10	20	21.71	40.75
6	25	31.27	39.44
8	25	20.70	39.05
10	25	17.28	37.13



Graph 1: Compressive strength at 7 and 28 Days of age at 0%, 6%, 8%, 10% and 0%, 10%, 15%, 20%, 25% of Silica Fume and Metakaolin

Table 10

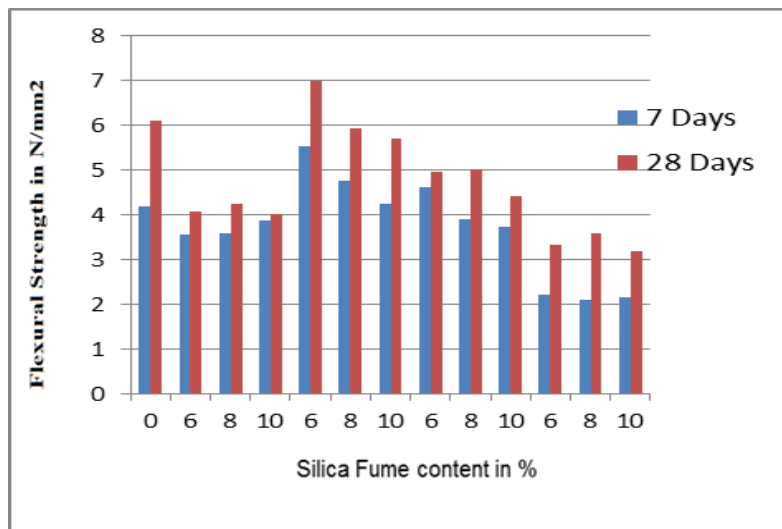
Replacement level (%)		Split tensile Strength N/mm <sup>2</sup>	
Silica fume	Metakaolin	7 Days	28 Days
0	0	2.16	2.82
6	10	0.64	1.87
8	10	0.76	1.31
10	10	0.63	1.53
6	15	1.35	2.97
8	15	1.25	2.59
10	15	0.96	2.41
6	20	0.96	1.27
8	20	0.87	0.98
10	20	1.06	1.20
6	25	0.55	1.21
8	25	0.46	1.01
10	25	0.45	1.02



Graph 2: Split Tensile strength at 7 and 28 Days of age at 0%, 6%, 8%, 10% and 0%, 10%, 15%, 20%, 25% of Silica Fume and Metakaolin

Table 11

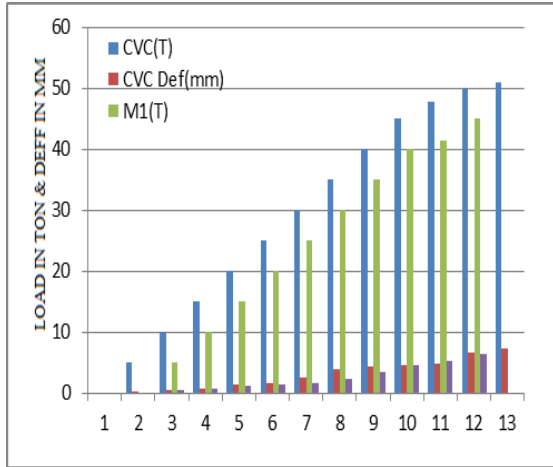
Replacement level (%)		Flexural Strength N/mm <sup>2</sup>	
Silica fume	Metakaolin	7 Days	28 Days
0	0	4.2	6.11
6	10	3.56	4.09
8	10	3.58	4.25
10	10	3.89	4.02
6	15	5.55	7.0
8	15	4.77	5.95
10	15	4.25	5.71
6	20	4.61	4.96
8	20	3.91	5.03
10	20	3.73	4.43
6	25	2.21	3.34
8	25	2.12	3.60
10	25	2.16	3.20



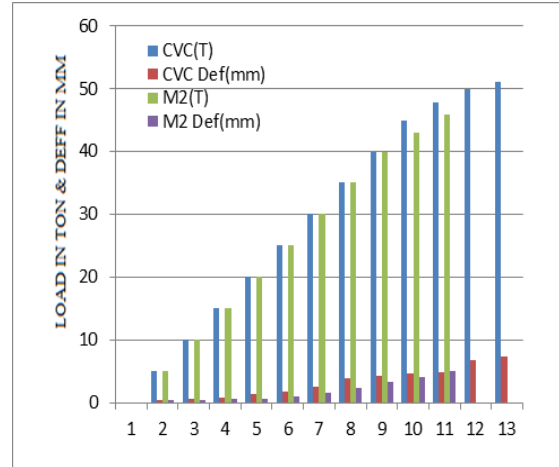
Graph 3: Flexural strength at 7 and 28 Days of age at 0%, 6%, 8%, 10% and 0%, 10%, 15%, 20%, 25% of Silica Fume and Metakaolin

The various mixes OF M30 grade with silica fume and metakaolin partially replaced with cement are designated as follows for beams;

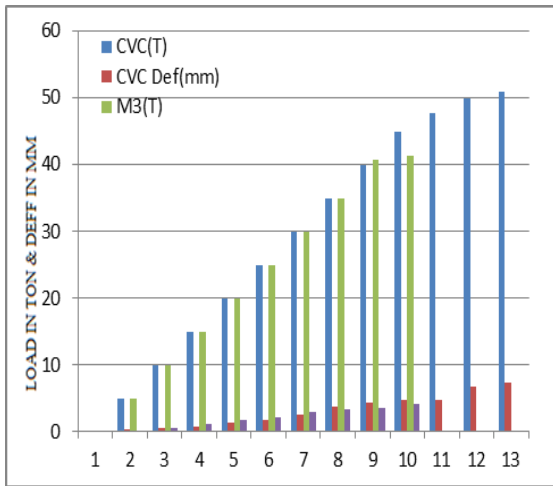
CVC	Conventional Concrete
M1	S.F. 6% & M.K. 10%
M2	S.F. 8% & M.K. 10%
M3	S.F. 10% & M.K. 10%
M4	S.F. 6% & M.K. 15%
M5	S.F. 8% & M.K. 15%
M6	S.F. 10% & M.K. 15%
M7	S.F. 6% & M.K. 20%
M8	S.F. 8% & M.K. 20%
M9	S.F. 10% & M.K. 20%
M10	S.F. 6% & M.K. 25%
M11	S.F. 8% & M.K. 25%
M12	S.F. 10% & M.K. 25%



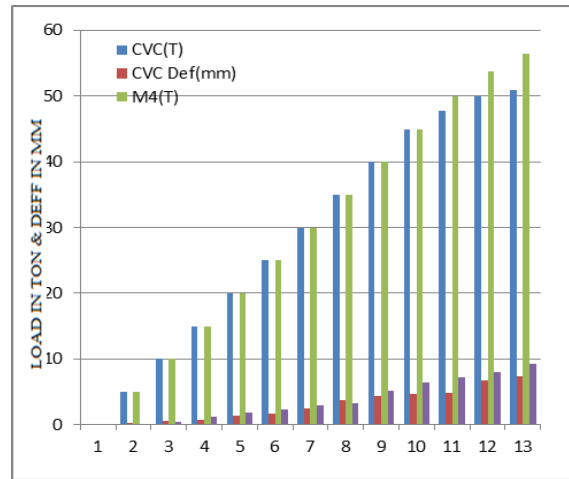
Graph 4 : Load Vs Deflection for CVC RCC beam and M1 beam



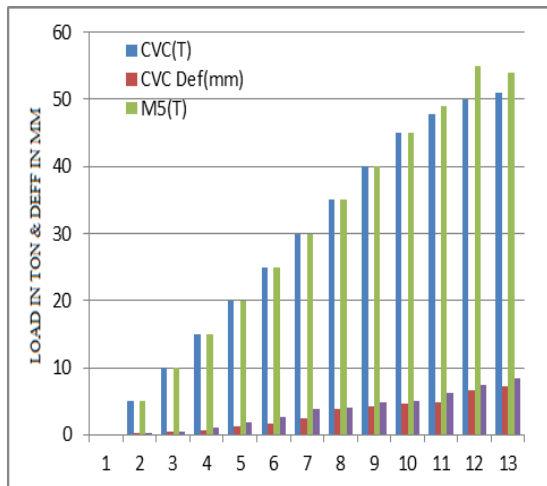
Graph 5 : Load Vs Deflection for CVC RCC beam and M2 beam



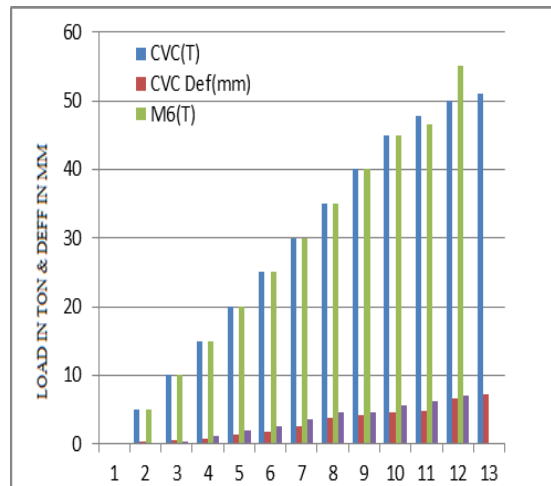
Graph 6 : Load Vs Deflection for CVC RCC beam and M3 beam



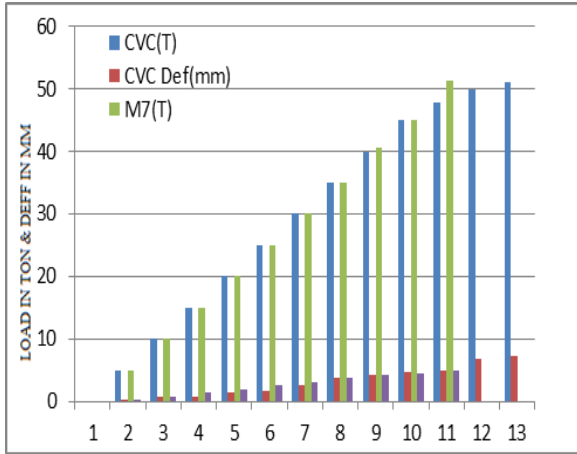
Graph 7 : Load Vs Deflection for CVC RCC beam and M4 beam



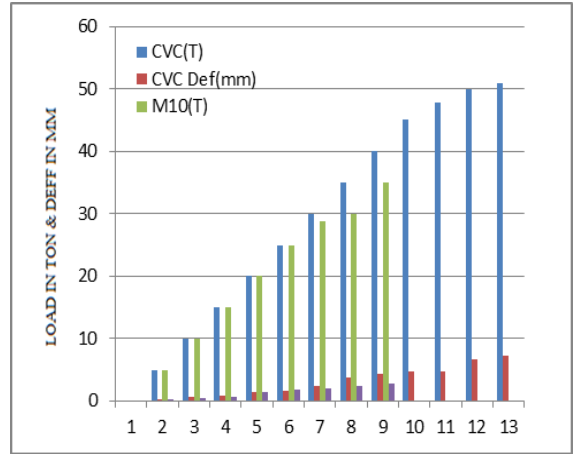
Graph 8: Load Vs Deflection for CVC RCC beam and M5 beam



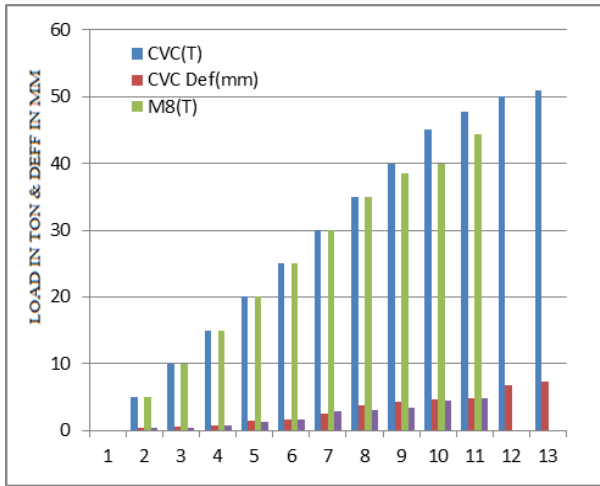
Graph 9: Load Vs Deflection for CVC RCC beam and M6 beam



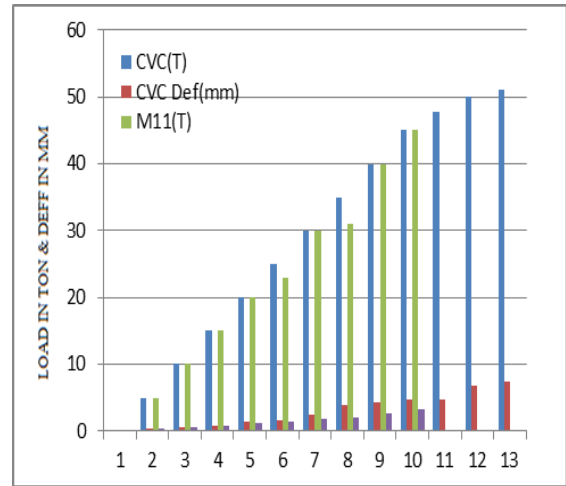
Graph 10: Load Vs Deflection for CVC RCC beam and M7 beam



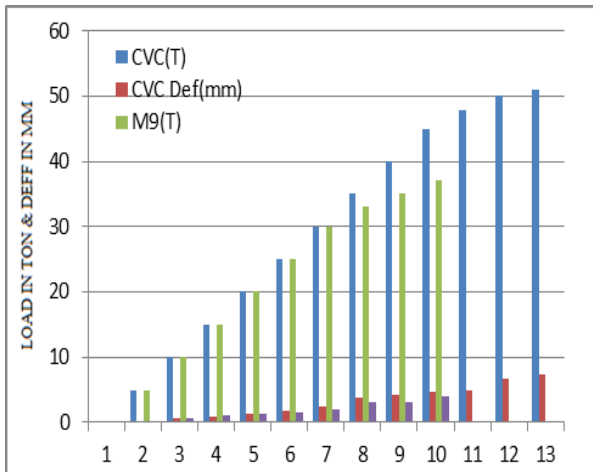
Graph 13: Load Vs Deflection for CVC RCC beam and M10 beam



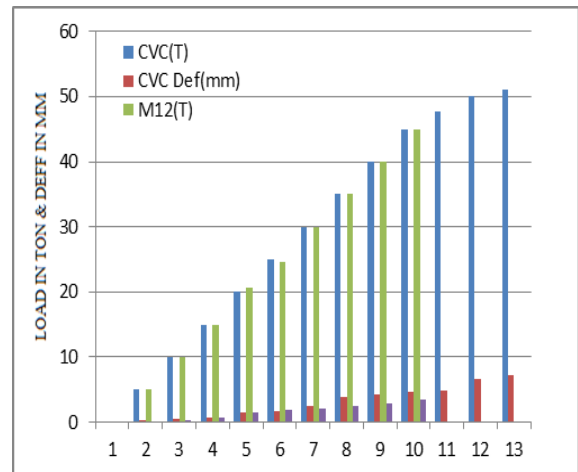
Graph 11: Load Vs Deflection for CVC RCC beam and M8 beam



Graph 14: Load Vs Deflection for CVC RCC beam and M11 beam



Graph 12: Load Vs Deflection for CVC RCC beam and M9 beam



Graph 15: Load Vs Deflection for CVC RCC beam and M12 beam

## VI. CONCLUSIONS

Following observations have been made from the study of using silica fume and metakaolin in concrete:

- The 28 day Compressive strength increases with increase in percentage of metakaolin while in case of silica fume strength increases upto 15% replacement level and then starts decreasing. And the 7 day compressive strength of concrete generally decreases with the increasing Metakaolin content at all the Silica fume contents.
- Split tensile strength in Silica fume (6, 8, 10) and 10 % Metakaolin content is found to be 0.64, 0.76, 0.63. In this case after days curing the strength has increased more than 7 days curing.
- Similarly in case of Split Tensile strength of Silica fume (6, 8, 10) and 15%, 20%, 25% Metakaolin contents.
- In Split Tensile Strength, the difference between 7 days strength and 28 days strength is large.
- The concrete mixes developed flexural strength of 3.89, 5.55 and 4.61, 2.21 N/mm<sup>2</sup> in 7 days with the metakaolin replacement of 10%, 15%, 20% and 25% respectively. While it achieves strength of 4.25, 7.00 and 5.03, 3.60 N/mm<sup>2</sup> at the age of 28 days.
- The slump is found to decrease with increase in Metakaolin content at all the Silica fume contents considerably.
- In case of RS Mix S.F (6%) M.K (10%) beams the deflection is high compared to the CVC RCC beam of M-30. And the load carrying capacity is low in case of RS Mix S.F (6%) M.K (10%) beams when compared to CVC RCC beams.
- In case of RS Mix S.F (8%) M.K (10%) beams the deflection is low compared to the CVC RCC beam of M-30. And the load carrying capacity is low in case of RS Mix S.F. (8%) M.K (10%) beams when compared to CVC RCC beams.
- In case of RS Mix S.F (10%) M.K (10%) beams the deflection is low compared to the CVC RCC beam of M-30. And the load carrying capacity is low in case of RS Mix S.F. (10%) M.K (10%) beams when compared to CVC RCC beams.
- In case of RS Mix S.F (6%, 8%) M.K (15%) beams the deflection is high compared to the CVC RCC beam of M-30. And the load carrying capacity is high in case of RS Mix S.F. (6%, 8%) M.K (15%) beams when compared to CVC RCC beams.
- In case of RS Mix S.F (10%) M.K (15%) beams the deflection is high compared to the CVC RCC beam of M-30. And the load carrying capacity is low in case of RS Mix S.F. (10%) M.K (15%) beams when compared to CVC RCC beams. In case of RS Mix S.F (6%, 8%, 10%) M.K (20%, 25%) beams the deflection is low compared to the CVC RCC beam of M-30. And the load carrying capacity is low in case of RS Mix S.F. (6%, 8%, 10%) M.K (20%, 25%) beams when compared to CVC RCC beams.

## REFERENCES

- [1]. Jian-Tong Ding and Zongjin Li “Effects of Metakaolin and Silica Fume on Properties of Concrete”.
- [2]. M. S. Morsy, a. M. Rashad and s. S. Shebl, “Effect of Elevated Temperature On Compressive Strength Of Blended Cement Mortar”.
- [3]. ASTM C150/C150M-12 Standard Specification for Portland Cement.
- [4]. Silica Fume Association: Silica fume manual.38860 Sierra Lane, Lovettsville, VA 20180, USA (2005).
- [5]. Mix Design Code Books IS 10262 – 1982.
- [6]. IS 516-1959 Method of Test for Strength of concrete.
- [7]. IS 5816-1970 Splitting Tensile Strength of concrete.
- [8]. IS 456-2000 plain and Reinforced concrete code of practice.
- [9]. “concrete Technology” Theory and practice By MS SHETTY.

## Design and Implementation of VLSI Architecture for Image Scaling Processor

Bukya. Balaji<sup>1</sup>, Yarra. Naresh<sup>2</sup>

<sup>1</sup>Associate Professor, <sup>2</sup>Assistant professor/Gandhi Academy of technical Education/JNTUH/T.S/ INDIA.

**Abstract:** In many Digital image processing applications, for processing of images or displaying the images on different size displays, they are use image scaling techniques in order to scale up/scale down of an image. In this paper, we are implement the 7 stage VLSI architecture at low cost with the edge oriented area-pixel scaling technique for achieve better image quality compared to other techniques. This method achieves better visual quality compared to previous methods. The seven-stage VLSI architecture of our image scaling processor yields a processing rate of about 200 MHz by using TSMC 0.18- m technology.

### I. Introduction

In computer graphics, image scaling is the process of resizing a digital image. Scaling is a non-trivial process that involves a trade-off between efficiency, smoothness and sharpness. As the size of an image is increased, so the pixels which comprise the image become increasingly visible, making the image appears "soft". Conversely, reducing an image will tend to enhance its smoothness and apparent sharpness.

Apart from fitting a smaller display area, image size is most commonly decreased (or sub sampled or down sampled) in order to produce thumbnails. Enlarging an image (up sampling or interpolating) is generally common for making smaller imagery fit a bigger screen in full screen mode, for example. In "zooming" an image, it is not possible to discover any more information in the image than already exists, and image quality inevitably suffers. However, there are several methods of increasing the number of pixels that an image contains, which evens out the appearance of the original pixels. Pixel art scaling algorithms are image scaling algorithms specifically designed to up sample (enlarge) low-resolution pixel and line art that contains thin lines, solid areas of color rather than gradient fills or shading, and has not been anti-aliased.

IMAGE scaling is widely used in many fields, ranging from consumer electronics to medical imaging. It is indispensable when the resolution of an image generated by a source device is different from the screen resolution of a target display. For example, we have to enlarge images to fit HDTV or to scale them down to fit the mini-size portable LCD panel. The most simple and widely used scaling methods are the nearest neighbour and bilinear techniques.

An image size can be changed in several ways. The Fig 1(a) is Consider to doubling the size, The easiest way of doubling its size is nearest-neighbor interpolation, replacing every pixel with four pixels of the same color in Fig 1(b). The resulting image is larger than the original, and preserves all the original detail, but has undesirable jaggedness. The diagonal lines of the W, for example, now show the characteristic "stairway" shape. Other scaling methods are better at preserving smooth contours in the image. For example, bilinear interpolation produces the result in Fig 1(c). Linear (or bilinear, in two dimensions) interpolation is typically better than the nearest-neighbor system for changing the size of an image, but causes some undesirable softening of details and can still be somewhat jagged. Better scaling methods include bi cubic interpolation in Fig 1(d). For magnifying computer graphics with low resolution and/or few colors (usually from 2 to 256 colors) the best results will be achieved by hqx or other pixel art scaling algorithms. These produce sharp edges and maintain high level of detail. hq2x is in Fig 1(e). For scaling photos (and raster images with lots of colors) see also anti-aliasing algorithms called super sampling.

**Fig 1: Different Scaled Images (a) Original image (b) Nearest-neighbor interpolation (c) Linear Interpolation (d) bi cubic (e) hq2x**

According to the required computations and memory space, we can divide the existing scaling methods into two classes' lower complexity and higher complexity scaling techniques. The complexity of the former is very low and comparable to conventional bilinear method. The latter yields visually pleasing images by utilizing more advanced scaling methods. In many practical real-time applications, the scaling process is included in end-user equipment, so a good lower complexity scaling technique, which is simple and suitable for low-cost VLSI implementation, is needed. In this project, to be consider the lower complexity scaling techniques only.

In this method area-pixel model is used instead of common point-pixel model. From the original image it takes four pixels for calculating the one pixel of a scaled image. The modified area pixel scaling algorithm is used in this method for obtain better edge preservation requires two times more of computations than the bilinear method.

The main goal is to achieve low cost, for that edge-oriented area pixel scaling is used in this method. In this design VLSI circuit is approximated and implemented at low cost.

## II. Analysis of Image Scaling Technique

### A. Area –Pixel Model

Instead of Common point model area pixel scaling technique performs scale-up/scale-down transformation by taking each pixel is treated as one small rectangle but not a point. For example A source image of 4 X 4 pixels is scaled up to the target image of 5 X 5 pixels. Obviously, the area of a target pixel is less than that of a source pixel. the number of source pixels overlapped by the current target pixel window is one, two, or a maximum of four. Let the luminance values of four source pixels overlapped by the window of current target pixel at coordinate (k,l) be denoted as  $F_s(m,n)$ ,  $F_s(m+1,n)$ ,  $F_s(m,n+1)$  and  $F_s(m+1,n+1)$  and, respectively.

The estimated value of current target pixel denoted as  $\hat{F}_T(k,l)$  can be calculated by weighted averaging the luminance values of four source pixels with area coverage ratio as

$$\hat{F}_T(k,l) = \sum_{i=0}^1 \sum_{j=0}^1 [F_s(m+i,n+j) \times W(m+i,n+j)] \quad (1)$$

Where  $W(m,n)$ ,  $W(m+1,n)$ ,  $W(m,n+1)$ , and  $W(m+1,n+1)$  represent the weight factors of neighbouring source pixels for the current target pixel at (k,l). Assume that the regions of four source pixels overlapped by current target pixel window are denoted as  $A(m+1,n)$ ,  $A(m,n+1)$ , and  $A(m+1,n+1)$ , respectively, and the area of the target pixel window is denoted as  $A_{sum}$ . The weighted factors of four source pixels can be given as

Where  $A_{sum} = A(m,n) + A(m+1,n) + A(m,n+1) + A(m+1,n+1)$ ,

Let the width and height of the overlapped region  $A_{sum}$  be denoted as  $left(k,l)$  and  $top(k,l)$ , and the width and height of  $A(m+1,n+1)$  be denoted as  $right(k,l)$  and  $bottom(k,l)$ . Then, the areas of overlapped regions can be calculated by

$$[A(m,n), A(m+1,n), A(m,n+1), \text{and } A(m+1,n+1)] = [left(k,l) \times top(k,l), right(k,l) \times top(k,l), left(k,l) \times bottom(k,l), right(k,l) \times bottom(k,l)]. \quad (3)$$

The hardware implementation of area pixel model is very difficult at low cost. It requires many manipulation operations like additions, multiplications, floating point operations to calculate one target pixel. In order to reduce this computational complexity, we implement VLSI architecture to determine those necessary coordinate values efficiently and quickly

We know that the direct implementation of area-pixel scaling requires some extensive floating-point computations for the current target pixel at (k,l) to determine the four parameters,  $left(k,l)$ ,  $top(k,l)$ ,  $right(k,l)$ , and  $bottom(k,l)$ . In the proposed process, we use an approximate technique suitable for low-cost VLSI implementation to achieve that goal properly.

$$\hat{F}_T(k,l) = \sum_{i=0}^1 \sum_{j=0}^1 [F_s(m+i,n+j) \times W(m+i,n+j)] \quad (1)$$

$$[W(m,n), W(m+1,n), W(m,n+1), W(m+1,n+1)] = [A(m,n)/A_{sum}, A(m+1,n)/A_{sum}, A(m,n+1)/A_{sum}, A(m+1,n+1)/A_{sum}] \quad (2)$$

Where  $A_{sum} = A(m,n) + A(m+1,n) + A(m,n+1) + A(m+1,n+1)$

$$[A(m,n), A(m+1,n), A(m,n+1), \text{and } A(m+1,n+1)] = [left(k,l) \times top(k,l), right(k,l) \times top(k,l), left(k,l) \times bottom(k,l), right(k,l) \times bottom(k,l)]. \quad (3)$$

We modify (3) and implement the calculation of areas of the overlapped regions as

$$[A'(m,n), A'(m+1,n), A'(m,n+1), A'(m+1,n+1)]$$

$$= [\text{left}'(k,l) \times \text{top}'(k,l), \text{right}'(k,l) \times \text{top}'(k,l), \text{left}'(k,l) \times \text{bottom}'(k,l), \text{right}'(k,l) \times \text{bottom}'(k,l)]. \quad (4)$$

Those  $\text{left}'(k,l), \text{top}'(k,l), \text{right}'(k,l)$  and  $\text{bottom}'(k,l)$  are all 6-b integers and given as  $[\text{left}'(k,l), \text{top}'(k,l), \text{right}'(k,l), \text{bottom}'(k,l)] = \text{Appr}[\text{left}(k,l), \text{top}(k,l), \text{right}(k,l), \text{bottom}(k,l)]$  (5)

Where Appr represents the approximate operator adopted in this design and will be explained in detail later. To obtain better visual quality, a simple low-cost edge catching technique is employed to preserve the edge features effectively by taking into account the local characteristic existed in those available source pixels around the target pixel.

The final areas of the overlapped regions are given as  $[A''(m,n), A''(m+1,n), A''(m,n+1), A''(m+1,n+1)] = \Gamma ([A'(m,n), A'(m+1,n), A'(m,n+1), A'(m+1,n+1)])$  (6)

Where we adopt a tuning operator  $\Gamma$  to tune the areas of four overlapped regions according to the edge features obtained by edge-catching technique. By applying (6) to (1) and (2), we can determine the estimated luminance value of the current target pixel. Then we describe the low-cost edge-catching technique in detail.

### III. VLSI Architecture for Edge- Oriented Image Scaling

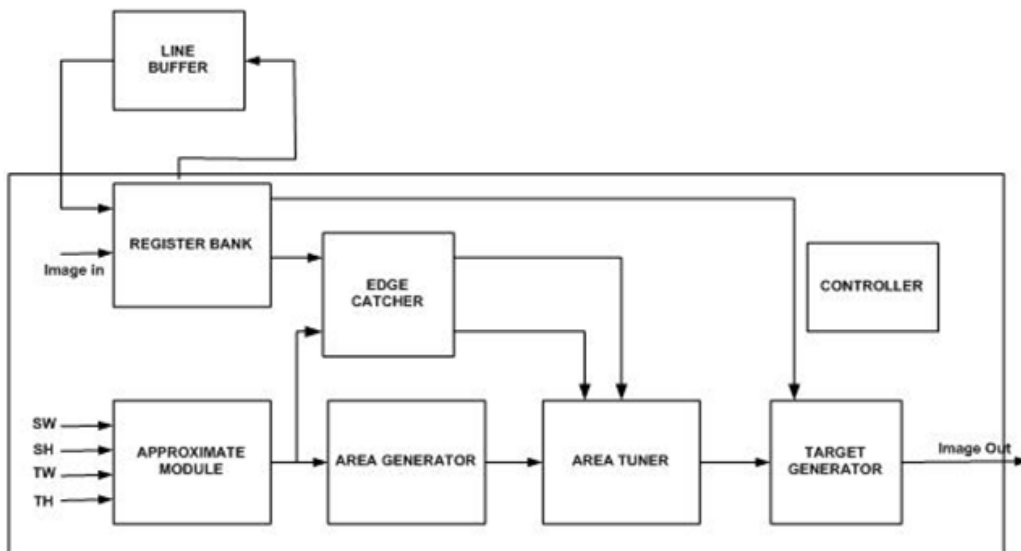


Fig 2: Block diagram of VLSI architecture for Edge oriented Area Pixel scaling Method.

Edge oriented Area Pixel scaling method requires low computational complexity and only one line memory buffer, so it is suitable for low-cost VLSI implementation. Fig.2 shows block diagram of the seven-stage VLSI architecture for this scaling method. The architecture consists of seven main blocks: approximate module (AM), register bank (RB), area generator (AG), edge catcher (EC), area tuner (AT), target generator (TG), and the controller. Each of them is described briefly in the following subsections.

#### A Approximate Module

When a source image of  $SW \times SH$  pixels is scaled up or down to the target image of  $TW \times TH$  pixels, the AM generates  $\text{left}(k,l), \text{top}(k,l), \text{right}(k,l), \text{bottom}(k,l)$ , respectively, for each target pixel from left to right and from top to bottom. In this VLSI implementation  $n$  is set to 3, so each rectangular target pixel is treated as  $2^3 \times 2^3$  uniform-sized grids. It is composed two stage pipelined architecture.

#### B Register Bank

In this design, the estimated value of the current target pixel is calculated by using the luminance values of  $2 \times 4$  neighbouring source pixels  $F_s(m-1,n), F_s(m,n), F_s(m+1,n), F_s(m+2,n), F_s(m-1,n+1), F_s(m,n+1), F_s(m+1,n+1),$  and  $F_s(m+2,n+1)$ . The register bank, consisting of eight registers, is used to provide those source luminance values at exact time for the estimated process of current target pixel. the

line buffer is used to store the pixel values of one row in the source image. It has totally eight registers. When the controller enables the shift operation in RB, two new values are read into RB (Reg3 and Reg7) and the rest 6-pixel values are shifted to their right registers one by one. The 8-pixel values stored in RB will be used by EC for edge catching and by TG for target pixel estimating.

**C Area Generator**

For each target pixel ,AG calculates the areas of the overlapped regions  $A'(m,n)$ ,  $A'(m+1,n)$ , and  $A'(m+1,n+1)$ . the architecture of area generator consists of pipeline register and 4 x 4 integer multipliers.

**D Edge catcher**

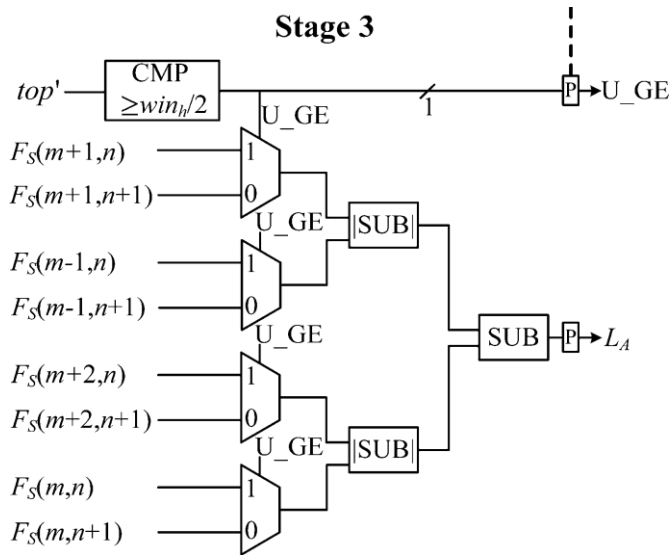


**Fig. 3: Architecture of edge catcher**

**E Area Tuner**

AT is used to modify the areas of the four overlapped regions based on the current local edge information ( $L_A$  and U GE provided by EC). Fig.4 shows the two-stage pipeline architecture of AT. If U GE is equal to 1, the upper row (row ) in current pixel window is more important. On the contrary, if U-GE is equal to 0, the lower row (row n+1) is more important. finally ,the tuned areas  $A''(m,n)$ ,  $A''(m+1,n)$ ,  $A''(m,n+1)$  and  $A''(m+1,n+1)$  are sent to TG.

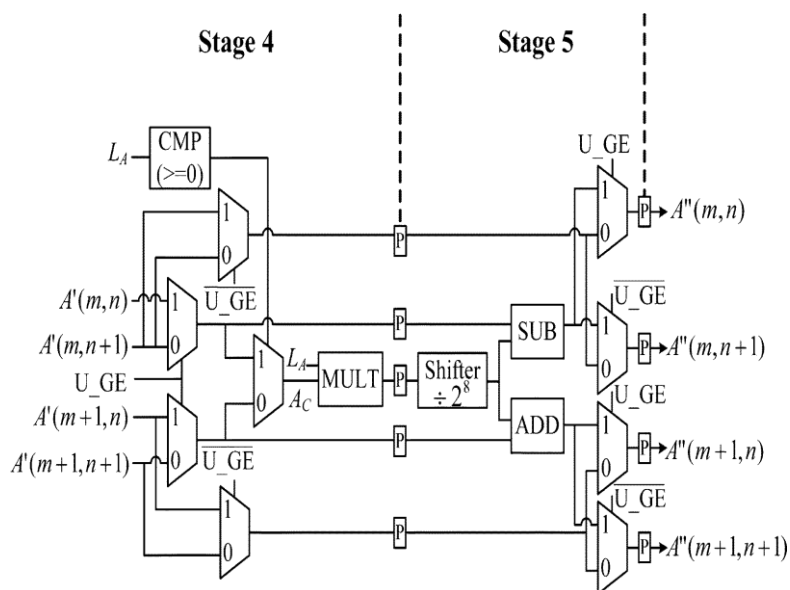


**Fig.4: Architecture of area tuner**

EC implements the proposed low-cost edge-catching technique and outputs the evaluating parameter  $L_A$ , which represents the local edge characteristic of current pixel at coordinate  $(k, l)$ . Fig.3 shows the architecture of EC where SUB unit generates the difference of two inputs and ISUBI unit generates the two inputs' absolute value of difference. The comparator CMP outputs logic 1 if the input value is greater than or equal to  $Win_h/2$ . The binary compared result, denoted as U\_GE, is used to decide whether the upper row (row n) in current pixel window is more important than the lower row (row n+1) in regards to catch edge features.

**F Target Generator**

By weighted averaging the luminance values of four source pixels with tuned-area coverage ratio, TG implements and determines the  $F^{\wedge}_T(k,l)$ . Fig.5 shows the two-stage pipe line architecture of TG. Four MULT units and three ADD units are used .

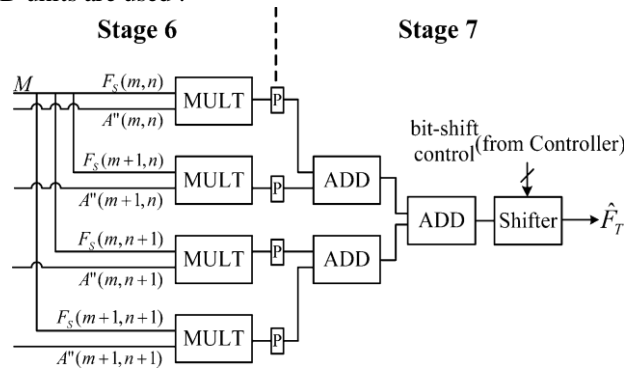


**Fig.5 Architecture of target generator**

**G CONTROLLER**

The controller, realized with a finite-state machine, monitors the data flow and sends proper control signals to all other components. In the design, AM, AT, and TG require two clock cycles to complete their functions, respectively. Both AG and EC need one clock cycle to finish their tasks, and they work in parallel because no data dependency between them exists. For each target pixel, seven clock cycles are needed to output the estimated value  $F^{\wedge}_T(k,l)$ .

**IV. Result Analysis**

To reduce hardware cost, we adopt the low-cost technique suitable for VLSI implementation to perform area-pixel scaling. To verify the computational complexity, the scaling method is implemented in VHDL language on the 2.8-GHz Pentium 4 processor with 512-MB memory and the 520-MHz INTEL XScale PXA270 with 64-MB memory, respectively. Table 6.1 shows the computing time (in the unit of second) of enlarging image from the size of 352 x 288 to the size of 300 x 200 for the two processors. Obviously, this method requires less computing time than previous method, and previous method needs much longer time due to extensive computations. To explore the performance of quantitative evaluation for image enlargement and reduction, first we scale the twelve 352 x 288 test images to the size of 400 x300, and 300 x 200, respectively, by using this method. Here, the output images of Edge- Oriented image scaling method are generated by the proposed VLSI circuit after post-layout transistor-level simulation. The output images of other scaling methods are all generated with software C programs. Simulation results show that this design achieves better quantitative quality than the previous low-complexity scaling methods.

**A Simulation Results:**

The below Fig.6 shows the simulation results of the Scaled down image. Various signals involved in the simulation of the Scaled down image are Input Signals: blue, green, image\_scaleion, imgcolumns, imglines, red, clk, image scaled image, Mono, processRGB, reset Output Signals: processingRGB, image\_scaleing, addr, din,we

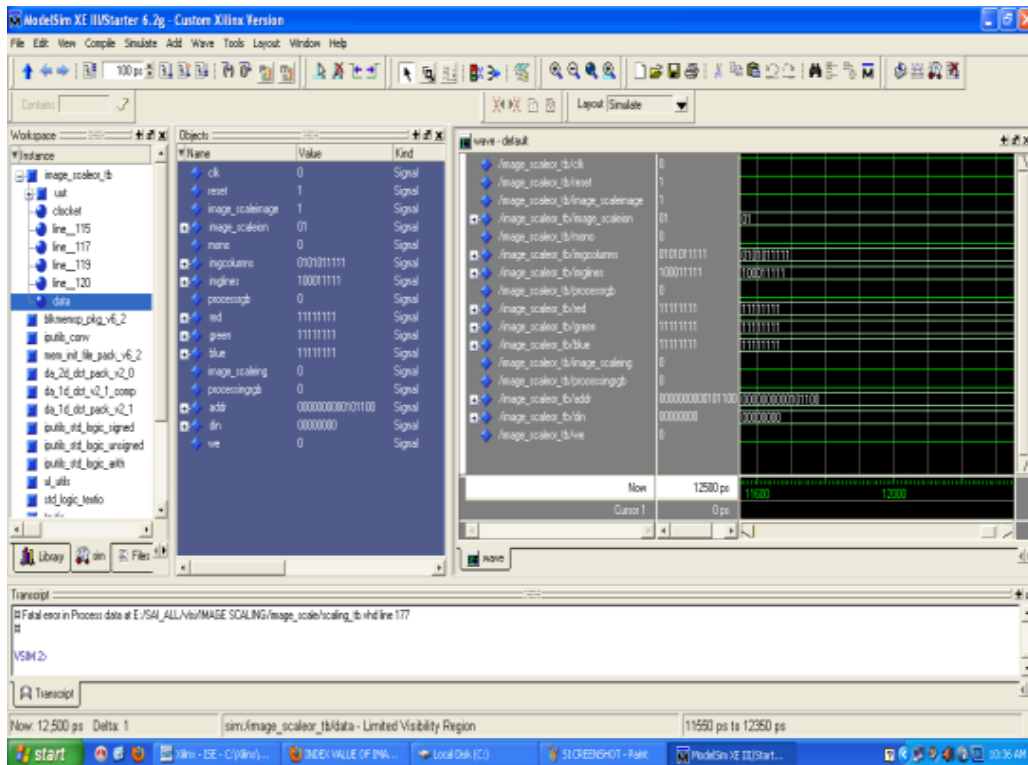


Fig.6: Simulation results of Scaled down Image

The below Fig.7 shows the simulation results of the Scaled up image. Various signals involved in the simulation of the Scaled up image are Input Signals: blue, green, image\_scaleion, imgcolumns, imglines, red, clk, image\_scaledimage, Mono, processRGB, reset Output Signals: processingRGB, image\_scaling, addr, din, we

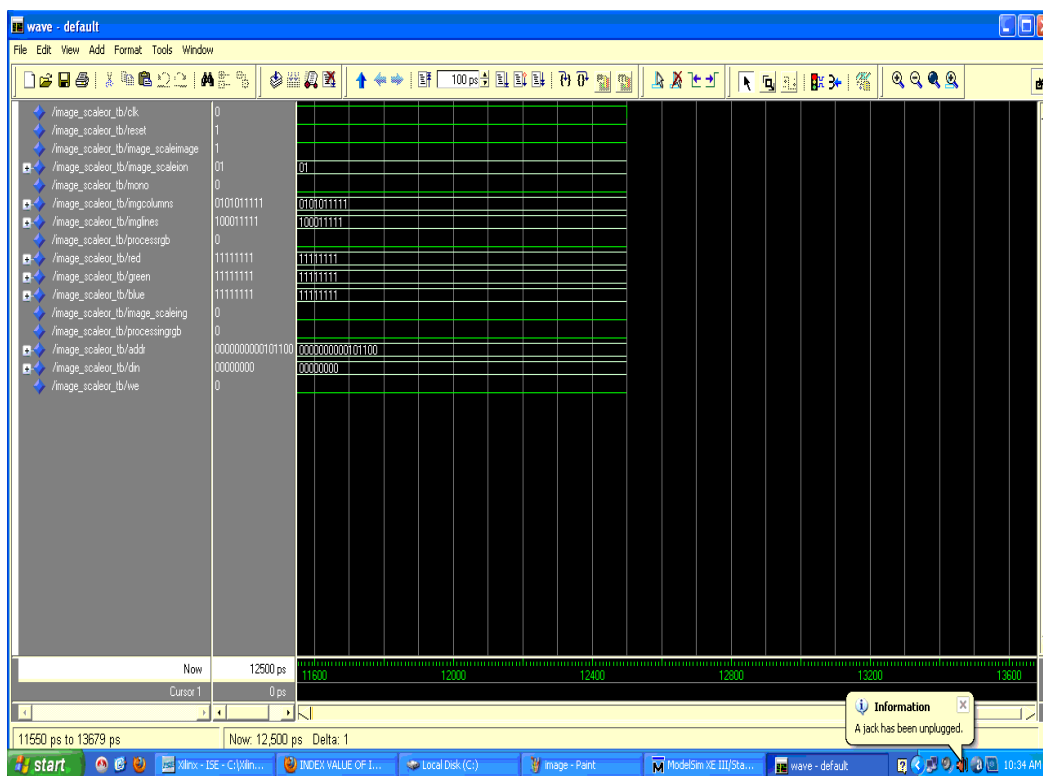
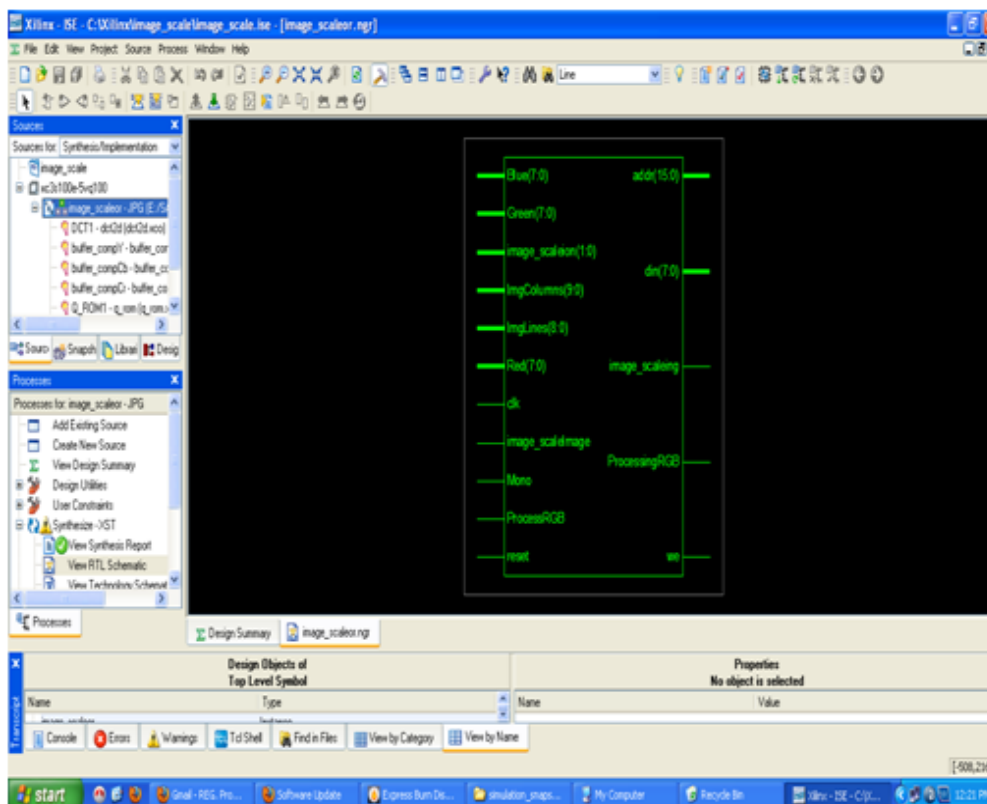


Fig.7 Simulation results of Scaled up Image

## B RTL (Register Transfer Level) Schematic View



**Fig.8 RTL (Register Transfer Level) View**

Observations:

The above Fig.8 Shows RTL view, which displays the top level Schematic symbol for the design. It is the integration of all sub modules as a whole. RTL view gives the various design elements and connectivity between them.

## C Input and Output Images:

### (a) Input Images



**Fig.9 Input images (a) Fruits image of 352 x 288 pixels (b) Building image of 352 x 288 pixels**

To achieve the goal of low cost, the edge oriented area-pixel scaling technique is implemented with low-complexity VLSI architecture in this design. Here we apply images of size 352x288 as an input.

### (b) Output images:

**Scaled down images:**

The proposed architecture is edge oriented image scaling technique. It is adopted to preserve the image edge features effectively so as to achieve better image quality. Here we get scaled down images of size 300x200 as for requirement by using this technique.



**Fig.10 Output Scaled Down images (a) Fruits image of 300 x 200 pixels (b) Building image of 300 x 200 pixels**

**Scaled up images:**



**Fig.11 Output Scaled up images (a) Fruits image of 400 x 300 pixels (b) Building image of 400 x 300 pixels**

**V. Conclusion**

A low-cost image scaling process is proposed in this project. The experimental results demonstrate that our design achieves low computational complexity and only one line memory buffer, so it is suitable for low-cost better performances in both objective and subjective image quality than other low-complexity scaling methods. This scaling method requires VLSI implementation. Furthermore; an efficient VLSI architecture for the proposed method is presented. In this simulation, this project simulation is operates with a clock period of 5 ns and achieves a processing rate of 200 mega pixels/second. The architecture works with monochromatic images, RGB colour images easily. Finally it is implemented the image scaled up in 352x288 to 400x300 and scaled down in 352x288 to 300x200, and without effecting the input image. The output results show that our design achieves better quantitative quality than the previous low-complexity scaling methods. The simple edge catching technique is adopted to preserve the image edge features effectively, so it achieved better image quality.

## REFERENCES

- [1] C. Kim, S. M. Seong, J. A. Lee, and L. S. Kim, "Winscale: An image scaling algorithm using an area pixel model," *IEEE Trans. Circuits Syst. Video Technol.*, vol. 13, no. 6, pp. 549–553, Jun. 2003.
- [2] I. Andreadis and A. Amanatiadis, "Digital image scaling," in *Proc. IEEE Instrum. Meas. Technol. Conf.*, May 2005, vol. 3, pp. 2028–2032.
- [3] H. A. Aly and E. Dubois, "Image up-sampling using total-variation regularization with a new observation model," *IEEE Trans. Image Process.*, vol. 14, no. 10, pp. 1647–1659, Oct. 2005.
- [4] K. Ramchandran, A. Ortega, K. Metin Uz, and M. Vetterli, "Multiresolution broadcast for digital HDTV using joint source/channel coding," *IEEE Journal on Selected Areas in Communications*, 11(1):6–23, January 1993.
- [5] R. C. Gonzalez and R. E. Woods, *Digital Image Processing*. Reading, MA: Addison-Wesley, 1992.
- [6] W. K. Pratt, *Digital Image Processing*. New York: Wiley-Interscience, 1991.
- [7] T. M. Lehmann, C. Gonner, and K. Spitzer, "Survey: Interpolation methods in medical image processing," *IEEE Trans. Med. Imag.*, vol. 18, no. 11, pp. 1049–1075, Nov. 1999.
- [8] C. Weerasnghe, M. Nilsson, S. Lichman, and I. Kharitonenko, "Digital zoom camera with image sharpening and suppression," *IEEE Trans. Consumer Electron.*, vol. 50, no. 3, pp. 777–786, Aug. 2004.
- [9] S. Fifman, "Digital rectification of ERTS multispectral imagery," in *Proc. Significant Results Obtained from Earth Resources Technology Satellite-1*, 1973, vol. 1, pp. 1131–1142.
- [10] J. A. Parker, R. V. Kenyon, and D. E. Troxel, "Comparison of interpolation methods for image resampling," *IEEE Trans. Med. Imag.*, vol. MI-2, no. 3, pp. 31–39, Sep. 1983.

## BIOGRAPHIES



B. Balaji received the B.Tech degree in Electronics & Communication Engineering from JBIET college in JNTU Hyderabad and his Masters degree from NCET College-Kakinada in 2003 and 2009 respectively. He is currently working as Associate Professor in Gandhi Academy of Technical Education His interests are Image processing, VLSI Chip design, etc.



Yarra Naresh received the B.Tech degree in Electronics & Communication Engineering and his Masters degree from Anurag Engineering college in JNTU Hyderabad in 2008 and 2011 respectively. He is currently working as Assistant Professor in Gandhi Academy of Technical Education His interests are Image processing, VLSI Chip design, etc.

## An insight on transparent antennas

Pushpa U. S<sup>1</sup>, Smita Chopde<sup>2</sup>

<sup>1,2</sup> *Electronics and Telecom Department, Agnel Technical Education Complex, Mumbai University, India*

**Abstract:** *This paper mainly discusses about the Transparent Antenna's introduction, design, their feeding methods, the future scope and finally transition from 2D to 3D.*

### I. Introduction

Satellites have always played an important role in space. Their contributions for space research, extended global communications and surveillance have been instrumental for the advancement of the information age. As part of the effort to create this outer space network, satellites have evolved from simple transmitters to complex systems that incorporate a myriad of technologies into a single location. Cost and weight are always key issues for successful satellite deployment. Groups of researchers and budget-tight companies employ smaller and cheaper satellite solutions that are usually custom made for a specific application. These small satellites, such as USU sat1, shown in Fig.1, have created a constant demand for cheaper systems that do more with less [1]. Limitations on the size of these small satellites leave barely enough room for solar cells, which are necessary to power the satellite. This repeatedly impedes the placement of other external elements such as antennas. Without the required surface area for tropical antennas, often complex and failure prone antennas that must be deployed in orbit are used. This adds substantially to cost and labor hours as well as the potential for failure. Two solutions have arisen to mitigate the difficulty of solar cell and antenna integration. The first solution entails the placement of a slot antenna on the back side of the solar cell [7]. This solution has been proven effective if custom built solar cell antennas are assembled for small satellites, but is not viable if the small satellite is being built from off-the-shelf components. The second solution suggests the placement of meshed see-through copper antennas, such as the one seen in Fig.2, on top of the solar cell [9]. See-through meshed antennas are still in the early research phase, but show some promise as transparent antennas.

This paper considers another type of transparent antenna that can be integrated on an off-the-shelf solar panel. Indium Tin Oxide (ITO) antennas on solar cell panels. ITO antennas have been used for various types of antenna applications including [5], [6] and [3]. ITO has been shown to have high optical transparency while maintaining effective RF conductivity [5]. These properties could potentially make ITO a good candidate for the application of optically transparent antennas for solar cells, but many of these antennas have failed to meet expectations for efficiency while retaining transparency. This paper will analyze the effect of ITO materials on patch antenna design. The tradeoff between optical transparency and electrical conductivity will be evaluated for a wide range of frequencies. Methods to better predict the skin effects on patch antenna and their impact on antenna efficiency are also described. Another challenge for ITO and meshed patch antenna design is how to feed the antennas. Soldering a copper feed line to the ITO antenna melts the ITO, making the antenna worthless. Proximity feed, is used instead. The full understanding of that feed and its effects on efficiency gain, polarization and antenna matching is the second major contribution of this research. It is important to note that the application of transparent antenna design concepts is not limited to transparent oxides (TCOs), but can be applied to other emerging technologies that utilize materials with lower conductivity values, such as conducting fabrics.

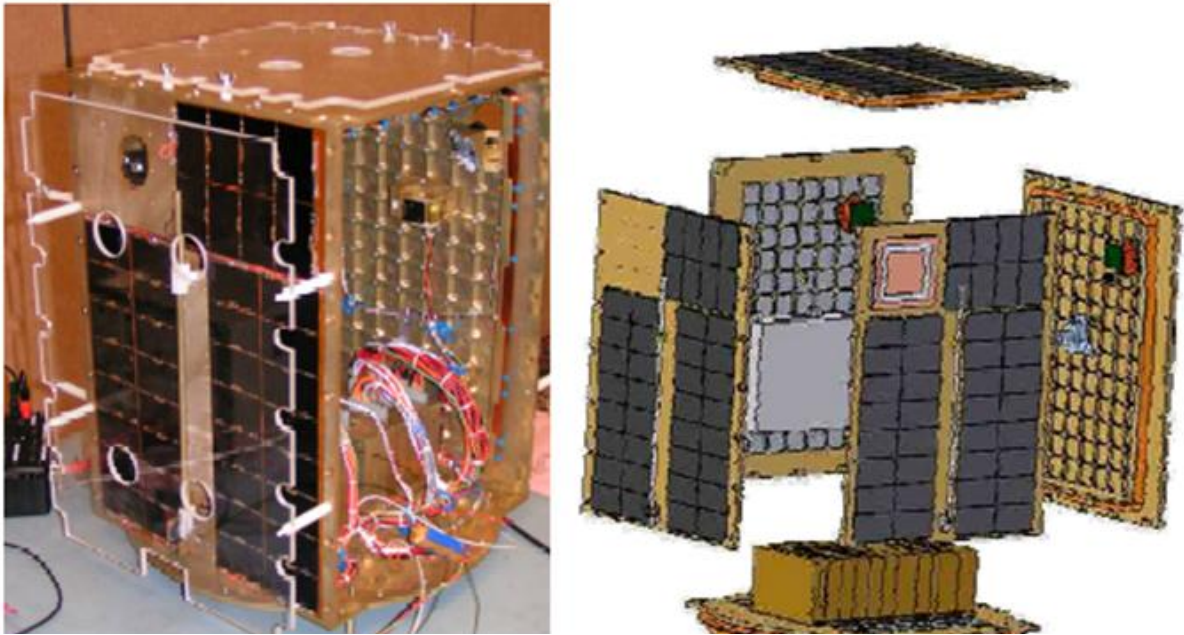


Figure1 ;USUsatl - TOROID [1]

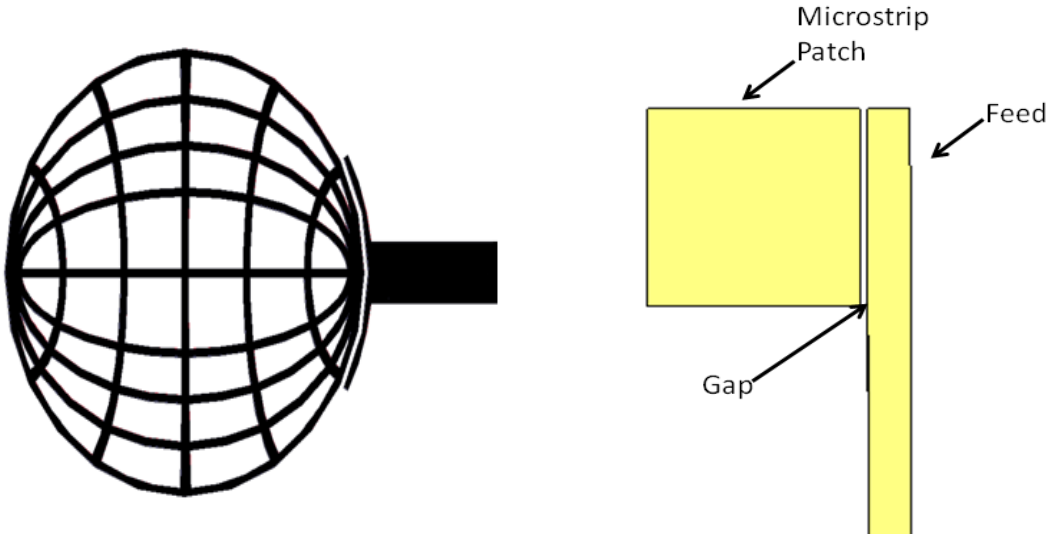


Figure 2: Meshed see-through copper antenna [16] Figure 3: Proximity coupled feed for a patch antenna

## II. Transparent Antenna Design

### 1.1 ITO (Indium Tin Oxide) Antennas

Monopole and patch antennas have been made with ITO [5]. It was found that patch antenna radiators are not as effective or as monopole antennas. Efficiency is controlled by how much current runs on the ITO imperfectly conducting antenna surface. In [5] PIFA (Planar Inverted F Antenna) was found to have a higher radiation resistance, because it behaves like a cavity and excites a larger current on the whole patch. The trapezoidal monopole requires less current to be excited on its surface and therefore is more efficient [5]. None of the previous designs have been placed on a solar cell. [6], [3] and [5] have found that ITO antennas optical transparency is inversely proportional to the sheet resistivity and therefore ITO antennas have poor conductivity. This results in a tradeoff between transparency and efficiency for ITO antennas for solar cell applications.

Chemical spray deposition, DC sputtering and RF sputtering are a few of the methods used for performing ITO deposition [3].

### **1.2 Meshed Patch Antennas**

An alternative to antennas made of transparent materials are meshed antennas. Although the optical transparency of meshed antennas is typically lower than ITO antennas, meshed antennas have higher efficiency and overall gain [9]

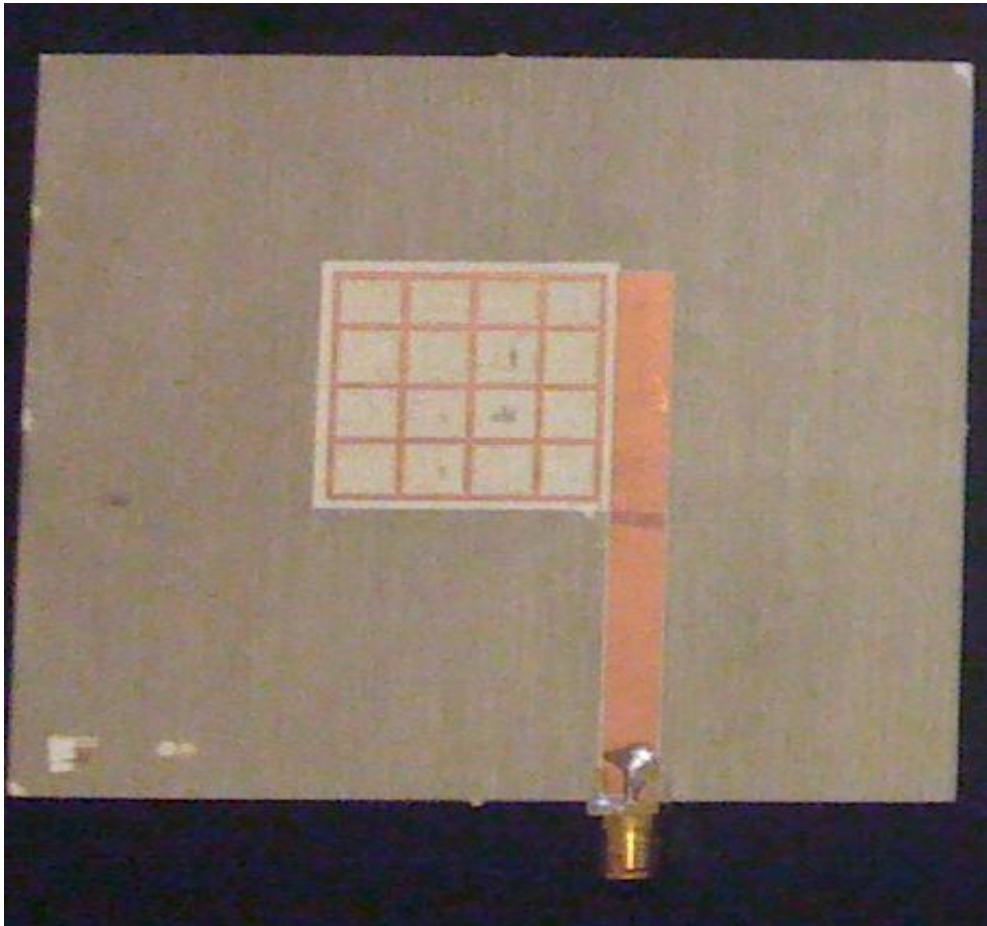


Figure 4: Meshed and solid patch antennas resonant at 2.4 GHz

### **1.3 Integrated Solar Cell Antennas**

Integrated solar cell antennas have been developed with great success. They provide virtually no obstruction or degradation to the solar cell and still are able to maintain high gains and radiation efficiency [7]. The SOLANT (SOLarANTennas) design incorporates a slot antenna in the ground plane of a solar panel [7]. With this design solar panels are able to function at their maximum capacity because the antenna blocks no light to the solar panel. The SOLANT design was able to achieve gains of up to 30 dBi. The integrated slot antenna design requires antennas to be custom fabricated, which is cost prohibitive for small satellites.

## **III. Feeding Methods For Transparent Antennas**

### **2.1 Direct Microstrip Feed**

The direct microstrip feed is the oldest and the most traditional feeding technique that works well when the antenna can be printed on a single layer. For patch antenna designs, quarter wave transformer or inset feed techniques have been developed to provide better matching [2]. These feeding techniques do not work well with meshed antennas. Visible feed lines on top of solar cells shadow the energy generating cells. Furthermore, the possibility of integrating meshed printed patch antennas onto the line feed is difficult due to the fragile and

unreliable bond of mesh lines and feed. For the reasons mentioned above, alternative techniques must be employed for optimally feeding of mesh antennas.

2.2 Coupled Microstrip Feed

An alternative approach to the direct feed described above is using a coupled feed. A passive feed works with a rectangular patch element that is capacitive or inductively coupled to a microstrip feed line. The capacitive coupling depends on the dimensions of the patch as well as the width of the gap between the patch and the feed [2]. At higher frequencies, this arrangement has very low coupling and bandwidth. Proximity fed antennas are a good alternative to more common direct feed methods due to the absence of direct connection between the antenna and the feed line. This type of coupled feed mitigates some difficulties between meshed copper bonding and frees up more solar cell area for increased power efficiency.

2.3 Passive feed method for meshed microstrip patch antennas

Recent advancements in transparent patch antenna designs have enabled the placement of antennas above the surface of solar cells [9] and on transparent surfaces, such as automobile windows [4]. Optically transparent antenna designs can be made of see-through meshed forms [9] or out of transparent materials such as Indium Tin Oxide (ITO) [8]. Much of the difficulty of feeding these antennas is attributed to the poor bonding of conductive materials, such as copper, to feed meshed see-through patch antennas. Furthermore, when implementing antenna arrays the difficulty of feeding optically transparent microstrip patches without blocking the power harvesting area of a solar cell can also be a challenge. Notwithstanding these shortcomings, a co-planar electromagnetically coupled passive feed method for transparent antennas can be considered. This feed is inexpensive and easy implementation of a feed line that can be used topically on solar cells or other transparent surfaces without blocking its light transmission.

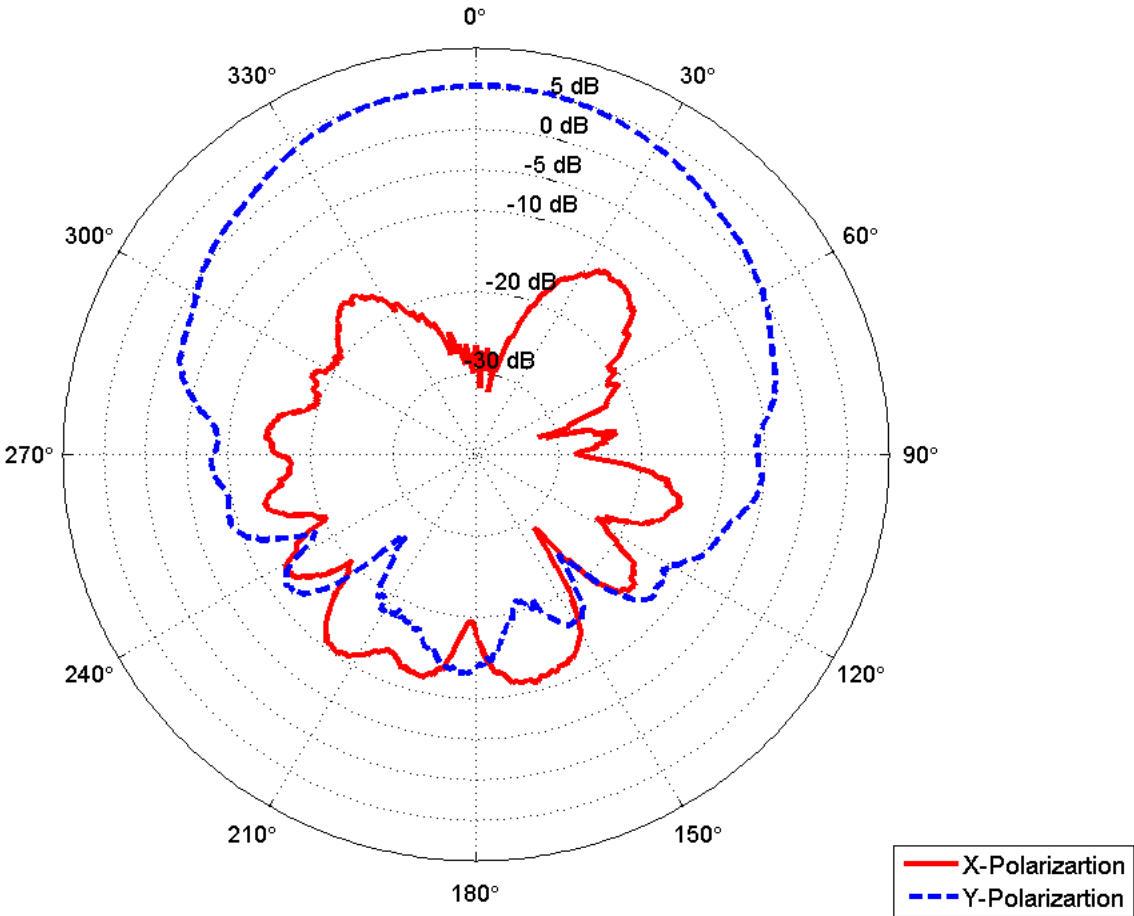


Figure 5: Radiation pattern of E-Plane in dB of a solid patch antenna fed through a passive feed with an inductive configuration

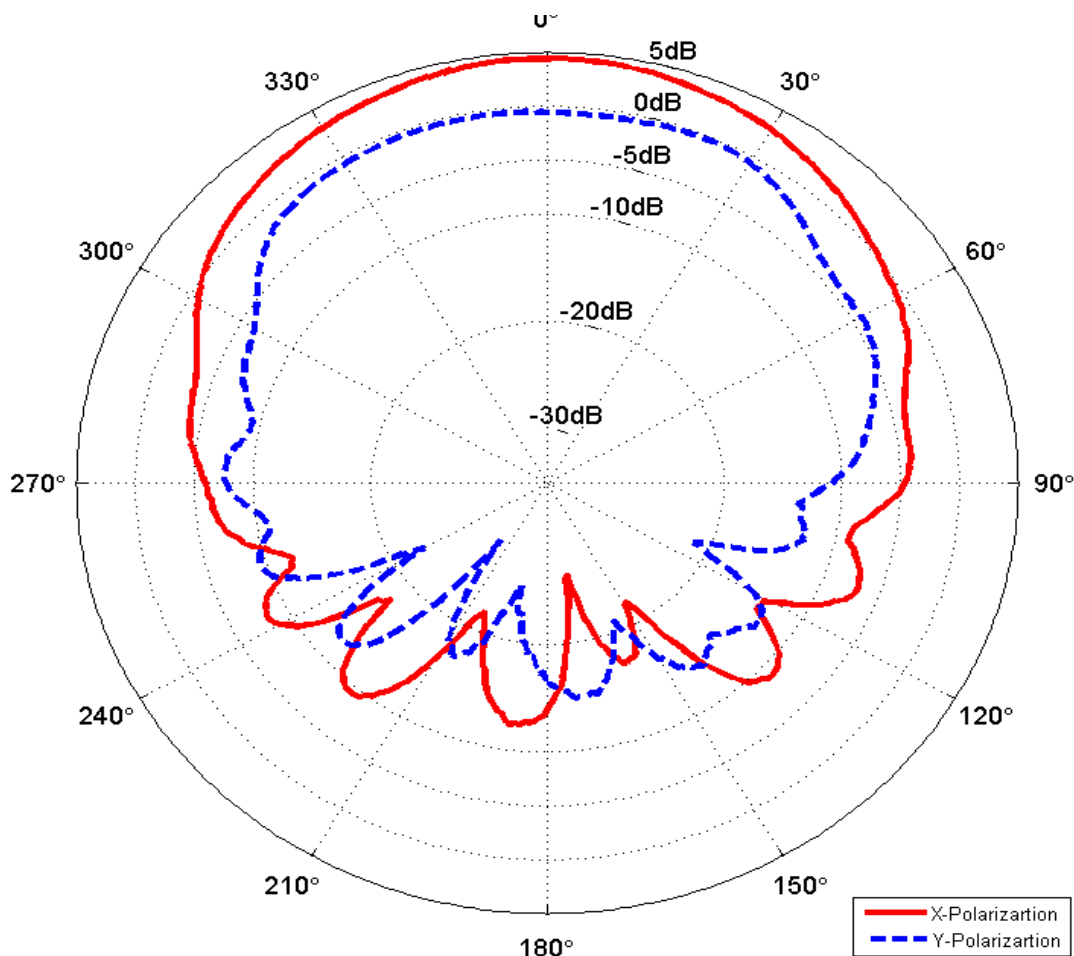


Figure 6: Radiation pattern of E-Plane in dB of meshed patch antenna fed through a passive feed with a capacitive configuration

**2.4 Co-planar Electromagnetically Coupled Feed**

A common configuration of a passive coupled feed is addressed as a two layer structure where the feed line is placed underneath the antenna [2]. In case of feeding antennas placed on an existing structure such as a solar cell, coupled feeds must be modified to feed the antenna from its side.

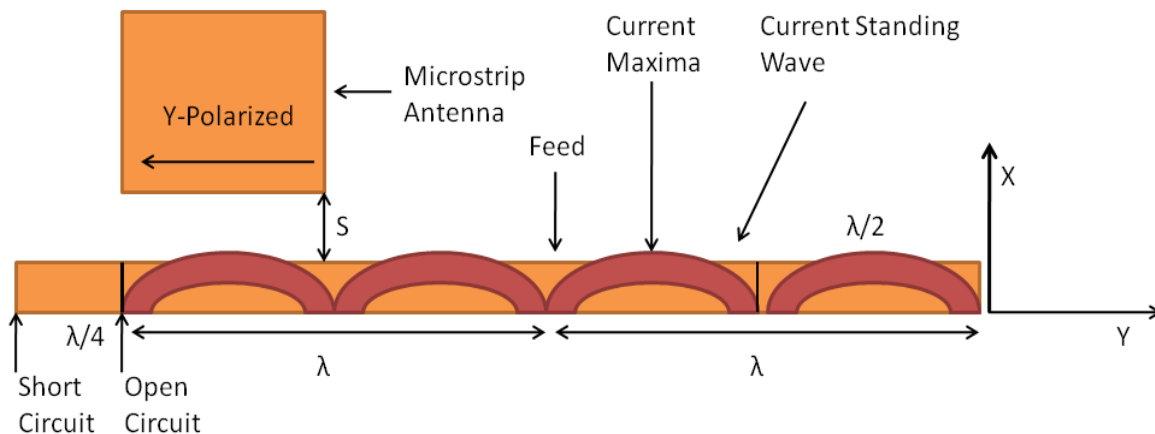


Figure 7: Geometry of a co-planar electromagnetically coupled feed

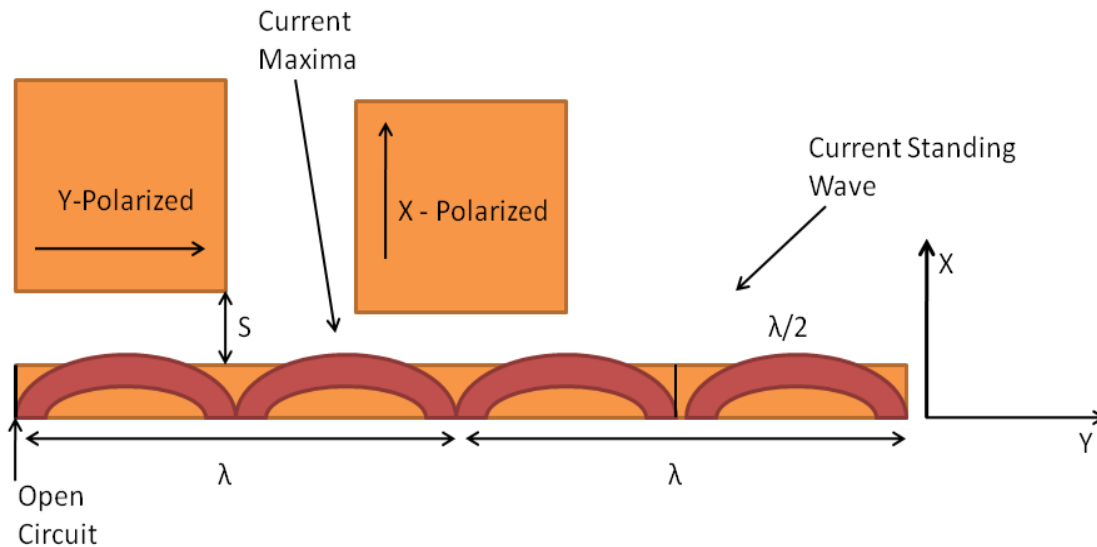


Figure 8: Direction of polarization for different rotation rectangular microstrip patches

#### IV. Future Work

Although this paper has mainly discussed the use of transparent antennas on solar cells, the application for such antennas is not limited to solar cells on small satellites. These transparent antennas can be also used in other areas such as windshields of cars and even as transparent circuits. The present state of TCOs has not matured enough to allow the implementation of TCOs in antenna design at microwave frequencies of 100 MHz to 10GHz but can be used at frequencies above 10GHz. This work gives some guidelines and requirements so that antenna engineers and material's scientists can push the boundaries and enable the usage of such materials. The use of transparent TCOs can enable implementation of transparent RF circuits for aviation, transportation and consumer electronics. Once TCOs are improved for use at frequencies of 300MHz to 10 GHz, the implementation of passive feeds will help with additional challenges such as bonding of TCOs to copper. Furthermore, co-planar coupled feeds can be used to feed materials that are more difficult to bond, such as the feeding of fabric antennas etc.

#### V. Transparent Antennas: From 2d To 3d

Transparent antennas are very attractive. They can be integrated with clear substrates such as window glass, or with solar cells to save surface areas of satellites. Transparent antennas are normally realized using (2D) planar structures based on the theory of patch antenna. The optical transparency can be obtained by fabricating meshed conductors or transparent conductors on an acrylic or glass substrate. Transparent designs using the meshed-conductor approach are straightforward because optical signals can pass through the opening of the meshes, while microwave signals can be transmitted or received by the conductors. The transparency and antenna property can be optimized by refining the width of the mesh. In the transparent-conductor approach, transparent conductive films are used as radiators. Commonly used transparent conductive films include indium tin oxide (ITO), silver coated polyester film (AgHT), and fluorine-doped tin oxide (FTO). A sheet resistance of at least 1-2 ohm/square is required to obtain an optical transmittance of around 70%. However, antennas made of such transparent conductor films are not efficient because of the high sheet resistance. This is one of the major obstacles to the widespread application of transparent antennas.

For a long time, transparent antennas have been of planar (2D) structures. Very recently, 3D transparent antennas have also been developed. This is a new topic. The principle of 3D transparent antenna is based on the theory of dielectric resonator antenna; the resonance is caused by the whole 3D structure rather than a confined cavity as found in the patch-antenna case. For glass, it is usually assumed that its refractive index is  $\sim 1.5$ , giving a dielectric constant of  $\sim 2.25$ . This value is too low for a DRA to have good polarization purity. However, it was generally overlooked that this dielectric constant was obtained at optical frequencies instead of microwave frequencies. Recently, a dielectric constant of  $\sim 7$  was measured for glass at 2 GHz and this value is sufficient for obtaining a good radiator. Since crystals are basically glass, they can also be used for antenna designs. It has been experimentally found that the lighting and antenna parts do not affect each other because they are operating in totally different frequency regions. Finally, 3D transparent antennas can be designed as aesthetic glass (or crystal) wares or artworks. This idea is especially useful when invisible antennas are needed due to psychological reasons.

## REFERENCES

- [1] Baktur, R., and Furse, C. Transparent solar cell antennas for small satellites. NSF Proposal Award 0801426. Utah State University and University of Utah.
- [2] Balanis, C. *Antenna Theory: Analysis and Design*. Wiley, New York, 1996.
- [3] Bourry, M., Sarret, M., and Drissi, M. Novel In<sub>2</sub>O<sub>3</sub> alloy for microwave and optical applications. 48th Midwest Symposium on Circuits and Systems 1 (August 2005), 615-618.
- [4] Clasen, G., and Langley, R. Meshed patch antennas. *IEEE Transactions on Antennas and Propagation* 52, 6 (June 2004), 1412-1416.
- [5] Guan, N., Furuya, H., Delaune, D., and Ito, K. Antennas made of transparent conductive oxides. In *PIERS Proceedings Online* (2008), vol. 4.
- [6] Outleb, N., Pinel, J., Drissi, M., and Bonnaud, O. Microwave planar antenna with rf-sputtered indium tin oxide oxides. *Microwave and Optical Technology Letters* 24, 1 (2000).
- [7] S. Vaccaro, J. Mosig, P. M. Two advanced solar antennas.
- [8] Saberlin, J., and Furse, C. Challenges with optically transparent antennas for solar cells. Preprint, July 2010.
- [9] Turpin, T., and Baktur, R. Integrated solar meshed patch antennas. *IEEE Antennas and Wireless Propagation Letters* 8 (2009), 693-696

# The Effect of Design Parameters of an Integrated Linear Electromagnetic Motor, At the Process of Pulling Away Anchor, From Its Breakaway Stage

Dr. Ginady G. Ugarov<sup>1</sup>, Dr. Vladimir Iv. Moshkin<sup>2</sup>, Dr. Amer Kh. Massad<sup>3</sup>

<sup>1</sup>Department of Power Supply of Industrial Enterprises, Saratov State Technical University, Russia

<sup>2</sup>Department of Energy and technological of materials, Kurgan State University Russia

<sup>3</sup>Department of Electrical & Mechanical Engineering, An-Najah National University, Palestine

**Abstract:** This paper assess the influence of design parameters of ferromagnetic guide housing at the possess of pulling away the anchor from the holding device which is integrated in the design of the motor. The design of an integrated circuit and the equivalent magnetic circuit of the integrated LEMM on breakaway stage was built, mathematical models of system were laid out. An expression for its magnetic induction, with which you can set the beginning of saturation of the shunt, defining moment of pulling away anchor from the holding area. an expression is derived for its magnetic induction, with which you can set the beginning of saturation of the shunt, define moment of anchor pulling away from the holding area, the zone of permissible combinations of cross-sectional area of the upper magnetic shunt and holding area, and the zone of change in the magnetic induction in the yoke at the pulling away moment of the motor anchor.

**Index Terms:** Linear electromagnetic motor, pulling away anchor, breakaway stage, holding force, holding device, ferromagnetic guide housing.

## I. Introduction

Electromagnetic linear machine generates linear motions directly without rotation-to-translation conversion mechanisms, which significantly simplifies system structure and improves system efficiency. It has wide applications in aeronautics [1, 2], transportation [3-5], medical devices [6,7] and so on. linear electric motors are able to accumulate energy for the usage, When the generated force is in opposite direction as the suspension velocity [8].

One way of increasing the specific power and energy performance of these linear motors is to force the accumulating of magnetic energy in the working gaps of pulsed electromagnetic linear motors (LEMM) by retaining its anchor, which implement the principle of increasing artificially accumulated magnetic energy of running clearances on breakaway stage by motors loading [9]. In this breakaway stage, the anchor artificially creates a static reaction force (holding force  $F_H$ ), which decreases abruptly to zero after the start of the armature. Consequently, the anchor will start moving under the influence of an increased tractive force [10, 11].

The Integration of the holding device of the anchor (HDOA) in the motor design in the magnetic core and MMF proposed in [12, 13], has allowed to simplify the design of pulse LEMM at the same time to increase its power and energy performance. Design parameters of both holding device of anchor and ferromagnetic guide housing of pulsed LEMM have an effect on the holding force of the motor's anchor.

## II. Problem Statement

Experimental research of the linear electromagnetic motor is a complicated task requiring use of special experimental equipment [14]. As mentioned in [15] experimental studies of such integrated LEMM showed that the regulation of holding force is difficult because it depends on several design parameters of the motor. Therefore, conducting such experimental research is not feasible (it is not practically possible), as such verification will take a long time.

The influence of varying the value of the holding area  $S_H$ , which holds the anchor and creates changes of the holding force  $F_H$  on breakaway stage, is the defined and determined in [16]. The motor which has this design is called integrated LEMM.

However obtained expressions in [16], do not allow us to investigate the influence of the design parameters of the ferromagnetic shunt during the process of pulling away the integrated LEMM anchor. The

flux magnitude of the upper shunt  $\Phi_{ush}$  and its cross-section  $S_{ush}$  have effect on the magnetization process and determine the moment when the breakaway anchor stage reaches saturation of the ferromagnetic guide housing.

As the value  $S_{ush}$ , especially at smaller  $\Phi_{ush}$  decreases, the shunt is saturated eventually causing holding force  $F_H$ , to be limited to the tractive force  $F_{st}$  in the moment of pulling away motor anchor. In [17] it is shown that with increasing  $F_{st}$  increased energy performance of pulsed LEMM is obtained.

The purpose of this paper, is to assess the influence of design parameters of ferromagnetic guide housing at the possess of pulling away the anchor from the holding device which is integrated in the design of the motor.

### III. Mathematical Models System

In such motor design, anchor on breakaway stage is held by its own magnetic field ferromagnetic guide housing 2 Fig.1, which is called an upper magnetic shunt relative to the upper running clearance  $\delta_u$ . Lower magnetic shunt is a ferromagnetic anchor guide 3. Thus, the LEMM in this design has two working clearances shunted by motor parts design - the upper and lower magnetic shunts. During operation in this LEMM with holding device (holding device integrated in design), both shunts saturate an eventually affect motor performance. In this LEMM design, holding force  $F_H$  occurs between mating surfaces, which is formed by the upper part of the flat anchor 1 and the top of the inside of the ferromagnetic shunt (2) when they are in contact or almost in contact the gap  $\delta_0$ .

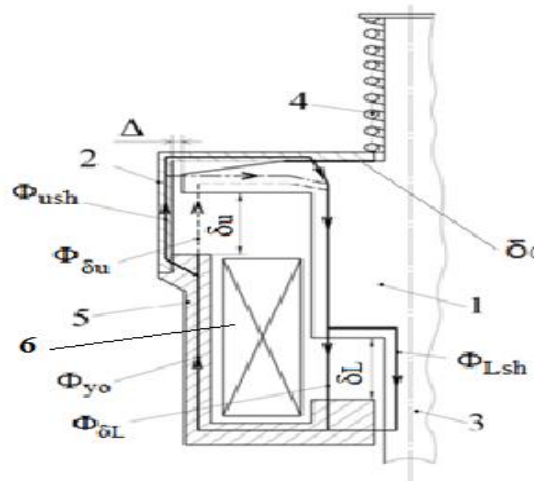


Fig. 1: The design of an integrated circuit LEMM

In such a motor design, when we connect the coil to the power supply for the first time and until the initial magnetic field has not yet unfolded, both the magnetic shunts are also not saturated and have small magnetic reluctance  $R_{ush}$   $R_{Lsh}$ , hence  $R_{ush} = R_{ush1} + R_{ush2}$ .

From the equivalent of the magnetic circuit LEMM and with neglecting the leakage flux Fig.2 which is corresponding to the design scheme in Fig. 1, the magnetic flux  $\Phi_{yo}$  yoke 5 appears as two components:

$$\Phi_{yo} = \Phi_{ush} + \Phi_{\delta u} = \Phi_{Lsh} + \Phi_{\delta l} \quad (1)$$

these two components pass in the anchor LEMM almost entirely through the upper shunt ( $R_{ush}$  and  $R_{up\delta}$ ), bypassing the upper working clearances  $\delta_u$ , which in this case have much bigger reluctance  $R_{\delta u}$  compared to the reluctance of the upper branch of the  $R_{ub}$  shunt Fig.2 and the technological gap  $\Delta$ :

$$R_{ub} = R_{ush} + R_{up\delta} \quad (2)$$

$$R_{up\delta} = \frac{\delta_{up}}{\mu_0 S_H};$$

$$R_{\Delta} = \frac{\Delta}{\mu_0 S_{upsh}} \quad (3)$$

Where  $R_{up\delta}$ , the reluctance of the air gap  $\delta_{up}$ , creates the holding force and forms mating surfaces of the upper shunt and the top of the anchor 1.

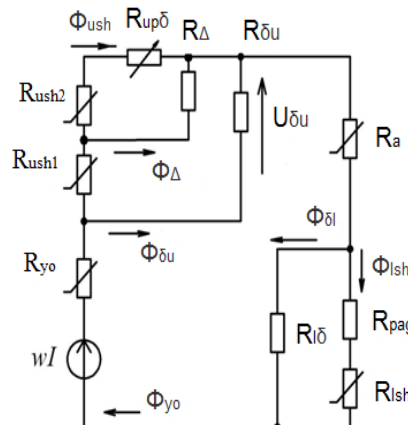


Fig. 2: The equivalent magnetic circuit of the integrated LEMM on breakaway stage

$R_{up\delta}$  at a given moment is much smaller than shunt  $R_{ush}$ , due to minimal value of air gap  $\delta_{up}$ , which is selected in the initial state of a return spring 4 and smaller than the reluctance technological gap  $R_{\Delta}$ .

Therefore, the expressions (1) and (2) can be written as:

$$\Phi_{yo} \approx \Phi_{ush} ; R_{ub} = R_{ush}$$

Then by the electromagnetic holding force which occurs between the upper shunt and the upper shunt of part anchor, the anchor is attracted to the stationary shunt, and despite the increase of the current in the coil anchor it is held in this position. The magnitude of holding force  $F_H$  in this case depends on the magnitude of the magnetic flux of the upper shunt  $\Phi_{ush}$  and its contact area with the flat part of the anchor - (Holding area)  $S_H$  (in Fig.1 shows a heavy line). The magnitude  $\Phi_{ush}$  with a certain saturation induction  $B_0$  material of the guide housing (upper shunt) is determined by its cross-sectional area  $S_{ush}$ . Accordingly, the value of holding force under these conditions will be a function of two design parameters - area  $S_H$  and area  $S_{ush}$ .

With increasing mmf motors winding 6 on breakaway anchors stage, the magnetic flux of the upper shunt  $\Phi_{ush}$  also increases. Thus, the holding force increases and saturates this ferromagnetic shunt, and reluctance  $R_{ush}$  begins to increase. As a result, shunt flux slowdown and a simultaneous redistribution of  $\Phi_{ush}$  and  $\Phi_{\delta u}$  occurs according to equation (1). That is, all the bulk of the flux in the yoke  $\Phi_{yo}$  in particular the flux component  $\Phi_{\delta u}$  extends through upper working clearance (the dotted line in Fig.1) which is represented by  $R_{\delta u}$  element in the equivalent magnetic circuit (Fig.2), that creates additional tractive force down, acting on a combined anchor 1 motor. Similar processes occur in the lower shunt with the difference that it is saturated before the upper shunt, and the reluctance of the parasitic air gap  $R_{pag}$  Fig.2 remains unchanged when the motor is operated and accordingly the tractive force in the parasitic air gap is not created.

To assess the influence of cross-sectional area  $S_{ush}$  at the anchor, at the instance of pulling-away, it is first necessary to establish the beginning of saturation of the upper shunt. According to the magnetization curve schedules, and particularly at its tabulated values it is difficult to find these conditions of saturation. By an approximation to the magnetization curve of a magnetic steel of ferromagnetic guide housing 2 (Fig. 1), these conditions are defined easily. For this purpose, the magnetization curve of the material shunt in saturation parts, is approximated by piecewise-linear segments and each segment is represented by polynomial of a certain degree as in the following form:

$$B(H) = B_0 + \mu_k \mu_0 H \quad (4)$$

where  $\mu_k$  relative permeability of the material of the magnetic shunt at the part of its saturation flux density corresponding to the maximum  $B_k$ ,  $H$  magnetic field strength,  $\mu_0 = 4\pi \times 10^{-7} \frac{H}{m}$  permeability of free space,  $B_0$  magnetic induction value (magnetic flux density), where saturation begins of the upper shunt.

Equation (4) is the equation of the line tangent to the magnetization curve at  $B = B_K$ , corresponding to the maximum induction indicated by this curve. The maximum magnetic induction  $B_K$  is usually given in the design of pulse LEMM [10, 18].

The value of  $B_0$  in equation (4) can be found by using power polynomial for the curve  $B = B_K$ , when the magnetic field strength of the material shunt equals zero. Then the magnetic flux of the upper shunt is:

$$\Phi_{ush} = (B_0 + \mu_K \mu_0 H_{ush}) S_{ush} \quad (5)$$

where  $S_{ush}$  is the cross sectional area of the upper shunt.

To determine the magnetic field strength in the upper shunt  $H_{ush}$  we use the equivalent circuit shown in Figure 2, which implies that, the upper working clearance with reluctance  $R_{\delta u}$  and shunt branch  $R_{ub}$  both are under the same magnetic field strength. By KCL (when leakage flux neglected), we obtain for this section of the magnetic circuit the following relationship:

$$H_{ush} L_{ush} + H_0 \delta_0 = H_{\delta u} L_{\delta u} \quad (6)$$

where  $H_{\delta u}$  magnetic field strength in the upper working clearance  $\delta_u$ ,  $H_0$  magnetic field strength in the air gap  $\delta_0$  (shown as a heavy line between the inner mating surfaces of the upper shunt and the top of the anchor 1 Fig.1), and  $H_{ush}$  magnetic field strength in the upper magnetic shunt,  $L_{\delta u} = \delta_u$  the length of the magnetic line of the upper working clearance,  $L_{ush}$  the length of the magnetic line of the upper magnetic shunt.

At breakaway stage of the anchor, the magnetic field strength  $H_0 \delta_0$  on the air gap  $\delta_0$  between the inner mating surfaces of the upper shunt and the top of the anchor is very small compared to the magnetic field strength on the upper shunt  $H_{ush} L_{ush}$ , therefore can be ignored. Accordingly, equation (6) can be simplified to :

$$H_{ush} L_{ush} = H_{\delta u} L_{\delta u} \quad (7)$$

The fact that  $L_{ush} > L_{\delta u}$ , result in longer length of the magnetic field line of the upper shunt . Which results in magnetic field strength in the upper shunt  $H_{ush}$  less than the magnetic field strength the upper working clearances  $H_{\delta u}$  which has shorter magnetic field line as indicated by the following equation.

$$H_{\delta u} = \frac{B_{\delta u}}{\mu_0} = \frac{\Phi_{\delta u}}{\mu_0 S_{yo}}$$

Then from equation (7), and above relationship we got:

$$H_{ush} = H_{\delta u} \frac{L_{\delta u}}{L_{ush}} = \frac{\Phi_{\delta u}}{\mu_0 S_{yo}} \times \frac{L_{\delta u}}{L_{ush}} \quad (8)$$

Considering the length of the magnetic line of the upper working clearance  $L_{\delta u} = \delta_u$  and taking  $L_{ush}$  relative to  $L_{\delta u}$  the following result can be obtained  $L_{ush}^* = \frac{L_{ush}}{L_{\delta u}}$ , and the relative magnitude of  $L_{ush}^*$  is greater than one.

Solving equation (8) for the magnetic field strength in the material of the upper magnetic shunt  $H_{ush}$ , under the condition implemented in equation (1) results in the following:

$$H_{ush} = \frac{\Phi_{\delta u}}{\mu_0 S_{yo}} \times \frac{1}{L_{ush}^*} = \frac{\Phi_{yo} - \Phi_{ush}}{\mu_0 S_{yo} L_{ush}^*}$$

$$H_{ush} = \frac{(1 - \Phi_{ush}^*) B_{yo}}{\mu_0 L_{ush}^*} \quad (9)$$

where:  $\Phi_{yo}^* = \frac{\Phi_{ush}}{\Phi_{yo}}$

$B_{yo}$  is the magnetic field density in the motor yoke

substituting equation (9) in to (5) we obtain the following expression for  $\Phi_{ush}$  :

$$\Phi_{ush} = (B_0 + \mu_k \frac{(1 - \Phi_{ush}^*) B_{yo}}{L_{ush}^*}) S_{ush} \quad (10)$$

Solving equation (10) for the flux density of the yoke  $B_{yo}$  as a function of design parameters of the upper magnetic shunt results in the following:

$$B_{yo} = B_0 \frac{S_{ush}^*}{\Phi_{ush}^* - S_{ush}^* \mu_K \frac{(1 - \Phi_{ush}^*)}{L_{ush}^*}} \quad (11)$$

where  $S_{yo}^* = \frac{S_{ush}}{S_{yo}}$

The expression for  $B_{yo}$  in (11) on the structure coincides with the ratio obtained in [19], and shows the induction value in the yoke LEMM above which the anchor will pull away from the holding area and will start moving. This induction in accordance with (11) depends on the cross-sectional area of the upper shunt  $S_{ush}$ , its average length of the magnetic line  $L_{ush}$ , the material of the shunt (coefficient  $\mu_K$ ), and early induction saturation  $B_0$ . Upper limit for the value  $S_{ush}$  is required, as any value higher than the permissible value  $S_{ush}$  will not cause saturation, which means that the anchor on the breakaway stage will not pull away from the holding area of the shunt. when the current in the coil causes saturation in the upper shunt before the yoke, then the induction in the upper shunt will be lower than the induction in the yoke LEMM, so the  $B_{yo} < B_0$  or:

$$\frac{B_{yo}}{B_0} < 1 \quad (12)$$

Then from equation (11) under the condition implemented in equation (12) the following equation results:

$$\frac{S_{ush}^*}{\Phi_{ush}^* - S_{ush}^* \mu_K \frac{(1 - \Phi_{ush}^*)}{L_{ush}^*}} < 1 \quad (13)$$

Manipulating (13) under the condition for pulling the anchor away :

$$S_{ush}^* < \frac{\Phi_{ush}^* L_{ush}^*}{L_{ush}^* + \mu_K (1 - \Phi_{ush}^*)} \quad (14)$$

Without fulfillment of (14), saturation of the upper shunt will not occur for any value of the current in the coil LEMM, and the anchor will not pull away (move). Using (14) we obtain the range of possible combinations of parameters  $S_{ush}^*$  and  $\Phi_{ush}^*$  for given values of the parameters  $L_{ush}^*$  and  $\mu_K$ . If we use steel St10 as material shunt, and according to [19]  $B_0 = 1.65T$ , and  $\mu_K = 9$ ,  $L_{ush}^* = 1.5$ , resulting in a simpler form, of equation (14) as follows:

$$S_{ush}^* < \frac{\Phi_{ush}^*}{1 + 6(1 - \Phi_{ush}^*)} \quad (15)$$

From the condition of the pulling away anchor from holding area:

$$\Phi_{ush}^* < \frac{-1 + \sqrt{\frac{2}{S_H^*} - 1}}{\frac{1}{S_H^*} - 1} \quad (16)$$

and by using (15) we define the various zones for cross-sectional area of the magnetic shunt  $S_{ush}^*$  and the value of holding area  $S_H^*$  for this case. This zone is in the form of inequality (17) as shown in Fig. 4 hatched, and the dotted line shows the boundary of the zone change of flux  $\Phi_{ush}^* = f(S_H^*)$ , constructed by (16).

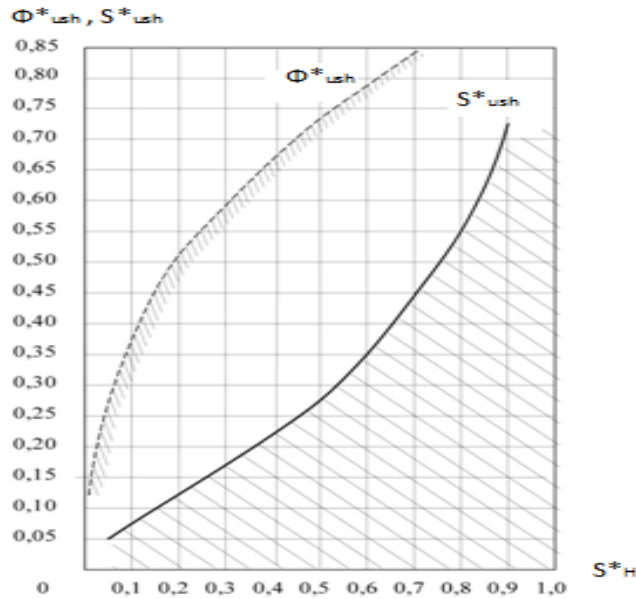


Fig. 4: change of zone cross sectional area of the magnetic shunt and its flux at the pulling away anchor moment when changing the values of holding area.

$$S^*_{ush} < \frac{1 - \sqrt{\frac{2}{S^*_H} - 1}}{1 - \frac{7}{S^*_H} + 6\sqrt{\frac{2}{S^*_H} - 1}} \quad (17)$$

At the border of the zone, when  $B_0 = B_{yo}$  the anchor will not pull away anchor from the holding device.

By using the limitations and recommendations set out above, we obtain from (11) the dependence of the relative magnetic flux in the yoke LEMM at the design parameters of the shunt  $S^*_{ush}$  and  $S^*_H$  when  $\mu_K = 9$ ,  $L^*_{ush} = 1.5$  and  $B_0 = 1.65T$  when the pulling away of anchor happens:

$$\frac{B_{yo}}{B_0} < \frac{S^*_{ush}}{\Phi^*_{ush} - 6S^*_{ush}(1 - \Phi^*_{ush})} \quad (18)$$

To do this, we express the flux  $\Phi^*_{ush}$  through the shunt design parameter  $S^*_H$  using (16) and Substituting the flux into (18) we obtain:

$$\frac{B_{yo}}{B_0} < \frac{S^*_{ush}(1 - \frac{1}{S^*_H})}{1 - (1 + 6S^*_{ush})\sqrt{\frac{2}{S^*_H} - 1} + \frac{6S^*_H}{S^*_H}} \quad (19)$$

Figures 5a and 5b show the change in the zones relative to the change in the magnetic induction in the yoke LEMM anchor at the moment of pulling away for various zones of design parameters.

In the boundaries of these zones a sharp increase in the induction of a yoke indicates invalid combination of geometrical dimensions LEMM with ferromagnetic guide housing. Also Equality  $B_0 = B_{yo}$  is unacceptable because it occurs during the saturation of the ferromagnetic yoke and the guide housing.

More over the tractive force of the pulse LEMM falls down due to the redistribution of the magnetic fluxes in the motor system.

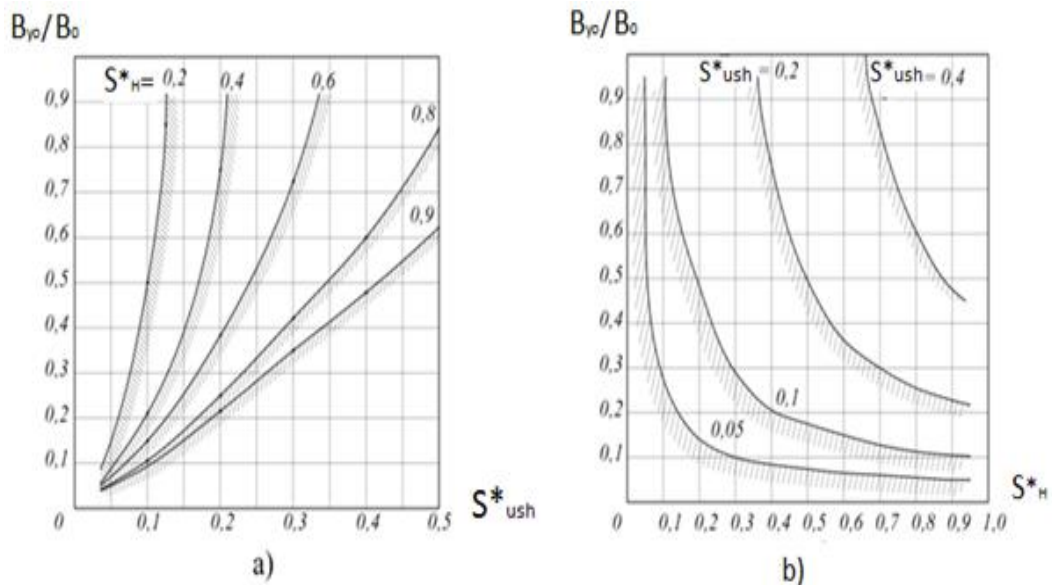


Fig. 5: Change zone of the magnetic induction in the yoke LEMM at the pulling away anchor moment while changing the design parameters  $S^*_{ush}$  and  $S^*_H$

#### IV. Conclusion

Based on a piecewise linear approximation of the magnetization curve of a ferromagnetic material of the guide housing (upper magnetic shunt), an expression is derived for its magnetic induction, with which you can set the beginning of saturation of the shunt, define moment of anchor pulling away from the holding area, the zone of permissible combinations of cross-sectional area of the upper magnetic shunt and holding area, and the zone of change in the magnetic induction in the yoke at the pulling away moment of the motor anchor. Any combination of these design parameters, beyond those zones, the integrated pulse LEMM doesn't work.

#### REFERENCES

- [1] Stumberger, G., M. T. Aydemir, D. Zarko, and T. A. Lipo, "Design of a linear bulk superconductor magnet synchronous motor for electromagnetic aircraft launch systems," *IEEE Transactions on Applied Superconductivity*, Vol. 14, No. 1, 54-62, 2004.
- [2] Kou, B. Q., X. Z. Huang, H. X. Wu, and L. Y. Li, "Thrust and thermal characteristics of electromagnetic launcher based on permanent magnet linear synchronous motors," *IEEE Transactions on Magnetics*, Vol. 45, No. 1, 358-362, 2009.
- [3] Thornton, R., M. T. Thompson, B. M. Perreault, and J. R. Fang, "Linear motor powered transportation," *Proceedings of the IEEE*, Vol. 97, No. 11, 1754-1757, 2009.
- [4] Yan L. G., "The linear motor powered transportation development and application in China," *Proceedings of the IEEE*, Vol. 97, No. 11, 1872-1880, 2009.
- [5] Katerina Hyniova, Antonin Stribrsky, Jaroslav Honcu, Ales Kruczek "Active Suspension System with Linear Electric Motor" *WSEAS TRANSACTIONS on SYSTEMS*, Vol. 8, No. 2, pp. 278-287, 2009.
- [6] Yamada, H., M. Yamaguchi, M. Karita, Y. Matsuura, and S. Fukunaga, "Acute animal experiment using a linear motor-driven total artificial heart," *IEEE Translation Journal on Magnetics in Japan*, Vol. 9, No. 6, 90-97, 1994.
- [7] Yamada, H., M. Yamaguchi, K. Kobayashi, Y. Matsuura, and H. Takano, "Development and test of a linear motor-driven total artificial heart," *IEEE Engineering in Medicine and Biology Magazine*, Vol. 14, No. 11, 84-90, 1995.
- [8] Katerina Hyniova "Experiments Taken on Energy Management in Active Suspension of Vehicles" *WSEAS TRANSACTIONS on SYSTEMS*, Vol. 11, No. 8, 426-335, 2012.
- [9] Ugarov G.G, "Principles of increasing the specific power and energy performance of pulsed electromagnetic linear motors" // *Pulse linear electric machines. Collection of scientific papers.* -Novosibirsk: Institute of Mining, Academy of Sciences of the USSR, 1991. - pp. 43-50.
- [10] N.P. Ryashentsev .G.G. Ugarov., A.B. Lvytsin "Electromagnetic press", Nauka Publishers, sibirsk branch, Novosibirsk, 1989.- 216p.
- [11] Patent RU2018652, E21C 3/16. Electric hammer. / A.F Maer, V. I Moshkin, IP Popov (Russian Federation). 4712733/03; appl. 07.03.89, publ. 30.08.1994.
- [12] Patent RU2084071, HO2K 33/02. The linear electromagnetic motor / G.G Ugarov. VY Neumann (Russian Federation). 95110459/07; appl. 22.06.1995, publ. 10.07.1997.
- [13] Usanov K. M, Moshkin V. I, Ugarov GG, "Linear electromagnetic pulse drive Autonomous power supply", Monograph. - Kurgan: Publishing House of the KSU Press, 2006. - 284 p.

- [14] M. Molis, E. Matkevičius, L. Radzevičius, "The Experimental Research of the Linear Motor" *ELECTRONICS AND ELECTRICAL ENGINEERING*, 2008. No. 7(87), pp.57- 60.
- [15] G.G Ugarov , V.IV Moshkin and A. Kh. Massad "The Influence of Holding Device Anchor Parameters On The Holding Force Magnitude, Of An Integrated Linear Electromagnetic Motor" *IJES*, Vol.3, No.4, 1-6, 2014.
- [16] V.I Moshkin and G.G Ugarov, "Estimation of parameters of the device forced accumulation of magnetic energy of a linear electromagnetic motor", *Innovative technology in teaching and production, Proceedings of the VI All-Russian scientific-practical conference Kamishyn, 15-16 December 2009 Volume 2. - Volgograd Volgograd State Technical University Publishing House, 2010. - pp 75-78.*
- [17] Moshkin V.I, Egorov A.A, and Ugarov G.G, "The study of the forced modes of magnetic energy storage in pulse linear electromagnetic motors", *Vestnik of the Saratov State Technical University, - Saratov: SSTU 2006, № 1 (10), no.1. - pp. 39-44.*
- [18] Moshkin V.I, Ugarov G.G.: "By choosing a fundamental base dimensions of linear electromagnetic motors " , *Proceedings of the Volgograd State Technical University: Interuniversity. Inter-college. Collection of scientific papers. Art. 8, number (81). - Volgograd: VSTU Publishing House, 2011. pp.108-111. - (Series processes of energy conversion and power plants. Issue 3).*
- [19] I.M. Husainov and A.Kh. Massad "The accelerated accumulation of magnetic energy in the pulse electromechanical transducer", *Problems of the electric power industry. Inter-college. scientific collection, - Saratov: SSTU 2000, pp.36-38.*

## Thermal Analysis of Clay Pot in Pot Refrigerator

Harish. H. G<sup>1</sup>, Y. T. Krishne Gowda<sup>2</sup>

<sup>1</sup>Department of mechanical engineering, Maharaja Institute of Technology, India)

<sup>2</sup>Professor, Department of mechanical engineering, Maharaja Institute of Technology, India)

**Abstract:** Cooling through evaporation is an ancient effective method of lowering temperature. The simple clay pot refrigerator is ideally suited for preserving vegetarian food and water in hot and dry climates. The refrigeration takes place by evaporation through the porous pot material. The present work includes experimental analysis of a clay pot in pot by varying height of water in the inner pot, by varying water level in the annulus of two pots and by subjecting the pot in pot refrigerator for free and forced convection. Results obtained from experimental analysis shows that Temperature T1 is highest when inner pot is filled with 5.5litres of water and lowest when it is filled with 1.5 litres of water. Temperature T1 decreases by increasing water level in the annulus of two pots and rate of cooling is lowest when pot in pot refrigerator is subjected to free convection and highest when it is subjected to forced convection.

**Keywords:** Evaporation, Free and forced convection, Porous, Refrigeration, Temperature

### I. Introduction

Cooling through evaporation is an ancient and effective method of lowering temperature. Both plants and animals use this method to lower their temperature. Trees, through the method of Eva transpiration remain cooler than their environment. [5]

The principle underlying evaporative cooling is conversion of sensible heat to latent heat. The warm and dry outdoor air is forced through porous wall or wetted pads that are replenished with water from cooler's reservoir. Due to low humidity of the incoming air some of the water gets evaporated. Some of the sensible heat of the air is transferred to water and become latent by evaporating some of water. The latent heat follows the water vapor and diffuses into the air. Evaporation causes a drop in the dry-bulb temperature and a rise in the relative humidity of the air. [1]- [7]

Evaporation cooling is dependent on the condition of the air and it is necessary to determine the weather condition that may be encountered to properly evaluate the possible effectiveness of evaporative cooler. On the other hand, the amount of water vapor that can be taken up and held by the air is not constant: it depends on two factors: the first is the temperature of the air, which determines the potential of the air to take up and hold vapor. The second involves the availability of water: if little or no water is present, the air will be unable to take up very much amount of water. [5]

In rural areas of India, vegetarian food is often preserved in a clay pot refrigerator. The cooling space is smaller clay pot inserted within a larger clay pot. The annular space between the two pots is filled with sand are occupied by water. Convective and radiative heat transfer from hot and dry surrounding evaporates this water and brings about cooling of space in the inner pot where food is kept. This slows both the respiratory process and activities of micro-organism which are destructive activity during storage of food. The mathematical model of pot in pot refrigerator using Reynolds flow model is presented by A.W. Date. [1]

An evaporative cooler is made up of a porous material that is fed with water. Hot dry air is drawn over the material. The water evaporates into the air raising the humidity and at the same time reducing the temperature of the air. [5]

The different type of evaporative cooler designs under review includes pot-in-pot, cabinet, statics, and charcoal cooling chamber. The gap between them is either filled with jute, damp cloth, or sand .Water is linked to the cooler at the top, thus keeping chamber cooled. [5]

In the literature cited above it was found that experimental analysis has not carried out by varying load in the inner pot, by varying proportion of sand and water in the annulus of two pots and also it was found that experimental analysis has not been carried out on pot in pot under forced and free convection environment.

In the present study experimental investigation is carried out by varying height of the water in the inner pot, by varying ratio of sand to water and by varying wind speed in the range of 0 to 4.4 m/s.

## II. Description Of Clay Pot In Pot Refrigerator

The clay pot refrigerator is designed with locally available material that is clay which is excavated from a nearby stream and before casting of its structure it was mixed thoroughly with water to increase its plasticity. The clay was chosen because of its low conductivity of heat and porosity. It is very cheap and abundantly available. The pots are cylindrical in shape and are made by using wheel. The top and bottom surface of pot in pot refrigerator are insulated using thermo Cole. Pot in pot refrigerator having dimension of larger pot 32cm in diameter, 31cm in height and thickness of wall 0.6cm and smaller pot having dimension 16cm in diameter, 31cm in height and thickness of wall is 0.6cm is used for the analysis. The top and bottom surface of pot in pot refrigerator are insulated using thermo Cole. The cooling space is a smaller pot inserted within a larger pot. The annular space between the two pots is filled with sand and sand particles are of the size between 300 microns to 600 microns which is sieved by using sieve shaker motorized.

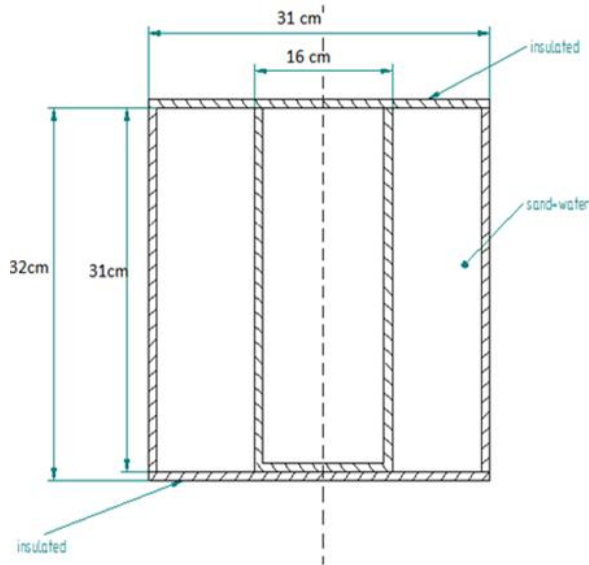


Fig 1: Schematic clay pot in pot



Fig 2: A prototyped developed clay pot in pot

## III. Experimental Setup

Fig 3 shows the experimental setup of a pot in pot refrigerator which is kept for natural convection. It consists of two pots where a smaller pot is inserted into the larger pot, thermocouples (T1, T2, T3 and T4), a 4 channel scanner, GPRS RTU, AC adaptor, and a power supply. Thermocouple T1 with a reading accuracy  $1^{\circ}\text{C}$  from 0 to  $100^{\circ}\text{C}$  and % F.S. error  $\pm 0.6\%$  F.S is used to measure the temperature at the center of the inner pot, T2 is used to measure inner wall temperature of the inner pot, T3 is used to measure temperature of sand and water that is filled between inner and outer pot and T4 is used to measure the temperature of outer wall of the outer pot. A 4 channel scanner with reading accuracy  $\pm 0.1\%$  of FS  $\pm 1$  Count scans and displays the temperature which is sensed by the thermocouple. It consists of a voltmeter which converts small voltage variation into temperature. Serial Communication with RS 485 is also provided for the scanner through which data of temperature are sent to GPRS RTU.

GPRS connected Remote Terminal Unit which has been used in the experiment monitors the analog inputs like temperature from various sensors and also does all the signal processing and digitizes the signal. The collected data using GPRS RTU are sent to the cloud through a secured protocol using GPRS technology; we can view and download sensor wise analytics and graphs on a centralized monitoring system using desktops, laptops, mobiles etc. anywhere and anytime. Experiments are conducted and data's are collected by varying the quantity of water in the inner pot and by varying the proportion of sand and water that is filled between the inner and outer pot. Dry bulb and wet bulb temperature of the atmosphere at regular intervals of time is measured by using a psychrometer having  $20^{\circ}\text{F}$  to  $120^{\circ}\text{F}$  measuring range.

Fig 4 shows the experimental setup of a pot in pot which is kept for forced convection. The experimental setup is similar to natural convection but in this case the experiment is conducted and data's are collected by varying the velocity of air which is blown by a fan kept at a distance of 1.5 meters from the pot in pot. The velocity of the wind is measured by using a digital vane type anemometer with a reading accuracy of  $\pm (2\% + 1d)$ .

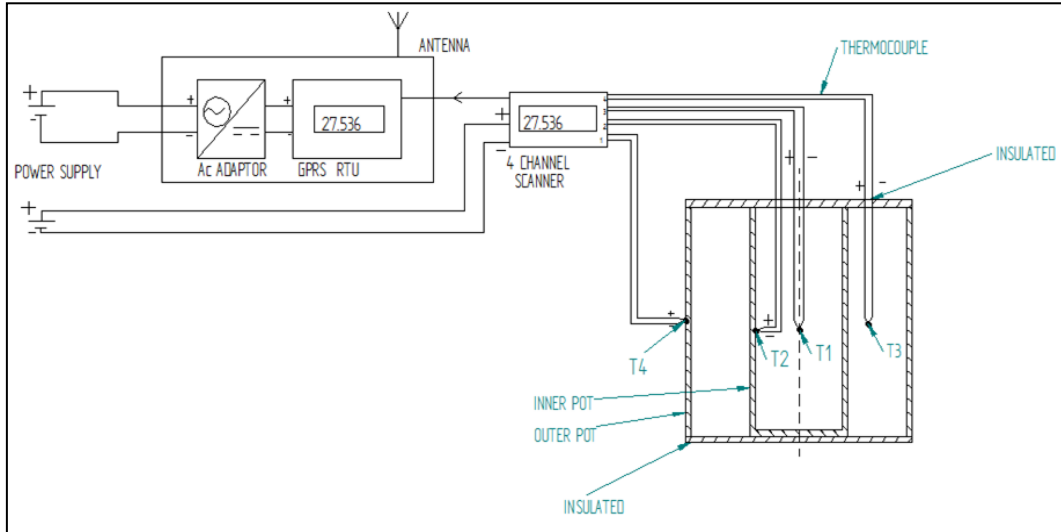


Fig 3: Experimental setup of clay pot in pot for natural convection

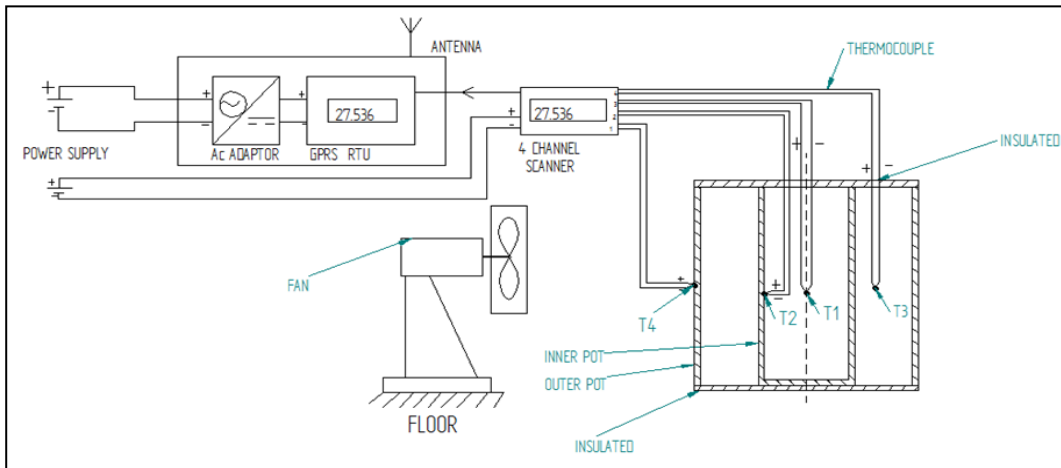


Fig 4: Experimental setup of clay pot in pot for forced convection

#### IV. Results And Discussion

By using the same pots in all cases, the size of the pores in the clay, as well as thickness of their walls are held constant.

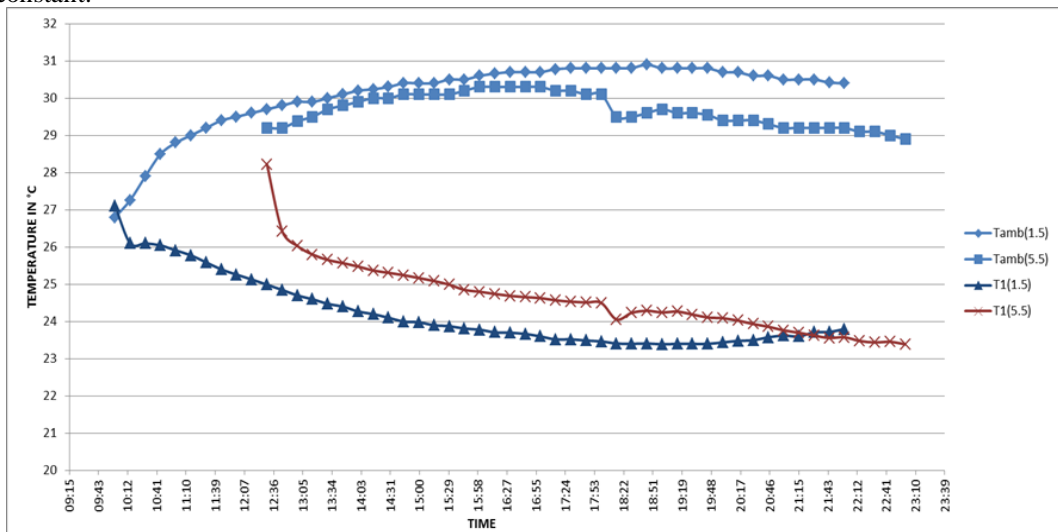


Fig 5: Variation of Temperature T1 with height

Investigation is carried out by varying height of the water in the inner pot by 1.5, 3.0, 4.5 and 5.5 liters of water. Ratio of sand to water in the annulus of the two pots is 15:2.5 and it is constant for all cases. In all cases pot in pot refrigerator is kept for natural convection. Where  $T_1$  is the temperature at the center of inner pot and  $T_{amb}$  is the ambient temperature.

FIG 5 shows the variation of temperature  $T_1$  when pot in pot refrigerator is filled with 1.5 and 5.5 liters of water. Rate of cooling is highest when the water quantity is 1.5 liters and lowest when the water quantity is 5.5liters. This is because area available for evaporation is same for both the cases but when load in the inner pot is maximum then more amount of heat has to be removed to produce maximum cooling effect. From the graph it can also be observed that plots for 1.5 and 5.5 liters coincide at the end of the experiment.

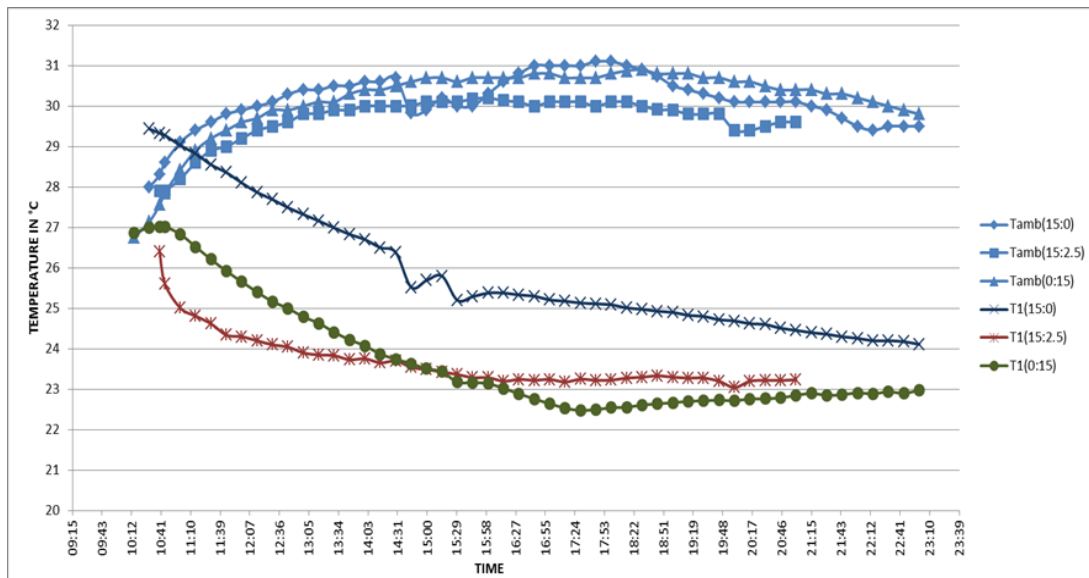


Fig 6: Variation of Temperature T1 with ratio of sand to water

Experimental analysis is carried out by varying ratio of sand to water in the annulus of the two pots by 15:0, 15:0.5, 15:1.5, 15:2.5 and 0:15. Water in the inner pot is 1.5litres and it is constant for all cases. In all cases pot in pot refrigerator is kept for natural convection.

FIG 6 shows the variation of temperature  $T_1$  when the ratio of sand to water is 15:0, 15:2.5 and 0:15. It shows that temperature  $T_1$  decreases by increasing the water level in the annulus of the two pots. Temperature  $T_1$  is higher throughout the experiment when the ratio of sand to water is 15:0 (no water in the annulus of two pots) this is because when water level in the annulus of the two pot is less, large area is not available for evaporation as a result evaporation rate is low. From the graph it can also be further observed that reduction of  $T_1$  is maximum when ratio of sand to water is 0: 15(annulus of the two pots is filled with water with no sand). At the end of the experiment it can be observed that temperature  $T_1$  increases when the ratio of sand to water is 0:15 but the temperature  $T_1$  remains constant when the ratio of sand to water is 15:2.5 this is because sand acts as a thermal insulator for the entry of heat from atmosphere into the inner pot.

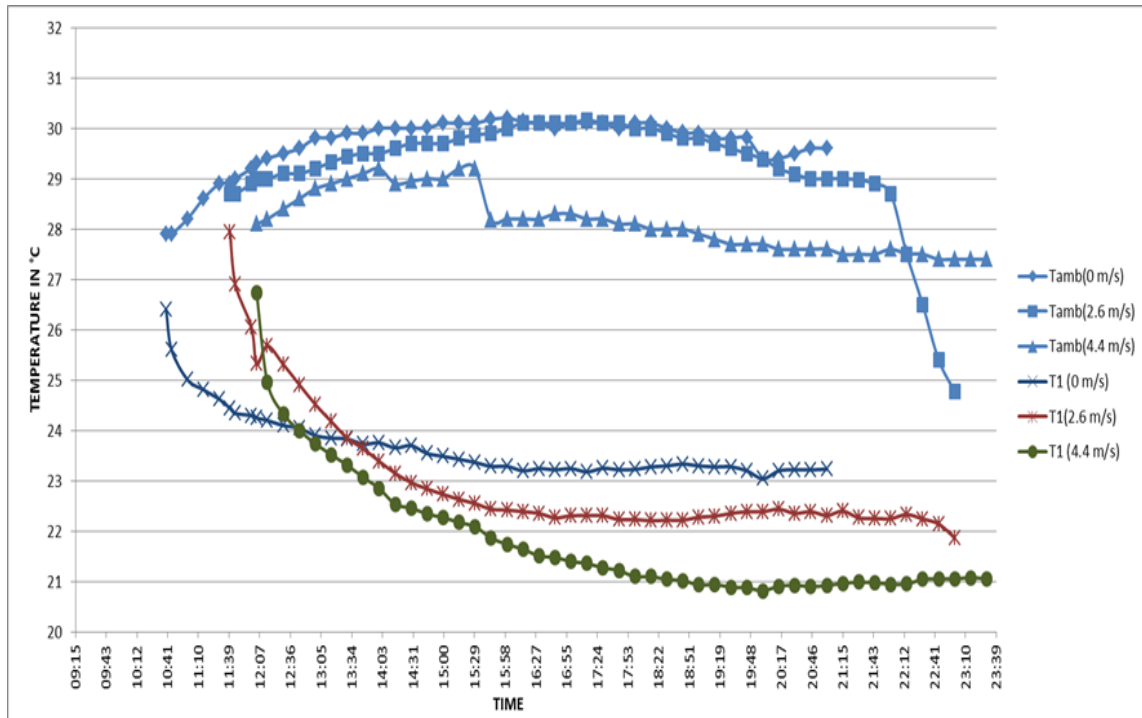


Fig 7: Variation of temperature T1 with wind speed

Experimental investigation is carried out by varying wind speed by 0, 2.6, 3.4 and 4.4 m/s. Ratio of sand to water in the annulus of the two pots and water in the inner pot is 15:2.5 and 1.5litres respectively and they are constant for all cases. Fig 7 shows the variation of T1 with the wind speed. From the graph it can be observed that rate of cooling is higher when the wind speed is 0 m/s and lower when wind speed is 4.4 m/s this is because of low rate of evaporation during natural convection and high rate of evaporation during forced convection. As a result temperature T1 is highest when wind speed is 0 m/s and lowest when wind speed is 4.4 m/s.

### V. Conclusions

Experimental analysis of a clay pot in pot is carried out by varying height of water in the inner pot, by varying water level in the annulus of two pots and by subjecting the pot in pot refrigerator for free and forced convection. The following conclusions have been drawn

- 1.) Temperature T1 is higher throughout the experiment when the ratio of sand to water is 15:0 (no water in the annulus of two pots) in a pot in pot refrigerator.
- 2.) Reduction of temperature T1 is maximum when ratio of sand to water is 0: 15(annulus of the two pots is filled with water with no sand) in a pot in pot refrigerator.
- 3.) When a pot in pot refrigerator is considered temperature T1 reduces to a minimum value when ratio of sand to water is 0:15 and increases at the end of the experiment but the temperature T1 reduces and remains constant when the ratio of sand to water is 15:2.5 indicating effect of sand which acts as insulator for the flow of heat from inner pot to atmosphere.
- 4.) Rate of cooling is highest when the water quantity is 1.5 liters and lowest when the water quantity is 5.5liters for a pot in pot refrigerator indicating the effect of load.
- 5.) Temperature T1 is highest when the wind speed is 0 m/s and lowest when wind speed is 4.4 m/s for a pot in pot refrigerator which indicated the effect of speed on rate of cooling.

**REFERENCES**

- [1] A.W.Date “Heat and Mass transfer analysis of a clay-pot refrigerator” *International Journal of Heat and Mass Transfer* 55(2012) 3977-3983
- [2] Ashutosh Mittal a ,Tarun Katariaa,1 ,Gautam K. Dasb , and Siddhartha G. Chatterjeea,2 “Evaporative Cooling of Water in a small vessel under varying Ambient Humidity” *Faculty of Paper and Engineering, SUNY college of Environmental Science and Forestry,1 Forestry Drive, Syracuse , New York 13210, U.S.A*
- [3] Victor O. Aimiuwu “Evaporative Cooling Of Water In Hot Arid Regions” *Energy conversion and Management* volume 33, No. 1. pp. 69-74, 1992
- [4] E.E. Anyanwu “Design and measured performance of a porous evaporative cooler for preservation of fruits and vegetable” *Energy Conversion and Management* 45(2004) 2187-2195
- [5] Isaac F. Odesola, Ph.D. and Onwuka Onyebuchi, B. Sc “A Review of Porous Evaporative cooling for the Preservation of Fruits and Vegetables” *A Pacific Journal of Science and Technology* volume 10, Number 2. November 2009.
- [6] Ndukwu. Macmanus Chinenye “Development of Clay Evaporative Cooler For Fruits and Vegetables Preservation” *Agriculture Engineering International: CIGR Journal. Manuscript No.1781. Vol.13, No.1, 2011*
- [7] Kamaldeen O.S\*, Anugwom Uzoma, Olymeni F.F and Awagu E.F “*International Journal of Engineering and Technology*, 2(1) (2013) 63-69

# Effects of applied voltage and flow rates of ozone generator fed by dry air and O<sub>2</sub> on the coaxial wire-cylinder reactor by varying various electrodes parameters

Hamid. H. Murbat.

Department of physics/ College of Science for Women/ University of Baghdad.

**Abstract:** Production of ozone is one of the most typical industrial and commercial applications. The ozone generator was designed according to the coaxial wire-cylinder reactor with pure oxygen gas and atmospheric air as feed gases for ozone production. The effect of the flow rate and discharge voltage on the concentration of the ozone were studied, the applied voltage was varied from (1- 9 kV) for two values of the gap space between electrodes  $D= 2$  and  $4$  mm, and two values of the electrode area  $A_e= 20$  and  $36$  cm<sup>2</sup>. It is found that the concentration of ozone increases with increasing discharge voltage and area of electrode and decrease with increasing flow gas rate and gap space.

**Keywords:** Ozone generation, Non-thermal plasma, coaxial wire-cylinder reactor, Gap space, Electrode area.

## I. Introduction

There are several types of the electrical discharges that have been used for generating nonthermal (cold) plasmas under different experimental techniques. These techniques include the corona discharges, the glow discharges, the dielectric barrier discharge (DBD), the radio frequency (RF) discharges, and the microwave (MW) discharges [1]. All these techniques able to generate localized concentrations of reactive oxygen species, including O-atom [2], O<sub>2</sub> [3], and ozone [4], these species have many technologically applications including treatment of biological media and surface modification of textiles and semiconductors [5]. Ozone production, in particular,

is one of the oldest applications of electrical discharges, dating to 19th century [6].

While dielectric barrier discharges (DBDs) have been a standard means of ozone production for commercial industry, ozone also generated by many other sources, including pulsed streamer corona discharge sources in point-plane [7,8], spiral wire-cylinder [9] and wire-cylinder [10] configurations. Recently, ozone has been generated by other cold plasma sources, including microplasma arrays [11–14] and dielectric barrier plasma jet devices [15–19].

Ozone produced by atmospheric pressure plasma is a powerful oxidizer that could destroy microorganisms effectively. Ozone concentration in nature varies between 0.01 ppm to 0.05 ppm, depending on geographic location and season. High voltage discharge ozone generators produce ozone/gas mixture, which contains 1 % to 3 % ozone when using dry air, and from 3 % to 6 % ozone when the feed gas is the high purity oxygen only is used [20]. Ozone is a strong oxidizing agent with a low environmental impact [21]. Therefore, ozone has been used in wide industrial applications such as water treatment, sterilization, bleaching, and decolorizing. The very important reasons for using ozone water treatment are it can destroy organic compounds and can kill bacteria [22,23]. Ozone is a disinfectant that does not leave the rest of the reaction in the water because the ozone will decompose back in to oxygen and also the ability of ozone to dissolve in water thirteen times more easily than oxygen. [24,25]. With more applications and increasing consumption, improvements in ozone production efficiency are required [26].

The paper studies maximization of the ozone yield in a coaxial wire-cylinder reactor by maximising the various parameters that are involved, including the applied discharge voltage, the gas flow rate, the gap spacing between electrodes and the area of the electrode.

## II. Experimental Work

The scheme of ozone generating system by using dielectric barrier discharge plasma that was designed can be seen in Figure (1). The ozone cell consists of tube made of Pyrex glass with length of 14 cm and inner diameter of 1.2cm. The cell was connected to the high voltage power

supply by two electrodes, the anode was conned through copper rode, concentrated inside the tube, and the cathode was connected by sheet of copper shielded the outside of the tube. The tube have two opened one to entry the gas and other to exit the ozone. The gas passes inside the tube through the gap between the anode and the edge of the glass tube. The high voltage Ac transformer (0 – 15 kV, f=50 Hz) was used to supply ozone chamber with high voltage. The gas flow was monitored by flow meter (Rotameter 1100 GEC-Elliott), and the ozone concentration was measured by ozone monitor (ECO Sensors OS-6 Ozone Swich). To study the effect of the geometry of the ozone chamber, two different electrode areas ( $A_e= 20, 36 \text{ cm}^2$ ) and two different gap space between electrodes ( $D=2, 4 \text{ mm}$ ) were used.

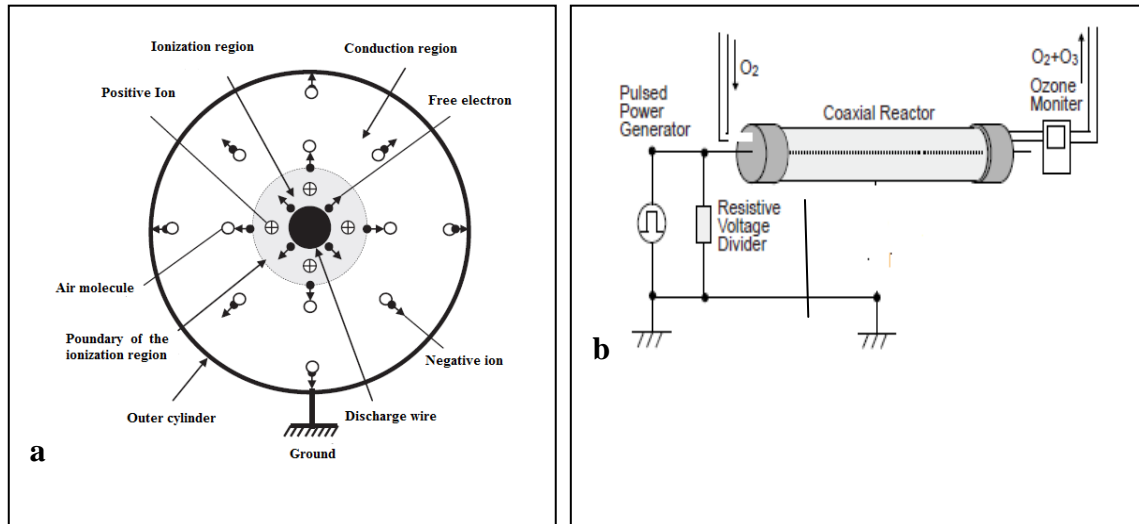


Fig.1. a) Cross section of a coaxial reactor, b) Schematic diagram the ozone production system using a coaxial reactor.

### III. Results And Discussions

This paper includes the production of ozone by using two supplied gases:

- a. Pure oxygen gas (O<sub>2</sub>).
- b. Dry air.

#### a - A pure oxygen O<sub>2</sub> as supplied gas.

##### 3.1 Effect of flow rate on ozone concentration.

To study the effect of the flow rate on the concentration of the ozone produced by an ozone generator, the concentration of ozone has been measured with the flow rate for different discharge voltage (4.5, 5, 6, 7, 8, 9) kV, for two electrodes area ( $A_e= 20, 36 \text{ cm}^2$ ), and two gap space ( $D=2, 4 \text{ mm}$ ), the results are shown in Fig. 3.

It can be shown that decrease of the concentration of the ozone with increasing of the flow rate. This is because of the residence time of the gas on the ozone chamber inversely related to the gas flow rate, with an increased residence time providing time for a reaction to occur and a correspondingly higher ozone concentration to be produce.

##### 3.2 Effect of discharge voltage on ozone concentration.

From Fig. 2 it can be shown that at a given flow rate the increasing of the ozone concentration with increasing discharge voltage, this can be interpreted as follows:

As the voltage is increased the electrical energy density increase leads to more energy being transferred to the electrons, thereby increasing the possibility of collisions with the oxygen atoms in the chamber.

##### 3.3 Effect of gap space on ozone concentration.

Fig. 3. shows that the effect of reducing gap space from (4 mm to 2 mm) is clearly from the generation of ozone, it is produced a significantly higher at any given gas flow. This is clearly related to the increased energy density as the gap space is decreased, together with increased number

of oxygen molecule/electron collisions and correspondingly increased combination of oxygen atoms with oxygen molecules.

**3.4 Effect of electrode area on ozone concentration.**

Fig. 4. Shows ozone concentration as a function of discharge voltage for two different electrode area ( A<sub>e</sub>=20, 36 cm<sup>2</sup> ). It can be shown that the production of ozone is higher for wider electrode area. This is because of the residence time of the gas on the ozone chamber proportional to the electrode area, therefore, with an increased residence time providing time for reaction to occur and correspondingly higher ozone production occur.

**b - The supplied gas is dry air.**

To compare the concentration of ozone produced by oxygen as a supplied gas and dry air, the experiment was repeated by using the dry air as supplied gas instead of pure oxygen the results were shown in Fig. 6. It is found the concentration of ozone is also increase with increasing flow rate as the situation when the pure oxygen had been used except the concentration of ozone somewhat lower in second situation, because the concentration depends on the number of the oxygen molecules. Fig. 7 shows the difference

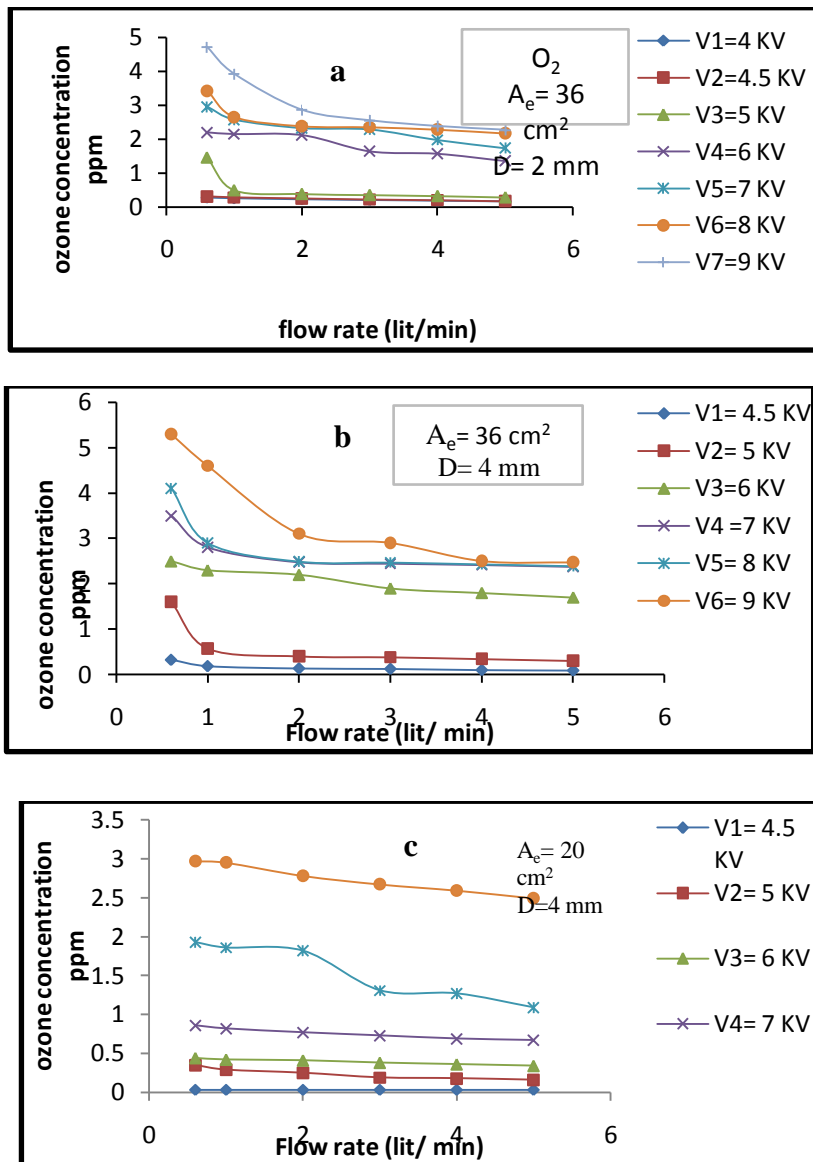


Fig. 2. The ozone concentration as a function of a gas flow rate for different discharge voltage: a) A<sub>e</sub>=36 cm<sup>2</sup>, D=4 mm, b) A<sub>e</sub>=36 cm<sup>2</sup>, D=2 mm, c) A<sub>e</sub>=20 cm<sup>2</sup>, D=4 mm.

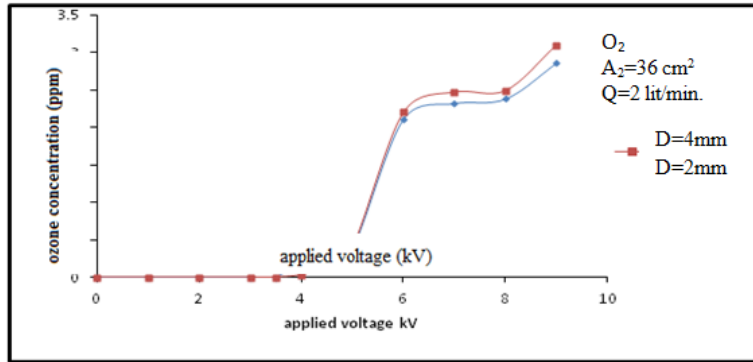


Fig.3. Ozone concentration as a function of applied voltage for two value of gap space (D=2, 4 mm) and given electrode area A<sub>e</sub>=36 cm<sup>2</sup>, and gas flow (Q=2 lit./min.).

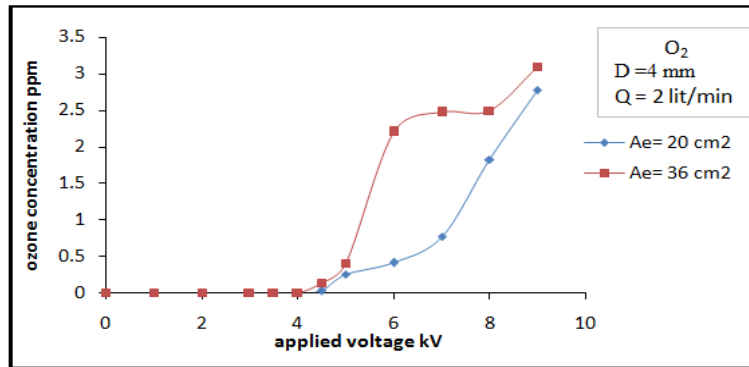


Fig. 4. Ozone concentration as a function of applied voltage for two different electrode area A<sub>e</sub>=20, 36 cm<sup>2</sup>.

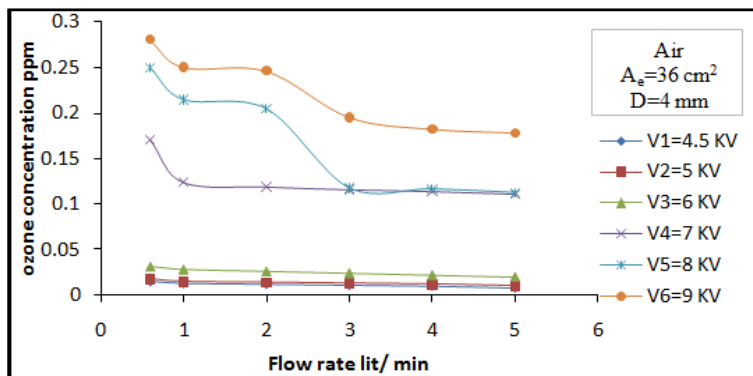


Fig. 5. Ozone concentration as a function of air flow rate for different discharge voltage and given electrode area A<sub>e</sub>=36 cm<sup>2</sup> and gap space D=4mm.

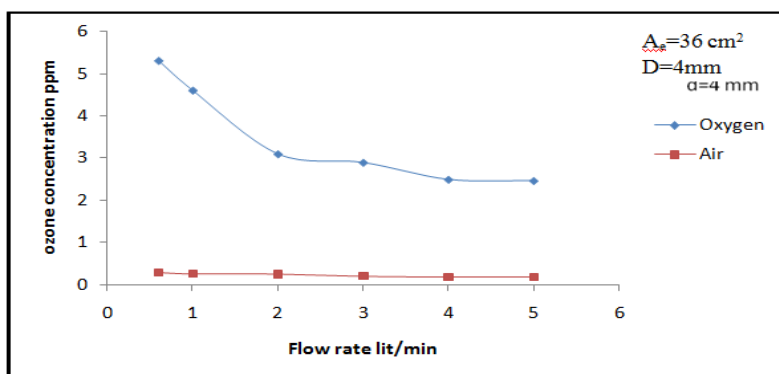


Fig. 6. Ozone concentration as a function of flow rate for Oxygen and air as a feeding gas.

#### IV. Conclusion

Production of ozone by the coaxial wire-cylinder reactor in pure Oxygen gas and air at atmospheric pressure. with two electrode area  $A_e=20, 36 \text{ cm}^2$ , and two gap space  $D=2, 4 \text{ mm}$ , different flow rates and discharge voltages has been experimentally investigated. It was found that concentration of ozone increase with discharge voltage and electrode area but decrease with and gap space.

The comparison between ozone production using oxygen gas and air as feed gas shows the concentration of ozone somewhat lower in second situation, but the difference between two values can be reduced by using low flow rate, wider electrode area and long discharge time.

These experimental results have provided information which will be useful in the decisions to be made about the commercialization of the plasma jet device for biomedical applications.

#### REFERENCES

- [1] A. Yehia, and A. Mizuno, JOURNAL OF APPLIED PHYSICS 113, 183301 (2013).
- [2] K. Niemi, V. Schulz-von der Gathen, Plasma Sources Sci. Technol. 14, 375 (2005).
- [3] J. S. Sousa, K. Niemi, L. J. Cox, Q. T. Algwari, T. Gans, and D. O'Connell, J. Appl. Phys. 109, 123302, (2011).
- [4] J. Y. Jeong, J. Park, I. Henins, S. E. Babayan, V. J. Tu, G. S. Selwyn, G. Ding, and R. F. Hicks, J. Phys. Chem. A 104, 8027 (2000).
- [5] Brian L. Sands<sup>1,a</sup> and Biswa N. Ganguly, JOURNAL OF APPLIED PHYSICS 114, 243301 (2013)
- [6] U. Kogelschatz, Plasma Chem. Plasma Process. 23, 1 (2003).
- [7] E. A. Gordeyena and A. A. Matveyev, Plasma Sources Sci. Technol. 3, 575 (1994).
- [8] R. Ono and T. Oda, J. Phys. D: Appl. Phys. 37, 730 (2004).
- [9] M. Simek and M. Clupek, J. Phys. D: Appl. Phys. 35, 1171 (2002).
- [10] W. J.M. Samaranyake, Y. Miyahara, T.Namihira, S. Katsuki, T. Sakugawa, R. Hackam, and H. Akiyama, IEEE Trans. Dielectr. Electr. 7, 254 (2000).
- [11] K. Shimizu, T. Sugiyama, and M. N. Samarantunge, IEEE Trans. Ind. Appl. 44, 506 (2008).
- [12] C. Y. Duluard, T. Dufour, J. Hubert, and F. Reniers, J. Appl. Phys. 113, 093303 (2013).
- [13] J. G. Eden, S.-J. Park, J. H. Cho, M. H. Kim, T. J. Houlahan, Jr., B. Li, E. S. Kim, T. L. Kim, S. K. Lee, and K. S. Kim et al., IEEE Trans. Plasma Sci. 41, 661 (2013).
- [14] M. H. Kim, J. H. Cho, S. B. Ban, R. Y. Choi, E. J. Kwon, S.-J. Park, and J. G. Eden, J. Phys. D: Appl. Phys. 46, 305201 (2013).
- [15] S. Reuter, J. Winter, S. Iseni, S. Peters, A. Schmidt-Bleker, M. D€unnbier, J. Sch€afer, R. Foest, and K.-D. Weltmann, Plasma Sources Sci. Technol. 21, 034015 (2012)
- [16] J. Winter, M. D€unnbier, A. Schmidt-Bleker, A. Meshchanov, S. Reuter, and K.-D. Weltmann, J. Phys. D: Appl. Phys. 45, 385201 (2012).
- [17] D. Ellerweg, J. Benedikt, A. von Keudell, N. Knake, and V. Schulz-von der Gathen, New J. Phys. 12, 013021 (2010).
- [18] D. Ellerweg, A. von Keudell, Plasma Sources Sci. Technol. 21, 034019 (2012).
- [19] S. Zhang, W. van Gaens, B. van Gessel, S. Hofmann, E. M. Veldhuizen, A. Bogaerts, and P. Bruggeman, J. Phys. D: Appl. Phys. 46, 205202 (2013).
- [20] Y. Bellebna, A. nTilmatine, Acta Electrotechnica et Informatica, Vol. 13, No. 3, 22–26, (2013).
- [21] C. Yamabe, , IEEJ Trans. FM, Vol. 126, No. 9, pp. 874-877, (2006).
- [22] Javier R., Olga G., and Fernando B. , Chemosphere, Vol. 74, Issue 6, pp. 854-859, (2009).
- [23] Tsugura H. , Watanabe T., H. Shimazaki and S. Sameshima, Water Science and Technology Vol. 37, Issue 12, pp. 285-292, (1998).
- [24] Viera M. R. , Guiamet , P. S. M. F. L. de Mele and H. A. Videla;; International Biodeterioration & Biodegradation ,Vol. 44, Issue 4, pp. 201-207, December (1999).
- [25] Clellan Mc., ENV America Incorporation, United States of America, (2003).
- [26] Y. Nakata, R. Mabuchi, Kenji Teranishi and Naoyuki Shimomura, IEEE Transactions on Dielectrics and Electrical Insulation Vol. 20, No. 4; August ( 2013).

## A Review of Routing Protocols for Wireless Sensor Network

Vikas Chaudhary<sup>1</sup>, Aasiya Khatoon<sup>2</sup>, Nalin Chaudhary<sup>3</sup>

<sup>1</sup> M.Tech (C.S) (Assistant Professor, Bhagwant University, Ajmer, India)

<sup>2</sup> M.Tech (C.S) (Scholar, Bhagwant University, Ajmer, India)

<sup>3</sup> M.Tech (C.S) (Scholar, Bhagwant University, Ajmer, India)

**Abstract-** A wireless sensor network is a collection of nodes organized into a cooperative network. Each node consists of processing capability, may contain multiple types of memory, have a RF transceiver, have a power source, and accommodate various sensors and actuators. The nodes communicate wirelessly and often self-organize after being deployed in an ad hoc fashion.

Routing protocols for wireless sensor networks are responsible for maintaining the routes in the network and have to ensure reliable multi-hop communication. The performance of the network is greatly influenced by the routing techniques. Routing is to find out the path to route the sensed data to the base station. In this paper the features of WSNs are introduced and routing protocols are reviewed for Wireless Sensor Network.

**Keywords-** Wireless Sensor Networks, Routing Protocols, Hierarchical Routing Protocols

### I. Introduction

Wireless sensor networks are quickly gaining popularity due to the fact that they are potentially low cost solutions to a variety of real-world challenges [1]. Their low cost provides a means to deploy large sensor arrays in a variety of conditions capable of performing both military and civilian tasks. Wireless Sensor Network (WSN) is intended for monitoring an environment. Wireless sensor network (WSN) is widely considered as one of the most important technologies for the twenty-first century [2]. In the past decades, it has received tremendous attention from both academia and industry all over the world. A WSN typically consists of a large number of low-cost, low-power, and multifunctional wireless sensor nodes, with sensing, wireless communications and computation capabilities [3, 4]. These sensor nodes communicate over short distance via a wireless medium and collaborate to accomplish a common task, for example, environment monitoring, military surveillance, and industrial process control [5].

The wireless sensor node is used to sense and collect data from a certain domain and transmit it to the sink where application lies. Ensuring the direct communication between a sensor and the sink may lead nodes to produce their messages with such a high power that it could result resources to be quickly consumed. Therefore, the collaboration of nodes to ensure that distant nodes communicate with the sink is a requirement. In this way, messages are generated by intermediate nodes so that a route with multiple links or hops to the sink is established.

The communication with the sink could be initially evolved without a routing protocol. Based on this statement, the flooding algorithm comes out as a solution. In this algorithm, the transmitter broadcasts the data which are consecutively retransmitted in order to make them arrive at the intended destination. However, its simplicity brings out significant drawbacks. An implosion is detected because nodes repeatedly receive multiple copies of the same data message.

One optimization relies on the gossiping algorithm [6]. Gossiping avoids implosion as the sensor transmits the message to a selected neighbor instead of informing all its neighbors as in the classical flooding algorithm. However, overlap and resource blindness are still present. Furthermore, these inconveniences are highlighted when the number of nodes in the network increases.

Due to shortcomings of the previous strategies, routing protocols become necessary in wireless sensor networks. Nevertheless, the inclusion of a routing protocol in a wireless sensor network is not a insignificant task. One of the main limitations is the identification of nodes. Since wireless sensor networks are formed by a significant number of nodes, the manual assignment of unique identifiers becomes infeasible [7].

However, this shortcoming is easily overcome in wireless sensor networks since an IP address is not required to identify the destination node of a specific packet. As a matter of fact, attribute-based addressing fits better with the explicitness of wireless sensor networks. In this case, an attribute such as node location and sensor type is used to identify the final destination. Once nodes are identified, routing protocols are in charge of

building and maintaining routes between distant nodes. The routing protocols operate in various ways which make them suitable for certain applications.

## **II. Network Characteristics And Design Objectives**

The characteristics of sensor networks and application requirements have a determine impact on the network design objectives in term of network capabilities and network performance [8].

### **2.1 Network Characteristics**

Wireless sensor networks as compared to traditional wireless networks have the following unique characteristics and constraints:

**Battery-powered sensor nodes:** Sensor nodes are usually powered by battery and are deployed in a harsh environment where it is very difficult to change or recharge the batteries.

**Unreliable sensor nodes:** Since sensor nodes are prone to physical damages or failures due to its deployment in harsh or hostile environment.

**Data redundancy:** In most sensor network application, sensor nodes are densely deployed in a region of interest and collaborate to accomplish a common sensing task. Thus, the data sensed by multiple sensor nodes typically have a certain level of correlation or redundancy.

**Self-configurable:** Sensor nodes are usually randomly deployed and autonomously configure themselves into a communication network.

**Frequent topology change:** Network topology changes frequently due to the node failures, damage, addition, energy depletion, or channel fading.

**Application specific:** A sensor network is usually designed and deployed for a specific application. The design requirements of a sensor network change with its application.

**Many-to-one traffic pattern:** In most sensor network applications, the data sensed by sensor nodes flow from multiple source sensor nodes to a particular sink, exhibiting a many-to-one traffic pattern.

### **2.2 Network Design Objectives**

Most sensor networks are application specific and have different application requirements. Thus, all or part of the following main design objectives is considered in the design of sensor networks:

- **Small node size**
- **Low power consumption**
- **Low node cost**
- **Scalability**
- **Reliability**
- **Adaptability**
- **Self-configurability**
- **Channel utilization**
- **Fault tolerance**
- **QoS support**
- **Security**

## **III. Design Constraints For Routing In Wireless Sensor Networks**

Due to the reduced computing, radio and battery resources of sensors, routing protocols in wireless sensor networks are expected to fulfill the following requirements [9]:

- **Autonomy:** The assumption of a dedicated unit that controls the radio and routing resources does not stand in wireless sensor networks as it could be an easy point of attack. Since there will not be any centralized entity to make the routing decision, the routing procedures are transferred to the network nodes.
- **Energy Efficiency:** Routing protocols should prolong network lifetime while maintaining a good grade of connectivity to allow the communication between nodes. It is important to note that the battery replacement in the sensors is infeasible since most of the sensors are randomly placed. Under some circumstances, the sensors are not even reachable. For instance, in wireless underground sensor networks, some devices are buried to make them able to sense the soil [10].
- **Scalability:** Wireless sensor networks are composed of hundred of nodes so routing protocols should work with this amount of nodes.
- **Resilience:** Sensors may unpredictably stop operating due to environmental reasons or to the battery consumption. Routing protocols should cope with this eventuality so when a current-in-use node fails, an alternative route could be discovered.

- **Device Heterogeneity:** Although most of the civil applications of wireless sensor network rely on homogenous nodes, the introduction of different kinds of sensors could report significant benefits. The use of nodes with different processors, transceivers, power units or sensing components may improve the characteristics of the network. Among other, the scalability of the network, the energy drainage or the bandwidth is potential candidates to benefit from the heterogeneity of nodes [11].
- **Mobility Adaptability:** The different applications of wireless sensor networks could demand nodes to cope with their own mobility, the mobility of the sink or the mobility of the event to sense. Routing protocols should render appropriate support for these movements.

#### IV. Classification Of Routing Protocols In Wireless Sensor Networks

As per the involvement of sensor node in the network, the routing protocols are mainly classified into three categories:

- **Data-centric or negotiation based protocol**
- **Hierarchical or cluster based protocol**
- **location-based protocol**

##### 4.1 DATA-CENTRIC OR NEGOTIATION BASED PROTOCOL

*Data-centric or negotiation based protocol* [9,12], these protocols are basically query based and depend on the desired data (name of the data), which help us to remove or eliminate the redundancy of the data. Data-centric model assures to combine the applications needed to access data (instead of individual nodes) with a natural framework for in-network processing [13]. Wireless sensor networks have many applications where due to lack of global identification along with random deployment of sensor nodes, it is hard to select a specific set of sensor nodes to be queried. This consideration differentiates data centric routing from traditional address based routing where routes are created between addressable nodes. SPIN [14] is the first data-centric protocol, which considers data negotiation between nodes in order to eliminate redundant data and save energy. Later, Directed diffusion has been developed and has become a breakthrough in data-centric routing.

S

**PIN (Sensor protocol for information exchange):** SPIN (sensor protocol for information exchange) is the first category of data centric protocol. The key feature of this routing protocol is to name the data using meta-data which describes the characteristics of data. SPIN is the 3-stage protocol since there are three messages in order to have communication between nodes.

- ADV (Advertisement): To advertise new data.
- REQ (Request): To Request for data.
- DATA: Carry the actual data.

One of the advantages of SPIN is that topological changes are localized since each node needs to know only its single-hop neighbors. SPIN gives a factor of 3.5 less than flooding in terms of energy dissipation and meta-data negotiation almost halves the redundant data.

**Directed Diffusion:** Directed Diffusion is very significant finding in the data-centric routing research of sensor networks. The idea aims at diffusing data through sensor nodes by using a naming scheme for the data. Directed Diffusion avoids unnecessary operation of network layer routing in order to serve its best purpose i.e. to save energy. Directed diffusion has several key elements namely data naming, interests and gradients, data propagation, and reinforcement. A sensing task can be described by a list of attribute-value pairs. At the beginning of the directed diffusion process, the sink specifies a low data rate for incoming events. After that, the sink can reinforce one particular sensor to send events with a higher data rate by resending the original interest message with a smaller interval. Likewise, if a neighboring sensor receives this interest message and finds that the sender's interest has a higher data rate than before, and this data rate is higher than that of any existing gradient, it will reinforce one or more of its neighbors.

##### 4.2 HIERARCHICAL PROTOCOL

*Hierarchical or cluster based protocol*, as the name suggests in this protocol, the group of some nodes in the network makes one or more clusters (depend on the size of the networks). In a cluster one node works as a cluster head. All nodes in a cluster first send the data to the cluster head; the cluster head perform some aggregation function upon this data then send to the sink or base station. Similar to other communication networks, scalability is one of the major design attributes of sensor networks. A single-tier network can cause the gateway to overload with the increase in sensors density. Such overload might cause latency in communication and inadequate tracking of events. In addition, the single-gateway architecture is not scalable for

a larger set of sensors covering a wider area of interest since the sensors are typically not capable of long-haul communication. Clustering is the best approach to increase the scalability of the system and cover a wide area without degrading the performance.

The main aim of hierarchical routing is to efficiently maintain the energy consumption of sensor nodes by involving them in multi-hop communication within a particular cluster and by performing data aggregation and fusion in order to decrease the number of transmitted messages to the sink. LEACH [15] is the first cluster based routing protocol for the sensor network.

**LEACH (Low Energy Adaptive Clustering Hierarchy):** LEACH [15, 16] is a most popular clustering-based protocol for the sensor network. The idea is to form clusters of the sensor nodes based on the received signal strength and use local cluster heads as routers to the sink. This will save energy since the transmissions will only be done by such cluster heads rather than all sensor nodes. It utilizes randomized rotation of the cluster-heads to evenly distribute the energy load among the sensor nodes in the network. All nodes in the network are homogeneous and energy-constrained. The main energy saving of LEACH protocol comes from the combination of data compression and routing.

All the data processing such as data fusion and aggregation are local to the cluster. Cluster heads change randomly over time in order to balance the energy dissipation of nodes. This decision is made by the node choosing a random number between 0 and 1. The node becomes a cluster head for the current round if the number is less than the following threshold:

$$T(n) = \begin{cases} p/(1-P^{*(r \bmod 1/P)}) & \text{if } n \text{ belongs to } G \\ 0 & \text{Otherwise} \\ 1 & \end{cases}$$

Where  $p$  is the desired percentage of cluster heads (e.g. 0.05),  $r$  is the current round, and  $G$  is the set of nodes that have not been cluster heads in the last  $1/p$  rounds.

LEACH is completely distributed and requires no global knowledge of network. It reduces energy consumption by (a) minimizing the communication cost between sensors and their cluster heads and (b) turning off non-head nodes as much as possible. LEACH uses single-hop routing where each node can transmit directly to the cluster-head and the sink. Therefore, it is not applicable to networks deployed in large regions. Furthermore, the idea of dynamic clustering brings extra overhead, e.g. head changes, advertisements etc., which may diminish the gain in energy consumption.

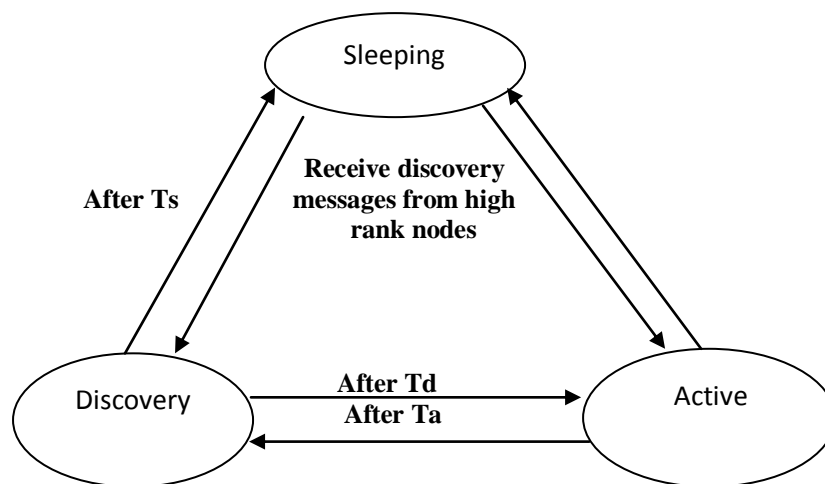
**PEGASIS (Power-Efficient Gathering in Sensor Information Systems):** PEGASIS [17] is an extension of the LEACH protocol, which forms chains from sensor nodes so that each node transmits and receives from a neighbor and only one node is selected from that chain to transmit to the base station (sink). The data is gathered and moves from node to node, aggregated and eventually sent to the base station. The chain construction is performed in a greedy way. Simulation results showed that PEGASIS is able to increase the lifetime of the network twice as much the lifetime of the network under the LEACH protocol. Such performance gain is achieved through the elimination of the overhead caused by dynamic cluster formation in LEACH and through decreasing the number of transmissions and reception by using data aggregation. PEGASIS is a chain-based power efficient protocol based on LEACH.

#### 4.3 LOCATION-BASED PROTOCOL

*location-based protocol*, these protocol utilize the position information of the desired data in the desired region than rather considering the whole network [9, 12]. Most of the routing protocols for sensor networks require location information for sensor nodes. In most cases location information is needed in order to calculate the distance between two particular nodes so that energy consumption can be estimated. Since, there is no addressing scheme for sensor networks like IP-addresses and they are spatially deployed on a region, location information can be utilized in routing data in an energy efficient way. For instance, if the region to be sensed is known, using the location of sensors, the query can be diffused only to that particular region which will eliminate the number of transmission significantly. The location-based routing protocols take into account the mobility of sensor nodes and perform very well when the density of network increases. But, the performance is very poor when the network deployment is sparse, and there is no data aggregation and further processing by the header node. In this section, we present a sample of location-aware routing protocols proposed for WSNs.

**Geographic Adaptive Fidelity (GAF):** Geographic adaptive fidelity (GAF) [18] is an energy-aware location-based routing algorithm designed primarily for mobile ad hoc networks, but may be applicable to sensor networks as well.

GAF is based on mechanism of turning off unnecessary sensors while keeping a constant level of routing fidelity (or uninterrupted connectivity between communicating sensors). In GAF, sensor field is divided into grid squares and every sensor uses its location information, which can be provided by GPS or other location systems, to associate itself with a particular grid in which it resides. This kind of association is exploited by GAF to identify the sensors that are equivalent from the perspective of packet forwarding.



As shown in Figure 1, the state transition diagram of GAF has three states, namely, discovery, active, and sleeping. When a sensor enters the sleeping state, it turns off its radio for energy savings. In the discovery state, a sensor exchanges discovery messages to learn about other sensors in the same grid. Even in the active state, a sensor periodically broadcasts its discovery message to inform equivalent sensors about its state. The time spent in each of these states can be tuned by the application depending on several factors, such as its needs and sensor mobility. GAF aims to maximize the network lifetime by reaching a state where each grid has only one active sensor based on sensor ranking rules. The ranking of sensors is based on their residual energy levels. Thus, a sensor with a higher rank will be able to handle routing within their corresponding grids.

**Geographic and Energy-Aware Routing (GEAR):** GEAR [19] is an energy-efficient routing protocol proposed for routing queries to target regions in a sensor field. In GEAR, the sensors are supposed to have localization hardware equipped, for example, a GPS unit or a localization system [20] so that they know their current positions. Furthermore, the sensors are aware of their residual energy as well as the locations and residual energy of each of their neighbors. GEAR uses energy aware heuristics that are based on geographical information to select sensors to route a packet toward its destination region. Then, GEAR uses a recursive geographic forwarding algorithm to disseminate the packet inside the target region.

## V. Conclusion

Routing emerges as a challenge in wireless sensor network as compared to traditional wireless networking. In this paper, we reviewed routing protocols in wireless sensor networks based on the various performance characteristics (like scalability, efficient use of resources, Energy saving). Overall, depending upon the network structure, routing techniques are divided into three categories. Data centric or flat routing, hierarchical or cluster routing and location based routing. All these routing techniques have common goal to increase the life of the network.

## REFERENCES

- [1]. I.F. Akyildiz, W. Su, Y. Sankarasubramaniam, and E. Cayirci. A survey on sensor networks. *IEEE Communications Magazine*, 40(8):102–114, August 2002.
- [2]. “21 ideas for the 21<sup>st</sup> century”, *Business Week*, Aug. 30 1999, pp. 78-167.
- [3]. S.K. Singh, M.P. Singh, and D.K. Singh, “A survey of Energy-Efficient Hierarchical Cluster-based Routing in Wireless Sensor Networks”, *International Journal of Advanced Networking and Application (IJANA)*, Sept.–Oct. 2010, vol. 02, issue 02, pp. 570–580.

- [4]. S.K. Singh, M.P. Singh, and D.K. Singh, "Energy-efficient Homogeneous Clustering Algorithm for Wireless Sensor Network", *International Journal of Wireless & Mobile Networks (IJWMN)*, Aug. 2010, vol. 2, no. 3, pp. 49-61.
- [5]. Jun Zheng and Abbas Jamalipour, "Wireless Sensor Networks: A Networking Perspective", a book published by A John & Sons, Inc, and IEEE, 2009.
- [6]. Zanjaj, E.; Baldi, M.; Chiaraluca, F. Efficiency of the Gossip Algorithm for Wireless Sensor Networks. In *Proceedings of the 15th International Conference on Software, Telecommunications and Computer Networks (SoftCOM)*, Split–Dubrovnik, Croatia, September, 2007.
- [7]. Zhou, H.; Mutka, M.W.; Ni, L.M. Reactive ID Assignment for Sensor Networks. In *Proceedings of the 2nd IEEE International Conference on Mobile Ad-hoc and Sensor Systems (MASS)*, Washington, DC, USA, November, 2005.
- [8]. Jun Zheng and Abbas Jamalipour, "Wireless Sensor Networks: A Networking Perspective", a book published by A John & Sons, Inc, and IEEE, 2009.
- [9]. Akkaya, K.; Younis, M. A Survey on Routing Protocols for Wireless Sensor Networks. *Ad Hoc Netw.* 2005, 3, 325–349.
- [10]. Akyildiz, I.; Pompili, D.; Melodia, T. Underwater Acoustic Sensor Networks: Research Challenges. *Ad Hoc Netw.* 2005, 3, 257–279.
- [11]. Karl, H.; Willig, A. *Protocols and Architectures for Wireless Sensor Networks*. John Wiley & Sons: Chichester, West Sussex, UK, 2005.
- [12]. Qiangfeng Jiang, D. Manivannan "Routing Protocols for Sensor Networks" in *IEEE trans.* 2004.
- [13]. P. Jiang, Y. Wen, X. Shen and A.Xue. "A Study of Routing Protocols in Wireless Sensor Networks", in *Proc. of the 6<sup>th</sup> World Congress on Intelligent Control and Automation*, vol. 1, pp. 266-270, June, 2006.
- [14]. Q. Jiang and D. Manivannan, "Routing Protocols for Sensor Networks," in *Proc. of IEEE Consumer Communications and Networking Conference (CCNC)*, pp. 93-98, January, 2004.
- [15]. W. Heinzelman, A. Chandrakasan, and H. Balakrishnan, "Energy efficient Communication Protocol for Wireless Micro Sensor Networks," in *Proc. of the 33rd Annual Hawaii International Conf. on System Sciences*, 2000, pp. 3005–3014.
- [16]. Dezheng Song "Probabilistic Modeling of Leach Protocol and Computing Sensor Energy Consumption Rate in Sensor Networks" CS Department, Texas A&M University Technical Report: TR 2005-2-2, February 22, 2005
- [17]. S. Lindsey and C.S. Raghavendra, "PEGASIS: Power-efficient Gathering in Sensor Information System", *Proceedings IEEE Aerospace Conference*, vol. 3, Big Sky, MT, Mar. 2002, pp. 1125-1130.
- [18]. Y. Xu, J. Heidemann, D. Estrin, Geography-informed energy conservation for ad hoc routing, in: *Proceedings of the 7th Annual ACM/IEEE International Conference on Mobile Computing and Networking (MobiCom01)*, Rome, Italy, July 2001.
- [19]. Y. Yu, R. Govindan, and D. Estrin, "Geographical and energy aware routing: A recursive data dissemination protocol for wireless sensor networks", *Technical Report UCLA/CSD-TR-01-0023*, UCLA Computer Science Department, May 2001.
- [20]. N. Bulusu, J. Heidemann, and D. Estrin, "GPS-less Low Cost Outdoor Localization for Very Small Devices", *IEEE Personal Communication Magazine*, vol. 7, no. 5, Oct. 2000, pp. 28-34.